Properties, distribution and radiative effect of aerosols in Ile-de-France by a coupled measurement-modelling approach

Ludovico Di Antonio

THÈSE DE DOCTORAT

UPEC
Connaissance - Action

UNIVERSITÉ
PARIS-EST CRÉTEIL
VAL DE MARNE

PARIS EST SUP

Propriétés, distribution et effet radiatif des aérosols en Ile-de-France par une approche couplée mesure-modélisation

Thèse de doctorat de l'Université Paris-Est Créteil

École doctorale n° 531, Sciences, Ingénierie et Environnement – SIE
Sciences de l'Univers et de l'Environnement

Thèse préparée dans les unités de recherche **MEREIA** et **MODÉLISATION** du
Laboratoire Interuniversitaire des Systèmes Atmosphériques
sous la direction de **Jean-François DOUSSIN,** Directeur de recherche,
la co-direction de **Gilles FORET**, Maître de conférences,
le co-encadrement de **Claudia DI BIAGIO**, Chargée de recherche,
le co-encadrement de **Matthias BEEKMANN**, Directeur de recherche,

Thèse soutenue à Créteil, le 08 Juillet 2024, par

Ludovico Di Antonio

Composition du jury :
Membres du jury avec voix délibérative :

Maria KANAKIDOU, Professeure, University of Crete, Department of Chemistry	Rapportrice
Oleg DUBOVIK, Directeur de recherche, Université de Lille, CNRS, LOA	Rapporteur
Jean-Christophe RAUT, Maître de conférences, Sorbonne Université, CNRS, LATMOS	Examinateur
Solène TURQUETY, Professeure, Sorbonne Université, CNRS, LATMOS	Examinatrice
Jean-François DOUSSIN, Directeur de recherche, CNRS, LISA	Directeur
Gilles FORET, Maître de conférences, UPEC, LISA	Co-directeur
Claudia DI BIAGIO, Chargée de recherche, CNRS, LISA	Co-encadrante
Matthias BEEKMANN, Directeur de recherche, CNRS, LISA	Co-encadrant

“Per natura amiamo e siamo onesti. E per natura vogliamo sapere di più. E continuiamo a imparare. La nostra conoscenza del mondo continua a crescere. Ci sono frontiere, dove stiamo imparando, e brucia il nostro desiderio di sapere. Sono nelle profondità più minute del tessuto dello spazio, nelle origini del cosmo, nella natura del tempo, nel fato dei buchi neri, e nel funzionamento del nostro stesso pensiero. Qui, sul bordo di quello che sappiamo, a contatto con l’oceano di quanto non sappiamo, brillano il mistero del mondo, la bellezza del mondo, e ci lasciano senza fiato.”

Carlo Rovelli

“By nature, we love and we are honest. And by nature, we want to know more. And we keep learning. Our knowledge of the world continues to grow. There are frontiers where we are learning, and our desire to know burns brightly. They are in the deepest fabric of the space, in the origins of the cosmos, in the nature of time, in the fate of black holes, and in the functioning of our own thoughts. Here, on the edge of what we know, in contact with the ocean of what we don't know, the mystery of the world shines, the beauty of the world shines, and it leaves us breathless.”

Carlo Rovelli

Acknowledgments

Before we dive into the meanders of science, let me spend some time thanking the people who contributed to the success of this PhD journey.

I would like to start by expressing my sincere gratitude to Prof. Maria Kanakidou and Dr. Dubovik for agreeing to revise the manuscript and be part of the jury. I would also like to extend my gratitude to Prof. Solène Turquety and Prof. Jean-Christophe Raut for accepting to be part of the jury as well. Thanks also to Dr. Marc Mallet, Dr. Yevgeny Derimian and Prof. Jean-Christophe Raut for agreeing to be part of the thesis committee and for the valuable discussions that have led to improvements in the quality of this PhD thesis.

I would like to spend some words to express my sincere gratitude to my team of supervisors: Claudia, Matthias, Jean-François, Gilles, Paola and Guillaume. All of you contributed in your own way to make this journey pleasant and constructive. Few people can have the rare fortune I have had in benefiting from such a rich team of supervisors, who have followed and advised me throughout this journey.
I will always be grateful to you for the time you spent with me and for your invaluable contribution to my personal and professional growth.

My sincere gratitude also goes to the LISA laboratory, which has been my second home for the entire PhD years. I would like to start thanking the Prof. Patrice Coll, LISA director, and all the administrative staff (Genevieve, Pascale, Fazia, Isabelle, Natalie…) for allowing me to integrate into the laboratory.
In particular, I would like to thank Genevieve, who helped me many times with the French bureaucracy and to whom I wish my sincerest wishes for a "calm" retirement.
Honestly, I am jealous, I wish I had your time to go hiking and mushroom picking, I admit it!

I spent almost the last four years between the MEREIA and MODÉLISATION groups of LISA and it was a great opportunity to meet wonderful people. Thanks to all the people with whom I was lucky to exchange of science and life. There are so many of you, and my sincerest thanks go to all of you.

I would like to thank the ACROSS and RI-URBANS projects for funding my thesis. In particular, I would like to thank all the people involved in the ACROSS project that I had the chance to meet and with whom I had the chance to collaborate. It was a pleasure to spend almost six dense weeks together in such a rich and fruitful environment.
I will never forget all the sunrises and sunsets at PRG, changing the filters (thanks also to the nice security guys with whom after six weeks I had made friends) and all the efforts we made together!

A very special thanks goes to all the students, PhDs and Post-docs with whom I had the pleasure of sharing time, laughs, joys and sorrows: Sergio, Francesco, François, Mathilde, Stephanie, Camilo, Lucy, Anil, Johannes, Chenjie, Diana, Farouk, Prem, Taos, Elie, Mathieu, Nicolas, Martin, Ines, Fidji, Nadia, Maxime, Giulia, Angélique… and to all those I might have unintentionally forgotten.
Many thanks to my office mates Marco, Johannes, Chris, Hichem and Tony, with whom I shared the office during almost the last four years.

Special thanks to Sergio, a true friend without whom my integration here and my level of French would never have improved. Thank you for all the days we spent together. And thank you for all the videos of Lebanon you showed me. Only a patriotic Italian from Abruzzo can stand a patriotic Lebanese, we should ask for a twinning sooner or later! Now I have no more excuses and I will visit you in Lebanon! To you, I can just wish you all the success for your life!

Thanks also to Francesco. Thank you for making me re-evaluate the north of Italy and fall in love with the “Mandorlato”. Without you vecio, I would have felt much more homesick for the Bel Paese. Thank you for all the “Camera Café” moments and laughs we shared.

I would love to thank also Annalina, Barbara and Paolo.
Without your precious advice, this journey wouldn't have been the same.

A very special thanks also to Prof. Frank Silvio Marzano, who passed away prematurely during this PhD journey. A source of inspiration for me. As he always said, “*gutta cavat lapidem*”**!**

Before finishing, I would like to thank my family.
Thank you for supporting me and helping me whenever I needed.
Without your support, I would never have gone this far.

I wish to conclude these acknowledgements by deeply thanking my beloved Alessandra.
Thank you for choosing to share not only this journey with me.
I could always count on you, no matter what.
Thank you for always being there.

INDEX

Résumé

Propriétés, distribution et effet radiatif des aérosols en Ile-de-France par une approche couplée mesure-modélisation

Les aérosols atmosphériques sont l'une des composantes clés du système climatique et sont également des acteurs majeurs de la pollution atmosphérique. L'interaction entre les aérosols et le rayonnement solaire et infrarouge (l'Effet Radiatif Direct, ERD) reste l'une des principales incertitudes dans la compréhension du système climatique à l'échelle régionale et globale. Le dernier rapport du Groupe d'experts intergouvernemental sur l'évolution du climat (GIEC) atteste que l'Interaction Aérosols-Rayonnement (IAR) représente un forçage effectif global négatif moyen de -0.22±0.25 Wm^{-2} qui s'oppose et contrebalance une fraction du forçage radiatif direct positif des gaz à effet de serre. À ce jour, l'estimation de l'intensité et du signe de l'ERD des aérosols reste très incertain, en particulier à l'échelle régionale et lorsque des aérosols d'origine et de type différents se mélangent. Ceci est particulièrement le cas pour les environnements mixtes anthropogéniques et biogéniques, tels que les flux sortants des grandes agglomérations urbaines. La façon dont les composants anthropogéniques et biogéniques interagissent et affectent les propriétés des aérosols et l'ERD est une question majeure et ouverte, pour laquelle les connaissances scientifiques sont encore faibles.

L'objectif de cette thèse est de mettre en œuvre une approche synergique de mesure et de modélisation afin d'atteindre deux objectifs principaux: i) mieux comprendre les propriétés optiques spectrales des aérosols (épaisseur optique des aérosols, albédo de diffusion simple et indice de réfraction complexe) à l'échelle régionale où se produit le mélange entre les aérosols anthropogéniques et biogéniques, et évaluer leur variabilité temporelle et spatiale dans des conditions variables ; ii) produire une estimation robuste de l'effet radiatif direct des aérosols et étudier la dépendance de l'ERD à l'état de mélange des aérosols et à la contribution des différentes espèces d'aérosols. Le cadre d'application de cette étude est l'Ile-de-France, une zone très peuplée d'Europe théâtre de l'interaction entre les émissions anthropiques de l'agglomération métropolitaine Parisienne et biogéniques des zones forestières limitrophes.

La stratégie de ce travail se base sur la combinaison des observations de la campagne internationale ACROSS (**A**tmospheric **C**hemist**R**y **O**f the **S**uburban Fore**S**t) et des observations des bases de données existantes au sol et par satellite, avec les simulations du modèle de chimie-transport 3-D WRF-CHIMERE, permettant une évaluation la plus complète possible de la masse d'aérosol simulée, de la composition chimique et des propriétés optiques spectrales, qui sont des paramètres clés pour l'estimation de l'ERD.

Mot-clé : *aérosols, interaction aérosol-rayonnement, iar, effet radiatif direct, mesure, modélisation, synergie, propriétés optiques spectrales, indice de réfraction complexe, albédo de diffusion simple, ACROSS, campagne de terrain, modèle de chimie-transport, WRF, CHIMERE*

Abstract

Properties, distribution and radiative effect of aerosols in Ile-de-France by a coupled measurement-modelling approach

Atmospheric aerosols are one of the key components of the climate system and also major contributors to air pollution. One of the most significant uncertainties in the understanding of the climate system at both regional and global scales is the interaction between aerosols and solar and infrared radiation (the Direct Radiative Effect, DRE). The latest Intergovernmental Panel on Climate Change (IPCC) report attests that the aerosol Aerosol-Radiation Interaction (ARI) represents an average negative global effective forcing of -0.22±0.25 Wm^{-2}, which opposes and counteracts a fraction of the positive direct radiative forcing by greenhouse gases. At present, there is still large uncertainty in estimating the magnitude and sign of the aerosol DRE, in particular at the regional scale, where aerosol of different origin and types mix. This is particularly the case for the mixed anthropogenic-biogenic environments, such as in the outflow of big urban agglomerations. How the anthropogenic and biogenic components interact and affect aerosol properties and DRE is an open and relevant question, for which scientific knowledge is still low.

The objective of this thesis work is to apply a synergistic measurement-modelling approach in order to achieve two main objectives: i) get more deeper understanding of the aerosol spectral optical properties (aerosol optical depth, single scattering albedo and complex refractive index) at the regional scale where the mixing between anthropogenic and biogenic aerosols occurs and evaluate their temporal and spatial variability under varying conditions; ii) produce a robust direct radiative effect estimate in the region and investigate the DRE dependency on the aerosol mixing state and the contribution of the different aerosol species.

This thesis focuses on the Ile-de-France region, a densely populated area in central Europe affected by the interaction between anthropogenic emissions from the Paris metropolitan area and biogenic emissions from surrounding forested areas. The strategy of this work is based on the combination of field campaign observations from the international ACROSS (**A**tmospheric **C**hemist**R**y **O**f the **S**uburban Fore**S**t) campaign and observations from ground-based and remote sensing existing databases with the WRF-CHIMERE 3-D chemistry transport model (CTM), allowing for a comprehensive evaluation of the simulated aerosol loading, chemical composition and spectral optical properties, which are key parameters to drive the DRE estimation.

Keywords: *aerosols, aerosol-radiation interaction, ari, direct radiative effect, measurement, modelling, synergy, spectral optical properties, complex refractive index, single scattering albedo, ACROSS, field campaign, CTM, WRF, CHIMERE*

Introduction

Scientific context and thesis motivation

The contemporary era is facing one of its most pressing challenges: the climate change. Scientific consensus, as highlighted by the Intergovernmental Panel on Climate Change (IPCC, 1995, 2001, 2013, 2022), establishes an unambiguous connection between human activities and global warming, exposing all living beings to experience significant increase in global average temperatures by the end of this century, even at very low emission scenarios. Indeed, Figure 1.1 depicts the global temperature changes for three representative generations (born in 1950, 1980 and 2020), illustrating that both the older and newer generations might be subjected to a significant temperature increase even before 2050, depending on the greenhouse gases (GHG) emission scenario.

Climate change is already impacting weather patterns and precipitation across various regions worldwide (Douville et al., 2021). In this context, atmospheric aerosols, i.e. liquid and solid particles

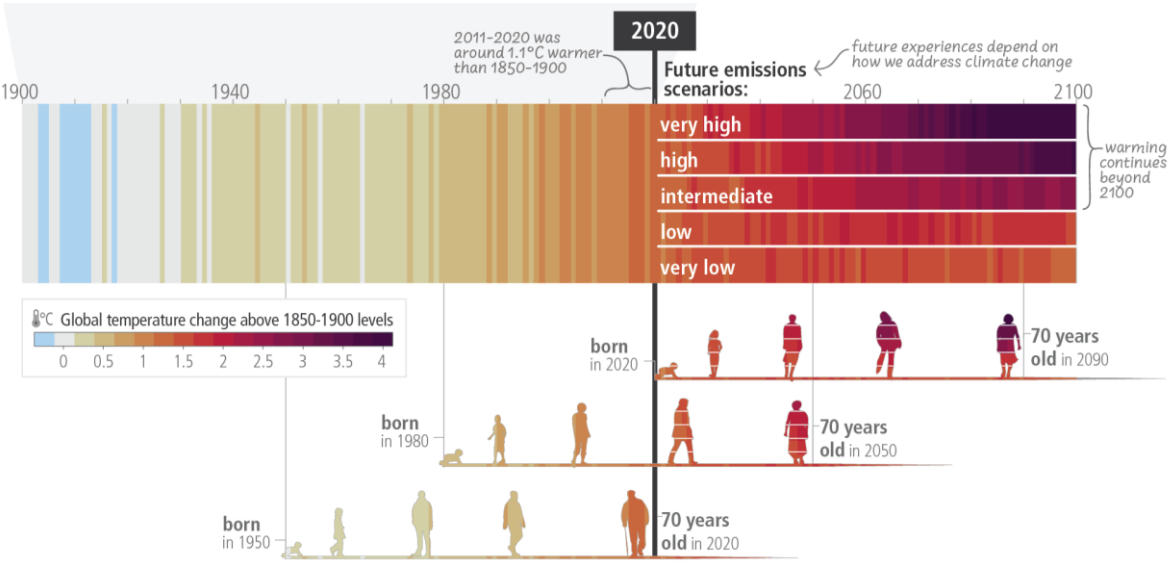

Figure 1.1: Observed (1900–2020) and projected (2021–2100) changes in global surface temperature (relative to 1850–1900). The figure illustrates the surface global temperature change (as stripes) to which three representative generations (born in 1950, 1980 and 2020) will be exposed under different greenhouse gas (GHG) emission scenarios. Simplified and adapted from IPCC (2023).

suspended in the air and emitted both by anthropogenic and natural sources, exert a major role on the Earth's energy budget and affect the climate system (IPCC, 2013). Due to their lifetime (of the order of days to weeks in the troposphere) aerosols are included within the Short-Lived Climate Forcers (SLCFs, defined by a lifetime less than two decades) together with other chemical reactive gases such as methane and ozone (Szopa et al., 2021). Aerosols directly scatter or absorb the solar radiation (the Direct Radiative Effect, DRE, from the aerosol-radiation interaction, ARI), inducing instantaneous perturbations to the radiative balance (Bellouin et al., 2020). A negative (positive) direct radiative effect at the top of the atmosphere indicates that more (less) radiation is reflected back to the space. In addition, aerosols modify the earth's radiative balance by acting on cloud micro-physics and changing the cloud distribution (ACI) (IPCC, 2022). To compensate this radiative imbalance induced by aerosols, each component of the climate system adjusts on a different temporal scale (Bellouin et al., 2020). The increasing of the aerosol loads in the second half of the last century have counterbalanced part of the global warming induced by greenhouse gases at that time, due to the cooling effect of aerosols. On the contrary, the decrease of the global aerosol burden since the last two to three decades has led to an apparent acceleration of global warming (Forster et al., 2021; IPCC, 2022).

In the recent decades, Chemistry-Transport Models (CTMs) have been extensively employed to simulate the aerosol temporal and spatial variability at the global and regional scale, to evaluate their direct radiative effect magnitude and sign (Drugé et al., 2022; Konovalov et al., 2023a; Myhre et al., 2013, 2020; Stier et al., 2013). The regional scale (of hundreds to about thousands of km) is relevant to describe the aerosol – climate interaction, since aerosol sources and lifetimes are spatially strongly heterogeneous, leading to regionally varying aerosol distributions and amplified effects. Nonetheless, reproducing the lifecycle of aerosols is highly challenging for CTM's and global models. Aspects that contribute to this difficulty include the capacity to reproduce:

- aerosol emissions and secondary sources, their transport and lifetime which determine their spatial and temporal distribution and loadings.
- The aerosol chemical composition and mixing state, the spatial and vertical spectral optical properties (such as the complex refractive index), and the size distribution, which in turn delineate the particle-radiation interaction.
- The cloud coverage, vertical distribution and optical properties, which in all-sky conditions is crucial to describe the aerosol behaviour above and below clouds.
- An accurate land surface representation, such as the surface albedo, which quantifies the reflected radiation from the surface.

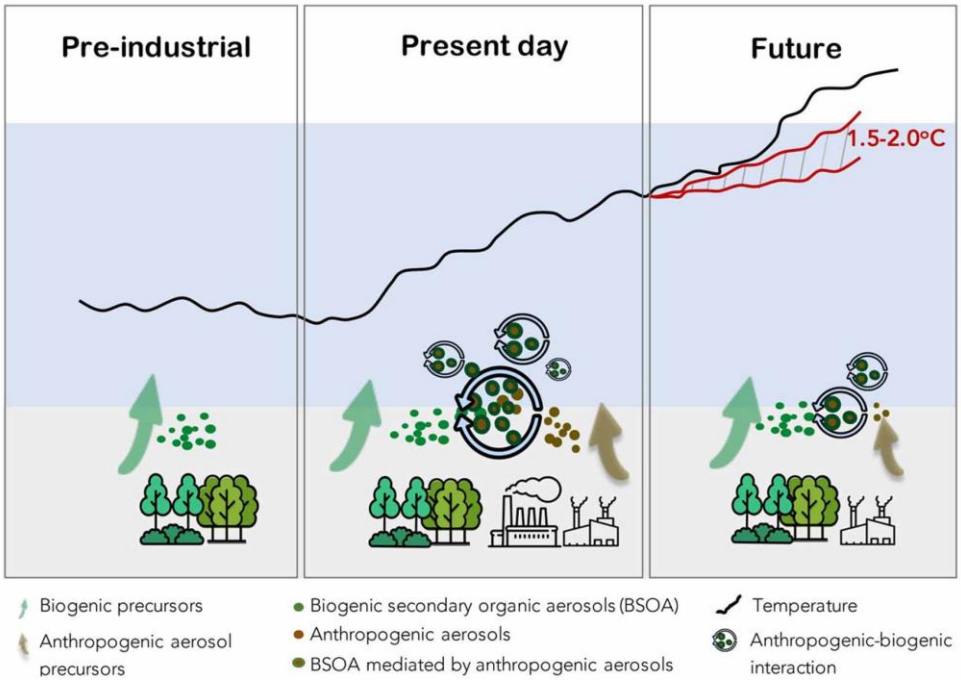

Figure 1.2: Illustration of the anthropogenic-biogenic interaction on different time scales. Compared to the pre-industrial period, a large increase in anthropogenic emissions in the present increases the formation of BSOA, which attenuates the global warming effect. However, a reduction in both anthropogenic and biogenic aerosols can result in a strong enhancement of global warming. The black line shows the temperature increase, while the red line shows the possible temperature increase under future scenarios. From Liu et al. (2021).

The specific contribution of each of the aforementioned aspects to the DRE is still matter of scientific investigation and the overall uncertainties still large (IPCC, 2023; Thorsen et al., 2021; Bellouin et al., 2020; Thorsen et al., 2020). One additional important source of the DRE uncertainty is due to the accurate representation of the anthropogenic-biogenic interaction which impacts the aerosol yields, chemical composition and spectral optical properties, and in particular the complex refractive index (He et al., 2021; Liu et al., 2016; Mao et al., 2022a; Moise et al., 2015; Zheng et al., 2023). Compared to pre-industrial times, the present day large increase of the anthropogenic emissions is indeed accompanied by a concurrent increase of biogenic aerosols which enhances the effect of anthropogenic changes (See Fig. 1.2, Liu et al., 2021).

Given the social and scientific relevance of this current topic, it is important to investigate whether it is possible to evaluate and constrain the aerosol direct radiative effect magnitude and sign and in particular over region where the mixing of anthropogenic and biogenic emissions regularly occurs. Is the DRE sensitive to the aerosol composition? Which is the specific contribution of the biogenic-anthropogenic interaction to aerosol properties and DRE? Which aerosol species contribute the most to the DRE in such mixed regions?

This thesis aims at addressing these scientific questions, taking advantage of an integrated modelling-measurement approach to better constrain the aerosol variability and uncertainties, as well as their composition and properties, in order to estimate the aerosol direct radiative effect at the regional scale of the Paris area (the Ile-de-France region) during summer 2022. According to the recent Meteo France report (Meteo France, 2022), summer 2022 has been classified as "the summer of extremes" due to strong positive temperature anomalies registered during the summer 2022 season, the strong deficit in precipitation, the long duration of the heat waves episodes and the several forest fires that occurred in Europe, leading to unusually strong aerosol loadings over France and Ile-de-France (IDF).

The Ile-de-France region has been selected since it is an area of mixing of both anthropogenic and biogenic aerosol sources. In fact, the densely populated Paris area, surrounded by the forested and rural environments, represents the ideal scenario in the European framework, to investigate the possible anthropogenic-biogenic aerosols interaction and their impact on the aerosol radiative effect on a regional scale perspective. Both types of aerosols, anthropogenic and biogenic, can be emitted and formed within the region and transported to it under conditions of continental advection.

This work benefits of two complementary resources: 1) the WRF-CHIMERE CTM onine model (Menut et al., 2021), allowing for the direct radiative effect and meteorological feedbacks estimations, and its offline version (developed in the framework of this thesis) to perform sensitivity studies to aerosol type and mixing state; 2) a comprehensive set of measurements, including aerosol physico-chemical and spectral optical properties, in particular those from the ACROSS (**A**tmospheric **C**hemist**R**y **O**f the **S**uburban fore**S**t) field campaign 2022 (Cantrell and Michoud, 2022), that took place in the Paris area in the June-July 2022 period. Part of this thesis project is committed to the data acquisition and processing of the ACROSS campaign in situ measurements, which are used to validate the model outputs and drive sensitivity modelling studies.

This thesis work, as part of the ACROSS project, can be separated in observations and modelling contributions. On the scientific point of view this thesis contributed to the scientific goals of the ACROSS project by:

- providing a deeper understanding of the Paris aerosol loading compared to other regions and cities in Europe, allowing the contextualisation of the Paris mixed anthropogenic-biogenic conditions with respect to other regions;
- providing more insights on the surface aerosol spectral optical properties variability at different sites (rural, peri-urban and rural), characteristics of the region and under the

challenging conditions of summer 2022, investigating the link with the bulk aerosol chemical composition and the different meteorological conditions observed during the campaign;

- performing high-resolution 3D numerical simulations to investigate the gas and aerosol variability at the regional and local scale, bounding the role of the BSOA and ASOA within the Paris area and evidencing the different meteorological and chemical conditions in order to support the ACROSS experimental community in the interpretation of the results;
- estimating the aerosol direct radiative effect both over France and at the regional scale of the Ile-de-France region, for a better understanding of the role of the anthropogenic-biogenic interaction on the direct radiative effect.

My specific contribution to the different activities in link with the ACROSS project and the intensive field campaign can be summarised as follows:

- contribution to the setup, deployment, operation and maintain of the instrumentation (e.g. nephelometers, aethalometer…) at the two supersites of the ACROSS campaign: Paris Rive Gauche (PRG, urban) and Rambouillet Forest (rural). In particular, I have participated to the whole campaign, acting as a focal point of the daily activities at the PRG site, ensuring correct operations of several instruments throughout most of the campaign period.
- Software development for data acquisition and processing of gas and aerosol instruments such as nephelometers, aethalometers and particle counters (OPC), at the Paris Rive Gauche urban site, and processing of aerosol observations at the Rambouillet site.
- Support in scientific and technical activities (e.g. quartz filters changes the early morning and the late afternoon at the PRG site).
- Data submission and publication on the AERIS website for the in situ measurements during the ACROSS campaign, including, but not limited to, aerosol and gas observations (see to the annex for further details on the published datasets).
- Analysis of long term data series from remote sensing observations (ground-based, satellite) to perform preliminary climatological analyses and to support model simulation validation.
- Production of daily forecast reports, as part of the forecasting cell, on meteorological and chemical conditions, aimed at assisting the scientific team, in charge of the ACROSS airborne component, in selecting the right time and flight pattern to follow the direction of the Paris plume and other scientific goals.
- Setup, run, validation and full analysis of the high resolution WRF-CHIMERE model simulations (three nested domains up to 2 km x 2km spatial resolution over the Ile-de-France region) to estimate the aerosol DRE, also used to support the ACROSS aircraft and ground-

based teams in the interpretation of the field campaign results. The model simulations served also as input to the HYSPLIT back trajectories model.

- Development of a tracer analysis aiming at supporting the ground-based and aircraft ACROSS teams in following the Paris plume evolution.

The thesis manuscript is organized as follows:

Chapter 1 illustrates a general introduction on the main characteristics of atmospheric aerosols (size distribution, chemical composition and spectral optical properties) driving the direct radiative effect. A state-of-art knowledge of the DRE variability at the global and regional scale, with a particular focus on the radiation-absorbing aerosols (e.g. black and brown carbon) and the possible source of uncertainties in the DRE estimations are outlined. The main scientific questions of this thesis manuscript are also presented.

Chapter 2 describes a general overview of the ACROSS campaign deployment, weather conditions as well as the methodology, the tools, the resources and the CTM model description and developments performed during the thesis project.

Chapter 3 presents the results of the climatological study on the aerosol optical depth from the high resolution satellite data at the European, regional and local scale. The objective is providing a deeper understanding of aerosol load and distribution in the Paris area compared to other region and cities in Europe, allowing to interpret Paris conditions and the DRE results obtained within this thesis.

Chapter 4 illustrates the aerosol spectral complex refractive index (CRI) retrieval during the ACROSS campaign from the spectral optical measurements used to validate the CRI gradients (from the rural to urban) simulated with the WRF-CHIMERE model.

Chapter 5 and Chapter 6 illustrate the results of the WRF-CHIMERE simulations performed for the ACROSS field campaign 2022. Chapter 5 is dedicated to discuss the validation of the meteorological fields (from WRF simulations), the aerosol loadings, chemical composition and optical properties (from CHIMERE simulations), with a particular focus and the different weather and chemical conditions of summer 2022.

The results of the sensitivity tests performed on the DRE, linked to the aerosol CRI and mixing state (from external to core-shell), as well as the contribution of the different species (e.g. black carbon) to DRE are discussed in Chapter 6.

Conclusions and perspectives are drawn in the last chapter of this thesis manuscript.

Chapter 1

1. Atmospheric aerosols and climate: the direct radiative effect

1.1 Sources, types and broad role of aerosols in the climate system

Aerosol particles are ubiquitous in the atmosphere, originate from a large range of sources, both natural and anthropogenic, and have a lifetime of several days in the troposphere (IPCC, 2021). Aerosols can be both "primary", as they are directly emitted in the atmosphere, or "secondary" as result of condensation processes of gas-phase species on pre-existing particles or by nucleation of new particles (Seinfeld and Pandis, 2016). Primary aerosols include inorganic species, such as mineral dust, volcanic ashes, sea sprays, inorganic material from human activities, and organic species, also called Primary Organic Aerosols (POA), like those emitted from fossil fuel combustion (due to traffic or ships), biofuels, biomass burning and biological material. Figure 1.3 depicts the main natural and anthropogenic aerosol sources. Secondary aerosols, produced both from gas-phase and aqueous in cloud reactions (Seinfeld and Pandis, 2016) consist mostly of sulphate, nitrate, and Secondary Organic Aerosols (SOA). The SOA, which represent a major fraction of total atmospheric organic aerosols (OA=POA+SOA) (Crippa et al., 2014; Kanakidou et al., 2005; Srivastava et al., 2022; Turpin and Huntzicker, 1995), are formed due to the oxidation of biogenic and anthropogenic volatile organic compounds (VOCs) by different gaseous species as ozone (O_3), and hydroxyl radicals (OH), dominating daytime chemistry and nitrate (NO_3) playing a crucial role in night-time chemistry. The SOA can be formed through a chain of processes consisting in direct emission or evaporation of semi-volatile POA emissions, their gas phase oxidation decreasing their volatility, and re-condensation (e.g., Robinson et al., 2007). The BSOA and ASOA represent the biogenic and anthropogenic-derived secondary organic aerosols respectively. Hallquist et al., (2009) estimate that the SOA fluxes (TgC/yr) are dominated by BSOA (88 TgC/yr), while a lower fraction is due to ASOA (10 TgC/yr). Among all the biogenic VOCs precursors, isoprene is the most abundant (Guenther et al., 1995), while alkanes and aromatic compounds dominate the SOA precursors (Srivastava et al., 2022; Volkamer et al., 2006; Ziemann and Atkinson, 2012). It can also be noted that there is indeed a continuum of volatilities of organic compounds which allows them to be classified according to their saturation vapour concentration (C^*): extremely-low (ELVOC, $C^*<3x10^{-4}$ μgm^{-3}), low (LVOC,

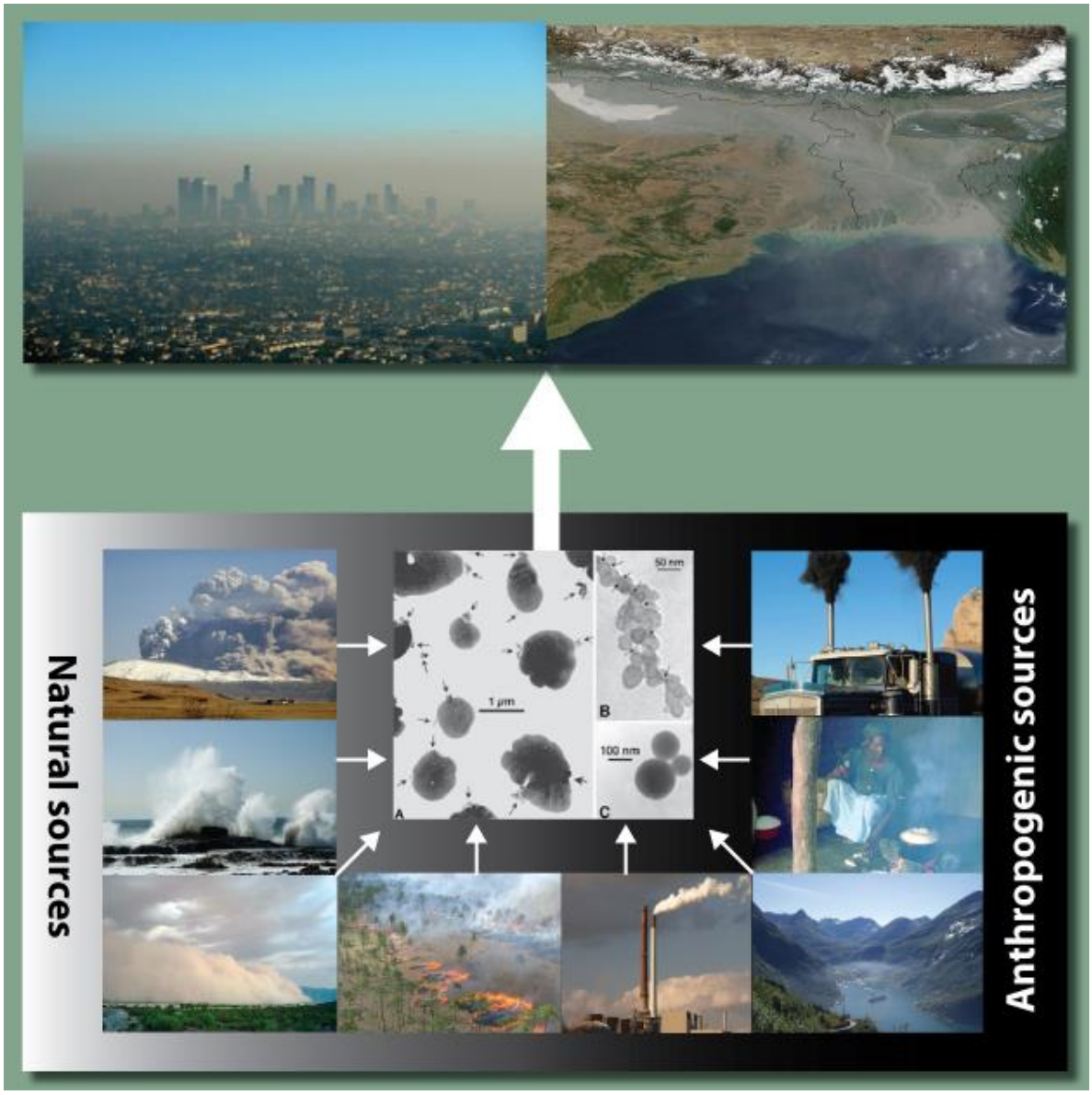

Figure 1.3: Schematic representation of the major natural and anthropogenic aerosol sources including: volcanic eruptions (e.g. ash and sulphate), sea spray (e.g. sea salt and sulphate), dust events (e.g. mineral dust), biomass burning (e.g. black carbon and organics), industrial (e.g. fossil fuel black carbon, organics, sulphate and nitrate), cooking (e.g. black carbon and organics) and transportation (e.g. sulphate, black carbon and VOCs). From Myhre et al. (2013).

$3x10^{-4}$ µgm^{-3} <C*<0.3µgm^{-3}), semi-volatile (SVOC, 0.3µgm^{-3} <C*<300 µgm^{-3}), intermediate (IVOC, 300 µgm^{-3} <C*<10^{6} µgm^{-3}) and volatile (VOC, C*>10^{6} µgm^{-3}).

Atmospheric aerosols have been demonstrated to play a key role in the climate system (Bellouin et al., 2020; Boucher et al., 2013; Fiore et al., 2012; Robotto et al., 2022; Seinfeld et al., 2016; Viana et al., 2014).

The aerosols, depending on their size distribution, mixing state, morphology, and chemical composition, directly interact with solar and terrestrial atmospheric radiation through processes of

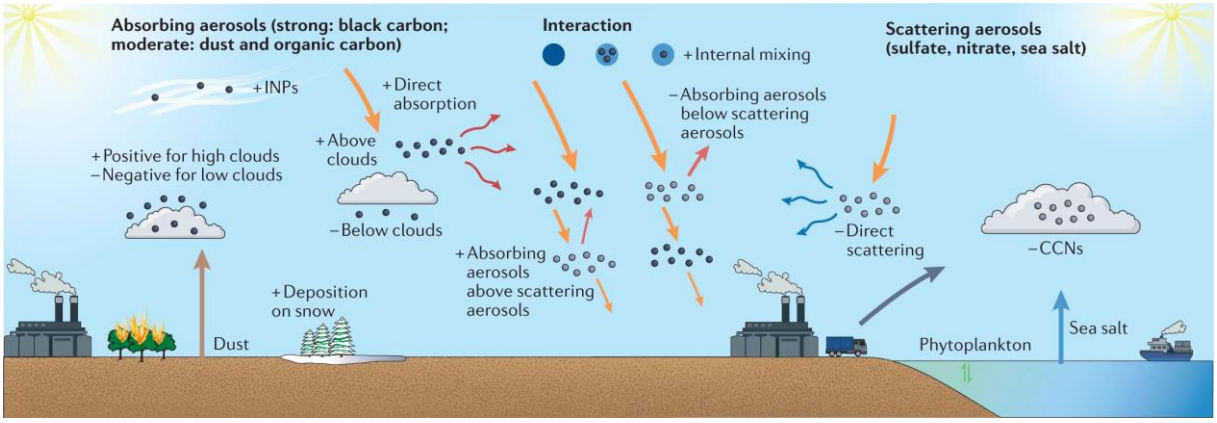

Figure 1.4: Illustration depicting the radiative effects of absorbing (dark grey dots) and scattering aerosols (light grey dots), along with their combined effects. Scattering aerosols contribute negatively (−) by reflecting sunlight and interacting with clouds, while absorbing aerosols typically exert a positive influence (+), albeit with the possibility of a negative effect through cloud interaction. The interaction between scattering and absorbing aerosols enhances their absorption, thereby reinforcing the overall positive radiative effect. From Li et al. (2022).

scattering and absorption (the *aerosol−radiation interaction effect*, ARI), which influences the Earth−atmosphere system's radiative budget. In order to assess the role of aerosols in the radiative budget, the definitions of Direct Radiative Effect (DRE) and Direct Radiative Forcing (DRF) have been introduced. The DRE (expressed in Wm^{-2}) is the change in net radiation at a specific level (surface, tropopause, top-of-atmosphere) compared to an aerosol-free atmosphere. A schematic representation of the aerosol direct radiative effect across its lifecycle is shown in Fig. 1.4 from (Li et al., 2022a). The DRE can be calculated at different temporal (instantaneous, daily, monthly, annual) and spatial (local, regional, global) scales and for different spectral ranges. The DRF (Wm^{-2}) is the change in DRE from pre-industrial to present-day (Heald et al., 2014; IPCC, 2014; Tuccella et al., 2020). The effective radiative forcing (ERF) defined by the IPCC further includes atmospheric and surface temperature adjustments due to imposed perturbations (IPCC, 2023).

Figure 1.5 from Bellouin et al. (2020) illustrates the ERF concept as a schematic representation of the temporal evolution of the atmospheric system's response due to an external perturbation. It evidences how the various components react on different time scales and that the return to radiative equilibrium manifests as changes in surface temperature.

Aerosols also affect the microphysical properties and lifetime of clouds, which in turn has an effect on precipitation patterns, contributing to the *aerosol−cloud interaction effect* (ACI) (IPCC, 2023; Bellouin et al., 2020; Boucher et al., 2013) also called the "indirect effect". Indeed, aerosol particles can behave as cloud condensation nuclei (CCN) or ice nucleation (IN) particles, affecting the cloud droplet growth and the ice crystal concentration, leading to several indirect effects (Bellouin et al.,

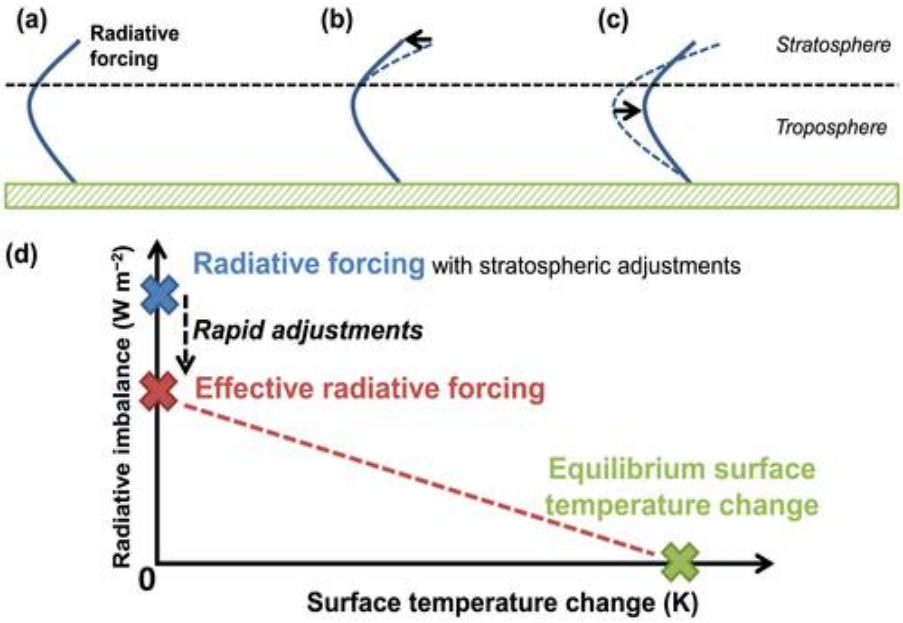

Figure 1.5: Schematic illustration on how the climate system responds differently due to instantaneous radiative forcing. From Bellouin et al. (2020).

2020; Forster et al., 2021). Another aerosol indirect effect is the *snow-albedo effect*: the snow surface reflectivity may change when more absorbing aerosols (e.g. black carbon, mineral dust) deposit on the surface, darkening it, lowering the reflectivity and increasing the snowmelt (Shi et al., 2021; Szopa et al., 2021b; Tuccella et al., 2021; Usha et al., 2022; Weihs et al., 2021). An additional indirect effect is related to the aerosol impact on the biogeochemical cycle (i.e., Mahowald, 2011). Since atmospheric particles last in the atmosphere for several days and may get transported by winds even far from the emission sources, when deposited, they represent a significant source of nutrient for the biosphere and the oceans. In fact, mineral dust and wildfires as well as anthropogenic emissions, constitute important aerosol sources of minerals such as potassium, iron, aluminium, quartz and alumina-silicates that could affect the terrestrial and ocean ecosystems (Hamilton et al., 2022; Karydis et al., 2016; Ryder et al., 2018; Zhang et al., 2023).

Besides the direct and indirect effects, another significant effect is the aerosol "semi-direct effect". It consists in the possible local increase of the temperature due to solar and infrared radiation absorption (also defined as rapid adjustment to the ARI effect), leading to changes in atmospheric stability, which can suppress atmospheric convection and alters the cloud distribution and thickness (Bender, 2020; Hansen et al., 2007; Rao and Dey, 2020).

Anthropogenic and biogenic aerosols are recognized by their direct, semi-direct and indirect effects to significantly contribute to the global and regional radiative forcing. However, due to the

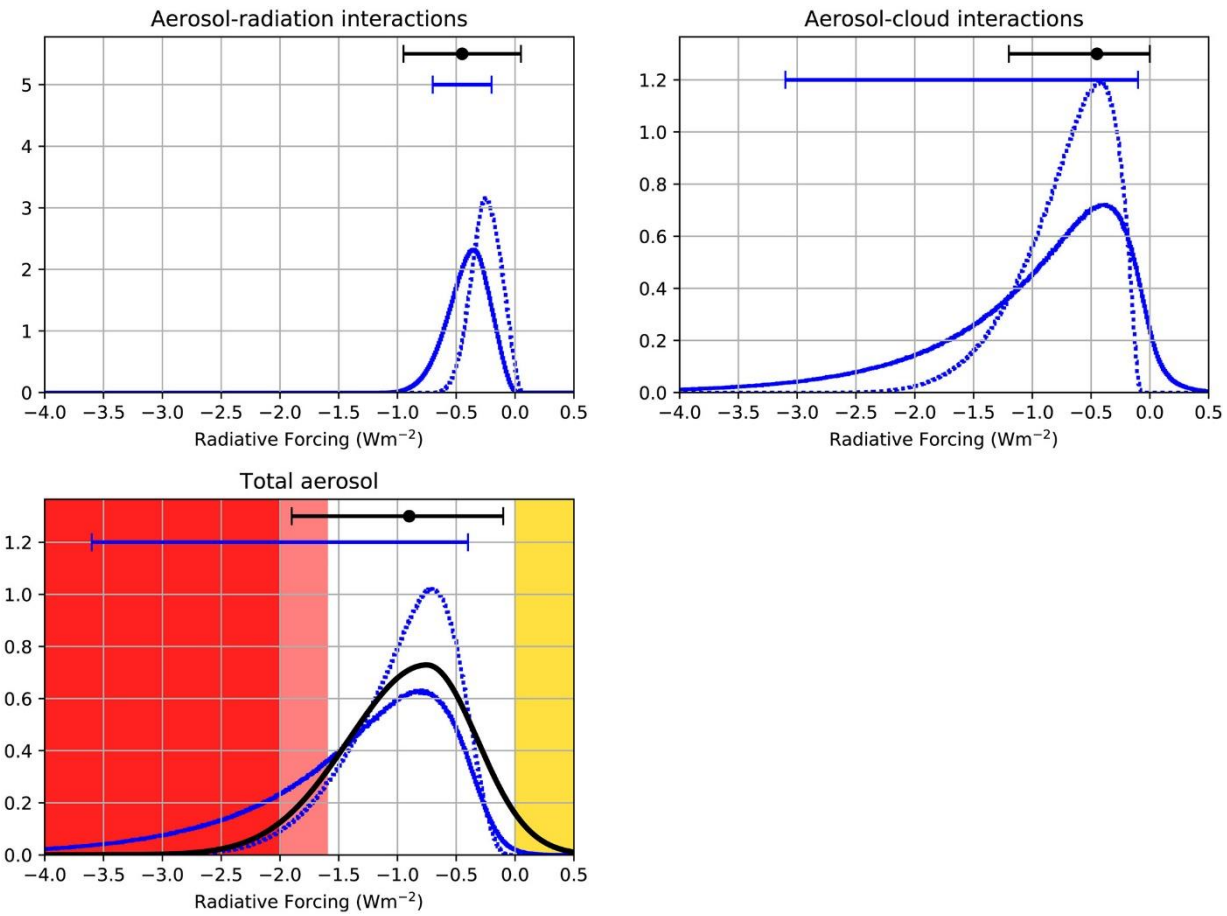

Figure 1.6: Probability distribution functions of aerosol radiative forcing (dashed lines) and effective radiative forcing (solid lines), in W m^{-2}, as derived by Bellouin et al. (2020) and by the Fifth Assessment Report of the IPCC (Myhre, Shindell, et al., 2013) (black) for the aerosol-radiation interaction (ARI) and the aerosol cloud interaction (ACI). From Bellouin et al. (2020).

complexity in characterizing their spatial and temporal variability, their chemical composition, mixing state, size and vertical distribution, determining the aerosol radiative forcing magnitude and sign remains uncertain (IPCC, 2023). Reducing uncertainty on the aerosol-radiation interaction is crucial both in reference to the DRE, to assess the role of aerosols in the climate system, and to the DRF, to understand the impact of human perturbations to the climate state and evolution.

Figure 1.6 depicts the Probability Distribution Functions (PDF) of the aerosol RF and ERF due to ARI and ACI from (Bellouin et al., 2020). The ARI's effective radiative forcing PDF shows a negative peak within the [-0.71, -0.14] Wm^{-2} confidence interval, while the total ERF (due to ACI+ARI), within the [-3.15, -0.35] Wm^{-2} confidence interval, attesting the high uncertainty that remains in the RF estimates. In comparison, the positive effective radiative forcing by GHGs is very well constrained and estimated 3.32 ±0.29 Wm^{-2} by the last IPCC report.

In the next section, we will describe the key parameters that drive the aerosol direct radiative effect as it represents a fundamental concept of this thesis manuscript (Sect. 1.2) and will extend on the discussion of aerosol DRE variability and sources of uncertainty (Section 1.3).

1.2 Aerosol properties of relevance for the direct radiative effect

1.2.1 Aerosol size distribution

In order to assess the aerosol radiative impact on climate, it is essential to model their size distribution, as the particle size is a key parameter both in the interaction with the radiation (solar and infrared) and particle activation as a cloud condensation and ice nuclei (CCN, IN). The aerosols particle diameters vary from a few nanometers up to tens of micrometers, affecting their lifetime in the atmosphere, their interaction with radiation, and their health effects, among others. The aerosols distribution within a range of diameters can be described by the number, surface and volume size distribution as:

$$n_n(D) = \frac{dN(D)}{dD} \tag{1.1}$$

$$n_s(D) = \pi D^2 \frac{dN(D)}{dD} \tag{1.2}$$

$$n_v(D) = \frac{\pi}{6} D^3 \frac{dN(D)}{dD} \tag{1.3}$$

where $n_n(D), n_s(D), n_v(D)$ represent the number, surface or volume of particles per cm^3 having a diameter between D and D+dD. The integral of the number/surface/volume size distribution (N) represents the total number/surface/volume concentration of the particles over a certain diameter range. As the particles sizes range between several orders of magnitude the size distribution is often represented in a logarithmic space as:

$$n_n(\log(D)) = \frac{dN(D)}{dlog(D)} \tag{1.4}$$

Where $n_n(\log(D))$ represents the number of particles per cm^3 having a diameter between log(D) and log(D)+dlog(D). Aerosol particles are classified according to different sizes defined as 'modes", depending mainly on their microphysical and chemical formation processes: the *nucleation mode* consists of particles in the 0.001-0.01 µm range; the *Aitken mode* in the range of 0.01-0.1 µm; the *accumulation mode* between 0.1-1 µm and the *coarse mode* between 1 and 10 µm. A comprehensive description of the aerosol distribution and the main physical and chemical processes acting on the different size ranges is depicted in Fig. 1.7. Particles in the nucleation and Aitken mode do not heavily contribute to the mass loading, while they govern the number size distribution. On the contrary, particles in the accumulation mode (which contains particles directly emitted or grown by coagulation and condensation) represent a substantial contributor to the aerosol mass. Coarse fraction particles

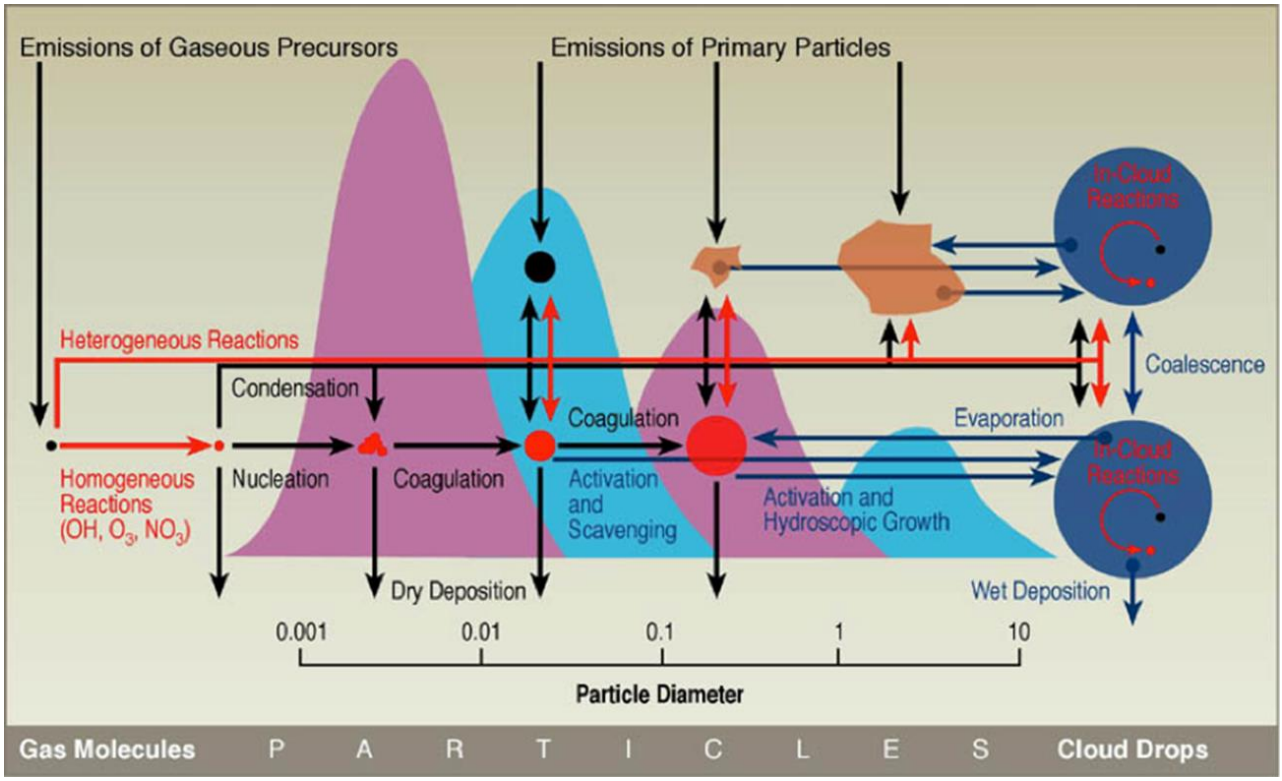

Figure 1.7: Schematic representation of the i) different aerosol modes: nucleation (0.001-0.01µm), Aitken (0.01-0.1µm), accumulation (0.1-1 µm) and coarse (1-10µm) and ii) and the different microphysical process determining the formation and growth of an aerosol particle. From Brasseur and Jacob (2017).

tend to be directly emitted in the atmosphere, especially dust and volcanic ash particles which can be lifted in upper layers of the atmosphere (from free troposphere to the Upper Troposphere - Lower Stratosphere) and then be transported over long distances. Accumulation mode particles are also of strong interest for the aerosol radiative effects as they have a comparably longer lifetime, a substantial impact on the atmosphere's radiation budget and contribute to the majority of the CCN concentration (Houghton et al., 2001). Additionally, the coarse mode particles strongly contribute to the ARI by scattering and absorbing both shortwave and longwave radiation, and ACI, by influencing cloud formation, distribution as well as precipitation patterns and biogeochemical cycles (Adebiyi et al., 2023; Di Biagio et al., 2020).

Urban and rural aerosol number size distributions are dominated by fine-mode particles with diameter less than 0.1µm, while volume and mass size distribution show two main modes in the accumulation and coarse mode (Seinfeld and Pandis, 2016). Figure 1.8 shows the volume size distribution integrated over the column from the AERONET network for the urban rural and peri-urban sites in the Ile-de-France region and averaged over the ACROSS 2022 field campaign period (from 15 june to 25 July 2022). From the column point of view, all the three sites show an accumulation and coarse

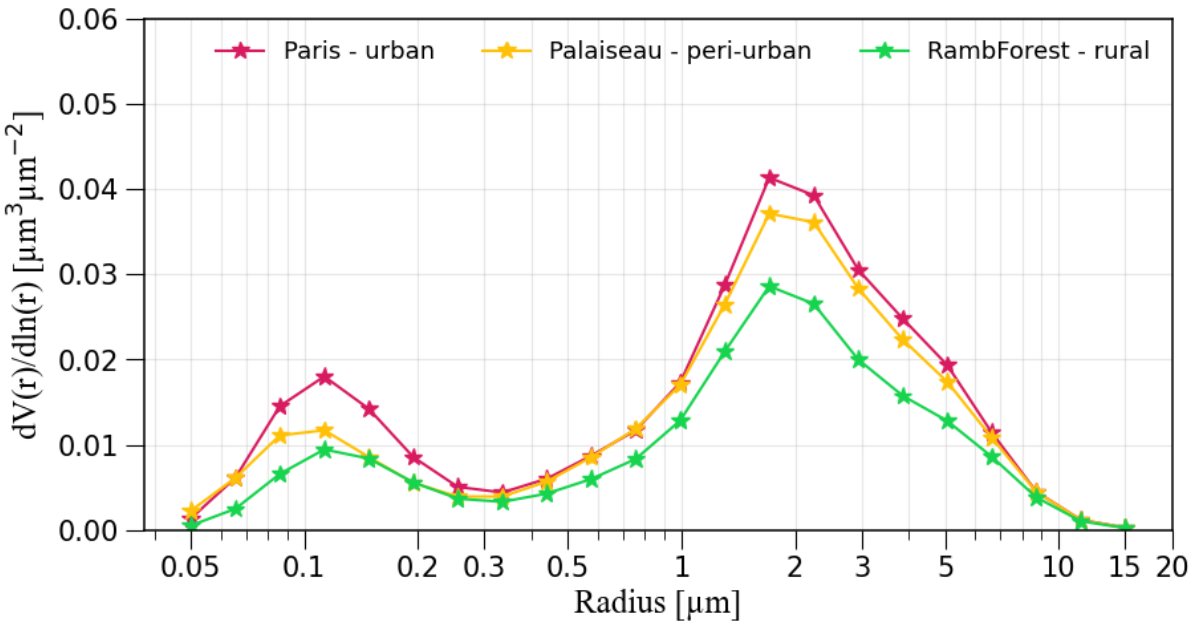

Figure 1.8: Volume size distribution for the Paris (urban), Palaiseau (peri-urban) and Rambouillet (rural) as derived from optical inversion from Level 1.5 (RambForest) and Level 2 (Paris, Palaiseau) AERONET data averaged on the ACROSS field campaign period (from 15 June to 25 july 2022).

mode during the ACROSS campaign, with stronger (lower) at the urban (rural) site. The strong coarse signal at the three sites (urban, peri-urban and rural) can be attributed to the dust outbreaks over the region during the various heatwave periods of summer 2022.

In the framework of the health regulations and the atmospheric pollution, the term "PM_x" (particulate matter having an aerodynamic diameter less than "x" µm) has been defined to evaluate the particle loadings and distinguish between three main classes: the *ultrafin*e (or $PM_{0.1}$ with aerodynamic diameter less than 0.1µm), the *fine* (or $PM_{2.5}$ with aerodynamic diameter less than 2.5 µm) and the *coarse* (or PM_{10} with aerodynamic diameter less than 10µm). Ultrafine particles contribute more on the number compared to mass aerosol distribution (Bouma et al., 2023; da Costa e Oliveira et al., 2019; WHO, 2006). Depending on their size, aerosols can penetrate more or less deeply into the respiratory tract, and for ultrafine particles, even cross the air blood barrier. Aerosol affects human health in numerous ways, through cancerogenity of chemical compounds related to soot particles to a general inflammatory action due to reactive oxygen species (ROS) (Beelen et al., 2014; Bouma et al., 2023; Dockery, 2009).

Globally, outdoor air pollution causes about 4 millions of premature deaths annually (https://www.who.int/news-room/fact-sheets/detail/ambient-(outdoor)-air-quality-and-health, last access: 08 May 2024).

1.2.2 Aerosol chemical composition

Among all the aerosol components, ammonium (NH_4^+), nitrate (NO_3^-), sulfate (SO_4^{2-}), black carbon (BC), organic aerosols (OA), inorganic minerals and sea salt represent the major contributors to the aerosol atmospheric load at the global and regional scale (Boucher et al., 2013). Ammonium, nitrate and sulfate are the major contributors to the secondary inorganic aerosol (SIA) mass, mostly found in the atmosphere in the fine mode of the size distribution (Zhang et al., 2021a). Nitrate is formed in areas with high ammonia and nitric acid (HNO_3) concentrations, the latter produced by NO_x oxidation NH_3 reacting with sulphuric acid (H_2SO_4, a product of the SO_2 oxidation) produces ammonium sulfate or ammonium bi-sulfate. Organic aerosols, both primary and secondary (POA, SOA) in turn denote the most abundant single fraction in the PM_1 and $PM_{2.5}$ mass within urban and rural environments, as shown for example for Europe in Fig.1.9 in (Chen et al., 2022b) for urban and non-urban sites and worldwide from (Zhang et al., 2007).

Another important anthropogenic aerosol species is black carbon (BC). Although it does not strongly contribute to the aerosol mass, it is present in urban areas and regions shaped by human activities and plays a key role in the climate system (Bond et al., 2013). It may exist as cluster of fractal aggregates, it is insoluble in water, refractory and it shows the highest absorption in the whole visible spectrum (Bond et al., 2013). Large sources of BC come from traffic, industrial emissions and wildfires (Bond et al., 2013). The BC, together with OA, form the so-called "*carbonaceous aerosols*".

However, BC is not the only aerosol light-absorber. A part of the organic carbon (defined as Brown carbon, BrC), absorbs the solar radiation, mainly in the near-ultraviolet part of the solar spectrum (Kirchstetter et al., 2004). The BrC can originate as primary incomplete combustion product, as well as secondary species from biogenic and anthropogenic emissions through gas and aqueous phase reactions (Betz et al., 2022; He et al., 2021; Laskin et al., 2015; Liu et al., 2016, 2015a; Moise et al., 2015; Updyke et al., 2012; Xiong et al., 2022).

Secondary brown carbon due to anthropogenic and biogenic origin can be found either within rural and urban atmosphere (Sun et al., 2021). Therefore, in environments where mixing between anthropogenic and biogenic emissions occurs, their interaction leads to the formation of secondary matter with different optical characteristics (Moise et al., 2015).

Additionally, most of the coarse fraction of the size distribution is dominated by the mineral dust and sea spray aerosols. Mineral dust particles are emitted by the natural wind erosion (e.g. from desert and arid areas) or by human activities (e.g. agricultural and industrial) and they may have irregular shape (Lindqvist et al., 2014; Luo et al., 2022). Mineral dust is also a light absorber (Baldo et al., 2023; Di Biagio et al., 2017, 2019). Mineral dust aerosols are composed of a variety of minerals such

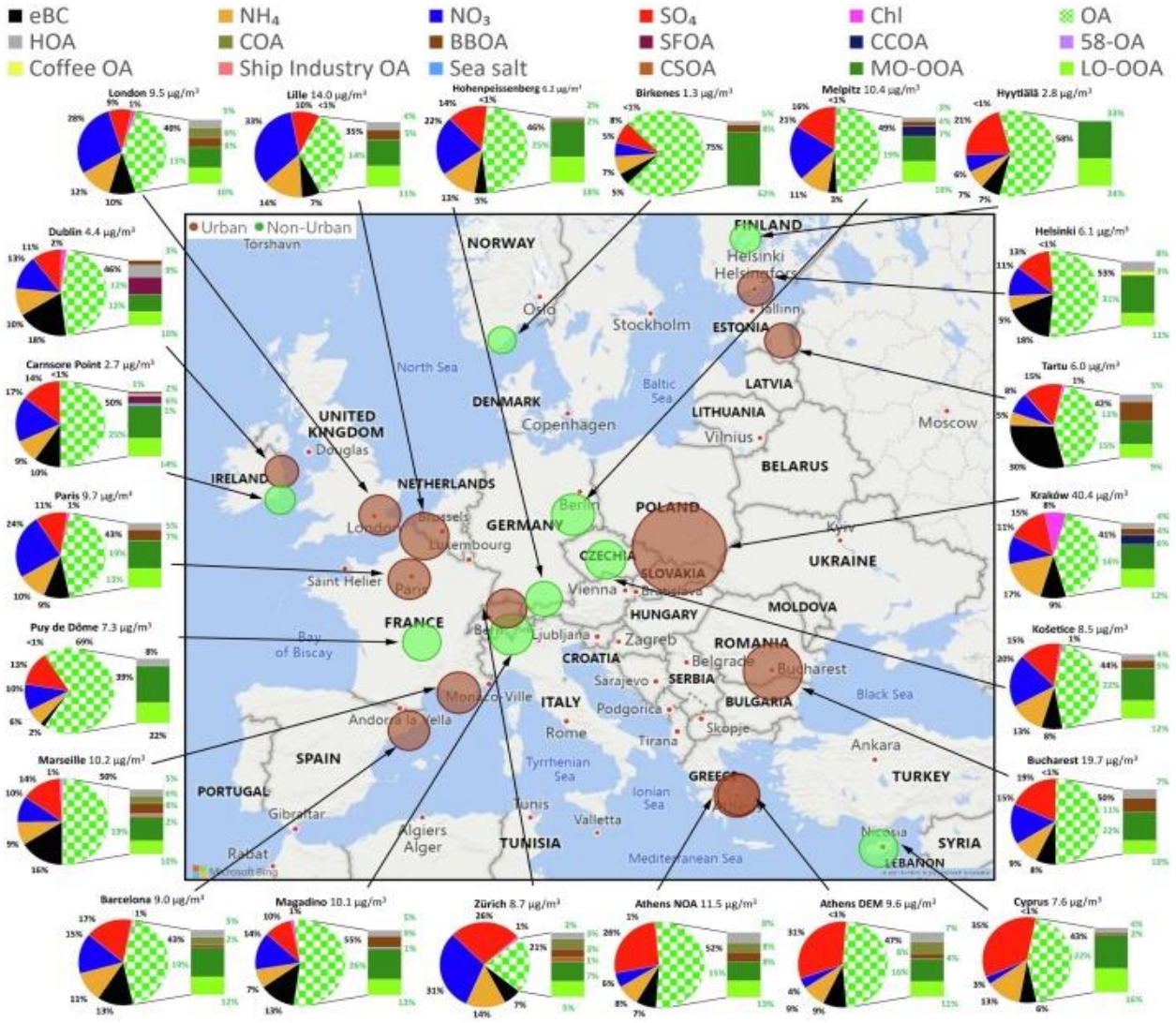

Figure 1.9: Submicron particulate matter (PM_1) mass concentration (in µg/m3) and mass fractions of non-refractory inorganic species, equivalent black carbon and organic aerosol. The size of the markers corresponds to the PM1 mass concentration. Urban and non-urban sites are represented respectively with the brown and green colours. From Chen et al. (2022).

as iron oxides, calcite, quartz and clays, impacting the spectral absorption and scattering signature (Sokolik and Toon, 1999). The dust contribution to the radiative effect is still subject of scientific debate (Di Biagio et al., 2020; Granados-Muñoz et al., 2019; Tuccella et al., 2020; Boucher et al., 2013; Kok et al., 2017). Saharan dust may strongly affect the aerosol chemical composition and loadings at urban and rural European atmospheres during outbreaks and heatwave conditions (Córdoba-Jabonero et al., 2021; Gkikas et al., 2018; Masson et al., 2010; Santese et al., 2010). Over Europe, there are around 30 dust events per year, with peaks over spring and summer (https://stories.ecmwf.int/forecasting-dust-storms/index.html, last access 8 May 2024). However, Cuevas-Agulló et al. (2024) show for the Western Euro-Mediterranean (WEM) region, an increase in

the dust frequency during the 2020-2022 winter period compared to the 2003-2019. This suggests, that mineral dust can affect air quality over the WEM, even in the months where the lowest frequency of Saharan dust transport is expected.

Ultimately, sea spray or marine aerosol particles, which significantly scatter the solar radiation, are primarily emitted by the wind erosion on water surfaces. They also represent a major player in the climate system and major source of coarse aerosols in coastal areas (Ayash et al., 2008; Claeys et al., 2017; Jiang, 2022; Sellegri and Mallet, 2022).

1.2.3 Aerosol spectral optical properties and mixing state

In this section we define the key parameters driving the aerosol-radiation interactions. If we consider an ensemble of aerosol particles inside a volume described by the number size distribution $n_n(D)$, each particle individually contributes to the light extinction (sum of absorption and scattering) through the extinction cross section $\sigma_{ext}(CRI, \chi)$ (units of m^2) or if normalized to the aerosol cross-sectional area, to the extinction efficiency $Q_{ext}(CRI, \chi)$. The factor χ is the size parameter and expressed as:

$$\chi = \pi D \lambda^{-1} \quad (1.5)$$

where D is the particle diameter and λ is the wavelength of the incident wave on the particle. χ represents a key parameter in the scattering theory, useful to discern among the different scattering regimes (Rayleigh, Mie and geometric). As a matter of fact, the interaction of aerosol with radiation is determined by the ratio between particle diameter and wavelength of radiation. Aerosol particles are often modelled as homogeneous spherical particles through the Mie theory which applies to conditions where $\chi \sim 1$ (Bohren et Huffman, 1983). Mie theory provides an analytical solution to Maxwell's equations for the scattering of electromagnetic radiation by spherical particles, which in turn allows to define the scattering efficiency $Q_{sca}(CRI, \chi)$ as:

$$Q_{sca}(CRI, \chi) = \frac{2}{\chi^2} \sum_{k=0}^{\infty} (2k+1)(|a_k|^2 + |b_k|^2) \quad (1.6)$$

where a_k and b_k are the Mie coefficient of the series. Analogous formulations can be defined both for Q_{ext} and Q_{abs}. Hence, assuming to have an ensemble of particles distributed according to $n_n(D)$, the total volumetric scattering coefficient (β_{sca}) [m^{-1}], representing the total radiation scattered due an ensemble of particles having minimum and maximum diameters (D_{min}, D_{max}), can be defined as:

$$\beta_{sca}(CRI, \lambda) = \int_{D_{min}}^{D_{max}} \sigma_{sca}(CRI, \chi) n_n(D) dD = \frac{1}{4} \int_{D_{min}}^{D_{max}} Q_{sca}(CRI, \chi) \pi D^2 n_n(D) dD \quad (1.7)$$

Analogous formulations can be defined both for the absorption (β_{abs}) and the extinction (β_{ext}) coefficients. Consequently, since $\beta_{ext} = \beta_{sca} + \beta_{abs}$, the fraction of light scattered with respect to the total extinction is defined as the single scattering albedo (SSA) as:

$$SSA = \frac{\beta_{sca}(m,\lambda)}{\beta_{ext}(m,\lambda)} \quad (1.8)$$

The SSA is a key parameter (which further depends on particle size and morphology) to represent the optical behaviour of aerosols. The SSA can vary between 0 (indicating a purely absorbing aerosol ensemble) and 1 (indicating a purely scattering aerosol ensemble). Global seasonal maps of single scattering albedo at 550 nm for the 2014-2018 period from the CERES-MODIS are available in Fig 1.10. (Devi and Satheesh, 2022) found an average value 0.93 and 0.97 at 550 nm respectively over land and ocean. Minimum values are observed within the 30°N-10°S belt during the MAM and SON seasons due to the strong wildfire activity (Ranaivombola et al., 2023). Low SSA values are observed also over high polluted regions such as China and India. On the contrary, high SSA values during all the seasons (>0.9) are observed for the European region.

Another important factor driving the DRE effect is the angular distribution of the incident light scattered by an aerosol particle. Hence, the asymmetry parameter (g) is defined as:

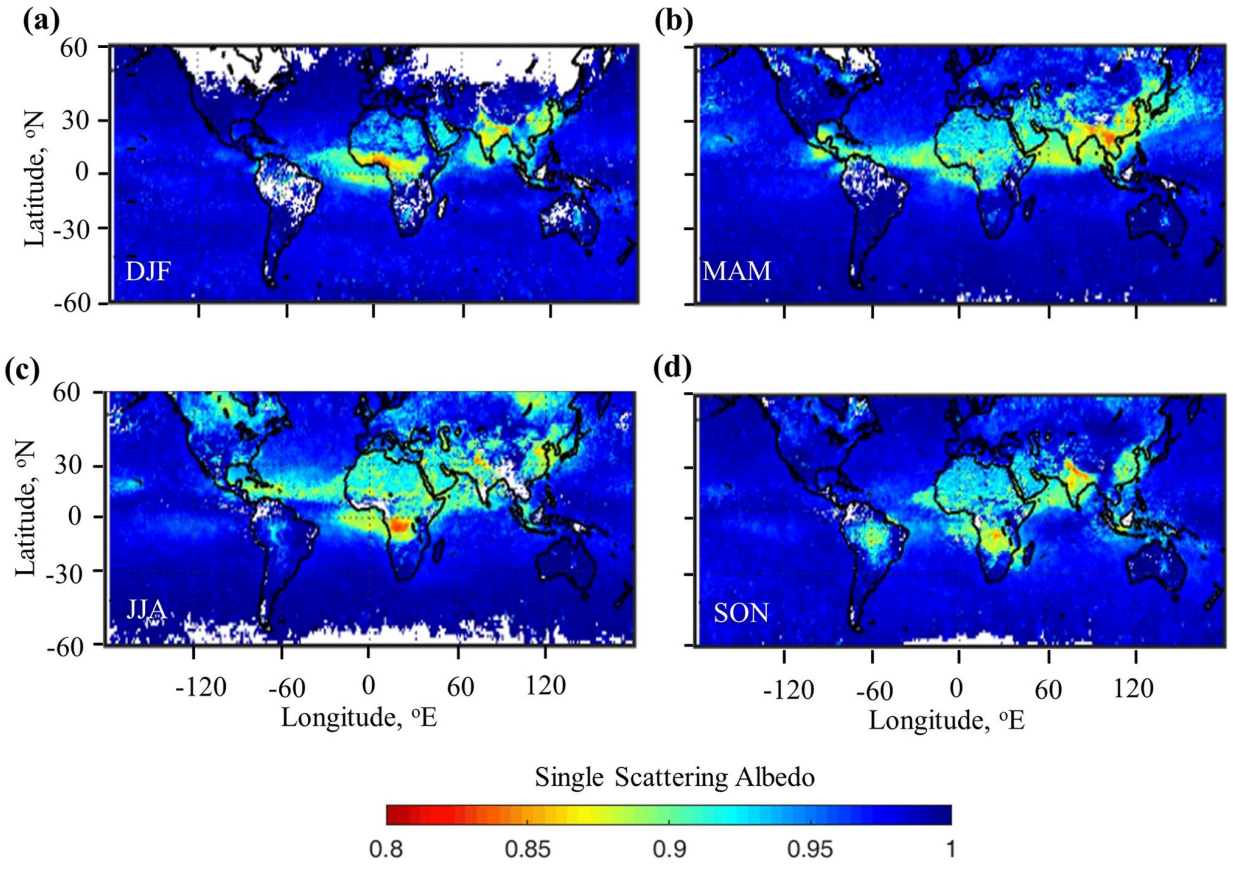

Figure 1.10: From Devi and Satheesh (2022): global seasonal maps of single scattering albedo (SSA) at 550 nm from the CERES-MODIS and averaged over the different seasons and for the 2014-2018 period. (a) December–January–February (DJF), (b) March–April–May (MAM), (c) June–July–August (JJA), and (d) September–October–November (SON).

$$g(CRI,\chi) = \frac{1}{2}\int_0^{\pi} \cos(\theta) P(\theta, CRI, \chi) \sin(\theta)\, d\theta \quad (1.9)$$

where $P(\theta, CRI, \chi)$ is the scattering phase function corresponding to the ratio between the scattering intensity from a specific angular direction θ and the integral of the scattering intensity from all the possible directions. The asymmetry parameter can vary between -1 and 1. The value -1 indicates that all the incident light is scattered in the backward direction, while the value of 1 indicates that all the incident light is scattered in the forward direction. A value of 0 indicates that the light is isotropically scattered in all directions.

Aerosol loadings at local, regional and global scale are often quantified through the aerosol optical depth (AOD), which is a unitless parameter. In fact, the AOD at a specific wavelength λ is defined as the vertical integral (between two levels z_{min} and z_{max}) of the extinction coefficient (units of m^{-1}) as:

$$AOD(CRI,\chi) = \int_{z_{min}}^{z_{max}} \beta_{ext}(z, CRI, \chi) dz \quad (1.10)$$

AOD measurements are used to analyse the spatio-temporal distribution and loadings of aerosols and improve the air quality forecasts since they can be assimilated in regional or global models (Ha et al., 2020; Kondragunta et al., 2008; Lee et al., 2022). The spectral AOD and SSA can also be used to differentiate different aerosol types (Bahadur et al., 2012; Dubovik et al., 2002; Smirnov et al., 2002; Tuccella et al., 2020). Figure 1.11 shows the annual mean climatology of AOD observed at 550 nm by several ground-based and satellite observations. AOD less than 0.2 are observed for Europe, with the highest values observed over the 0°-45N° belt, due to the strong wildfire activity, anthropogenic pollution and dust events.

The absorbing fraction of the aerosol optical depth can be further investigated through the absorption aerosol optical depth which is defined as:

$$AAOD = AOD\ (1 - SSA) \quad (1.11)$$

Additionally, the AOD wavelength dependency can be described according to a power law function involving the Angstrom exponent (Ångström, 1929) as:

$$AOD_{\lambda} = AOD_{\lambda_0} \left(\frac{\lambda}{\lambda_0}\right)^{-AE} \quad (1.12)$$

The AE is often used also to retrieve information on the particle size (Schuster et al., 2006). The aerosol spectral absorption dependence can be estimated through the absorption angstrom exponent (AAE). The values of 1 are often attributed to BC-dominated aerosol ensembles (Liu et al., 2018), while stronger values to BrC and mineral dust particles (Chakrabarty et al., 2023; Devi et al., 2016; Valenzuela et al., 2015; Zhang et al., 2021b), because the latter compounds more strongly absorb at shorter wavelengths.

All the aforementioned parameters strongly depend on the particle complex refractive index (CRI), the intrinsic variable describing the capacity of the material to interact with radiation. The CRI(λ) is

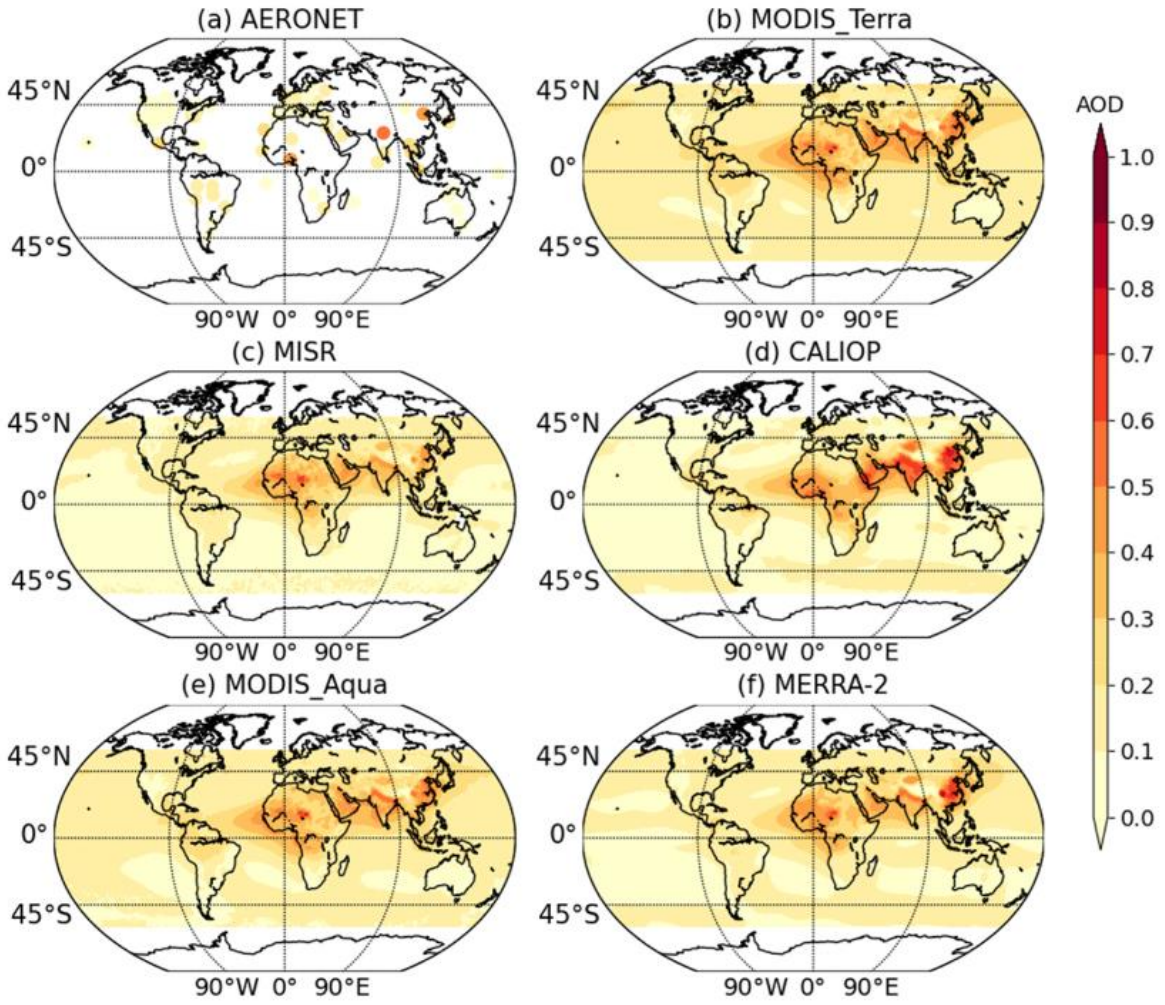

Figure 1.11: Annual mean climatology of AOD at 1°x1° spatial resolution from the major satellite missions across the globe for the 2001-2020 period, with exception for the CALIOP and MODIS_Aqua instruments where the period is from 2006-2020 and 2002-2020 respectively. From Gupta et al. (2022).

complex number $n(\lambda) + ik(\lambda)$. Its real part (n) is related to the non−absorbing aerosol component, while its imaginary part (k) is related to the absorbing component (Bohren et Huffman, 1983; Seinfeld and Pandis, 2016).

The complex refractive index depends on the particle chemical composition and mixing state. Inorganic aerosols show very weak absorption components (Seinfeld and Pandis, 2016), while the imaginary component in the visible part of spectrum is non zero for carbonaceous aerosols containing black and brown carbon (Cappa et al., 2019; Corbin et al., 2018; Yao et al., 2022). On the one hand, BC dominates the absorption in the urban environment showing low SSA values and high imaginary component (Bond and Bergstrom, 2006; Samset et al., 2018; Xie et al., 2019). On the other hand,

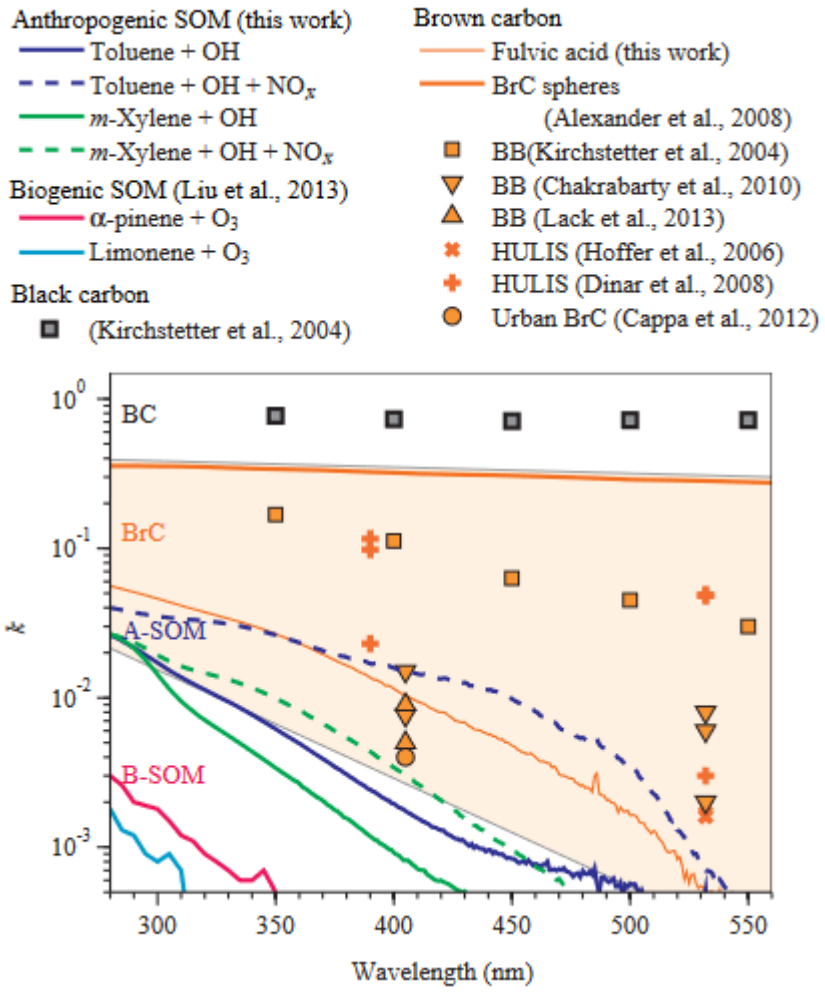

Figure 1.12: Wavelength-dependent k values for the black carbon (BC), anthropogenic and biogenic secondary organic matter (A- and B- SOM) and Brown carbon. Anthropogenic SOM is derived from toluene or m-xylene at different NO_x level, while biogenic SOM is derived for ozonolysis of α-pinene-and limonene. From Liu et al. (2015).

recent studies support the hypothesis that the absorbing capacity of BrC, and therefore its spectral CRI and SSA, might vary along with the process of formation, the precursors type, the oxidation patterns and the NO_x levels for secondary species (Dingle et al., 2019; Flores et al., 2014b; He et al., 2021; Kim and Paulson, 2013; Liu et al., 2015a; Moise et al., 2015; Nakayama et al., 2012, 2015; Yang et al., 2022), as well as due to chemical ageing, potentially inducing either whitening or darkening of the brown aerosols (Zhang et al., 2020; Wang et al., 2018; Liu et al., 2015; Moise et al., 2015). Characterizing the CRI in environments where the mixing of biogenic and anthropogenic aerosols occurs thus proves challenging due to the complex chemical composition. Figure 1.12 and 1.13 depict how the biogenic−derived secondary organic aerosols shows a weaker CRI imaginary component at UV compared to the anthropogenic SOA, in particular anthropogenic volatile organic compounds (VOCs) oxidization at high NOx levels leads to highly absorbing SOA with an order of

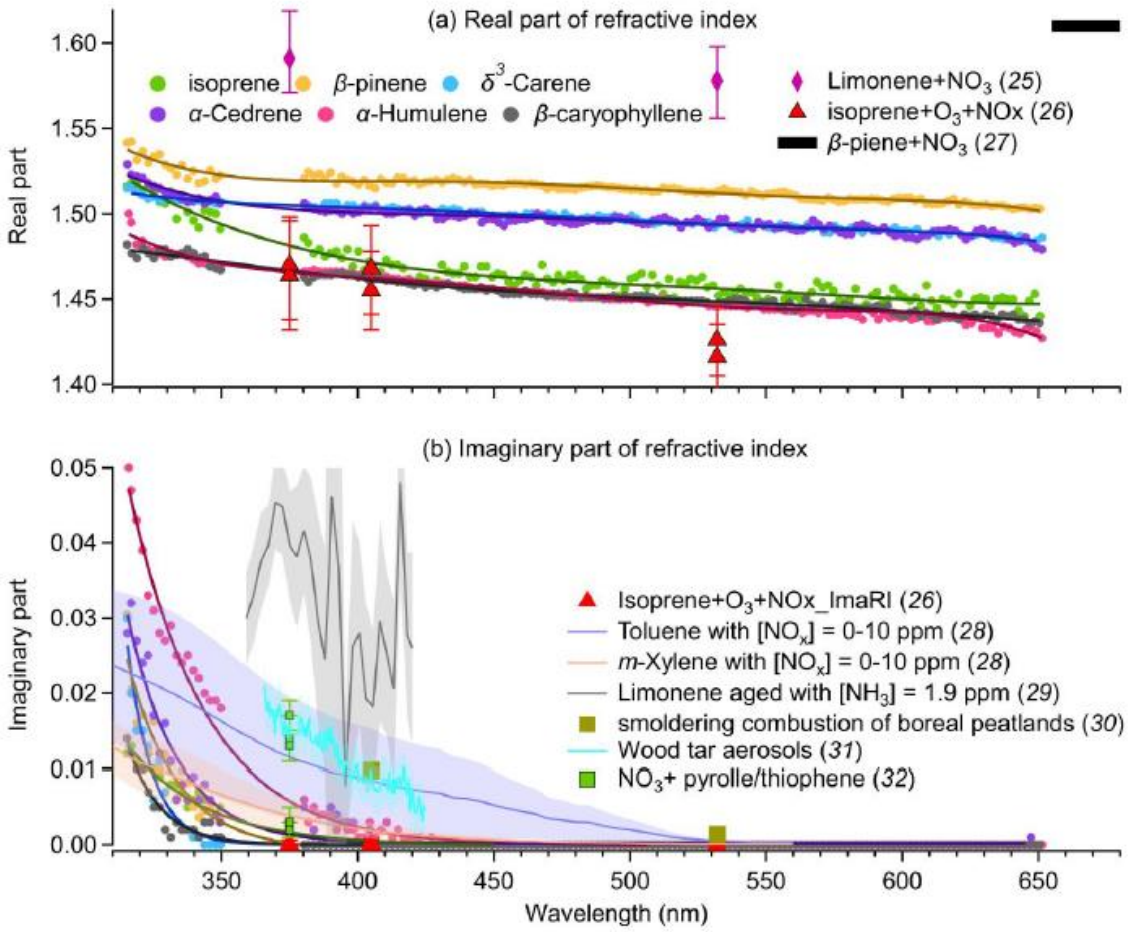

Figure 1.13: Literature survey for (top) real refractive index from the NO_3-derived secondary organic aerosol (bottom) imaginary refractive index derived from anthropogenic and biogenic sources, biomass burning and from unsaturated heterocyclic VOCs. From He et al. (2021).

magnitude of difference (He et al., 2021; Liu et al., 2015). Laboratory and field investigations suggest that the mixing of anthropogenic and biogenic precursors under several NO_x levels may impact the absorption properties of the SOA (He et al., 2022; Liu et al., 2016; Moise et al., 2015; Hecobian et al., 2010). Therefore, the CRI proves to be an important source of uncertainty in calculating optical properties within urban and rural environments.

Finally, another important feature is the particle mixing state, which provides insight on how individual particles are mixed together to form an aerosol particle, impacting its scattering and absorption properties. Two different extreme mixing states can be defined for an aerosol population: i) a "fully internal mixture" which contains equally distributed and well mixed mass fractions of all the available aerosol chemical species whose CRI can be assumed as a volume-averaged refractive index, and ii) an "external mixture" representing an aerosol particle formed only by specific species with a specific CRI. Figure 1.14 depicts an idealised representation of the aerosol population mixing

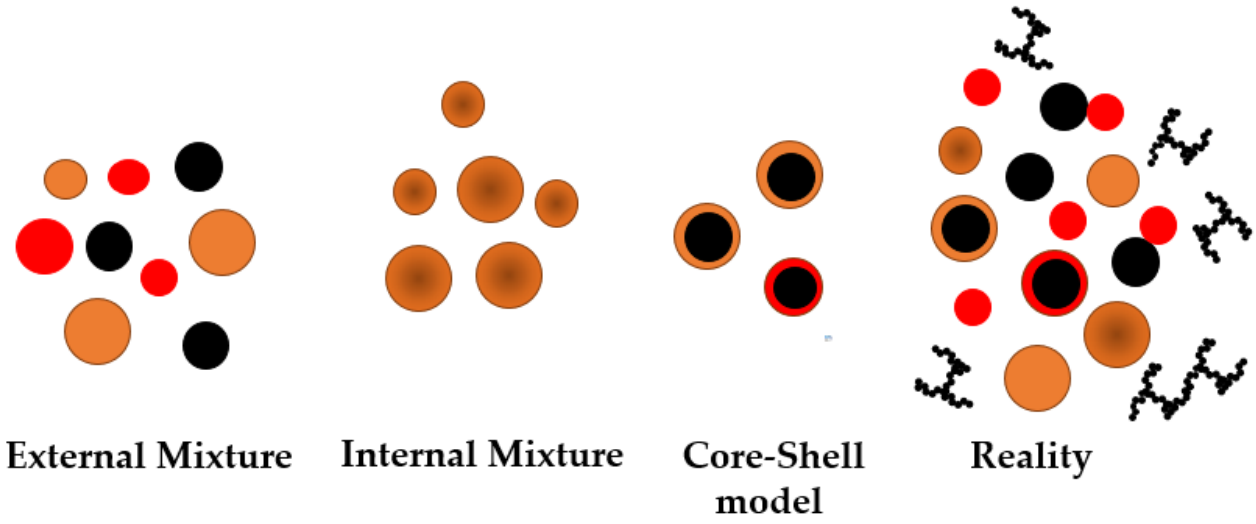

Figure 1.14: Idealised representation of the aerosol population mixing state: "external mixture" representing an aerosol population formed by aerosol species not mixed together; "internal mixture" formed only by equally distributed and well mixed mass fractions of all the available aerosol chemical species whose complex refractive index can be assumed as a volume-averaged refractive index; the "core-shell" model which is designed to represent a particle with a black carbon core coated with soluble aerosols.

state. The real aerosol mixing state lies between these two extremes (Riemer et al., 2019). As black carbon dominates the absorption, its mixing state with other compounds such as organics (e.g brown carbon, BSOA and ASOA) and inorganics, is of significant interest. Freshly emitted black carbon aerosols tends to be in an external mixing state compared to the surrounding aerosol population, while in an internal mixing state few hour after the emission (Cheng et al., 2006; Curci et al., 2019; Müller et al., 2017). One of the popular internal mixing state models is the 'core-shell' model. This model assumes a black carbon (BC) core surrounded by a shell of internally mixed soluble material. It has been shown to well reproduce the BC absorption (Bond and Bergstrom, 2006). Due to the scattering material in the shell, a further enhancement of the BC absorption due to multiple light scattering towards the BC core, defined as "lensing effect" has been observed (Curci et al., 2019; Liu et al., 2017; Zhang et al., 2018). However, pure external or internal core-shell mixing are only extreme states of mixing, while real aerosol populations mostly show intermediate mixing states (Curci et al., 2019; Riemer et al., 2019; Yao et al., 2022). Figure 1.15 shows how an aerosol population mixing state can evolve crossing diversified environments. Crossing an urban area, a background air mass can charge of freshly emitted particles and undergo physical and chemically aging while moving away, forming a more internal mixture. Despite being able to analytically solve the absorption and diffusion of spherical particles through the Mie theory, the particles in the real atmosphere may not be spherical and have a complex morphology and fractal dimensions, impacting the aerosol spectral optical properties and thus leading to a discrepancy between simulation and observations (Pang et al.,

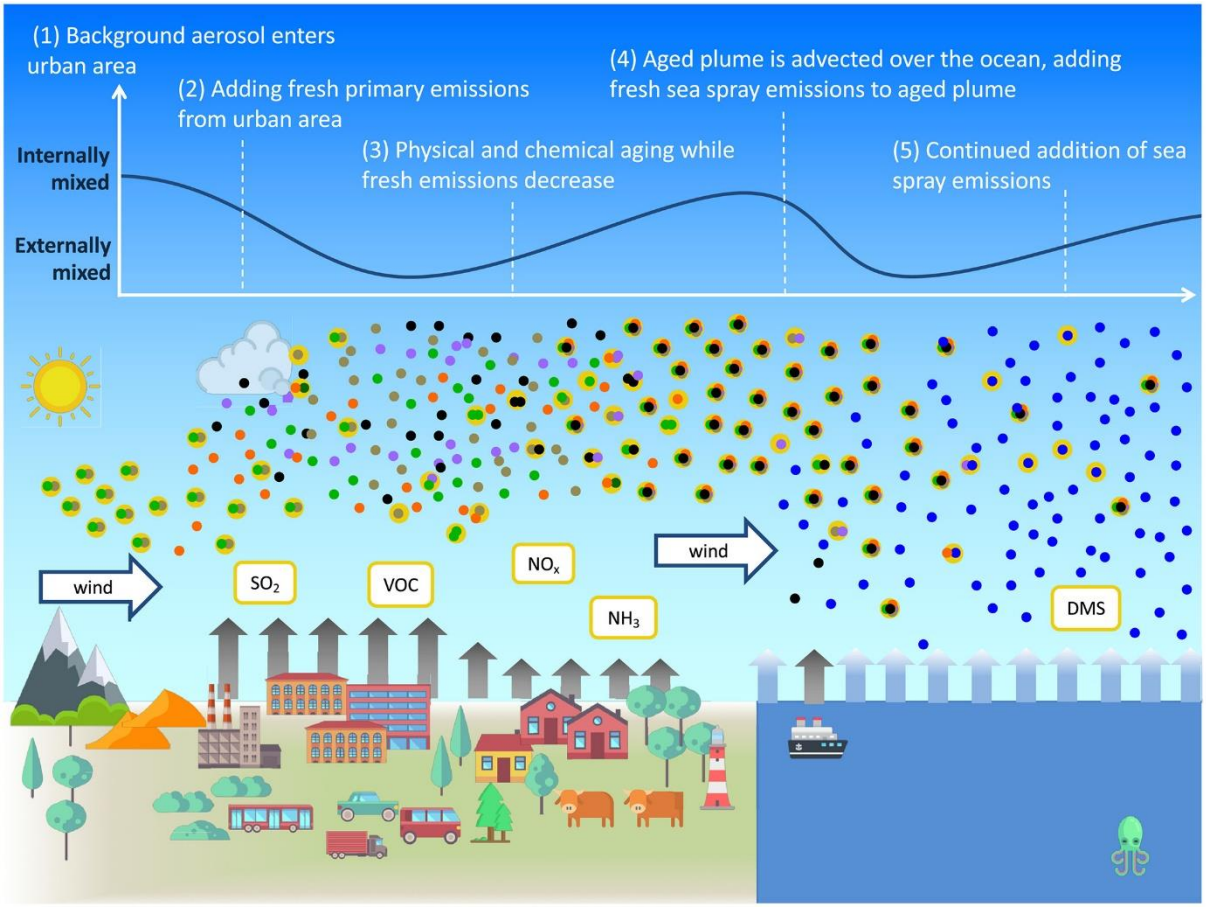

Figure 1.15: A schematic representation of the mixing state evolution of an aerosol particle traversing different environments due to atmospheric transport. As the aerosol particle traverses an urban area, new fresh particles are introduced, resulting in a more externally mixed aerosol population. Physical and chemical aging can occur as the air mass moves away from the emission sources and the aerosol population becomes more internally mixed. This process can occur at any time when the air mass passes through new emission sources (e.g. the ocean). From Riemer et al. (2019).

2023; Xu et al., 2020). Therefore, other methods, such as the Rayleigh-Debye-Gans or T-Matrix amongst others, should be considered to calculate the aerosol optical properties (Liu et al., 2008; Sorensen et al., 2018; Tazaki et al., 2016). A picture of freshly emitted soot particles which shows a chain-like structure compared to fully-coated soot, which are completely embedded into soluble materials is available in Figure 1.16. Those shape-advanced methods are however computationally-demanding, and require advanced morphology characterization to be applied.

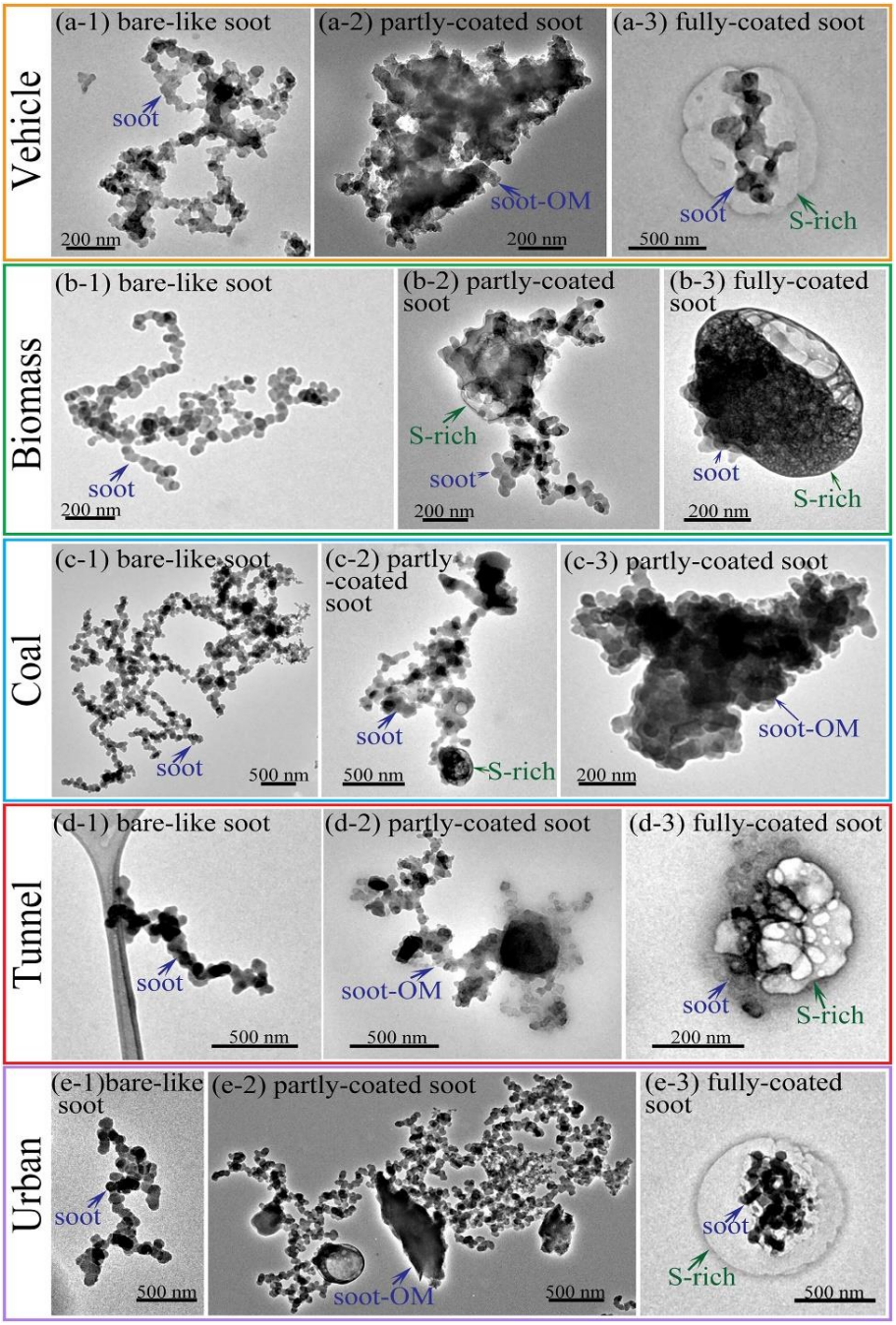

Figure 1.16: Morphology and mixing state of individual soot particles emitted from vehicular emissions, biomass burning, and coal combustion and collected in tunnel air and urban air. From Pang et al. (2023)

1.3 Aerosol direct radiative effect

1.3.1 Direct radiative effect global and regional variability

There exist a variety of methodologies to estimate the direct radiative effect of aerosols: from ground-based and satellite observations up to modelling studies (Bellouin et al., 2013, 2020; Chand et al., 2009; Di Biagio et al., 2020; Kinne, 2019; Konovalov et al., 2023b; Lacagnina et al., 2017; Péré et al., 2011; Yu and Huang, 2023). The DRE, under all-sky and clear-sky conditions (respectively with and without clouds), is defined as the net (ΔF, downward minus upward, units of Wm^{-2}) radiative flux with (F^{aer}) and without aerosols (F^{clean}) at the top of the atmosphere (TOA), surface (BOA) and within the atmosphere (ATM) respectively as:

$$DRE_{TOA}^{net} = \Delta F_{TOA}^{aer} - \Delta F_{TOA}^{clean} = (F_{\downarrow TOA}^{aer} - F_{\uparrow TOA}^{aer}) - (F_{\downarrow TOA}^{clean} - F_{\uparrow TOA}^{clean}) \quad (1.13)$$

$$DRE_{BOA}^{net} = \Delta F_{BOA}^{aer} - \Delta F_{BOA}^{clean} = (F_{\downarrow BOA}^{aer} - F_{\uparrow BOA}^{aer}) - (F_{\downarrow BOA}^{clean} - F_{\uparrow BOA}^{clean}) \quad (1.14)$$

$$DRE_{ATM}^{net} = DRE_{TOA}^{net} - DRE_{BOA}^{net} \quad (1.15)$$

The DRE can be expressed as the sum of a shortwave (SW, lower than 4 μm) and longwave component (LW, higher than 4 μm). Positive (negative) DRE values attest more (less) radiation is captured within the Earth-atmosphere system. Analogous formulations can be retrieved for the DRF but in reference to values prior to industrial revolution (1750). Another important parameter, the direct radiative efficiency (DREE, units of Wm^{-2} AOD^{-1}) relates the DRE and the aerosol loading through the AOD and it is defined as:

$$DREE = \frac{DRE}{AOD_{550nm}} \quad (1.16)$$

The DREE has the advantage of being independent of the aerosol loading, but to be modulated by aerosol intrinsic optical properties and surface/atmospheric conditions. Figure 1.17 shows an example of global model estimates of the AOD and global annual average clear-sky DRE at the TOA for the longwave and shortwave component and each specific aerosol contribution (Heald et al., 2014). Accounting for all the aerosols species a negative DRE SW component at TOA can be observed inducing a cooling (after each component has responded to the external forcing on different timescales) of the Earth-atmosphere system (more energy radiated back to space). In the shortwave range, a negative contribution is observed for all the species, with the exception for the black carbon which shows a positive effect. In the longwave, only dust and sea salt show a significant contribution to the DRE because of their coarse size distribution, therefore being more efficient in interacting with LW radiation. Fine anthropogenic aerosols mostly contribute to the shortwave part of the DRE.

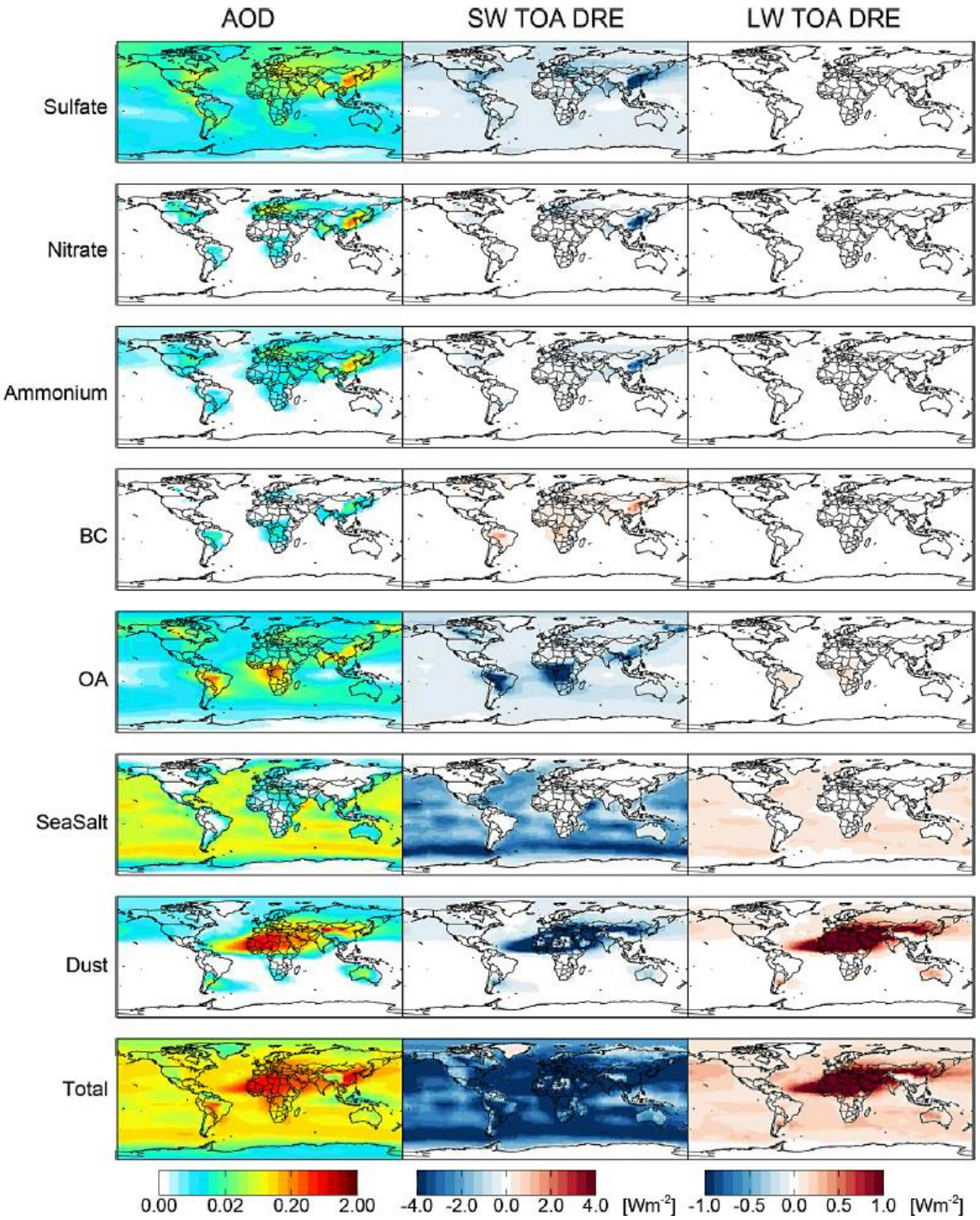

Figure 1.17: Annual mean AOD (left), shortwave TOA clear-sky direct radiative effect (center) and long-wave TOA clear-sky direct radiative effect (right) simulated by GC–RT for the 2010. Color bars are saturated at respective values. From Heald et al. (2014).

However, the DRE magnitude and sign have been demonstrated to be inhomogeneous and varying globally and regionally due to the high variability in the aerosol spectral optical properties, loading, and surface properties (Kasoar et al., 2018; Korras-Carraca et al., 2019; Lacagnina et al., 2017; Subba

et al., 2020; Yu and Huang, 2023). Temporal variability of DRE is also strong. It is for example particularly increased during fire events or dust outbreaks (Adebiyi et al., 2023; Konovalov et al., 2023b; Saleh et al., 2015; di Sarra et al., 2011). Examples of DRE and the DREE global average values as obtained from literature studies (including modelling and observations) at TOA and BOA at the global scale under clear-sky and all-sky conditions for all aerosol species have been reported in Table 1.1. The DRE TOA varies between -7.3 and -2.62 (-2.4 and -1.46) Wm^{-2} under clear-sky (all-sky) conditions. The magnitude of the DRE TOA under all-sky condition is in general lower compared to clear-sky, because clouds already scatter back a part of the incoming shortwave radiation. Moreover, the magnitude of the DRE BOA is stronger compared to the DRE TOA and varies between -10.8 and -6.64 Wm^{-2} for the considered literature studies under clear-sky conditions. The DRE BOA is always more negative than DRE TOA because it depends on extinction of incoming radiation, thus the sum of scattering and absorption, while for DRE TOA scattering and absorption are in competition.

As anticipated, the DRE shows strong regional differences due to regionally variable aerosol loadings. The all-sky Northern Hemisphere shows stronger values (DRE TOA of -1.87 Wm^{-2}) compared to the Southern Hemisphere (DRE TOA of -1.79 Wm^{-2}) due to the higher aerosol loading (Bellouin et al., 2013; Korras-Carraca et al., 2019). Korras-Carraca et al. (2021) show by long-term climatological

	All-sky				Clear Sky			
	TOA		**BOA**		**TOA**		**BOA**	
	DRE	**DREE**	**DRE**	**DREE**	**DRE**	**DREE**	**DRE**	**DREE**
(Bellouin et al., 2013)	-	-	-	-	-7.3±1.3	-41	-10.8±1.9	-60
(Heald et al., 2014)	−1.83	-30	-	-	-2.75	-20	-	-
(Lacagnina et al., 2017)	−2.1 ± 0.7	-	-	-	−4.6 ± 1.5	-30^{o}/-20^{l}	-	-
(Kinne, 2019)	-1.8	-	-4.0	-	-3.5	-	-7.4	-
(Korras-Carraca et al., 2019)	-1.83	-15	-4.23	-35	-3.89	-32	-6.64	-55
(Matus et al., 2019)	-2.4±0.6	-	-	-	-2.62±0.6	-	-	-
(Thorsen et al., 2020)	-1.46	-	-	-	-3.17	-	-	-
(Korras-Carraca et al., 2021)	-	-	-	-	-5.2	-37	-7.6	-54
(Thorsen et al., 2021)	-1.9±1.1	-	-	-	-4.6±0.85	-	-	-
(Elsey et al., 2023)	-	-	-	-	-4.55	-	-8.3	-
(Yu and Huang, 2023)	-1.64	-	-	-	-3.41	-	-	-

Table 1.1: Recent literature survey on the aerosol direct radiative effect (Wm^{-2}) and efficiency ($Wm^{-2}AOD^{-1}$) global averages for the top of the atmosphere (TOA) and the bottom of the atmosphere (BOA). "o" and "l" superscript stands for ocean and land respectively. The "-" sign stands for not available information.

analysis of MERRA-2 reanalysis data that global average DRE TOA is −5.2 Wm^{-2}, but it significantly varies between the different regions: Southern Africa and the Mediterranean region show DRE TOA values of -5.2 Wm^{-2} and -7.2 Wm^{-2} respectively, while stronger values are observed for India and East Asia respectively of -9.3 Wm^{-2} and -11.08 Wm^{-2}. The Mediterranean region is interesting due to the presence of mixture of biogenic, anthropogenic and dust aerosols (Chazette et al., 2019; Dayan et al., 2020; Michoud et al., 2017; Pace et al., 2006). Indeed, the magnitude of the DRE may depend on the temporal averages, as stronger values have been observed during shorter time scales and episodic events (Mallet et al., 2022; Chauvigné et al., 2021; di Sarra et al., 2011; Mallet et al., 2006; Meloni et al., 2004). The literature survey in Mallet et al. (2022), shows that local aerosol variability (e.g. anthropogenic- or dust- dominated) significantly affects the daily SW averages over the Mediterranean region. The shortwave DRE TOA and DRE BOA vary within the [-9, -1.5] Wm^{-2} and [-66, -24] Wm^{-2} range over the Mediterranean region for instantaneous values. Regional simulations performed by Gkikas et al. (2018) show that all-sky DRE over the region is sensible to the dust outbreaks and range in the [-8.5 ,0.5] Wm^{-2} at the TOA. Santese et al. (2010) simulated maximum daily SW averages for DRE_{TOA} and DRE_{BOA} of -3.5 Wm^{-2} and -25 Wm^{-2} for the summer 2003 and for a regional domain partially covering the Sahara desert and Southern Europe. Tafuro et al. (2007) observed a stronger monthly DRE TOA during summer (-9 Wm^{-2}), while lower during winter (-6 Wm^{-2}) on southeast Italy and under clear-sky conditions.

Concerning other regions, Thomas et al. (2013) reported the DRE TOA and DRE BOA for several regions worldwide using the GlobAEROSOL-AATSR dataset. Annual regional mean of DRE TOA and DRE BOA globally vary respectively between [-16, -2.6] Wm^{-2} and [-43, -5.3] Wm^{-2}. Average DRE TOA values of -16 Wm^{-2} and – 9.3 Wm^{-2} are respectively observed for Europe and South Africa. Other literature studies such as Song et al. (2018), estimated a DRE TOA in the [-15.43, -7.3] Wm^{-2} over North China, while Nair et al. (2017) estimated a DRE TOA in the [-11, +0.4] Wm^{-2} and [-11.6, -0.9] Wm^{-2} for spring and winter seasons respectively, over the South Asia. This study also reports a literature survey over different Indian locations showing that DRE TOA can vary in the [-15, +0.7] Wm^{-2} range.

The DRE magnitude can be strongly enhanced even in regions usually not affected by high aerosol loads due to atmospheric transport. As an example, during the summer fire seasons a DRE TOA between - 2.6 and -5.8 Wm^{-2} and DRE BOA between -3.0 and -6.1 Wm^{-2} have been estimated in the eastern Arctic region depending on the aerosol scheme used (Konovalov et al., 2023b).

Of significant interest is to investigate the magnitude and sign of the DRE due to black carbon, brown carbon and mineral dust, constituting the radiation-absorbing aerosols. Since they absorb the SW and LW radiation, their DRE specific contribution is matter of scientific debate, as they might counteract

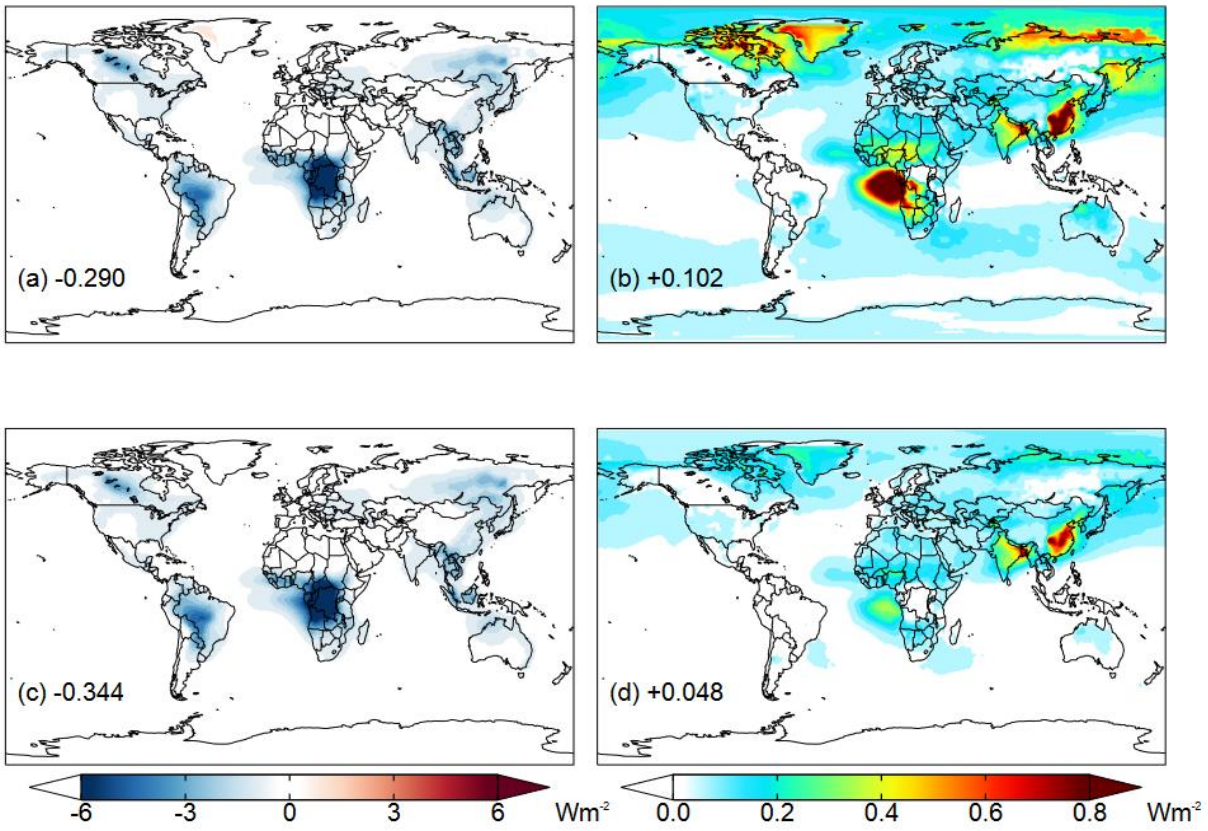

Figure 1.18: Global annual mean all-sky direct radiative effect at the top of the atmosphere for 2014 for organic aerosols (a) and brown carbon absorption (b) without considering the aging processes. (c) and (d) are the same as (a) and (b) but including the aging processes.

the aerosol negative radiative effect of the other mostly scattering species (IPCC, 2021). Positive BC direct radiative effect (DRE), direct radiative forcing (DRF) and effective radiative forcing (ERF) have been observed in literature (Bond et al., 2013; Chen et al., 2022a; Feichter and Stier, 2012; Forster et al., 2021; Kelesidis et al., 2022; Matsui et al., 2018; Myhre et al., 2013; Saleh et al., 2015; Tuccella et al., 2020; Wang et al., 2016, 2014). The literature survey in Saleh et al. (2015) points out that the BC DRE strongly depends on the BC mixing state and varies between +0.3 and +1.05 Wm^{-2} (if accounting for both model and observationally constrained studies). The latest IPCC report attests a positive BC effective radiative forcing of +0.11 [–0.20,0.42] Wm^{-2} (Szopa et al., 2021b).

Concerning the BrC, studies as (Drugé et al., 2022; Jo et al., 2016; Saleh et al., 2015; Tuccella et al., 2020; Wang et al., 2018; Zeng et al., 2020) show that BrC positively contributes to the DRE TOA in the [+0.04, +0.57] Wm^{-2} range. Figure 1.18 shows the global annual mean all-sky DRE TOA distribution for OA and BrC DRE. Wang et al. (2018) observed that taking into account for aging processes the average DRE from OA decreases (from +0.102 to +0.048), representing around the 30% of the BC DRE.

Finally, while mineral dust DRE shows a clear positive DRE TOA contribution in the longwave part of the spectrum and a negative effect in the shortwave, the total DRE TOA still remains unconstrained both in magnitude and sign due to uncertainties linked to the complex refractive index, size and particle shape representation in models (Di Biagio et al., 2020; Kok et al., 2017, 2023; Song et al., 2022; Tuccella et al., 2020).

1.3.2 Factors and processes contributing to the direct radiative effect uncertainties and how reduce them

State−of−the−art knowledge recognises that the DRE uncertainties in magnitude and sign depend on the accurate representation of the aerosol spectral optical properties, size distribution, loading and mixing state in model schemes (Curci et al., 2015; Haywood and Shine, 1997; Li et al., 2022a; Ma et al., 2021; Mallet et al., 2020; Thorsen et al., 2021; Tuccella et al., 2020; Yu et al., 2006; Zhang et al., 2022). The latest IPCC report indicates that, the magnitude of the aerosol radiative effect due to aerosol radiation-interaction is reduced by 50% compared to the previous report (-0.22 Wm^{-2} compared to -0.45 Wm^{-2}). At the same time, the uncertainty on the ERF remains higher than 100 % (Forster et al., 2021). Figure 1.19 depicts a literature survey, which synthesizes uncertainties in all-sky and clear-sky DRE and DRF studies from both modelling and observations and concludes on still high values, in the range from 0.15 to nearly 0.5 Wm^{-2}.

In this paragraph, we discuss the potential sources of uncertainties in modelling the aerosol direct radiative effect. In broad terms, modelling the DRE needs an accurate representation of several input data and processes, such as:

- the total aerosol mass loading in the atmospheric column;
- the aerosol size-resolved vertical distribution, given that the aerosol interaction with radiation depends on the particle diameter;
- the aerosol chemical composition given the very different spectral optical properties of different aerosol species;
- the aerosol mixing state (e.g. internal or external), given the impact on the optical properties;
- the aerosol spectral optical properties such as the complex refractive index;
- the validity of the Mie theory which is accurate for spherical particles, but an approximation for non-spherical particles;
- a correct representation of the surface albedo and cloud cover, distribution and optical properties (the latter for the case of all-sky DRE).
- the radiative transfer across the atmospheric column;

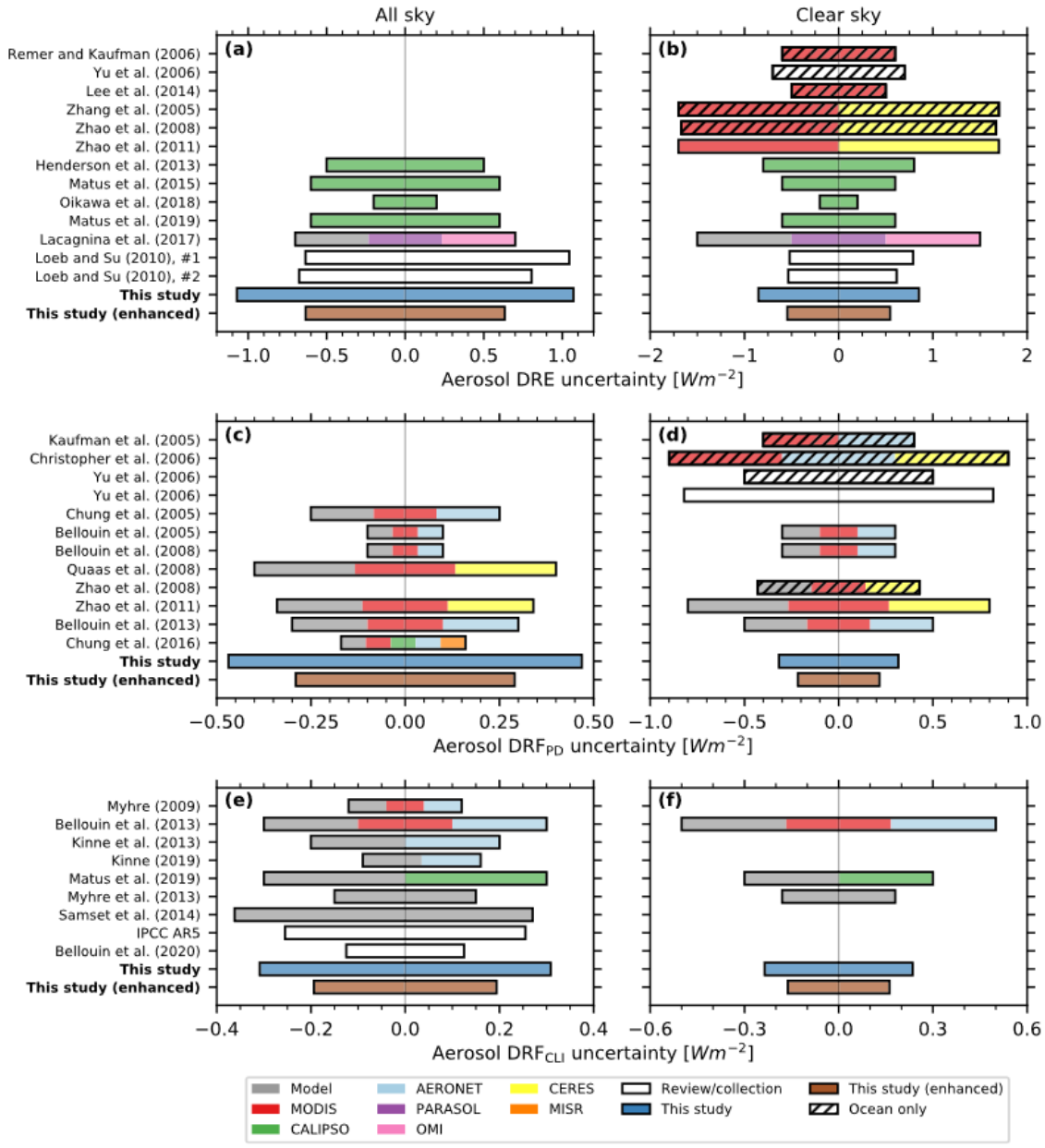

Figure 1.19: aerosol direct radiative effect at the top of the atmosphere uncertainty (calculated as the net shortwave flux with and without aerosol), DRF_{CLI} (calculated as the difference in DRE from present-day to preindustrial times) uncertainty due to ARI and DRF_{PD} (calculated as the difference in DRE from present-day to preindustrial times). Ocean-only estimates are denoted with hatching. The uncertainty estimation of the "enhanced" approach in this study is based on the assumption of exact knowledge of the aerosol mixture and type. From Thorsen et al. (2021).

The first five uncertainties can be partly assessed in comparing modelled and observed AOD field. Indeed, due to this integrative character, a strong link between AOD and DRE has been observed (Haywood and Shine, 1995; Satheesh and Ramanathan, 2000; Wu et al., 2016).

For AOD below extreme values (<2) (e.g., Stone et al. (2011)), and for a given aerosol chemical speciation and size distribution, the DRE magnitude is proportional to the AOD, meaning that high (low) AOD leads to high (low) negative DRE (Zhang et al., 2022). However, as aerosol radiation

extinction is mainly due to scattering, AOD only gives a weak constraint on absorption. The AAOD (absorption AOD) and SSA give additional information on aerosol absorption, while g provides details on the angular distribution of the scattered light. Literature studies show that there is still high uncertainty in the characterisation of the AAOD (Chen et al., 2022a; Samset et al., 2018; Sand et al., 2021). This term dominates the absorption part of the direct radiative effect, which is the result of the sum of radiation-absorbing aerosol contributions. An example of the global annual mean absorption aerosol optical depth at 550 nm from different models is shown in Fig. 1.20. The large spread in model results (by up to a factor 3) demonstrates the high uncertainty in reproducing distribution and amount of absorbing aerosols, an uncertainty that is expected to propagate into the direct radiative effect estimation.

This uncertainty in AAOD is directly related to that in SSA (for a given AOD, as SSA is defined as 1-AAOD/AOD). The SSA is another uncertain parameter for the DRE estimation (Chauvigné et al., 2021; Thorsen et al., 2021; Yao et al., 2022; Zhang et al., 2022). It strongly depends on the aerosol chemical composition, absorption (i.e. complex refractive index), mixing state and particle size (Chauvigné et al., 2021; Curci et al., 2015, 2019; Tian et al., 2023; Yao et al., 2022). Curci et al. (2015) estimated an uncertainty between 30-35% in SSA and AOD, while lower (10%) for the asymmetry parameter (g), due to the different mixing state assumption. Zhang et al. (2022) also estimated that SSA dominates the uncertainty under internal mixing assumption due to aerosol absorption uncertainties, while AOD dominates under external mixing. Thorsen et al. (2021) shows how the DRE uncertainty is dominated by the SSA, in particular at low AOD values. The sign of the DRE can even shift from positive to negative if a critical SSA (between 0.85 and 0.9, depending on surface albedo) value is reached (Tian et al., 2023; Li et al., 2022; Seinfeld and Pandis, 2016; Hansen et al., 1997; Haywood and Shine, 1995). Additionally, the effect of SSA on DRE is further modulated by the vertical distribution: aerosols located above clouds may lead to stronger absorption as the reflected light is further absorbed by the aerosol layer (Li et al., 2022a). On the other hand, aerosol particles located under the cloud may reduce the absorption as much of the light is reflected by the above cloud.

Further uncertainties affecting the simulated DRE variability at the regional scale, concern the correct simulation of the aerosol chemical composition, significantly affecting the uncertainties in the complex refractive index, AOD, and SSA (Song et al., 2021). In particular, the aerosol chemical composition may vary from urban to rural environments (Crippa et al., 2014; Sandrini et al., 2016; Seinfeld and Pandis, 2016) leading to spatial and temporal heterogeneity in the spectral optical properties (Che et al., 2018; Liu and Smith, 1995; Nascimento et al., 2021; Rizzo et al., 2011, 2013; Zhang et al., 2017). Among all the aerosol species, models have strong limitations in simulating the

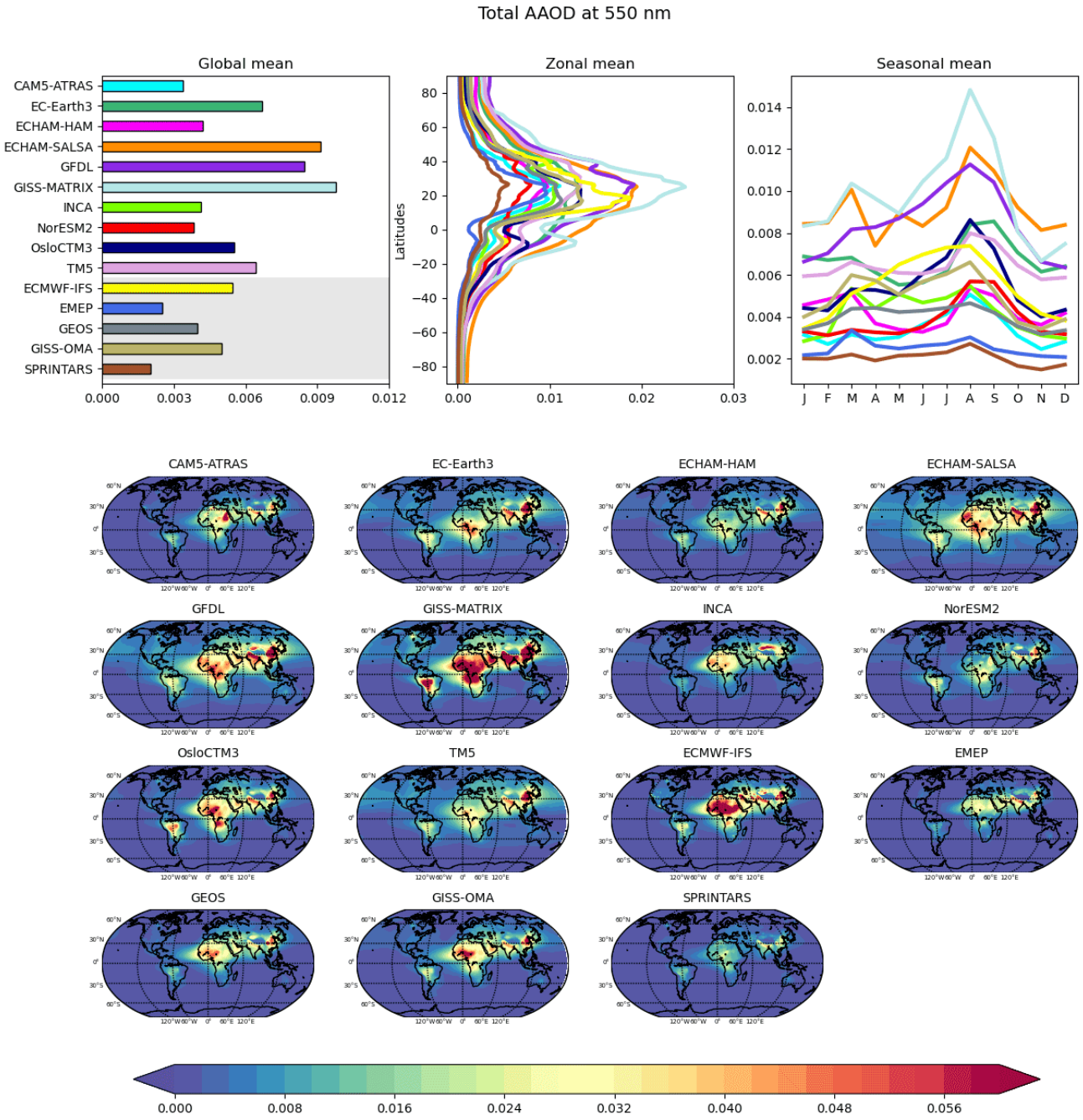

Figure 1.20: Global annual mean absorption aerosol optical depth at 550 nm from different models. The models with grey shading have externally mixed BC. From Sand et al. (2021).

SOA concentrations due to uncertainties in the emissions inventories (Navarro-Barboza et al., 2024) and the lack of a complete description of the VOCs oxidation pathways (initiated by OH, O_3 and NO_3). As a result, simulations of SOA loading and also optical properties, and in particular the absorbing component of their CRI can be biased. This absorbing component depends on the process of formation of SOA, i.e. the precursors type, the oxidation patterns and the NO_x levels for secondary species (Dingle et al., 2019; Flores et al., 2014b; He et al., 2021; Kim and Paulson, 2013; Liu et al.,

2016; Moise et al., 2015; Nakayama et al., 2012, 2015; Yang et al., 2022). This represents a significant source of complexity and uncertainties, even more in regions where mixing between biogenic and anthropogenic aerosols occurs (such as the Ile-de-France). During summer, in presence of heatwave conditions, significant aerosol loadings may occur (due to urban pollution stagnation) and possible biogenic SOA build-up due to the temperature increase, regionally inducing the anthropogenic-biogenic mixing around urban agglomerations. Several studies have identified and quantified the pathways of interactions between biogenic and anthropogenic emissions, and in particular how much BSOA can be controlled by anthropogenic emissions (Carlton et al., 2018):

- anthropogenic NO_x emissions are necessary for building-up oxidant capacity, through formation of ozone, the NO_3 and also the OH radical. These oxidants promote BSOA build-up from BVOC precursors.
- Anthropogenic NO_x ad SO_2 emissions modulate the oxidation pathways of BVOC: sulphuric acid favours the build-up of BSOA from isoprene through the epoxide pathway (Goldstein et al., 2009); formation of organic nitrates can be linked to enhanced BSOA formation (Carlton et al., 2018); however the absence of NO favours the formation of peroxide dimers during terpene oxidation (e.g Mohr et al., 2017) also leading to enhanced BSOA formation.
- The presence of POA and ASOA can act as seed aerosol and promote the aerosol partitioning of semi-volatile species of biogenic origin in the particle phase (and in the same way BSOA favours the partitioning of semi-volatile species of anthropogenic origin in the particle phase).

These effects lead to strong build-up of BSOA up to a factor of four in the anthropogenic pollution plume over Manaus in the amazon region (Shrivastava et al., 2019), mainly through the effect on oxidant capacity. Over US, removal of anthropogenic NOx, SO_2 and POA emissions during the simulated summertime period can reduce nationally averaged BSOA by 23%, 14% and 8%, respectively (Carlton et al., 2018). All these mixing processes with their related uncertainties ultimately impact uncertainties in the DRE estimation. Nascimento et al. (2021) has shown for simulations in the Amazon area downwind of a large pollution source (Manaus), that the presence of the pollution plume may affect the aerosol optical properties leading to a 10% SSA reduction (i.e. more absorbing aerosols). Liu et al. (2021) showed that the reduction of atmospheric aerosol cooling due to pollution control is much enhanced over the south-western US due to the interaction with BSOA formation (through a less efficient epoxide formation pathway).

All these results highlight the importance of well-simulating the aerosol chemical formation mechanisms and ageing, and therefore the composition, in particular accounting for the biogenic-anthropogenic mixing in regional models to further constrain the regional DRE variability.

As said before, a strong uncertainty on the DRE estimation for absorbing aerosols is related to the sufficient knowledge for the black and brown carbon complex refractive index (Laskin et al., 2015; Liu et al., 2016; Moteki et al., 2023; Shamjad et al., 2016, 2018; Zhao et al., 2020a). Current models attribute the well-known CRI of 1.95-0.79i from Bond and Bergstrom (2006) to black carbon. Moteki et al. (2023) suggest that a value of 1.95-0.96i is further recommended for uncoated black carbon, which implies a 16% underestimation in the shortwave absorption in current models, for freshly emitted uncoated BC (keeping in mind that under real atmospheric conditions BC is rapidly coated). Due to the complex nature of brown carbon, also its refractive index may be highly variable and strongly dependent on the source of emission (e.g. biomass burning or biofuel, anthropogenic or biogenic SOA, etc.), pattern of formation and physico-chemical aging and wavelength (Laskin et al., 2015; Liu et al., 2016; Moise et al., 2015; Saleh et al., 2014; Wang et al., 2018). Freshly emitted BrC might have very different optical properties compared to aged BrC due to possible bleaching and photochemical aging (Laskin et al., 2015). This requires that the chemical-physical processes are dynamically represented within CTMs and climate models.

Alongside the accurate characterization of the CRI, there is the need for an accurate representation of the particle mixing state. A real aerosol population mixing state may evolve in time, showing a more external mixing near the source and more internal far from the sources (Curci et al., 2015, 2019; Riemer et al., 2019). Curci et al. (2019) showed that empirically parametrising the mixing state calculating the fraction of internally with respect to externally mixed aerosols reduced the bias in the SSA estimation. Black carbon plays a major role in the particle mixing state and the absorption enhancement due to the lensing effect (Liu et al., 2015b; Saleh et al., 2015; Zhang et al., 2018). Figure 1.21 from Wu et al. (2016) shows that the BC related radiative forcing strongly depends on the particle mixing state and aging (from fresh to heavily coated), which in turn affect the SSA and complex refractive index. This certainly causes significant uncertainty because not all models are capable to follow the mixing state evolution.

Recent studies have further exploited the DRE sensitivity to the particle size distribution and morphology, demonstrating as it is a crucial parameter to well reproduce the spectral optical properties (Di Biagio et al., 2020; Song et al., 2022; Tian et al., 2023). Particles may also grow due to hygroscopic growth (growth of a particle due to water uptake), which is a process that further introduces modifications in the complex refractive index, also affecting the shape of the particles (Curci et al., 2015; Kuang et al., 2016; Li et al., 2022a; Xia et al., 2023; Yu et al., 2006). Most of the CTMs and climate models apply the Mie theory for spherical particles to simulate the optical efficiencies. Even if this theory is exact for spheres it may be not accurate for real atmospheric

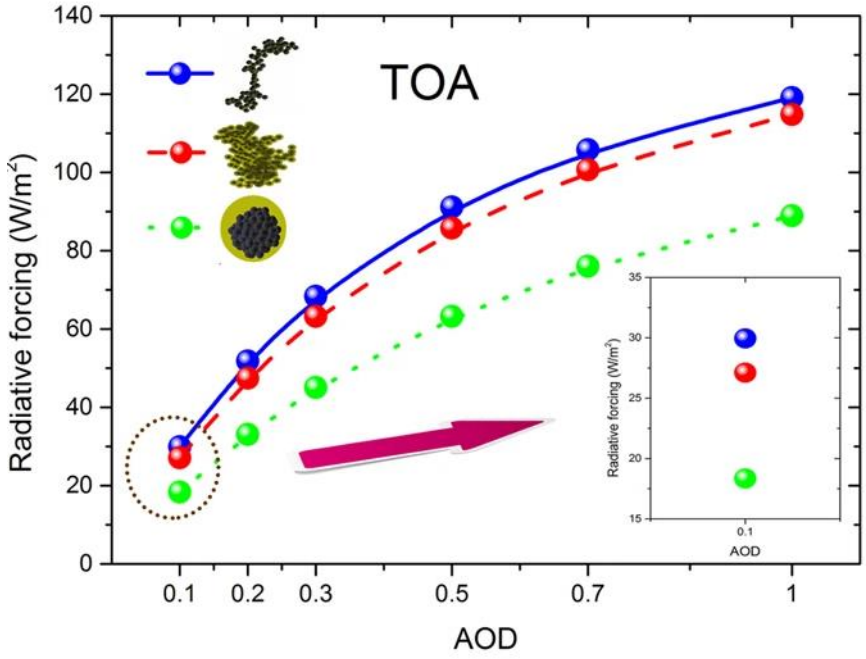

Figure 1.21: Black carbon radiative forcing for different aging and mixing states (freshly emitted (blue) , thinly coated (red) and heavily coated (green). From Wu et al., (2016).

aerosols due to the complex morphology and fractal dimensions of some species, such as soot and dust (Pang et al., 2023).

The DRE uncertainties strongly depend also on land-surface representation, such as the surface albedo, and cloud coverage, distribution and optical properties. The magnitude of the surface albedo may change the DRE sign and magnitude (Yu and Huang, 2023). The aerosol DRE TOA is higher over dark (ocean) surfaces than over bright (deserts, snow/ice) surfaces. Over bright surfaces, the upward irradiance may be stronger due to the increase of the upward reflected radiation, reducing the net DRE effect (Wu et al., 2016). On the other hand, the presence of clouds and their vertical distribution and thickness has an impact on the radiation propagation, which, combined with aerosol vertical distribution, can introduce significant variability in the all-sky DRE (Myhre et al., 2020).

Lastly, uncertainties in the DRE can arise from the Radiative Transfer Models (RTMs) applied to simulate the quantities such as the irradiance, actinic flux and the polarised radiance. In fact, RTMs simulate the electromagnetic radiation propagation through a medium (e.g the atmosphere) and there exist various solvers to numerically evaluate the radiative transfer equations with their respective assumptions and uncertainties. An example of RTM is the Rapid Radiative Transfer Model (RRTM), which provides clear-sky direct and diffuse fluxes with an accuracy less than 2 Wm^{-2} (Iacono et al., 2008).

As a matter of fact, in order to reduce the DRE estimate, models should be able to reproduce the aerosol lifecycle and evolution of its physico-chemical state and spectral optical properties.

Observational data, such as ground-based and satellite remote sensing, and in-situ aerosol measurements can provide precious information to validate and constraint:

- the aerosol chemical composition and loading;
- the simulated aerosol 3D distribution;
- the aerosol spectral properties (from the SSA to complex refractive index) and the size distribution;

Additional measurements can be used to improve the model representation of surface properties, and to test the correctness of the simulated radiation fluxes.

Actually, combining measurement and models is required to initiate, constraint, and validate simulations, to provide a best evaluation of the aerosol DRE and its evolution.

1.4 Scientific questions of the thesis

This thesis is motivated by the objective to better understand the impact of different anthropogenic and biogenic aerosol sources, and their mixing and interaction, on the regional-scale direct radiative effect. In this general framework, this paragraph outlines the scientific questions that arise from the previous sections and that will be addressed in this thesis manuscript:

1. Can we better constrain the regional scale DRE magnitude and sign over a region affected by the mixing of anthropogenic and biogenic emissions?
2. How sensitive is the DRE to the aerosol composition and mixing state and the possible contribution of the biogenic-anthropogenic interaction?
3. Which aerosol species contribute the most to the DRE in such mixed regions? What is the specific contribution of the BC, ASOA, BSOA and BB-POA to the DRE?

In order to address these questions, this thesis manuscript relies on the application of a synergistic measurement-modelling approach at the regional scale of the Paris area (the Ile-de-France region) which represents an excellent case-study to investigate the biogenic-anthropogenic mixing. The region hosts the densely populated Paris agglomeration of over 12 million people (www.insee.fr), surrounded by woods and national forests.

The advantage of the choice of this area lies in the fact that this project benefits from the international ACROSS field campaign (occurred in Paris area in the summer 2022, https://across.aeris-data.fr/, last access: 18 May 2024). Its aim is to deeply understand the physics and chemistry leading to the biogenic-anthropogenic interaction by a comprehensive set of in-situ and aircraft measurements.

About twelve years after the last major campaign MEGAPOLI (MEGAcities: Emissions, urban, regional and Global Atmospheric POLlution and climate effects, and Integrated tools for assessment and mitigation; (Beekmann et al., 2010)) within the Paris urban area, the ACROSS project extends

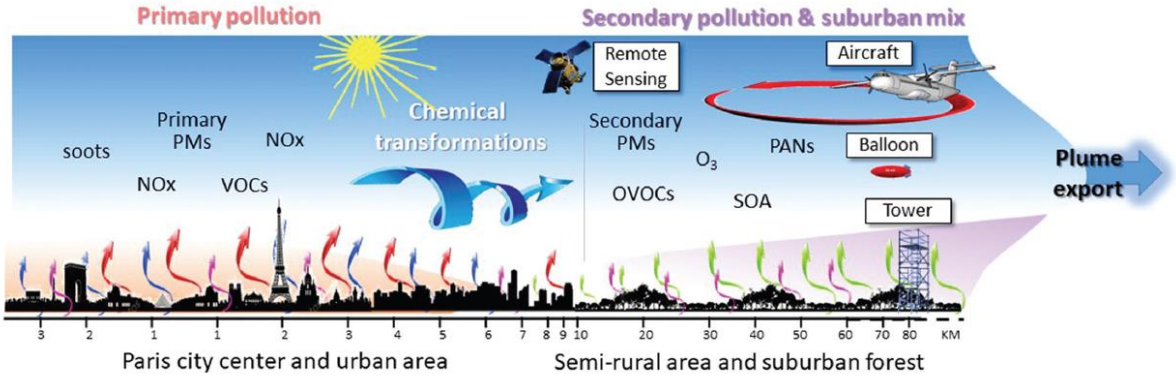

Figure 1.22: Schematic representation of the ACROSS project configuration. On the one hand, the Paris urban area. On the other hand, the surrounding forest area. As the anthropogenic emissions from Paris move towards the forested area, mixing between biogenic and anthropogenic air masses occurs. Therefore, a comprehensive set of measurements from ground-based, airborne and space-based platforms was deployed during the ACROSS campaign to further investigate the biogenic-anthropogenic mixing interaction. From Cantrell and Michoud (2022).

the domain of investigation to the surrounding forested environment and follows the progress of a state-of-the-art comprehensive instrumentation (Ait-Helal et al., 2014; Baudic et al., 2016; Bressi et al., 2014; Healy et al., 2013; Jurányi et al., 2013). The ACROSS project, supported by the MOPGA (Make Our Planet Great Again) initiative, has involved 22 French and international partners and providing a considerable number of instrumentations. Figure 1.22 depicts an idealised sectional representation of the Paris area and the possible "golden case" for the ACROSS field campaign. On the left, there is the Paris urban agglomerate, which is supposed to emit a considerable amount of primary pollutants (e.g. organics, black carbon, NO_x, AVOCs). On the right, the forested areas where anthropogenic secondary aerosol continues to be formed in the pollution plume and where biogenic emissions lead to additional BSOA build-up. Interestingly, BSOA build-up over forested areas in vicinity of the Paris agglomeration can be compared when these areas are aloft or downwind of the Paris anthropogenic pollutions. The differences in the chemical aerosol chemical composition and optical properties can be analysed for the different wind regime.

Several ACROSS scientific questions (Cantrell and Michoud, 2022, "ACROSS White paper") fit the thesis aims. They involve in particular the interaction between the biogenic and anthropogenic environments. Among those there are:

- Does the anthropogenic-biogenic mixing impact the aerosol properties and chemical composition?
- Are we able to represent the mixing within numerical models? Do current parameterisations accurately reproduce the mixing and the secondary aerosol formation and loading?

To address the scientific questions posed by the thesis and the ACROSS project, three main working axes have been followed and presented in the following chapters:

1. **Climatological aerosol optical depth studies from satellite over Europe**. This part of the work aims at investigating the local and regional aerosol contributions around main European cities, Paris included, to contextualize the Paris aerosol loads in a wider European framework; that is to analyse if conditions in terms of aerosol load and local to regional aerosol distribution in the Paris agglomeration are representative of other cities and regions.
2. **Investigation of the aerosol spectral optical properties (i.e., complex refractive index) at the scale of Ile-de-France during the summer 2022 ACROSS field campaign.** This work is aimed at establishing a dataset documenting the variability of the complex refractive index at three sites representatives of different conditions within the Ile-de-France region: a urban, a peri-urban and a rural site. This dataset will allow acquiring knowledge on the variability of spectral optical properties and the link to the bulk chemical composition, which in turn will be used to validate the CTM simulations and guide sensitivity studies.
3. **Estimate of the aerosol DRE from high resolution WRF-CHIMERE simulations constrained by observations at the Ile-de-France and France regional scale.** This work benefits from the synergy with observations to address the aforementioned scientific questions. The WRF-CHIMERE simulations evaluated with several observations, including those from the ACROSS field campaign, enable us to give sound model based answers to such questions. Sensitivity tests guided by experimental data allow for investigating which aerosol source contributes the most within the Paris area, and possible biogenic-anthropogenic interactions.

Addressing the scientific questions of this PhD work lays the foundations for a deeper understanding of the anthropogenic-biogenic interactions at the regional scale. Summer 2022, which corresponds to the framework in which this thesis analysis is situated, has been classified as “the summer of extremes” due to strong positive temperature anomalies registered during all the season, the strong deficit in precipitation, the long duration of the heat waves episodes and the several forest fires occurred in Europe. These events lead to unusually strong aerosol loadings over France and the Ile-de-France region. In a continuously warming and changing climate, there will be a growing opportunity to observe noteworthy aerosol loading episodes linked to the increase in the frequency of heatwave conditions. This opens up the opportunity to consider the results obtained within this thesis a proxy for potential future scenarios.

Chapter 2

2. Tools, methods and models

In this paragraph we present the methodology of the measurements-modelling approach applied to fulfil the thesis goals. The workflow strategy is shown in Figure 2.1. On the one hand there are the "MEASUREMENTS", in particular those of the ACROSS field campaign 2022. On the other hand, the "MODELLING", through the ONLINE WRF-CHIMERE coupling and the OFFLINE radiative interface.

Measurements are used for several distinct objectives:

i) build an AOD climatology, looking at the impact of cities on their regional surrounding based on long-term high resolution satellite data.

ii) Get knowledge of aerosol distribution and spectral optical properties of three points characteristics of the Ile-de-France region (urban, peri-urban, rural) during the summer 2022 period (the ACROSS campaign)

iii) Validate the WRF-CHIMERE gas and aerosol simulation (from the regional to the local scale) using both ACROSS field campaign data and existing network databases to fulfil two distinct objectives:

- Spatial and temporal validation, in order to evaluate the model capability of reproducing the gas and aerosol spatial patterns for major pollutants ($PM_{2.5}$, PM_{10}, O_3, NO_2).
- To evaluate the model capability of reproducing the regional (Ile-de-France) and local aerosol variability (from the chemical to the optical properties point of view).

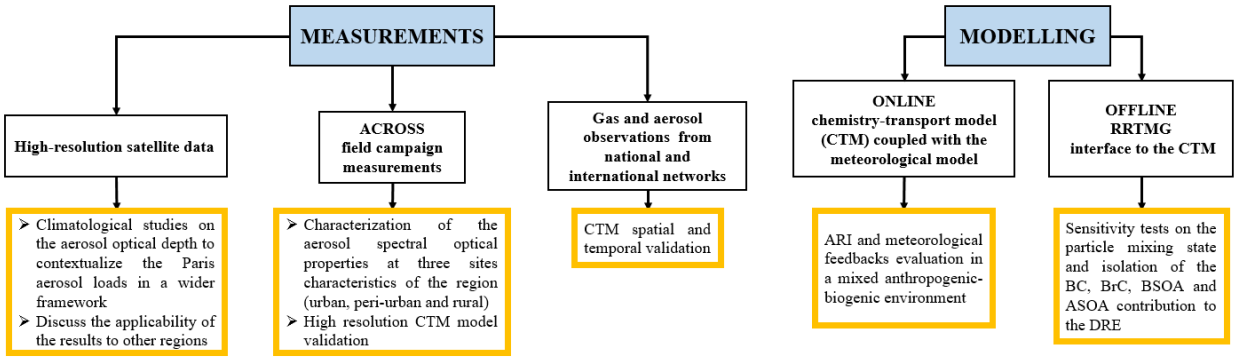

Figure 2.1: Mind map of the synergistic modelling-measurement approach employed during this thesis. Observations have been used both for climatological studies and WRF-CHIMERE CTM simulation's validation. Two main simulation approaches have been used: i) the ONLINE method with a coupling between WRF and CHIMERE, where WRF receives information on the aerosol load and optical properties from CHIMERE and takes it into account in the simulation of meteorological fields transferred back to CHIMERE and ii) the OFFLINE method where no coupling is employed. The OFFLINE interface to the CTM has been developed within this thesis project. RRTMG stands for Rapid Radiative transfer model for GCM applications.

Model simulations are applied with the objectives of:

- performing high-resolution 3D numerical simulations to investigate the gas and aerosol variability at the regional and local scale of the Ile-de-France region.
- Estimating the aerosol direct radiative effect at the regional scale of the Ile-de-France, for a better understanding of the role of the anthropogenic-biogenic interaction on the direct radiative effect.

In the next section the instrumental deployment of the ACROSS campaign and the overview of the atmospheric conditions during the campaign are described. Section 2.2 describes the additional datasets further used to validate the WRF-CHIMERE simulation. The WRF-CHIMERE model and other modelling tools (especially used for calculation of the optical parameters and the direct radiative effect), together with the OFFLINE model developments during the thesis and the specific products developed for the ACROSS community are presented in Sec. 2.3.

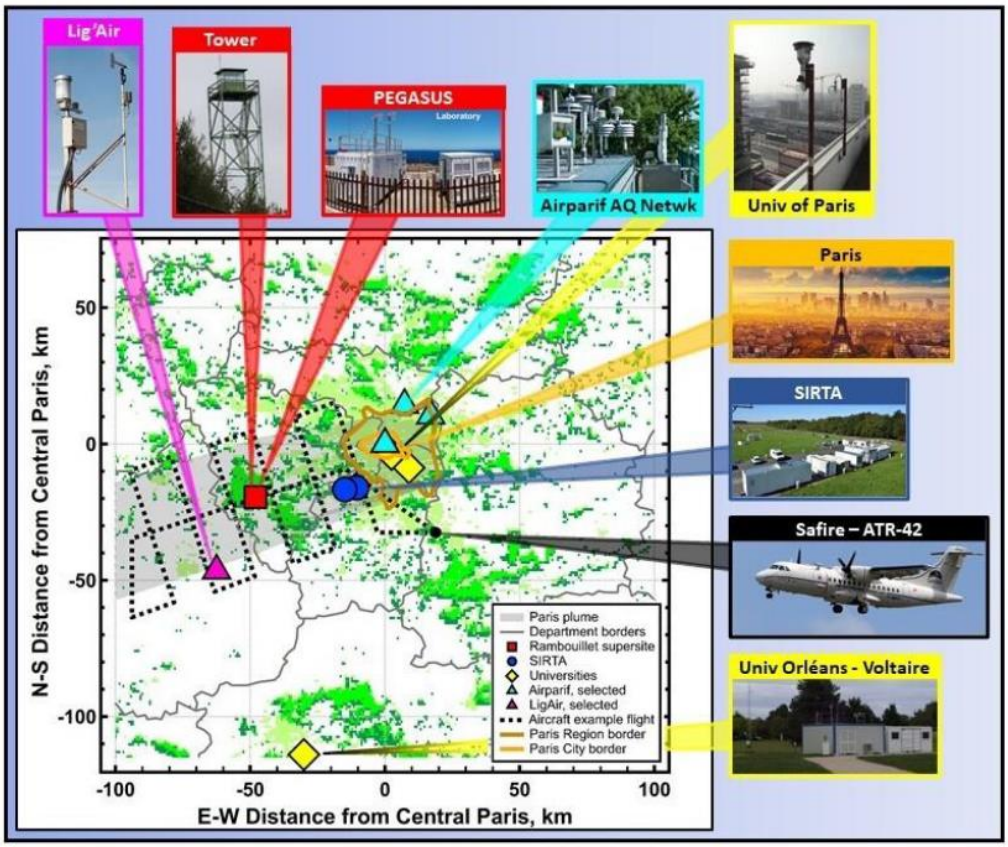

Figure 2.2: Map of the ground-based sites and aircraft deployment during the ACROSS field campaign 2022. The grey area delineates the possible Paris plume development.

2.1 The ACROSS field campaign: experimental deployment

The **A**tmospheric **C**hemistRy **O**f the **S**uburban Fore**S**t (ACROSS) field campaign occurred between the 13 June and the 25 July 2022 in the Ile-de-France region (Cantrell and Michoud, 2022). A considerable number of instruments and sites have been deployed during the ACROSS campaign (Figure 2.2) and the contribution of 22 between French and international partners. The strategy involved three different sites and some airborne operations. A forested super-site was set up specifically to conduct the campaign: the Rambouillet Forest site which included one 40 m instrumented tower, many mobile ground-based mobile platforms, and the dedicated installation of an AERONET sunphotometer. Additional ground based sites were deployed, covering part of the Ile-de-France region, in particular the transect Paris-Rambouillet, including the PRG site, a discontinuous air quality station from LISA specifically upgraded for the campaign, the SIRTA ACTRIS observatory who also contributed to the project, a ground-based site in Jussieu (Paris center), together with a ground-based site in Orléans, plus existing networks such as AIRPARIF. The campaign integrated by scientific flights with the CNRS SAFIRE (Service des Avions Français Instrumentés

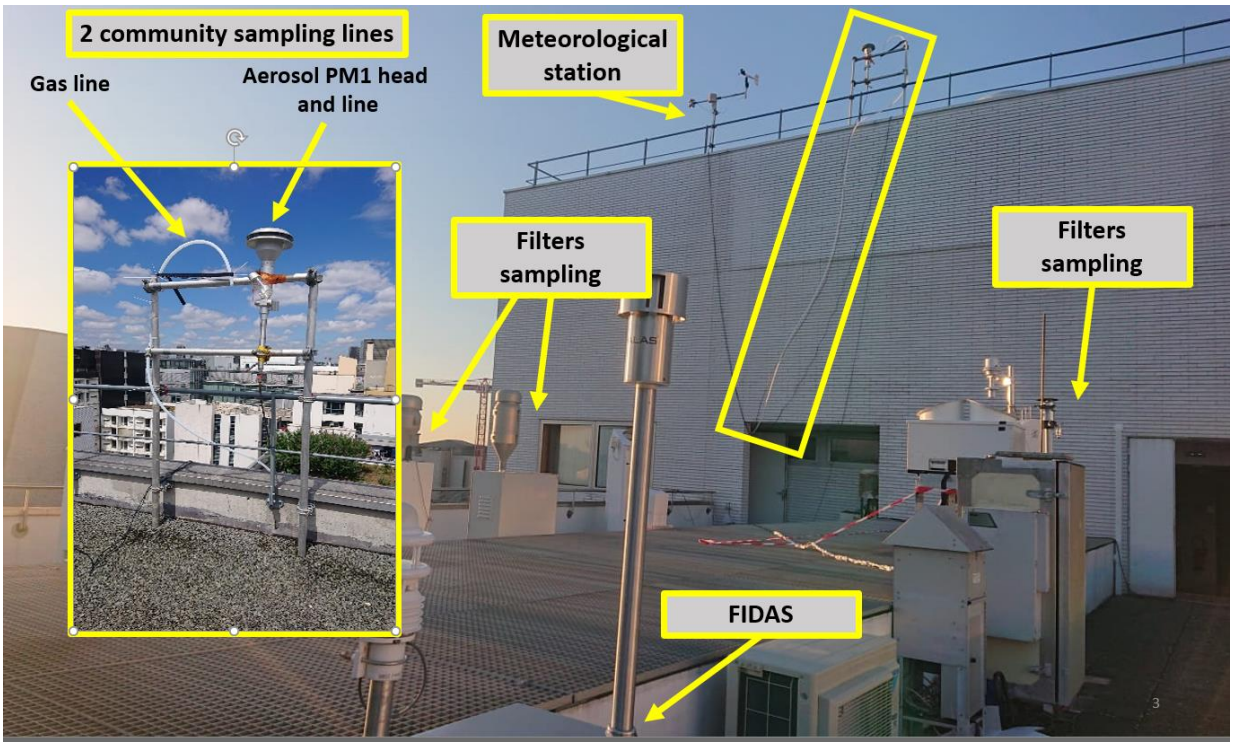

Figure 2.3: Picture and schematic illustration of the Paris-Rive Gauche deployment on the roof and the terrace of the Batiment Lamark.

pour la Recherche en Environnement) ATR-42 research aircraft (See Fig. 2.2). The aircraft campaign took place in the first phase of the ACROSS campaign, between the 16 June and the 5 July 2022 and consisted of 14 flights performed at an altitude between 300 and 600 meters above ground level, with 11 vertical profiles. On all of the sites and platforms, a comprehensive set of gas and aerosols instruments have been deployed, including also those of aerosol spectral optical parameters. This huge experimental effort was accomplished by a large consortium of national and international laboratories (see Tables 2.1 – 2.3) and was led by LISA.

In the following paragraphs, we describe more in detail the setup and measurements at the two main ACROSS ground-based sites used in this study, PRG and Rambouillet, as well as the measurements performed at the SIRTA site. Surface in situ measurements at these three sites are used to derive the complex refractive index and SSA and interpret their variability and link to chemical composition (Chapter 4). As well, some of the surface data are used to compare to the WRF-CHIMERE simulations as discussed in Chapter 5.

- **Paris–Rive Gauche**

The Paris–Rive Gauche (PRG) site (48.8277° N, 2.3806 °E; hereafter PRG) was hosted at the Lamark building at Université Paris Cité, on the southeastern part of the Paris administrative borders. Within

PRG INSTRUMENTATION		
Instrument	**Parameters**	**Responsible institution**
Aerosol characterization		
Thermo Inc. TEOM 1405-DF microbalance	Total mass concentration	LISA
Single-stage filter sampling on polycarbonate ® Nuclepore filters	Elemental composition by X-ray fluorescence (XRF)	LISA
Single stage filter sampling on teflon filters	Organic speciation of total aerosol by infrared spectrometry analysis; X-ray photoelectron spectrometry (XPS) for O:C at aerosol surface	LISA
High-volume filter sampling on quartz filters + PUF	Elemental and organic carbon composition of total aerosol by thermo-optical analysis; Organic speciation of total aerosol by various gas-chromatography mass-spectrometry (GC-MS) analysis; Ion chromatography (IC) analysis; absorption HPLC-UV/Vis-ESI/HRMS for identification and characterization of the chromophores	LISA / INERIS/ LCE
Aerodyne Aerosol Chemical Speciation Monitor (ACSM)	**Non-refractory aerosol submicron composition (sulfate, ammonium, nitrate, organics..) – dry aerosols**	**LISA**
PTR-MS CHARON	sub-µm particulate matter	LCE
TSI Scanning Mobility Particle Sizer (SMPS)	**Particle size distribution (23-982.2 nm mobility diameter)**	**LCE**
GRIMM Inc. optical particle counters (OPC, 1.109)	**Particle size distribution (0.3–20 µm optical diameter)**	**LISA**
nanoSMPS	Particle size distribution (10-64 nm mobility diameter)	IRCELYON
FIDAS	Total mass concentration in PM_1, $PM_{2.5}$, PM_4, and PM_{10} size fractions	Mairie de Paris
AURORA 4000 nephelometer	**Scattering coefficient @ 450, 525, 635 nm (units Mm^{-1} =10^{-6} m^{-1})**	**LISA / Univ. Nova Goritza**
Magee Sci. aethalometer (AE33)	**Absorption coefficient @ 370, 420, 470, 590, 660, 880, 950 nm (units Mm^{-1} =10^{-6} m^{-1}) 1-min resolution**	**LISA / INERIS**
Ceilometer	Aerosol backscatter and extinction coefficient and depolarization ratio @ 355 nm 5-deg from zenith pointing 1-s resolution	LMD
Gas phase		
Horiba APSA monitor	SO_2 mixing ratio 2-min resolution, detection limit 1 ppb	LISA
Horiba APOA monitor	O_3 mixing ratio, 2-min resolution, detection limit 1 ppb	LISA
Horiba APNA monitor	NO_x mixing ratio, 2-min resolution, detection limit 1 ppb	LISA
AP2E	Ammonia	LISA
PTR-MS VOCUS, PTR-MS CHARON, TD-GC-FID	VOCs	LISA/LCE/IRCELYON
Meteorology		
Meteo station PM1 head level	Temperature, pressure, wind direction, wind speed	LISA
Meteo station FIDAS – terrace level	Temperature, pressure, wind direction, wind speed	LISA
Meteo France instrumentation: Cartridges Radiometer (RPG HATPRO) BASTA (cloud radar) DIAL lidar dial water vapor (VAISALA)	oxygenated VOCs Temperature, Humidity profiles, LWP (liquid water path), IWV (integrated watervapor) CTOP, Cbase (cloud radar) attenuated backscatter, water vapor mixing ratio	Meteo France

Table 2.1: Summary of the instruments and the measured parameters deployed at the Paris-Rive Gauche site. Acronyms of instituions : LISA ((Laboratoire Interuniversitaire des Systèmes Atmosphériques), LCE (Laboratoire Chimie Environnement), IRCELYON (Institut de recherches sur la catalyse et l'environnement), INERIS (Institut national de l'environnement industriel et des risques), LMD (Laboratoire de Météorologie Dynamique). The data used within Chapter 4 are highlighted in bold.

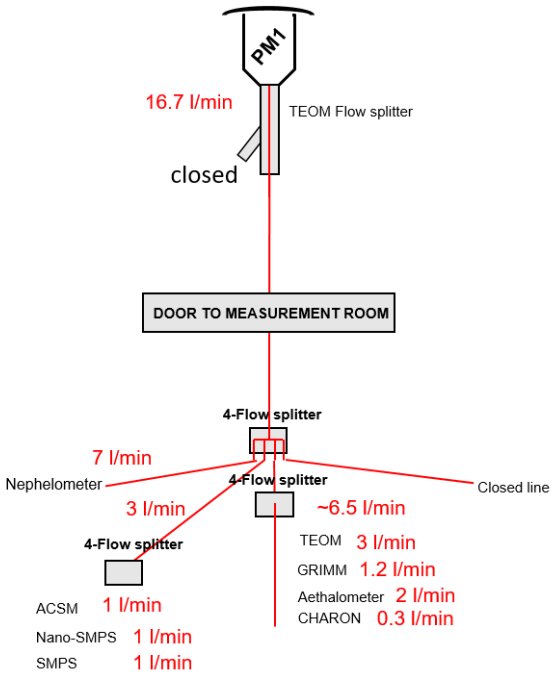

Figure 2.4: Idealised schematisation of the aerosol line deployed at the Paris-Rive Gauche. In red the flowrate is shown.

the Paris urban agglomeration and in close proximity to the still dense sub-urban area in the south-east, this site presents urban background features: it is at a distance of a few hundred meters from strong emission sources such as bus and train stations, main roads and city highway intersections. Aerosol and gas sampling was performed from the roof of the building at about 30 m a.g.l. Measurements at the PRG sites included both gas and aerosol phases, and meteorological parameters. Two main sampling lines, one for the gas and the other one for the aerosol phase were deployed from the roof of the building, and additional instruments were installed on the terrace of the 7th floor, about 10 m below the intake point of the gas and aerosol lines Figure 2.3. A comprehensive list with all the instruments connected to the sampling line or on the terrace is provided in Table 2.1.

The aerosol sampling system (see Figure 2.4) for the ACROSS campaign was composed of a certified PM_1 head (PM_X model, Leckel GmbH, Berlin, Germany), letting only particles with an aerodynamic D<1 µm to flow in the tubes, with an optimal flow requirement of 16.7 l min^{-1}. A copper tube was linking the PM_1 head to the laboratory where the instruments measuring room were located about 10 m below. At the extremity of the copper tube, there was a 4–way stainless steel flow splitter. One of the four lines was closed, while all the aerosol instruments were connected to the other three lines.

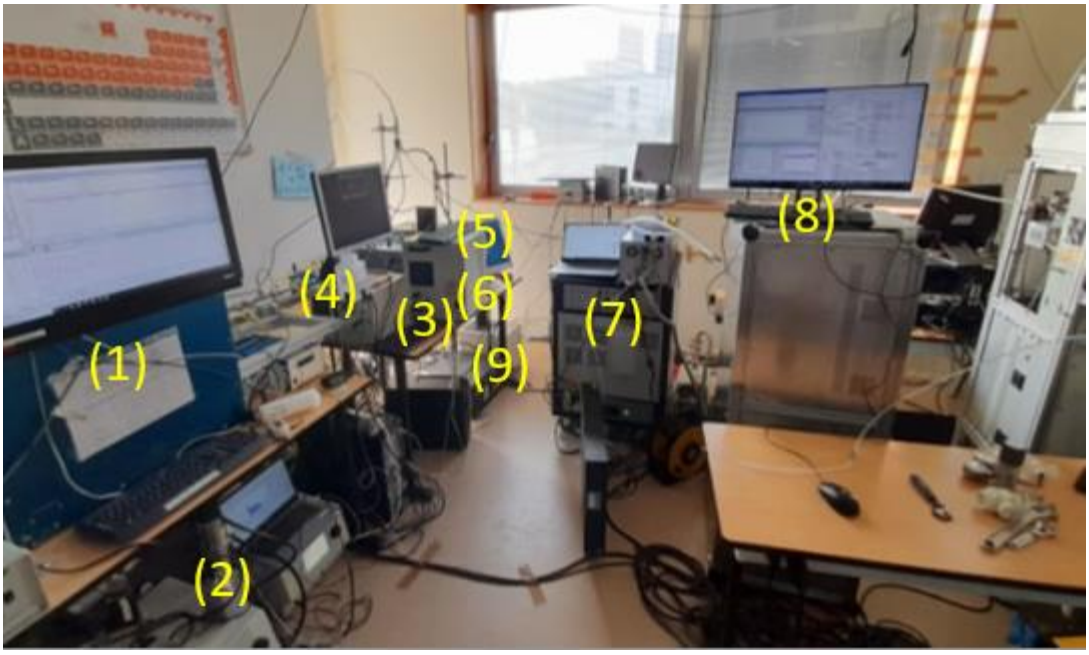

Figure 2.5: The Paris-Rive Gauche measuring room: (1) the ACSM (Aerosol Chemical Speciation Monitor), (2) the SMPS (Scanning Mobility Particle Sizer), (3) Nano-SMPS (Scanning Mobility Particle Sizer), (4) the Nephelometer (Aurora 4000), (5) the Aethalometer (AE33), (6) GRIMM OPC 1.108, (7) PTR-MS CHARON (CHemical Analysis of aeRosol ON-line), (8) PTR-MS VOCUS (CHemical Analysis of aeRosol ON-line

The ensemble of the measuring instruments connected to the PM_1, shown in Figure 2.5, are also listed in Table 2.1, and where contributed by several laboratories and coordinated by LISA. Finally, Figure 2.6 illustrates the instrument deployment outside the measuring room and the position of the instruments and sampling lines deployed during the campaign.

- **The Rambouillet Forest**

The Rambouillet forest ground–based supersite (48.6866° N, 1.7045° E) was hosted at the "Boissiere–Ecole" French commune, located in the eastern part of the Rambouillet forest, within the Ile-de-France region and at around 50 km southwest of the Paris administrative borders. The site covers a surface area of 625 m^2 and include a 40 m high tower, originally dedicated to the surveillance of forest fires above the canopy (about 25 m high). The area is surrounded by the Rambouillet national forest, a mixed deciduous and evergreen trees forest. The three classification according to the IGN (French institute national de l'information géographique et forestière) is available in Figure 2.7.

A large panel of instrumentation was installed below and above the canopy, from the ground to the top of the tower, in order to measure biogenic and anthropogenic VOCs, gas pollutants, and aerosols. Measurements below the canopy were performed by several laboratories and mobile platforms (LISA, EPOC, ICARE, PC2A, IMT Nord Europe, etc), including The PEGASUS (PortablE Gas and Aerosol Sampling UnitS) mobile platform from LISA (Formenti et al., in preparation) and the "Barracuda"

RAMBOUILLET INSTRUMENTATION			
Instrument	**Parameters**	**Platform/ Responsible institution**	**Above or Below canopy**
Aerosol characterization			
Thermo Inc. TEOM 1405-DF microbalance	Total mass concentration	PEGASUS/LISA	Below
Single-stage filter sampling on polycarbonate ® Nuclepore filters	Elemental composition by X-ray fluorescence (XRF)	PEGASUS/LISA	Below
Single stage filter sampling on teflon filters	Organic speciation of total aerosol by infrared spectrometry analysis; X-ray photoelectron spectrometry (XPS) for O:C at aerosol surface	PEGASUS/LISA	Below
High-volume filter sampling on quartz filters + PUF	Elemental and organic carbon composition of total aerosol by thermo-optical analysis; Organic speciation of total aerosol by various gas-chromatography mass-spectrometry (GC-MS) analysis; Ion chromatography (IC) analysis; absorption HPLC-UV/Vis-ESI/HRMS for identification and characterization of the chromophores	PEGASUS/LISA	Below
Aerodyne Aerosol Mass Spectrometer (ASM)	**Non-refractory aerosol submicron composition (sulfate, ammonium, nitrate, organics..) – dry aerosols**	**IMT Nord Europe**	**Above and Below**
Aerodyne CAPS-SSA	aerosol extinction/scattering	PEGASUS/LISA	Below
Aerodyne CAPS-PMEX	aerosol extinction coefficient	PEGASUS/LISA	Below
TSI Scanning Mobility Particle Sizer (SMPS)	**Particle size distribution (19.5-881.7 nm mobility diameter)**	**BARRACUDA/ EPOC**	**Below**
GRIMM Inc. optical particle counters (OPC, 1.109)	**Particle size distribution (0.25–32 µm optical diameter)**	**PEGASUS/LISA**	**Below**
TSI 3563 nephelometer	**Scattering coefficient @ 450, 550, 700 nm (units Mm^{-1} =10^{-6} m^{-1})**	**PEGASUS/LISA**	**Below**
Magee Sci. aethalometer (AE33)	**Absorption coefficient @ 370, 420, 470, 590, 660, 880, 950 nm (units Mm^{-1} =10^{-6} m^{-1}) 1-min resolution**	**PEGASUS/LISA**	**Below**
Gas phase			
Horiba APSA monitor	SO_2 mixing ratio 2-min resolution, detection limit 1 ppb	PEGASUS/LISA	Below
Horiba APOA monitor	O_3 mixing ratio, 2-min resolution, detection limit 1 ppb	PEGASUS/LISA	Below
Horiba APNA monitor	NO_x mixing ratio, 2-min resolution, detection limit 1 ppb	PEGASUS/LISA	Below
Meteorology			
Meteo France instrumentation	Temperature, pressure, wind direction, wind speed	Meteo France	

Table 2.2: List of the instruments and the measured parameters deployed by the LISA laboratory and other partners at the Rambouillet Forest at ground (PEGASUS platform) and the top of the 40 m high tower above the canopy. The measurements highlighted in bold have been collected and used as inputs to the complex refractive index retrieval. Only measurements used in this thesis work are listed due to the extensive list of instruments deployed during the ACROSS campaign. Acronyms of instituions and platforms : LISA ((Laboratoire Interuniversitaire des Systèmes Atmosphériques), PEGASUS (PortablE Gas and Aerosol Sampling UnitS), IMT (Institut Mines-Télécom), EPOC (EPOC Environnements et Paléoenvironnements Océaniques et Continentaux).

Figure 2.6: Illustration of the instrument deployment outside the measuring room at the Paris-Rive-Gauche site. (left) roof, (right) terrace.

from EPOC (Kammer et al., 2020) measuring aerosol load and properties in the PM_1 fraction. The PEGASUS platform grouped most of the instruments below the canopy, having both gas and aerosol optical and size distribution measurements. The PEGASUS sampling line, presented two PM_1 heads: high-volume (38 l min-1; PM_X model, Leckel GmbH, Berlin, Germany) and low-volume (16.7 l min^{-1}; BGI - PQ TSP, Mesa Laboratories, Butler, NJ). The ambient air was distributed to instruments through Teflon® Coated Aluminum 5- and 2- Port Manifolds (URG-2000-30HF and URG-2000-30HF-3, URG Inc, Chapel Hill, NC, USA). The gas sampling lines were composed of ¼" diameter Teflon tubes shielded by aluminium tubes and equipped with an inverted funnel to safeguard against rain and condensed water. The Rambouillet forest 40 m tower and the view of the containers from the top of the tower is given in Figure 2.8.

Figure 2.9 illustrates most of the instruments installed on the PEGASUS measuring platform, while a summary of the available measurements, together with other instrumentation of relevance for the present thesis work, is given in Table 2.2.

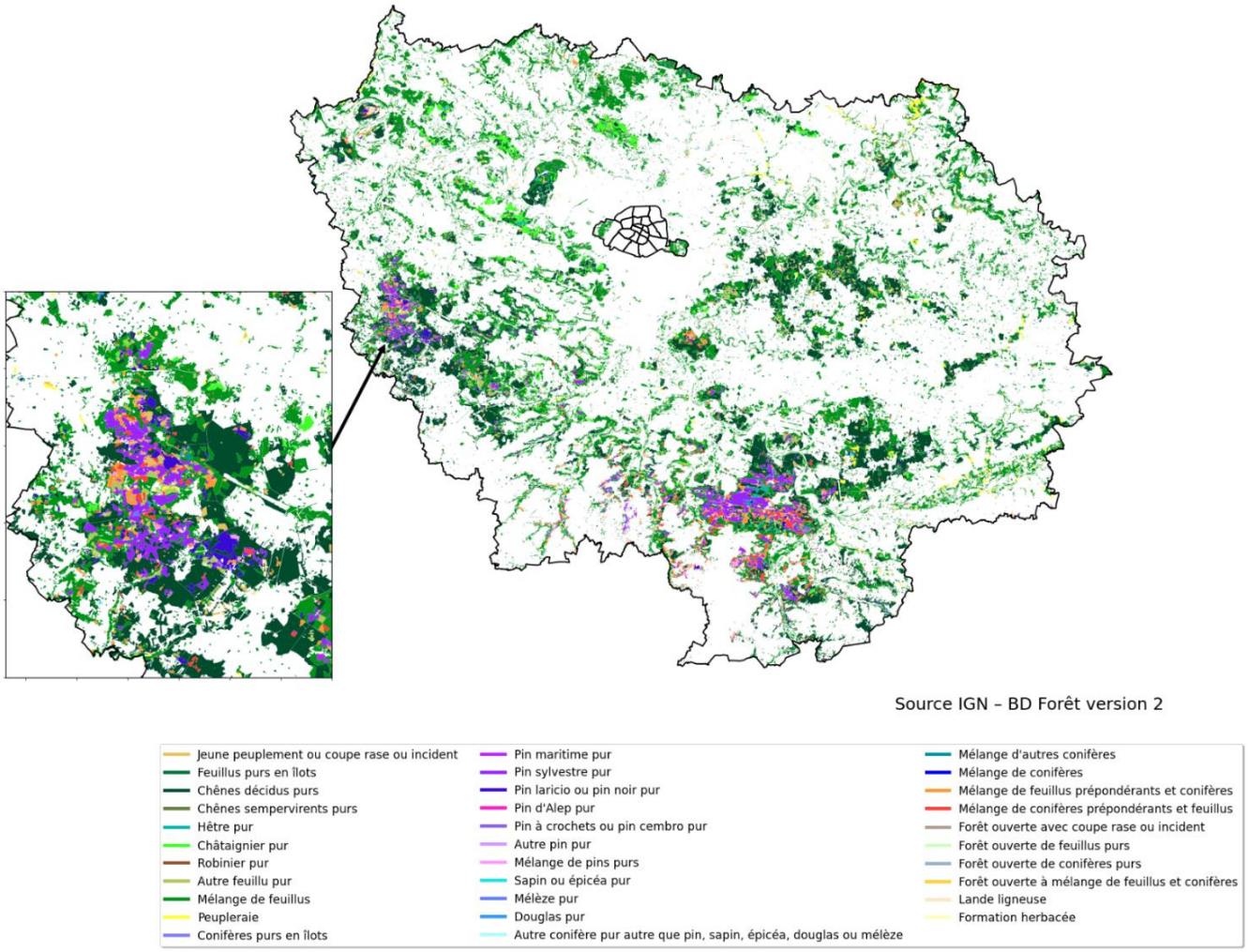

Figure 2.7: IGN (Institut national de l'information géographique et forestière) tree species classification for the Ile-de-France region. Black lines represent the Paris and the Ile-de-France administrative borders. In the bottom left, there is a zoom on the Rambouillet forest. This figure has been produces from the forest inventory (BD Foret version 2 product, https://inventaire-forestier.ign.fr/spip.php?article646).

Figure 2.8: The Rambouillet forest 40 m tower (left) and the view from the top of the tower of the containers : (1) represents the Max Planck Institute (MPI) the (2) and (3) indicate the Portable Gas and Aerosol Sampling UnitS (PEGASUS) facilities, (4) the INRAE (Institut national de recherche pour l'agriculture, l'alimentation et l'environnement) platform, (5) the PC2A (PhysicoChimie des Processus de Combustion et de l'Atmosphère) and (6) the LPC2E (Laboratoire de Physique et de Chimie de l'Environnement et de l'Espace) platforms.

Figure 2.9: PEGASUS (PortablE Gas and Aerosol Sampling UnitS) measuring platform: (1) the TEOM (2) Aethalometer (3) water CPC (condensation particle counter), (4) the GRIMM OPC and Nephelometer, (5) CAPS, (6) SP2, (7) HTDMA, (8) PILS (9) ACSM and gas analyzer

Instrument	Parameters	Responsible institution
Aerosol characterization		
Aerodyne Aerosol Chemical Speciation Monitor (ACSM)	Non-refractory aerosol submicron composition (sulfate, ammonium, nitrate, organics..) – dry aerosols	SIRTA/LSCE
AURORA 3000 nephelometer	Scattering coefficient @ 450, 525, 635 nm (units Mm^{-1} =10^{-6} m^{-1})	
Magee Sci. aethalometer (AE33)	Absorption coefficient @ 370, 420, 470, 590, 660, 880, 950 nm (units Mm^{-1} =10^{-6} m^{-1}) 1-min resolution	
TSI Mobility Particle Size Spectrometer (MMPS)	Particle size distribution (8.9–829.0 nm mobility diameter)	SIRTA/TROPOS

Table 2.3: Summary of the instruments and the measured parameters deployed from the SIRTA during the ACROSS campaign and used as inputs to the complex refractive index retrieval. Acronyms of instituions and platforms : SIRTA (Site instrumental de recherche par télédétection), LSCE (Laboratoire Interuniversitaire des Systèmes Atmosphérique Laboratoire des Sciences du Climat et de l'Environnement), TROPOS (Leibniz Institute for Tropospheric Research).

- **The SIRTA site**

Among the other sites that participated in the ACROSS campaign, there is the SIRTA (Site Instrumental de Recherche par Télédétection Atmosphérique, https://sirta.ipsl.fr/) (48.7090° N, 2.1488° E), which is an Aerosol, Clouds, and Trace gases Research Infrastructure (ACTRIS) long−term observational site in the Paris area (Haeffelin et al., 2005). Located at around 20 km southwest of the Paris administrative borders, the SIRTA is considered a peri–urban site due to its proximity to forest, urban areas as well as agriculture fields and traffic roads. Measurements carried out at SIRTA have been classified as background values for the Paris area (Bedoya-Velásquez et al., 2019) and represents the peri-urban site of the complex refractive index retrieval (See Chapter 4). The summary of the instruments used for the complex refractive index retrieval is available in Table 2.3. The table is not exhaustive as many other measurements are currently installed since the site represents a reference observatory for the Paris region. Some of the instruments were added specifically during the ACROSS campaign.

❖ **Relevant measurements used from PRG, Rambouillet forest and SIRTA for this work**

Within the many instruments deployed at PRG, Rambouillet forest and SIRTA during the ACROSS campaign, the ones of interest for my work and that I analysed in detail (Chapter 4) are:

- nephelometer (Aurora 4000 at PRG, TSI 3563 at Rambouillet) and Aethalometer (AE33 at the three sites), providing respectively the aerosol scattering (at 450, 525, 635 nm for PRG and 450, 550, 700 nm) and absorption coefficients (at 370, 420, 470, 590, 660, 880, 950 nm).

- ACSM (Aerosol Chemical Speciation Monitor), providing the non-refractory aerosol chemical composition (organics, nitrate…) at PRG and SIRTA or AMS (Aerosol Mass Spectrometer) at Rambouillet forest.
- SMPS (Scanning Mobility Particle Sizer), providing the particle number size distribution in the submicron mobility diameter range.
- GRIMM OPC (Optical Particle Counter, model 1.108 at PRG and 1.109 at Ramb Forest), providing the particle number size distribution in the optical diameter range starting at 0.3 µm up to 20 or 32 µm.

Aerosol spectral scattering and absorption coefficients and size distribution from the Nephelometer, Aethalometer, SMPS and GRIMM OPC have been used for the complex refractive index and SSA retrieval at the three sites. A further analysis on the bulk chemical composition correlating the ACSM/AMS data with the retrieved CRI has been also performed (See Chapter 4).

2.1.1 Overview of the sampled ACROSS campaign conditions

The ACROSS field campaign occurred during the summer 2022 with exceptionally hot and dry conditions over Western Europe, and which therefore has been considered as a proxy of a future 2050 climate (Ribes et al., 2022). According to the recent Meteo France report (Meteo France, 2022), summer 2022 has been classified as “the summer of extremes” due to strong positive temperature anomalies (see Figure 2.10) registered during all the summer 2022 season, a strong deficit in

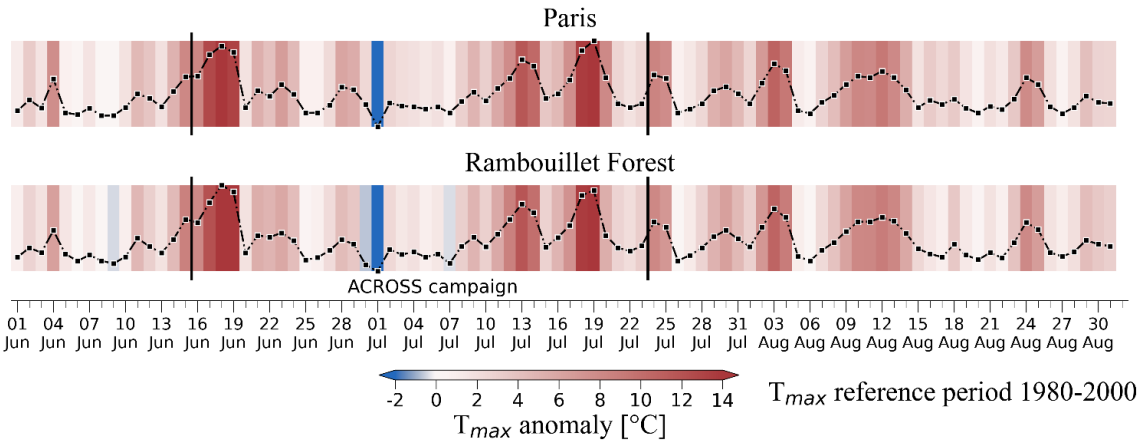

Figure 2.10: Daily max temperature anomaly compared to the 1980-2000 reference period from the E-OBS dataset for the Paris and Rambouillet Forest sites for the summer 2022 (Cornes et al., 2018). The black vertical lines show the starting and ending of the ACROSS field campaign. The black curve shows the normalised daily max temperature anomaly. Positive anomalies are observed during the entire summer 2022.

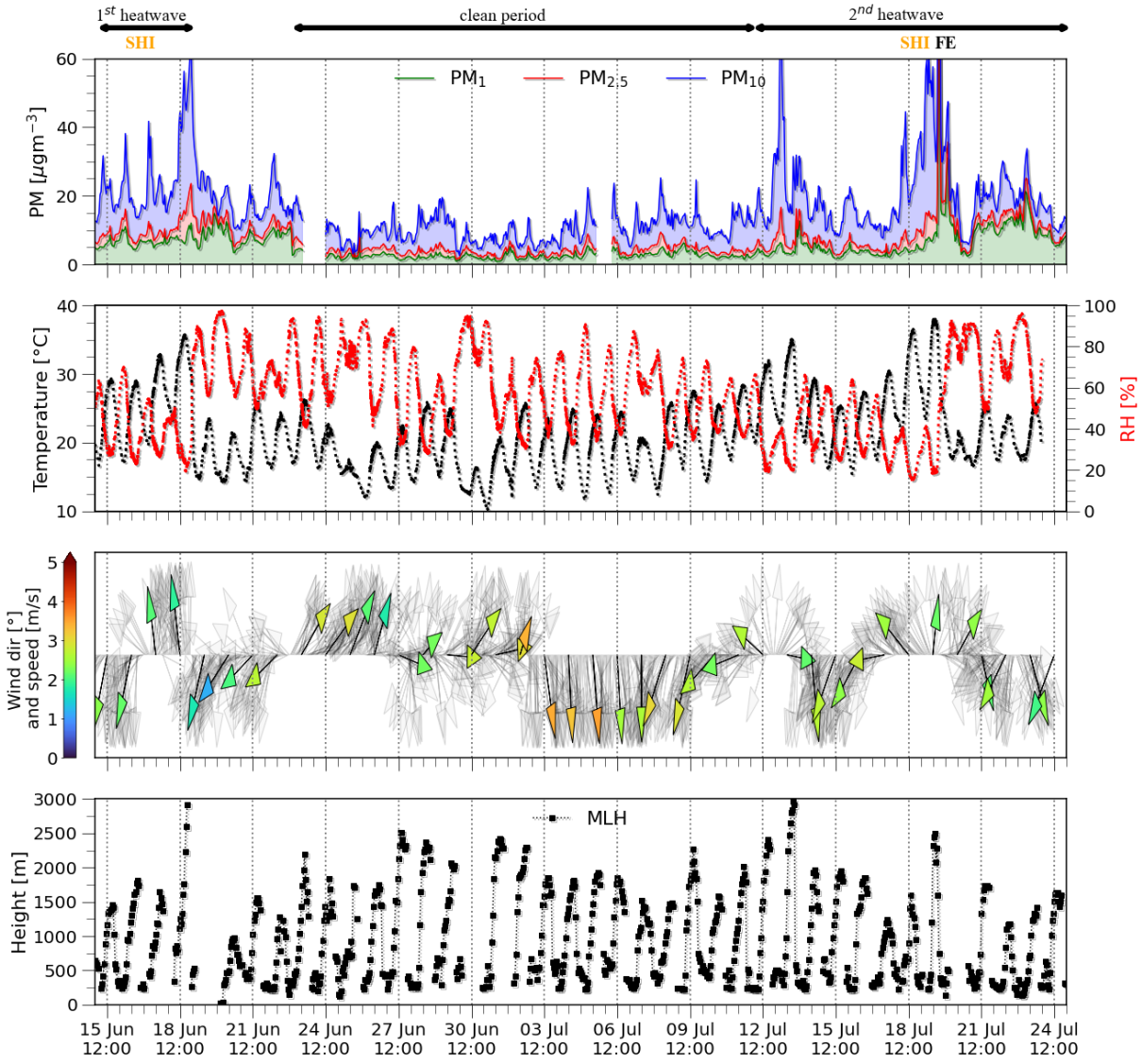

Figure 2.11: Temporal variation at the urban background site at Paris Rive Gauche (PRG) of a) particulate matter (PM_1, $PM_{2.5}$, PM_{10}) (Di Antonio et al., 2023), b) temperature and relative humidity, c) wind speed and direction, d) mixing layer height (MLH) at SIRTA (Kotthaus et al., 2023), during the ACROSS campaign 2022. SHI stands for "Saharan dust intrusion", while "FE" stands for "Fire episode".

precipitation, the long duration of the heat waves episodes and the several forest fires occurred in Europe.

The WMO defines the term "heatwave" as a prolonged period of unusually hot days and nights (https://wmo.int/topics/heatwave). Accordingly, two strong heatwaves hit Europe within the ACROSS field campaign period, in particular the Western France. Meteo France classified these dates as the 15-19 June and the 12-25 July over France. This classification fits more Southern and Western France and slightly the Paris area, since the second heatwave could be further divided into two smaller periods due to a temperature decrease between the 14th and 17th July (See Figure 2.10). These weather

conditions impacted air quality over the area, due to the strong weather stability and weak winds. For instance, light easterly winds under sunny anticyclonic conditions allow for regional advection, local accumulation, and for efficient photochemical formation of secondary pollutants. Hot temperatures trigger enhanced biogenic VOC emissions within the forests. In Figure 2.11 we show temporal variability of particulate matter measurements at the PRG site, together with several meteorological variables during the campaign: temperature and relative humidity, wind speed and direction and the mixing layer height (measured at SIRTA). Strong PM_{10} values (>50 µg m^{-3}) occurred during the first and second heatwaves, affected also by Saharan dust intrusion (SHI) over de region. These high PM_{10} concentrations are strongly correlated with the increase of temperature (>35°) which is in turn anti-correlated with the relative humidity profile (<25%). These heatwaves, characterised mostly by southerly winds and average wind speed of ~2 ms^{-1}, lead also to a strong mixing layer height development (~3 km). Between the two heatwaves, a period with temperature values closer to the climatological average of 23° for the reference 1980-2000 period (see Fig. 2.10) has been observed. This period was characterised by the advection of cleaner air masses from W to SW, leading to lower aerosol loadings (PM_{10}<20 µgm^{-3}).

Figure 2.12 shows an overview of the atmospheric conditions over the three main periods registered during the ACROSS campaign. Panel (a), (b) and (c) show the geopotential height from the ERA5 reanalysis dataset. During the two heatwave periods, a deep anticyclonic system over Europe, constrained by two cycloninc systems (respectively over the Atlantic Ocean and Italy), allowed to the warm air of Saharan origin to rise towards northern latitudes, lasting several days and leading to strong heatwave periods over western France the 18 June and the 19 July 2022. On the contrary, cleaner conditions are observed on the 1 July 2022 due to the arrival of a low-pressure system over Northern France. During the heatwaves, the ozone reached daily maximum values above 180 µgm^{-3}, while the daily average PM_{10} distribution values above 40 µgm^{-3} for the western part, while lower than 30 µgm^{-3} over the eastern part of France. It is worth mentioning, that due to strong temperatures and thunderstorms the experimental conditions during the filed campaign at all sites, and for the aircraft, were extremely challenging. Several power cuts and air conditioning problems were faced during the campaign.

Conversely, the cleaner conditions registered between the two heatwaves is observed over large parts of France (see Figure 2.11 and 2.12), and the $PM_{2.5}$ and PM_{10} were lower than 14 and 20 µg m^{-3} respectively over the region.

In addition to the heatwaves and cleaner conditions, the summer 2022 was also characterised by an exceptionally strong wildfire activity (Menut et al., 2023). In particular, a strong fire episode occurred over the Aquitaine region, in South-Western France, and strongly impacted the air quality over that

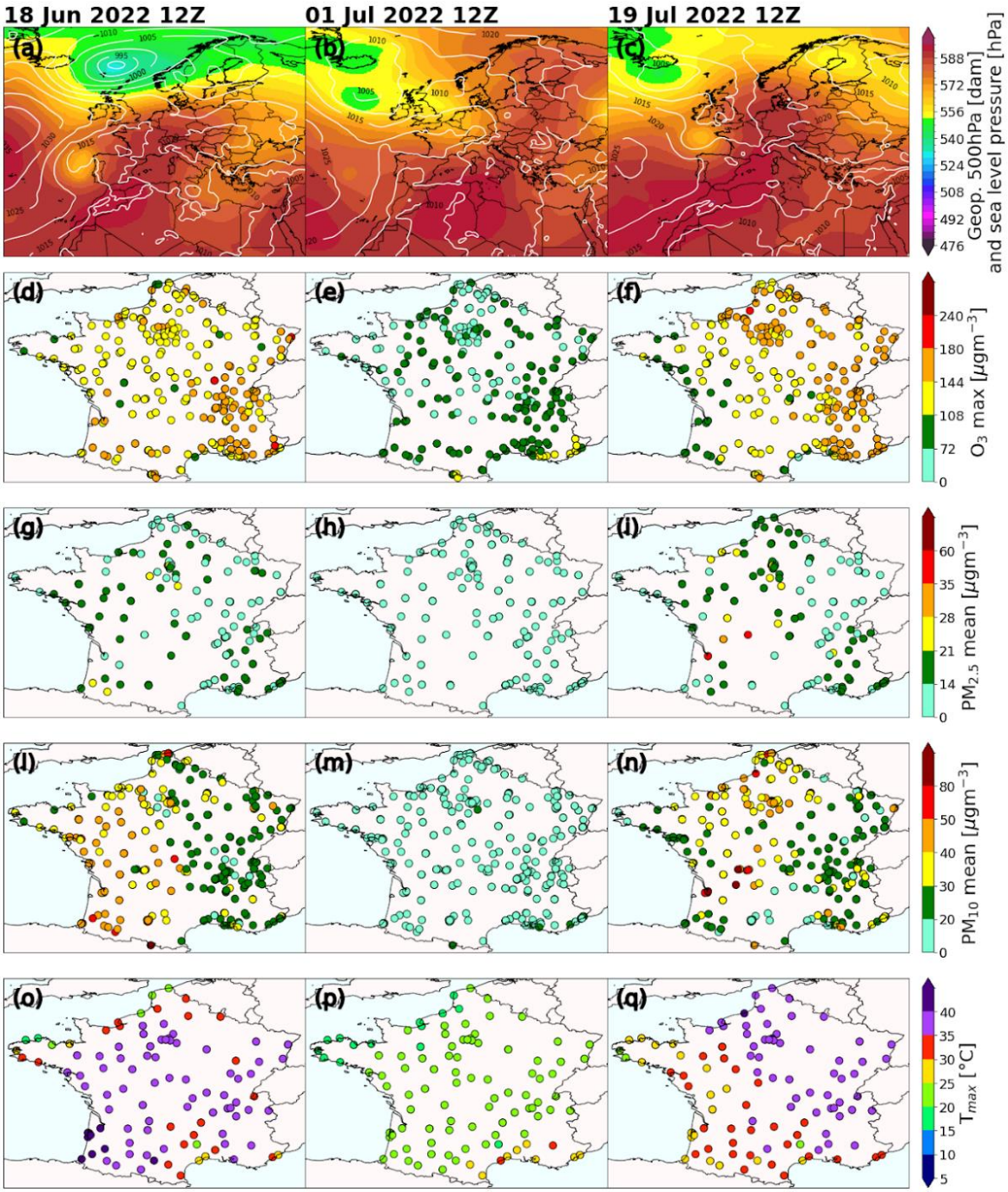

Figure 2.12: Geopotential height and surface pressure at 12 UTC of the here main periods registered during the ACROSS campaign from the ERA5 reanalysis (Hersbach et al., 2023b, a). Panels (d)-(f) represent the daily max O_3, panels (g)-(i) represent the daily mean $PM_{2.5}$, panels (l)-(n) represent the daily mean PM_{10} and panels (o)-(q) the daily max temperature. O_3, $PM_{2.5}$, and PM_{10} are provided by the EEA, while daily max temperature data are provided by the MIDAS database.

region, but also over distant regions where the fire plume was advected during several days (https://www.ineris.fr/fr/ineris/actualites/feux-forets-gironde-mesures-concentrations-composition-chimique-particules, last access 30 January 2024). Due to southerly winds and the intensity of this fire episode, the biomass burning plume was exceptionally registered also over the Paris area, and in

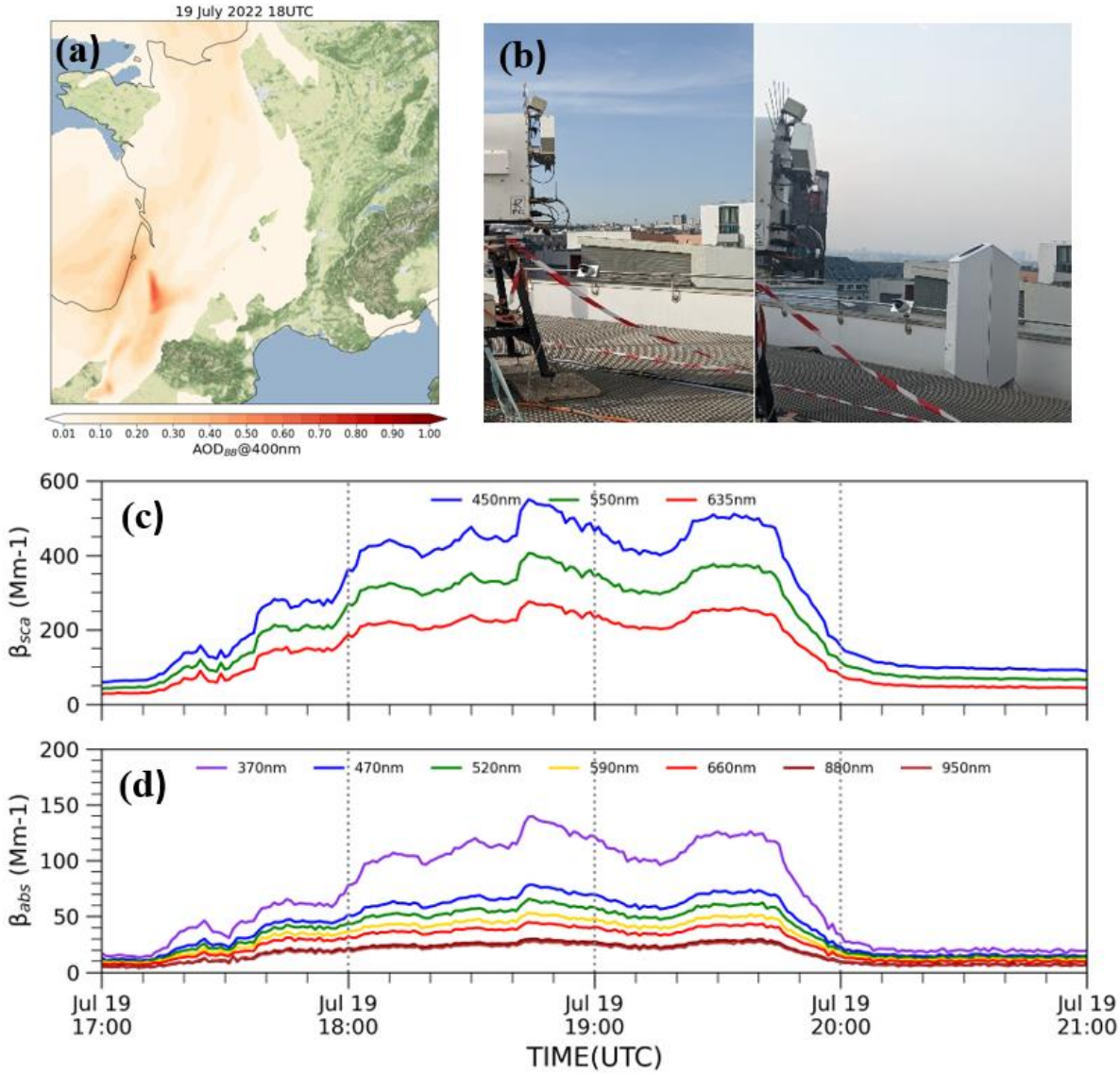

Figure 2.13: Panel (a) represents the biomass burning AOD simulated from the WRF-CHIMRE model for the 19 July at 18 UTC, panel (b) represents the visibility conditions before and after the fire plume and dust episodes of this day. Panels (c) and (d) represent the absorption and scattering coefficients measured at the Paris Rive Gauche site. Strong visibility reduction and air quality degradation, as well as a strong increase in the optical signal occurred on the evening of the 19 July 2022.

combination with a dust episode, leading to strong visibility reduction, high PM concentrations and high optical signals. An illustration of the PM_1 registered at the PRG site during the event is provided in Figure 2.11. On the afternoon of 19th July, a sudden increase of the scattering coefficient at 450 nm more than 400 Mm^{-1} and a strong spectral dependence in the absorption coefficient have been observed in coincidence with the arrival of the fire plume at the Paris urban site. Figure 2.13 shows that with the arrival of the fire plume from southern France (panel a) at about 18 UTC at the urban site, there was a strong decrease in visibility (panel b) and a strong increase in the scattering (panel

c) and absorption (panel d) coefficients, which lasted a few hours due to a sudden change in the wind direction.

To summarize, the ensemble of exceptional and contrasted conditions registered, the dataset acquired over the Ile-de-France region during the ACROSS campaign represents a unique resource to study aerosol properties and effects under the impact of diverse situations, including heatwave periods when the mixing between anthropogenic and biogenic aerosols is favoured, both by meteorological patterns and strong biogenic VOCs production.

2.2 Climatological datasets for the long-term variability analysis and the WRF-CHIMERE model validation

Along with the ACROSS field campaign measurements, other observations (including ground-based and satellite remote sensing and in-situ measurements) have been considered in this work, both to contribute to answer the main scientific questions and to validate the WRF-CHIMERE model simulation. The variables that need to be validated, both in their spatial and temporal variability, are:

- the radiation fields and meteorology;
- the aerosol mass and chemical composition ($PM_{2.5}$, PM_{10}, organic fraction in $PM_{1,}$ …);
- the aerosol spectral optical properties (e.g. complex refractive index, AOD, SSA);
- the gaseous concentration (e.g. O_3, NO_2);

In this paragraph we provide details on the main sources of data, complementary to the ACROSS observations, used to perform long-term variability analysis of aerosol load and distribution and validation of model simulations.

2.2.1 Observations from the AERONET network

The AERONET (AErosol RObotic NETwork, website) database is an international network of ground-based sunphotometers (Cimel Electronique) distributed worldwide (See Fig. 2.14) that provides columnar aerosol optical depth measurement, and retrieval of spectral optical properties, size distribution and column water vapour. The sun photometers take direct sun measurements every ~15 minutes at several wavelengths in the UV-VIS and Near Infrared (e.g. 440, 675 and 1020 nm) and are used to quantify the radiation extinct due to aerosol, allowing to estimate the AOD, with an uncertainty due to calibration ~0.02 (Sinyuk et al., 2020). Combining CIMEL measurements with the retrieval algorithm from (Dubovik et al., 2000, 2006), the AERONET network provides other columnar aerosol properties such as the single scattering albedo, the absorbing aerosol optical depth (AAOD), the complex refractive index and the volume size distribution for 22 logarithmically

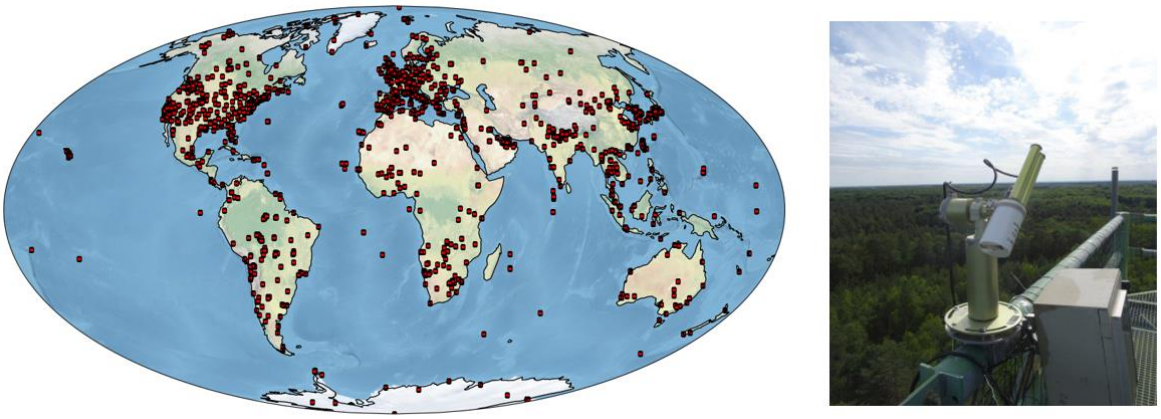

Figure 2.14: The AERONET version 3 locations across the globe (left), the AERONET sun photometer installed at the top of the 40 m tower during the ACROSS Field campaign.

equidistant discrete points with radius between 0.05µm < r < 15.0µm. The uncertainties on the retrieval has been discussed in (Dubovik et al., 2000) and more recently by (Sinyuk et al., 2020).

All the data are available on the AERONET website (https://aeronet.gsfc.nasa.gov/) with three different quality levels:

• LEVEL1.0: Raw data and unscreened.

• LEVEL1.5: A first post-processing on clouds has been applied and quality checked.

• LEVEL2.0: Quality assured and cloud screened data.

In this thesis, the AERONET Version 3 (Giles et al., 2019) Level 1.5 and 2 data of AOD and SSA have been used for diverse finalities: 1/ realise preliminary climatological studies on the AOD and SSA over the Paris and Palaiseau sites; 2/ provide the framework of validation at the European scale for the satellite high-resolution MAIAC AOD product (Chapter 3) and 3/ to evaluate the WRF-CHIMERE model AOD and SSA simulated for the ACROSS campaign (Chapter 5).

2.2.2 The MAIAC high resolution satellite data

The Multi–Angle Implementation of Atmospheric Correction (MAIAC) algorithm (Lyapustin et al., 2018), provides the aerosol optical depth at 470 and 550 nm at the spatial resolution of 1 km. The product, distributed on a daily basis, contains the collection of each Moderate Resolution Imaging Spectroradiometer (MODIS) Aqua and Terra satellites overpasses, whose number varies according to the latitude. The MAIAC algorithm benefits of the multi–angle satellite observations, retaining in memory up to 16 days of consecutive satellite overpasses, to better constrain the surface reflectance, improving the AOD retrievals in particular over complex scenes as urban areas (Chen et al., 2021; Gupta et al., 2016; Wang et al., 2010). The MAIAC aerosol algorithm uses eight different background

aerosol models over land (Look Up Tables, LUT) and it has developed a more stable algorithm that reduces the AOD bias over bright surfaces (in absence of smoke and dust), typical for the Dark Target (Remer et al., 2005, 2020) and Deep Blue (Hsu et al., 2004) algorithms (Lyapustin et al., 2018). Furthermore, MAIAC can retrieve AOD over partial cloudy conditions and distinguish between smoke and dust scenes (Lyapustin et al., 2012). The AOD from the MAIAC algorithm has been validated over different areas of the world and shown to perform better with respect to the Deep Blue, the Dark Target algorithms when compared to AERONET observations (Falah et al., 2021; Just et al., 2015; Martins et al., 2017, 2019; Mhawish et al., 2019; Qin et al., 2021; Su et al., 2023; Tao et al., 2019; Zhang et al., 2019).

The MAIAC data have been validated against the AERONET network at the European scale and used to provide climatological studies at the European, regional and local scale on the aerosol optical depth. The uncertainty attributed to the MAIAC AOD retrievals has been defined through the expected error EE = ± ($0.1AOD_{AERONET}$ + 0.05), indicating the percentage of AOD_{MAIAC} retrievals falling in the envelope (expressed in percent). The EE has been established following (Falah et al., 2021) and (Lyapustin et al., 2018), considering both absolute and relative errors and by attributing an absolute error of 0.05 and a relative error of 0.1. Results are presented in Chapter 3. These data will be also used to spatially validate the AOD from the WRF-CHIMERE model simulation. The MAIAC data are accessible at https://doi.org/10.5067/MODIS/MCD19A2.006.

2.2.3 The GEOD'AIR database

The Geod'air (GEstion des données d'Observation de la qualité de l'AIR) database (https://www.geodair.fr/) is a French air quality database, managed by the LCSQA (Laboratoire Central de Surveillance de la Qualité de l'Air) and aiming at centralizing the pollutant data on the French national territory. The data can be delivered at hourly, daily, seasonal and annual temporal resolution.

In this thesis manuscript we use the hourly data from the Aerosol Chemical Speciation Monitor (ACSM), providing the non-refractory aerosol chemical composition (nitrate, sulfate…) and the Aethalometer (AE33), providing the equivalent black carbon concentration, in order to validate the aerosol WRF-CHIMERE simulated chemical composition over France.

2.2.4 The European Environmental Agency database

The European Environmental Agency (EEA) is a network involving 38 European countries, aiming at collecting and disseminating atmospheric observables quality-assured datasets. Data are available online at https://discomap.eea.europa.eu/map/fme/AirQualityExport.html. The EEA annually

releases the E1a datasets covering data from the previous year. Hourly concentration of $PM_{2.5}$, PM_{10}, O_3, NO_2 are available.

These data are used in this thesis to spatially validate the WRF-CHIMERE simulation performed during the ACROSS campaign 2022 (Chapter 5).

2.2.5 The MIDAS and E-OBS datasets

The Met Office Integrated Data Archive System (MIDAS) and the E-OBS gridded dataset are two databases providing meteorological observables used to validate the surface meteorology of the WRF-CHIMERE simulation. The MIDAS database is available at (https://catalogue.ceda.ac.uk/uuid/220a65615218d5c9cc9e4785a3234bd0 (last access: 08 May 2024) and provides globally hourly meteorological parameters, such as the surface temperature, relative humidity and wind direction and speed, collected from ground-based stations. The E-OBS dataset (https://www.ecad.eu/download/ensembles/download.php, last access 08 May 2024), is based on an ensemble approach to regrid the scattered observations on a regular grid (at 0.25° or 0.1° spatial resolution) and disseminated on a daily basis (such as maximum and minimum temperature). The temperature, wind direction and wind speed, and the surface shortwave downwelling radiation data are a combination of in situ stations and ensemble modelling, with the aim of reconstructing the 2-D fields at the European scale. Those data are used to evaluate the WRF-CHIMERE simulation (Chapter 5).

2.2.6 Sentinel-5P TROPOMI

The TROPOspheric Monitoring Instrument (TROPOMI) (Veefkind et al., 2012) single payload of the Sentinel 5P satellite provides daily global coverage of atmospheric observables with a maximum spatial resolution of $7x3.5km^2$ at near nadir. It is a push-broom passive remote sensing instrument and measures the reflected sunlight at the top of the atmosphere (TOA) from the UV to the infrared part of the light spectrum. TROPOMI data are available at the Copernicus Open Access Hub https://scihub.copernicus.eu/ (last access: 08 May 2024). Among the available Level 2 data, the one used in the present work is the Formaldehyde (HCHO) total column concentration (L2_HCHO) used to validate the simulates HCHO from the WRF-CHIMERE simulation, taken as a proxy of isoprene concentrations. The TROPOMI HCHO number density (units of molecules per cm^2) was bias-corrected using Oomen et al. (2024) and converted to Dobson Unit (DU). We did not apply averaging kernels as in Oomen et al. (2024), because we think that the bias correction already includes a large part of the lack of sensitivity of TROPOMI in the lower layers, and then its application would

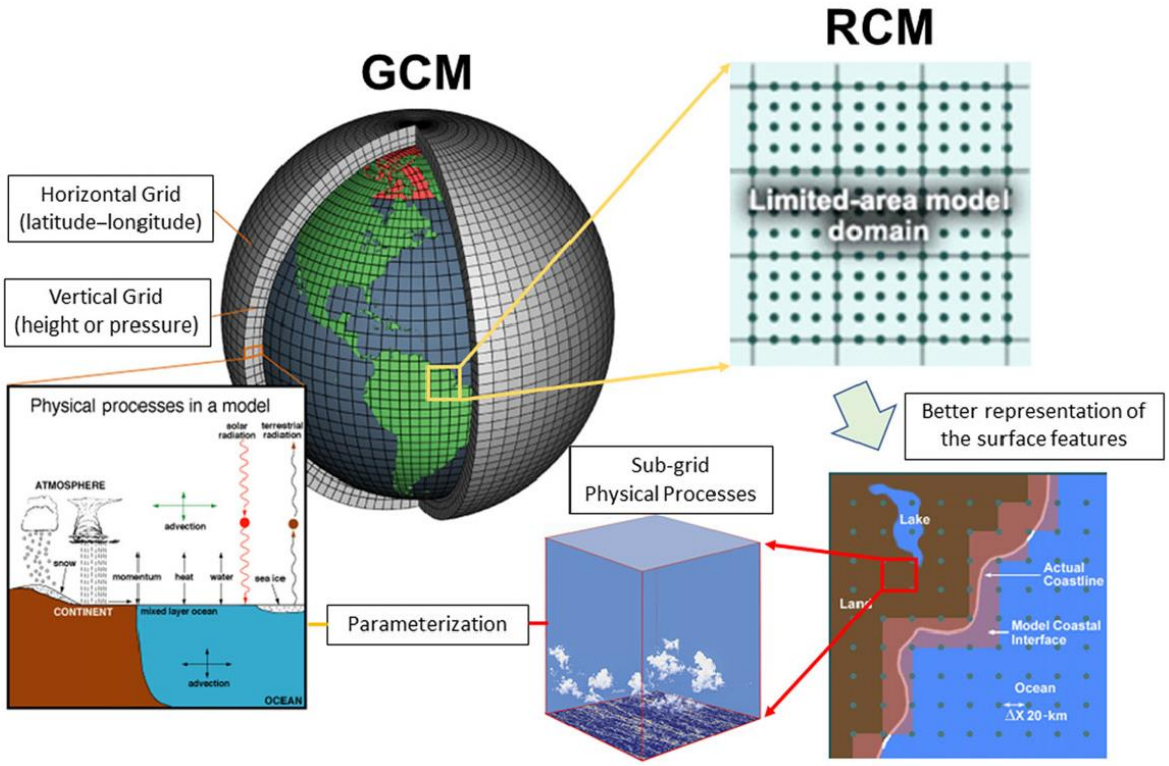

Figure 2.15: Schematic representation of global climate model (GCM) and a regional climate model (RCM). The grid has a spatial and vertical resolution. Physical processes that occur on a lower spatial resolution compared to that of the model (such as convection) have to be parametrised. From Ambrizzi et al. (2019).

overcorrect the data. Finally, in order to perform the model validation, the WRF-CHIMERE model and the TROPOMI data have been regridded to a common 0.5°x0.5° spatial resolutions.

2.3 The WRF-CHIMERE model

2.3.1 General overview of the WRF-CHIMERE model and setup for the ACROSS campaign simulation

The CHIMERE model (https://www.lmd.polytechnique.fr/chimere/, last access: 08 May 2024) is a 3-D regional Eulerian chemistry transport model (CTM), used both for research and operational purposes, and developed between the LMD (Laboratoire de Météorologie Dynamique) and the LISA (Laboratoire Interuniversitaire des Systèmes Atmosphériques). It can simulate gas and aerosol concentrations and optical properties with a spatial resolution between 1 and 100 km.

The basis of a CTM relies on solving the continuity equation of infinitesimal variations of the simulated chemical species mixing ratios (C_i, i.e. gas and aerosol). The equation can be decomposed as the sum of the different production (P) and losses (L) terms due to advection, turbulent mixing, dry and wet deposition, the chemistry and the emissions developed within the model as:

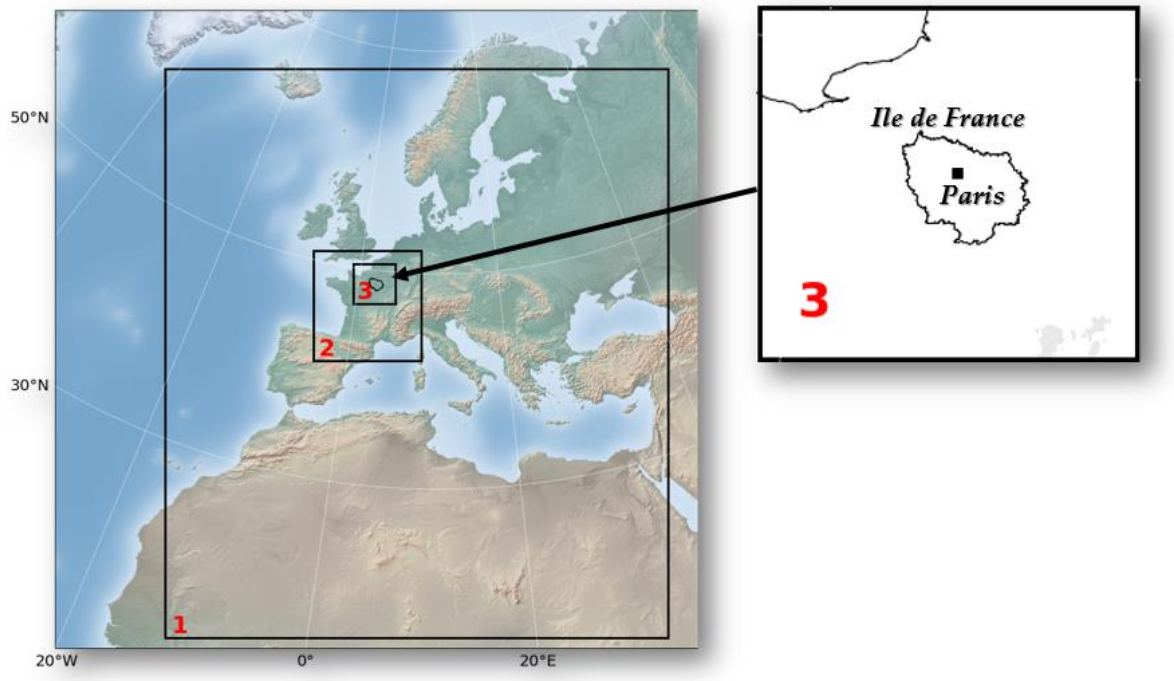

Figure 2.16: The three nested domains configured for the WRF-CHIMERE simulation of the ACROSS campaign 2022. The first domain (1) is at 30x30km spatial resolution, the second (2) at 6x6 km spatial resolution, and the third (3) at 2x2 km spatial resolution covering the Ile-de-France region.

$$\frac{dC_i}{dt} = P - L = \left[\frac{dC_i}{dt}\right]_{advection} + \left[\frac{dC_i}{dt}\right]_{mixing} + \left[\frac{dC_i}{dt}\right]_{deposition} + \left[\frac{dC_i}{dt}\right]_{chemistry} + \left[\frac{dC_i}{dt}\right]_{emissions} \quad (2.1)$$

Solving this equation provides the concentration of the species C_i at a given time and space. In order to solve the ensemble of equations for a set of species i, it is necessary to discretize and numerically solve them on a finite spatial and vertical grid. Figure 2.15, shows an illustration of discretized global and regional climate models grids. The finite spatial resolution imposes that processes occurring at small spatial scales (e.g. physical sub-grid processes) must be parameterized, thus becoming a potential significant source of uncertainty in models. Eulerian CTMs numerically resolve these equations for any species at a given time and space to provide a 3-D resolved output.

The first CHIMERE version was released in the 1997 as a quasi-box model and capable of simulating only the gas-phase chemistry over the Paris area (Vautard et al., 2001). Further developments have followed, such as the possibility of simulating 3D aerosols and gas concentrations, or including the ONLINE coupling with a meteorological model, making it a French national tool. In this thesis we used the CHIMERE v2020r3 version (Menut et al., 2021), which is coupled with the WRF 3.7.1 meteorological model version (Skamarock et al., 2008), through the OASIS-MCT coupler (Craig et al., 2017). The coupling capability allows the meteorological model to receive aerosol concentration

Inputs	Description	Resolution
Meteorology	WRF v. 3.7.1 model forced with the GFS initial and boundary condition	1°x1° (NCEP) WRF nested domains at 30, 6, 2 km
Initial and boundary conditions for chemistry	The CAMS reanalysis (EAC4)	0.75°x0.75°
Anthropogenic emissions	CAMS-GLOB-ANT v5.3	0.1°x0.1°
Biogenic emissions	Online with the MEGAN v. 2.1 model	WRF nested domains at 30, 6, 2 km
Fire Emissions	CAMS Global Fire Assimilation System (GFAS)	0.1°x0.1°
Land use	GLOBCOVER	~300m

Table 2.4: Summary of the CHIMERE model inputs for the simulation for the ACROSS campaign 2022

fields and spectral optical properties from CHIMERE, which in turn, by taking into account aerosol-radiation interactions, update the radiation fields.

In order to run a model simulation, it is necessary to define the simulation domain. Three nested domains respectively at 30, 6, and 2 km resolution have been configured for the 15 June-25 July 2022 ACROSS period simulation (see Figure 2.16). The nesting is a one-way, allowing only larger domain (i.e. lower spatial resolution) simulations to provide the boundary conditions for the higher spatial resolution domain. The simulations for each domain are therefore sequential (from the lower to the higher resolution domain). The objectives of high-resolution simulations (i.e. 2 km spatial resolution) over the Ile-de-France region are to perform a more detailed study of the biogenic and anthropogenic environments during the ACROSS field campaign. Such a fine resolution is also necessary in order to make the model simulations as much as possible representative for the observation sites, from which measurements are used for model evaluation. In order to run the simulation, it is necessary to provide the meteorological fields, the emissions (biogenic, anthropogenic and fire) and the chemical initial and boundary conditions (e.g. from global models for the largest domain). A summary detailing all inputs (meteorology, boundary conditions…) used for the WRF-CHIMERE simulation considered in this work is available in Table 2.4.

The WRF model ((Skamarock et al., 2008), forced with the NCEP initial and boundary conditions) provides the meteorological fields to CHIMERE.

The anthropogenic emissions (CO, NH_3, BC, OC…) are provided by the CAMS-GLOB-ANT product for 17 sectors, 36 species (Soulie et al., 2023) and then reported to the 11 SNAP (Selected Nomenclature for reporting of Air Pollutants) sectors of CHIMERE model through the emiSURF2020r3 pre-processor (provided by the CHIMERE community, https://www.lmd.polytechnique.fr/chimere/ , last access: 08 May 2024).

Flag/Parameter	Description
Number vertical levels	15 for the 30km and 6km domains, 10 for the 2km domain
Top layer pressure	300 hPa for the 30km and 6km domains, 500 hPa for the 2km domain
Vertical advection scheme	(iadvv=2) The first-order antidissipative scheme (Lachatre et al., 2020)
Vertical wind diagnostic	False. Vertical winds are directly interpolated from the WRF model.
Chemistry mechanism	(mecachim=3) SAPRC-07A (Carter, 2010)
Number of aerosols bins	10 between 0.1 and 10µm
Microphysics parametrisation	(mp_physics=8) Thompson et al. scheme: A new scheme with ice, snow and graupel processes suitable for high-resolution simulations (Thompson et al., 2008)
Boundary layer	(bl_pbl_physics=1) Yonsei University scheme (Hong, 2010)
Secondary organic aerosol formation	(soatyp=7 and carb=3) VBS scheme with functionalisation and fragmentation for POA and SOA (Cholakian et al., 2018, 2019)

Table 2.5: Summary of the main CHIMERE configuration parameters for the microphysics, dynamics and the chemistry of gas and aerosol for the ACROSS campaign 2022.

Biogenic emissions are simulated with the Model of Emissions of Gases and Aerosols from Nature (MEGAN) v.2.1 routine (Guenther et al., 2006) implemented within the CHIMERE model. Emissions are calculated as a function of landuse. For each forest type and climate zone, an average tree species distribution is used, and standard emission factors are given for each species. Their temporal variation of these emissions then depends on several parameters: the short-wave radiation, the surface temperature simulated by the WRF model and the leaf area index (LAI) derived from MODIS observations (Yuan et al., 2011). In this thesis we use the LAI referred to the 2013 year with a temporal resolution of 8-days and the emission factors from Sindelarova et al. (2014). The emission scheme does not consider the relative humidity dependence (at least the version we use here).

Fire emissions are taken from the CAMS Global Fire Assimilation System (GFAS, Kaiser et al., 2012) and processed with the CAMS FIRE v2020r1 pre-processor (provided by the CHIMERE community (https://www.lmd.polytechnique.fr/chimere/, last access: 08 May 2024). Once the inputs prepared, it is important to compile the parameter file, which contains the parameterisations that the model adopts for the dynamics, the physics and the chemistry to follow the gas and aerosol concentration spatial and temporal evolution. A summary of the main parametrization chosen for the ACROSS simulation is available in Table 2.5 and described in the following.

- **Gas-phase chemistry**

There are three main gas-phase chemical schemes within the CHIMERE model: MELCHIOR1, MELCHIOR2 and SAPRC-07A. The MELCHIOR1 scheme contains around 80 gaseous species and 300 reactions and its reduced version MELCHIOR2 with 44 species and 120 reactions. The SAPRC-07A scheme is a reduced version of the original SAPRC-07 (Carter, 2010) and that contains 72 species and 218 reactions (Mailler et al., 2017). The SAPRC scheme has been adopted for the

ACROSS field campaign simulation based on the fact that the SAPRC scheme shows a more detailed VOCs description compared to the MELCHIOR scheme implemented in the standard version of CHIMERE.

- **Aerosol microphysics**

The CHIMERE model can simulate the aerosol concentrations through a sectional bin approach and for different aerosol species depending on the aerosol chemistry scheme. The main species simulated are: black carbon, organic aerosol, dust, anthropogenic primary particulate matter (PPM), nitrate, sulfate and ammonium, sea salt (including sodium and chloride) and water. Note that organic aerosol consists in a number of different species with different physico-chemical properties depending on the organic aerosol scheme chosen (see below). The default 10 sectional bins between about 0.01 and 40 µm have been chosen. The diameter between the upper and lower boundary of a bin varies in general by a factor of two.

The evolution of the aerosol size distribution is regulated by the aerosol microphysical processes such as nucleation, absorption and coagulation.

The nucleation involves the aggregation of gas molecules to form new aerosol clusters. In the CHIMERE model the parameterisation of Kulmala et al. (1998) for sulfuric acid is implemented, neglecting nucleation for organic species.

The coagulation is the process in which particles collide and adhere to each other to form bigger particles, the different coagulation terms are based on Debry et al. (2007). Gas-particle partitioning is based on Pandis et al. (1993). Thermodynamic modules are applied to calculate the gas-particle concentration at equilibrium.

The ISORROPIA model (Nenes et al., 1998) is used to calculate the equilibrium concentration of semi-volatile inorganic species and the water content in each size bin, assuming that only inorganic species and sea salt may be sufficiently hygroscopic to absorb water. For the semi volatile organics the equilibrium concentration follows Pankow (1994) and it shows a temperature dependence.

- **The VBS scheme**

The number of the organic aerosol species simulated by the model depends on which scheme is adopted to reproduce the complexity of the organic fraction. Indeed, simplified representations are used in CTM models due to the high computational demand, and because details of an explicit representation at molecular level are in general not known from laboratory experiments.

In this thesis we adapted the Volatility set basis (VBS) scheme (See Fig 2.17) to simulate the POA and SOA. The VBS was first conceptualised by Donahue et al. (2006) and it classifies organic aerosol and more generally organic matter into bins according to its volatility. By default, a bin covers a volatility range of one order of magnitude. Given their volatility, expressed as a saturation

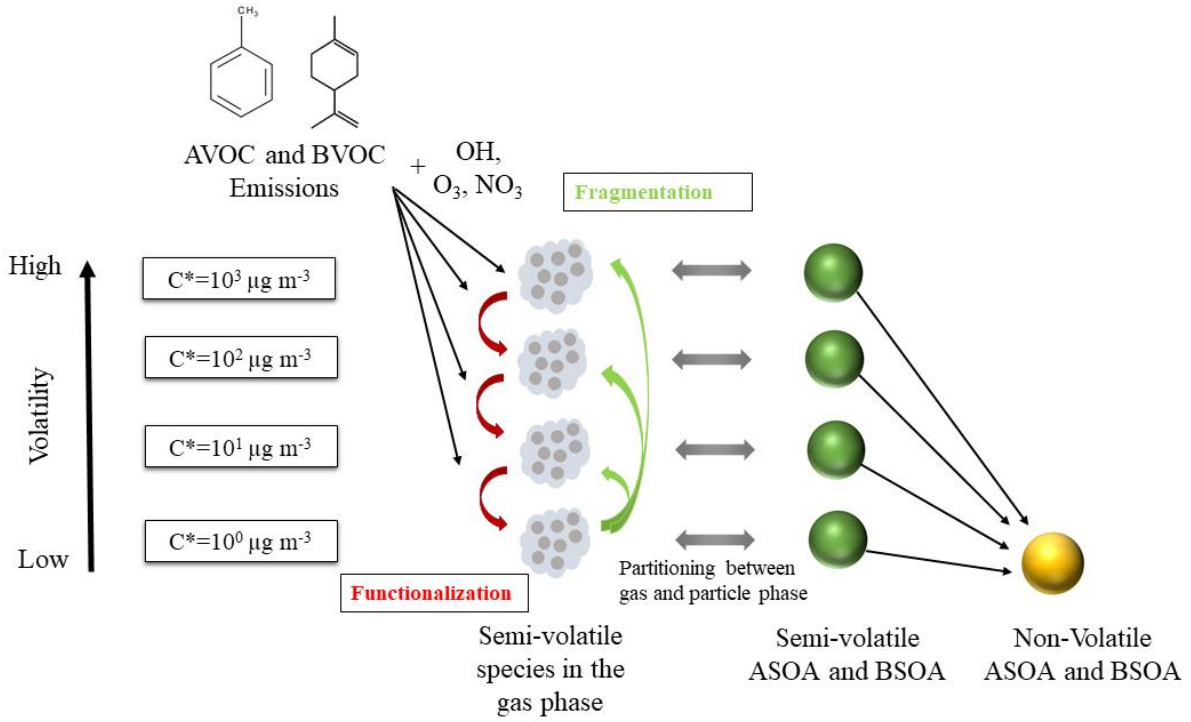

Figure 2.17: Schematic representation of the VBS scheme adapted for the biogenic and anthropogenic SOA modelling within the CHIMERE model for the ACROSS campaign. Anthropogenic and biogenic VOCs are emitted within the 4 bins available at different saturation concentration C*, allowing for functionalisation (lower volatility) and fragmentation (higher volatility) as well as non-volatile aerosol formation.

concentration C_i^*, and the abundance of seed aerosols (C_{OA}), organic species can distribute between the aerosol ($C_{i,aer}$) and the gas phase ($C_{i,gas}$).

$$\frac{C_{i,aer}}{C_{i,gas}} = \frac{C_{OA}}{C_i^*} \quad (2.2)$$

As a first consequence, primary organic aerosol emissions, which are taken by default as non-volatile in traditional aerosol schemes, are affected to specific volatility bins, and partly evaporate, as C_{OA} decreases.

Second, organic compounds present in the gas phase can change their volatility class, they can acquire lower volatility by functionalisation (being more present in the aerosol phase then), or larger one by fragmentation of the carbon chains (being less present in the aerosol phase then).

One of the VBS schemes available within CHIMERE is based on Cholakian et al. (2019) which allows for the fragmentation (transfer to higher volatility bins) and the functionalisation (transfer to lower volatility bins) processes, as well as formation of non-volatile aerosols unable to return to the gas phase. The intermediate-volatile organic compounds (IVOC) and the semi-volatile organic compounds (SVOC) are partitioned into nine volatility bins according to their saturation concentration C^* ranging from 0.01 to 10^6 µgm^{-3}. Therefore, primary emitted organic aerosols are splitted into the nine volatility bins. The POA vaporized into the gas phase can be oxidized by OH

and form the oxidized POA, thus OPOA, O2POA, O3POA (2 and 3 stands for more functionalized products), or become non-volatile and form the oxidized non-volatile POA (ONVSOA). Only VOC with a saturation concentration lower than 10^3 μgm^{-3} are allowed to be converted to the particle phase, because under current organic aerosol concentrations, roughly not exceeding the order of 100 μgm^{-3}, the fraction of mass present in the aerosol phase would be very low. This reduces the number of size bins for a category to six. The total number of tracer species due to POA oxidation is therefore 30.

Four different volatility bins in the 1 to 1000 μgm^{-3} saturation concentration C^* range and a non-volatile species have been implemented to represent the anthropogenic SOA (ASOA) and the biogenic SOA (BSOA). A schematic representation of the VBS scheme is presented in Figure 2.17. Fragmentation occurs at 75% rate independently of the volatility following (Shrivastava et al., 2015), leaving the 25% to functionalisation. These percentages are based on the best agreement between simulated and measured SOA in chamber experiments and described in (Shrivastava et al., 2013). Biogenic and anthropogenic non-volatile secondary organic aerosols (BNVSOA and ANVSOA) are formed attributing a reaction constant corresponding to a 1h of lifetime (Cholakian et al., 2018). Chemical reactions allow both for the high-NO_x and low-NO_x regimes, with the possibility of forming biogenic and anthropogenic non-volatile species through OH, NO_3 and O_3 oxidations pathways. The total number of aerosol species due to AVOC and BVOC simulated is 10 (5 for ASOA and 5 for BSOA). This VBS aerosol scheme contains therefore 40 species, which multiplied by 10 aerosol bins lead to 400 simulated species for the SOA.

- **The WRF-CHIMERE online radiative coupling**

The WRF-CHIMERE model can be run in two different ways: offline and online. The offline mode implies first to independently perform a WRF meteorological simulation which will be used as input by the subsequent CHIMERE simulation. On the other hand, the online coupling allows for an interaction at each physical time step between the two models, with the possibility of simulating the feedbacks on the meteorology and chemical species. In this work we adopted a physical time step of ten minutes with a maximal permitted Courant-Friedrich-Levy (CFL) parameter of 0.4.

As a function of a positive or negative DRE at each vertical level, each component of the Earth system responds differently at the perturbation, which in turn may translate in a change in the surface temperature to react to the radiative imbalance (Bellouin et al., 2020). This also impacts the planetary boundary layer development, humidity and cloud distribution and finally wind speed.

This translates into an impact on aerosol emissions as well, such as those from mineral dust and sea salt (which are wind-dependent). The WRF-CHIMERE direct coupling provides therefore the possibility to estimate the ARI, which includes both the direct effect and the semi-direct effect on clouds (even if this effect is not activated here).

Coupling case	Radiative effect	Description
cpl=0	-	No coupling between the WRF and the CHIMERE model. The simulations are performed consecutively.
cpl=1	-	Coupling between the WRF and the CHIMERE model. The two simulations are performed in parallel and meteorological fields are sent from WRF to CHIMERE every physical time step through the OASIS coupler.
cpl=2	Direct effect	Same as cpl=1 with the addition of the CHIMERE AOD, SSA and g sent to WRF and interpolated on the WRF vertical levels impacting the radiative calculations and the meteorology.
cpl=3	Indirect effect	Same as cpl=1 with the addition of the CHIMERE aerosol number distribution, hygroscopicity and ice nuclei sent to WRF and interpolated on the WRF vertical levels impacting the radiative calculations and the meteorology
cpl=4	Direct+Indirect effect	Combination of cpl=2 and cpl=3

Table 2.6: Summary of the possible coupling options between the WRF and the CHIMERE model. In bold, the options used in this thesis manuscript are highlighted.

The downward and the upward radiation fluxes necessary to estimate the direct radiative effect are simulated by the Rapid Radiative Transfer Model for GCMs (RRTMG) included in the WRF model (Iacono et al., 2008). Additionally, the options cpl=3 and cpl=4 include the indirect effect on radiation and clouds, impacting the cloud microphysics, the CCN concentration and precipitation patterns (ACI). In this thesis we adopted the Thompson microphysical scheme to simulate the ice, snow and graupel processes (Thompson et al., 2008). The different coupling (cpl) configurations available in the CHIMEREv2020r3 version are shown in Table 2.6.

In this thesis project, the cpl=1 and the cpl=2 configurations have been used to simulate the aerosol direct radiative effect. The cpl=1 allows for simulating the aerosol concentrations without feedbacks from CHIMERE to WRF, permitting WRF to simulate a pristine atmosphere (i.e. AOD=0). The cpl=2, allows CHIMERE to send aerosol spectral optical properties to WRF, impacting the radiation and the meteorology. Therefore, following the notation of Sec 1.3 the direct radiative effect at the top of the atmosphere has been estimated as:

$$DRE_{TOA}^{net} = \Delta F_{TOA}^{cpl=2} - \Delta F_{TOA}^{cpl=1} \quad (2.3)$$

Where F is the downward or upward flux. We define this procedure as the "ONLINE" method due to the online exchange between WRF and CHIMERE. Since this approach allows for the adjustments in the meteorology, the aerosol direct effect simulated includes the semi-direct effect (SDRE).

Since we are interested in simulating the direct effect and above all the contribution of the various aerosol species to the DRE, I developed an offline interface between the RRTMG and the CHIMERE model outputs (allowing for sensitivity tests) and details are provided in Sec. 2.3.4.

2.3.2 The WRF-CHIMERE refractive index database and its update for the ACROSS campaign 2022

In order to evaluate the shortwave spectral optical properties and therefore the aerosol direct radiative effect, the WRF-CHIMERE model needs as input the complex refractive index (CRI) data at 200, 300, 400, 600 and 1000 nm and the density for each simulated species. Table 2.7 shows the refractive index database from the CHIMERE v2020r3 standard version. The BSOA, ASOA and OPOA have the same spectral refractive index, assumed to be constant with the wavelength.

As discussed in Sec. 1.3.2, the complex refractive index of SOA, strongly depends on wavelength, on the different precursors and oxidations patterns. In order to better simulate the spectral optical properties of SOA from biogenic and anthropogenic precursors and take into account their absorption properties, as discussed in Sec 1.3.2, it has emerged the need to update the CRI data for ASOA, BSOA and OPOA at input to CHIMERE. A summary of the modified CRI is provided in Table 2.8. However, since we do not dispose of enough literature values, only average CRI will be attributed for each aerosol species, thus independent of the oxidation pathway.

In addition, for a more refined treatment, we would have needed to add new specific compounds in the aerosol scheme still increasing the computational demand. Concerning the SOA, the CHIMERE

Species	**Complex refractive index**					
	200	300	400	600	1000	Density
λ	[nm]	[nm]	[nm]	[nm]	[nm]	[g/cm^3]
BCAR	1.95-7.9x10^{-1}i	1.95-7.9x10^{-1}i	1.95-7.9x10^{-1}i	1.95-7.9x10^{-1}i	1.95-7.9x10^{-1}i	1.8
PPM	1.53-8.0x10^{-3}i	1.52-8.0x10^{-3}i	1.52-8.0x10^{-3}i	1.51-8.0x10^{-3}i	1.50-8.0x10^{-3}i	2.3
POA	1.53-9.0x10^{-2}i	1.53-8.0x10^{-3}i	1.53-5.0x10^{-3}i	1.53-6.3x10^{-3}i	1.53-1.6x10^{-2}i	1.3
OPOA	1.56-3.0x10^{-3}i	1.56-3.0x10^{-3}i	1.56-3.0x10^{-3}i	1.56-3.0x10^{-3}i	1.56-3.0x10^{-3}i	1.5
ASOA	1.56-3.0x10^{-3}i	1.56-3.0x10^{-3}i	1.56-3.0x10^{-3}i	1.56-3.0x10^{-3}i	1.56-3.0x10^{-3}i	1.5
BSOA	1.56-3.0x10^{-3}i	1.56-3.0x10^{-3}i	1.56-3.0x10^{-3}i	1.56-3.0x10^{-3}i	1.56-3.0x10^{-3}i	1.5
Cl^-	1.38-8.7x10^{-7}i	1.38-3.5x10^{-7}i	1.37-6.6x10^{-9}i	1.36-1.2x10^{-8}i	1.35-2.6x10^{-5}i	1.5
Na^+	1.38-8.7x10^{-7}i	1.38-3.5x10^{-7}i	1.37-6.6x10^{-9}i	1.36-1.2x10^{-8}i	1.35-2.6x10^{-5}i	1
DUST	1.53-5.5x10^{-3}i	1.53-5.5x10^{-3}i	1.53-2.4x10^{-3}i	1.53-8.9x10^{-4}i	1.53-7.6x10^{-4}i	2.3
NH_4^+	1.53-5.0x10^{-4}	1.52-5.0x10^{-4}	1.52-5.0x10^{-4}	1.52-5.0x10^{-4}	1.52-5.0x10^{-4}	1.7
NO_3^-	1.53-6.0x10^{-3}	1.53-6.0x10^{-3}	1.53-6.0x10^{-3}	1.53-6.0x10^{-3}	1.53-6.0x10^{-3}	1.7
SO_4^{2-}	1.50-1.0x10^{-8}	1.47-1.0x10^{-8}	1.44-1.0x10^{-8}	1.43-1.3x10^{-8}	1.42-1.2x10^{-6}	1.8
WATER	1.35-2.0x10^{-9}	1.34-2.0x10^{-9}	1.34-1.8x10^{-8}	1.33-3.4x10^{-8}	1.33-3.9x10^{-7}	1

Table 2.7: Summary of the CHIMERE refractive indices and densities from the v2020r3 version

Species	Complex refractive index				
λ	200 [nm]	300 [nm]	400 [nm]	600 [nm]	1000 [nm]
BB-POA[a]	$1.70\text{-}1.0\times10^{-1}i$	$1.70\text{-}6.0\times10^{-2}i$	$1.70\text{-}3.0\times10^{-2}i$	$1.70\text{-}2.0\times10^{-2}i$	$1.70\text{-}7.0\times10^{-3}i$
OPOA[b]	$1.53\text{-}1.0\times10^{-4}i$	$1.53\text{-}1.0\times10^{-4}i$	$1.53\text{-}1.0\times10^{-4}i$	$1.53\text{-}1.0\times10^{-4}i$	$1.53\text{-}1.0\times10^{-4}i$
ASOA[c]	$1.63\text{-}4.0\times10^{-2}i$	$1.58\text{-}2.0\times10^{-2}i$	$1.55\text{-}5.0\times10^{-3}i$	$1.53\text{-}1.0\times10^{-4}i$	$1.52\text{-}1.0\times10^{-4}i$
BSOA[d]	$1.6\text{-}5.0\times10^{-3}i$	$1.55\text{-}1.2\times10^{-3}i$	$1.52\text{-}1.0\times10^{-4}i$	$1.50\text{-}1.0\times10^{-4}i$	$1.50\text{-}1.0\times10^{-4}i$

[a](Saleh et al., 2015; Wang et al., 2018)
[b]Real part as POA, imaginary part non absorbing
[c](Liu et al., 2015a)
[d](Liu et al., 2013, 2015a)

Table 2.8: CHIMERE refractive indices update for some specific aerosol species and introduction of a new aerosol species (BB-POA) to trace the primary biomass burning aerosols.

model attributes the same spectral invariant refractive index (1.56-0.003i) both to BSOA and ASOA CRI (Table 2.7).

However, (Liu et al., 2013, 2015a) found by laboratory experiments on major anthropogenic and biogenic precursors, that the anthropogenic derived SOA shows a ten times stronger imaginary component compared to the biogenic SOA, under different NO_x conditions, which might enhance the light absorption. Furthermore, they observed a strong spectral dependence on the BSOA and ASOA imaginary component of the CRI, with maximum in the UV. The BSOA and ASOA CRI have been extracted from (Liu et al., 2013, 2015a) since they retrieved the CRI for anthropogenic and biogenic precursors that provide high SOA yields. The imaginary ASOA refractive index has been taken as the logarithmic mean of the curves available in Figure 4 of (Liu et al., 2015a), while the real part is based on the average values in Figure 2 of (Liu et al., 2015a). The imaginary part of the BSOA has been taken as the logarithmic mean of the curves available in Figure 4 of (Liu et al., 2015a), while the real part has been taken from (Liu et al., 2013). For POA, we kept the CRI values from the standard CHIMERE version in Table 2.7 as we did not find any specific literature warranting for updates. The real part of OPOA has the same characteristics of POA, while the imaginary component has been considered non-absorbing at all the wavelengths, in the absence of any specific literature indicating absorption.

A new aerosol tracer, having primary organic aerosols features, has been introduced within the CHIMERE model to trace the biomass burning plumes (BB-POA) during the ACROSS simulation from the CAMS fire emissions. The complex refractive index for this species has been assumed following the formulation of (Saleh et al., 2015), which regardless the chemical age and fuel type, identified a relationship between the organic aerosol effective absorptivity and the BC-to-OA ratio

for biomass and biofuel burning OA that can be easily applied to our simulations. The imaginary component is parametrised as:

$$k_{OA} = k_{OA,550}\left(\frac{550}{\lambda}\right)^{w} \quad (2.4)$$

$$k_{OA,550} = 0.016\log_{10}(\mathrm{BC-to-OA}) + 0.04 \quad (2.5)$$

$$w = \frac{0.21}{\mathrm{BC-to-OA}+0.07} \quad (2.6)$$

A BC-to-OA=0.05 has been assumed following (Wang et al., 2018). All the aforementioned updates have been taken into account to perform the CHIMERE simulation for the ACROSS campaign 2022.

2.3.3 The spectral optical properties evaluation under external and core-shell assumptions

In this section, we will present the different optical models and mixing state assumptions made during this thesis work for regional model simulations.

Three different models, simulating the external and core-shell mixing state are available: The WRF-CHIMERE optical routine, the FlexAOD (Curci, 2012) and the OPTSIM (Stromatas et al., 2012) models, which we all will present hereafter.

- **The WRF-CHIMERE and spectral optical properties (external mixing, ONLINE)**

The WRF-CHIMERE model provides the aerosol spectral optical properties online and under the external mixing assumption. The WRF-CHIMERE aerosol concentrations are interpolated on a finer size distribution of 12 bins between 40 nm and 10µm (as compared to the original 10 bins between about 10nm and 40 µm) and the extinction efficiencies (Q_{ext}), the mean radius (r_{mean}) and the single scattering albedo of each aerosol species within the bin are calculated following the Mie theory and the numerical algorithm from (Mishchenko et al., 1999) for polydisperse spherical particles. Therefore, every species has its own refractive index and the spectral AOD is calculated at each layer and for each species and each size bin, then aggregated as:

$$AOD(\lambda) = \sum_{\mathrm{ibin}=1}^{\mathrm{nbin}}\sum_{\mathrm{ilev}=1}^{\mathrm{nlev}}\sum_{\mathrm{ispec}=1}^{\mathrm{nspec}}\frac{3}{4}\frac{Q_{ext}(\lambda,\mathrm{ispec,ibin})}{r_{mean}(\mathrm{ibin})\rho(\mathrm{ispec})}\mathrm{conc}(\mathrm{ibin},\mathrm{ilev},\mathrm{ispec})\Delta z(\mathrm{ilev}) \quad (2.7)$$

Where nbin is the total number of size bins, nlev is the total number of vertical layers and nspec is the total number of species, while ρ is the aerosol species' density. The terms "conc" and Δz stand for the aerosol concentration and layer thickness respectively. Vertically resolved optical properties are needed for the radiative calculations. The vertically-resolved SSA is calculated as:

$$\mathrm{SSA}(\lambda,z) = \frac{\sum_{\mathrm{ibin}}^{\mathrm{nbin}}\sum_{\mathrm{ispec}}^{\mathrm{nspec}}\mathrm{SSA}(\lambda,\mathrm{ispec})\mathrm{AOD}(\lambda,\mathrm{ispec,ibin},z)}{\mathrm{AOD}(\lambda)} \quad (2.8)$$

While g follows the formulation of (Irvine, 1963):

$$g(\lambda, z) = \frac{\sum_{ibin}^{nbin} \sum_{ispec}^{nspec} \frac{P_1(\lambda,ispec,ibin)}{3} SSA(\lambda) AOD(\lambda,ispec,ibin,z)}{\sum_{ibin}^{nbin} \sum_{ispec}^{nspec} SSA(\lambda) AOD(\lambda,ispec,ibin,z)} \quad (2.9)$$

where P_1 is the first coefficient of the Legendre polynomials (i.e. the first moment of the scattering phase function).

- **The FlexAOD optical model (external mixing, OFFLINE)**

The Flexible Aerosol Optical Depth (FlexAOD, (Curci, 2012)) is an optical model that provides offline spectral optical properties under the external mixing assumption starting from the WRF-CHIMERE output.

The spectral optical properties are calculated in a similar way compared to the WRF-CHIMERE model with the exception of the aerosol size distribution which is maintained at its original 10 bins resolution. The AOD, SSA and g are calculated as:

$$AOD(\lambda, z) = \sum_{ispec=1}^{nspec} AOD(\lambda, ispec) \quad (2.10)$$

$$SSA(\lambda) = \frac{1}{AOD(\lambda)} \sum_{i=1}^{nspec} AOD(\lambda, ispec) SSA(\lambda, ispec) \quad (2.11)$$

$$g(\lambda, ispec) = \frac{1}{AOD(\lambda,ispec) SSA(\lambda,ispec)} \sum_{i=1}^{nspec} AOD(\lambda, ispec) SSA(\lambda, ispec) g(\lambda, ispec) \quad (2.12)$$

This model provides the spectral optical properties for the offline direct radiative effect described in Sec. 2.3.4.

- **The OPTSIM optical model (core-shell internal mixing, OFFLINE)**

The OPTical properties SIMulation (OPTSIM, (Stromatas et al., 2012)) model provides the spectral aerosol optical properties under both homogeneous and core-shell assumption. In this thesis we used the OPTSIM model to perform calculations under the core-shell assumption.

The core-shell (CS) model is described as an aerosol particle composed of an insoluble core material (e.g. black carbon), surrounded by soluble material (e.g. sulfate). Assuming spherical particles, the mass of the core (M_{core}) and the shell (M_{shell}) can be expressed as:

$$M_{core} = \rho_{core} \frac{4}{3} \pi r_{core}^3 \quad (2.13)$$

$$M_{shell} = \rho_{shell} \frac{4}{3} \pi (r_{shell}^3 - r_{core}^3) \quad (2.14)$$

Where ρ_{core} and r_{core} and ρ_{shell} and r_{shell} are respectively the average density and the radius of the core and the shell (r_{shell} is the sum of the radius of the core and the coating thickness). Dividing the M_{shell}/M_{core} it is possible to express the r_{core} as a function of the r_{shell} as:

$$\frac{M_{shell}}{M_{core}} = \frac{\rho_{shell}}{\rho_{core}} \left(\left(\frac{r_{core}}{r_{shell}} \right)^{-3} - 1 \right) \quad (2.15)$$

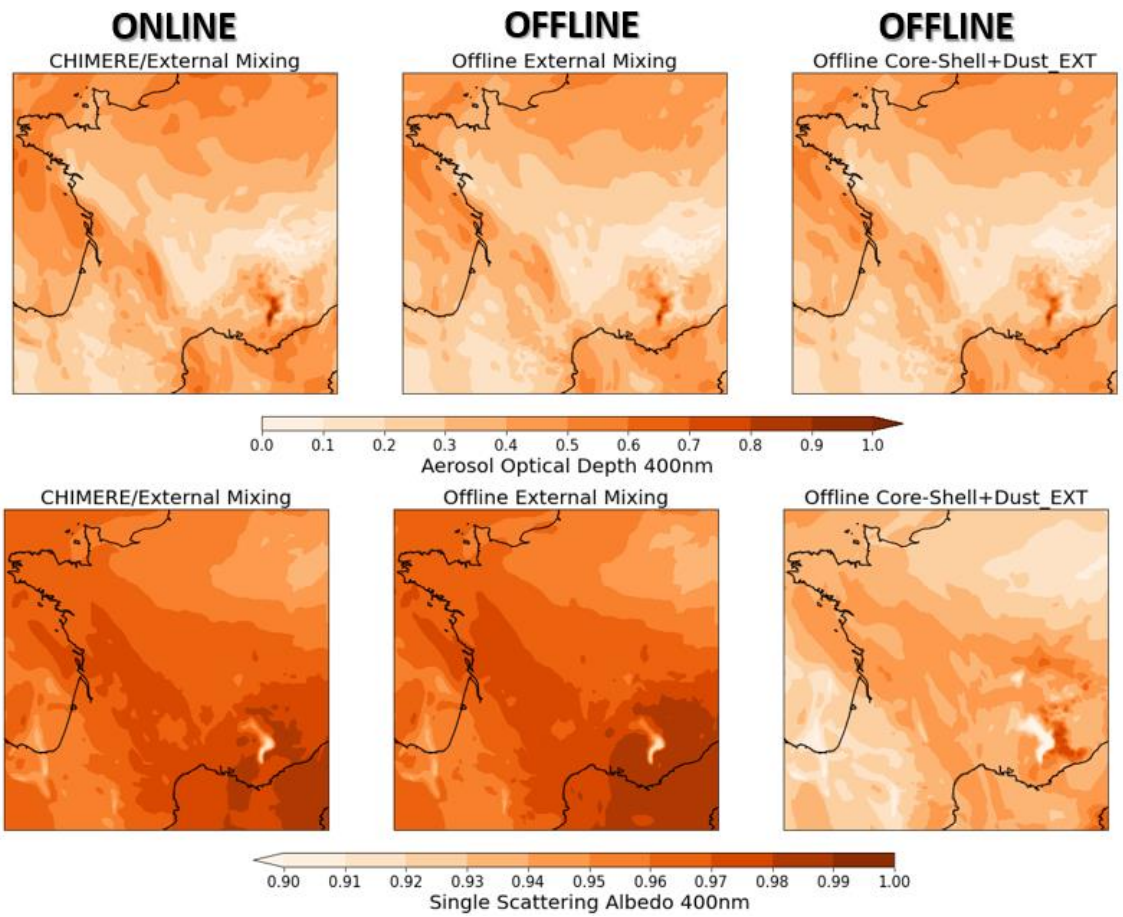

Figure 2.18: Aerosol optical depth (AOD) and single scattering albedo for the 18 June at 12 UTC simulated from the CHIMERE, FlexAOD and OPTSIM models. CHIMERE and FlexAOD provides the AOD and SSA under external mixing, while the OPTSIM model under core-shell. The core shell model has been applied for all the species except dust, which has been considered not to mix with the other aerosol species (i.e. external mixing).

$$r_{core} = \frac{r_{shell}}{\left(\frac{M_{shell}\rho_{core}}{M_{core}\rho_{shell}}+1\right)^{1/3}} = \frac{r_{shell}}{\left(\frac{V_{shell}}{V_{core}}+1\right)^{1/3}} \quad (2.16)$$

Where the V_{shell} and the V_{core} are respectively the total volume occupied by the core and the shell. The size dependent V_{shell} and the V_{core} can be expressed as:

$$V_{core}(ibin) = \sum_{ispec=1}^{nspec_{core}} \frac{conc(ibin,ispec)}{\rho(ispec)} \quad (2.17)$$

$$V_{shell}(ibin) = \sum_{ispec=1}^{nspec_{shell}} \frac{conc(ibin,ispec)}{\rho(ispec)} \quad (2.18)$$

Therefore, knowing that the r_{shell} is the median radius (r_{median}) of the aerosol bin (calculated from the cut-off radii of the bin), it is possible to estimate the r_{core}. Under the core-shell assumption the size dependent complex refractive index (n-ik) of the core (CRI_{core}) and the shell (CRI_{shell}) represented by a volume weighted average as:

$$CRI_{core}(ibin) = \sum_{ispec=1}^{nspec_{core}} \frac{V(ibin,ispec)n(ispec)}{V_{core}(ibin)} - \sum_{ispec=1}^{nspec_{shell}} \frac{V(ibin,ispec)k(ispec)}{V_{core}(ibin)} i \quad (2.19)$$

$$\mathrm{CRI_{shell}(ibin)} = \sum_{\mathrm{ispec=1}}^{\mathrm{nspec_{shell}}} \frac{\mathrm{V(ibin,ispec)n(ispec)}}{\mathrm{V_{shell}(ibin)}} - \sum_{\mathrm{ispec=1}}^{\mathrm{nspec_{shell}}} \frac{\mathrm{V(ibin,ispec)k(ispec)}}{\mathrm{V_{shell}(ibin)}}\mathrm{i} \quad (2.20)$$

n($ispec$), k($ispec$) and $V(ibin, ispec)$ represent the real and imaginary part of the refractive index of the aerosol species and the volume occupied within the core or the shell.

Finally, the extinction, the scattering efficiencies and g are calculated using the Wiscombe Mie code for stratified sphere based on (Toon and Ackerman, 1981).

The size-resolved AOD is calculated and integrated as:

$$\mathrm{AOD}\ (\lambda, \mathrm{z}) = \sum_{\mathrm{ibin=1}}^{\mathrm{nbin}} \frac{\mathrm{Q_{ext}}(\lambda, \mathrm{ibin})}{\mathrm{r_{median}(ibin)}\overline{\rho}} \mathrm{conc_{sum}(ibin, z)}\Delta\mathrm{z} = \beta_{ext}(\lambda)\Delta\mathrm{z} \quad (2.21)$$

where nbin represents the number of aerosol bins (10 from the WRF-CHIMERE model), $\overline{\rho}$ is the mass-weighted average density between the core and the shell, and $\mathrm{conc_{sum}}$ is the total aerosol concentration within the aerosol bin. The AOD can be further expressed as the extinction coefficient (β_{ext}) multiplied by the layer thickness Δz. The size-resolved SSA is calculated and integrated as the ratio between the extinction (β_{ext}) and the scattering coefficient (β_{sca}) as:

$$\mathrm{SSA}(\lambda, \mathrm{z}) = \sum_{\mathrm{ibin=1}}^{\mathrm{nbin}} \frac{\beta_{sca}(\lambda, \mathrm{ibin,z})}{\beta_{ext}(\lambda, \mathrm{ibin,z})} \quad (2.22)$$

And the asymmetry parameter g as the β_{sca} weighted average as:

$$\mathrm{g}(\lambda, \mathrm{z}) = \frac{1}{\beta_{sca}(\lambda)} \sum_{\mathrm{ibin=1}}^{\mathrm{nbin}} \beta_{sca}(\lambda, \mathrm{ibin}, \mathrm{z})\, g(\lambda, \mathrm{ibin}, \mathrm{z}) \quad (2.23)$$

In order to perform the core-shell simulation, black carbon has been attributed to the core with the complex refractive index identified in Sec. 2.3.2. The other species, with the exception of the dust species that has been treated as externally mixed (i.e. $\mathrm{AOD=AOD_{CS}+AOD_{DUST\text{-}EXT}}$), have been attributed to the shell. An example of the AOD and SSA simulated with the three different models is available in Figure 2.18, showing the much lower SSA (due to the lensing effect and absorption enhancement (Zhang et al., 2018)) of the core-shell model compared to the external mixture.

2.3.4 The WRF-CHIMERE-RRTMG offline radiative coupling for the direct radiative estimation

Estimating the regional scale direct radiative effect over the Paris area represents one the scientific question of this thesis. The WRF-CHIMERE online coupling method described in 2.4.1, allows only for a radiative effects estimation considering the ensemble of all the aerosol species included in the CHIMERE simulation, while estimating the contribution of a specific aerosol species (e.g. black carbon, brown carbon) would be too computationally heavy as it would require multiple simulation runs. Furthermore, the online coupling includes the meteorological feedbacks to a radiative perturbation (i.e. on surface temperature), allowing for rapid adjustments and therefore simulating both the sum of direct and semi-direct radiative effects.

To evaluate the direct radiative effect of aerosols and the specific contribution of each aerosol species, (such as black carbon and SOA) and to perform sensitivity tests (e.g. on the aerosol mixing state), it is necessary to couple the WRF-CHIMERE (cpl=1 i.e. without considering the meteorological feedbacks) offline with a radiative transfer model to solve the radiative transfer equation (RTE). We define this method as the OFFLINE approach (See Figure 2.1). Indeed, the shortwave Rapid Radiative Transfer Model for Global Climate Models (RRTMG_SW) v.5.0.0 (http://rtweb.aer.com/) was interfaced to the WRF-CHIMERE outputs following the RRTMG configuration within the WRF model (i.e. the module module_ra_rrtmg_sw.F) to be as much consistent as possible with the online simulation.

The RRTMG is a reduced version (optimised for GCMs) of the RRTM model and it applies the correlated-k method to accurately estimate the shortwave and longwave fluxes, as well as the heating rates. The RRTMG_SW model is divided into 14 bands within the 0.2-12.2 µm spectral range, chosen according to the major gas absorbers within the bands (Clough et al., 2005).

In order to run the RRTMG model several parameters (listed also in Table 2.9) must be provided:

- vertically resolved gas mixing rations such as CO_2, CH_4, N_2O, O_2, O_3 and water vapour (H_2O).
- Temperature and pressure profiles both at half-level (between two consecutive vertical model layers) and at the interface (of the vertical model layer), as well as the temperature of the surface.

Parameters	Sources and assumptions
CO_2, CH_4, N_2O, O_2	Assumed constant values from the WRF model
H_2O	Water vapour mixing ratio from the WRF model
O_3	Calculated from the WRF model climatological values (ozone.formatted)
Temperature and pressure profiles at half-levels and interface	Calculated from the hydrostatic pressure and potential temperature outputs of the WRF model
Spectral AOD, SSA, g	Output from the optical models and interpolated at the SW bands of RRTMG
In-cloud ice and liquid water paths	Calculated from the liquid and ice mixing ratios from the WRF model
Effective ice and liquid radii, cloud fraction	Output from the WRF model
UV-Visible and Near-Infrared surface albedo	Output from the WRF model, same values for UV-Visible and Near-Infrared

Table 2.9 Summary of the inputs to the RRTMG_SW model and how they are calculated within this work.

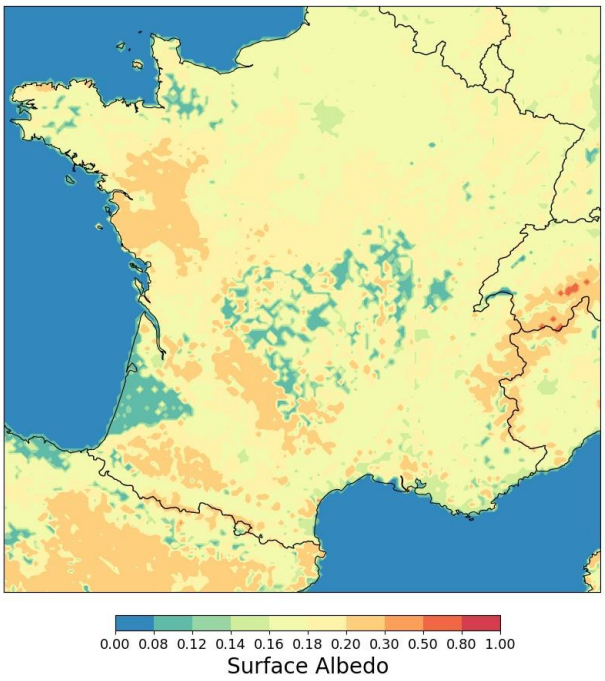

Figure 2.19: Simulated surface albedo from the WRF model at the 6km spatial resolution domain.

- Aerosol spectral optical properties (AOD, SSA, g) at the 14 spectral bands of the RRTMG model.
- In-cloud ice and liquid water content, effective ice and liquid radii for cloud optical properties, cloud fraction.
- The surface albedo.

The RRTMG_SW model outputs are the vertically resolved upward and downward radiative fluxes and atmospheric heating rates under clear-sky and all-sky conditions.

An example of the surface albedo simulated by the WRF model is available in Figure 2.19, showing darker surfaces over ocean and brighter surfaces over land.

The cloud optical properties are calculated within the RRTMG model and the sub-grid variability of clouds is represented by the statistical technique of the Monte-Carlo Independent Column approximation (McICA, (Barker et al., 2008)). The optical depths of water clouds is calculated based on the parameterisation of (Hu and Stamnes, 1993), while optical depths for ice clouds are based on (Fu, 1996).

The offline coupling allows for estimating the instantaneous DRE and isolating each species contribution, (e.g. the black carbon), simulating the difference between the DRE with ($DRE_{BC_{TOA}}^{BC}$) and without ($DRE_{BC_{TOA}}^{noBC}$) as:

$$DRE_{BC_{TOA}}^{net} = DRE_{BC_{TOA}}^{BC} - DRE_{BC_{TOA}}^{noBC} \quad (2.24)$$

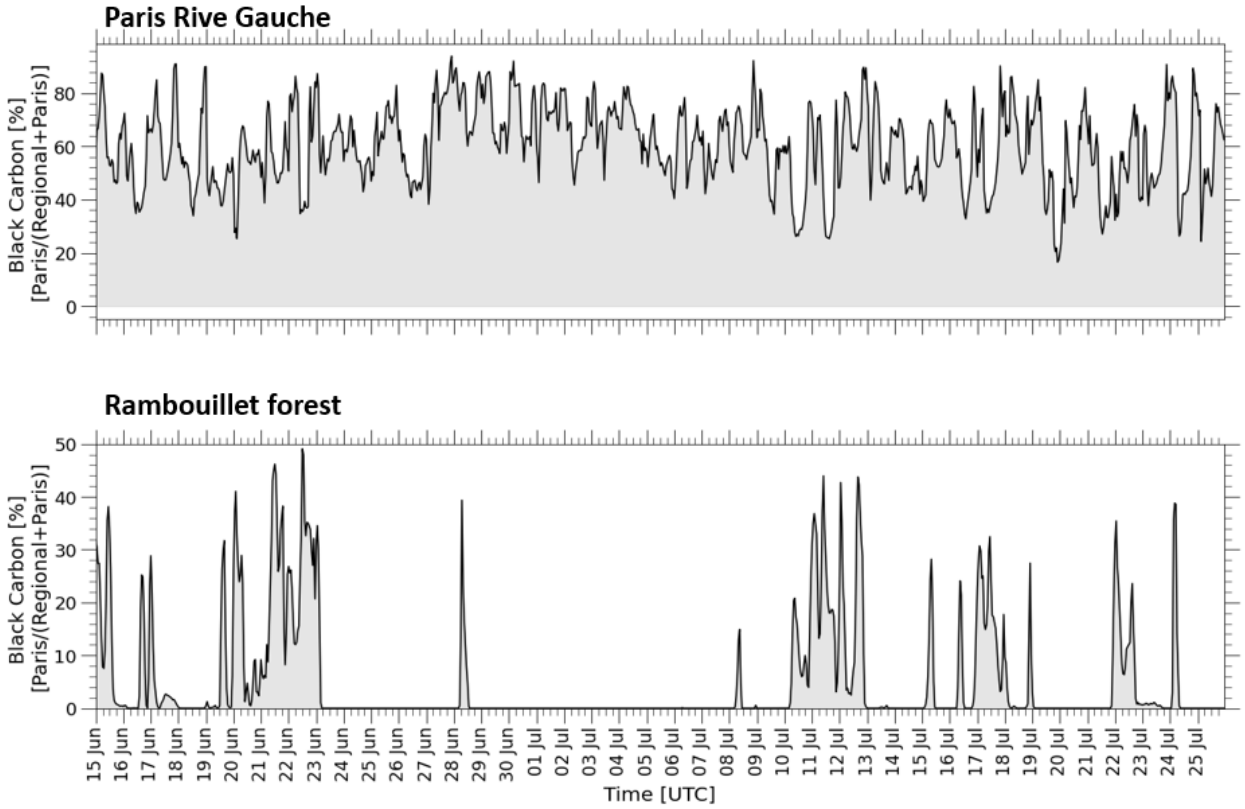

Figure 2.20: The BC_{ratio} extracted at the PRG and RambForest locations, showing when the ground based sites are under the influence of the Grand-Paris emissions.

Analogous formulations can be obtained for the other species such as BSOA, ASOA and BB-POA at BOA and within the atmosphere (ATM).

Finally, another formulation can be retrieved as the difference between i) a simulation considering the imaginary refractive index of the aerosol species as "absorbing" and ii) a simulation with a zero imaginary component:

$$DRE_{BC_{TOA}}^{net_{abs}} = DRE_{BC_{TOA}}^{BC_{absorption}} - DRE_{BC_{TOA}}^{BC_{scattering}} \quad (2.25)$$

Analogous formulations can be obtained again for the other species. This formulation allows testing the DRE response and sensitivity to the imaginary component of the refractive index (e.g. biomass burning POA, BSOA and ASOA UV absorption).

2.3.5 BC Paris-to-regional ratio

During the thesis, support to the ACROSS community was also provided by developing and disseminating simulation products. The black carbon Paris–to–regional ratio (BC_{ratio}), Di Antonio et al. (2023), is a product derived from the 2km CHIMERE v2020r3 chemistry transport model simulation (Menut et al., 2021) and motivated by the ACROSS community's need of knowing when the ground-based sites were under the influence of the Paris plume. This product aims at tracing the

modelled BC emissions in the Grand Paris domain (Grand-Orly Seine Bièvre, 2018) compared to the regional background levels. The ratio is calculated at each 2x2 km spatial resolution and at hourly temporal resolution as:

$$\mathrm{BC_{ratio}}\ (\mathrm{lon, lat, time}) = \frac{\mathrm{BC_{Paris}(lon,lat,time)}}{\mathrm{BC_{Paris}(lon,lat,time)+BC_{regional}(lon,lat,time)}} \quad (2.26)$$

where for each pixel within the considered domain the $\mathrm{BC_{Paris}(lon, lat, time)}$ represents a tracer for the simulated BC emissions within the Grand Paris domain, while the $\mathrm{BC_{regional}}$ accounts for the BC simulated concentrations without taking into account the Grand Paris area's BC emissions. A value of 1 of the BC_{ratio} indicates that all the BC is due to advection from the Grand Paris area. On the contrary, a value of 0 in the BC_{ratio} means that no contribution from Grand Paris area is traced. Intermediate values weight the contribution of Grand Paris area over the total BC concentration simulated in the regional domain. The extraction of the BC_{ratio} over the Paris-Rive Gauche and Rambouillet Forest site is available in Figure 2.20. The results show that the simulated black carbon concentrations due to the regional contribution are not negligible at the PRG site, while they are as expected major for the Rambouillet site. Conversely, a BC_{ratio} greater than zero indicates the presence of the Paris plume at the Rambouillet site, which during the ACROSS campaign reached values up to 50% under favorable weather conditions.

2.3.6 The HYSPLIT-WRF model setup for the ACROSS field campaign

Understanding the history of air masses helps to understand the physical-chemical processes that the aerosols might have undergone travelling over land and ocean. In this regards, back-trajectories simulations are useful tools to statistically investigate (via a single or an ensemble approach) the origin and evolution of an air mass.

HYSPLIT (Stein et al., 2015) back-trajectories simulations were performed for the ACROSS campaign period at the Paris Rive Gauche (PRG), SIRTA and Rambouillet (RambForest) ground-based sites and for the aircraft campaign aiming at supporting the research activities of the ACROSS community (Siour and Di Antonio, 2023).

The WRF-CHIMERE meteorological fields from the 6x6 km and 2x2 km spatial resolution simulations have been used as HYSPLIT backtrajectory meteorological model inputs. The meteorological fields have 10 minutes of temporal resolution.

The dataset is grouped on a daily basis and contains four backtrajectories runs per day starting at 00, 06, 12 and 18 UTC and with a maximum duration of 48 hours. Two different options are available: 1) one single backtrajectory starting at 25 m, 10 m, 40 m above ground level (a.g.l.) respectively for the PRG, SIRTA and RambForest locations; 2) an ensemble backtrajectory simulation composed by

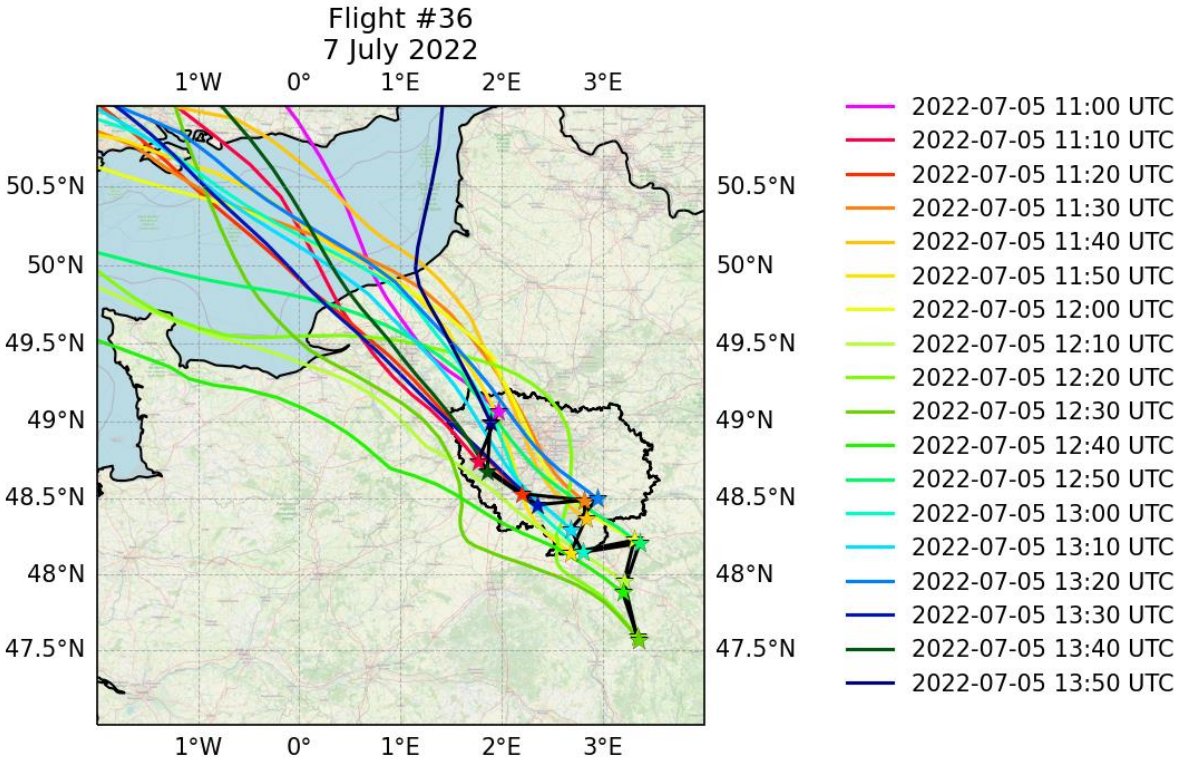

Figure 2.21 HYSPLIT backtrajectories initialized with the WRF-CHIMERE meteorological fields at 10 minutes resolution for the Flight #36 occurred on the 7 July 2022.

27 ensemble members. These members include all the possible offset combinations due to perturbations in the initial meteorological data: ±1 grid point in the horizontal direction (X and Y directions), ±0.01 sigma units corresponding to ~±250 m. The dataset contains the longitude, the latitude and the altitude of the simulated air parcel as well as the ambient pressure, temperature, relative humidity and specific humidity. All the dataset variables have 3D dimensions and depend on i) the number of runs per day (run_starting_time), ii) the number of backtrajectories simulated hours (ntime_backtraj) and iii) the number of trajectories (ntraj, 1 for single backtrajectory, 27 for the ensemble simulation). An example of the backtrajectory plot is available in Figure 2.21.

Chapter 3

3. Aerosol optical depth climatology from the high-resolution MAIAC product over Europe: differences between major European cities and their surrounding environments

This chapter is in the form of an article, published in Atmospheric Chemistry and Physics on the 6 October 2023 and further included in the "Atmospheric Chemistry of the Suburban Forest – multiplatform observational campaign of the chemistry and physics of mixed urban and biogenic emissions" special issue.

In particular, within this study we performed a climatological analysis (from 2000 to 2021) on the aerosol optical depth at 550 nm from the high-resolution (1km of spatial resolution) Multi-Angle Implementation of Atmospheric Correction (MAIAC) satellite data (Lyapustin et al., 2018). This work aims to investigate the climatological AOD variability and trend at three different scales over Europe: a continental, a regional and an urban-local scale in order to evidence the impact of the local scale urban emissions on the regional background aerosol load. The objective is also to understand whether the order of magnitude of the AOD obtained at the local and regional scale around Paris is representative of other cities and regions in Europe, thus enabling the contextualization and interpretation of the results and the applicability of the methods presented in this thesis project within a broader framework. The analysis of the long-term MAIAC dataset reveals that the average AOD at 550 nm values range from 0.06 to 0.16 at the urban-local scale, exhibiting a significant north-south gradient in Europe. By computing the average ratio between the AOD at the local scale the regional scale, the findings indicate that there are average enhancements of local AOD compared to regional, with percentages of 57%, 55%, 39%, and 32% observed for major metropolitan areas like Barcelona, Lisbon, Paris, and Athens, respectively. This suggests a significant increase in aerosol levels at the regional scale due local emissions and therefore human activities. The magnitude of the observed AOD fat 550 nm or Paris falls in the middle among the cities analysed. This suggests that the results obtained in this thesis may be indicative of average conditions in a European urban environment.

Atmos. Chem. Phys., 23, 12455–12475, 2023
https://doi.org/10.5194/acp-23-12455-2023

Atmospheric Chemistry and Physics
Open Access
EGU

Aerosol optical depth climatology from the high-resolution MAIAC product over Europe: differences between major European cities and their surrounding environments

Ludovico Di Antonio[1], Claudia Di Biagio[2], Gilles Foret[1], Paola Formenti[2], Guillaume Siour[1], Jean-François Doussin[1], and Matthias Beekmann[2]

[1]Univ Paris Est Creteil, Université Paris Cité, CNRS, LISA, F-94010 Créteil, France
[2]Université Paris Cité, Univ Paris Est Creteil, CNRS, LISA, F-75013 Paris, France

Correspondence: Ludovico Di Antonio (ludovico.diantonio@lisa.ipsl.fr) and Matthias Beekmann (matthias.beekmann@lisa.ipsl.fr)

Received: 12 June 2023 – Discussion started: 27 June 2023
Revised: 9 August 2023 – Accepted: 12 August 2023 – Published: 6 October 2023

Abstract. The aerosol optical depth (AOD) is a derived measurement useful to investigate the aerosol load and its distribution at different spatio-temporal scales. In this work we use long-term (2000–2021) MAIAC (Multi-Angle Implementation of Atmospheric Correction) retrievals with 1 km resolution to investigate the climatological AOD variability and trends at different scales in Europe: a continental (30–60° N, 20° W–40° E), a regional ($100 \times 100\,km^2$) and an urban–local scale ($3 \times 3\,km^2$). The AOD climatology at the continental scale shows the highest values during summer (JJA) and the lowest during winter (DJF) seasons. Regional and urban–local scales are investigated for 21 cities in Europe, including capitals and large urban agglomerations. Analyses show AOD average (550 nm) values between 0.06 and 0.16 at the urban–local scale while also displaying a strong north–south gradient. This gradient corresponds to a similar one in the European background, with higher AOD being located over the Po Valley, the Mediterranean Basin and eastern Europe. Average enhancements of the local with respect to regional AOD of 57 %, 55 %, 39 % and 32 % are found for large metropolitan centers such as Barcelona, Lisbon, Paris and Athens, respectively, suggesting a non-negligible enhancement of the aerosol burden through local emissions. Negative average deviations are observed for other cities, such as Amsterdam (−17 %) and Brussels (−6 %), indicating higher regional background signal and suggesting a heterogeneous aerosol spatial distribution that conceals the urban–local signal. Finally, negative statistically significant AOD trends for the entire European continent are observed. A stronger decrease rate at the regional scale with respect to the local scale occurs for most of the cities under investigation.

1 Introduction

Climate change and air quality preservation represent two of the greatest challenges of our times, especially in densely populated areas. Aerosol particles have been shown to play a key role in climate change and to affect air quality over many regions of the world (Robotto et al., 2022; Viana et al., 2014; Fiore et al., 2012). Aerosols affect the radiative budget both directly, by scattering and absorption of solar and thermal radiation (the aerosol–radiation interaction, ARI), and indirectly, by influencing the cloud formation and properties (aerosol–cloud interaction, ACI) (Bellouin et al., 2020). Constraining the aerosol contribution to climate and its change is still a challenge (Bender, 2020), as further demonstrated by the Climate Change 2021 IPCC report, indicating large remaining spread in ARI and ACI estimations (Masson-Delmotte et al., 2021). Atmospheric aerosols are also a concern for air quality and human health (Yang et

Published by Copernicus Publications on behalf of the European Geosciences Union.

al., 2018; Li et al., 2017, 2016; Dockery, 2009). Millions of people in Europe and around the world, especially over dense urban agglomerations, industrial areas and rural environment, experience significant particulate matter exposure (Sicard et al., 2021). Under favorable weather conditions such as high radiation levels, high temperature, low precipitation and low winds during summer or temperature inversions and low planetary boundary layer height during winter, local primary and secondary aerosol formation have been shown to build up to create the so-called "aerosol pollution episodes" (Foret et al., 2022; Groot Zwaaftink et al., 2022; Diémoz et al., 2019). These episodes correspond to daily average particulate matter (PM) levels above the European threshold of $50\,\mu g\,m^{-3}$ and last for several consecutively days. They lead to significant air quality and visibility degradation (Majewski et al., 2021; Singh et al., 2020) and increase the potential health risk (Luo et al., 2021; Grigorieva and Lukyanets, 2021). However, the aerosol anthropogenic precursors, abundant in urban agglomerations, can also spread around emission hotspots and affect larger areas, including rural and forested environments, leading to situations of mixed anthropogenic–biogenic scenarios (Xu et al., 2021). This would lead to aerosols having different chemical, physical and radiative properties and therefore to a potentially different impact on both human health (Tuet et al., 2017; Liu et al., 2009) and the environment (Nascimento et al., 2021; Shrivastava et al., 2019; Martin et al., 2016). In this regard, how the local- and regional-scale anthropogenic and biogenic precursors, their mixing, and their processing affect aerosol loading and properties, in particular around major city agglomerations, is still unknown and is a matter of scientific investigation (Cantrell and Michoud, 2022; Liu et al., 2021; Ma et al., 2021).

The aerosol optical depth (AOD) is a key parameter to investigate aerosol load and distribution over local- to large-scale areas (Bai et al., 2022; Faisal et al., 2022; Raptis et al., 2020; Sun et al., 2019; Just et al., 2015; Smirnov et al., 2002). The AOD is defined as the integral of the aerosol extinction coefficient (inverse units of length) over the whole atmospheric column, and it depends on the aerosol mass concentration, size distribution, shape and complex refractive index. Measurements of AOD are used to improve the air quality forecasts since they can be assimilated in regional or global models (Lee et al., 2022; Ha et al., 2020; Kondragunta et al., 2008), and they can also be linked to visibility measurements (Aman et al., 2022; Zhang et al., 2016; Boers et al., 2015; Kessner et al., 2013; Bäumer et al., 2008). Moreover, the AOD spectral variability can also be used to discern among different aerosol types and help source apportionment (Tuccella et al., 2020; Bahadur et al., 2012). However, since AOD observations are vertically integrated, the correlation with surface aerosol measurements may not be straightforward (He et al., 2021; Grgurić et al., 2014; Segura et al., 2017; Guo et al., 2009; Schaap et al., 2009; Schäfer et al., 2008). In fact, AOD is sensitive to dust and biomass burning plumes transported at high altitude, which may not affect surface measurements (Eck et al., 2023; Gkikas et al., 2022; Song et al., 2009). Different studies reported AOD trends at a global scale (Gupta et al., 2023, 2022; Zhao et al., 2017; He et al., 2016; Mehta et al., 2016; Mao et al., 2014), supporting a decreasing AOD trend over Europe (Gupta et al., 2023, 2022; Filonchyk et al., 2020b; Alpert et al., 2012). The overall decreasing trend at the European regional scale has been attributed to mitigation policies applied in recent years for the aerosol and the aerosol precursor emissions (Gupta et al., 2022; Hammer et al., 2020; Provençal et al., 2017; Zhao et al., 2017).

The AOD is routinely retrieved across the globe by both ground-based sun photometer measurements, such as those of the widespread AERONET (Aerosol Robotic Network) (Giles et al., 2019), and by satellite sensors, among them the Moderate Resolution Imaging Spectroradiometer (MODIS). Three complementary algorithms, developed at NASA, exist for the MODIS AOD retrieval: the Deep Blue (DB) (Hsu et al., 2004), the Dark Target (DT) (Remer et al., 2020, 2005) and the more recent Multi-Angle Implementation of Atmospheric Correction (MAIAC) algorithm (Lyapustin et al., 2018). The DB and DT algorithms, extensively used in the literature (e.g., Shi et al., 2021; Spencer et al., 2019; Sayer et al., 2018; Lee et al., 2017; Hsu et al., 2017), provide aerosol retrievals at a spatial resolution of 3 and 10 km. The MAIAC algorithm provides atmospheric retrievals of AOD at 470 and 550 nm at the more advanced spatial resolution of 1 km. As a matter of fact, an accurate estimation of surface reflectance, discerning among atmospheric and surface contributions, is necessary to provide the best-quality AOD retrievals (Bilal et al., 2019). In this regard, the MAIAC algorithm benefits the multi-angle satellite observations, retaining in memory up to 16 d of consecutive satellite overpasses to better constrain the surface reflectance, improving the AOD retrievals in particular over complex scenes such as urban areas (Chen et al., 2021; Gupta et al., 2016; Wang et al., 2010). The MAIAC aerosol algorithm uses eight different background aerosol models over land (look-up tables, LUTs), and it has developed a more stable algorithm that reduces the AOD bias over bright surfaces (in the absence of smoke and dust), typical for the DT and DB algorithms (Lyapustin et al., 2018). Furthermore, MAIAC can retrieve AOD over partially cloudy conditions and distinguish between smoke and dust scenes (Lyapustin et al., 2012). The AOD from the MAIAC algorithm has been validated over different areas of the world and shown to perform better with respect to the DT and DB algorithms when compared to AERONET observations (Su et al., 2023; Falah et al., 2021; Qin et al., 2021; Martins et al., 2019; Zhang et al., 2019; Tao et al., 2019; Mhawish et al., 2019; Martins et al., 2017; Just et al., 2015). The estimated expected error (EE) for MAIAC AOD is evaluated at $\pm(0.05 + 0.1)$ AOD, but it is shown to vary as a function of surface reflectivity, aerosol loading and size, as well as aerosol type (Falah et al., 2021). Because of its 1 km reso-

lution and good performance, the MAIAC AOD product is increasingly used in air quality studies (Pedde et al., 2022; Gladson et al., 2022; Yang et al., 2022; van Donkelaar et al., 2021; Jung et al., 2021; Hough et al., 2021).

In this paper, we benefit from the high-spatial-resolution long-term MAIAC data (from 2000 to 2021) to investigate AOD over Europe. This work is part of the ACROSS (Atmospheric ChemistRy Of the Suburban foreSt; https://across.aeris-data.fr/, last access: June 2023) project, whose objective is to deepen the current physical–chemical knowledge of the interaction between anthropogenic emissions in the Paris area and its surrounding environment through an intensive field campaign, which took place in the summer 2022 (Cantrell and Michoud, 2022). Within the ACROSS context, this study aims to achieve three different objectives:

- Investigate the urban–local- vs. regional-scale aerosol optical depth variability starting from a broader context over the European domain (30–60° N, 20° W–40° E) up to the urban–local scale ($3 \times 3\,km^2$) around major urban agglomerations in Europe.
- Explore the long-term trends at the urban–local ($3 \times 3\,km^2$), regional ($100 \times 100\,km^2$) and continental scales (30–60° N, 20° W–40° E).
- Contextualize the results for the Paris agglomeration with respect to other European cities.

The paper is organized as follows. The MAIAC product and its use are described in Sect. 2. Previous validation studies of the MAIAC product in Europe have been performed in Italy (Stafoggia et al., 2017), the Moscow metropolitan area (Zhdanova et al., 2020) and Germany (Falah et al., 2021), but no analysis has considered the entire European continent. Therefore, a validation analysis for Europe is also provided in Sect. 2. The discussion of the AOD climatology and trends over Europe and local/regional analysis are presented in Sect. 3, before giving conclusions in Sect. 4.

2 Methods

2.1 MAIAC dataset extraction and analysis

The daily MCD19A2 product (Lyapustin and Wang, 2018) providing the AOD at 470 and 550 nm has been used over the period February 2000–August 2021. All the observations are delivered in the HDF4 format and stored at 1 km resolution in sinusoidal grid mapping. The product, distributed on a daily basis, contains the collection of each MODIS Aqua and Terra satellite overpasses, whose number varies according to the latitude. The uncertainty attributed to the MAIAC AOD retrievals has been defined through the expected error $EE = \pm(0.1AOD_{AERONET} + 0.05)$, indicating the percentage of AOD_{MAIAC} retrievals falling in the envelope (expressed in percent). The EE has been established following Falah et al. (2021) and Lyapustin et al. (2018), considering both absolute and relative errors and by attributing an absolute error of 0.05 and a relative error of 0.1. As discussed in the next section, the validation against AERONET is considered to re-evaluate the EE over Europe and subsequently update the MAIAC uncertainty. In this product, in order to merge the satellite data to perform the climatological averages at the European scale (30–60° N, 20° W–40° E), the daily average of each tile has been taken, followed by horizontal and vertical concatenation over the different MODIS tiles of interest. Only data classified as best-quality AOD (quality check flag "0000") have been used in the following analysis. Although this choice reduces the number of available data, it guarantees the quality of the retrieval, which is an important aspect to perform high-resolution studies over urban areas.

Starting from the merged MAIAC data, the following treatment is applied.

- The sinusoidal grid coordinate system is converted to WGS 84.
- AOD daily averages are calculated for each grid point using available cloud-free observations from Terra and Aqua (i.e., two to five observations per day are available for the different grid points with Terra and Aqua overpass times between 09:00 and 14:00 local time).
- Local- and regional-scale AOD extractions have been performed to investigate the effect of the aerosol formation and city emissions over the surrounding areas. To this aim a list of 21 cities has been established, including European capital cities and big agglomerates with more than 1 million inhabitants. Those cities are listed in Table 1, and their location is plotted in Fig. 1. The MAIAC AOD data have been extracted around the city locations using two different concentric kernels (centered on the nearest pixel to the longitude and latitude values of each city in Table 1): $3 \times 3\,km^2$ ($9\,km^2$ area) for the local scale and $100 \times 100\,km^2$ ($10\,000\,km^2$) for the regional scale. The regional domain was chosen to be large enough to minimize effects of the city's pollution; i.e., the local-scale product occupies only $\sim 0.09\,\%$ of its regional background. Days for which a minimum of 40 % spatial data coverage is available are considered for both the local and the regional scale, and the others are discarded for the analysis. The local-to-regional AOD ratio (LTRR) has been calculated for each available kernel extraction (after averaging over all the available AOD data satisfying the spatial threshold in the kernels) to quantify the local-scale enhancement of the regional AOD by using the following formula:

$$LTRR = \frac{AOD_{local}}{AOD_{regional}} - 1. \quad (1)$$

Positive deviations of the LTRR highlight the positive contribution of the urban–local scale to the regional

Figure 1. Localization of European cities used for the analysis of the local-to-regional ratio. Map created with Cartopy (Elson et al., 2023).

background signal, considering that AOD_{local} intrinsically represents the sum of the local production and the possible regionally advected AOD fractions. Conversely, negative deviations can be linked to the presence of a non-homogenous spatial aerosol distribution at the regional scale, as well as to a possible local sink of pollution. The former may result in a stronger regional background signal related to different aerosol sources surrounding the city which may conceal the urban–local signal and reduce the pollution gradients.

Trend assessment on AOD has been conducted over annual averages of daily AOD data using the original Mann–Kendall test (Hussain and Mahmud, 2019). Annual AOD averages are performed if at least 50 daily AOD observations are available in the year, and trend evaluations are performed if at least 5 years of data are available in the dataset. The output of the Mann–Kendall test provides the significance of the test (p value) and the Theil–Sen slope (Theil, 1992; Sen, 1968). All the tests have been calculated assuming a significance level (α) of 0.05, and the trend is considered significant if the p value $< \alpha$. The relative change has been calculated following (Colette et al., 2016)

$$\mathrm{RC}\left(\%\,\mathrm{yr}^{-1}\right) = \frac{s}{y0}, \tag{2}$$

where s is the Theil–Sen slope, and $y0$ is the first available year for the trend evaluation.

Table 1. List of European cities used for the city-scale analysis. City names in bold are the cities (not metropolitan regions) with more than 1 million of inhabitants according to the Eurostat database (Eurostat, 2023).

Longitude	Latitude	City
4.88	52.37	Amsterdam
23.72	37.98	Athens
2.15	41.39	**Barcelona**
20.43	44.80	**Belgrade**
13.40	52.52	**Berlin**
11.32	44.49	Bologna
4.38	50.83	**Brussels**
12.57	55.68	Copenhagen
−6.26	53.349	Dublin
−9.13	38.72	Lisbon
−0.12	51.50	**London**
−3.70	40.41	**Madrid**
5.4	43.3	Marseille
9.18	45.46	**Milan**
10.75	59.91	Oslo
2.33	48.86	**Paris**
14.43	50.07	**Prague**
12.49	41.90	**Rome**
18.06	59.33	Stockholm
16.36	48.21	**Vienna**
15.97	45.81	Zagreb

2.2 Validation against AERONET observations and revised MAIAC estimated error (EE) for Europe

The MAIAC AOD validation has been performed by comparing the 550 nm AOD with all the available acquisitions (207 sites) in the AERONET Version 3 ground-based sun photometer network over continental Europe (Giles et al., 2019). Version 3, Level 2 AERONET data have been used (https://aeronet.gsfc.nasa.gov/, last access: June 2023). AERONET provides AOD measurements at four different wavelengths: 440, 675, 860, 1020 nm. The AOD at 550 nm has been extrapolated by assuming a power law relationship with the Ångström exponent α (Ångström, 1929; Schuster et al., 2006) calculated between 440 and 675 nm:

$$\mathrm{AOD}_{550} = \mathrm{AOD}_{675\,\mathrm{nm}}\left(\frac{550}{675}\right)^{-\alpha} \tag{3}$$

$$\alpha = -\frac{\log\left(\frac{\mathrm{AOD}_{440\,\mathrm{nm}}}{\mathrm{AOD}_{675\,\mathrm{nm}}}\right)}{\log\left(\frac{440}{675}\right)}. \tag{4}$$

Since the AERONET measurements are taken at different elevation angles depending on the sun elevation over the horizon, the measurements may be considered representative of a larger area around the point of acquisition (Chen et al., 2020; Schutgens, 2020; Kinne et al., 2013). In order to improve the meaningfulness against the AERONET observations, the MAIAC AODs have been additionally extracted

by taking an arbitrary average area of $0.06° \times 0.06°$ over the AERONET site, corresponding to $\sim 7 \times 7\,km^2$, chosen between the 1×1 and $9 \times 9\,km^2$ boxes, for which Falah et al. (2021) show that MAIAC–AERONET comparisons give similar results. Furthermore, AERONET AOD data between ± 1 h of the satellite passage have been considered to compare with MAIAC. The uncertainty in the AERONET AOD is $\Delta AOD_{AERONET} = 0.02$ and is linked to calibration uncertainty (Sinyuk et al., 2020). As the differences between MAIAC and AERONET observations are attributed entirely to MAIAC uncertainty, the derived MAIAC expected error is conservative. Different statistical indicators have been calculated to evaluate the comparison between MAIAC and AERONET AOD data. The mean bias error (MBE), the normalized mean bias (NMB), the root mean square error (RMSE) and the fraction of data within a factor of 2 (FAC2) are defined below (N is the number of data points):

$$\mathrm{MBE} = \frac{1}{N}\left(\mathrm{AOD_{MAIAC}} - \mathrm{AOD_{AERONET}}\right) \quad (5)$$

$$\mathrm{NMB} = \frac{\sum\left(\mathrm{AOD_{MAIAC}} - \mathrm{AOD_{AERONET}}\right)}{\sum \mathrm{AOD_{MAIAC}}} \quad (6)$$

$$\mathrm{RMSE} = \sqrt{\frac{\sum\left(\mathrm{AOD_{MAIAC}} - \mathrm{AOD_{AERONET}}\right)^2}{N}} \quad (7)$$

$$\mathrm{FAC2}(\%) = \text{fraction of data satisfying } 0.5 \leq \frac{\mathrm{AOD_{MAIAC}}}{\mathrm{AOD_{AERONET}}} \leq 2. \quad (8)$$

The correlation between AOD_{MAIAC} and $AOD_{AERONET}$ has been evaluated through the Pearson correlation coefficient R. The slope and the intercept of the regression line have been calculated taking into account the uncertainty in both coordinates using the York regression (York et al., 2004). The comparison between MAIAC and AERONET AOD at 550 nm for all available European AERONET measurements from 2000 to 2021 is shown in Fig. 2. The overall validation performed considering the entire dataset (Fig. 2a) shows a slight underestimation of the AOD from MAIAC with respect to AERONET, with an MBE (-0.02) and an RMSE (0.06) values similar to those retrieved in previous validation studies (Chen et al., 2020; Lyapustin et al., 2018; Martins et al., 2017). The probability density function (PDF) of the MAIAC–AERONET absolute differences (Fig. 2b) shows a mean value and a σ of -0.02 and 0.06, respectively. A total of 77 % of the AOD retrievals fall in an $EE = \pm(0.05AOD + 0.05)$, with a relative error lower than the validation $EE = \pm(0.1AOD + 0.05)$ from Falah et al. (2021), accounting for observations in northern Africa, California and Germany, but comparable to the EE envelope (~ 74 % of points falling within the EE) obtained in Qin et al. (2021) over the Köppen climate classification of normally humid and warm climate (Cf) regions, including part of the European domain.

Since dependency of EE on aerosol type and size has been evidenced by Falah et al. (2021) a further detailed validation depending on the Ångström exponent (AE) between 440 and 870 nm has been performed and is presented in Fig. 2c, d and e. The AE, combined with AOD, is an indicator of the particle type and size. AE values lower than 1 can be associated with coarse-mode aerosols (sea salt and dust), whereas AE values higher than 2 can be associated with fine-mode aerosols (urban pollution and smoke) (Schuster et al., 2006). In this regard, three different classes depending on AE have been identified, respectively referred to as coarse, mixed and fine aerosol particles: $AE < 0.5$, $0.5 \leq AE < 1.5$, $AE \geq 1.5$. The MAIAC validation shows an R value of 0.84 for the overall validation (Fig. 2a) comparable with the 0.85, 0.81 and 0.87 for the coarse, mixed and fine classes, respectively. The validation for the mixed- and fine-dominated classes show a satisfactory accuracy of the product, with an MBE of -0.02 for both and 79 % and 81 % of the points, respectively, within the envelope of $EE = \pm(0.1AOD + 0.05)$ from Falah et al. (2021). However, for the coarse mode, the MAIAC validation shows an MBE of -0.08 and 46 % of points, within the envelope of $EE = \pm(0.1AOD + 0.05)$ from Falah et al. (2021), significantly lower with respect to the other two classes. In the case of $AOD < 0.25$ (84 % of points in the coarse-mode validation), attributable to a marine-dominated aerosol scene (Toledano et al., 2007), 51 % of points are within the EE, whereas for $AOD \geq 0.25$ (16 % of points in the coarse-mode validation), attributable to dust-dominated aerosols (Rogozovsky et al., 2023; Bodenheimer et al., 2021; Toledano et al., 2007), the percentage of points within EE is significantly lower than 1σ (i.e., 68 % of points falling in the EE envelope). As a matter of fact, a higher EE is needed to contain the 68 % of the MAIAC–AERONET differences for the coarse-mode validation. Rogozovsky et al. (2023) and Qin et al. (2021) show that the MAIAC algorithm is sensitive to the aerosol size. Rogozovsky et al. (2023) observed that the underestimation of MAIAC compared to AERONET is related to the presence of dust (characterized by high depolarization ratio and small AE). This result suggests that further improvements are needed in the case of coarse-mode-dominated classification.

In summary, results of the validation against AERONET suggest that the EE for MAIAC for observations over Europe between 2000 and 2021 can be estimated at $EE = \pm(0.05AOD + 0.05)$, lower than the EE estimated by Falah et al. (2021). The total MAIAC AOD uncertainty has therefore been revised to take into account this new estimation.

3 Results and discussions

3.1 European-scale analysis

Before looking at the fine-scale variability in the major European cities (Sect. 3.2), we address here the question of their

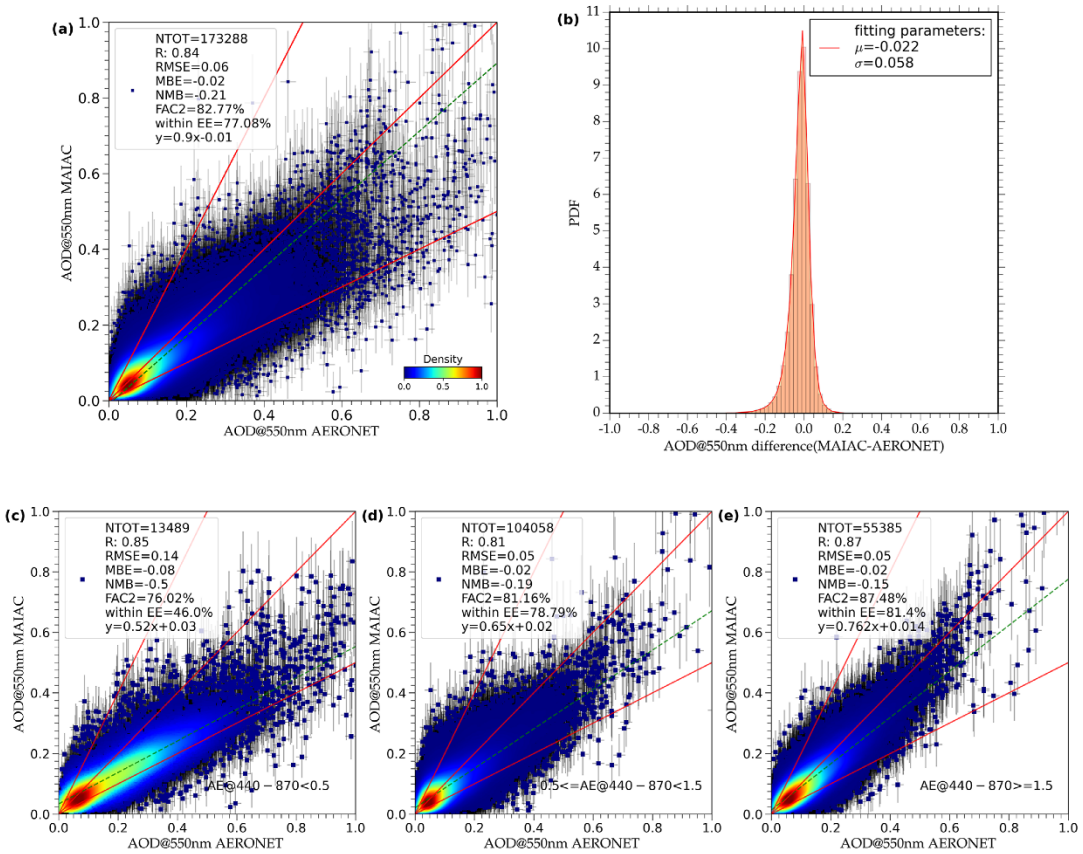

Figure 2. Scatterplot of the MAIAC against AERONET observations considering **(a)** all the available data points in Europe and points selected based on the Ångström exponent (AE) assuming **(c)** AE < 0.5, **(d)** $0.5 \leq$ AE < 1.5 and **(e)** AE ≥ 1.5. Panel **(b)** shows the PDF of the difference between MAIAC and AERONET values in reference to data points in **(a)**. The abbreviations indicate total number of points (NTOT), correlation coefficient (R), root mean square error (RMSE), mean bias error (MBE), normalized mean bias (NMB), fraction of y data between 0.5 and 2 times x (FAC2) expressed in percentage, fraction of retrievals within the expected error (EE $= 0.05 + 0.05$ AOD), and the equation of the regression line. Vertical and horizontal bars represent the x and y errors. Solid red lines represent the straight lines passing through the origin with slope coefficients of 2, 1 and 0.5, respectively. The dotted green line represents the regression line.

European AOD background levels and their seasonal variation, as seen by multi-year MAIAC observations. We place our findings in the context of previous analysis mainly based on spatially less refined MODIS observations (Gupta et al., 2023; Filonchyk et al., 2020a; Wei et al., 2019), introducing an analysis based on 2 decades of data, extending and validating studies performed in shorter time periods.

The aerosol optical depth variability at the European scale is shown in Fig. 3, reporting seasonal averages, and in Fig. S1 in the Supplement, reporting the monthly averages of the AOD at 550 nm. The summer (JJA) season shows the highest AOD values, ranging between 0.12–0.22 in the 30–60° N band, whereas DJF shows the lowest AOD values, ranging between 0.06–0.09. Figure S1 depicts maps of monthly AOD averages and shows maximum values between April and July and minimum between November and January. A north–south latitudinal gradient is present for all the seasons, as shown in Figs. 3 and S2, with a maximum gradient during the summer (JJA) and minimum during the winter (DJF) season. According to Fig. S2, seasonal AOD averages range between 0.06–0.11 and 0.09–0.22 and in the 55–60 and 30–35° N bands, respectively.

These findings with the MAIAC dataset are broadly in line with a previous analysis of MODIS and MISR data (Gupta et al., 2023, 2022; Filonchyk et al., 2020a; Mehta et al., 2016). A north–south AOD gradient over Europe has also

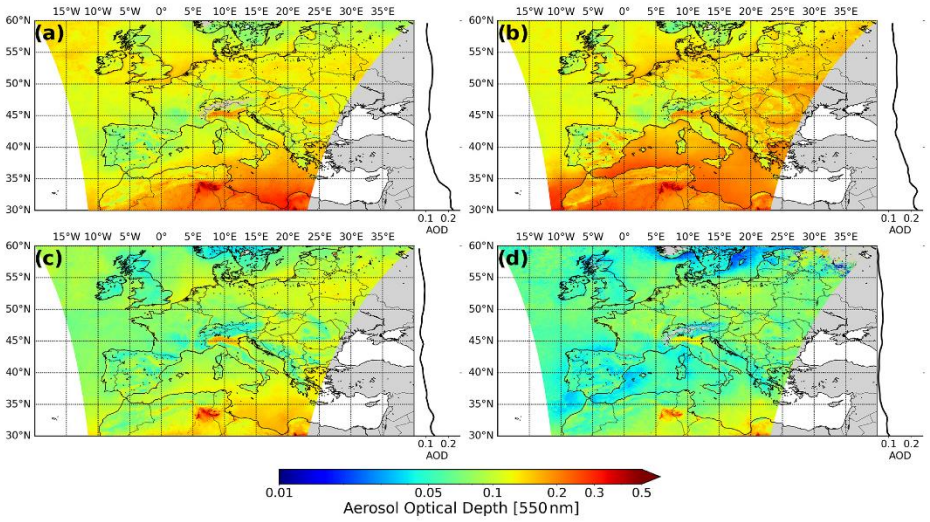

Figure 3. Climatological seasonal mean of the aerosol optical depth at 550 nm from the MAIAC algorithm over the period 2000–2021. Seasons are in the following order: **(a)** March–April–May, **(b)** June–July–August, **(c)** September–October–November and **(d)** December–January–February. The right side of each figure shows the latitudinal average of AOD.

been found in other MODIS studies (Merdji et al., 2023; Floutsi et al., 2016; Israelevich et al., 2012; Barnaba and Gobbi, 2004). Concerning averages over western Europe for the 2007–2016 period, Zhao et al. (2018) find a broad spring–summer AOD maximum of around 0.2 extending from April to July for MODIS Aqua and Terra and around 0.15 for MISR and a winter (December and January) minimum between 0.08 and 0.10. Ma and Yu (2015) attribute the simulated spring maximum over southern France and Corsica over the western Mediterranean Basin especially to sulfate and dust, while other primary aerosol species (sea salt, primary carbonaceous aerosol) show lower contributions and a flat seasonal variation. For secondary aerosol as sulfates, these larger AOD values during the late spring–summer season are attributed to stronger photochemical activity due to increased oxidant capacity (enhanced OH and ozone levels), whereas the contrary is expected for the late autumn–early winter minima. However, these authors did not take into account secondary organic aerosol; it can be expected to be at a maximum during summer due to the higher biogenic volatile organic compounds (BVOCs), and increased photochemical activity during this season (Gao et al., 2022). Possible fire events can also affect summer AOD peaks over Europe since they are more frequent during this period (European Commission et al., 2022; Zhao et al., 2018).

Different aerosol hotspots, as previously identified in the literature (Coelho et al., 2022; Backes et al., 2016; Gkikas et al., 2016; Bovchaliuk et al., 2013; Vecchi et al., 2009), are also visible in Fig. 3, especially the Mediterranean Sea, the Po Valley and eastern Europe. The Mediterranean Basin (30–46° N, 6° W–36° E) is affected by both anthropogenic, biogenic and dust emissions (Dayan et al., 2020; Chazette et al., 2019; Michoud et al., 2017; Pace et al., 2006). Its AOD seasonal cycle shown in Fig. 3, ranging between 0.07–0.19 (average values obtained from the ocean part of the basin), follows the Saharan dust transport cycle for the southern part, whereas the northern part is mostly dominated by human activities. In fact, the high MAM AOD values (between 0.2 and 0.3) shown over the south-southeastern part of the Mediterranean Basin are caused by the onset of the Saharan dust transport due to a low-pressure system (the Sharav cyclone), which pushes the dust plumes to the eastern basin (Floutsi et al., 2016; Moulin et al., 1998). During summer, the Balearic cyclogenesis causes the spreading of the dust plumes northwards from the Saharan source region, explaining the high JJA values (AOD > 0.2) over large areas of the southern part of the basin (Formenti et al., 2018; Floutsi et al., 2016; Moulin et al., 1998). The AOD average over the February 2000–August 2021 period over the Mediterranean Basin (30–46° N, 6° W–36° E) resulted in an AOD of 0.13 at 550 nm, comparable to the result obtained in Chiapello et al. (2021) at 865 nm based on POLDER-3 observations.

In the Po Valley (43°36′–46°12′ N, 7–12°30′ E), the seasonal cycle ranges between 0.09 (for DJF) and 0.15 (for JJA), with maxima in June and July (AOD > 0.16). PM composition measurements at the ground are shown to be dominated by traffic, biomass burning emissions, and ammonium nitrate and sulfate formation (Scotto et al., 2021), and the largest

ground PM values can occur in the DJF and SON seasons due to recurrent low temperatures and possible intense residential biomass burning (Pietrogrande et al., 2015) and ammonium nitrate precursor emissions (Scotto et al., 2021; Vecchi et al., 2018). The MAM and JJA levels at the ground can be caused by local agricultural sources (e.g., burning of pruning and fertilizers) (Scotto et al., 2021; Bucci et al., 2018; Clarisse et al., 2009). In summertime high levels of secondary organic aerosols in the presence of stagnation conditions have also been observed in Sandrini et al. (2016). Since AOD values are columnar values, the difference observed in the seasonal cycle between the ground (mainly DJF–MAM peaks) and AOD (JJA) can be attributed to different reasons: (1) the planetary boundary layer height (PBL), lower in the winter and higher in the summer, which conversely to ground PM does not affect the AOD measurements, and (2) possible dust events and biomass burning fires that can contribute to the stronger AOD levels during the spring and summer seasons. In addition, high AOD levels are also favored by insufficient pollution dispersion and removal, the valley being surrounded by mountains (the Alps and the Apennines), especially under stable weather conditions, promoting pollutant accumulation and air mass stagnation (Putaud et al., 2014). As a matter of fact, this reasoning is general and not restricted to the Po Valley.

Concerning eastern Europe (42–55° N, 13–30° E), Fig. 3 shows a strong seasonal variability in AOD for regions like Poland and Serbia, with a maximum AOD of up to 0.2 during the JJA season and minimum over the DJF season, with AOD generally below 0.15. The seasonal cycle for 2001–2014, with a maximum over summer and spring, was also observed by Chubarova et al. (2016), studying the Moscow AERONET site. Furthermore, Bovchaliuk et al. (2013) found AOD values ranging between 0.05 and 0.2 at 870 nm for the 2003–2011 period, with peaks over the spring, which the authors explain by agricultural fires correlated with an observed increase in the fine-fraction-mode particles.

Finally, western Europe (35–60° N, 11° W–18° E) also shows an AOD seasonal variability over land in the 0.06–0.12 range, with the maximum in the JJA season. A summer AOD maximum attributable to dust, smoke and sea spray aerosols has also been found in Zhao et al. (2018) for this area. These values are lower compared to other regions within Europe. This result can be justified by its proximity to the Atlantic Ocean, which contributes to the exposure these areas to more humid and less polluted air masses as well as to a greater pollutant dispersion capability.

3.2 City-scale analysis

The 1 km resolution MAIAC AOD data are used to explore AOD levels over cities and evaluate and quantify the different AOD levels of cities with respect to their surrounding areas. Figure 4 shows the distribution and the heterogeneity of the aerosol optical depth over the different sites. European cities

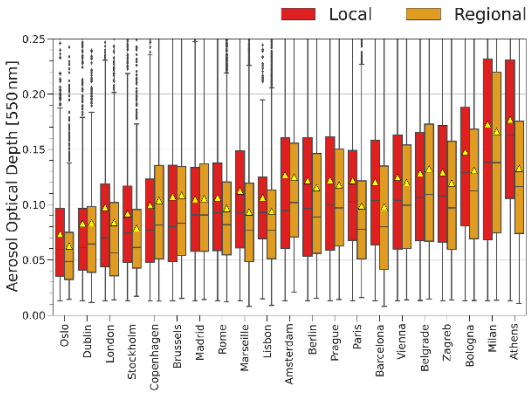

Figure 4. Climatology of the aerosol optical depth at 550 nm from the MAIAC algorithm at different cities in Europe for (red) the local scale and (orange) the regional scale, as defined in Sect. 2.1. The location of the cities is shown in Fig. 1. The figure aims to enhance the contribution to AOD enhancement due to the local source of pollution. The yellow triangles represent the AOD mean, whereas the median has been reported as the line crossing the boxplot. Black dots represent the outliers.

are ordered by increasing 50th-percentile values of the local-scale AOD from left to right. Table 1 gives the coordinates of city centers. An example of AOD time series for some of the cities is shown in Fig. S3. In line with Sect. 3.1, a north–south gradient can be found among the cities as well, highlighting that European cities located at more northern latitudes have AOD levels at 550 nm that are in general lower compared to cities at more southern latitudes: Oslo, Dublin and London show median AOD values (the 25th and 75th percentiles are also reported in brackets) of 0.06 (0.03–0.10), 0.06 (0.04–0.10) and 0.07 (0.04–0.12), respectively, whereas the more southern cities of Bologna, Milan and Athens show 0.13 (0.08–0.19), 0.14 (0.07–0.23) and 0.16 (0.11–0.23), respectively. Sites located in the middle range of Fig. 4, like Lisbon, Berlin and Amsterdam, show median AOD values of 0.09 (0.07–0.12), 0.10 (0.05–0.16) and 0.09 (0.06–0.16). The AOD values in the northern cities only rarely exceed a threshold of 0.3, which we arbitrarily relate to pollution (anthropogenic, dust, fires etc.) events (0.6 %, 2.5 % and 4.0 % of the total observations for Oslo, Dublin and London, respectively; see Table 2). For more southern cities like Milan and Athens, this fraction is 14.7 % and 10.6 %, respectively. Looking more closely to the timing of these occurrences, 18 % and 10 % of these "high-pollution" cases occurred before and after 2010, respectively, for Milan and 14 % and 8 % for Athens.

Figure 4 shows that the city centers' local-scale AOD levels in most of the cities considered in our study (58.8 %) are larger than the regional AOD. In addition, an increase

Table 2. Aerosol optical depth statistics at 550 nm from the MAIAC algorithm at different sites for both the local and regional scale: number of days when AOD > 0.3, 25th and 75th distribution percentiles, LTRR mean ± its standard deviation, and LTRR 25th and 75th distribution percentiles are reported.

	AOD > 0.3 (%)	Lower/upper bound (25th/75th)	AOD > 0.3 (%)	Lower/upper bound (25th/75th)	Mean ± SD	Lower/upper bound (25th/75th)	
N days	AOD local		AOD regional		LTRR		City
886	5.3	0.06/0.16	4.1	0.07/0.16	−0.17 ± 0.01	−0.31/−0.04	Amsterdam
4081	10.6	0.11/0.23	3.2	0.07/0.18	0.32 ± 0.01	−0.04/0.52	Athens
3121	3.5	0.06/0.16	1.6	0.04/0.13	0.57 ± 0.02	0.02/0.93	Barcelona
2424	5.2	0.07/0.17	5.9	0.07/0.17	0.07 ± 0.01	−0.15/0.24	Belgrade
1631	5.3	0.05/0.16	4.1	0.06/0.15	−0.03 ± 0.01	−0.17/0.11	Berlin
3222	7.1	0.08/0.19	4.8	0.07/0.17	0.14 ± 0.01	−0.07/0.28	Bologna
1389	4.2	0.05/0.14	4.1	0.05/0.13	−0.06 ± 0.01	−0.21/0.07	Brussels
1037	3.1	0.05/0.12	2.4	0.05/0.14	−0.01 ± 0.02	−0.25/0.18	Copenhagen
910	2.5	0.04/0.10	2.6	0.04/0.10	−0.01 ± 0.02	−0.32/0.16	Dublin
445	1.3	0.07/0.12	1.5	0.05/0.11	0.55 ± 0.03	0.15/0.88	Lisbon
1080	4.0	0.04/0.12	3.1	0.04/0.10	0.13 ± 0.02	−0.08/0.29	London
3049	1.5	0.06/0.13	1.6	0.06/0.14	0.14 ± 0.01	−0.04/0.29	Madrid
4394	2.4	0.06/0.15	1.2	0.05/0.12	0.26 ± 0.01	−0.13/0.48	Marseille
3220	14.7	0.07/0.23	12.5	0.07/0.22	−0.01 ± 0.01	−0.18/0.15	Milan
1042	0.6	0.03/0.10	0.6	0.03/0.07	0.07 ± 0.02	−0.11/0.19	Oslo
1293	4.4	0.07/0.15	2.5	0.05/0.12	0.39 ± 0.02	0.01/0.64	Paris
1502	4.5	0.06/0.16	3.6	0.06/0.15	−0.03 ± 0.01	−0.21/0.14	Prague
3670	1.9	0.06/0.14	1.2	0.05/0.12	0.10 ± 0.01	−0.13/0.27	Rome
1119	1.8	0.05/0.12	1.8	0.04/0.10	0.04 ± 0.02	−0.10/0.15	Stockholm
2015	4.9	0.06/0.16	3.5	0.06/0.15	0.03 ± 0.01	−0.19/0.2	Vienna
2531	5.2	0.07/0.17	3.8	0.06/0.16	0.08 ± 0.01	−0.10/0.24	Zagreb

in the frequency of AOD > 0.3 can also be observed for the city AOD (See Table 2). The local-to-regional ratio (LTRR) calculated using Eq. (1) for the 2000–2021 period and for the different cities is summarized in Table 2. Again, positive LTRR values are characteristic of an urban-scale contribution to the aerosol burden on top of the regional one, highlighting the importance of local anthropogenic emissions and atmospheric conditions favorable to pollutant accumulation. For instance, an LTRR value of 1 would correspond to a 50 % contribution of urban–local aerosol to total AOD, while a value of 0.5 would correspond to a contribution of a third. It should be noted that the local contribution to surface PM is necessarily stronger than that to AOD, as the importance of the regional background is greater for the vertical column.

In contrast, negative LTRR values indicate a lower local city AOD than the regional one, suggesting a possible inhomogeneity in AOD within the rather large ($100 \times 100\,km^2$) regional domain since the observed negative LTRR values were in general very small (a low percentage). This could be true especially for coastal sites or partly mountainous sites, where topography plays an important role. Furthermore, this inhomogeneity may be related to (i) the spatial extent of the city, which may impact the AOD levels of the regional scale, or (ii) the different location of emission sources, such as the location of industrial areas, which, combined with favorable meteorological conditions, can lead to inhomogeneous spatial patterns in the regional domain.

An alternative explanation to negative LTRR values would be local aerosol loss at the urban scale. However, systematic urban loss processes are not easy to identify. Sedimentation and dry deposition processes are not expected to be particularly enhanced over urban areas, nor is precipitation, compared to its regional surrounding. On the other hand, the urban heat island with increased temperatures could lead to evaporation of particles. For instance, Pirhadi et al. (2020) finds that due to its semi-volatile character, about 50 % of ambient $PM_{2.5}$ aerosol mass evaporated when heated up in a thermo-denuder from ambient temperature (∼ 13 °C in winter, 23 °C in summer and up to 50 °C). The urban heat island effect depends on the size and additional heat production within an urban area. It is restricted to light-wind meteorological conditions, and it is more pronounced during night, while MAIAC observations are made during daytime. For these reasons, we consider that evaporation of semi-volatile aerosol under higher urban temperatures could only have a limited effect on our dataset. In the framework of the present analysis it is in general difficult to distinguish between these two loss and inhomogeneity effects.

Maximum mean values of LTRR are shown for Barcelona (0.57 ± 0.02), Lisbon (0.55 ± 0.03), Paris (0.39 ± 0.02) and Athens (0.32 ± 0.01). In contrast, significantly negative LTRR values are shown for Brussels (-0.06 ± 0.01), Amsterdam (-0.17 ± 0.01) and Berlin (-0.03 ± 0.01). The uncertainty has been calculated here as the standard error of the mean: $\sigma/\sqrt{N}$, where σ is the standard deviation of the LTRR distribution, and N is the number of points available over the 2000–2021 period. The most negative LTRR is found for Amsterdam. For this coastal city, larger AODs are observed over the sea than over the continent (see Fig. 3, especially for the spring and autumn seasons), which could be caused by enhanced sea salt, but possibly also by slight differences in the retrieval algorithm for sea and land surfaces. Thus, the regional background cannot be considered to be homogeneous for this case.

In this study we focus on the Paris area, which shows an LTRR of 0.39 ± 0.02. The aim of this interest is to support the preceding climatological studies performed for the ACROSS field campaign (Cantrell and Michoud, 2022). Paris represents a strongly centralized agglomeration with about 11 million inhabitants. It is located in western Europe, in a rural area without strong orography, some 200 km from the Atlantic Ocean. This leads to generally favorable pollutant dispersion conditions (Vautard et al., 2003). The median local AOD value at 550 nm is 0.10 (0.07–0.15) for Paris, which falls slightly over the median of the cities' distribution in Fig. 4. Results from the MEGAPOLI (Beekmann et al., 2010) campaign have shown that a large fraction of fine PM at the ground is transported from the European continent and southern France towards Paris, while local emissions represent a smaller fraction (Beekmann et al., 2015; Bressi et al., 2014). Later studies with multi-year datasets (mid-2011–mid-2013; Petit et al., 2015) or pointing to specific pollution episodes (December 2016; Foret et al., 2022) make the local emission contribution to fine aerosol pollution peaks evident. Skyllakou et al. (2014) show by source apportionment that primary organic aerosol (POA) and elemental carbon (BC) control the $PM_{2.5}$ fraction of the local Paris emissions, whereas regional advection controls the secondary $PM_{2.5}$ fraction. Organic aerosols have been shown to play a key role in the Paris air quality assessment (Zhang et al., 2019; Petit et al., 2015; Bressi et al., 2014). Sulfate and secondary organic aerosols are mainly attributed to long-range transport (Foret et al., 2022; Skyllakou et al., 2014). For the period 2000–2021, the percentage of days with AOD > 0.3 is found to be 4 % at the local Paris scale.

Barcelona shows a local/regional distribution that is rather similar to Paris (Fig. 4), although its LTRR is larger (0.57 ± 0.02, actually the largest in our study), and the geomorphology of the two sites is significantly different. It is located in the northeastern part of the Iberian Peninsula, bordering the Mediterranean Sea and the foothills of the Pyrenees mountains. Recirculation caused by mountain winds and sea breeze (Jaén et al., 2021; Pérez et al., 2004) could enhance the urban–local AOD. In addition, the regional background over the mountainous area next to Barcelona is relatively low with respect to that over the Mediterranean Sea (Fig. 3), which could contribute to the large LTRR.

Bologna and Milan are surrounded by the well-known Po Valley, as previously discussed, where recirculation and stagnation events of aerosol and precursors may occur and cause enhanced pollution levels (Putaud et al., 2014). Vecchi et al. (2018) showed by source apportionment analysis that, during the winter season, the major PM contribution to light extinction for the Milan urban area is nitrate (42 %), followed by sulfate and primary aerosol due to traffic- and biomass-burning-related organic aerosol. In another study, secondary inorganic aerosols have also been shown to contribute 35 % of the PM over the Milan urban area on average annually (Amato et al., 2016). As a consequence, the large regional PM background leads to comparatively small additional local contributions and small LTRR values for both of these cities.

Concerning Athens, with an LTRR of 0.32 ± 0.01, aerosols of anthropogenic origin have been shown to dominate. Indeed Taghvaee et al. (2019) showed by source apportionment analysis that traffic emissions, secondary organic aerosol (SOA) and biomass burning correspond to major sources of $PM_{2.5}$ samples, contributing 44 %, 16 % and 9 %, respectively, with higher PM values during summer than winter. During the latter season high-$PM_{2.5}$ episodes are linked to dust and biomass burning episodes (Raptis et al., 2020). Furthermore, the organic aerosol concentrations in Athens have been shown to be dominated by regional SOA during summertime (Tsiflikiotou et al., 2019), also highlighting the importance of long-range transport in this area (Manousakas et al., 2020). As a conclusion of this discussion, $PM_{2.5}$ sources over the Athens region are a mixture of regional and local origin, which is reflected in its LTRR value.

For the seasonal variation in LTRR values, Fig. 5 shows the scatterplot between the local and regional AOD as a function of the season for all cities. The fitting line considering all seasons shows a slope of 1.08 and a linear correlation of 0.89, highlighting the overall average positive contribution to air quality degradation at the local and the regional scale over the different seasons. Figure 5 shows that the fraction of points where $AOD_{local} > AOD_{regional}$ is 84 %, 65 %, 75 % and 97 % for DJF, MAM, JJA and SON, respectively. This result suggests that the local contribution is higher during winter and lower during summer. In order to explain this difference, it should be considered that during summertime, favorable weather conditions, stronger photochemistry activity and enhanced BVOC emissions can lead to increased secondary aerosol formation and increase the secondary to primary aerosol ratio. As secondary aerosol formation is a regional phenomenon (Beekmann et al., 2015; Skyllakou et al., 2014; Karl et al., 2009), the regional contribution to AOD is increased. Furthermore, possible dust and fire events can

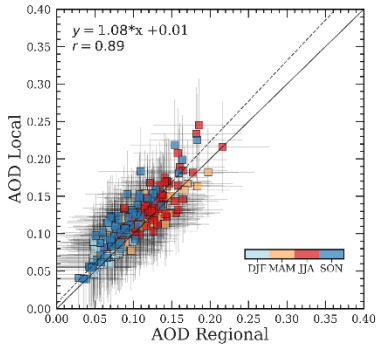

Figure 5. Local vs. regional scatterplot in different seasons (December–January–February, DJF; March–April–May, MAM; June–July–August, JJA; September–October–November, SON). The largest differences between local and regional are found during the DJF and MAM seasons. Vertical and horizontal bars represent the x and y errors. Solid and dashed lines represent the 1 : 1 and regression lines, respectively.

also contribute to the increase in the regional signal during summer and spring over Europe. However, during wintertime secondary aerosol formation is less pronounced; in addition primary aerosol emissions are increased due to increased heating demand.

3.3 Trend analysis

The analysis of the high-resolution MAIAC product can contribute to the further investigation of the aerosol optical depth tendency over the European region. Statistically significant (p value < 0.05) absolute and relative AOD trends over the European continent are reported in Fig. 6. Negative AOD trends have been found over the domain of interest, in the $[-3, -0.6]\,\%\,\mathrm{yr}^{-1}$ range, representing the 5th and 95th percentile, respectively, of Fig. 6b. Furthermore, more negative trends are mostly found over the regional hotspots outlined in Sect. 3.1 (Po Valley, Mediterranean Basin, parts of eastern Europe). Decreasing relative and absolute trends of $-1.34 \pm 0.29\,\%\,\mathrm{yr}^{-1}$ and $-0.0021 \pm 0.0005\,\mathrm{units\,yr}^{-1}$ for the Mediterranean Basin have been found for the 2001–2021 period. A decreasing absolute trend of $-0.003\,\mathrm{units\,yr}^{-1}$ for the 2002–2014 period has also been found with the MAIAC data in agreement with the $-0.003\,\mathrm{units\,yr}^{-1}$ observed in Floutsi et al. (2016). A trend of $-1.66 \pm 0.58\,\%\,\mathrm{yr}^{-1}$ at 550 nm has been estimated for the Po Valley, lower than what has been observed at the Ispra AERONET site in the period 2004–2010 (Putaud et al., 2014), where they estimated a decreasing trend of $-4.0 \pm 1.8\,\%\,\mathrm{yr}^{-1}$ and $-2.5 \pm 1.3\,\%\,\mathrm{yr}^{-1}$ for the 440 and 675 nm, respectively. Negative AOD tendency has also been registered for the Benelux and the Peloponnese area of $-2.46 \pm 0.96\,\%\,\mathrm{yr}^{-1}$ and $-1.49 \pm 0.45\,\%\,\mathrm{yr}^{-1}$, respectively. A statistically absolute significant trend of $-0.003 \pm 0.002\,\mathrm{units\,yr}^{-1}$ has been observed for the eastern Europe area, in line with what is observed in Filonchyk et al. (2020a) for the 2002–2018 period, where values in the range of $[-0.0025, -0.0028]\,\mathrm{units\,yr}^{-1}$ are observed for the Czech Republic, Bulgaria, Slovakia and Hungary with MODIS TERRA data. However stronger trends for the 2002–2019 period, in the range of $[-0.0031, -0.0076]\,\mathrm{units\,yr}^{-1}$, are observed in Filonchyk et al. (2020b) for several cities in eastern Europe by using MODIS AQUA data. Chubarova et al. (2016) attribute the significant negative trends observed in Moscow for the 2001–2014 period to the strong decrease in SO_x, non-methane volatile organic compounds (NMVOCs) and NO_x emissions. As a matter of fact, Tsyro et al. (2022) predicted, through a six-model ensemble approach, decreasing surface $PM_{2.5}$ and PM_{10} over Europe for the 1990–2010 period, attributed to a large impact on sulfate, ammonium and nitrate precursor emission reductions. Nevertheless, this decrease appeared to have a greater impact over central and eastern Europe. For instance, trends stronger than $-2.5\,\%\,\mathrm{yr}^{-1}$ are observed over Germany, the Czech Republic, Hungary, Slovakia and Ukraine for both $PM_{2.5}$ and PM_{10}.

Taking advantage of the high spatial resolution of the MAIAC product, the analysis has been extended to a local scale to estimate the AOD trends over the cities listed in Table 2 and to compare them to the trends for the surrounding regional background. Results are shown and summarized in Table 3. For most of the sites, a significant negative trend can be identified consistently both within the city center ($3 \times 3\,\mathrm{km}^2$) and in the surrounding area ($100 \times 100\,\mathrm{km}^2$). For instance, Athens, Prague, Vienna, Milan, Zagreb and Bologna show AOD trends in the range of $[-0.9, -1.7]\,\%\,\mathrm{yr}^{-1}$ and $[-1.3, -2.0]\,\%\,\mathrm{yr}^{-1}$ for the regional and local scale, respectively. This result is in line with the aforementioned observations at the European scale and with other studies focusing on European megacities (Papachristopoulou et al., 2022; Gupta et al., 2022; Zhao et al., 2017). Papachristopoulou et al. (2022) observed a decrease in AOD of up to -0.03 units per decade over the 2003–2020 period for European megacities like Paris, Barcelona, Madrid and London. This result is comparable to the range of $[-0.01, -0.03]$ units per decade observed for the European cities analyzed in this study. Conversely, cities where AOD levels are relatively low (positioned in the leftmost part of Fig. 4) do not generally show statistically significant results. Among all the cities, Prague shows the strongest relative trend at both the regional and local scale of $-2.0\,\%\,\mathrm{yr}^{-1}$ and $-1.7\,\%\,\mathrm{yr}^{-1}$, respectively. The absolute value obtained in this study for the local scale is comparable to that of -0.0022 obtained in Filonchyk et al. (2020a) for the 2000–2018 period. Moreover, the estimated trend of $-1.0\,\%\,\mathrm{yr}^{-1}$ over Athens is in line with the $-1.1\,\%\,\mathrm{yr}^{-1}$ obtained at 440 nm at the AERONET urban site in Raptis et al. (2020) for the 2000–2018 period. In the case of Paris, a trend of $-1.5\,\%\,\mathrm{yr}^{-1}$ is obtained for the regional

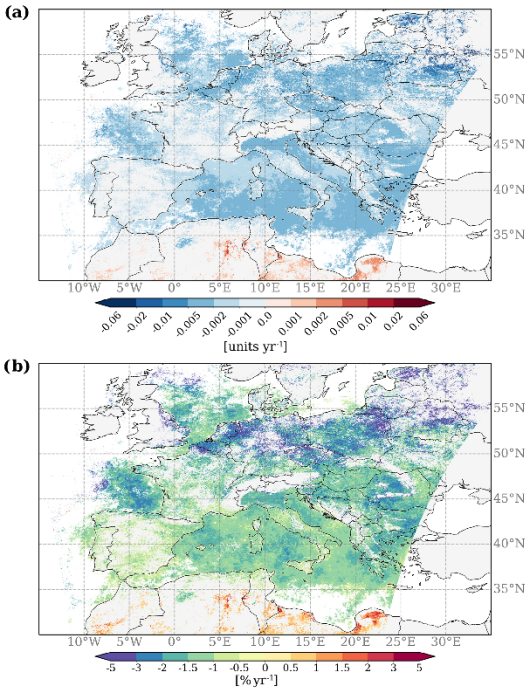

Figure 6. Theil–Sen **(a)** absolute and **(b)** relative change in aerosol optical depth at 550 nm over the European domain for the 2000–2021 period. Only the significant (p value < 0.05) pixels are reported.

Table 3. Optical depth trends at the local and regional scale for the different analyzed cities. Only significant trends are shown (p value < 0.05).

Trend				
AOD local		AOD regional		
Absolute (units yr^{-1})	Relative (% yr^{-1})	Absolute (units yr^{-1})	Relative (% yr^{-1})	City
–	–	–	–	Amsterdam
−0.0017	−1.0	−0.0020	−1.3	Athens
−0.0010	−0.9	−0.0017	−1.5	Barcelona
−0.0016	−1.6	−0.0014	−1.2	Belgrade
−0.0015	−1.4	–	–	Berlin
−0.0021	−1.4	−0.0025	−1.8	Bologna
−0.0020	−1.5	−0.021	−1.5	Brussels
–	–	–	–	Copenhagen
–	–	–	–	Dublin
–	–	–	–	Lisbon
–	–	–	–	London
–	–	–	–	Madrid
−0.0005	−0.5	−0.0014	−0.9	Marseille
−0.0034	−1.4	−0.0033	−1.7	Milan
–	–	–	–	Oslo
–	–	−0.0015	−1.5	Paris
−0.0030	−1.7	−0.0030	−2.0	Prague
−0.0012	−1.1	−0.0014	−1.3	Rome
–	–	–	–	Stockholm
−0.0011	−0.9	−0.0025	−1.9	Vienna
−0.0020	−1.6	−0.0022	−1.8	Zagreb

scale, while the city center trend is not significant. Interestingly, the regional relative trend for most cities (9 of 11 in Table 3) is stronger (i.e., more negative) than the local one. One possible reason of this outcome could be a stronger decrease in secondary aerosols due to stringent pollution control of precursors (SO_2; NO_x; volatile organic compounds, VOCs) than that of primary aerosol, as found for several French EMEP/MERA network sites (Font et al., 2023). Indeed, the primary to secondary aerosol ratio is expected to be larger for urban than for regional background sites.

4 Conclusions

This study presents a quantitative estimation of the aerosol optical depth variability in Europe using long-term measurements (2000–2021) from the MAIAC algorithm applied to MODIS satellite observations. The MAIAC validation, performed at the European scale against ground-based sun photometer data, demonstrates a slight underestimation of MAIAC AOD, showing an MBE of −0.02 and an RMSE of 0.06, respectively. An expected error EE $= \pm(0.05\text{AOD} +$ 0.05) has been found for the European continent, which is lower with respect to what was suggested by Lyapustin et al. (2018). Moreover, according to the AERONET AE splitting analysis, the validation, which provides satisfactory results for mixed and fine aerosol mode, does not perform as strongly in the presence of coarse-dominated aerosols. This suggests that further improvements of the MAIAC algorithm are needed for scenes dominated by dust or other coarse-sized particles.

Regarding the AOD seasonal climatology over the European continent, the AOD exhibits maximum and minimum values during the summer (JJA) and winter (DJF) seasons, respectively, showing a strong north–south latitudinal gradient. Values of AOD in the range of 0.12–0.22 (JJA) and 0.06–0.09 (DJF) are observed in the 30–60° N band.

Concerning the link between regional- and local-scale air quality across the main European cities, which was the main objective of this work, both the regional background and city level AOD show a general north–south gradient with increasing AOD and several hotspots over the Po Valley and the Mediterranean Sea. The analysis of the local-to-regional ratio shows that most of the cities contribute to the enhancement of the AOD loading with respect to their regional background. In contrast, for some cities a slightly negative LTRR could be explained by either specific losses or an inhomogeneity of the regional background. On a relative scale the

city contribution to regional AOD is maximum during the winter season because the primary vs. secondary aerosol ratio is expected to be the largest. Concerning the Paris area, most of the pollution has been considered to be transported from the European continent in previous studies (Beekmann et al., 2015). In fact, Paris represents an important isolated agglomeration with respect to the surrounding area. Indeed, the long-term analysis conducted in this work indicates an average local-to-regional excess ratio of 39 %, suggesting a non-negligible impact of the city emissions in addition to the regional aerosol burden in Paris. Further investigation is needed to understand the nature of this AOD difference. As a matter of fact, the interaction between the regional background and the local emissions cannot be exploited through AOD measurements directly, although we know that changes in the chemical and optical properties lead to changes in the aerosol extinction profile. Further investigation of the interaction between biogenic and anthropogenic local and regional air masses and the impact on aerosol properties will be provided in the ACROSS project (Cantrell and Michoud, 2022).

Different studies have already shown negative decreasing AOD trends over the European continent using MODIS satellite data in particular, however, most of the time with a broader spatial resolution with respect to the product used in this study. The MAIAC high-spatial-resolution product has been exploited to investigate the AOD trends at both the European and local city scale. The result shows a general AOD decrease over the entire European continent, consistent with the recent literature and in connection with the mitigation policies over the European countries. In particular, spatially homogeneous trends have been found over known European hotspots (e.g., $-1.34\,\%\,\mathrm{yr}^{-1}$ and $-1.66\,\%\,\mathrm{yr}^{-1}$ for the Mediterranean Sea and the Po Valley, respectively). In addition, taking advantage of the high spatial resolution, the analysis has also been extended at the city level, showing a statistically significant yearly decrease in AOD at 550 nm during the last 2 decades in the range of $[-0.5, -1.7]\,\%\,\mathrm{yr}^{-1}$ at the city level and $[-0.9, -2.0]\,\%\,\mathrm{yr}^{-1}$ in the surroundings. This result highlights the faster decrease in regional AOD levels with respect to those at the urban–local scale. Nevertheless, over the Paris area, we observed a statistically significant negative trend only at the regional scale. A potential explanation could be linked to the more stringent control of aerosol precursor emissions (SO_2, NO_x, VOCs) with respect to direct aerosol emissions (Font et al., 2023).

Data availability. The MAIAC MCD19A2 data used in this study are accessible at https://doi.org/10.5067/MODIS/MCD19A2.006 (Lyapustin et al., 2018). The AERONET data are available at https://aeronet.gsfc.nasa.gov/ (AERONET, 2023). Population data reported in Table 1 can be accessed at the following link: http://data.europa.eu/88u/dataset/yfspvoibibfesstjomhcg (Eurostat, 2023). The data and the codes that support the findings of this study are available upon request from the corresponding authors.

Supplement. The supplement related to this article is available online at: https://doi.org/10.5194/acp-23-12455-2023-supplement.

Author contributions. LDA, CDB and MB designed the study and discussed the results. LDA performed the data analysis with contributions from CDB and MB. GF, PF, GS and JFD contributed to the discussion of the results. LDA, CDB and MB wrote the paper with contributions from all co-authors.

Competing interests. The contact author has declared that none of the authors has any competing interests.

Disclaimer. Publisher's note: Copernicus Publications remains neutral with regard to jurisdictional claims in published maps and institutional affiliations.

Special issue statement. This article is part of the special issue "Atmospheric Chemistry of the Suburban Forest – multiplatform observational campaign of the chemistry and physics of mixed urban and biogenic emissions". It is not associated with a conference.

Acknowledgements. This work has been supported by the ACROSS and the RI-URBANS projects. The ACROSS project has received funding from the French National Research Agency (ANR) under the investment program integrated into France 2030, with the reference ANR-17-MPGA-0002, and it was supported by the French National program LEFE (Les Enveloppes Fluides et l'Environnement) of the CNRS/INSU (Centre National de la Recherche Scientifique/Institut National des Sciences de L'Univers). The RI-URBANS project has received funding from the European Union's Horizon 2020 research and innovation program under grant agreement no. 101036245. We thank all the AERONET PIs and their staff for establishing and maintaining all the sites used in this investigation. Useful discussions with Marc Mallet, Yevgeny Derimian and Jean-Christophe Raut are gratefully acknowledged. We thank Christopher Cantrell and Vincent Michoud, PIs of the ACROSS project. Helpful comments by the reviewers are gratefully acknowledged.

Financial support. This research has been supported by the European Commission, Horizon 2020 (grant no. 101036245); the Agence Nationale de la Recherche (grant no. ANR-17-MPGA-0002); and the Centre National de la Recherche Scientifique, Institut National des Sciences de L'Univers (ACROSS-GO).

Review statement. This paper was edited by Stelios Kazadzis and reviewed by Alexei Lyapustin and one anonymous referee.

References

AERONET: Version 3 Aerosol Optical Depth, https://aeronet.gsfc.nasa.gov/, last access: June 2023.

Alpert, P., Shvainshtein, O., and Kishcha, P.: AOD Trends over Megacities Based on Space Monitoring Using MODIS and MISR, American Journal of Climate Change, 1, 117–131, https://doi.org/10.4236/ajcc.2012.13010, 2012.

Aman, N., Manomaiphiboon, K., Suwattiga, P., Assareh, N., Limpaseni, W., Suwanathada, P., Soonsin, V., and Wang, Y.: Visibility, aerosol optical depth, and low-visibility events in Bangkok during the dry season and associated local weather and synoptic patterns, Environ. Monit. Assess., 194, 322, https://doi.org/10.1007/s10661-022-09880-2, 2022.

Amato, F., Alastuey, A., Karanasiou, A., Lucarelli, F., Nava, S., Calzolai, G., Severi, M., Becagli, S., Gianelle, V. L., Colombi, C., Alves, C., Custódio, D., Nunes, T., Cerqueira, M., Pio, C., Eleftheriadis, K., Diapouli, E., Reche, C., Minguillón, M. C., Manousakas, M.-I., Maggos, T., Vratolis, S., Harrison, R. M., and Querol, X.: AIRUSE-LIFE+: a harmonized PM speciation and source apportionment in five southern European cities, Atmos. Chem. Phys., 16, 3289–3309, https://doi.org/10.5194/acp-16-3289-2016, 2016.

Ångström, A.: On the Atmospheric Transmission of Sun Radiation and on Dust in the Air, Geogr. Ann., 11, 156–166, https://doi.org/10.1080/20014422.1929.11880498, 1929.

Backes, A. M., Aulinger, A., Bieser, J., Matthias, V., and Quante, M.: Ammonia emissions in Europe, part II: How ammonia emission abatement strategies affect secondary aerosols, Atmos. Environ., 126, 153–161, https://doi.org/10.1016/j.atmosenv.2015.11.039, 2016.

Bahadur, R., Praveen, P. S., Xu, Y., and Ramanathan, V.: Solar absorption by elemental and brown carbon determined from spectral observations, P. Natl. Acad. Sci. USA, 109, 17366–17371, https://doi.org/10.1073/pnas.1205910109, 2012.

Bai, R., Xue, Y., Jiang, X., Jin, C., and Sun, Y.: Retrieval of High-Resolution Aerosol Optical Depth for Urban Air Pollution Monitoring, Atmosphere, 13, 756, https://doi.org/10.3390/atmos13050756, 2022.

Barnaba, F. and Gobbi, G. P.: Aerosol seasonal variability over the Mediterranean region and relative impact of maritime, continental and Saharan dust particles over the basin from MODIS data in the year 2001, Atmos. Chem. Phys., 4, 2367–2391, https://doi.org/10.5194/acp-4-2367-2004, 2004.

Bäumer, D., Vogel, B., Versick, S., Rinke, R., Möhler, O., and Schnaiter, M.: Relationship of visibility, aerosol optical thickness and aerosol size distribution in an ageing air mass over South-West Germany, Atmos. Environ., 42, 989–998, https://doi.org/10.1016/j.atmosenv.2007.10.017, 2008.

Beekmann, M., Chiappini, L., Favez, O., Aymoz, G., Bessagnet, B., Rouil, L., and Rossignol, S.: The megapoli paris campaign for urban aerosol characterisation – a comprehensive data set for air quality model evaluation, in: 13. International Conference on Harmonisation within Atmospheric Dispersion Modelling for Regulatory Purposes (HARMO 13), 1–4 June 2010, Paris, France, 519–523, ISBN 978-286815062-2, 2010.

Beekmann, M., Prévôt, A. S. H., Drewnick, F., Sciare, J., Pandis, S. N., Denier van der Gon, H. A. C., Crippa, M., Freutel, F., Poulain, L., Ghersi, V., Rodriguez, E., Beirle, S., Zotter, P., von der Weiden-Reinmüller, S.-L., Bressi, M., Fountoukis, C., Petetin, H., Szidat, S., Schneider, J., Rosso, A., El Haddad, I., Megaritis, A., Zhang, Q. J., Michoud, V., Slowik, J. G., Moukhtar, S., Kolmonen, P., Stohl, A., Eckhardt, S., Borbon, A., Gros, V., Marchand, N., Jaffrezo, J. L., Schwarzenboeck, A., Colomb, A., Wiedensohler, A., Borrmann, S., Lawrence, M., Baklanov, A., and Baltensperger, U.: In situ, satellite measurement and model evidence on the dominant regional contribution to fine particulate matter levels in the Paris megacity, Atmos. Chem. Phys., 15, 9577–9591, https://doi.org/10.5194/acp-15-9577-2015, 2015.

Bellouin, N., Quaas, J., Gryspeerdt, E., Kinne, S., Stier, P., Watson-Parris, D., Boucher, O., Carslaw, K. S., Christensen, M., Daniau, A.-L., Dufresne, J.-L., Feingold, G., Fiedler, S., Forster, P., Gettelman, A., Haywood, J. M., Lohmann, U., Malavelle, F., Mauritsen, T., McCoy, D. T., Myhre, G., Mülmenstädt, J., Neubauer, D., Possner, A., Rugenstein, M., Sato, Y., Schulz, M., Schwartz, S. E., Sourdeval, O., Storelvmo, T., Toll, V., Winker, D., and Stevens, B.: Bounding Global Aerosol Radiative Forcing of Climate Change, Rev. Geophys., 58, e2019RG000660, https://doi.org/10.1029/2019RG000660, 2020.

Bender, F. A.-M.: Aerosol Forcing: Still Uncertain, Still Relevant, AGU Adv., 1, e2019AV000128, https://doi.org/10.1029/2019AV000128, 2020.

Bilal, M., Nazeer, M., Nichol, J. E., Bleiweiss, M. P., Qiu, Z., Jäkel, E., Campbell, J. R., Atique, L., Huang, X., and Lolli, S.: A Simplified and Robust Surface Reflectance Estimation Method (SREM) for Use over Diverse Land Surfaces Using Multi-Sensor Data, Remote Sens., 11, 1344, https://doi.org/10.3390/rs11111344, 2019.

Bodenheimer, S., Nirel, R., Lensky, I. M., and Dayan, U.: The synoptic skill of aerosol optical depth and angstrom exponent levels over the Mediterranean Basin, Int. J. Climatol., 41, 1801–1820, https://doi.org/10.1002/joc.6931, 2021.

Boers, R., Weele, M. van, Meijgaard, E. van, Savenije, M., Siebesma, A. P., Bosveld, F., and Stammes, P.: Observations and projections of visibility and aerosol optical thickness (1956–2100) in the Netherlands: impacts of time-varying aerosol composition and hygroscopicity, Environ. Res. Lett., 10, 015003, https://doi.org/10.1088/1748-9326/10/1/015003, 2015.

Bovchaliuk, A., Milinevsky, G., Danylevsky, V., Goloub, P., Dubovik, O., Holdak, A., Ducos, F., and Sosonkin, M.: Variability of aerosol properties over Eastern Europe observed from ground and satellites in the period from 2003 to 2011, Atmos. Chem. Phys., 13, 6587–6602, https://doi.org/10.5194/acp-13-6587-2013, 2013.

Bressi, M., Sciare, J., Ghersi, V., Mihalopoulos, N., Petit, J.-E., Nicolas, J. B., Moukhtar, S., Rosso, A., Féron, A., Bonnaire, N., Poulakis, E., and Theodosi, C.: Sources and geographical origins of fine aerosols in Paris (France), Atmos. Chem. Phys., 14, 8813–8839, https://doi.org/10.5194/acp-14-8813-2014, 2014.

Bucci, S., Cristofanelli, P., Decesari, S., Marinoni, A., Sandrini, S., Größ, J., Wiedensohler, A., Di Marco, C. F., Nemitz, E., Cairo, F., Di Liberto, L., and Fierli, F.: Vertical distribution of aerosol optical properties in the Po Valley during the 2012 summer campaigns, Atmos. Chem. Phys., 18, 5371–5389, https://doi.org/10.5194/acp-18-5371-2018, 2018.

Cantrell, C. and Michoud, V.: ACROSS: A Field Experiment to Study Atmospheric Oxidation Chemistry and Physics of Mixed Anthropogenic-Biogenic Air Masses in

the Greater Paris Area, B. Am. Meteorol. Soc., 1, 599–603, https://doi.org/10.1175/BAMS-D-21-0115.1, 2022.

Chazette, P., Totems, J., and Shang, X.: Transport of aerosols over the French Riviera – link between ground-based lidar and spaceborne observations, Atmos. Chem. Phys., 19, 3885–3904, https://doi.org/10.5194/acp-19-3885-2019, 2019.

Chen, C., Dubovik, O., Fuertes, D., Litvinov, P., Lapyonok, T., Lopatin, A., Ducos, F., Derimian, Y., Herman, M., Tanré, D., Remer, L. A., Lyapustin, A., Sayer, A. M., Levy, R. C., Hsu, N. C., Descloitres, J., Li, L., Torres, B., Karol, Y., Herrera, M., Herreras, M., Aspetsberger, M., Wanzenboeck, M., Bindreiter, L., Marth, D., Hangler, A., and Federspiel, C.: Validation of GRASP algorithm product from POLDER/PARASOL data and assessment of multi-angular polarimetry potential for aerosol monitoring, Earth Syst. Sci. Data, 12, 3573–3620, https://doi.org/10.5194/essd-12-3573-2020, 2020.

Chen, L., Wang, R., Wei, G., Han, J., and Zha, Y.: A surface reflectance correction model to improve the retrieval of MISR aerosol optical depth supported by MODIS data, Adv. Space Res., 67, 858–867, https://doi.org/10.1016/j.asr.2020.10.033, 2021.

Chiapello, I., Formenti, P., Mbemba Kabuiku, L., Ducos, F., Tanré, D., and Dulac, F.: Aerosol optical properties derived from POLDER-3/PARASOL (2005–2013) over the Western Mediterranean Sea – Part 2: Spatial distribution and temporal variability, Atmos. Chem. Phys., 21, 12715–12737, https://doi.org/10.5194/acp-21-12715-2021, 2021.

Chubarova, N. Y., Poliukhov, A. A., and Gorlova, I. D.: Long-term variability of aerosol optical thickness in Eastern Europe over 2001–2014 according to the measurements at the Moscow MSU MO AERONET site with additional cloud and NO_2 correction, Atmos. Meas. Tech., 9, 313–334, https://doi.org/10.5194/amt-9-313-2016, 2016.

Clarisse, L., Clerbaux, C., Dentener, F., Hurtmans, D., and Coheur, P.-F.: Global ammonia distribution derived from infrared satellite observations, Nat. Geosci., 2, 479–483, https://doi.org/10.1038/ngeo551, 2009.

Coelho, S., Ferreira, J., Rodrigues, V., and Lopes, M.: Source apportionment of air pollution in European urban areas: Lessons from the ClairCity project, J. Environ. Manage., 320, 115899, https://doi.org/10.1016/j.jenvman.2022.115899, 2022.

Colette, A., Aas, W., Banin, L., Braban, C. F., Ferm, M., Gonzalez Ortiz, A., Ilyin, I., Mar, K., Pandolfi, M., Putaud, J.-P., Shatalov, V., Solberg, S., Spindler, G., Tarasova, O., Vana, M., Adani, M., Almodovar, P., Berton, E., Bessagnet, B., Bohlin-Nizzetto, P., Boruvkova, J., Breivik, K., Briganti, G., Cappelletti, A., Cuvelier, K., Derwent, R., D'Isidoro, M., Fagerli, H., Funk, C., Garcia Vivanco, M., Haeuber, R., Hueglin, C., Jenkins, S., Kerr, J., de Leeuw, F., Lynch, J., Manders, A., Mircea, M., Pay, M. T., Pritula, D., Querol, X., Raffort, V., Reiss, I., Roustan, Y., Sauvage, S., Scavo, K., Simpson, D., Smith, R. I., Tang, Y. S., Theobald, M., Torseth, K., Tsyro, S., van Pul, A., Vidic, S., Wallasch, M., and Wind, P.: Air pollution trends in the EMEP region between 1990 and 2012, 2016, Norwegian Institute for Air Research, Kjeller, Norway, EMEP: CCC-Report 1/2016, 105 pp., 2016.

Dayan, C., Fredj, E., Misztal, P. K., Gabay, M., Guenther, A. B., and Tas, E.: Emission of biogenic volatile organic compounds from warm and oligotrophic seawater in the Eastern Mediterranean, Atmos. Chem. Phys., 20, 12741–12759, https://doi.org/10.5194/acp-20-12741-2020, 2020.

Diémoz, H., Barnaba, F., Magri, T., Pession, G., Dionisi, D., Pittavino, S., Tombolato, I. K. F., Campanelli, M., Della Ceca, L. S., Hervo, M., Di Liberto, L., Ferrero, L., and Gobbi, G. P.: Transport of Po Valley aerosol pollution to the northwestern Alps – Part 1: Phenomenology, Atmos. Chem. Phys., 19, 3065–3095, https://doi.org/10.5194/acp-19-3065-2019, 2019.

Dockery, D. W.: Health Effects of Particulate Air Pollution, Ann. Epidemiol., 19, 257–263, https://doi.org/10.1016/j.annepidem.2009.01.018, 2009.

Eck, T. F., Holben, B. N., Reid, J. S., Sinyuk, A., Giles, D. M., Arola, A., Slutsker, I., Schafer, J. S., Sorokin, M. G., Smirnov, A., LaRosa, A. D., Kraft, J., Reid, E. A., O'Neill, N. T., Welton, E. J., and Menendez, A. R.: The extreme forest fires in California/Oregon in 2020: Aerosol optical and physical properties and comparisons of aged versus fresh smoke, Atmos. Environ., 305, 119798, https://doi.org/10.1016/j.atmosenv.2023.119798, 2023.

Elson, P., Sales de Andrade, E., Lucas, G., May, R., Hattersley, R., Campbell, E., Dawson, A., Little, B., Raynaud, S., scmc72, Snow, A. D., Comer, R., Donkers, K., Blay, B., Killick, P., Wilson, N., Peglar, P., Igolston, Ibdreyer, Andrew, Szymaniak, J., Berchet, A., Bosley, C., Davis, L., Filipe, Krasting, J., Bradbury, M., Kirkham, D., stephenworsley, and Havlin, C.: SciTools/cartopy: v0.22.0, Zenodo [code], https://doi.org/10.5281/zenodo.1182735, 2023.

European Commission, Joint Research Centre, San-Miguel-Ayanz, J., Durrant, T., Boca, R., Maianti, P., Libertá, G., Artés-Vivancos, T., Oom, D., Branco, A., Rigo, D., Ferrari, D., Pfeiffer, H., Grecchi, R., and Nuijten, D.: Advance report on wildfires in Europe, Middle East and North Africa 2021, Publications Office of the European Union, https://doi.org/10.2760/039729, 2022.

Eurostat: Population on 1 January by age groups and sex – cities and greater cities, European Commission [data set], http://data.europa.eu/88u/dataset/yfspvoibibfcsstjomhcg (last access: September 2023), 2023.

Faisal, A.-A., Rahman, M. M., and Haque, S.: Retrieving spatial variation of aerosol level over urban mixed land surfaces using Landsat imageries: Degree of air pollution in Dhaka Metropolitan Area, Phys. Chem. Earth Parts ABC, 126, 103074, https://doi.org/10.1016/j.pce.2021.103074, 2022.

Falah, S., Mhawish, A., Sorek-Hamer, M., Lyapustin, A. I., Kloog, I., Banerjee, T., Kizel, F., and Broday, D. M.: Impact of environmental attributes on the uncertainty in MAIAC/MODIS AOD retrievals: A comparative analysis, Atmos. Environ., 262, 118659, https://doi.org/10.1016/j.atmosenv.2021.118659, 2021.

Filonchyk, M., Hurynovich, V., Yan, H., Zhou, L., and Gusev, A.: Climatology of aerosol optical depth over Eastern Europe based on 19 years (2000–2018) MODIS TERRA data, Int. J. Climatol., 40, 3531–3549, https://doi.org/10.1002/joc.6412, 2020a.

Filonchyk, M., Hurynovich, V., and Yan, H.: Trends in aerosol optical properties over Eastern Europe based on MODIS-Aqua, Geosci. Front., 11, 2169–2181, https://doi.org/10.1016/j.gsf.2020.03.014, 2020b.

Fiore, A. M., Naik, V., Spracklen, D. V., Steiner, A., Unger, N., Prather, M., Bergmann, D., Cameron-Smith, P. J., Cionni, I., Collins, W. J., Dalsøren, S., Eyring, V., Folberth, G. A., Ginoux, P., Horowitz, L. W., Josse, B., Lamarque, J.-F., MacKenzie, I. A., Nagashima, T., O'Connor, F. M., Righi, M., Rumbold, S. T.,

Shindell, D. T., Skeie, R. B., Sudo, K., Szopa, S., Takemura, T., and Zeng, G.: Global air quality and climate, Chem. Soc. Rev., 41, 6663–6683, https://doi.org/10.1039/C2CS35095E, 2012.

Floutsi, A. A., Korras-Carraca, M. B., Matsoukas, C., Hatzianastassiou, N., and Biskos, G.: Climatology and trends of aerosol optical depth over the Mediterranean basin during the last 12 years (2002–2014) based on Collection 006 MODIS-Aqua data, Sci. Total Environ., 551–552, 292–303, https://doi.org/10.1016/j.scitotenv.2016.01.192, 2016.

Font, A., Bourin, A., Gouillou, C., Debevec, C., Bonnaire, N., Sauvage, S., F. de Brito, J., and Riffault, V.: Aerosol composition at EMEP remote sites in France : mass balance and de-weathered trends of $PM_{2.5}$ and its main components, EGU General Assembly 2023, Vienna, Austria, 24–28 April 2023, EGU23-940, https://doi.org/10.5194/egusphere-egu23-940, 2023.

Foret, G., Michoud, V., Kotthaus, S., Petit, J.-E., Baudic, A., Siour, G., Kim, Y., Doussin, J.-F., Dupont, J.-C., Formenti, P., Gaimoz, C., Ghersi, V., Gratien, A., Gros, V., Jaffrezo, J.-L., Haeffelin, M., Kreitz, M., Ravetta, F., Sartelet, K., Simon, L., Té, Y., Uzu, G., Zhang, S., Favez, O., and Beekmann, M.: The December 2016 extreme weather and particulate matter pollution episode in the Paris region (France), Atmos. Environ., 291, 119386, https://doi.org/10.1016/j.atmosenv.2022.119386, 2022.

Formenti, P., Mbemba Kabuiku, L., Chiapello, I., Ducos, F., Dulac, F., and Tanré, D.: Aerosol optical properties derived from POLDER-3/PARASOL (2005–2013) over the western Mediterranean Sea – Part 1: Quality assessment with AERONET and in situ airborne observations, Atmos. Meas. Tech., 11, 6761–6784, https://doi.org/10.5194/amt-11-6761-2018, 2018.

Gao, Y., Ma, M., Yan, F., Su, H., Wang, S., Liao, H., Zhao, B., Wang, X., Sun, Y., Hopkins, J. R., Chen, Q., Fu, P., Lewis, A. C., Qiu, Q., Yao, X., and Gao, H.: Impacts of biogenic emissions from urban landscapes on summer ozone and secondary organic aerosol formation in megacities, Sci. Total Environ., 814, 152654, https://doi.org/10.1016/j.scitotenv.2021.152654, 2022.

Giles, D. M., Sinyuk, A., Sorokin, M. G., Schafer, J. S., Smirnov, A., Slutsker, I., Eck, T. F., Holben, B. N., Lewis, J. R., Campbell, J. R., Welton, E. J., Korkin, S. V., and Lyapustin, A. I.: Advancements in the Aerosol Robotic Network (AERONET) Version 3 database – automated near-real-time quality control algorithm with improved cloud screening for Sun photometer aerosol optical depth (AOD) measurements, Atmos. Meas. Tech., 12, 169–209, https://doi.org/10.5194/amt-12-169-2019, 2019.

Gkikas, A., Hatzianastassiou, N., Mihalopoulos, N., and Torres, O.: Characterization of aerosol episodes in the greater Mediterranean Sea area from satellite observations (2000–2007), Atmos. Environ., 128, 286–304, https://doi.org/10.1016/j.atmosenv.2015.11.056, 2016.

Gkikas, A., Proestakis, E., Amiridis, V., Kazadzis, S., Di Tomaso, E., Marinou, E., Hatzianastassiou, N., Kok, J. F., and García-Pando, C. P.: Quantification of the dust optical depth across spatiotemporal scales with the MIDAS global dataset (2003–2017), Atmos. Chem. Phys., 22, 3553–3578, https://doi.org/10.5194/acp-22-3553-2022, 2022.

Gladson, L., Garcia, N., Bi, J., Liu, Y., Lee, H. J., and Cromar, K.: Evaluating the Utility of High-Resolution Spatiotemporal Air Pollution Data in Estimating Local $PM_{2.5}$ Exposures in California from 2015–2018, Atmosphere, 13, 85, https://doi.org/10.3390/atmos13010085, 2022.

Grgurić, S., Križan, J., Gašparac, G., Antonić, O., Špirić, Z., Mamouri, R. E., Christodoulou, A., Nisantzi, A., Agapiou, A., Themistocleous, K., Fedra, K., Panayiotou, C., and Hadjimitsis, D.: Relationship between MODIS based Aerosol Optical Depth and PM_{10} over Croatia, Cent. Eur. J. Geosci., 6, 2–16, https://doi.org/10.2478/s13533-012-0135-6, 2014.

Grigorieva, E. and Lukyanets, A.: Combined Effect of Hot Weather and Outdoor Air Pollution on Respiratory Health: Literature Review, Atmosphere, 12, 790, https://doi.org/10.3390/atmos12060790, 2021.

Groot Zwaaftink, C. D., Aas, W., Eckhardt, S., Evangeliou, N., Hamer, P., Johnsrud, M., Kylling, A., Platt, S. M., Stebel, K., Uggerud, H., and Yttri, K. E.: What caused a record high PM_{10} episode in northern Europe in October 2020?, Atmos. Chem. Phys., 22, 3789–3810, https://doi.org/10.5194/acp-22-3789-2022, 2022.

Guo, J.-P., Zhang, X.-Y., Che, H.-Z., Gong, S.-L., An, X., Cao, C.-X., Guang, J., Zhang, H., Wang, Y.-Q., Zhang, X.-C., Xue, M., and Li, X.-W.: Correlation between PM concentrations and aerosol optical depth in eastern China, Atmos. Environ., 43, 5876–5886, https://doi.org/10.1016/j.atmosenv.2009.08.026, 2009.

Gupta, G., Venkat Ratnam, M., Madhavan, B. L., and Narayanamurthy, C. S.: Long-term trends in Aerosol Optical Depth obtained across the globe using multi-satellite measurements, Atmos. Environ., 273, 118953, https://doi.org/10.1016/j.atmosenv.2022.118953, 2022.

Gupta, G., Venkat Ratnam, M., Madhavan, B. L., and Jayaraman, A.: Global trends in the aerosol optical, physical, and morphological properties obtained using multi-sensor measurements, Atmos. Environ., 295, 119569, https://doi.org/10.1016/j.atmosenv.2022.119569, 2023.

Gupta, P., Levy, R. C., Mattoo, S., Remer, L. A., and Munchak, L. A.: A surface reflectance scheme for retrieving aerosol optical depth over urban surfaces in MODIS Dark Target retrieval algorithm, Atmos. Meas. Tech., 9, 3293–3308, https://doi.org/10.5194/amt-9-3293-2016, 2016.

Ha, S., Liu, Z., Sun, W., Lee, Y., and Chang, L.: Improving air quality forecasting with the assimilation of GOCI aerosol optical depth (AOD) retrievals during the KORUS-AQ period, Atmos. Chem. Phys., 20, 6015–6036, https://doi.org/10.5194/acp-20-6015-2020, 2020.

Hammer, M. S., van Donkelaar, A., Li, C., Lyapustin, A., Sayer, A. M., Hsu, N. C., Levy, R. C., Garay, M. J., Kalashnikova, O. V., Kahn, R. A., Brauer, M., Apte, J. S., Henze, D. K., Zhang, L., Zhang, Q., Ford, B., Pierce, J. R., and Martin, R. V.: Global Estimates and Long-Term Trends of Fine Particulate Matter Concentrations (1998–2018), Environ. Sci. Technol., 54, 7879–7890, https://doi.org/10.1021/acs.est.0c01764, 2020.

He, Q., Zhang, M., and Huang, B.: Spatio-temporal variation and impact factors analysis of satellite-based aerosol optical depth over China from 2002 to 2015, Atmos. Environ., 129, 79–90, https://doi.org/10.1016/j.atmosenv.2016.01.002, 2016.

He, Q., Wang, M., and Yim, S. H. L.: The spatiotemporal relationship between $PM_{2.5}$ and aerosol optical depth in China: influencing factors and implications for satellite $PM_{2.5}$ estimations using MAIAC aerosol optical depth, Atmos. Chem. Phys., 21, 18375–18391, https://doi.org/10.5194/acp-21-18375-2021, 2021.

Hough, I., Sarafian, R., Shtein, A., Zhou, B., Lepeule, J., and Kloog, I.: Gaussian Markov random fields improve ensemble predictions of daily 1 km $PM_{2.5}$ and PM_{10} across France, Atmos. Environ., 264, 118693, https://doi.org/10.1016/j.atmosenv.2021.118693, 2021.

Hsu, N. C., Tsay, S.-C., King, M. D., and Herman, J. R.: Aerosol properties over bright-reflecting source regions, IEEE T. Geosci. Remote, 42, 557–569, https://doi.org/10.1109/TGRS.2004.824067, 2004.

Hsu, N. C., Lee, J., Sayer, A. M., Carletta, N., Chen, S.-H., Tucker, C. J., Holben, B. N., and Tsay, S.-C.: Retrieving near-global aerosol loading over land and ocean from AVHRR, J. Geophys. Res.-Atmos., 122, 9968–9989, https://doi.org/10.1002/2017JD026932, 2017.

Hussain, M. M. and Mahmud, I.: pyMannKendall: a python package for non parametric Mann Kendall family of trend tests., J. Open Source Softw., 4, 1556, https://doi.org/10.21105/joss.01556, 2019.

Israelevich, P., Ganor, E., Alpert, P., Kishcha, P., and Stupp, A.: Predominant transport paths of Saharan dust over the Mediterranean Sea to Europe, J. Geophys. Res.-Atmos., 117, D02205, https://doi.org/10.1029/2011JD016482, 2012.

Jaén, C., Udina, M., and Bech, J.: Analysis of two heat wave driven ozone episodes in Barcelona and surrounding region: Meteorological and photochemical modeling, Atmos. Environ., 246, 118037, https://doi.org/10.1016/j.atmosenv.2020.118037, 2021.

Jung, C.-R., Chen, W.-T., and Nakayama, S. F.: A National-Scale 1-km Resolution $PM_{2.5}$ Estimation Model over Japan Using MAIAC AOD and a Two-Stage Random Forest Model, Remote Sens., 13, 3657, https://doi.org/10.3390/rs13183657, 2021.

Just, A. C., Wright, R. O., Schwartz, J., Coull, B. A., Baccarelli, A. A., Tellez-Rojo, M. M., Moody, E., Wang, Y., Lyapustin, A., and Kloog, I.: Using high-resolution satellite aerosol optical depth to estimate daily $PM_{2.5}$ geographical distribution in Mexico City, Environ. Sci. Technol., 49, 8576–8584, https://doi.org/10.1021/acs.est.5b00859, 2015.

Karl, M., Tsigaridis, K., Vignati, E., and Dentener, F.: Formation of secondary organic aerosol from isoprene oxidation over Europe, Atmos. Chem. Phys., 9, 7003–7030, https://doi.org/10.5194/acp-9-7003-2009, 2009.

Kessner, A. L., Wang, J., Levy, R. C., and Colarco, P. R.: Remote sensing of surface visibility from space: A look at the United States East Coast, Atmos. Environ., 81, 136–147, https://doi.org/10.1016/j.atmosenv.2013.08.050, 2013.

Kinne, S., O'Donnel, D., Stier, P., Kloster, S., Zhang, K., Schmidt, H., Rast, S., Giorgetta, M., Eck, T. F., and Stevens, B.: MAC-v1: A new global aerosol climatology for climate studies, J. Adv. Model. Earth Syst., 5, 704–740, https://doi.org/10.1002/jame.20035, 2013.

Kondragunta, S., Lee, P., McQueen, J., Kittaka, C., Prados, A. I., Ciren, P., Laszlo, I., Pierce, R. B., Hoff, R., and Szykman, J. J.: Air Quality Forecast Verification Using Satellite Data, J. Appl. Meteorol. Climatol., 47, 425–442, 2008.

Lee, J., Hsu, N. C., Sayer, A. M., Bettenhausen, C., and Yang, P.: AERONET-Based Nonspherical Dust Optical Models and Effects on the VIIRS Deep Blue/SOAR Over Water Aerosol Product, J. Geophys. Res.-Atmos., 122, 10384–10401, https://doi.org/10.1002/2017JD027258, 2017.

Lee, S., Park, S., Lee, M.-I., Kim, G., Im, J., and Song, C.-K.: Air Quality Forecasts Improved by Combining Data Assimilation and Machine Learning With Satellite AOD, Geophys. Res. Lett., 49, e2021GL096066, https://doi.org/10.1029/2021GL096066, 2022.

Li, M.-H., Fan, L.-C., Mao, B., Yang, J.-W., Choi, A. M. K., Cao, W.-J., and Xu, J.-F.: Short-term Exposure to Ambient Fine Particulate Matter Increases Hospitalizations and Mortality in COPD: A Systematic Review and Meta-analysis, Chest, 149, 447–458, https://doi.org/10.1378/chest.15-0513, 2016.

Li, Z., Wen, Q., and Zhang, R.: Sources, health effects and control strategies of indoor fine particulate matter ($PM_{2.5}$): A review, Sci. Total Environ., 586, 610–622, https://doi.org/10.1016/j.scitotenv.2017.02.029, 2017.

Liu, J., Mauzerall, D. L., and Horowitz, L. W.: Evaluating inter-continental transport of fine aerosols: (2) Global health impact, Atmos. Environ., 43, 4339–4347, https://doi.org/10.1016/j.atmosenv.2009.05.032, 2009.

Liu, Y., Liu, Y., Wang, M., Dong, X., Zheng, Y., Shrivastava, M., Qian, Y., Bai, H., Li, X., and Yang, X.-Q.: Anthropogenic–biogenic interaction amplifies warming from emission reduction over the southeastern US, Environ. Res. Lett., 16, 124046, https://doi.org/10.1088/1748-9326/ac3285, 2021.

Luo, M., Ji, Y., Ren, Y., Gao, F., Zhang, H., Zhang, L., Yu, Y., and Li, H.: Characteristics and Health Risk Assessment of $PM_{2.5}$-Bound PAHs during Heavy Air Pollution Episodes in Winter in Urban Area of Beijing, China, Atmosphere, 12, 323, https://doi.org/10.3390/atmos12030323, 2021.

Lyapustin, A. and Wang, Y.: MCD19A2 MODIS/Terra+Aqua Land Aerosol Optical Depth Daily L2G Global 1km SIN Grid V006, NASA EOSDIS Land Processes DAAC [data set], https://doi.org/10.5067/MODIS/MCD19A2.006, 2018.

Lyapustin, A., Wang, Y., Laszlo, I., and Korkin, S.: Improved cloud and snow screening in MAIAC aerosol retrievals using spectral and spatial analysis, Atmos. Meas. Tech., 5, 843–850, https://doi.org/10.5194/amt-5-843-2012, 2012.

Lyapustin, A., Wang, Y., Korkin, S., and Huang, D.: MODIS Collection 6 MAIAC algorithm, Atmos. Meas. Tech., 11, 5741–5765, https://doi.org/10.5194/amt-11-5741-2018, 2018.

Ma, X. and Yu, F.: Seasonal and spatial variations of global aerosol optical depth: multi-year modelling with GEOS-Chem-APM and comparisons with multiple-platform observations, Tellus B, 67, 25115, https://doi.org/10.3402/tellusb.v67.25115, 2015.

Ma, Y., Xin, J., Zhang, W., Gong, C., Wen, T., Wu, X., Wang, Y., Wang, L., Wu, F., and Ding, X.: Uncertainties of Simulated Aerosol Direct Radiative Effect Induced by Aerosol Chemical Components: A Measurement-Based Perspective From Urban-Forest Transition Region in East China, J. Geophys. Res.-Atmos., 126, e2020JD033688, https://doi.org/10.1029/2020JD033688, 2021.

Majewski, G., Szeląg, B., Mach, T., Rogula-Kozłowska, W., Aniol, E., Bihałowicz, J., Dmochowska, A., and Bihałowicz, J. S.: Predicting the Number of Days With Visibility in a Specific Range in Warsaw (Poland) Based on Meteorological and Air Quality Data, Front. Environ. Sci., 9, 623094, https://doi.org/10.3389/fenvs.2021.623094, 2021.

Manousakas, M. I., Florou, K., and Pandis, S. N.: Source Apportionment of Fine Organic and Inorganic Atmospheric Aerosol

in an Urban Background Area in Greece, Atmosphere, 11, 330, https://doi.org/10.3390/atmos11040330, 2020.

Mao, K. B., Ma, Y., Xia, L., Chen, W. Y., Shen, X. Y., He, T. J., and Xu, T. R.: Global aerosol change in the last decade: An analysis based on MODIS data, Atmos. Environ., 94, 680–686, https://doi.org/10.1016/j.atmosenv.2014.04.053, 2014.

Martin, S. T., Artaxo, P., Machado, L. A. T., Manzi, A. O., Souza, R. A. F., Schumacher, C., Wang, J., Andreae, M. O., Barbosa, H. M. J., Fan, J., Fisch, G., Goldstein, A. H., Guenther, A., Jimenez, J. L., Pöschl, U., Silva Dias, M. A., Smith, J. N., and Wendisch, M.: Introduction: Observations and Modeling of the Green Ocean Amazon (GoAmazon2014/5), Atmos. Chem. Phys., 16, 4785–4797, https://doi.org/10.5194/acp-16-4785-2016, 2016.

Martins, V. S., Lyapustin, A., de Carvalho, L. a. S., Barbosa, C. C. F., and Novo, E. M. L. M.: Validation of high-resolution MAIAC aerosol product over South America, J. Geophys. Res.-Atmos., 122, 7537–7559, https://doi.org/10.1002/2016JD026301, 2017.

Martins, V. S., Lyapustin, A., Wang, Y., Giles, D. M., Smirnov, A., Slutsker, I., and Korkin, S.: Global validation of columnar water vapor derived from EOS MODIS-MAIAC algorithm against the ground-based AERONET observations, Atmos. Res., 225, 181–192, https://doi.org/10.1016/j.atmosres.2019.04.005, 2019.

Masson-Delmotte, Zhai, P., Pirani, A., Connors, S. L., Péan, C., Berger, S., Caud, N., Chen, Y., Goldfarb, L., Gomis, M. I., Huang, M., Leitzell, K., Lonnoy, E., Matthews, J. B. R., Maycock, T. K., Waterfield, T., Yelekçi, Ö., Yu, R., and Zhou, B. (Eds.): Climate Change 2021: The Physical Science Basis. Contribution of Working Group I to the Sixth Assessment Report of the Intergovernmental Panel on Climate Change, Cambridge University Press, Cambridge, United Kingdom and New York, NY, USA, https://doi.org/10.1017/9781009157896, 2021.

Mehta, M., Singh, R., Singh, A., Singh, N., and Anshumali: Recent global aerosol optical depth variations and trends – A comparative study using MODIS and MISR level 3 datasets, Remote Sens. Environ., 181, 137–150, https://doi.org/10.1016/j.rse.2016.04.004, 2016.

Merdji, A. B., Lu, C., Xu, X., and Mhawish, A.: Long-term three-dimensional distribution and transport of Saharan dust: Observation from CALIPSO, MODIS, and reanalysis data, Atmos. Res., 286, 106658, https://doi.org/10.1016/j.atmosres.2023.106658, 2023.

Mhawish, A., Banerjee, T., Sorek-Hamer, M., Lyapustin, A., Broday, D. M., and Chatfield, R.: Comparison and evaluation of MODIS Multi-angle Implementation of Atmospheric Correction (MAIAC) aerosol product over South Asia, Remote Sens. Environ., 224, 12–28, https://doi.org/10.1016/j.rse.2019.01.033, 2019.

Michoud, V., Sciare, J., Sauvage, S., Dusanter, S., Léonardis, T., Gros, V., Kalogridis, C., Zannoni, N., Féron, A., Petit, J.-E., Crenn, V., Baisnée, D., Sarda-Estève, R., Bonnaire, N., Marchand, N., DeWitt, H. L., Pey, J., Colomb, A., Gheusi, F., Szidat, S., Stavroulas, I., Borbon, A., and Locoge, N.: Organic carbon at a remote site of the western Mediterranean Basin: sources and chemistry during the ChArMEx SOP2 field experiment, Atmos. Chem. Phys., 17, 8837–8865, https://doi.org/10.5194/acp-17-8837-2017, 2017.

Moulin, C., Lambert, C. E., Dayan, U., Masson, V., Ramonet, M., Bousquet, P., Legrand, M., Balkanski, Y. J., Guelle, W., Marticorena, B., Bergametti, G., and Dulac, F.: Satellite climatology of African dust transport in the Mediterranean atmosphere, J. Geophys. Res.-Atmos., 103, 13137–13144, https://doi.org/10.1029/98JD00171, 1998.

Nascimento, J. P., Bela, M. M., Meller, B. B., Banducci, A. L., Rizzo, L. V., Vara-Vela, A. L., Barbosa, H. M. J., Gomes, H., Rafee, S. A. A., Franco, M. A., Carbone, S., Cirino, G. G., Souza, R. A. F., McKeen, S. A., and Artaxo, P.: Aerosols from anthropogenic and biogenic sources and their interactions – modeling aerosol formation, optical properties, and impacts over the central Amazon basin, Atmos. Chem. Phys., 21, 6755–6779, https://doi.org/10.5194/acp-21-6755-2021, 2021.

Pace, G., di Sarra, A., Meloni, D., Piacentino, S., and Chamard, P.: Aerosol optical properties at Lampedusa (Central Mediterranean). 1. Influence of transport and identification of different aerosol types, Atmos. Chem. Phys., 6, 697–713, https://doi.org/10.5194/acp-6-697-2006, 2006.

Papachristopoulou, K., Raptis, I.-P., Gkikas, A., Fountoulakis, I., Masoom, A., and Kazadzis, S.: Aerosol optical depth regime over megacities of the world, Atmos. Chem. Phys., 22, 15703–15727, https://doi.org/10.5194/acp-22-15703-2022, 2022.

Pedde, M., Kloog, I., Szpiro, A., Dorman, M., Larson, T. V., and Adar, S. D.: Estimating long-term $PM_{10-2.5}$ concentrations in six US cities using satellite-based aerosol optical depth data, Atmos. Environ., 272, 118945, https://doi.org/10.1016/j.atmosenv.2022.118945, 2022.

Pérez, C., Sicard, M., Jorba, O., Comerón, A., and Baldasano, J. M.: Summertime re-circulations of air pollutants over the north-eastern Iberian coast observed from systematic EARLINET lidar measurements in Barcelona, Atmos. Environ., 38, 3983–4000, https://doi.org/10.1016/j.atmosenv.2004.04.010, 2004.

Petit, J.-E., Favez, O., Sciare, J., Crenn, V., Sarda-Estève, R., Bonnaire, N., Močnik, G., Dupont, J.-C., Haeffelin, M., and Leoz-Garziandia, E.: Two years of near real-time chemical composition of submicron aerosols in the region of Paris using an Aerosol Chemical Speciation Monitor (ACSM) and a multi-wavelength Aethalometer, Atmos. Chem. Phys., 15, 2985–3005, https://doi.org/10.5194/acp-15-2985-2015, 2015.

Pietrogrande, M. C., Bacco, D., Ferrari, S., Kaipainen, J., Ricciardelli, I., Riekkola, M.-L., Trentini, A., and Visentin, M.: Characterization of atmospheric aerosols in the Po valley during the supersito campaigns – Part 3: Contribution of wood combustion to wintertime atmospheric aerosols in Emilia Romagna region (Northern Italy), Atmos. Environ., 122, 291–305, https://doi.org/10.1016/j.atmosenv.2015.09.059, 2015.

Pirhadi, M., Mousavi, A., Taghvaee, S., Shafer, M. M., and Sioutas, C.: Semi-volatile components of $PM_{2.5}$ in an urban environment: volatility profiles and associated oxidative potential, Atmos. Environ. Oxf. Engl. 1994, 223, 117197, https://doi.org/10.1016/j.atmosenv.2019.117197, 2020.

Provençal, S., Kishcha, P., da Silva, A. M., Elhacham, E., and Alpert, P.: AOD distributions and trends of major aerosol species over a selection of the world's most populated cities based on the 1st version of NASA's MERRA Aerosol Reanalysis, Urban Clim., 20, 168–191, https://doi.org/10.1016/j.uclim.2017.04.001, 2017.

Putaud, J. P., Cavalli, F., Martins dos Santos, S., and Dell'Acqua, A.: Long-term trends in aerosol optical characteristics in the Po Valley, Italy, Atmos. Chem. Phys., 14, 9129–9136, https://doi.org/10.5194/acp-14-9129-2014, 2014.

Qin, W., Fang, H., Wang, L., Wei, J., Zhang, M., Su, X., Bilal, M., and Liang, X.: MODIS high-resolution MAIAC aerosol product: Global validation and analysis, Atmos. Environ., 264, 118684, https://doi.org/10.1016/j.atmosenv.2021.118684, 2021.

Raptis, I.-P., Kazadzis, S., Amiridis, V., Gkikas, A., Gerasopoulos, E., and Mihalopoulos, N.: A Decade of Aerosol Optical Properties Measurements over Athens, Greece, Atmosphere, 11, 154, https://doi.org/10.3390/atmos11020154, 2020.

Remer, L. A., Kaufman, Y. J., Tanré, D., Mattoo, S., Chu, D. A., Martins, J. V., Li, R.-R., Ichoku, C., Levy, R. C., Kleidman, R. G., Eck, T. F., Vermote, E., and Holben, B. N.: The MODIS Aerosol Algorithm, Products, and Validation, J. Atmos. Sci., 62, 947–973, https://doi.org/10.1175/JAS3385.1, 2005.

Remer, L. A., Levy, R. C., Mattoo, S., Tanré, D., Gupta, P., Shi, Y., Sawyer, V., Munchak, L. A., Zhou, Y., Kim, M., Ichoku, C., Patadia, F., Li, R.-R., Gassó, S., Kleidman, R. G., and Holben, B. N.: The Dark Target Algorithm for Observing the Global Aerosol System: Past, Present, and Future, Remote Sens., 12, 2900, https://doi.org/10.3390/rs12182900, 2020.

Robotto, A., Barbero, S., Bracco, P., Cremonini, R., Ravina, M., and Brizio, E.: Improving Air Quality Standards in Europe: Comparative Analysis of Regional Differences, with a Focus on Northern Italy, Atmosphere, 13, 642, https://doi.org/10.3390/atmos13050642, 2022.

Rogozovsky, I., Ohneiser, K., Lyapustin, A., Ansmann, A., and Chudnovsky, A.: The impact of different aerosol layering conditions on the high-resolution MODIS/MAIAC AOD retrieval bias: The uncertainty analysis, Atmos. Environ., 309, 119930, https://doi.org/10.1016/j.atmosenv.2023.119930, 2023.

Sandrini, S., van Pinxteren, D., Giulianelli, L., Herrmann, H., Poulain, L., Facchini, M. C., Gilardoni, S., Rinaldi, M., Paglione, M., Turpin, B. J., Pollini, F., Bucci, S., Zanca, N., and Decesari, S.: Size-resolved aerosol composition at an urban and a rural site in the Po Valley in summertime: implications for secondary aerosol formation, Atmos. Chem. Phys., 16, 10879–10897, https://doi.org/10.5194/acp-16-10879-2016, 2016.

Sayer, A. M., Hsu, N. C., Lee, J., Bettenhausen, C., Kim, W. V., and Smirnov, A.: Satellite Ocean Aerosol Retrieval (SOAR) Algorithm Extension to S-NPP VIIRS as Part of the "Deep Blue" Aerosol Project, J. Geophys. Res.-Atmos., 123, 380–400, https://doi.org/10.1002/2017JD027412, 2018.

Schaap, M., Apituley, A., Timmermans, R. M. A., Koelemeijer, R. B. A., and de Leeuw, G.: Exploring the relation between aerosol optical depth and $PM_{2.5}$ at Cabauw, the Netherlands, Atmos. Chem. Phys., 9, 909–925, https://doi.org/10.5194/acp-9-909-2009, 2009.

Schäfer, K., Harbusch, A., Emeis, S., Koepke, P., and Wiegner, M.: Correlation of aerosol mass near the ground with aerosol optical depth during two seasons in Munich, Atmos. Environ., 42, 4036–4046, https://doi.org/10.1016/j.atmosenv.2008.01.060, 2008.

Schuster, G. L., Dubovik, O., and Holben, B. N.: Angstrom exponent and bimodal aerosol size distributions, J. Geophys. Res.-Atmos., 111, D07207, https://doi.org/10.1029/2005JD006328, 2006.

Schutgens, N. A. J.: Site representativity of AERONET and GAW remotely sensed aerosol optical thickness and absorbing aerosol optical thickness observations, Atmos. Chem. Phys., 20, 7473–7488, https://doi.org/10.5194/acp-20-7473-2020, 2020.

Scotto, F., Bacco, D., Lasagni, S., Trentini, A., Poluzzi, V., and Vecchi, R.: A multi-year source apportionment of $PM_{2.5}$ at multiple sites in the southern Po Valley (Italy), Atmos. Pollut. Res., 12, 101192, https://doi.org/10.1016/j.apr.2021.101192, 2021.

Segura, S., Estellés, V., Utrillas, M. P., and Martínez-Lozano, J. A.: Long term analysis of the columnar and surface aerosol relationship at an urban European coastal site, Atmos. Environ., 167, 309–322, https://doi.org/10.1016/j.atmosenv.2017.08.012, 2017.

Sen, P. K.: Estimates of the Regression Coefficient Based on Kendall's Tau, J. Am. Stat. Assoc., 63, 1379–1389, https://doi.org/10.2307/2285891, 1968.

Shi, Y. R., Levy, R. C., Yang, L., Remer, L. A., Mattoo, S., and Dubovik, O.: A Dark Target research aerosol algorithm for MODIS observations over eastern China: increasing coverage while maintaining accuracy at high aerosol loading, Atmos. Meas. Tech., 14, 3449–3468, https://doi.org/10.5194/amt-14-3449-2021, 2021.

Shrivastava, M., Andreae, M. O., Artaxo, P., Barbosa, H. M. J., Berg, L. K., Brito, J., Ching, J., Easter, R. C., Fan, J., Fast, J. D., Feng, Z., Fuentes, J. D., Glasius, M., Goldstein, A. H., Alves, E. G., Gomes, H., Gu, D., Guenther, A., Jathar, S. H., Kim, S., Liu, Y., Lou, S., Martin, S. T., McNeill, V. F., Medeiros, A., de Sá, S. S., Shilling, J. E., Springston, S. R., Souza, R. a. F., Thornton, J. A., Isaacman-VanWertz, G., Yee, L. D., Ynoue, R., Zaveri, R. A., Zelenyuk, A., and Zhao, C.: Urban pollution greatly enhances formation of natural aerosols over the Amazon rainforest, Nat. Commun., 10, 1046, https://doi.org/10.1038/s41467-019-08909-4, 2019.

Sicard, P., Agathokleous, E., De Marco, A., Paoletti, E., and Calatayud, V.: Urban population exposure to air pollution in Europe over the last decades, Environ. Sci. Eur., 33, 28, https://doi.org/10.1186/s12302-020-00450-2, 2021.

Singh, A., Avis, W. R., and Pope, F. D.: Visibility as a proxy for air quality in East Africa, Environ. Res. Lett., 15, 084002, https://doi.org/10.1088/1748-9326/ab8b12, 2020.

Sinyuk, A., Holben, B. N., Eck, T. F., Giles, D. M., Slutsker, I., Korkin, S., Schafer, J. S., Smirnov, A., Sorokin, M., and Lyapustin, A.: The AERONET Version 3 aerosol retrieval algorithm, associated uncertainties and comparisons to Version 2, Atmos. Meas. Tech., 13, 3375–3411, https://doi.org/10.5194/amt-13-3375-2020, 2020.

Skyllakou, K., Murphy, B. N., Megaritis, A. G., Fountoukis, C., and Pandis, S. N.: Contributions of local and regional sources to fine PM in the megacity of Paris, Atmos. Chem. Phys., 14, 2343–2352, https://doi.org/10.5194/acp-14-2343-2014, 2014.

Smirnov, A., Holben, B. N., Eck, T. F., Slutsker, I., Chatenet, B., and Pinker, R. T.: Diurnal variability of aerosol optical depth observed at AERONET (Aerosol Robotic Network) sites, Geophys. Res. Lett., 29, 30-1–30-4, https://doi.org/10.1029/2002GL016305, 2002.

Song, C. K., Ho, C. H., Park, R. J., Choi, Y. S., Kim, J., Gong, D. Y., and Lee, Y. B.: Spatial and seasonal variations of surface PM_{10} concentration and MODIS aerosol optical depth over China, Asia-Pac. J. Atmos. Sci., 45, 33–43, 2009.

Spencer, R. S., Levy, R. C., Remer, L. A., Mattoo, S., Arnold, G. T., Hlavka, D. L., Meyer, K. G., Marshak, A., Wilcox, E. M., and Platnick, S. E.: Exploring Aerosols Near Clouds With High-Spatial-Resolution Aircraft Remote Sensing Dur-

ing SEAC4RS, J. Geophys. Res.-Atmos., 124, 2148–2173, https://doi.org/10.1029/2018JD028989, 2019.

Stafoggia, M., Schwartz, J., Badaloni, C., Bellander, T., Alessandrini, E., Cattani, G., de' Donato, F., Gaeta, A., Leone, G., Lyapustin, A., Sorek-Hamer, M., de Hoogh, K., Di, Q., Forastiere, F., and Kloog, I.: Estimation of daily PM_{10} concentrations in Italy (2006–2012) using finely resolved satellite data, land use variables and meteorology, Environ. Int., 99, 234–244, https://doi.org/10.1016/j.envint.2016.11.024, 2017.

Su, X., Cao, M., Wang, L., Gui, X., Zhang, M., Huang, Y., and Zhao, Y.: Validation, inter-comparison, and usage recommendation of six latest VIIRS and MODIS aerosol products over the ocean and land on the global and regional scales, Sci. Total Environ., 884, 163794, https://doi.org/10.1016/j.scitotenv.2023.163794, 2023.

Sun, E., Xu, X., Che, H., Tang, Z., Gui, K., An, L., Lu, C., and Shi, G.: Variation in MERRA-2 aerosol optical depth and absorption aerosol optical depth over China from 1980 to 2017, J. Atmos. Sol.-Terr. Phy., 186, 8–19, https://doi.org/10.1016/j.jastp.2019.01.019, 2019.

Taghvaee, S., Sowlat, M. H., Diapouli, E., Manousakas, M. I., Vasilatou, V., Eleftheriadis, K., and Sioutas, C.: Source apportionment of the oxidative potential of fine ambient particulate matter ($PM_{2.5}$) in Athens, Greece, Sci. Total Environ., 653, 1407–1416, https://doi.org/10.1016/j.scitotenv.2018.11.016, 2019.

Tao, M., Wang, J., Li, R., Wang, L., Wang, L., Wang, Z., Tao, J., Che, H., and Chen, L.: Performance of MODIS high-resolution MAIAC aerosol algorithm in China: Characterization and limitation, Atmos. Environ., 213, 159–169, https://doi.org/10.1016/j.atmosenv.2019.06.004, 2019.

Theil, H.: A Rank-Invariant Method of Linear and Polynomial Regression Analysis, in: Henri Theil's Contributions to Economics and Econometrics: Econometric Theory and Methodology, edited by: Raj, B. and Koerts, J., Springer Netherlands, Dordrecht, the Netherlands, 345–381, https://doi.org/10.1007/978-94-011-2546-8_20, 1992.

Toledano, C., Cachorro, V. E., Berjon, A., de Frutos, A. M., Sorribas, M., de la Morena, B. A., and Goloub, P.: Aerosol optical depth and Ångström exponent climatology at El Arenosillo AERONET site (Huelva, Spain), Q. J. Roy. Meteor. Soc., 133, 795–807, https://doi.org/10.1002/qj.54, 2007.

Tsiflikiotou, M. A., Kostenidou, E., Papanastasiou, D. K., Patoulias, D., Zarmpas, P., Paraskevopoulou, D., Diapouli, E., Kaltsonoudis, C., Florou, K., Bougiatioti, A., Stavroulas, I., Theodosi, C., Kouvarakis, G., Vasilatou, V., Siakavaras, D., Biskos, G., Pilinis, C., Eleftheriadis, K., Gerasopoulos, E., Mihalopoulos, N., and Pandis, S. N.: Summertime particulate matter and its composition in Greece, Atmos. Environ., 213, 597–607, https://doi.org/10.1016/j.atmosenv.2019.06.013, 2019.

Tsyro, S., Aas, W., Colette, A., Andersson, C., Bessagnet, B., Ciarelli, G., Couvidat, F., Cuvelier, K., Manders, A., Mar, K., Mircea, M., Otero, N., Pay, M.-T., Raffort, V., Roustan, Y., Theobald, M. R., Vivanco, M. G., Fagerli, H., Wind, P., Briganti, G., Cappelletti, A., D'Isidoro, M., and Adani, M.: Eurodelta multi-model simulated and observed particulate matter trends in Europe in the period of 1990–2010, Atmos. Chem. Phys., 22, 7207–7257, https://doi.org/10.5194/acp-22-7207-2022, 2022.

Tuccella, P., Curci, G., Pitari, G., Lee, S., and Jo, D. S.: Direct Radiative Effect of Absorbing Aerosols: Sensitivity to Mixing State, Brown Carbon, and Soil Dust Refractive Index and Shape, J. Geophys. Res.-Atmos., 125, e2019JD030967, https://doi.org/10.1029/2019JD030967, 2020.

Tuet, W. Y., Chen, Y., Fok, S., Champion, J. A., and Ng, N. L.: Inflammatory responses to secondary organic aerosols (SOA) generated from biogenic and anthropogenic precursors, Atmos. Chem. Phys., 17, 11423–11440, https://doi.org/10.5194/acp-17-11423-2017, 2017.

van Donkelaar, A., Hammer, M. S., Bindle, L., Brauer, M., Brook, J. R., Garay, M. J., Hsu, N. C., Kalashnikova, O. V., Kahn, R. A., Lee, C., Levy, R. C., Lyapustin, A., Sayer, A. M., and Martin, R. V.: Monthly Global Estimates of Fine Particulate Matter and Their Uncertainty, Environ. Sci. Technol., 55, 15287–15300, https://doi.org/10.1021/acs.est.1c05309, 2021.

Vautard, R., Menut, L., Beekmann, M., Chazette, P., Flamant, P. H., Gombert, D., Guédalia, D., Kley, D., Lefebvre, M.-P., Martin, D., Mégie, G., Perros, P., and Toupance, G.: A synthesis of the Air Pollution Over the Paris Region (ESQUIF) field campaign, J. Geophys. Res.-Atmos., 108, 8558, https://doi.org/10.1029/2003JD003380, 2003.

Vecchi, R., Bernardoni, V., Fermo, P., Lucarelli, F., Mazzei, F., Nava, S., Prati, P., Piazzalunga, A., and Valli, G.: 4-hours resolution data to study PM_{10} in a "hot spot" area in Europe, Environ. Monit. Assess., 154, 283–300, https://doi.org/10.1007/s10661-008-0396-1, 2009.

Vecchi, R., Bernardoni, V., Valentini, S., Piazzalunga, A., Fermo, P., and Valli, G.: Assessment of light extinction at a European polluted urban area during wintertime: Impact of PM_1 composition and sources, Environ. Pollut., 233, 679–689, https://doi.org/10.1016/j.envpol.2017.10.059, 2018.

Viana, M., Pey, J., Querol, X., Alastuey, A., de Leeuw, F., and Lükewille, A.: Natural sources of atmospheric aerosols influencing air quality across Europe, Sci. Total Environ., 472, 825–833, https://doi.org/10.1016/j.scitotenv.2013.11.140, 2014.

Wang, Y., Lyapustin, A. I., Privette, J. L., Cook, R. B., SanthanaVannan, S. K., Vermote, E. F., and Schaaf, C. L.: Assessment of biases in MODIS surface reflectance due to Lambertian approximation, Remote Sens. Environ., 114, 2791–2801, https://doi.org/10.1016/j.rse.2010.06.013, 2010.

Wei, J., Li, Z., Peng, Y., and Sun, L.: MODIS Collection 6.1 aerosol optical depth products over land and ocean: validation and comparison, Atmos. Environ., 201, 428–440, https://doi.org/10.1016/j.atmosenv.2018.12.004, 2019.

Xu, L., Du, L., Tsona, N. T., and Ge, M.: Anthropogenic Effects on Biogenic Secondary Organic Aerosol Formation, Adv. Atmos. Sci., 38, 1053–1084, https://doi.org/10.1007/s00376-020-0284-3, 2021.

Yang, B.-Y., Qian, Z., Li, S., Chen, G., Bloom, M. S., Elliott, M., Syberg, K. W., Heinrich, J., Markevych, I., Wang, S.-Q., Chen, D., Ma, H., Chen, D.-H., Liu, Y., Komppula, M., Leskinen, A., Liu, K.-K., Zeng, X.-W., Hu, L.-W., Guo, Y., and Dong, G.-H.: Ambient air pollution in relation to diabetes and glucose-homocostasis markers in China: a cross-sectional study with findings from the 33 Communities Chinese Health Study, Lancet Planet. Health, 2, e64–e73, https://doi.org/10.1016/S2542-5196(18)30001-9, 2018.

Yang, X., Xiao, D., Fan, L., Li, F., Wang, W., Bai, H., and Tang, J.: Spatiotemporal estimates of daily $PM_{2.5}$ concentrations based on 1-km resolution MAIAC AOD in the

Beijing–Tianjin–Hebei, China, Environ. Chall., 8, 100548, https://doi.org/10.1016/j.envc.2022.100548, 2022.

York, D., Evensen, N. M., Martínez, M. L., and De Basabe Delgado, J.: Unified equations for the slope, intercept, and standard errors of the best straight line, Am. J. Phys., 72, 367–375, https://doi.org/10.1119/1.1632486, 2004.

Zhang, Y., Favez, O., Petit, J.-E., Canonaco, F., Truong, F., Bonnaire, N., Crenn, V., Amodeo, T., Prévôt, A. S. H., Sciare, J., Gros, V., and Albinet, A.: Six-year source apportionment of submicron organic aerosols from near-continuous highly time-resolved measurements at SIRTA (Paris area, France), Atmos. Chem. Phys., 19, 14755–14776, https://doi.org/10.5194/acp-19-14755-2019, 2019.

Zhang, Z. Y., Wong, M. S., and Lee, K. H.: Evaluation of the representativeness of ground-based visibility for analysing the spatial and temporal variability of aerosol optical thickness in China, Atmos. Environ., 147, 31–45, https://doi.org/10.1016/j.atmosenv.2016.09.060, 2016.

Zhao, B., Jiang, J. H., Gu, Y., Diner, D., Worden, J., Liou, K.-N., Su, H., Xing, J., Garay, M., and Huang, L.: Decadal-scale trends in regional aerosol particle properties and their linkage to emission changes, Environ. Res. Lett., 12, 054021, https://doi.org/10.1088/1748-9326/aa6cb2, 2017.

Zhao, B., Jiang, J. H., Diner, D. J., Su, H., Gu, Y., Liou, K.-N., Jiang, Z., Huang, L., Takano, Y., Fan, X., and Omar, A. H.: Intra-annual variations of regional aerosol optical depth, vertical distribution, and particle types from multiple satellite and ground-based observational datasets, Atmos. Chem. Phys., 18, 11247–11260, https://doi.org/10.5194/acp-18-11247-2018, 2018.

Zhdanova, E. Y., Chubarova, N. Y., and Lyapustin, A. I.: Assessment of urban aerosol pollution over the Moscow megacity by the MAIAC aerosol product, Atmos. Meas. Tech., 13, 877–891, https://doi.org/10.5194/amt-13-877-2020, 2020.

Chapter 4

4. Aerosol spectral optical properties in the Paris urban area and its peri−urban and forested surroundings from ACROSS surface observations during summer 2022

This chapter is in the form of an article, and it will shortly be submitted to Atmospheric Chemistry and Physics journal, to the "Atmospheric Chemistry of the Suburban Forest – multiplatform observational campaign of the chemistry and physics of mixed urban and biogenic emissions" special issue.

Within this study we performed the spectral complex refractive index retrieval (CRI) and single scattering albedo (SSA) at three different sites deployed during the ACROSS field campaign 2022 and characteristic of three different environment of the Ile-de-France region: the urban-background (Paris-Rive Gauche), the peri-urban (SIRTA) and the rural (Rambouillet Forest) sites.

Hourly complex refractive indices and SSA at seven different wavelengths were retrieved iteratively by optical calculations (by applying the Mie Theory for homogeneous spherical particles), providing the measured number size distribution to reproduce the observed scattering and absorption measurements. Observations were performed under a PM_1 head during the summer June-July 2022, in the framework of the ACROSS field campaign. These retrievals have allowed us to investigate the aerosol spectral optical properties at diverse environments in the region and under diverse conditions, including:

- two intense and prolonged heatwave periods leading to high aerosol load over the Paris area.
- An intermediate period with low aerosol concentrations and temperature closer to climatological values.
- Additionally, a long−range transported fire episode on the 19 July which strongly affected the optical signal over the Paris area.

The spectral CRI (average 1.45-0.043i, 1.56-0.041i, 1.52-0.026i, for the urban, peri-urban and rural sites at 520 nm) and SSA (average 0.73, 0.80, 0.83 for the urban, peri-urban and rural sites at 520 nm) show an urban-to-rural gradient modulated by the weather conditions. The imaginary component of the CRI increases at the peri-urban and rural environments under the influence of the Paris urban plume (i.e. north-easterly winds), suggesting the potential mixing of biogenic-anthropogenic air masses, as well as the effect of possible coating that enhances the absorbing component far from the emission sources. Indeed, the CRI and SSA correlation with the bulk chemical composition analysis has shown that aerosol absorption is modulated by black carbon concentration at all three sites, and even a small BC concentration affects the imaginary CRI component, demonstrating the role of the

anthropogenic aerosols also at rural environments. The important role of organic aerosols, dominating the mass load, is also evidenced.

The retrieved complex refractive indices from field observations provides new knowledge on the properties of aerosols in mixed urban-rural environments. These data will be used to validate the estimated volume-average CRI from the WRF-CHIMERE modelling at the three different locations, in order to test the model capabilities of well-reproducing the aerosol spectral optical properties at the regional scale from urban to rural environments.

Aerosol spectral optical properties in the Paris urban area and its peri−urban and forested surroundings during summer 2022 from the ACROSS surface observations

L. Di Antonio[1], C. Di Biagio[2], P. Formenti[2], A. Gratien[2], V. Michoud[2], C. Cantrell[1,13], A. Bauville[1], A. Bergé[1], M. Cazaunau[1], S. Chevaillier[1], M. Cirtog[1], P.Coll[2], B. D'Anna[3], J. F. de Brito[4], D. O. De Haan[5], S. Deshmukh[6], O. Favez[7,8], P.M. Flaud[9], C. Gaimoz[1], L. N. Hawkins[10], J. Kammer[3], B. Language[1,a], F. Maisonneuve[1], G. Močnik[11], E. Perraudin[9], J.E. Petit[12], B. Picquet−Varrault[1], L. Poulain[6], P. Pouyes[9], D. Pronovost[10], V. Riffault[4], S. Riley[10], M. Shahin[3], G. Siour[1], E. Villenave[9], P. Zapf[2], G. Foret[1], J.F. Doussin[1], and M. Beekmann[2]

1Univ Paris Est Creteil and Université Paris Cité, CNRS, LISA, F−94010 Créteil, France
2Université Paris Cité and Univ Paris Est Creteil, CNRS, LISA, F−75013 Paris, France
3Aix Marseille Univ, CNRS, LCE, Marseille, France
4Centre for Energy and Environment, IMT Nord Europe, Institut Mines−Télécom, Université de Lille, Lille, 59000, France
5Department of Chemistry and Biochemistry, University of San Diego, 5998 Alcala Park, San Diego, California 92110, United States
6Leibniz Institut für Troposphärenforschung (TROPOS), Leipzig 04318, Germany
7Institut National De L'environnement Industriel et Des Risques (INERIS), Parc Technologique Alata BP2, 60550 Verneuil−en−Halatte, France
8Laboratoire Central de Surveillance de la Qualité de l'Air (LCSQA), 60550, Verneuil−en−Halatte, France
913 Univ. Bordeaux, EPOC UMR 5805 CNRS, 33405 Talence, France
10Department of Chemistry, Harvey Mudd College, 301 Platt Blvd, Claremont, California 91711, United States; 11Center for 11Atmospheric Research, University of Nova Gorica, Nova Gorica SI−5000, Slovenia
12Laboratoire des Sciences du Climat et de l'Environnement, CEA−CNRS−UVSQ, IPSL, Université Paris−Saclay, 91191 Gif−sur−Yvette, France
13University of Colorado, Atmospheric and Oceanic Sciences (ATOC), Boulder, CO 80309
anow at Unit for Environmental Sciences and Management, North−West University, Potchefstroom, South Africa

Correspondence to: Ludovico Di Antonio (ludovico.diantonio@lisa.ipsl.fr), Claudia Di Biagio (claudia.dibiagio@lisa.ipsl.fr)

Abstract. The complex refractive index (CRI, n-ik) and the single scattering albedo (SSA) are key parameters driving the aerosol direct radiative effect. Their spatial, temporal, and spectral variability for anthropogenic−biogenic mixed environments stems under-measured and therefore poorly understood. In this study we retrieve the spectral CRI and SSA (370-950 nm) from in situ surface optical measurements and number size distribution of submicron aerosols at three ground−based sites in the greater Paris area representatives of the urban city and its peri−urban and forested rural environment. Measurements were taken as part of the ACROSS (Atmospheric ChemistRy Of the Suburban forest) campaign occurred in June−July 2022 and affected by highly diversified conditions: 1) two strong heatwaves leading to high aerosol load; 2) an intermediate period with low aerosol concentrations; 3) a long−range transported fire episode. The retrieved CRI and SSA exhibit a gradient from the urban to the rural site, whose intensity is modulated by the weather conditions. The k (SSA) increases (decreases) at the peri-urban and rural sites when exposed to the influence of the Paris urban plume under north-easterly winds. An average CRI of 1.45-0.043i (urban), 1.56-0.041i (peri-urban), 1.52-0.026i (rural) is retrieved under heatwave conditions. Black carbon is identified to strongly contribute to absorption at the urban and peri−urban sites, while brown carbon accounts for up to 10% (urban), 17% (peri-urban) and 22% (rural) absorption at 370 nm. The long−range transported fire episode that occurred on the 19 July 2022 lead to a k of 0.022 (370 nm) at the urban site.

Introduction

Climate change represents one of the most serious challenges that society is facing today. The scientific community has demonstrated that human activities have favored a global temperature increase, impacting the weather and climate over different regions of the world (IPCC, 2022). In this framework, aerosol particles-from natural and anthropogenic sources play a major role (Boucher et al., 2013; Forster et al., 2021; Szopa et al., 2021a). Due to their size distribution, mixing state and chemical composition, aerosols directly affect the radiative budget of the Earth−atmosphere system by scattering and absorption of solar and thermal radiation (the aerosol−radiation interaction effect, ARI), and indirectly by affecting the surface albedo and the microphysical properties and lifetime of clouds (the aerosol−cloud interaction effect, ACI) (Bellouin et al., 2020; Boucher et al., 2013). As of today, while tropospheric anthropogenic aerosols are considered as the second most important contributors to the global and regional radiative forcing, the estimation of the magnitude and sign of this effect still remains uncertain (IPCC, 2021). In fact, due to the high spatial and temporal variability in aerosol sources, distribution and properties, the representation of aerosols in models remains still a challenge (Bellouin et al., 2020; Bender, 2020; Li et al., 2022b).

The magnitude and sign of the aerosol direct radiative effect is determined by the particles' spectral optical properties, represented by the complex refractive index (CRI) and the single scattering albedo (SSA) (Samset et al., 2018; Zhou et al., 2018). The CRI ($n(\lambda)$-$ik(\lambda)$) represents the particles ability to scatter and absorb radiation. Its real part (n) is related to the aerosol non−absorbing component, while its imaginary part (k) to the absorbing one (Bohren et Huffman, 1983; Seinfeld and Pandis, 2016). The SSA is the fraction of scattered light compared to the total extinction (absorption plus scattering), and is 1(0) for fully scattering (absorbing) particles. Most of the aerosol inorganic species (e.g. sulfate and nitrate) show a very weak CRI imaginary part and an SSA close to 1 in the solar spectrum (Aouizerats et al., 2010; Chang et al., 2022; Freedman et al., 2009; Mao et al., 2022b; Moore et al., 2021). Black carbon (BC) and brown carbon (BrC; i.e. the absorbing fraction of organic aerosols), as well as mineral dust, absorb incoming solar or outgoing thermal infrared radiation and may cause local warming, inducing the evaporation of cloud droplets and the reduction of the atmospheric stability (the semi−direct effect, (Allen et al., 2019)). The contribution of absorbing aerosols to the climate at regional and global scales is among the highest uncertainties in the climate forcing assessment (Bond et al., 2013; Kelesidis et al., 2022; Räisänen et al., 2022; Tuccella et al., 2020, 2021).

The BC is emitted predominantly by combustion processes associated to traffic, industries and wildfires (Bond et al., 2013) and is ubiquitous in urban areas and regions influenced by human activities. One of the most widely used CRI in climate models for BC is 1.95-0.79i (wavelength independent), showing a strong CRI imaginary component and resulting in an SSA of around 0.3 (550 nm) (Bond and Bergstrom, 2006; Samset et al., 2018). However, BC may exist under different mixing states: i) external mixing (e.g. freshly emitted BC) and ii) internal mixing with other aerosol species (e.g. aged BC), inducing light absorption enhancement (Bond et al., 2006; Hu et al., 2022; Jacobson, 2001; Liu et al., 2017; Saleh et al., 2015).

While for a long time organic carbon (OC) has been assumed to be not absorbing in models, this species is now recognized to play an important role in the radiative forcing (Li et al., 2023; Saleh et al., 2015; Tuccella et al., 2020, 2021; Wang et al., 2018; Zhang et al., 2020). The BrC absorbs light, mainly in the near−ultraviolet part of the light spectrum (Kirchstetter et al., 2004). It is emitted primary by fossil fuel, biofuel and biomass burning combustion or generated as a secondary species as a result of gas and aqueous phase reactions, including oxidation of anthropogenic and biogenic volatile organic compounds leading to absorbing secondary biogenic− and anthropogenic− organic aerosol (ASOA and BSOA) (Betz et

al., 2022; He et al., 2021; Laskin et al., 2015; Liu et al., 2016, 2015a; Moise et al., 2015; Updyke et al., 2012; Xiong et al., 2022) . State−of−the−art knowledge supports the hypothesis that the absorbing capacity of BrC, and therefore its spectral CRI and SSA, might vary along with the process of formation, the precursors type, the oxidation patterns and the NO_x levels for secondary species (Dingle et al., 2019; Flores et al., 2014a; He et al., 2021; Kim and Paulson, 2013; Liu et al., 2015a; Moise et al., 2015; Nakayama et al., 2012, 2015; Yang et al., 2022), as well as due to chemical ageing, potentially inducing either whitening or darkening of the brown aerosols (Liu et al., 2015a; Moise et al., 2015; Wang et al., 2018; Zhang et al., 2020). The biogenic−derived secondary organic aerosols shows a weaker CRI imaginary component compared to the anthropogenic SOA, in particular anthropogenic volatile organic compounds (VOCs) oxidation at high NO_x levels leads to highly absorbing SOA (He et al., 2021; Liu et al., 2015a). However laboratory and field investigations suggest that the mixing of anthropogenic and biogenic precursors under various NO_x levels may impact the absorption properties of the SOA (He et al., 2022; Hecobian et al., 2010; Liu et al., 2016; Moise et al., 2015).

Mineral dust particles are emitted by wind erosion from desert and arid areas or by human activities (e.g. agricultural and industrial) (Lindqvist et al., 2014; Luo et al., 2022)., They contribute up to 10% absorption in the solar spectrum (Di Biagio et al., 2019), while they strongly absorb in the thermal infrared (Di Biagio et al., 2017b). Significant dust loadings over northern Europe are recorded due to long-range transport from Sahara, with peaks of occurrence during spring and summer (Marinou et al., 2017; Merdji et al., 2023).

While aerosol composition and properties have been studied extensively in urban polluted environments dominated by BC, anthropogenic VOCs and high NO_x levels in the past decades (Boedicker et al., 2023; Cappa et al., 2019; Che et al., 2009; Ebert et al., 2004; Hu et al., 2016; Kahnert and Kanngießer, 2020; Kirago et al., 2022; Nault et al., 2021; Xie et al., 2019), the regional scale evolution and fate of urban polluted air has been addressed in only few studies such as the recent GO−Amazon or KORUS campaigns in the Amazon basin and Korea (Crawford et al., 2021; LeBlanc et al., 2022; Nascimento et al., 2021; Shrivastava et al., 2019). The outflow of urban pollution towards peri−urban and rural environments leads to the mixing of primary and secondary anthropogenic and biogenic compounds and varying BC, VOCs, and NO_x levels, in turn influencing the aerosol production, ageing, composition, mixing state and climate−relevant properties. The lack of observations on such evolving conditions hampers the proper representation of aerosols in chemical−transport and regional climate models, and our capacity to understand and predict the current and future evolution of climate and its feedbacks.

In this paper we investigate the spectral aerosol CRI and SSA (from 370 to 950 nm) and its regional gradient from urban to rural environment from in situ surface measurements of optical properties (absorption and scattering coefficients) and number size distribution of submicron aerosols at three ground−based sites in the Paris area (Ile-de-France region, see Fig. 1). Measurements were taken in June-July 2022 as part of the ACROSS (Atmospheric ChemistRy Of the Suburban forest) project (Cantrell and Michoud, 2022). The Paris metropolitan area targeted by ACROSS is the most populated city in France (around 12 million inhabitants, https://www.insee.fr/), located more than 200 km from other major agglomerations, and surrounded by forested and agricultural areas. In order to measure the diversity of emissions and the evolution of air mass properties in the region, three different ground−based measurement sites were deployed during ACROSS and considered in the present analysis: i) a site in central urban Paris (Paris Rive−Gauche, PRG), ii) a site in the Paris peri−urban environment (Site Instrumental de Recherche par Télédétection Atmosphérique, SIRTA), and iii) a site in the Rambouillet rural forested area (RambForest, supersite of the project, located 50 km downwind of Paris). The ACROSS campaign took place between 14 June to 25 July 2022, a period characterized by extreme weather conditions

and high temperatures for Europe (Copernicus Climate Change Service report;(C3S, 2023)). Various situations were sampled during ACROSS, including: 1) two strong heatwaves, promoting the biogenic SOA build−up and wind conditions favoring the export of the Paris emission plume towards the peri−urban and rural sites; 2) periods with low aerosols concentrations and limited urban outflow. Additionally, two concurrent situations occurred during the campaign: 3) an intense biomass burning episode rising up from southern France to the Ile-de-France area; 4) Saharan dust events transported from the upper atmosphere to the ground.

The paper is organized as follows: the ground−based sites, instrumentation, and measurements are presented in Section 2. The CRI and SSA retrieval procedures are illustrated in Section 3. The aerosol absorption and scattering coefficients, the CRI and the SSA variability within the different ACROSS periods, as well as the link to meteorology and aerosol bulk chemical composition are presented and discussed in Section 4 and 5. Conclusions are drawn in Section 6.

2. Methods

2.1 Site description

The ACROSS campaign included ground−based and aircraft observations across the Ile-de-France region deploying a large panel of instruments for measuring both the gas and the aerosol phases (Cantrell and Michoud, 2022). The three ground based sites considered in this study (Fig. 1) are briefly described in the following.

The Paris–Rive Gauche (PRG) site (48.8277° N, 2.3806 °E; hereafter PRG) was hosted at the Lamark building at Université Paris Cité, on the southeastern part of the Paris administrative borders. Within the Paris urban agglomeration and in close proximity to the urban area in the east, this site presents urban background features: it is at a distance of a few hundred meters from strong emission sources such as bus and train stations, main roads and city highway intersections. Aerosol and gas sampling was performed from the roof of the building at about 30 m a.g.l. A complete description of the site deployment during ACROSS, including gas and aerosol measurements will be provided separately (Di Biagio et al., in preparation).

The SIRTA (Site Instrumental de Recherche par Télédétection Atmosphérique, 48.7090° N, 2.1488° E) is an Aerosol, Clouds, and Trace gases Research Infrastructure (ACTRIS) long−term observational site (Bedoya-Velásquez et al., 2019; Chahine et al., 2018; Haeffelin et al., 2005; Zhang et al., 2019). Located at around 20 km southwest of the Paris administrative borders, the SIRTA is considered a peri–urban site due to its lower population density in an environment mixing forest, urban areas as well as agriculture fields and traffic roads. Therefore, measurements carried out at SIRTA have been classified as background values for the Paris area (Bedoya-Velásquez et al., 2019). Full instrumentation available at SIRTA is described at https://SIRTA.ipsl.fr/data−overview/ (last access: 31 December 2023).

The Rambouillet forest ground–based supersite (48.6866° N, 1.7045° E; hereafter RambForest), was hosted at the "Boissiere–Ecole" French commune, located in the eastern part of the Rambouillet forest, within the Ile-de-France region and at around 50 km southwest of the Paris administrative borders. The site covers a surface area of 625 m^2 and include a 40 m high tower, originally dedicated to the surveillance of forest fires above the canopy (about 25 m high). The area is surrounded by the Rambouillet national forest, a mixed (pine and oak primarly) deciduous and evergreen trees forest. A large panel of instrumentation was installed below and above the canopy, from the ground to the top of the tower, in order to measure biogenic and anthropogenic VOCs, gas pollutants, and aerosols. Measurements below the canopy

relevant to this paper were performed with the PEGASUS (PortablE Gas and Aerosol Sampling UnitS) (Formenti et al., in preparation) and the mobile facility "Barracuda" (Kammer et al., 2020).

2.2 In situ instrumentation

The optical CRI retrieval and SSA calculations are based on measurements of the aerosol light absorption and scattering coefficients (β_{abs}, β_{sca}, units of Mm^{-1}) and the particle number size distribution (units of particles per cm^3), as will be described in Sect. 3. In this section, we describe the different instruments providing these observables at PRG, SIRTA and RambForest, the data treatment and evaluation of their uncertainties. Aerosol measurements at the three sites were performed with a submicron (<1µm) particulate matter (PM_1) certified inlet. Data presented in this paper were averaged over 1−hour and reported at Standard Temperature and Pressure (STP) conditions (T=273.15 and P=1013.25 hPa).

2.2.1 Spectral aerosol absorption coefficient

Aerosol light absorption coefficient at seven wavelengths (370, 470, 520, 590, 660, 880, and 950 nm), together with equivalent black carbon (eBC) concentration, were measured at 1−min resolution by the dual–spot Aethalometer (AE33) Magee (Drinovec et al., 2015) for all the sites under investigation. The AE33 measures the light attenuation coefficient β_{atn} through a filter–based optical method. The absorption coefficient is calculated as $\beta_{abs}=\beta_{atn}/C_{ref}$, where C_{ref} is the multiple scattering correction parameter, accounting for absorption overestimation due to multi-scattering by the filter fiber (Collaud Coen et al., 2010; Weingartner et al., 2003). In this paper we used the spectral invariant C_{ref} ($C_{ref} = FF \bullet H^* = 2.45$, where H^*=1.76, an harmonization factor and FF =1.39, the base C_{ref} provided by the manufacturer for the M8060 filter type) recommended by the pan−European ACTRIS research infrastructure (ACTRIS, 2023). However, literature shows a large variability of C_{ref}, potentially linked to the aerosol composition, mixing state and SSA, with values ranging between 2 and 5 (Fig. S1) (Bernardoni et al., 2021; Di Biagio et al., 2017a; Drinovec et al., 2015, 2022; Kalbermatter et al., 2022; Moschos et al., 2021; Valentini et al., 2020; Weingartner et al., 2003; Yus-Díez et al., 2021). In order to take into account this major source of uncertainty in aethalometer absorption measurements, a wavelength–independent average C_{ref} from the ensemble of literature values depicted in Fig. S1 was calculated, corresponding to a value of 3.38. As 3.38 provides 38% deviation from the ACTRIS reference C_{ref} value, we assume 38% to be the uncertainty on β_{abs} due to uncertainties in the multiple scattering correction. An uncertainty of 10% due to noise was assumed from (Cuesta-Mosquera et al., 2021). The uncertainty due to temporal average (calculated as the standard deviation divided by the mean of the hourly average) was estimated to contribute from 15% at 520 nm up to up to 44% at 950 nm. The total uncertainty on β_{abs} was calculated as the quadratic sum of the uncertainty due to noise, standard deviation and C_{ref} reaching values up to 50% at all three sites and at all wavelengths.

The spectral variability of aerosol absorption coefficient was parametrized by the Absorption Angstrom Exponent (AAE) calculated as:

$$AAE = \ln\left(\frac{\beta_{abs}(\lambda_1)}{\beta_{abs}(\lambda_2)}\right)/\ln\left(\frac{\lambda_1}{\lambda_2}\right), \qquad \lambda_1 = 370, \lambda_2 = 950 \text{ nm} \tag{1}$$

2.2.2 Spectral aerosol scattering coefficient

The aerosol spectral light scattering coefficient was measured at the three different sites by three different models of nephelometers measuring at a temporal resolution between 1 and 5 seconds and operating at different wavelengths: the Ecotech Aurora 4000 (PRG, 450, 525 and 635 nm; (Teri et al., 2022)), the Ecotech Aurora 3000 (SIRTA, 450, 525 and 635 nm; (Teri et al., 2022)), and the TSI 3563 (RambForest, 450, 550 and 700 nm; (Anderson and Ogren, 1998)). Due to nephelometers geometry, the scattering coefficient was measured within a specific angular range (near-forward and near-

backward are not measured), introducing a systematic error known as truncation error. Both the Aurora 3000 and 4000 measure β_{sca} in the angle range $\theta_1 - \theta_2$=9°–170°, while the TSI 3563 measures within $\theta_1 - \theta_2$=7°–170°. The truncation error was corrected by following the formulations for submicron aerosols provided by (Teri et al., 2022) for the Ecotech Aurora 4000, (Müller et al., 2011) for the Ecotech Aurora 3000, and (Anderson and Ogren, 1998) for the TSI 3563, based on the knowledge of the Scattering Angstrom Exponent (SAE) representing the spectral variation of β_{sca}. The SAE was estimated as:

$$\mathrm{SAE} = \ln\left(\frac{\beta_{\mathrm{sca}}(\lambda_1)}{\beta_{\mathrm{sca}}(\lambda_2)}\right)/\ln\left(\frac{\lambda_1}{\lambda_2}\right), \qquad \lambda_1 = 450\ \lambda_2 = 635 \text{ or } 700 \text{ nm} \tag{2}$$

The truncation correction varies between [5,9] % at 520 nm. For the following of the paper we will use β_{sca} to refer to native nephelometer measurements (non-corrected for truncation), while the truncation–corrected scattering coefficient will be referred as $\beta_{\mathrm{sca,trunc-corr}}$.

The aerosol light scattering coefficient was extrapolated at the seven wavelengths of the AE33 using the SAE as:

$$\beta_{\mathrm{sca}}(\lambda_{\mathrm{x}}) = \beta_{\mathrm{sca}}(\lambda_2) \cdot \left(\frac{\lambda_{\mathrm{x}}}{\lambda_2}\right)^{-(\mathrm{SAE})}, \quad \lambda_x = 370, 470, 520, 590, 660, 880, 950 \text{ nm} \tag{3}$$

The uncertainty due to noise on β_{sca} was assumed as 3% for the Ecotech Aurora 3000 and 4000 (Teri et al., 2022) and 10% for the TSI 3563 (Anderson et al., 1996). The uncertainty due to hourly temporal average (calculated as the standard deviation divided by the mean of the hourly average) was estimated to contribute from 10% at 520 nm up to 30% at 950 nm at the rural site. The total uncertainty on the β_{sca} was estimated as the quadratic sum of the noise and standard deviation uncertainties (neglecting uncertainties due to spectral extrapolation and truncation correction).

2.2.3 Aerosol number size distribution

The aerosol number size distribution was provided by a scanning mobility particle sizer (SMPS, TSI Model 3080) and optical particle counter (OPC, GRIMM Inc.,). The SMPS classifies and counts particles which are selected based on the electrical mobility diameter (D_m). Particles flowing into the SMPS system are firstly neutralized by a soft X-Ray radioactive source secondly classified by their size according to their electrical mobility through a Differential Mobility Analyser (DMA 3081) and finally counted by a Condensation Particle Counter (CPC 3775). The SMPS can provide counting up to 1 µm of mobility diameter (D_m) with a time resolution of 3-min. The GRIMM OPC classify particles based on their optical diameter (D_{opt}) defined by the light scattering signal intensity derived from interaction with a monochromatic light source (Heim et al., 2008) and works at a temporal resolution of few seconds. During the ACROSS campaign the SMPS was deployed at the three sites with slightly different configurations leading to diverse sampled D_m ranges (23.3–982.2 nm (PRG), 8.9–829.0 nm (SIRTA), 19.5–881.7 nm (RambForest)), while the GRIMM OPC was deployed at PRG (GRIMM 1.108; optical diameter range 0.3–20 µm, 780 nm operating wavelength) and RambForest (GRIMM 1.109 model; optical diameter range 0.25-32 µm, 655 nm operating wavelength), but not at SIRTA.

The D_m measured by the SMPS can be converted into geometrical (or volume equivalent) diameter D_g by dividing for the dry dynamic shape factor (DeCarlo et al., 2004), in our study set equal to 1 in the assumption of spherical particles. The D_{opt} measured by the OPC can be converted into D_g by the knowledge of the CRI of the aerosol at the operating wavelength of the instrument (Formenti et al., 2021; Heim et al., 2008). As will be described in Sect. 3.1, the optical to geometrical OPC conversion is used to derive the real part of the unknown refractive index for sampled aerosols at PRG and RambForest.

The uncertainty of the particle size distribution ($dN(Dp)/dlogDp$) was calculated both for SMPS and OPC as the counting uncertainty due to Poisson statistics ($\Delta dN(Dp) = \pm\sqrt{dN(Dp)}$), resulting in an average 10% uncertainty in the submicron range. The total number concentration N_{tot} in the PM_1 fraction was calculated by summing up number concentrations from SMPS size bins.

2.3 Ancillary measurements and products

Together with the relevant optical and size measurements, other ancillary data are considered in this work:

- meteorological observations, including temperature, pressure, wind speed, wind direction, and mixing layer height (MLH), were obtained by in–situ meteorological station and from attenuated backscatter signals measured by a ceilometer at the SIRTA site. Data from the SIRTA observatory, located in the middle between the urban and the rural sites, were chosen as representative of regional average conditions;
- aerosol non–refractory composition (organic, nitrate, sulfate, ammonium, chloride) in the PM_1 fraction was measured by a Time–of–Flight Aerosol Chemical Speciation Monitor (TOF–ACSM, Aerodyne Research, (Fröhlich et al., 2013), 6−min resolution) at PRG and SIRTA sites and by a TOF Aerosol Mass Spectrometer (TOF–AMS, Aerodyne Research, (Drewnick et al., 2005), 3−min resolution) at the RambForest site. Uncertainty on the total non−refractory mass concentration from ACSM is evaluated to be around 25% (Budisulistiorini et al., 2014; Crenn et al., 2015).
- the black carbon Paris–to–regional ratio (BC_{ratio}), is a product derived from the WRF-CHIMERE v2020r3 CTM (chemistry transport model, Menut et al., 2021) simulation for the ACROSS campaign 2022 (Di Antonio et al., 2023). The CHIMERE model is a 3D regional Eulerian CTM, used to simulate gas and aerosols concentrations. The WRF meteorological model (v.3.7.1, forced with the NCEP initial and boundary conditions) is coupled with CHIMERE and provides the input meteorological fields. The anthropogenic emissions (BC, OC…) are provided by the CAMS-GLOB-ANT product with a spatial resolution of 0.1°x0.1° (Soulie et al., 2023). Three nested domains were configured respectively at 30km, 6km and 2km spatial resolution and centered over the Ile-de-France region. Aerosol dry deposition was simulated according to (Zhang et al., 2001), and wet deposition below-clouds due to rain according to (Willis and Tattelman, 1989).

  The BC_{ratio} product (retrieved only for the simulation at 2x2km spatial resolution) aims at tracing the modelled BC emissions in the Grand Paris domain (Grand-Orly Seine Bièvre, 2018) compared to the regional domain (Fig. 1), in order to be able to identify periods where the SIRTA and RambForest sites were under the influence of the Paris air masses. A tracer of BC from Greater Paris area emissions (BC_{Paris}) was introduced, such as the total black carbon concentration can be split into the Paris and a regional contribution as: $BC_{tot} = BC_{Paris} + BC_{regional}$. The BC_{ratio} is calculated at 2x2 km spatial resolution and at hourly temporal resolution as:

$$BC_{ratio}\,(lon, lat, time) = \frac{BC_{Paris}(lon,lat,time)}{BC_{Paris}(lon,lat,time)+BC_{regional}(lon,lat,time)} \quad (4)$$

  where for each pixel within the considered domain the $BC_{regional}$ accounts for the BC simulated concentrations without taking into account the Grand Paris area's BC emissions (i.e. BC emissions within the Grand Paris area equal zero), while BC_{Paris} (lon,lat,time) represents the simulated BC concentrations, within which only emissions from the Grand Paris area are considered. A value of 1 of the BC_{ratio} indicates that all the BC is due to

simulated concentrations from the Grand Paris area. On the contrary, a value of 0 in the BC_{ratio} means that no contribution from Grand Paris area is traced. Intermediate values weight the contribution of Grand Paris area over the total BC concentration simulated in the regional domain. An example of the BC_{ratio} useful to trace the evolution of the Grand Paris area plume is shown in Fig. 1.

- The Brown Carbon (BrC) contribution to the 370 nm absorption coefficient ($\beta_{abs-BrC}$) was calculated following Eq. (4) in (Zhang et al., 2020b) as:

$$\beta_{abs-BrC}(370\text{nm}) = \beta_{abs}(370nm) - \beta_{abs-BC}(370nm) \quad (5)$$

Where $\beta_{abs-BC}(370nm)$ is the BC absorption contribution to the total absorption at 370 nm parametrized as:

$$\beta_{abs-BC}(370\text{nm}) = \beta_{abs}(880nm) \cdot \left(\frac{370\text{nm}}{880\text{nm}}\right)^{-AAE_{BC}} \quad (6)$$

where AAE_{BC} is the AAE due to black carbon, assumed to be 1.

3. Spectral aerosol CRI and SSA assessment

3.1 CRI retrieval procedure

Hourly CRI at seven wavelengths were retrieved using the iterative method illustrated in Fig. S2 and detailed in text S1. The iterative method, consists at identifying n and k values that allows, by optical calculation using the measured number size distribution as input, to reproduce at each wavelength the measured spectral β_{sca} and β_{abs}. Calculations were made under the assumption of homogeneous spherical particles (Mie theory) and considering nephelometer measurements non−corrected for truncation, therefore simulating β_{sca} in the instrument measurement angle range. Size distribution measurements from the SMPS were used as input to the calculations. The n and k free parameters were varied in the [1.2, 2.0] range for n (at 0.01 step) and [0, 0.02] for k (at 0.001 step) and the optimal (n, k) pairs were determined by minimizing at each wavelength the root mean squared difference (RMSD) between observed and modelled β_{sca} and β_{abs} calculated as:

$$\text{RMSD} = \sqrt{\left(\frac{\beta_{sca\text{-}obs} - \beta_{sca\text{-}mod}}{\beta_{sca\text{-}mod}}\right)^2 + \left(\frac{\beta_{abs\text{-}obs} - \beta_{abs\text{-}mod}}{\beta_{abs\text{-}mod}}\right)^2} \quad (7)$$

Sensitivity calculations were performed to evaluate the uncertainties on the retrieved n and k values in relation to the uncertainty on the input parameters such as: i) instrumental error and ii) dataset variability (median and percentiles of the inputs) as detailed in Table S1. The average CRI ± SD of the results from the different simulations is reported.

In addition, for PRG and RambForest, where OPC measurements were also available, a second approach, named OPC−SMPS overlap method, was used to derive the CRI. This approach, detailed in Text S2 and Text S3, is based on the fact that the conversion of the OPC aerosol number size distribution from optical diameters ($dN(D_{opt})/d\log D_{opt}$) to geometrical diameter $dN(D_g)/d\log D_g$ depends on CRI. Comparing the OPC and SMPS measurements in their overlap region, and minimizing their differences by varying the optical-to-geometric conversion, allows retrieving information on the CRI at 780 nm (PRG) and 655 nm (RambForest), respectively, being 780 and 655 nm the operating wavelength of the OPC installed at the two sites. In order to apply this method, look up tables for OPC optical−to−geometrical diameter conversion values reported by (Formenti et al., 2021) for n varying in the range [1.33,1.74] (at 0.01 step) and k in the range [0,0.4] (at 0.001 step), both at 655 and 780 nm were considered. As the OPC optical to geometric corrections are mostly sensitive to n and less sensitive to k variations (see Fig. S3 and Fig. S4), this method does not permit to constrain both parameters but only n, while k is kept fixed at the spectral value of the optical−closure retrieval. The OPC−SMPS

overlap method, already applied in literature studies (Flores et al., 2009; Hand and Kreidenweis, 2002; Mack et al., 2010; Vratolis et al., 2018), was employed here with the aim of establishing a minimum aerosol load above which the optical-iterative method can considered as constrained (as discussed in Text S3). Results of the optical−iterative vs OPC−SMPS method comparison (shown in Fig. 2) suggest a threshold of 3 μg m^{-3}, corresponding to a β_{ext} of about 12 Mm^{-1}, to be applied to data to obtain well constrained retrievals. For the rest of the paper, the CRI results from the iterative method are reported and discussed assuming this threshold applied.

3.2 SSA calculation

Hourly averaged spectral aerosol SSA was calculated at the 7 operating wavelength of the aethalometer as:

$$SSA\ (\lambda) = \frac{\beta_{sca,trunc-corr}\ (\lambda)}{\beta_{ext}\ (\lambda)} = \frac{\beta_{sca,trunc-corr}\ (\lambda)}{\beta_{sca,trunc-corr}\ (\lambda)+\beta_{abs}\ (\lambda)} \quad (8)$$

where β_{ext} is the calculated extinction coefficient as the sum of $\beta_{sca,trunc-corr}$ and β_{abs}.The uncertainty on SSA, calculated with the statistical error propagation formula as:

$$\Delta SSA = \sqrt{\left(\frac{\beta_{abs}}{(\beta_{sca,trunc-corr}+\beta_{abs})^2}\right)\Delta\beta_{sca}\,)^2 + \left(\frac{\beta_{sca,trunc-corr}}{(\beta_{sca,trunc-corr}+\beta_{abs}\,)^2}\right)\Delta\beta_{abs})^2} \quad (9)$$

ranges on average within 14–43%, 11%–45%, 17–25% at the PRG, SIRTA and RambForest sites between 370 and 950 nm.

4. Results

4.1 Aerosol optical properties during the ACROSS campaign 2022

Figure 3 depicts the time series of β_{abs}, β_{sca} and β_{ext} at the 520 nm and the total particle number concentration N_{tot}, for the three sites in the June 15–July 25 2022 period together with temperature, mixing layer height and wind vector at the SIRTA site. Figure 4 shows the time series of the retrieved n, k, and SSA at 520 nm for the three different sites.

The ACROSS campaign was characterized by different atmospheric conditions, mirrored in the optical and CRI signal variability: i) two strong heatwaves occurred in the June 15–18 June and July 12–25 periods, with hourly temperatures above 35 °C registered at the peri−urban site during the first heatwave and close to 40 °C during the second one; ii) a "clean" period from the 23 June to the 11 July 2022, characterized by low aerosol loadings and temperatures close to climatological averages; iii) a strong long-range transport fire episode on the 19 July 2022. Note that for the RambForest site, because of the limited availability of the particle size distribution data and the mass−threshold applied and discussed in Sect. 3, the CRI retrievals are available only partially and during the clean and the second heatwave periods. While average aerosol optical properties for the different periods (full, clean, heatwaves) at 520 nm are summarized in Table 1, the following paragraphs provide insights on the clean and the heatwaves periods as well as the fire episode occurred on the 19 July 2022.

4.1.1 Clean Period (23 June-11 July 2022)

The "clean" period was marked by low scattering and absorption coefficients at 520 nm (below 20−40 Mm^{-1}). The mixing layer height extended up to 2.5 km, and the total number of particles reached the lowest values of (1.6, 1.2, 0.2) • 10^3 # cm^{-3} at PRG, SIRTA and RambForest respectively during the period. The imaginary CRI component at 520 nm varies from 0.01 to 0.16 between the three sites, reaching the maximum value at the SIRTA site, while the minimum at

RambForest. A SSA minimum value of 0.38 at 520 nm is also registered at PRG (urban) site. On the contrary, a maximum of 0.96 at RambForest (rural) is observed during this period. High average SSA absolute differences (~0.2) are observed between the urban and the rural site.

4.1.2 First (15–18 June 2022) and second (12–25 July 2022) heatwaves

The heatwave periods reflect in the highest scattering and absorption coefficients and particle number concentration during the campaign. High temperatures (above 35°) and highly developed mixing layer height (maximum value of 3km at the SIRTA site) were observed. The extinction coefficient at 520 nm maximizes at values between 40 and 80 Mm^{-1} during the first heatwave at the three sites, reaching up to 150 Mm^{-1} during the second one (excluding the 19 July evening and the 20 July early morning where two fire episodes occurred), and N_{tot} reaches maximum values of (22, 19, 9) • 10^3 particles cm^{-3} at PRG, SIRTA and RambForest sites respectively. The SSA reaches values up to 0.95 at the urban site, attenuating the average absolute differences with the RambForest site compared to the clean period (~0.1). The minimum SSA values (~0.43) registered during the night of 13 July are due to possible fireworks that may occur in the suburban Paris area even before the 14 July French national holiday. The imaginary CRI component is on average lower at the rural (lowest k value of 0.06 at 520nm), compared to the urban and peri-urban (highest k value at 520 nm of 0.13). The k is higher during the second heatwave compared to the first only at PRG and SIRTA (no size distribution data available for RambForest during the first heatwave).

During the heatwaves also two main Saharan dust transport events are observed, causing dust intrusions from the free troposphere to the surface. These episodes are marked by a decrease in the SAE signal showing a minimum value of 1.9 on the 18 July (first heatwave) compared to the 2.3 average value at the urban site, but not clearly distinguishable in absorption and scattering coefficients absolute signals, presumably due to the too low PM_1 sampling head cut−off for dust.

4.1.3 The fire episode of the 19 July 2022

An exceptionally intense event of long−range transport of biomass burning aerosols (identified as fire episode, FE) from southern France to the Ile-de-France region occurred in the evening of the 19 July (the fire plume arrived at around 17 UTC at the RambForest site, and at around 18 UTC at the urban site), corresponding to the hourly maxima of β_{sca} and β_{abs} of (340, 203, 253 Mm^{-1}) and (33, 22, 25 Mm^{-1}) at 520 nm and for the PRG, SIRTA and RambForest sites, respectively (See Fig. 3). This episode was documented in the recent CAMS2_71 report N°04 in 2022 (Tsyro et al., 2023).

Average hourly CRI values of $1.53-0.018i$ (PRG) and $1.57-0.020i$ (RambForest) at 520 nm are retrieved for the fire episode on the 19 July, showing an increase in the real part component, while a decrease in the imaginary part, compared to the average values of the period (size distribution data not available at the peri−urban site for CRI retrieval).

The AAE during the fire episode of 19 July reached maximum values of 1.64, 1.60 and 1.75 at the urban, peri−urban and rural sites, respectively, which indicates the contribution of brown carbon absorption at shorter wavelengths. The fraction of absorption due to BrC ($\beta_{abs-BrC}$) at 370 nm calculated following Eq. 5 is also reported in Table 1. The $\beta_{abs-BrC}$ significantly increased during the fire episode reaching hourly maximum values of 31, 19 and 29 Mm^{-1} and representing the 45%, 42% and 52% of the total absorption coefficient at 370 nm during the fire episode, significantly higher than compared to the estimated full period averages of 11%, 17% and 22% for the urban, peri–urban and rural sites respectively.

4.2 CRI and SSA diurnal cycle

The CRI and SSA show different diurnal cycle at the different sites, as illustrated in Fig. 5 for the full campaign. At both the urban and peri–urban locations n shows maximum values in the early afternoon at around 13–15 UTC, and lower values during the night. Together with higher values during the early afternoon, the real refractive index at the rural site shows an additional local maximum during night. Concerning the CRI imaginary part, both the urban and the peri–urban sites show morning and late afternoon peaks, suggesting the role of BC emissions due to traffic activity in affecting the imaginary CRI component. Also a local maximum value of k is identified at the rural site, but few hours later than the urban and peri–urban sites. The SSA shows the opposite behavior compared to k, with the highest values obtained during the early afternoon (peak of photooxidation activity), while lower values reached over the peak in absorption due to traffic emissions in the early morning and in the late afternoon.

4.3 CRI and SSA spectral variability

Both the scattering and the absorption coefficients decrease with λ at the PRG, SIRTA and RambForest sites (Fig. S5). These values show only slight variations during the heatwaves (AAE increases only at urban and rural sites; SAE increases only at the peri−urban site) and the clean period (Table 1, Fig. S6). The AAE values and gradients are in line with the previous observations reported by (Favez et al., 2009) who retrieved an average AAE of 1.07 for summertime in Paris (based on air quality observations in the same district as PRG station).

Figure 6 shows the CRI and SSA spectral variability at the three different sites for the whole ACROSS campaign. Full period averages show a slight wavelength−dependent CRI real component, with decreasing values in the 370-660 nm range (highest spectral variability for RambForest), in opposition to a mostly flat or slightly increasing CRI imaginary component with λ. The real CRI temporal full period averages ranges from 1.45 to 1.41, from 1.58 to 1.54, from 1.62 to 1.48 between 370 and 950 nm respectively for the urban, peri-urban and rural sites. For the imaginary component, higher values at 950 nm of 0.040 are retrieved at the urban site and peri−urban sites, whereas a lower value of 0.028 is retrieved at the rural site. The SSA decreases sharply with the wavelength at all sites, going from values of 0.81, 0.83, 0.90 at 370 nm to 0.58, 0.74, 0.69 at 950 nm. The spectral behaviour identified for the full average period both for n, k and SSA, remained unchanged during the heatwaves and clean periods (Fig. S8).

As shown in Fig. 6, during the 19 July fire episode, the absorption k increases at 370 and 470 nm, due to the possible increase in BrC contribution, in particular at the urban site where the derived k ranges between 0.022 and 0.019 in the 370-950 range. On the contrary, no significant changes in k have been observed at the rural site. Since, the FE plume has travelled more than 400 km to North, we expected the plume to be photochemically-aged, reducing its absorption due to bleaching effects (Laskin et al., 2015). As a matter of fact, literature studies shows how the BrC light refractive index may vary between 0.06 and 0.5 at 370 nm for biomass burning aerosols (Runa et al., 2022; Sumlin et al., 2018; Liu et al., 2015; Lack et al., 2013; Chakrabarty et al., 2010; Alexander et al., 2008; Kirchstetter et al., 2004).

5. Discussion

5.1 CRI and SSA link to meteorology conditions: an urban–to–rural gradients analysis

In this section we analyse the submicron (PM_1) single scattering albedo and complex refractive index at the three sites, under different meteorological conditions. As illustrated in Fig. 3 and Fig. 4 the entire June-July 2022 period was characterized by the strong temperature increase reaching above 35 °C, favouring only for few cases the MLH

development up to 3km, and weak winds (average values of 2.65 m s^{-1} and 2.46 m s^{-1} during the heatwaves), preventing the pollutant dispersion. A diagram of the SSA and CRI averages at 520 nm over the different periods (i.e. clean and heatwaves) is available in Figure 7, while an analysis by wind sector is summarised in Table 2. Figure 7 shows that on average an urban-to-rural gradient is present in SSA and CRI under the different ACROSS periods. Furthermore, as depicted in Table 2 (a further detailed version is available in Table S4), two main regimes can be identified. Under N, NE, E, SE wind conditions a positive gradient in SSA is identified (ΔSSA ($SSA_{RambForest}$–SSA_{PRG})~0.1), corresponding the largest k at SIRTA, intermediate values in PRG and lowest values in RambForest. Under S, SW, W and NW conditions the SSA positive gradient increases to ~0.2 and a systematic negative urban-to-rural gradient is identified also in k. The NE (north−easterly) wind directions represent the best wind scenarios to investigate the mixing between the Paris urban plume with the biogenic emissions of the rural site. These conditions are driven by a strong high pressure system over the Great Britain (not shown), characteristic of part of the two heatwave periods, leading to a potential advection of the urban air masses to the rural site, including both the fresh Paris emissions and the possible aged aerosols from upwind areas (e.g. the Benelux area). The MEGAPOLI campaign has shown that the regional aerosol advection dominates over the $PM_{2.5}$ fraction in the Paris area (Beekmann et al., 2015; Bressi et al., 2014). Indeed, the average CRI imaginary component increases at the peri−urban and rural sites (explained by the absorbing Paris pollution plume), while it decreases at the urban, under NE conditions compared to S/SW/W/NW conditions, due to advection of aged continental background aerosol, less absorbing than the fresh urban one with a larger BC fraction.

Under northerly winds more polluted air masses may be advected over the Paris area, originated from the Great Britain (Chazette et al., 2005). Average SSA and CRI values of (0.73, 0.79, 0.86) and (1.40−0.035i, 1.56−0.039i, 1.48−0.021i) have been observed during ACROSS for these conditions. Under SE and E wind directions, the strongest (lowest) average k (SSA) values is observed at the rural (0.053 and 0.73) and peri urban sites (0.032 and 0.80), while no significant increase is observed at the urban site. Conversely, the rural and peri−urban sites show the lower average CRI of $1.53-0.024i$ and $1.51-0.021i$ under south−westerly winds (air masses coming from the Loire Valley and SW France regions). Considering only the westerly, south−westerly, and southerly winds (representing the urban (rural) site as downwind (upwind)), cleaner air masses are expected (e.g. originating from the Atlantic Ocean under westerly winds). This is the case for the peri−urban and rural sites where higher wind sector average (W/SW/S) SSA of (0.84, 0.89) and low CRI of (0.026, 0.019) have been observed compared to other wind regimes, suggesting a cleaner environment, more dominated by scattering aerosols (e.g. marine or biogenic aerosols). On the contrary, the SSA (CRI) reaches the lowest (highest) values of 0.66 (0.051) at the urban site in particular during the first part of the clean period, suggesting a stronger influence of local anthropogenic emissions (BC−dominated) under low aerosol loading.

Finally, the strongest heatwave days (the 17−18 June and 19 July 2022), are mainly characterised by southerly winds, and are associated to the maximum MLH value during the campaign of nearly 3 km. The SSA maximum values at 370 nm of 0.93, 0.95 have been observed respectively at peri−urban and rural sites, reflecting the expected biogenic SOA enhancement in the SSA measurements. As a term of comparison, (Dingle et al., 2019) calculated SSA values of 0.98−0.99 at 375 nm for purely biogenic compounds, while aromatics derived SOA show lower SSA in the 0.75−0.95 range, more typical of the urban environment where maximum value of SSA at 370 nm during the heatwave period of 0.90 has been measured.

The real and imaginary CRI difference among the sites as a function of BC Paris−to−regional ratio and colored by the main wind sectors is shown in Fig. 8. Following the previous discussion, for N to SE wind sectors the $|\Delta n|$ and $|\Delta k|$ at

520 nm tends to be zero for the SIRTA and RambForest sites, supporting the hypothesis that the Paris area and the regional background influence the peri−urban and rural sites under these wind conditions. The $|\Delta n|$ and $|\Delta k|$ depicted in Fig. 8, shows that under N to SE wind sectors the advected regional pollution and the Paris emissions may homogenously affect the CRI over the Ile-de-France region. On the other hand, for S to NW, the highest (lowest) $|\Delta n|$ and $|\Delta k|$ (BC_{ratio}) are observed, suggesting a not-uniform aerosol spatial distribution across all three sites under these weather conditions.

5.2 Comparison of retrieved CRI with the literature

Figure 9 shows the spectral CRI retrievals comparison with ambient CRI literature studies, including in−situ and airborne studies and considering works that highlight refractive indices characteristic of urban and rural environments, as well as the past works in the Paris area. Additionally, AERONET columnar retrieval in the Ile-de-France region for the ACROSS period are also shown. In general, the real part of the CRI retrieved in our study at the three sites is in agreement with the ensemble of literature observations, while the range of k values sits in between literature observations and AERONET retrievals in the Ile-de-France region during the ACROSS campaign. The lower AERONET k values compared to the existent literature can be explained by the fact that AERONET is a columnar−integrated retrieval and therefore also representative of a wider area compared to in situ observations (measurements are performed at different elevation angles) (Chen et al., 2020; Di Antonio et al., 2023h; Schutgens, 2020). In situ CRI retrievals over the Paris area have been already performed during the ESQUIF (Etude et Simulation de la QUalité de l'air en Ile−de−France) and LISAIR (Lidar pour la Surveillance de l'AIR) campaigns, respectively in July 2000 and May 2005 by the synergy of lidar, sunphotometers and in−situ measurements from (Raut and Chazette, 2007, 2008) and reported in Fig. 9. Values of $1.56–0.034i$ at 355 nm and $1.59–0.040i$ at 532 nm have been observed over the Paris town hall for May 2005 (Raut and Chazette, 2007), while average PBL value of $1.51−0.017i$ has been obtained from (Raut and Chazette, 2008) from aircraft measurements and over the Paris area. Real components observed in (Raut and Chazette, 2007, 2008) show to be higher compared to the urban PRG site, while showing comparable results for the peri−urban background and rural sites. However, the imaginary component reflects the range of variability observed from (Raut and Chazette, 2007) and from the studies shown in Fig. 9 concerning airborne and in−situ observations (Aldhaif et al., 2018; Ebert et al., 2002, 2004; Espinosa et al., 2019; Ferrare et al., 2006, 1998; Hand and Kreidenweis, 2002; Müller et al., 2002; Redemann et al., 2000; Shingler et al., 2016; Yamasoe et al., 1998; Zhang et al., 2016, 2013). Concerning the SSA, the urban site shows lower values compared to the 0.82 and 0.93 found over the Paris area respectively on the 18 May 2005 and during the ESQUIF aircraft campaign (Raut and Chazette, 2007, 2008), while the CRI imaginary component is comparable the 0.032 estimated at 532 nm for the 18 May 2005 through the synergy of lidar and in−situ measurements by (Raut and Chazette, 2007). Finally, the SSA values observed in this study (W sector), range between 0.73 and 0.87 from the urban to the rural sites, lower compared to the 0.92 average values observed for the 31 July 2000 from (Raut and Chazette, 2007) during ESQUIF aircraft campaign under comparable weather scenarios.

5.3 CRI and SSA vs aerosol bulk chemical composition

Figure 10 illustrates the aerosol PM_1 bulk chemical composition measured at the three different sites and classified by several classes on CRI, SSA and AAE. The major contribution to the PM_1 mass and at the three sites is represented by the organic fraction, showing full campaign average values of (65%, 59% and 68%), followed by the sulfate (SO_4^-) fraction (17%, 23%, 19%) at the urban, peri−urban and rural sites. The eBC fraction contributes on average in the PM_1 for the 5%, 3% and 2%. Looking at the variation of the optical properties in relation to composition it emerges a clear

impact of the eBC fractions on the imaginary CRI and SSA components, both at the urban and peri−urban site, with an increase of the eBC fraction up to (14% and 11%) in the k>0.1 class. Therefore, a positive correlation between the aerosol absorption and the primary anthropogenic emissions is suggested at the urban and peri−urban locations. The highest (lowest) SSA (CRI) values >0.9 (<0.05), appear associated to higher concentrations of sulfates and nitrates fractions and a decrease in the organic and eBC fractions, in particular at the urban site. Furthermore, the increase of the AAE at the urban and peri−urban sites is associated to an increase of the organic fraction, suggesting an enhanced brown carbon absorption at shorter wavelengths in link with the decrease of inorganics non-absorbing compounds. Looking at Fig. 10, no clear correlation between the composition and the CRI, SSA, and AAE is observed at the rural forested site, suggesting a combination of different effects, such as absorption enhancement due to lensing effect with aerosol aging (Zhang et al., 2018) or the contribution of different absorbing secondary BrC species under diverse conditions. Finally, no significant variations in the real refractive index can be directly attributable to the bulk composition.

6. Conclusive remarks

In this paper we present the aerosol complex refractive index and single scattering albedo datasets retrieved during the ACROSS campaign in June-July 2022, under several contrasting atmospheric conditions, at three different ground−based sites representatives of urban (PRG), peri–urban (SIRTA) and rural (RambForest) conditions in the greater Paris area. Data refer to the submicron (PM_1) aerosol component, surface-level observations and cover the spectral range 370−950 nm. The CRI and SSA datasets were retrieved from a synergy between in−situ aerosol optical (scattering and absorption coefficients) and particle size distributions measurements and optical Mie calculations.

Results from the present study show a clear urban-to-rural gradient in SSA and CRI over the different periods, with varying intensity depending on meteorological conditions. The SSA (imaginary CRI) increases (decreases) going from urban to rural site, showing on average a 0.13 change between PRG and RambForest at 520 nm (full period average). The gradient is reduced under the influence of the Paris emissions on the surrounding sites under north-easterly wind regimes, as supported by the integration of observations and regional modelling products. Mixing of air masses of biogenic and anthropogenic origin are expected under these conditions, with consequent possible formation of mixed ASOA and BSOA products. On the contrary, a more marked positive urban−to−rural gradient in SSA (0.2 change between PRG and RambForest) is observed when the Paris urban site is downwind of the peri-urban and rural sites.

During the ACROSS campaign, the advection of an intense fire plume from the Southern of France caused a strong air quality and visibility degradation over the Ile-de-France region. The SSA at 370 (520) nm increased up to 0.93 (0.91) and the CRI spectral pattern changed at the urban site, showing an increase in the UV−visible wavelength, characteristic of possible aged−BrC in the plume. In fact, since the fire episode plume arised from long range transport, photochemically−aging procees may have occurred, reducing smoke aerosol absorption due to bleaching effects (Konovalov et al., 2021; Laskin et al., 2015). The retrieved k is within 0.022 and 0.019 across 370-950 nm at the urban site, while no significant changes in k have been observed at the rural and peri−urban sites in correspondence of the smoke plume.

−The bulk chemical composition analysis shows that the imaginary CRI is related to eBC fractions, suggesting the key role of primary emissions and even low eBC concentrations in affecting absorption, as particularly evident at the urban and peri-urban sites. Nevertheless, organics contribute more than 50% of the aerosol composition at the three sites, supporting the important contribution of brown carbon to spectral absorption. The BrC is estimated to contribute on

average up to 10% (urban), 17% (peri-urban) and 22% (rural) to the absorption at 370 nm. A more detailed and advanced analysis is necessary to provide insight on the molecular scale organic composition of the aerosols, in order to relate spectral absorption to the presence of different chromophores, as for example nitro-aromatics, at the different sites and under different conditions. Moreover, a more detailed characterization of the particle mixing state by particle-level in-situ measurements would be advantageous to better understand the particle chemical and optical evolution at the rural site, where more aged and internally mixed aerosols are expected.

According to the recent Meteo France report (Meteo France, 2022), summer 2022 has been called as "the summer of extremes" due to strong positive temperature anomalies registered during all the summer 2022 period, the strong deficit in precipitation, and the long duration of the heat waves episodes. The increase in the heatwave frequencies, lead to increased accumulation of anthropogenic emissions and biogenic VOC emissions, with possible SOA build-up that could have impacted the aerosol spectral optical properties (Cholakian et al., 2019; Gomez et al., 2023; Yli-Juuti et al., 2021). Average conditions at 520 nm shows that urban SSA is 12 % higher during the heatwaves compared to the clean period at the urban site, while no significant changes are observed at the SIRTA and RambForest. Nevertheless, on average, the CRI imaginary component is higher (respectively of 9% at PRG and SIRTA, while 13 % at RambForest) during the heatwaves compared to the clean period. Therefore, based on the unique dataset presented in this study, we suggest an average CRI at 520 nm of 1.45-0.043i, 1.56-0.041i, 1.52-0.026i respectively for locations showing urban background, peri-urban and rural features under heatwave conditions, while an average CRI of 1.39-0.039i, 1.52-0.038i, 1.47-0.023i is more appropriate under low aerosol loading scenarios.

The full dataset presented in this paper is made available to the scientific community as explained in the "Data availability" section, and can be used to better constraining the spectral aerosol optical properties representation in climate models and satellite retrievals under challenging climate conditions. As a first use, this dataset will be applied to validate the aerosol spectral optical properties simulated with the CHIMERE chemistry transport model, finalized at the estimation of the aerosol direct radiative effect at the regional scale of the Ile-de-France region for the ACROSS period.

Code availability

The CRI optical retrieval code can be made available upon request to the first author. The "miepython" routine from (Prahl, 2023) was used for Mie theory calculations.

Data availability

LEVEL 2 datasets used in the present study from the ACROSS field campaign for the PRG and RambForest sites are available or will be made soon available on the AERIS datacenter (https://across.aeris−data.fr/catalogue/) and DOI referenced. Some datasets already available are: the equivalent black carbon at the PRG site (Di Antonio et al., 2023c); the spectral scattering coefficient at the PRG site (Di Antonio et al., 2023f); the spectral absorption coefficient (Di Antonio et al., 2023b); the black carbon Paris-to-regional ratio (Di Antonio et al., 2023a); SMPS particle size distribution at the PRG site (KAMMER et al., 2024); the OPC particle size distribution at the PRG site (Di Antonio et al., 2023g); meteorological data at PRG site (Di Antonio et al., 2023e): the non-refractory aerosol composition below and above the canopy at the Rambouilet site (Ferreira de Brito et al., 2023b, a); the mixing layer height at SIRTA (Kotthaus et al., 2023). The SIRTA observatory data can be downloaded at https://sirta.ipsl.fr/ (last access: 7 April 2024).

Author contribution

LDA and CDB designed the study, in collaboration with MB, JFD, PF, GS and GF. LDA performed the full data analysis. CDB supervised all the analysis work. VM and CC designed the ACROSS field campaign. LDA, CDB, PF, AG, VM, CC, ABa, ABe, MCa, SC, MCi, BDA, JDB, DDH, SD, OF, PMF, CG, LH, JK, BL, FM, GM, EP, JEP, BPV, LP, PP, DP, VR, SR, MS, EV, and PZ, contributed to the campaign setup, deployment, calibration and operation of the instrumentation, and the data collection. LDA and CDB discussed the results and led the writing of the manuscript, with contributions by MB, JFD, PF, GS and GF. All authors commented and reviewed the manuscript.

Competing interest

One of the co-authors is a co-organizer of the editorial board of the Special Issue "Atmospheric Chemistry of the Suburban Forest – multiplatform observational campaign of the chemistry and physics of mixed urban and biogenic emissions". The authors have no other competing interests to declare.

Special issue statement

This article is part of the special issue "Atmospheric Chemistry of the Suburban Forest – multiplatform observational campaign of the chemistry and physics of mixed urban and biogenic emissions". It is not associated with a conference.

Acknowledgements

This work has been supported by the ACROSS and the RI−URBANS projects. The ACROSS project has received funding from the French National Research Agency (ANR) under the investment program integrated into France 2030, with the reference ANR−17−MPGA−0002, and it was supported by the French National program LEFE (Les Enveloppes Fluides et l'Environnement) of the CNRS/INSU (Centre National de la Recherche Scientifique/Institut National des Sciences de L'Univers). The RI−URBANS project has received funding from the European Union's Horizon 2020 research and innovation program under grant agreement no. 101036245. PEGASUS is a national facility of the CNRS-INSU as part of the French ACTRIS research infrastructure. IMT Nord Europe's group has been supported by Labex CaPPA (ANR-11-LABX-0005-01). L. N. Hawkins and D. O. De Haan were supported by NSF-IRES 1825094. Useful discussions with Marc Mallet, Yevgeny Derimian and Jean−Christophe Raut are gratefully acknowledged. The authors would like to acknowledge SIRTA for providing some of the data used in this study.

Figures

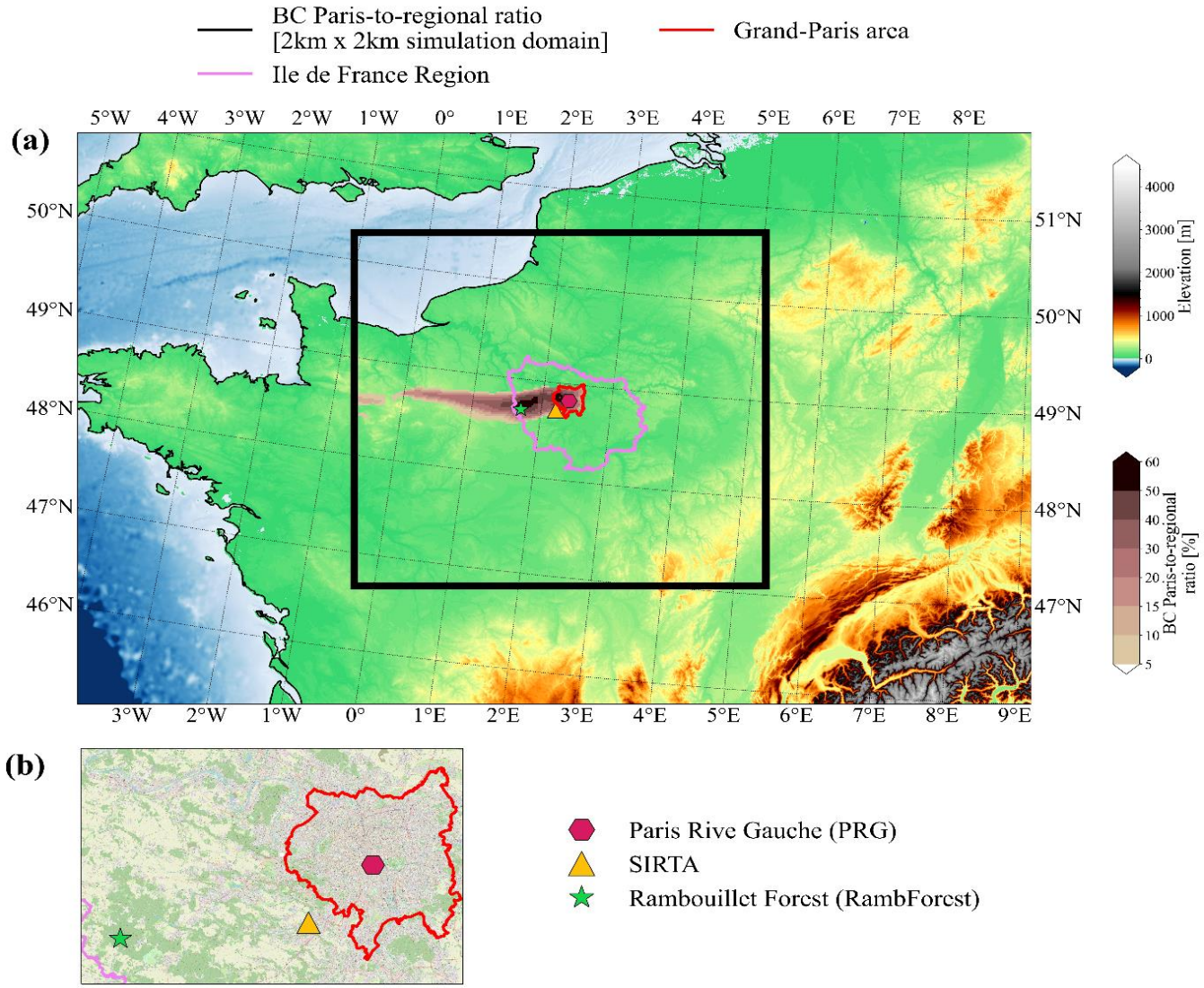

Figure 1: Geographical location of the Paris Rive Gauche (PRG, urban), SIRTA (peri−urban), and Rambouillet (RambForest, rural) ground−based sites deployed during the ACROSS campaign 2022 in the Ile-de-France region. Panel (a) shows in background the terrain elevation and the BC Paris−to regional ratio (BC_{ratio}) for the 22 June 2022 at 13 UTC. The violet line delimits the boundaries of the Ile-de-France region, while the red line delimits the boundaries of the Grand Paris domain. Digital elevation model source: SRTM15 (Tozer et al., 2019a, b). Panel (b) shows a zoom (1.6°−2.62°E, 48.60−49.05°N) over the Ile-de-France region to better visualize the ground−based sites locations. Background map source: Map data © OpenStreetMap contributors.

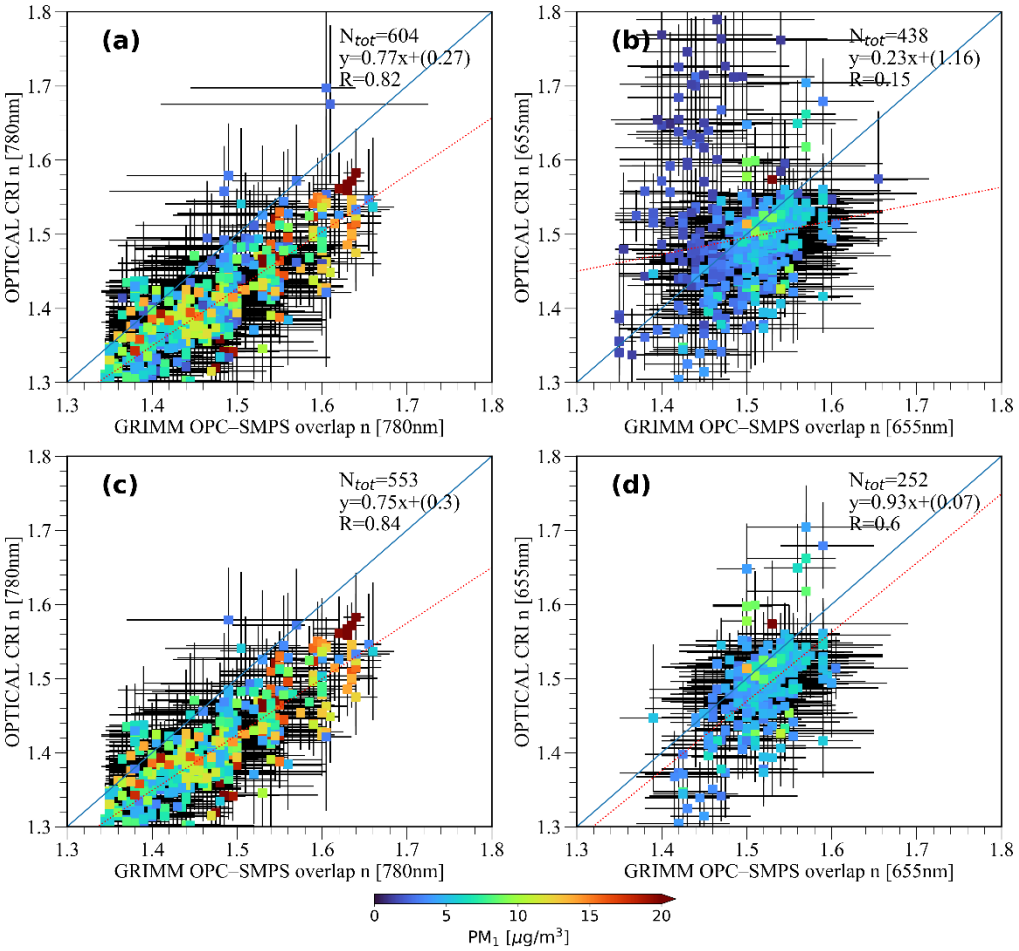

Figure 2: Scatter plot of the real part of the complex refractive index (CRI) retrieved by applying the optical−closure method versus the one retrieved with the OPC−SMPS overlap method at the PRG (780 nm, panels a) and c)) and RambForest (655 nm, panels b) and d)) sites. Points are colored by the PM_1 mass calculated from the SMPS size distribution data assuming an aerosol particle density of 1.4 g cm^{-3}. Panels a) and b) show all data while c) and d) reports data selected using a threshold of PM_1>3μgm^{-3}. The red dotted line represents the linear fit, while the 1:1 line is reported in blue.

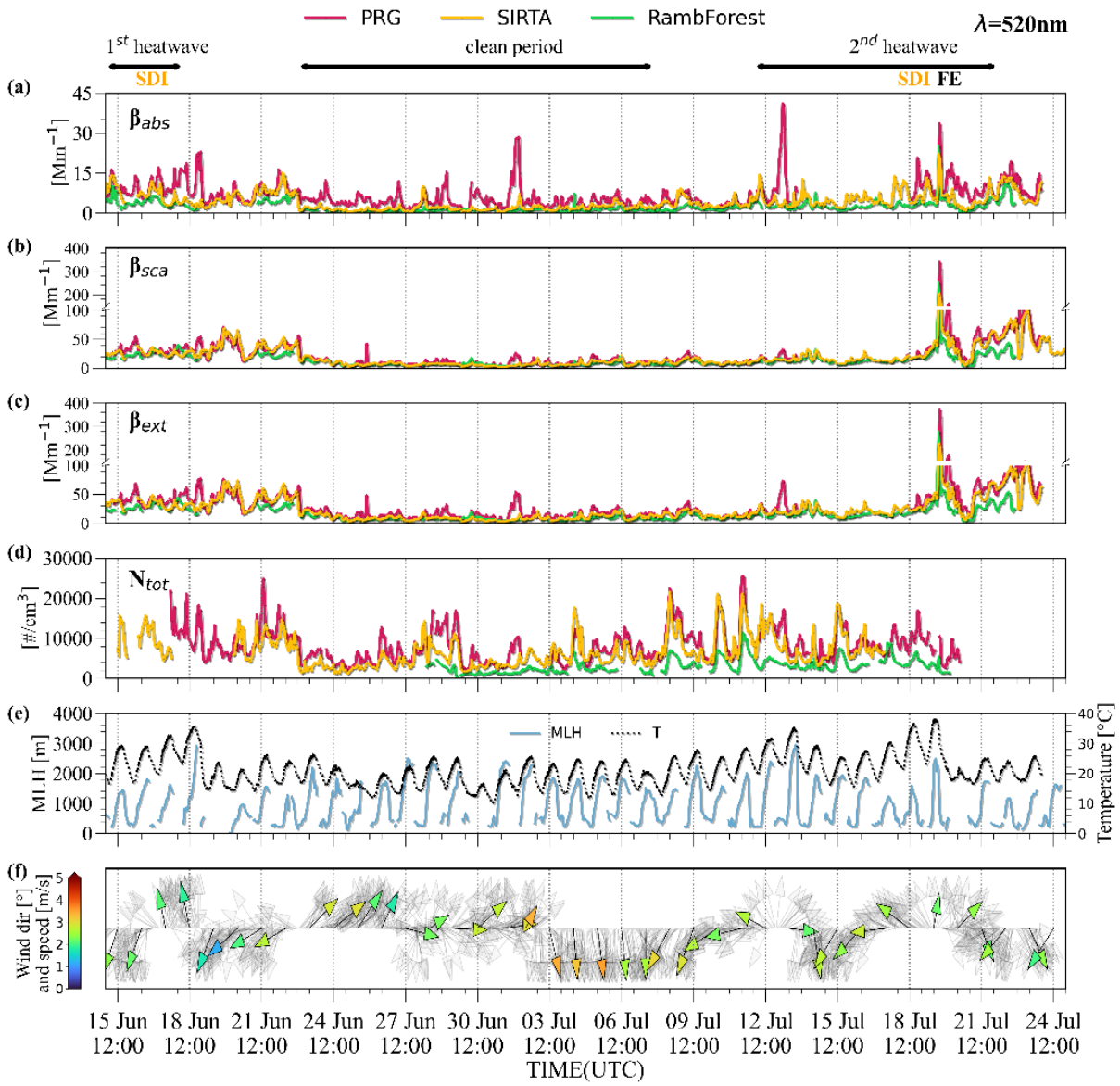

Figure 3: Absorption (βabs), scattering (βsca), and extinction (calculated as βabs+ βsca) coefficients time series at 520 nm at (a) Paris Rive Gauche (urban site) (b) SIRTA (peri–urban site) c) Rambouillet (RambForest) (rural site). Panel (d) represents the total number of particles at the three sites; the panel (e) represents the mixing layer height (MLH) and temperature registered at the SIRTA site. Panel (f) shows the daily wind speed and direction at the SIRTA site. Shaded arrows represent the hourly wind direction. Two different heatwaves periods correlated with the high optical signals during June and July 2022 months, interspersed by a low anthropogenic emission period (defined "clean period") are indicated by arrows at the top of panel a). The label SDI (colored in orange) and FE (colored in black) indicates periods affected by Saharan dust intrusion from the upper levels down to the ground and the long−range transport fire episode occurred on the 19th of July, respectively. The empty spaces represent periods where measurements were not validated.

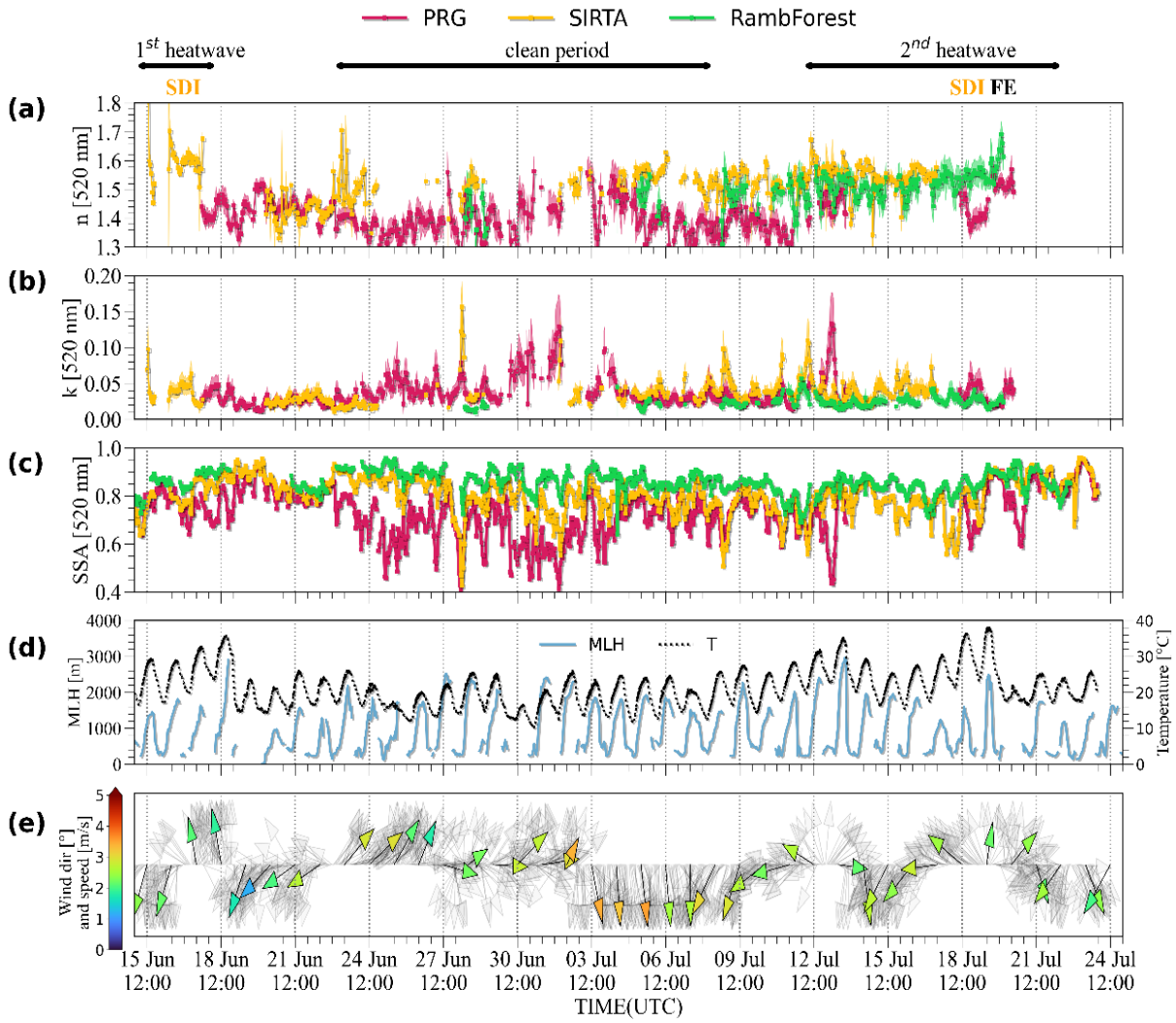

Figure 4: Time series of the a) real and b) imaginary part of the complex refractive index (CRI) and c) single scattering albedo (SSA at 520 nm retrieved for the ACROSS campaign at the PRG (urban), SIRTA (peri–urban) and RambForest (rural) sites. The mean CRI ± SD is reported. Black arrows at the top of the plots represent the different periods observed during the ACROSS campaign (see main text and 1) first heatwave from 15 June to 18 June 2022; 2) clean period from 23 June to 11 July 2022; 3) the second heatwave from the 12 July to 25 July 2022. The label SDI (colored in orange) and FE (colored in black) indicates periods affected by Saharan dust intrusion from the upper levels down to the ground and the long−range transport fire episode occurred on the 19th of July, respectively.

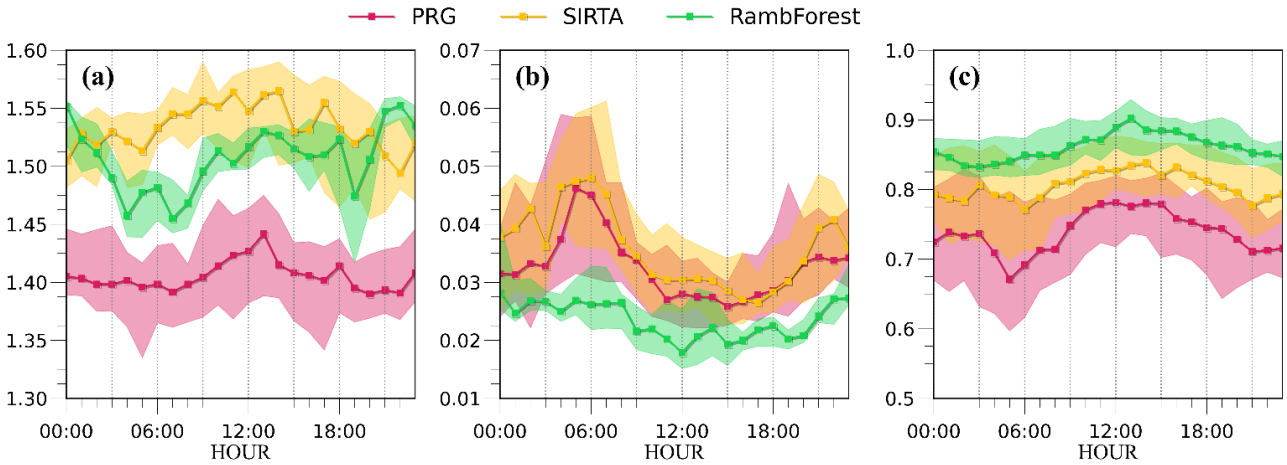

Figure 5: Diurnal cycle of hourly values of the (a) real and (b) imaginary part of the complex refractive index (CRI) and (c) single scattering albedo (SSA) at 520 nm retrieved for the full period of the ACROSS campaign at the PRG (urban), SIRTA (peri–urban) and RambForest (rural) sites. The median CRI and SSA are reported. Shaded area represents the 25 and 75 percentiles of the series.

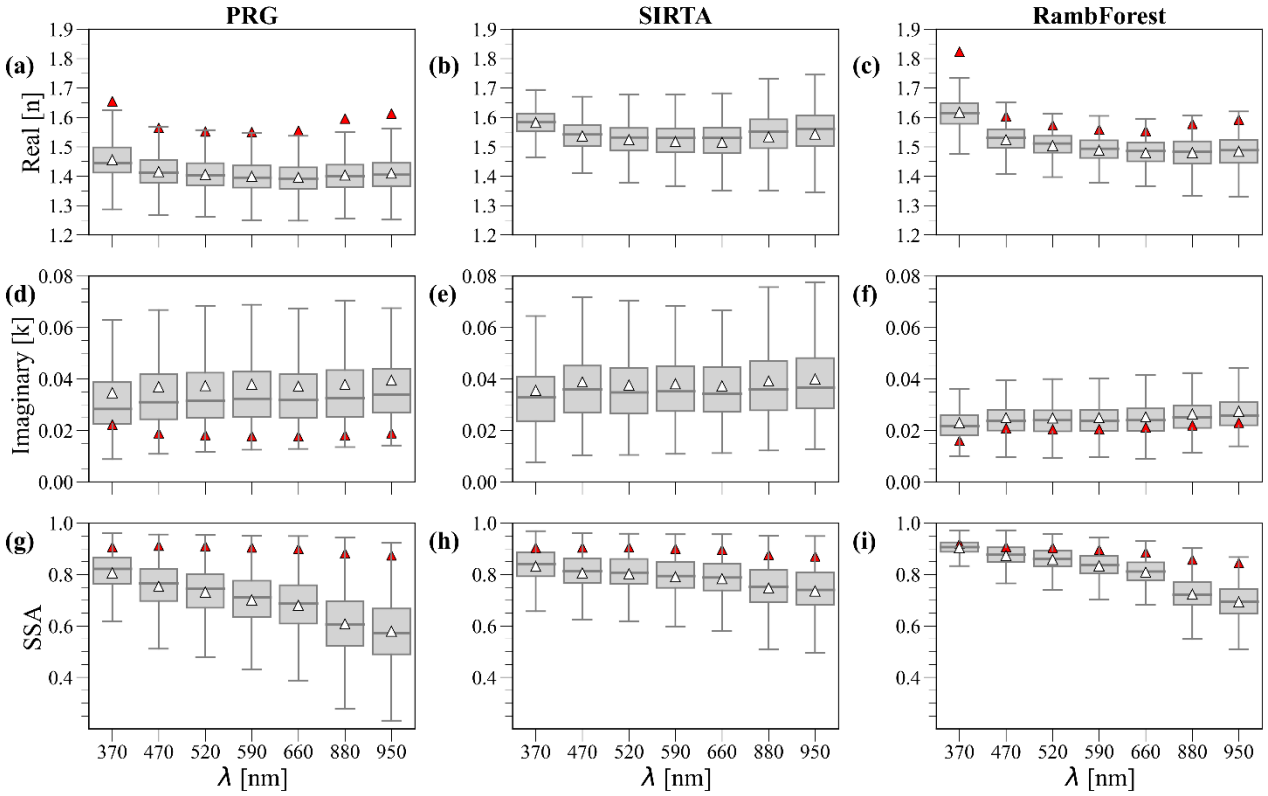

Figure 6: Wavelength dependence of the real and imaginary part of the complex refractive index (CRI) and single scattering albedo (SSA) for the full ACROSS period for the PRG (panels (a), (d), (g)), SIRTA (panels (b), (e), (h)) and RambForest (panels (c), (f), (i)) sites. Red triangles show the average values during the fire episode (FE): between 18 UTC and 19 UTC at the urban and peri−urban site, while between 16 UTC and 18 UTC at the rural site). No size distribution data are available for the complex refractive index retrieval at the peri−urban site during the FE. White triangles show the mean value, while black lines represent the medians. Outliers are not shown for the sake of readability.

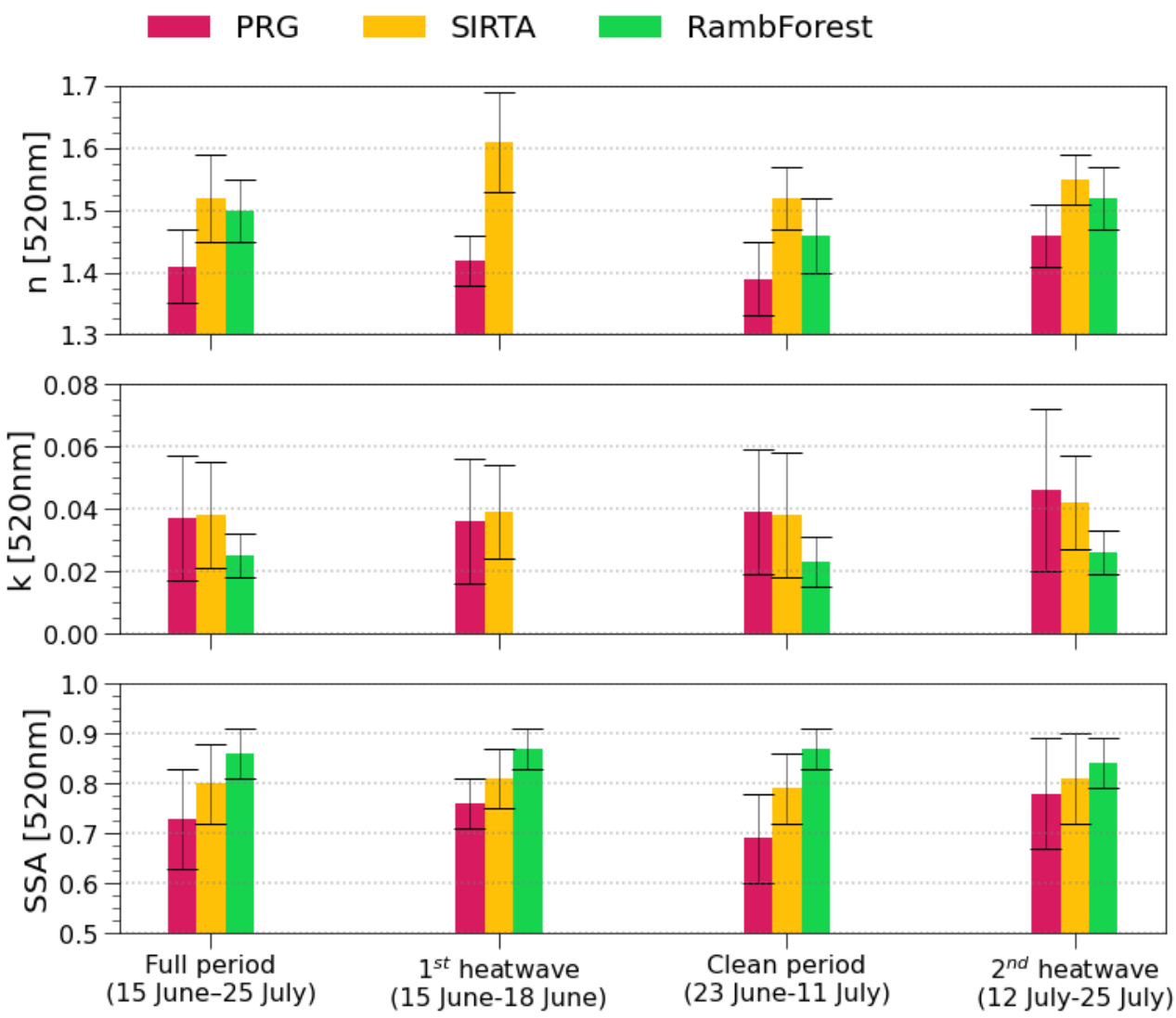

Figure 7: Average real (n) and complex (k) part of the CRI and single scattering albedo (SSA) at 520nm for the full period, the two heatwaves and the clean period for the PRG (urban), SRTA (peri-urban) and RambForest (rural). Black bars indicate the SD.

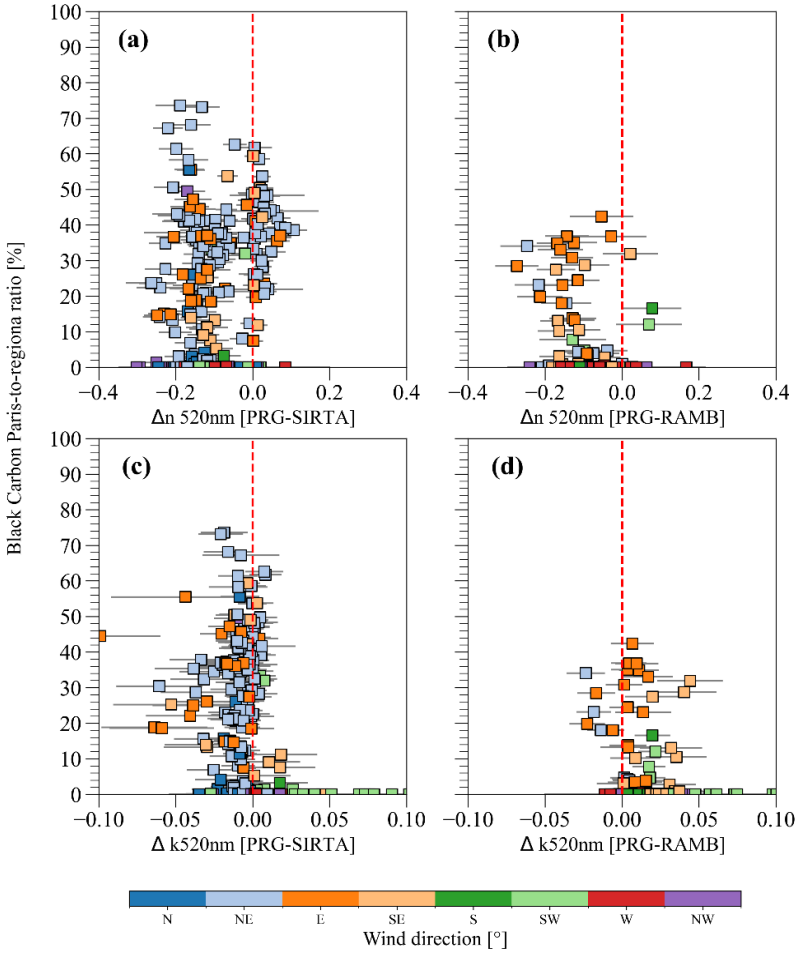

Figure 8: Scatter plot of absolute difference of the real (Δn, a, b) and imaginary (Δk, c, d) part of the complex refractive index at 470 nm vs the BC_{ratio} expressed in %, representing the Grand Paris area BC contribution to the total BC concentration extracted from the CHIMERE model simulation at a spatial resolution of 2km at the SIRTA (peri–urban, panel (a) and (c)) and the RambForest (rural, panel (b) and (c)) sites. Panels (a) and (c) show the Δn and Δk calculated as difference between PRG and SIRTA data, while (b) and (d) show the Δn and Δk for PRG minus RambForest. The vertical dashed line represents the zero difference line. Horizontal error bars represent ±SD and have been calculated as SD= $\sqrt{SD_1{}^2 + SD_2{}^2}$, where subscripts 1 or 2 stands for the specific site used to perform the difference.

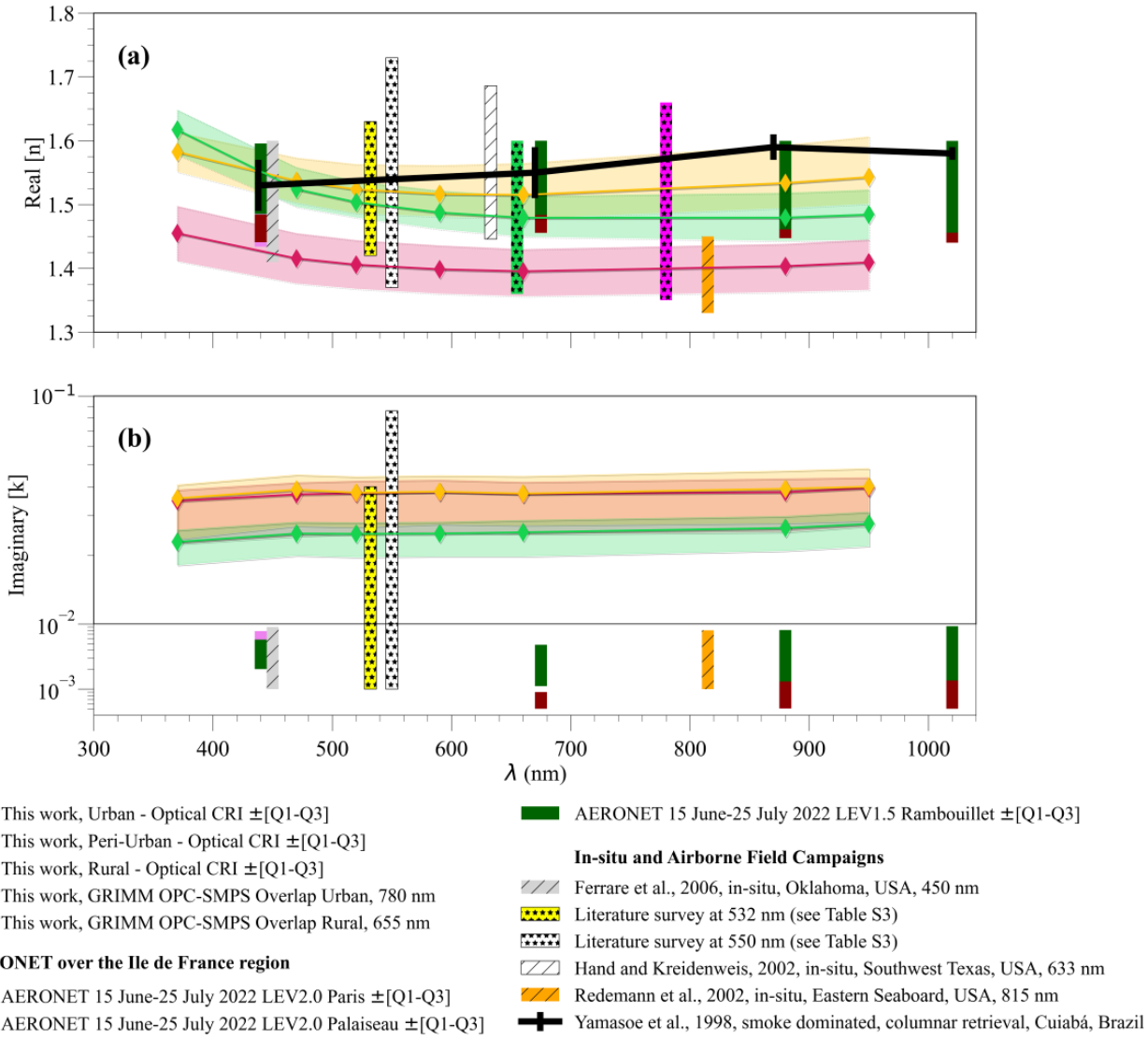

Figure 9: Comparison of the results obtained in this work with literature surveys of the (a) real (n) and (b) imaginary (k) part of the complex refractive index (CRI). Mean (solid line), 25th percentile (dotted line), 75th percentile (dashed line) and interquartile range (coloured area) of the CRI at Paris Rive Gauche (PRG, urban), SIRTA (peri–urban) and Rambouillet (RambForest) for the entire ACROSS period 2022 are represented. The legend identifies the line styles used for the literature works. Note that for k values the line for PRG is mainly hidden under that of SIRTA. The literature survey at 532 and 550 nm is detailed in Table S3.

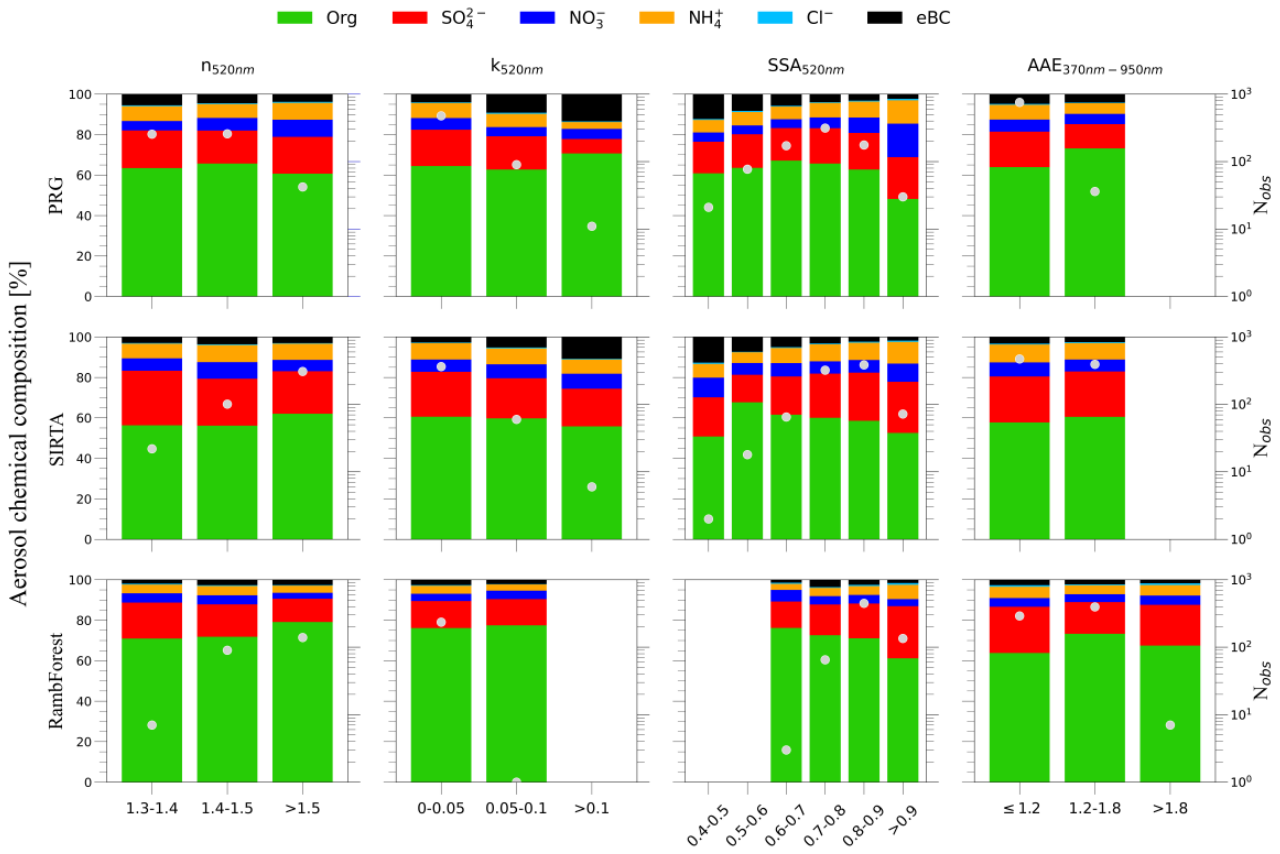

Figure 10: Aerosol chemical composition as a function of the complex refractive index (CRI), single scattering albedo (SSA) and absorption angstrom exponent (AAE) different classes for the PRG, SIRTA and RambForest sites. White points represent the number of observations in each section. The green color indicates the organic fraction, the red color indicates the sulfate fraction, the orange color indicates the nitrate fraction, the blue color indicates the ammonium fraction, cyan color indicates the chloride fraction, while black color indicates the equivalent black carbon contribution.

Tables

OBS	Full period (15 June–25 July)			1rst heatwave (15 June–18 June)			Clean period (23 June–11 July)			2nd Heatwave (12 July–25 July)		
	PRG	**SIRTA**	**Ramb Forest**	**PRG**	**SIRTA**	**Ramb Forest**	**PRG**	**SIRTA**	**Ramb Forest**	**PRG**	**SIRTA**	**Ramb Forest**
$N_{tot}/10^3$ [#/cm3]	8 ±4	7 ±4	3 ±2	12 ±4	10 ±3	–	7 ±4	6 ±4	3 ±2	9 ±4	8 ±4	4 ±1
β_{ext} [Mm^{-1}]	30 ±29	24 ±22	15 ±14	43 ±10	32 ±7	27 ±7	15 ±8	11 ±5	9 ±3	57 ±45	36 ±29	22 ±21
β_{sca} [Mm^{-1}]	24 ±26	20 ±20	13 ±13	32 ±7	26 ±5	23 ±6	11 ±6	9 ±4	7 ±3	47 ±42	30 ±26	18 ±18
β_{abs} [Mm^{-1}]	7 ±5	4 ±3	2 ±2	10 ±4	6 ±3	4 ±2	5 ±3	2 ±1	1 ±1	10 ±6	5 ±3	3 ±2
β_{abs}–BrC (370nm) [Mm^{-1}]	1.2 ±1.7	1.1 ±1.1	0.9 ±1.2	1.9 ±0.7	1.7 ±0.9	1.5 ±0.8	0.7 ±0.5	0.6 ±0.4	0.5 ±0.5	2.0 ±3.1	1.4 ±1.5	1.1 ±1.9
AAE	1.09 ±0.10	1.20 ±0.08	1.21 ±0.22	1.13 ±0.05	1.19 ±0.06	1.29 ±0.12	1.07 ±0.11	1.22 ±0.08	1.19 ±0.27	1.12 ±0.09	1.18 ±0.09	1.22 ±0.15
SAE	2.3 ±0.3	1.9 ±0.4	2.7 ±0.2	2.4 ±0.1	2.1 ±0.4	2.7 ±0.1	2.4 ±0.2	1.7 ±0.4	2.8 ±0.2	2.1 ±0.3	1.9 ±0.2	2.7 ±0.2
n	1.41 ±0.06	1.52 ±0.07	1.50 ±0.05	1.42 ±0.04	1.61 ±0.08	–	1.39 ±0.06	1.52 ±0.05	1.47 ±0.06	1.46 ±0.05	1.55 ±0.04	1.52 ±0.05
k	0.037 ±0.020	0.038 ±0.017	0.025 ±0.007	0.036 ±0.020	0.039 ±0.015	–	0.039 ±0.020	0.038 ±0.020	0.023 ±0.008	0.046 ±0.026	0.042 ±0.015	0.026 ±0.007
SSA	0.73 ±0.10	0.80 ±0.08	0.86 ±0.05	0.76 ±0.05	0.81 ±0.06	0.87 ±0.04	0.69 ±0.09	0.79 ±0.07	0.87 ±0.04	0.78 ±0.11	0.81 ±0.09	0.84 ±0.05

Table 1: Average values ± standard deviation (SD) of the: total number of particles (Ntot), extinction (β_{ext}) scattering (β_{sca}), and absorption (β_{abs}) coefficients at 520 nm, absorption coefficient fraction due to Brown carbon (βabs–BrC) at 370nm, real (n) and imaginary (k) part of CRI and SSA at 520 nm, and absorption and scattering angstrom exponents (AAE, SAE) calculated between 370 and 950 nm for the different periods defined during the ACROSS campaign 2022.

Wind direction	SSA ± SD			n ± SD			k ± SD		
	PRG	**SIRTA**	**Ramb Forest**	**PRG**	**SIRTA**	**Ramb Forest**	**PRG**	**SIRTA**	**Ramb Forest**
N	0.73 ±0.08	0.79 ±0.06	0.86 ±0.03	1.40 ±0.07	1.56 ±0.05	1.48 ±0.04	0.035± 0.011	0.039± 0.010	0.021 ±0.004
NE	0.77 ±0.08	0.79 ±0.07	0.84 ±0.04	1.40 ±0.05	1.51 ±0.07	1.49 ±0.05	0.028 ±0.011	0.039 ±0.013	0.026± 0.006
E	0.73 ±0.10	0.73 ±0.11	0.80 ±0.05	1.38 ±0.06	1.50 ±0.06	1.50 ±0.05	0.031 ±0.015	0.051 ±0.031	0.032 ±0.008
SE	0.72 ±0.10	0.77 ±0.10	0.85 ±0.05	1.42 ±0.04	1.53 ±0.07	1.53 ±0.04	0.043 ±0.024	0.053 ±0.024	0.028 ±0.007
S	0.70 ±0.08	0.84 ±0.05	0.90 ±0.02	1.42 ±0.06	1.56 ±0.04	1.51 ±0.08	0.043 ±0.013	0.031 ±0.014	0.018 ±0.005
SW	0.67 ±0.10	0.84 ±0.05	0.90 ±0.03	1.39 ±0.05	1.53 ±0.06	1.50 ±0.05	0.048 ±0.024	0.024 ±0.009	0.019 ±0.004
W	0.73 ±0.12	0.83 ±0.06	0.87 ±0.04	1.44 ±0.06	1.50 ±0.07	1.54 ±0.10	0.040 ±0.024	0.024 ±0.006	0.021 ±0.006
NW	0.77 ±0.11	0.82 ±0.08	0.87 ±0.04	1.41 ±0.07	1.55 ±0.05	1.49 ±0.06	0.034 ±0.016	0.032 ±0.009	0.021 ±0.006

Table 2: Single scattering albedo (SSA) and real (n) and imaginary (k) parts of the complex refractive index expressed as averages ± standard deviation (SD) at 520 nm as retrieved for the urban (PRG), peri−urban (SIRTA) and rural (RambForest) sites for the different main wind sectors. A more detailed version is available in the supplementary material (Table S4).

Appendix A: Useful list of abbreviations and symbols

D_p particle diameter

D_m mobility diameter

D_o optical diameter

D_g geometrical diameter

β_{sca} aerosol scattering coefficient

β_{abs} aerosol absorption coefficient

$\beta_{abs-BrC}$ Brown carbon absorption coefficient

β_{atn} light attenuation coefficient

$dN(D_p)/dlogD_p$ aerosol number size distribution

$dN(D_m)/dlogD_m$ aerosol number size distribution using mobility diameter D_m

$dN(D_o)/dlogD_o$ aerosol number size distribution using optical diameter D_o

$dN(D_g)/dlogD_g$ aerosol number size distribution using geometric diameter D_g

SAE Scattering Ångström exponent

N_{tot} total number of particles

χ shape factor

C_{ref} multiple–scattering coefficient

SSA Single scattering albedo

C_{sca} truncation correction coefficient

f(x) function of x

RMSD Root Mean Square Difference

RMSE Root Mean Square Error

MAE Mean Absolute Error

ERF Effective radiative forcing

ERFari Effective radiative forcing due to aerosol–radiation interactions

ERFaci Effective radiative forcing aerosol–cloud interactions

CRI complex refractive index

BC Black carbon

eBC Equivalent black carbon

BrC Brown Carbon

FE Fire episode

OC Organic aerosol

AVOC anthropogenic volatile organic compound

BVOC biogenic volatile organic compound

ASOA anthropogenic secondary organic aerosol

BSOA biogenic secondary organic aerosol

ACROSS Atmospheric ChemistRy Of the Suburban foreSt

ACTRIS Aerosol, Clouds and Trace Gases Research Infrastructure

FF filter factor

Cref Multiple scattering coefficient

H* harmonisation factor

VOC Volatile Organic Compound

PRG Paris Rive Gauche

RambForest Rambouillet Forest

ESQUIF Etude et Simulation de la QUalité de l'air en Ile−de−France

LISAIR Lidar pour la Surveillance de l'AIR

PM Particulate Matter

AAE Absorption Angstrom Exponent

SAE Scattering Angstrom Exponent

NCEP National Center for Environmental Prediction

Chapter 5

5. Evaluation of the meteorology, dynamics, chemistry, aerosol optical properties and radiation during the ACROSS campaign 2022

This chapter presents the evaluation against observations of the WRF-CHIMERE simulation conducted for the ACROSS campaign 2022. The chapter is subsequently divided into two main sections: the first, which is dedicated to the validation of the meteorology, dynamics and chemistry within the simulation, while the second which is dedicated to the evaluation of the aerosol optical parameters (surface and columnar) and surface radiation.

The first part is presented under the form of an article, and it will shortly be submitted to Atmospheric Chemistry and Physics journal and further included in the "Atmospheric Chemistry of the Suburban Forest – multiplatform observational campaign of the chemistry and physics of mixed urban and biogenic emissions" special issue, while the results from the second section will be included in a forthcoming article on the modelling of the aerosol direct radiative effect during the ACROSS field campaign.

Three nested domains respectively at 30 km (covering Europe and part of the North Africa), 6 km (covering France), and at 2 km (centred over the Ile-de-France region) spatial resolution have been deployed for the ACROSS field campaign.

Within the section 5.1 we used the already available measurements from the campaign in addition to observations from air quality and meteorological networks and satellites for the evaluation of the coupled WRF-CHIMERE model simulation over the June-July 2022 in the Ile-de-France region (at 2 km spatial resolution) and over France (at 6 km spatial resolution). The paper also provides an overview of meteorological conditions during the campaign period and related to major pollution variability over France and at the campaign sites. The work demonstrates that the WRF model is capable of well simulating key meteorological variables and their spatial and temporal variability throughout the campaign, with particular focus on the two heat waves that occurred at the beginning and end of the campaign.

On the contrary, while the WRF-CHIMERE model system generally well produces daily ozone maxima, all the major non-refractive aerosol species are affected by an overestimation at the France scale (at PM_1 size): +21% for organic aerosol, +16% for sulfate, +37% for ammonium, +53% for nitrate, and only +7% for BC. For organic aerosol (OA), the biases are more pronounced during the two heatwave periods (+49% and +38%), while they are slightly negative (-8%) during the clean period. This suggests the possibility of a bias in OA sensitivity to temperature, which could be related to a corresponding bias in biogenic volatile organic compound (VOC) emissions, or within the VBS

organic aerosol scheme. However, for the three sites in Ile-de-France, model overestimations are less systematic. Biases are -20% to +21% for the OA, -12% to +37% for sulfate, +1% to 89% for ammonium, +15% to +148% for nitrate and +27% to 66% for eBC. The large positive biases are obtained for the Rambouillet site (rural), where concentrations are very small (for example 0.38 μgm^{-3} for ammonium, 0.16 μgm^{-3} for nitrate and 0.14 μgm^{-3} for BC).

Additionally, within the section 5.2 we evaluate the model simulation optical and radiation observations such as:

- the surface single scattering albedo and complex refractive index at the urban peri-urban and rural sites of the ACROSS campaign
- The columnar aerosol optical depth (AOD), single scattering albedo (SSA) and absorption aerosol optical depth (AAOD) against the two different mixing state (extern and core-shell)
- The downwelling radiation at the surface with the E-OBS dataset.

This is a necessary step before using the WRF-CHIMERE simulation for the estimation of DRE in Chapter 6.

5.1 Modelling of atmospheric variability of gas and aerosols during the ACROSS campaign 2022 in the greater Paris area: evaluation of the meteorology, dynamics and chemistry

Ludovico Di Antonio[1], Matthias Beekmann[2], Guillaume Siour[1], Vincent Michoud[2], Christopher Cantrell[1,3], A. Beauville[1], A. Bergé[2], M. Cazaunau[1], S. Chevaillier[1], Manuela Cirtog[1], Joel F. de Brito[4], Paola Formenti[2], C. Gaimoz[1], O. Garret[5], Aline Gratien[2], Valérie Gros[6], Martial Haeffelin[7], Leila N. Hawkins[8], Simone Kotthaus[7], G. Noyalet[1], Diana Pereira[2], Jean-Eudes Petit[6], Veronique Riffault[4], Chenjie Yu[2], Gilles Foret[1], Jean-François Doussin[1], Claudia Di Biagio[2]

[1]Univ Paris Est Creteil and Université Paris Cité, CNRS, LISA, F−94010 Créteil, France
[2]Université Paris Cité and Univ Paris Est Creteil, CNRS, LISA, F−75013 Paris, France
[3]University of Colorado, Atmospheric and Oceanic Sciences (ATOC), Boulder, CO 80309
[4]Centre for Energy and Environment, IMT Nord Europe, Institut Mines−Télécom, Université de Lille, Lille, 59000, France
[5]Ville de Paris, Service parisien de santé environnementale, 75013, Paris, France
[6]Laboratoire des Sciences du Climat et de l'Environnement, CEA−CNRS−UVSQ, IPSL, Université Paris−Saclay, 91191 Gif−sur−Yvette, France
[7]Institut Pierre-Simon Laplace (IPSL), CNRS, École Polytechnique, Institut Polytechnique de Paris, 91128 Palaiseau CEDEX, France
[8]Department of Chemistry, Harvey Mudd College, 301 Platt Blvd, Claremont, California 91711, United States;

Correspondence to: Ludovico Di Antonio (ludovico.diantonio@lisa.ipsl.fr), Matthias Beekmann (matthias.beekmann@lisa.ipsl.fr)

Abstract. The interaction of anthropogenic and biogenic emissions around large urban agglomerations remains an important question for atmospheric research and is the key question of the ACROSS (Atmospheric Chemistry of the Suburban Forest) project leading an intensive field campaign in the Paris area during the exceptionally hot and dry summer 2022. The ACROSS campaign produced a wealth of observations from the Paris center to a suburban and a forest site, and from aircraft. 3D-modelling is an important part of ACROSS for disentangling processes like emissions, transport and physico-chemical transformations. Here we use the already available measurements from the ACROSS campaign in addition to observations from air quality and meteorological networks for anevaluation of the coupled WRF-CHIMERE model simulation over France. We find that the WRF model is able to reproduce meteorological variability during the campaign, in particular two heat waves towards its beginning and end. The model well reproduces daily ozone maxima, but overestimates $PM_{2.5}$ by a factor 1.5-2, partly due to an overestimation of secondary aerosol, both organic and inorganic. This overestimation was unexpected, and could be related to the specific hot summer conditions. For organic aerosol and BC in the Ile-de-France domain, biases are reduced, below about 20%. The model is used to explain how the interplay of different processes affects the fine aerosol variability and chemical composition over the campaign sites during two heatwave days: biogenic SOA build-up in different forests around the Paris area, advection of fire aerosols and long-range transport of Saharan dust.

Introduction

Megacities and large urban agglomerations are important hot spots of air pollution (e.g., Baklanov et al., 2010; Molina and Molina, 2004) several key questions concerning its interaction with regional pollution are still open. A first question concerns the share between the pollution produced locally within the urban areas and that imported from outside

(Lenschow et al., 2001). This aspect has been treated for several megacities, such as Mexico City (Calderón-Garcidueñas et al., 2015), New-York (Sun et al., 2011), London (Harrison et al., 2012), and Paris (Beekmann et al., 2015), evidencing a general unexpected large regional contributions to city pollution. For instance, (Beekmann et al., 2015) show that regional inflow contributes as high as 70% to the fine particle concentrations ($PM_{2.5}$) for the Paris agglomeration. On the other hand, recent analysis of long-term aerosol optical depth (AOD) measurements from the high-resolution MAIAC (Multi-Angle Implementation of Atmospheric Correction) product over 21 European large cities shows that although most of the aerosol load comes from regional sources, the city's emissions contribute to the deterioration of air quality by increasing AOD levels by 57, 55, 39, and 32% on average for large metropolitan agglomerations such as Barcelona, Lisbon, Paris and Athens (Di Antonio et al., 2023h).

A second main question concerns the impact and fate of concentrated urban emissions on regional pollution levels. From airborne observations in the plume of the Paris megacity during the MEGAPOLI campaign, (Freney et al., 2014) showed that anthropogenic secondary organic aerosol (ASOA) build-up as air masses travel away from the city agglomeration. A still debated question is the interaction between anthropogenic emissions, typically from the urban agglomeration, and biogenic emissions, typically from the surrounding areas. Both types of emissions lead to cumulative secondary pollutant (ozone, particulate matter) formation, and it is important to quantify the share of each source. A large panel of interactions (i.e., of additional effects beyond simple mixing) has been theoretically predicted, observed and modelled. For instance, both anthropogenic and biogenic species impact the oxidant capacity of the atmosphere (OH, NO_3, Cl, O_3) which governs secondary pollution production from anthropogenic and biogenic precursors (Sartelet et al., 2012; Shrivastava et al., 2019). Yields of biogenic secondary aerosol formation can be enhanced or lowered in the presence of anthropogenic emissions for instance, high yield BSOA formation pathway from isoprene implying an epoxide is favoured by low NO and large H_2SO_4 (for example (Carlton et al., 2018).

The interaction of anthropogenic and biogenic emissions in and around a large urban agglomeration is the central scientific question of the French and international ACROSS project (Atmospheric Chemistry of the Suburban Forest, https://across.aeris-data.fr/, last access: 24 April 2024) (Cantrell and Michoud, 2022)https://www.zotero.org/google-docs/?QCXzDa, focussing on the Paris agglomeration. With about 12 million inhabitants, the Paris agglomeration is one of Europe's largest megacities. It is surrounded by flat terrain including several large forested domains, thus an ideal playground to study anthropogenic-biogenic emission interactions. The key questions of the ACROSS project are: how do anthropogenic-biogenic interactions impact primary pollutant oxidation pathways and secondary pollutant build-up? How do they affect the organic carbon, reactive nitrogen and radical budgets? How are optical and hygroscopic aerosol properties affected and, as a consequence, their radiative effect and impact on cloud micro-physics? A large multi-site and multi-platform field campaign held from June 6th to July 25th has been the core of the ACROSS project. The campaign set-up consisted in three main instrumented surface sites on a NE-SW transect going from the Paris center to a suburban and a forest site. The French ATR 42 research aircraft was deployed to document the evolution of the Paris pollution plume over regional scale. Several secondary sites with less complete instrumentation were used to study specific processes or to characterise the spatial variability of major pollutants. Summer 2022 over Western Europe was exceptionally hot and dry and is considered as a proxy for future climate conditions (Ribes et al., 2022). Indeed, the ACROSS campaign was characterised by two strong heat waves towards the beginning and the end of the measurements period, and a more temperate background period in between. These meteorological conditions varying between extremes, together with two episodes of transport of African dust over Europe and the high occurrence of fires during the period

(Menut et al., 2023) make the campaign especially interesting to study also in the perspective of climate change and its impact on atmospheric composition and air quality.

Regional 3D simulation with the WRF-CHIMERE model system were performed covering the ACROSS field campaign domain and the whole France for the June-July 2022 period to support interpretation of campaign data going from local to regional scales or focussing on particular processes. In this paper, we present the configuration of the WRF-CHIMERE model simulation and first analysis of its output dataset, and provide some examples of the use of model data, together with observations, to derive the spatio-temporal variability of pollutants during the ACROSS campaign. In order to assess the robustness of the model output for it use in subsequent studies, and with particular emphasis at the challenging conditions during the ACROSS period, a thorough model evaluation is presented. This evaluation relies on the already available in situ measurements from the ACROSS campaign in the Ile-de-France area, but also to long term in situ and remote sensing measurements from established networks and satellite products. Particular focus is put on the evaluation of the meteorological simulations by the WRF-CHIMERE modelling system. The paper shows how different transport patterns and meteorological conditions, especially during the two heat waves, affected regional fields of major pollutants such as ozone and $PM_{2.5}$, through the interaction of anthropogenic and biogenic emissions.

2 Methods

2.1 WRF-Chimere model configuration

The WRF-CHIMERE model (Menut et al., 2021, https://www.lmd.polytechnique.fr/chimere/) is a 3-D regional Eulerian chemistry-transport model (CTM). It has been applied both for research and forecasting purposes over France and globally (Cholakian et al., 2018; Ferreyra et al., 2016; Lachatre et al., 2020; Tuccella et al., 2019). In this work we adopted the WRF (version 3.7.1, Skamarock et al., 2008) and CHIMERE v2020r3 coupled version (WRF-CHIMERE). Three one-way nested domains with spatial resolutions of 30, 6 and 2 km have been considered (Fig. 1). The 30 km domain covers the European continent and extends up to the Sahara Desert in order to be able to catch Saharan dust transport events over Europe. The 6 km domain covers the whole metropolitan France, while the 2 km domain covers the whole Paris area and the Ile-de-France region where the ACROSS field campaign occurred. The simulation extends from the 15 June 2022 to 25 July 2022, with two weeks of model spin-up. The 30 and 6 km domains have 15 vertical layers between the surface and 300 hPa, while 10 levels are used for the 2 km domain up to 500 hPa. In order to run the CHIMERE model, the meteorological data, initial and boundary conditions for the chemistry, anthropogenic, biogenic and fire emissions and land use have to be provided. All the data sources adopted for this work are summarised in Table 1. The WRF v 3.7.1 coupled with the CHIMERE model provides the meteorological data online (i.e. meteorological fields are exchanged at every physical time step of ten minutes with the CTM for the three domains). In this study, the National Centers of Environmental Predictions) NCEP analysis with 1°x1° spatial resolution has been used to force the meteorological initial and boundary conditions. The microphysics follow the Thompson scheme (Thompson et al., 2008), while the Yonsey University (YSU) planetary boundary layer height (PBL) scheme has been adopted for the PBL estimation (Hong, 2010). Radiation fluxes are calculated using the Rapid Radiative Transfer model for General Circulation Models (GCMs) (RRTMG, (Iacono et al., 2008). The nudging (i.e. the simulated meteorology adjustment on the analysis) has been activated outside the planetary boundary layer every six hours of simulation.

Gas and aerosols initial and boundary conditions to the WRF-CHIMERE model are taken from the CAMS global reanalysis product at 0.75°x0.75° of spatial resolution. Anthropogenic emissions are provided by the CAMS-GLOB-ANT

v5.3 products with a 0.1°x0.1° spatial resolution for 17 activity sectors (Soulie et al., 2023) and then reported to the 11 SNAP (Selected Nomenclature for reporting of Air Pollutants) sectors. For each activity sector, a chemical VOC profile is used from (Passant, 2002) (Passant et al., 2000), and VOCs are then regrouped into those present in the SAPRC chemical mechanism used (see below). The biogenic emissions are simulated with the Model of Emissions of Gases and Aerosols from Nature (MEGAN) v.2.1 module (Guenther et al., 2006) implemented within the CHIMERE model. Biogenic emissions depend on several parameters: the short-wave radiation, the surface temperature simulated by the WRF model and the leaf area index (LAI) derived from MODIS observations (Yuan et al., 2011). In this study we use the LAI referred to the 2013 year with a temporal resolution of 8-days and the emission factors from (Sindelarova et al., 2014). The emission scheme of biogenic VOCs considers dependence on temperature and radiation, but not on soil humidity, and so possible effects of dryness. Fire emissions are taken from the CAMS Global Fire Assimilation System (GFAS) (Kaiser et al., 2012) and processed with the CAMS FIRE v2020r1 pre-processor (provided by the CHIMERE developers, https://www.lmd.polytechnique.fr/chimere/ , last access 08 May 2024). The land use is based on GLOBCOVER with a spatial resolution of ~300m (Arino et al., 2008). The gas-phase chemistry mechanism adopted for the ACROSS campaign is SAPRC-07A, a reduced scheme based on the SAPRC from (Carter, 2010).

The CHIMERE aerosol module simulates the aerosol concentration through a sectional bin approach. In this work, 10 bins between the 0.01 and 40 µm diameter range have been chosen. The aerosol simulated species include black carbon (assumed as elemental carbon), sulfate, nitrate, dust, sea salt, primary particulate matter (PPM), and different primary (POA) and secondary organic aerosol (SOA) species. Secondary organic aerosols are simulated based on the volatility basis set (VBS) scheme (Donahue et al., 2006), allowing to take into account functionalisation (transfer to lower volatility bins) processes. The scheme was later extended to include fragmentation (transfer to higher volatility bins) and non-volatile aerosol formation (Shrivastava et al., 2013, 2015) and adapted by (Cholakian et al., 2019) for use in CHIMERE. The intermediate-volatile organic compounds (IVOC) and the semi-volatile organic compounds (SVOC) from primary organic aerosols are partitioned into nine volatility bins according to their saturation concentration C* ranging from 0.01 to 10^6 µgm^{-3}. The POA can be oxidized by OH to form the Oxidised POA (OPOA), with the possibility of forming more functionalized (O2POA, O3POA) and non-volatile (ONVSOA) products. Four different volatility bins in the 1 to 1000 µgm^{-3} saturation concentration C^* range and a non-volatile species have been used to represent the anthropogenic SOA (ASOA) and the biogenic SOA (BSOA) from VOC oxidation by OH, NO_3 and O_3. Fragmentation occurs at 75% rate independently of the volatility following (Shrivastava et al., 2015), leaving the 25% to functionalisation. These percentages are based on the best agreement between simulated and measured SOA as described in Shrivastava et al., (2013). Non-volatile biogenic and anthropogenic secondary organic aerosols (BNVSOA, ANVSOA) are formed attributing a reaction constant corresponding to a 1h of lifetime (Cholakian et al., 2018). The total number of aerosol species formed from VOC species of anthropogenic (AVOC) and biogenic origin (BVOC) is 10 (5 for ASOA and 5 for BSOA). This VBS aerosol scheme contains therefore 40 species, which multiplied by 10 aerosol bins lead to 400 simulated species for the SOA. Note however that primary fire organic aerosol is not treated with the VBS scheme, but as chemical inert. Nucleation, coagulation, condensation and dry and wet deposition processes are also addressed within this aerosol module.

2.2 Datasets for model evaluation

Datasets to discuss the campaign period analysis and for model evaluation integrate ACROSS field campaign ground-based observations, satellite data, and larger-scale databases.

In situ surface observations of the aerosol refractory and non-refractory chemical composition in the PM1 fraction and boundary layer height (PBLH)were retrieved at the three ground-based sites of the ACROSS campaign:

(i) the Paris–Rive Gauche (PRG) (48.8277° N, 2.3806 °E; hereafter PRG), hosted at the Lamark building at Université Paris Cité, on the southeastern part of the Paris administrative borders, in dense urban environment; instruments are installed at the 7th floor of an University building.

(ii) the SIRTA (Site Instrumental de Recherche par Télédétection Atmosphérique, 48.7090° N, 2.1488° E), located around 20 km southwest of the Paris administrative borders, it is a sub–urban site due to its lower population density in an environment mixing forest, urban areas as well as agriculture fields and traffic roads (Bedoya-Velásquez et al., 2019; Zhang et al., 2019; Chahine et al., 2018; Haeffelin et al., 2005);

(iii) the Rambouillet forest supersite (48.6866° N, 1.7045° E; hereafter RambForest), located around 50 km southwest of the Paris administrative borders, in the middle of the Rambouillet national forest, a mixed deciduous and evergreen trees. Measurements have been performed at ground, within the forest canopy, but also from a 40 m high tower, above the canopy of about 25 m height.

Data from the three ACROSS measurement sites include:

- aerosol non–refractory composition (organic, nitrate, sulfate, ammonium, chloride) as measured by a Time–of–Flight Aerosol Chemical Speciation Monitor (TOF–ACSM, Aerodyne Research, (Fröhlich et al., 2013), 6−min resolution) at PRG and SIRTA and by a TOF Aerosol Mass Spectrometer (TOF–AMS, Aerodyne Research, (Drewnick et al., 2005), 3−min resolution) at RambForest (Di Biagio et al., 2024; Ferreira de Brito et al., 2023b, a). Uncertainty on the total non−refractory mass concentration from ACSM is evaluated to be around 25% (Budisulistiorini et al., 2014; Crenn et al., 2015); equivalent black carbon concentration (eBC) concentration from dual-spot aethalometer (AE33, Magee Sci., 1-min resolution) (Di Antonio et al., 2023c), treated applying a site-invariant multiple scattering coefficient C_{ref} of 2.45 (ACTRIS, 2023).
- elemental and organic carbon (EC, OC) concentration from PM_1 head thermo-optical analysis on filter samples collected over daytime (16h from 8h to 22h UTC) and night-time (from 22 h to 8h UTC) at PRG and RambForest following the EUSAAR-2 protocol (Cavalli et al., 2010). Organic matter was calculated assuming an OC-to-OM ratio of 1.8 (Sciare et al., 2011);
- refractory black carbon (rBC) concentration at RambForest from a single particle soot photometer (SP2, DMT, 1 minute resolution) (Yu and Formenti, 2023);
- mixing layer height (PBLH) at SIRTA from automatic low-power lidars and ceilometers (ALC, Vaisala CL31, 15 minutes resolution) (Kotthaus et al., 2023);
- PM_1, $PM_{2.5}$, and PM_{10} aerosol concentration and meteorology (temperature, pressure, RH) at PRG from FIDAS 200E at 1 Minute resolution (Di Antonio et al., 2023d).

Additionally, to point surface observations at the ACROSS sites, aerosol non-refractory composition and eBC hourly data from ACSM and AE33 measurements on the PM_1 fraction were retrieved over whole France from the GEOD'AIR (GEstion des données d'Observation de la qualité de l'AIR) database (https://www.geodair.fr/). Measurements from 9 sites were considered (Table S1). The AE33 eBC were treated assuming a C_{ref}=2.45. as recommended by the pan-European ACTRIS (Aerosol, Clouds and Trace Gases Research Infrastructure) programme.

Hourly surface level observations of $PM_{2.5}$, PM_{10}, NO_2, and O_3 across Europe from the European Environmental Agency (EEA) database (https://discomap.eea.europa.eu/map/fme/AirQualityExport.html, last access: 24 April 2024) were further considered to assess aerosol and ozone concentration.

Level 2 formaldehyde (HCHO) total column concentration (L2_HCHO) from TROPOspheric Monitoring Instrument (TROPOMI) (Veefkind et al., 2012) were used as a proxy of isoprene concentrations. The TROPOMI HCHO number density (molecules cm^{-2}) was bias-corrected using (Oomen et al., 2024) and converted to Dobson Unit (DU). We did not apply averaging kernels as in (Oomen et al., 2024), because we think that the bias correction already includes a large part of the lack of sensitivity of TROPOMI in the lower layers, and then its application would overcorrect the data. Original data provided with a maximum spatial resolution of 7x3.5 km^2 at near nadir were re-gridded to a common 0.5°x0.5° spatial resolution.

Finally, the Met Office Integrated Data Archive System (MIDAS) (Met Office, 2012)) was considered for surface hourly meteorological parameters (temperature, pressure, RH, wind direction and speed) used to validate the surface meteorology of the WRF-CHIMERE simulation.

3 Description of the meteorological situation and evaluation

3.1 Evolution of the meteorological situation during the ACROSS campaign - between heat waves and oceanic flux

Here we give a first overview of the different meteorological conditions during the ACROSS campaign period based on in situ meteorological and aerosol measurements at the urban background PRG site, and also at a broader scale from meteorological observations and analysis data over Western Europe.

Hourly temperature averages at the urban PRG site (Fig. 2b) allow a broad classification into three periods: (1) a first heatwave period from June 15 to 18 with daily temperature maxima (T_{max}) between nearly 30°C and more than 36 °C; (2) a second long-lasting colder period from June 19 to July 11 with T_{max} between 15 °C and 25 °C; (3) a second heatwave period from July 12 to 23 with a mixture of very hot, but also colder days, with T_{max} varying between 22 °C and 38 °C. Relative humidity is strongly anti-correlated with temperature and varies from as low as 20-30% during the hottest days to more than 90% during the nights of the colder days. EUMETSAT satellite pictures available at(https://www.wetterzentrale.de, last access 11 April 2024), show mainly clear sky conditions during June 15 to 18, mixed cloudy and clear sky conditions from June 19 to July 11, mainly clear sky conditions from July 12 to 18, and then again mixed conditions form July 19 to 23 over Ile-de-France.

During the two hottest days of the first heatwave on June 17 and 18, moderate winds from SE (Fig. 2c) are measured at the PRG site. This corresponds to a generally southerly advection of hot and dry air masses of Mediterranean and even Saharan origin linked to a cut-off low located west of the Iberian Peninsula and a ridge over France visible in the 500hPa geopotential map of June 18 12 UTC (Fig. 3a). Daily temperature maxima over France are mostly over 35 °C except for some mountainous areas and coastal areas, and in the SW of France even above 40°C (Fig. 3o). This southerly advection is also well depicted in the 850 hPa temperature map (not shown) making evident that the French heatwave area is well connected to the Saharian heat reservoir. Linked to this is long range transport of Saharian dust to Northern France visible

in a large contribution to coarse aerosol (up to 40 µgm^{-3}, PM_{10} minus $PM_{2.5}$ concentrations, Fig. 2a) at PRG on June 18 indicative of coarse dust aerosol.

During the following colder and cleaner period, wind speed varies evidencing different sub periods: a first one from June 19 to 22, with moderate north-easterly winds (1-3 ms^{-1}) coming from N to NE bringing continental air masses to PRG in addition to local pollution, resulting in still elevated $PM_{2.5}$ levels of 10 to 15 µgm^{-3} nearly comparable to those during the first heat wave period. Then, from June 23 to July 2, south-westerly and westerly winds bringing clean oceanic air masses to the PRG site and northern France. A typical 500 hPa geopotential field for this period (Fig. 3b) shows a trough of low pressure extending from Iceland to the British Islands and Benelux and a high over the Mediterranean, according to this westerly flow. Daily temperature maxima are in the 15-20 and 20 to 25°C ranges over France (Fig. 3p). A last period from July 3 to July 11, characterised again by mainly northerly and somewhat stronger winds (3 - 4 ms^{-1}) leading to still clean conditions ($PM_{2.5}$ at PRG from 3 -7 µgm^{-3}).

The second heatwave period from July 12 onwards shows again varying meteorological conditions, but it includes 4 hot to very hot days with T_{max} between 32 and 38 °C (Fig. 2b) and in general southerly winds of moderate speed (from 2 to 3 ms^{-1}, Fig. 2c). For the hottest day on July 19, the 12 UTC 500 hPa geopotential field shows a cut-off low west of Britanny and a pronounced ridge extending northwards up to southern Scandinavia (Fig. 3c). The 850 hPa maps show again a tongue of hot air over Western and central Europe related to the Saharian heat reservoir (not shown). This ridge system is moving eastwards, letting at its rear enter somewhat colder air masses into Southwestern France with T_{max} in the range of 25-35 °C, while T_{max} is in the range of 35-40 °C over eastern France (Fig. 3q). The southward winds are again linked to Saharan dust transport for July 13 and 19, indicated again by large coarse PM_{10} of about 50 µgm^{-3} at the PRG site (Fig. 2a). The large and dry conditions over Western France have induced strong forest fires there advected to the Paris region for several hours in the evening of July 19 and leading to enhanced $PM_{2.5}$ concentrations (> 60 µgm^{-3} at the PRG site).

3.2 Evaluation of the WRF-CHIMERE meteorology

In this section, we will address the WRF-CHIMERE model capacity to simulate major meteorological variables: the mean and maximum daily temperature, wind speed and direction and PBLH.

Maximum daily temperature at 2m height (T_{max}) is in general well simulated, biases during the period are for most of the sites below ±1 °C, and this both for the whole campaign period and the three previously identified meteorological periods (Fig. 4, a-d). Larger biases exceeding ±2 °C are encountered for mountainous areas along an axis from the eastern Pyrenees to the Alps, passing by the Massif Central, and the French Jura. For the average of all sites, the mean bias error (MBE) for the whole period is -0.53 °C, it is slightly larger for the first and second heatwave periods (-0.70 °C and -0.64 °C, Fig. S1). Average correlation over the whole period and all sites in 0.93 (Fig. S2). Daily maximum temperatures are especially well restituted for the high temperature periods, as can be seen for the 90% percentiles in figure S4. For the mean daily temperature differences between simulations and observations are in general smaller than those for Tmax (MBE=-0.34 °C, Fig. S1e).

For wind speed, a slight overestimation is generally observed for the ensemble of sites, biases are most often within the ±1 ms^{-1} range for the different periods (Fig1, i-l). On the contrary, for Ile-de-France, a slight underestimation up to about -0.5 ms^{-1} is noted for most of the sites. On the average of all sites in the model domain, a positive bias of +0.3 ms^{-1} is observed when compared to the MIDAS sites (Figure S4,m). This overestimation is more pronounced for light wind days.

For both wind speed and direction the correlation is above 0.9 (Fig. S3). The wind direction is better simulated over flat terrain as in the Ile-de-France region with average deviations below only ±20 ° (RMSE), while for the whole model domain deviations above 50 ° are often identified (Fig. S4).

The observed daily evolution of the PBLH at the sub-urban SIRTA site is well simulated, showing a maximum in the early afternoon, and a long period of minimum values during night (Fig. 5a). Correlations of hourly values are respectively 0.77, 0.92 and 0.88 for three periods (Fig. 5, b-d). Daily maxima are well reproduced (±200 m) for a majority of days, but for about a third of cases the simulated PBLH is underestimated by more than 200 m and for two cases by more than a km. Indeed, for two amongst the hottest days with T_{max} higher than 33°C (June 18 and July 13), the observed PBLH heights nearly reach 3 km, while simulated values are only 1600 and 1900 m respectively. Reasons for this difference still need to be explored. During night time, a systematic model underestimation of PBLH occurs. While observed values are rarely below 200 m, simulated ones often are as low as 20 m, the lower limit in simulations. Average over both day and night leads to a mean bias of -281, -209, and -180 m for the three periods.

4 Analysis and WRF-CHIMERE model evaluation for major pollutants during the ACROSS campaign

4.1 Analysis of regulated pollutants at the French scale

The broad features of the evolution of major pollutants, ozone, NO_x, $PM_{2.5}$ and PM_{10}, at regional scale over France during the campaign period are presented in this section. We rely in this analysis on observations from French air quality networks (in particular on site having background features), for the examples of typical or significant days during the three periods (Fig. 3). First we analyse the spatio-temporal evolution of the daily ozone maximum (O_{3max}) as a tracer of photo-chemical activity in three periods (Fig. 3, d-f). As expected, O_{3max} is much larger during the heatwave days than during the clean period. On June 18, the day with the largest O_{3max} values during the first heatwave period, daily ozone maxima are in the range of 108-144 μgm^{-3} for Western and Central France including the Ile-de-France region. They are in the 144-180 μgm^{-3} range in South-Eastern France, where some sites exceed the French pollution information threshold of 180 μgm^{-3}. Apparently, this heat wave period does not correspond to a major ozone pollution episode in Ile-de-France and the northern half of France, despite hot temperatures, and low winds. For the example of Ile-de-France, HYSPLIT backward trajectories calculated with GFAS meteorology (arriving at 12 UTC at Paris center, 500 m height, Fig. S2a) show that air masses had turned anti-cyclonically and clockwise around the Ile-de-France region, and that some of them originated over the Morocco three days before. They indicate that air masses have mainly stayed over relatively low emission regions over rural France and south of England the last two days, which may explain the relatively moderate ozone peaks.

During the following intermediate clean period air masses are of oceanic origin, daily ozone maxima are below 108 or even below 72 μgm^{-3} on July 1. During the second heatwave, on July 19, daily O_3 maxima show a pronounced SW - NE gradient. In northern France including Ile-de-France and in South-Eastern France values are in the 144-180 μgm^{-3} range, while they are below 108 μgm^{-3} along the SW French coastline (Fig. 3e). This pattern, in good spatial correlation with the T_{max} field for this day (Fig. 3f). Indeed, the ozone heat pools are moving eastwards, letting on their rear enter clean oceanic air masses into SW France.

For particulate matter ($PM_{2.5}$ in Fig. 3g-i, PM_{10} in Fig. 3, l-n), concentrations are again larger during heatwave periods. On June 18, daily average PM_{10} concentrations show a pronounced E-W gradient, with values in the eastern part of the country mostly in the 20 -30 μgm^{-3} range, while they reach NW 30-40 μgm^{-3} in NW and 40-50 μgm^{-3} in SW France.

These latter elevated values are very probably due to dust transport from Sahara, made evident as enhanced AOD for this day over SW France and the Mediterranean region (Fig. S2c), and are concomitant to heat advection from the same region. As already noticed, PM_{10} peaks are also observed at the PRG urban site during the afternoon of June 18 (Fig. 3a). HYSPLIT back trajectories for this day starting at 2 km height show air masses originate over Morocco three days before (Fig. S2b). The PM E-W gradient is still visible for $PM_{2.5}$, daily average concentrations being in the range of 0-14 μgm^{-3} for most of the sites in Eastern France, while in the range of 14-21 μgm^{-3} for many sites in the western part, and even in the 21-28 μgm^{-3} range for some sites in the Ile-de-France region.

During the intermediate, clean period (July 1st), the $PM_{2.5}$ daily averages are below 14 μgm^{-3}, and the PM_{10} below 20 μgm^{-3}. During the second heat wave, the largest $PM_{2.5}$ daily averages above 35 μgm^{-3} occur at several sites in SW France values, due to the large fire activity in this region, related to repeated dry and hot weather conditions. They are still enhanced in Ile-de France and NW of France, in the 14 - 21 and 21 - 28 μgm^{-3} ranges, probably partly related to fire plume transport to these regions (see discussion in Sect. 5.2). PM_{10} daily averages show large values at the same sites in SW France (PM_{10} higher than 30 μgm^{-3}), probably again due to long range dust transport.

4.2 Model evaluation for major pollutants at French scale

We evaluate how the WRF-CHIMERE model simulations, here with their 6 km horizontal resolution, are able to reproduce the absolute concentrations of ozone, NO_2, $PM_{2.5}$ and PM_{10} and their spatio-temporal variability.

A statistical analysis over the whole campaign period shows that the daily maximum ozone concentrations are reasonably well simulated by the WRF-CHIMERE model, which is able to represent its spatial and temporal variability. For most of the French sites, negative O_3 biases fall in the 0-5 μgm^{-3} range, being larger during the first heat wave and within Ile-de-France where they can reach up to 20 μgm^{-3} (Fig. 6, a-d). They are also larger in mountain regions. On the average of all sites, ozone shows an average MBE (mean bias error of -3 μgm^{-3} corresponding to a NMB (normalized mean bias) of -4% (Fig. S5a). This figure shows that the agreement is rather homogeneous for the different percentiles of ozone concentrations. Taken all the sites and daily ozone maxima together, spatio-temporal correlation is 0.84 (Fig. 6a), with relatively little spatial heterogeneity (Fig. S1a).

For NO_2 daily means; average biases are between -5 to +5 μgm^{-3}, negative biases are prevailing in the Ile-de-France region (Figure 6i-h), may be due to the fact that urban features are not well enough resolved in the simulation with a 6 km resolution used here for model evaluation over France. Mean bias over all sites is -0.8 μgm^3 (Fig. S5e), mean NMB is -6%, and correlation is 0.51, but with a strong spatial inhomogeneity. As a matter of fact, sites in the alpine regions in SE France or over the Massif Central mountains in Central France show close to zero or even negative correlations, indicating that the WRF-CHIMERE model does not capture NO_2 variability for sites affected by orography.

For PM_{10}, biases in average concentrations during the campaign are similar for most of the sites and close to zero or slightly negative (down to -5 µgm3) (Fig. 6o). The mean negative bias (MBE) is -1.3 μgm^{-3}, which corresponds to -8% (NMB) (Fig. S5o). The negative bias (NMB) is larger during the clean air period, -17%, while it is only -5% and +2% during heat wave 1 and 2 (Fig. S5, p-r). The fraction of comparisons with less than a factor of two difference is always large, generally above 90%. Correlation is large (R=0.8), with a rather homogeneous distribution among sites (0.6-0.9).

Differently, the $PM_{2.5}$ fraction is overestimated in WRF-CHIMERE simulations. For most of the sites, this overestimation falls in the 0-5 μgm^{-3} range on average of the whole campaign (Fig. 6i), it is even larger during the first heatwave and in the Ile-de-France region (5-10 μgm^{-3}, Fig. 5l). The mean average positive bias is 6.0 μgm^{-3} (MBE), which corresponds to

an NMB of +73% (Fig. S5l). Average temporal correlation is as large as 0.84, with a rather homogeneous distribution among sites (0.7-0.95), thus WRF-CHIMERE is able to reproduce the spatio-temporal $PM_{2.5}$ variability, despite this overestimation. Due to the slight underestimation of PM_{10} and the pronounced overestimation of $PM_{2.5}$, an underestimation of coarse PM (PM_{10} - $PM_{2.5}$) is deduced, even if an explicit comparison was not performed. As a conclusion while WRF-CHIMERE reproduces PM_{10} in a satisfying manner, the finer $PM_{2.5}$ fraction shows a pronounced positive bias, which will be investigated in more detail in Sect. 4.4 and 4.5.

4.3 Evaluation of HCHO fields as constraint of isoprene emissions and photochemical activity

The VOC compounds of anthropogenic and biogenic origin are important precursors both for ozone and secondary organic aerosol. For the current work, in-situ VOC measurements obtained during the ACROSS campaign are not yet available. As an alternative, we analyse here satellite observations of formaldehyde columns obtained by the TROPOMI instrument to corresponding simulations. Formaldehyde is an intermediate oxidation product of many VOC's, but in the presence of strong enough isoprene emissions it is a good tracer of these emissions and has been used in inverse modelling (Dufour et al., 2009; Millet et al., 2008; Oomen et al., 2024). The comparison between daily simulated and observed HCHO columns over France (Fig. 7) shows an overall positive bias of 35% (28 – 48% for the different periods), correlation is 0.63, 74% of the simulations lie in between a factor of two of observations. Overestimations are very strong for very small values, but which are less sensitive to isoprene emissions and thus not investigated further. On the contrary, for the large HCHO columns, the overestimations are reduced. Therefore, isoprene emissions are suspected to be overestimated by a factor of about 1.35 in our simulations, which would then affect BSOA formed from during isoprene oxidation. However, if we applied the averaging kernels as in (Oomen et al., 2024), we can anticipate that we probably would find a negative bias in HCHO columns which would correspond to an isoprene emission underestimation. Because of this, and as in situ measurements for isoprene and terpenes are not yet available, we cannot conclude on a possible bias in BVOC emissions or concentrations and on their impact on BSOA formation.

4.4 Analysis and model evaluation of aerosol chemical composition at the French scale

In order to get more insight on the $PM_{2.5}$ fraction, we next analyse the aerosol chemical composition. This analysis is based on ACSM and aethalometer measurements at an approximate PM_1 cut-off made within the French Geod'air network (see Table S1). Visual inspection of Figure 8 shows an overall broad agreement in the simulated and observed chemical composition. For most of the sites, the organic fraction makes up 60 -70% of the PM_1 mass, followed by sulfate (15-25%), and nitrate, ammonia and black carbon (less than 10 % with the exception of nitrate for one site).

Statistical evaluation presented in Figure 9 shows systematic overestimations of the organic fraction of +21% (always in terms of NMB), of +16% for sulfate, + 37% for ammonium, +53% for nitrate, but only 7% for BC. For nitrate, the overestimation is most striking, a fraction of simulations shows nitrate concentrations in the 10 μgm^{-3} range, as compared to observations of only a few μgm^{-3}. Reasons for this behaviour need to be further investigated. These overestimations are modulated by meteorological conditions. They are stronger for the organic fraction during heat waves, and especially larger for enhanced concentrations, probably triggering excessive production of biogenic SOA (BSOA). On the contrary, they are stronger during the clean period for secondary inorganic aerosol (Fig. 9). Correlation is about 0.4 for all species except organic aerosol (R = 0.61). All in all, this analysis of different PM1 species is coherent with the previously made evident $PM_{2.5}$ overestimation, although the extent of overestimation is smaller. Thus, other aerosol species than those analysed here (non-refractory species and BC) are probably overestimated to an even stronger extent such as dust or

primary mineral particles. Unfortunately, no measurements for these species were available to us during the campaign period.

4.5 Analysis and model evaluation of aerosol chemical composition at the ACROSS sites in the greater Paris area

The ACSM and AMS derived PM_1 refractive aerosol chemical composition measurements for the PRG (Fig.S6), the SIRTA (Fig.S7), and the RambForest sites (Fig.S8) and the corresponding simulations at 2 km horizontal resolution, show many similarities: organic aerosol is by far the most abundant species class, its variability with enhanced concentrations during the two heat wave periods from June 15 to 18 and from July 12 to 23 drives the PM_1 variability. For most days, sulfate is the second most abundant species, while strong nitrate peaks appear on specific days.

Contrary to the French Geod'air sites, for the three ACROSS sites, organic aerosol is not anymore systematically overestimated by simulations (Fig. 10). Reasons for this behaviour are not clear and need further to be investigated. For the whole set of available measurements, relative biases (in terms of NMB) are -20% for PRG, -3% for SIRTA and +21% for Rambouillet (Tables 2 S2, S3 and S4). From Figure 11 and Figures S6-8, a tendency for overestimations for PM_1 chemical species is noted during heatwave periods, while during the clean period, relative biases are in general negative. For instance, for SIRTA, the NMB is +23% and +9% for the first and second heatwaves, while it is -25% for the clean period (Table S3). Similar tendencies are observed for the other two sites (Tables S2 and S4). Stronger positive biases during the heatwave periods have already been noted in the previous section for the GEODAIR data set.

Several strong simulated organic aerosol peaks are not observed or present in observations only to a lesser extent. For example, strong OA peaks in the morning hours of June 18 of more than 40 μgm^{-3} are simulated at Rambouillet and SIRTA, and nearly 30 $\mu\ gm^{-3}$ at PRG. The observed peak is only up to 25 μgm^{-3} at Rambouillet, while observations are missing at SIRTA, and concentrations are about 15 μgm^{-3} at PRG with a rather flat diurnal variation. These enhanced values are due to the advection of a plume of large BSOA concentrations originating at several forested areas south Ile-de-France as will be discussed in section 5.1. A strong and again sharp OA peak is simulated during the morning hours of July 13 only at the PRG site and not observed there. This overestimation is probably due to an underestimation of the simulated night-time and morning boundary layer height (below about 50 m, while several hundred meters are observed, Fig. 5). Finally, two OA peaks of between 30 and 40 μgm^{-3} are simulated at the three sites in the afternoon and night of July 19. While the first peak is not observed, the second one is and probably corresponds to the fire plume advected from the Aquitaine region in SW France. This event will be further described in Section 5.2. Despite these occasional failures, correlation between simulated and observed hourly concentrations, put at the three sites is rather large (R between 0.62 and 0.77, Table 2).

These comparisons are corroborated by the comparison with filter samples at PRG and Rambouillet sites (Figure 11). NMB with respect to simulations are between -5% and +1% for PRG and Rambouillet (under the hypothesis of a OM-to-OC ratio of 1.8 (Sciare et al., 2011)). Correlations (R) are large (0.74-0.83), indicating the averaging of 8 – 16 h facilitate the following of the time evolution, in particular a strong decrease in OM from more than 10 μgm^{-3} to about 5 μgm^{-3} in the afternoon of July 18 at the end of heatwave 1 and a peak of 15 - 20 μgm^{-3} during daytime July 19.

Also for secondary inorganic aerosol species, biases are much smaller for the three campaign sites than for French Geod'air sites. For sulfate, NMB values are -1% for PRG, -12% for SIRTA, and + 37 % for Rambouillet (Table 2). Especially during the first heat wave, simulated sulfate is more strongly underestimated than during the clean period (Fig. 10). For SIRTA, NMB is -63% and -16% for the first and second heatwaves, while it is only -11% for the clean period (Table S3). Similar tendencies are observed for the other two sites (Tables S2 and S4). These heatwave versus clean period differences are again in agreement with the comparison with the Geod'air sites in section 4.4. Again, as already made evident for the comparison with measurements from the Geod'air sites, nitrate is significantly overestimated at the three sites PRG, SIRTA and Rambouillet, with NMB of +15, +21 and +148% respectively. For nitrate this large relative bias corresponds to a small absolute one of +0.24 μgm^{-3}. A nitrate peak of about 15 μgm^{-3} is simulated in the morning of June 16 for the three sites, and observed to some extent (5 µgm-3) at PRG, the only site with available measurements at this time. It is due to advection of continental nitrate to the region under northerly wind conditions.

BC simulations are again evaluated against filter measurements (Figure 11). They show a general overestimation in terms of NMB, of +27 % at PRG and +66% at Rambouillet (Table 3), where for the latter absolute concentrations are very small (average eBC of 0.14 μgm^{-3}). Simulated concentrations at PRG larger than 1 µgm-3 are in general not observed. For PRG, this might be linked to the fact that this site is located on the 7th floor of a University building, and then could be less sensitive to primary emissions than the first model layer extending to 20 m above ground level. Simulated and observed eBC concentrations are much lower at Rambouillet, mostly below 0.4 μgm^{-3}. The largest simulated eBC peak of 0.6 μgm^{-3} during the night of July 11 to 12 is not observed. It is according to the BC origin product (Di Antonio et al., 2023a) partly due to advection from the Paris agglomeration. However, winds during this night are changing their direction (Fig. 2) and this attribution is then uncertain.

In summary, simulation to observation comparisons of particulate matter speciation are mostly satisfying with acceptable biases for all of the species below ±20% except for nitrate in terms of NMB. A good capacity to simulate the overall broad variability between different meteorological periods is observed, while individual peaks lasting several hours are often not simulated.

5. Case study illustration

In this section, we intend to illustrate with two examples, how the WRF-CHIMERE model is able to reproduce and disentangle complex advection and chemical formation patterns of organic aerosol, and in this way contributes in explaining the spatio-temporal variability encountered at the campaign measurement sites.

5.1 Regional BSOA formation and advection during the first heatwave

The first case is the night of June 17 to 18 during the first heatwave period, when strong OA peaks are simulated and observed. Figure 12 shows strong BSOA build-up over forested areas within and around the Ile-de-France region during the first part of the night starting between 18 and 20 UTC and continuing until June 18 at 2 UTC. These forested areas are the Sologne region (labelled S in Fig. 12) 130 km south of Paris, the Fontainebleau forest (F) 60 km in SSE of Paris, the Rambouillet forest (R) 40 km in the SWW, and the Chantilly forest (C) 50 km in the NNE. For example, at the Rambouillet forest, BSOA concentrations rise by about 20 μgm^{-3} between 18 and 22 UTC corresponding to an increase rate of 5 μgm^{-3} per hour. As no advection to this site is visible in Figure 13 during these hours, we interpret this as a BSOA formation rate at first order. This leads to a simulated OA peak at the Rambouillet site of about 40 μgm^{-3} which is

observed, although to a lesser extent (Fig. 10c). The BSOA formation is probably initiated more by O_3 than by NO_3, because simulated NO_3 levels are very low (about 0.5 ppt, not shown). However, analysis of the precise BSOA formation pathways is out of the scope of this paper, and would require taking into account initial oxidation of all BSOA precursor species, and their further oxidation.

During the following hours, south-easterly winds advect BSOA rich air masses from source regions north-eastwards, so that they diminish at Rambouillet from 2 UTC onwards (Fig. 12). The BSOA rich area originating at Sologne is advected to west of the Rambouillet site (and thus not measured during the campaign). The one originating at Fontainebleau forest is advected to the SIRTA and PRG sites. According to our simulations and Figure 12, it hits the SIRTA site at midnight, and the maximum BSOA levels of about 30 μgm^{-3} occur at 2 UTC (Fig.10b). Unfortunately, no ACSM measurements were available at SIRTA during this night. The SIRTA site being located at the edge of the Paris agglomeration, simulated NO_3 concentrations are more important there and northwards of it (about 2.0 ppt, not shown) allowing probably for additional terpene oxidation and BSOA formation. Concerning the PRG site, Figure 13 shows its localization at the eastern edge of the simulated BSOA plume. A small spatial mismatch in the simulation could then explain why the plume is simulated but not observed at PRG (only enhanced OA concentrations of about 15 μgm^{-3}, but no peak, Fig.10a).

As a conclusion major OA peaks simulated and partly observed at the campaign sites during the night of June 17 to 18 can be traced back to night-time BSOA build-up above forested areas within and south of Ile-de-France and to further advection of these BSOA rich air masses to the campaign sites.

5.2 Fire advection episode on the greater Paris area

The second case concerns the evening of July 19, during the second heatwave. For this evening, large OA concentrations around 15 μgm^{-3} were measured at the three campaign sites (Fig. S6, S7, S8). The WRF-CHIMERE simulation shows that these peaks are due to advection of both fire primary organic aerosol and BSOA from south-western France (Aquitaine region) to northern France (Fig. 13 and 14). The exceptionally hot and dry conditions during summer 2022 triggered large fire activity especially in the Landes forest in SW France leading to important forest destruction and very high local $PM_{2.5}$ concentrations (Menut et al., 2023). As stated before, in our simulation, aerosol fire emissions are taken as chemically inert, so they are by definition primary. Several VOC species are co-emitted with fires and, in our simulation, notable reactive α-pinene. These fires related BVOC emissions are locally much stronger than those form the surrounding Landes forest, but the latter occur over a much larger area in our simulation. As a result, strong BSOA formation occurs both due to fire and forest BVOC precursors. During June 19, this combined fire POA and BSOA plume moves more and more eastward (Fig S9), passing over the campaign sites in the evening, and hitting first the Rambouillet (19 UTC) and then the SIRTA and PRG (20 UTC). The model predicts for the maximum plume OA encountered during these hours that about two-thirds (~20 μgm^{-3}) are BSOA (both from fire and forest BVOC) and about one-third is due to primary fire POA (~10 μgm^{-3}). As a conclusion, regional advection from several hundred km upwind from strong (BSOA, fire) and exceptional (fire) sources can exceptionally affect the OA budget over the Ile-de France region and can be simulated with the WRF-CHIMERE model.

6 Conclusions and perspectives

In this paper, we used the available measurements from the ACROSS campaign in addition to observations from air quality and meteorological networks and satellites for a first evaluation of the coupled WRF-CHIMERE model simulation over the ACROSS campaign in June-July 2022 in the Ile-de-France region and France. This is a first requisite for using

the model system for further campaign analysis, as for example to disentangle chemical production/loss and transport processes. The paper also gives an overview over meteorological conditions over the campaign period and related major pollution (PM, ozone) variability over France and at the campaign sites.

From daily maximum temperature time series and pollutant fields at the Paris urban site, we classified the campaign period into three classes. A first heatwave period from June 15 to June 18 with daily temperature maxima (T_{max}) between nearly 30 °C and more than 36 °C. These elevated temperatures are partly due to heat advection from the Saharian heat reservoir (not shown). During this heatwave, connected also to dust transport, and enhanced PM_{10} levels over Western France for June 18. For the second heatwave period from July 12 to 23 with a mixture of very hot, but also colder days, T_{max} varying between 22 °C and 38 °C, southerly advection to the Ile-de-France region was again enhanced. During both heat waves, increased biogenic VOC emissions led to strong BSOA and also ozone build-up. For the intermediate period, between June 19 and July 11, ozone and PM levels were much lower, air mass origins more oceanic, and sometimes also partly continental.

Analysis from the present work shows that the WRF model is able to satisfactorily simulate key meteorological variables and to follow the meteorological variability during the campaign, and in particular the two heat waves towards the beginning and the end of the campaign. Maximum daily temperature is in general simulated within ± 1°C, while PBLH is generally underestimated by about 200 m. The adequate simulation of temperature is important as this parameter is a general indicator for the model ability to catch the meteorological conditions, and as in particular it governs among others the intensity of biogenic VOC emissions in the MEGAN module.

Also high and low wind periods and evolution of wind direction are reasonably well simulated (within ±1 ms^{-1}), in particular for the Ile-de-France region. This lends confidence in the simulation of different transport regimes during the campaign period, including simulation of the direction of the pollution plume originating in the Paris region. The WRF-CHIMERE model system generally well produces daily ozone maxima, with negative biases between -5 and 0 μgm^{-3} for the air quality network sites and some larger, unexplained under predictions up to -20 μgm^{-3} during the first heatwave especially in the Ile-de-France area.

While for PM_{10} the mean bias is slightly negative for the average of sites in the model domain (-1.3 μgm^{-3} or -8%), it is strongly positive for $PM_{2.5}$ (+6.0 μgm^{-3} or +73%). This overestimation was unexpected, and could be related to the specific hot summer conditions, for which the model is less well characterised. All major refractive aerosol species are concerned by this overestimation (at PM1 size), all though at lower level than for PM2.5: +21% for organic aerosol, +16% for sulfate, + 37% for ammonium, +53% for nitrate, but only +7% for BC. For OA, the biases are larger for the two heatwave periods (+49% and +38%), while slightly negative (-8%) during the clean period. So there is a possible bias in OA sensitivity to temperature, which could be related to a corresponding bias in biogenic VOC emissions, or within the VBS organic aerosol scheme. On the contrary, for the three sites in Ile-de-France, model overestimations are less systematic. Biases are -20% to +21% for OA, -12% to +37% for sulfate, +1% to 89% for ammonium, +15% to +148% for nitrate and +27% to 66% for eBC. The large positive biases are obtained for the Rambouillet site, where concentrations are very small (for example 0.38 μgm^{-3} for ammonium, 0.16 μgm^{-3} for nitrate and 0.14 μgm^{-3} for BC).

We perform here a first model based analysis for the two major heatwave days June 18 and July 19: major OA peaks simulated and partly observed at the campaign sites during the night of June 17 to 18 can be traced back to night-time BSOA build-up above forested areas within and south of Ile-de-France and to further advection of these BSOA rich air

masses to the campaign sites. For July 19, we make evident regional advection of both BSOA and the biomass burning aerosol from the Aquitaine region in SW France.

As short term perspectives, further evaluation of the WRF-CHIMERE model system is necessary, and will be performed continuously as new campaign data will become available. Especially for biogenic VOC, such data will help in evaluating biogenic VOC and especially terpene emissions for different meteorological conditions. Radical measurements (OH, NO_3) will be used to evaluate the model's oxidant capacity. For example, this will enable studies affecting organic aerosol formation to different pathways, i.e. distinguishing precursors and oxidants, and so to elucidate the interplay between anthropogenic and biogenic sources. Another line of future work is dealing with using the WRF-CHIMERE system to estimate the aerosol effect on the radiative budget and the role of anthropogenic / biogenic mixing. This requires correct, or at least evaluated, simulation of aerosol chemical composition, which is done here, and as further steps, evaluation of the aerosol size distribution and of its bulk and species-wise spectral optical properties, which will be the subject of future work.

Data availability.

Datasets used in the present study from the ACROSS field campaign for the PRG and RambForest sites are available or will be made soon available on the AERIS datacenter (https://across.aeris−data.fr/catalogue/) and DOI referenced. Some datasets already available are: the PM_1, $PM_{2.5}$ and PM_{10} (Di Antonio et al., 2023d); the equivalent black carbon at the PRG site (Di Antonio et al., 2023c); the black carbon Paris-to-regional ratio (Di Antonio et al., 2023a); the non-refractory black carbon concentration at the Rambouillet site (Yu and Formenti, 2023); the non-refractory aerosol composition below and above the canopy at the Rambouilet site (Ferreira de Brito et al., 2023b, a); the mixing layer height at SIRTA (Kotthaus et al., 2023).
The SIRTA observatory data can be downloaded at https://sirta.ipsl.fr/ (last access: 7 April 2024).
The GEOD'AIR data are available at https://www.geodair.fr/ (last access: 7 April 2024). EEA data are available at https://discomap.eea.europa.eu/map/fme/AirQualityExport.html (last access: 24 April 2024). The MIDAS (Met Office, 2012) data are available at https://catalogue.ceda.ac.uk/uuid/220a65615218d5c9cc9e4785a3234bd0 (last access: 7 April 2024). TROPOMI data are available at the Copernicus Open Access Hub https://scihub.copernicus.eu/.

Author contributions.

LDA and MB designed the study and discussed the results. LDA performed the full data analysis. MB and CDB supervised all the analysis work. VM and CC designed the ACROSS field campaign. LDA run the model simulations with contribution from GS and MB. LDA, VM, CC, MC, AB, ABe, SC, MCi, JFB, PF, CG, OG, AG, VG, MH, LH, SK, GN, DP, JEP, VR, CY, JFD, and CDB contributed to the campaign set-up, deployment, calibration and operation of the instrumentation, and the data collection from the PRG, SIRTA and RambForest sites. LDA, MB, and CDB wrote the paper with contributions from all co-authors.

Competing interests.

One of the co-authors is a co-organizer of the editorial board of the Special Issue “Atmospheric Chemistry of the Suburban Forest – multiplatform observational campaign of the chemistry and physics of mixed urban and biogenic emissions”. The authors have no other competing interests to declare.

Acknowledgments.

This work has been supported by the ACROSS and the RI-URBANS projects. The ACROSS project has received funding from the French National Research Agency (ANR) under the investment program integrated into France 2030, with the reference ANR-17-MPGA-0002, and it was supported by the French National program LEFE (Les Enveloppes Fluides et l’Environnement) of the CNRS/INSU (Centre National de la Recherche Scientifique/Institut National des Sciences de L’Univers). The RI-URBANS project has received funding from the European Union’s Horizon 2020 research and innovation program under grant agreement no. 101036245. The EEA is acknowledged for the air quality data for the stations which were used for the simulation validation. The NCEP is acknowledged for the meteorological input data used in the WRF meteorological model. The GEOD’AIR database is acknowledged for the aerosol composition data used to validate the model simulation. We thank S. Alage, E. AlMarj, T. Bertin, P. Coll, A. Feron, M. Feingesicht, O. Guillemant, S. Harb, J. Heuser, B. Language, O. Lauret, C. Macias, F. Maisonneuve, B. Piquet-Varrault, R. Torres, P Zapf, A. Albinet, J. Allan, M. Cayet, M. Des Forges, D. De Haan, X. Dignum, O. Favez, D. Pronovost, S. Riley, A. Rose, X. Roundtree, and M. Stepanovic for contribution to the ACROSS field campaign deployment and filter sampling.

Special issue statement.

This article is part of the special issue “Atmospheric Chemistry of the Suburban Forest – multiplatform observational campaign of the chemistry and physics of mixed urban and biogenic emissions”. It is not associated with a conference.

Figures

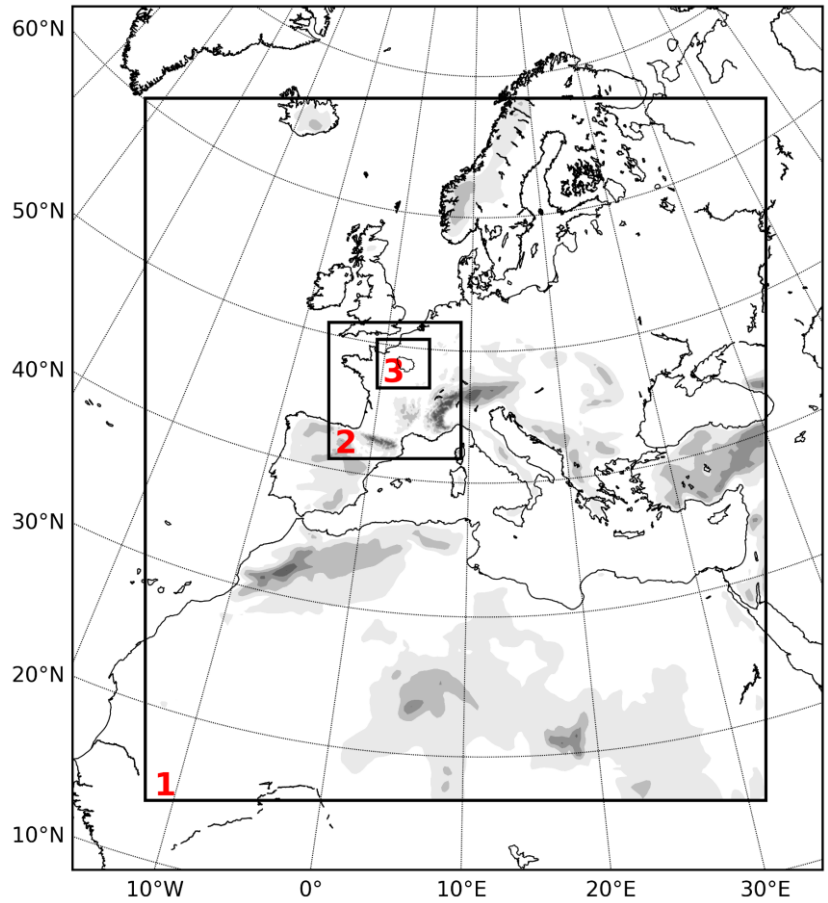

Figure 1: The three nested domains configured for the WRF-CHIMERE simulation of the ACROSS campaign 2022. The first domain (1) is at 30x30 km spatial resolution, the second (2) at 6x6 km spatial resolution, and the third (3) at 2x2 km spatial resolution covering an area centered over the Ile-de-France region. The boundaries of the Ile-de-France region are drawn in black within domain 3. The digital elevation model from the WRF output is shown in grayscale.

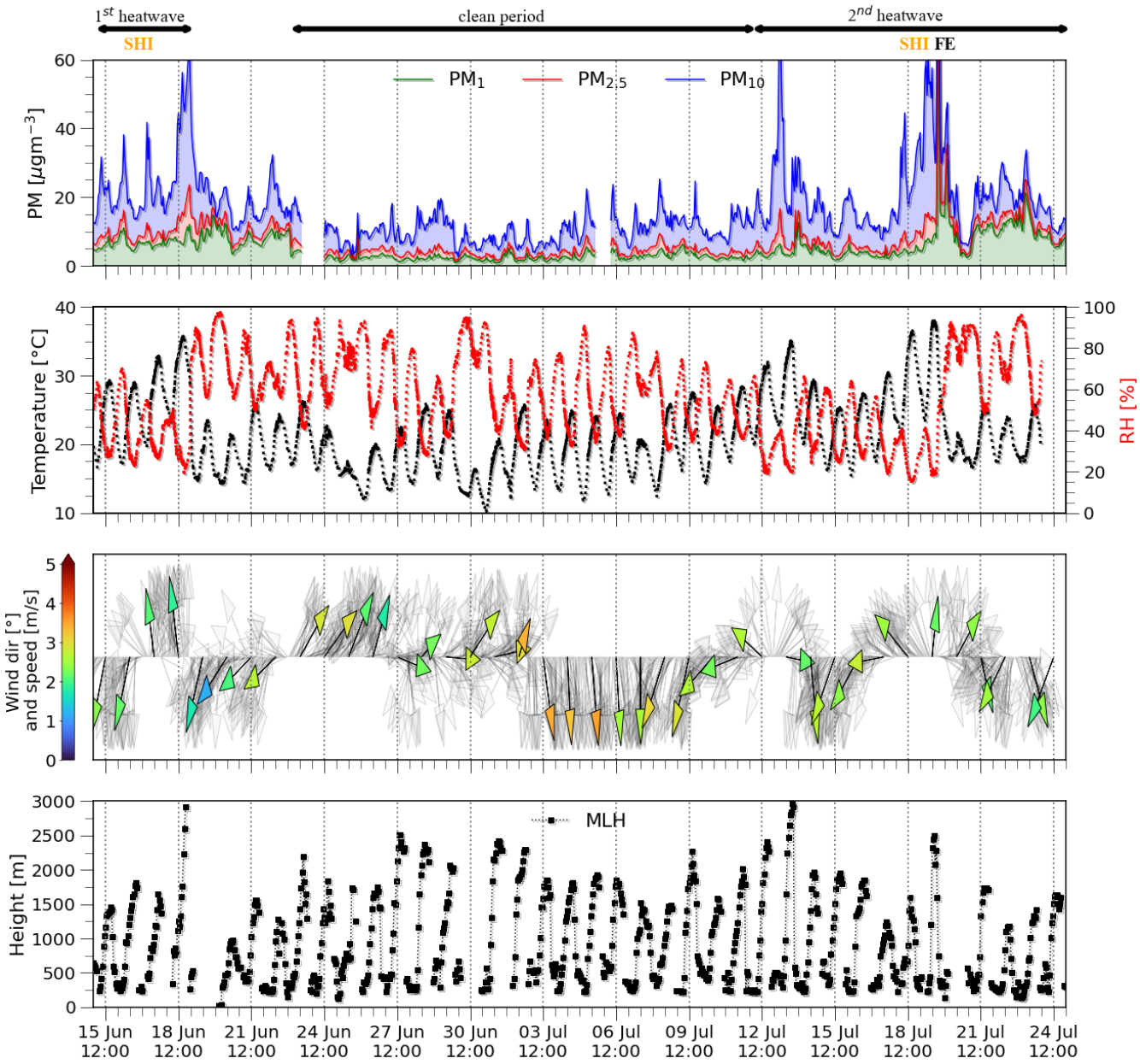

Figure 2: Temporal variation of observations during the ACROSS campaign for a) particulate matter concentration (PM_1, $PM_{2.5}$, PM_{10}) at the Paris-Rive Gauche (PRG) urban background site, b) temperature and relative humidity at the SIRTA site, c) wind speed and direction at the SIRTA site, d) mixing layer height (PBLH) from (Kotthaus et al., 2023), during the ACROSS campaign 2022. SHI stands for "Saharan dust intrusion", while "FE" stands for "Fire episode". The arrows represent daily average winds.

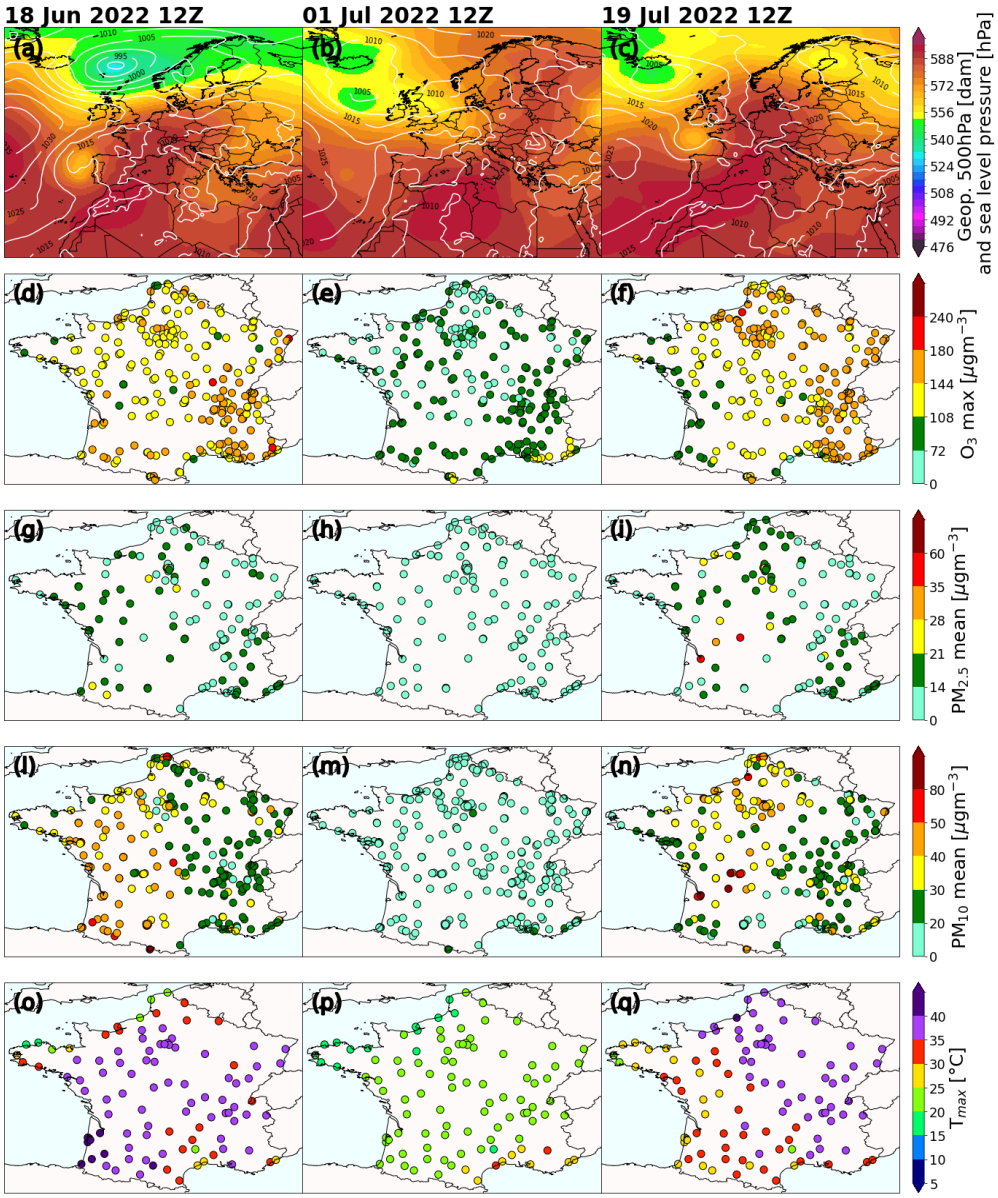

Figure 3: Several meteorological variables and major pollutant concentrations at 12 UTC for (left column) 18 June, (middle columns) 1 July and (right column) 19 July 2022 representative of the three main periods registered during the ACROSS campaign. Panels (a)-(c) represent geopotential height and surface pressure from the ERA5 reanalysis (Hersbach et al., 2023b, a) Panels (d)-(f) represent the daily maximum O_3, panels (g)-(i) represent the daily mean $PM_{2.5}$, panels (l)-(n) represent the daily mean PM_{10} and panels (o)-(q) the daily maximum temperature. The O_3, $PM_{2.5}$, and PM_{10} data are from the EEA database, while temperature data are from the MIDAS database.

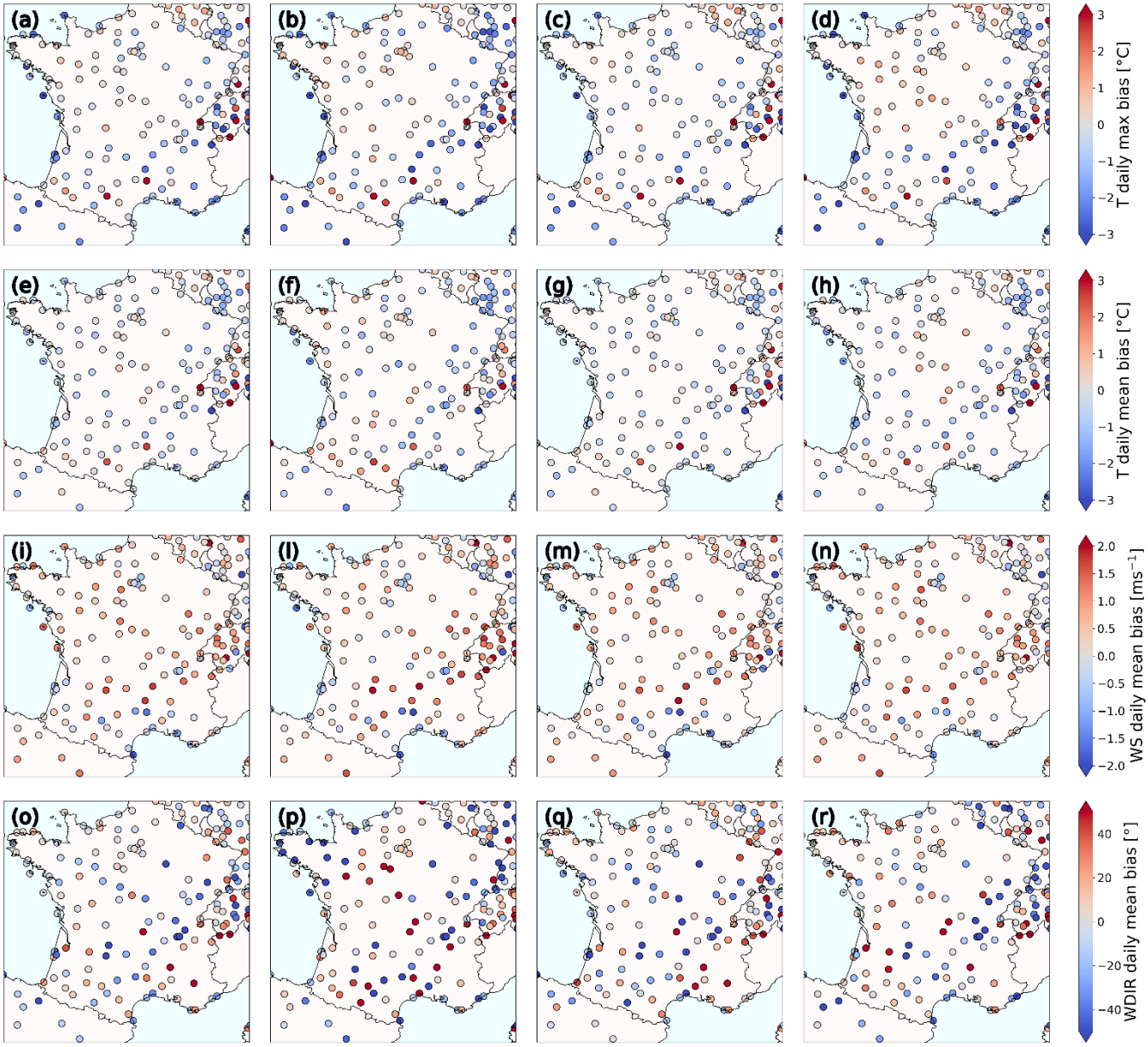

Figure 4: Daily bias obtained by comparing model output to observations from the MIDAS database, respectively for (left column) the full period, (middle left column) the first heatwave, (middle right column) the clean period and (right column) the second heatwave for the (a)-(d) max temperature, (e) - (h) mean temperature, (i)-(n) wind speed and (o)-(r) wind direction.

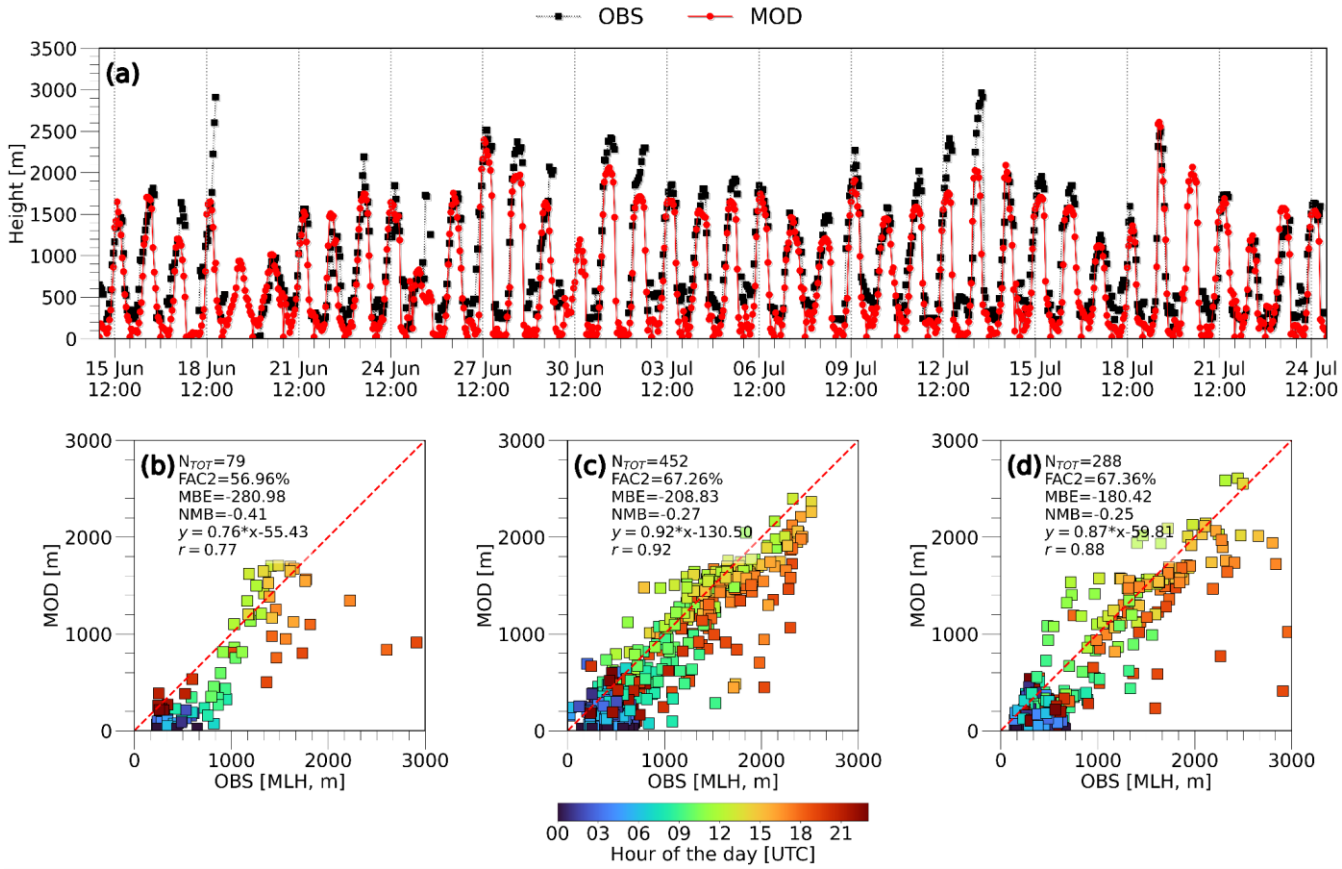

Figure 5: (a) Mixing layer height (PBLH) time series comparison at SIRTA between model simulations and observations; scatter plot of the modelled versus observed PBLH, coloured by the hour of the day for the firth heatwave (b), the clean period (c), the second heatwave (d).

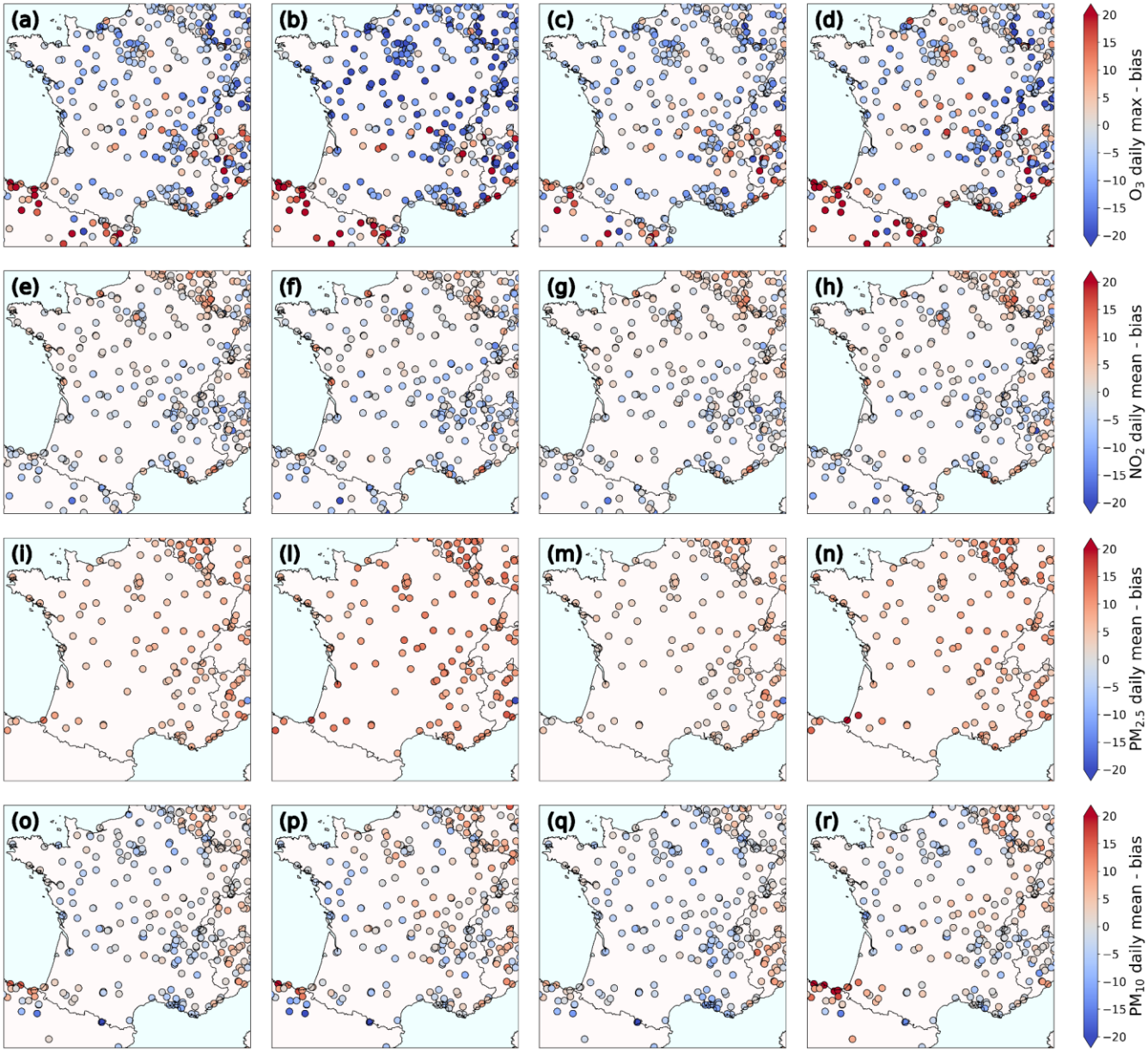

Figure 6: Daily bias obtained by comparing model output to the EEA observations respectively for the full period (left column), the first heatwave (middle left column), the clean period (middle right column) and the second heatwave (right column) for the (a)-(d) O_3 max, (e) - (h) NO_2 mean, (i)-(n) $PM_{2.5}$ mean and (o)-(r) PM_{10} mean.

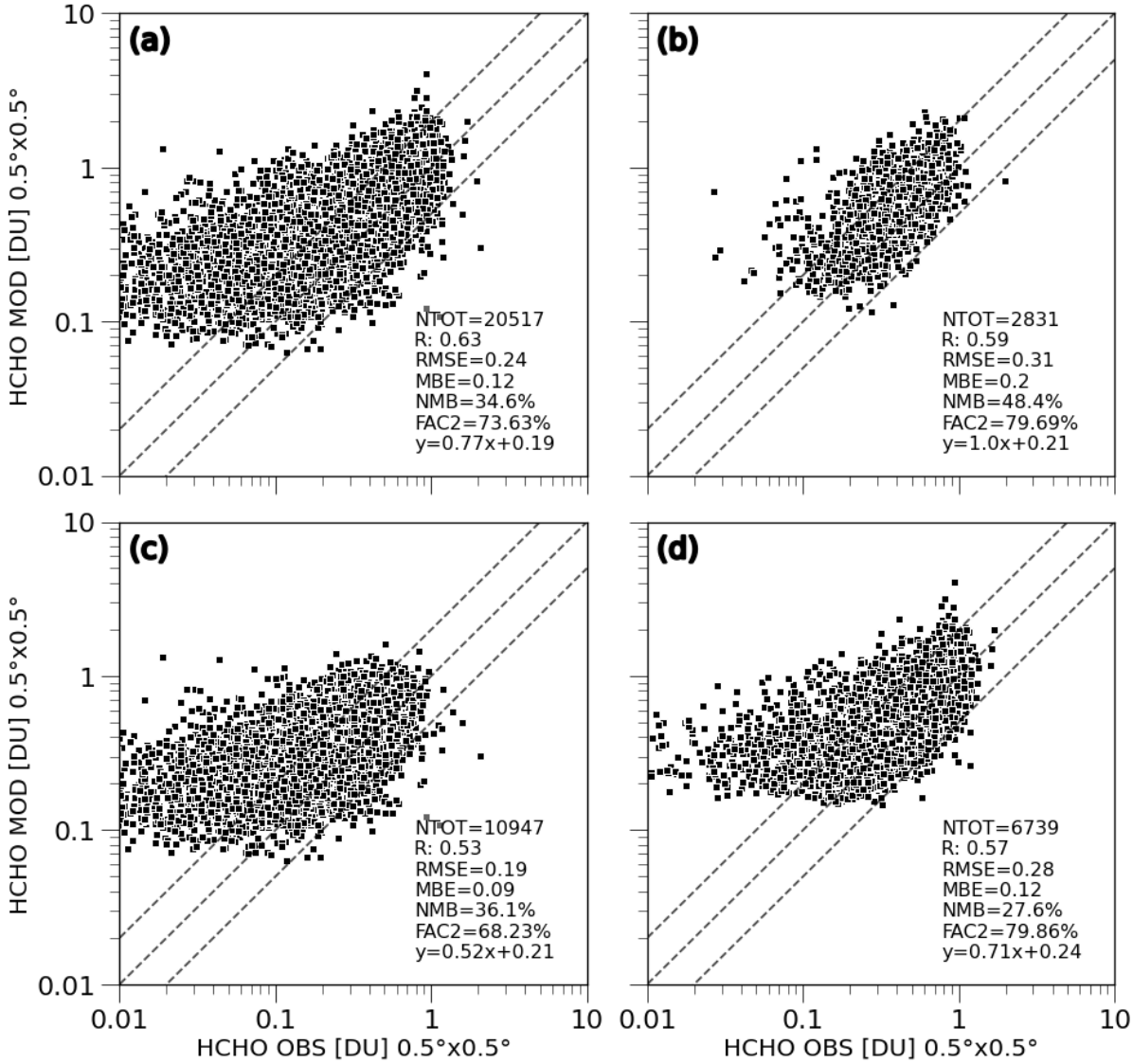

Figure 7: Modelled Formaldehyde (HCHO) versus TROPOMI data. Panel (a) stands for the full period, panel (b) the 1st heatwave period, panel (c) for the clean period and panel (d) the second heat wave respectively.

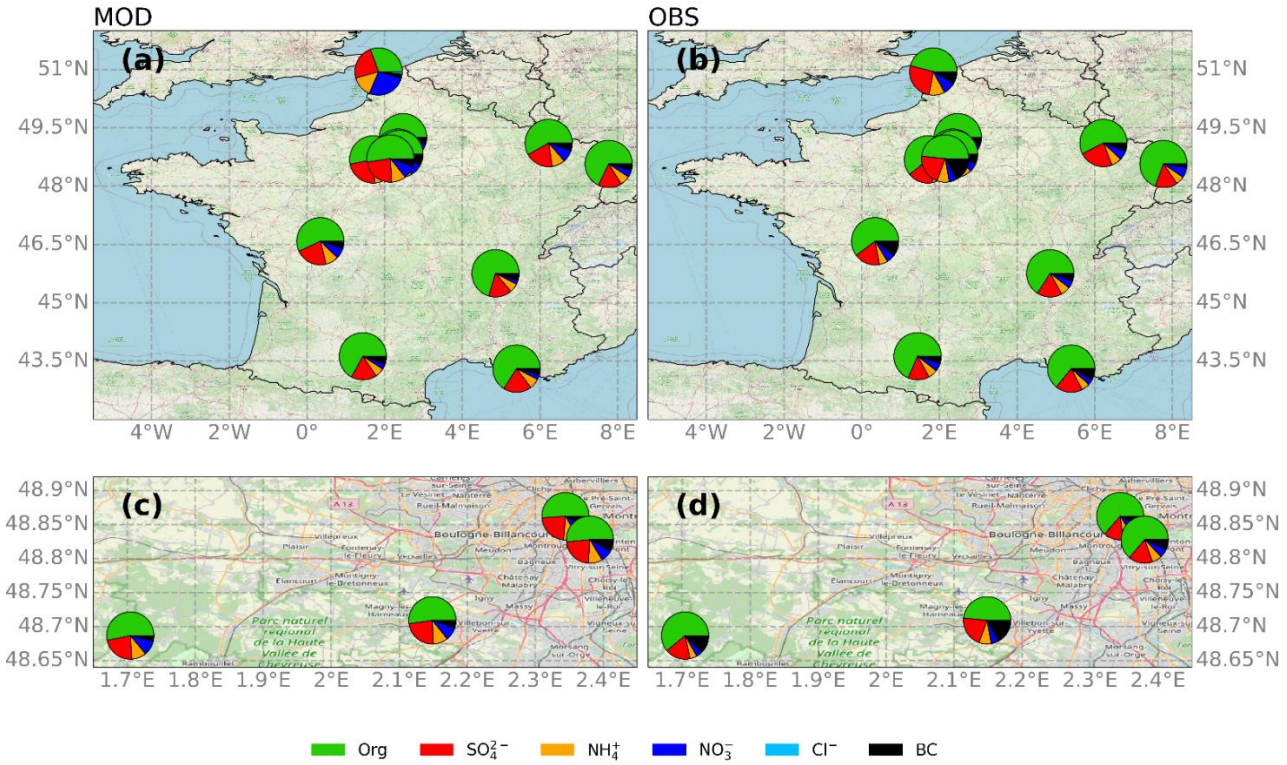

Figure 8: Average PM_1 aerosol composition from (a) the WRF-CHIMERE model, (b) the GEOD'AIR database and the PRG, SIRTA and RambForest sites. Panels (c) and (d) represent a zoom over the Ile-de-France region. Map data source: Map data © OpenStreetMap contributors.

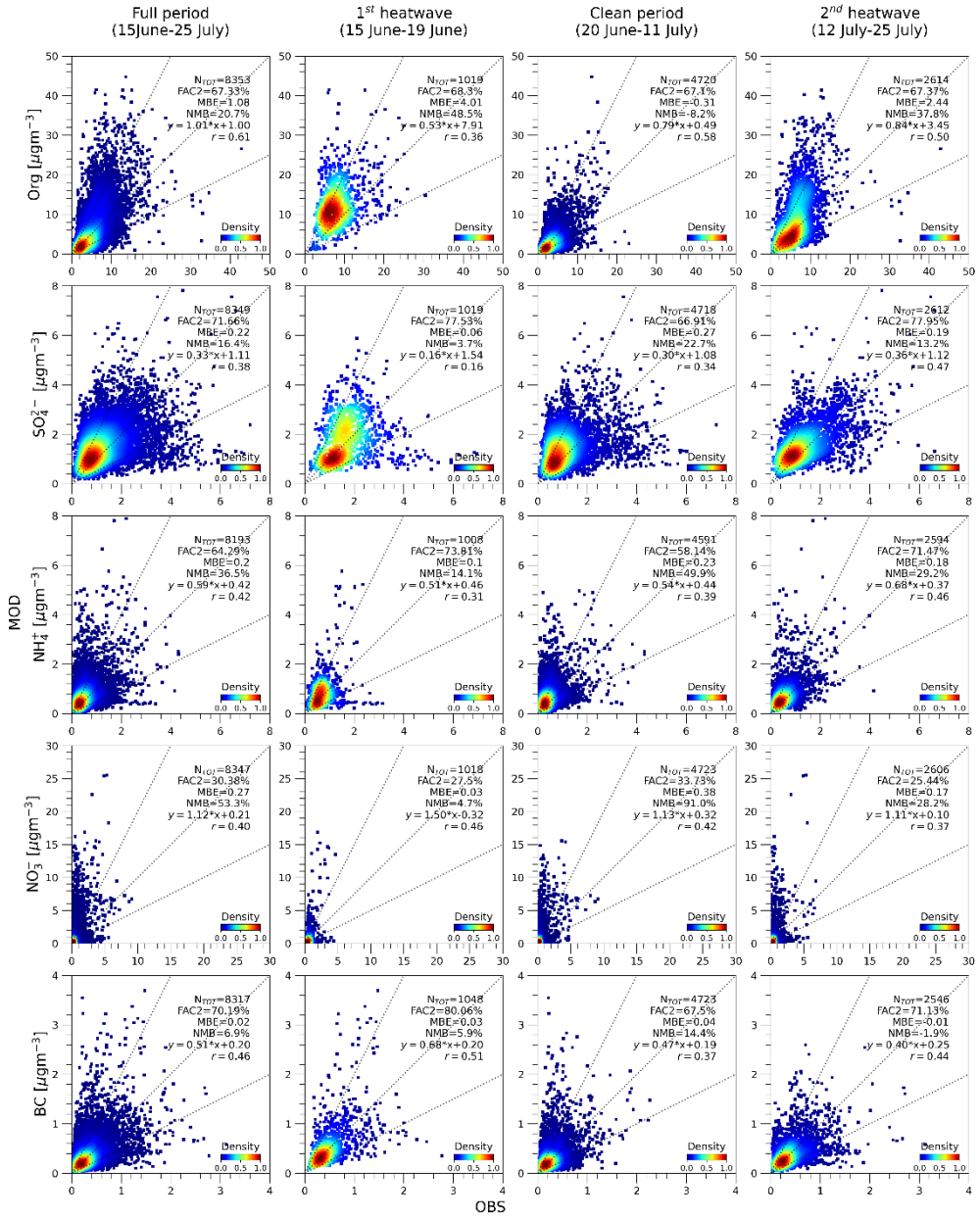

Figure 9: Comparison of simulated chemical composition to observations from the GEOD'AIR database and the PRG, SIRTA, RambForest sites for the full period (left column), the first heatwave (middle left column), the clean period (middle right column) and the second heatwave (right column). Statistical metrics are calculated from data merged for all sites: Ntot, number of observations, FAC2 fraction of points within a factor 2 limit, MBE mean bias error, NMB normalized mean bias, linear fit equation, R correlation coefficient.

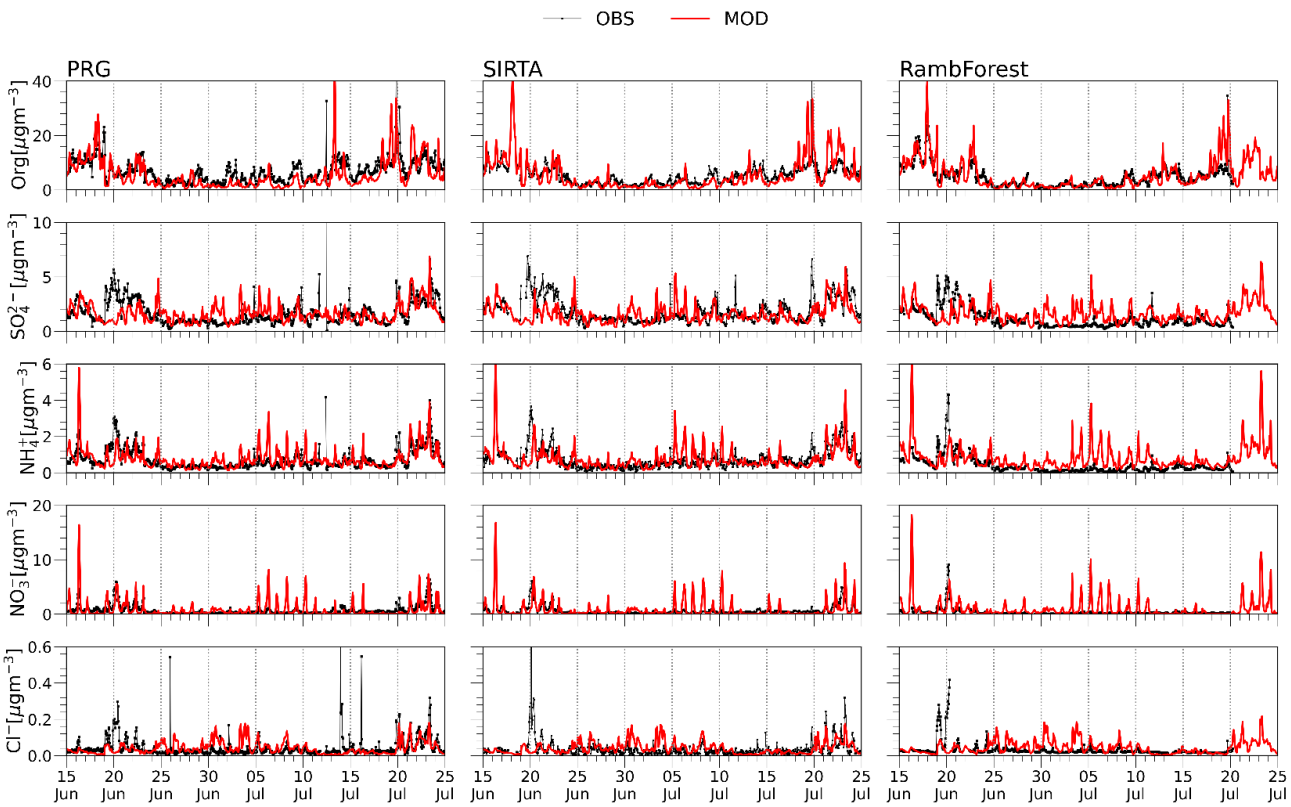

Figure 10: Comparison of simulated chemical composition to observations at the PRG (ACSM model), SIRTA (ACSM model), RambForest (AMS model) sites for the organics, sulfate, nitrate, ammonium and chloride. For the Rambouillet site, only data from the AMS below the canopy are shown for plot readability. Further details on the comparison are available in Figures S6-S8 for the PRG, SIRTA and RambForest sites.

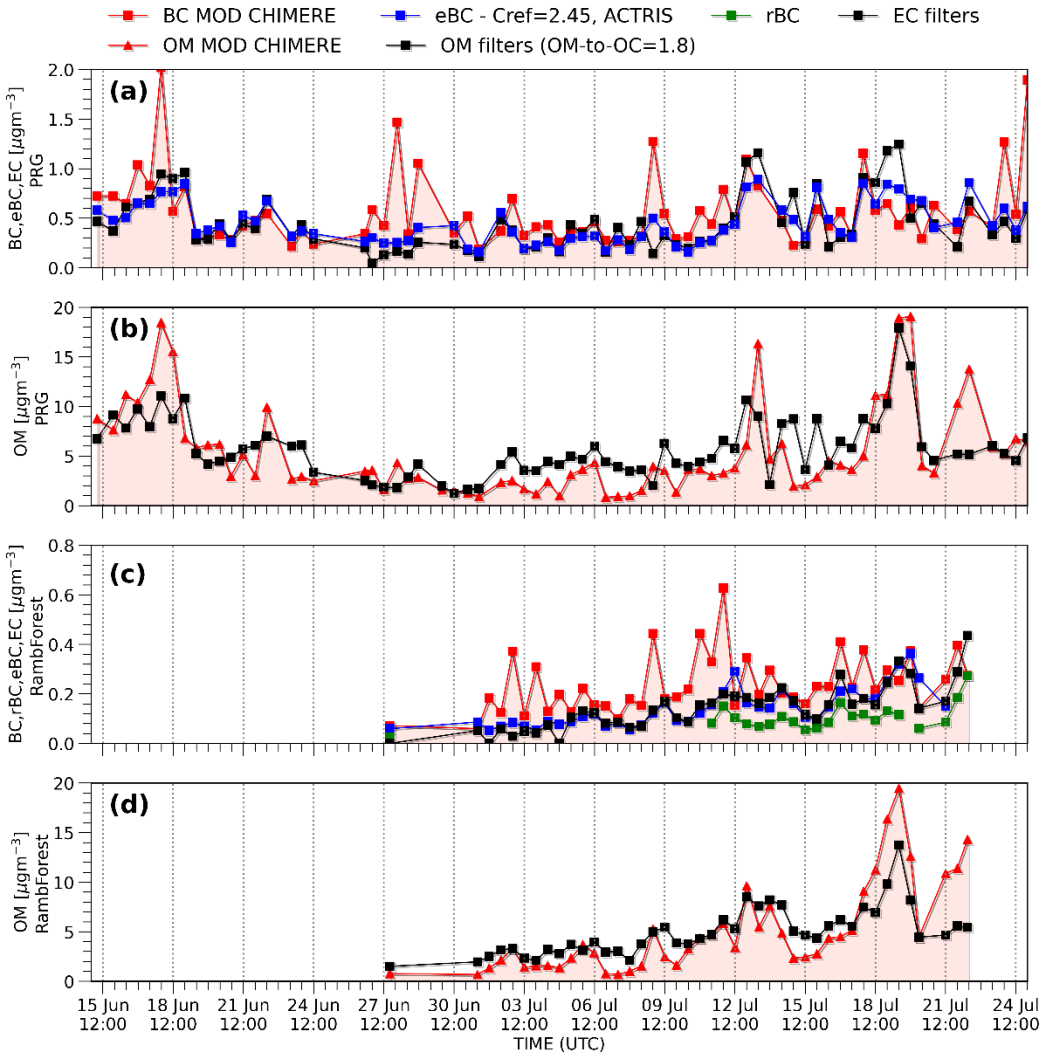

Figure 11: Panels (a) and (c) represent the comparison of CHIMERE simulated black carbon concentration with several observations at the PRG site and RambForest sites respectively: the black line represents the elemental carbon measurements (EC); the blue represents the equivalent black carbon (eBC, corrected for the multiple scattering coefficient from ACTRIS with a Cref=2.45) from AE33 measurements; the green the refractory black carbon from SP2 measurements. Panels (b) and (d) represent the comparison of CHIMERE simulated organic matter concentration with the organic matter from the filter sampling (assuming an OM-to-OC ratio of 1.8 from (Sciare et al., 2011). All the data are averaged on the filters starting and ending time.

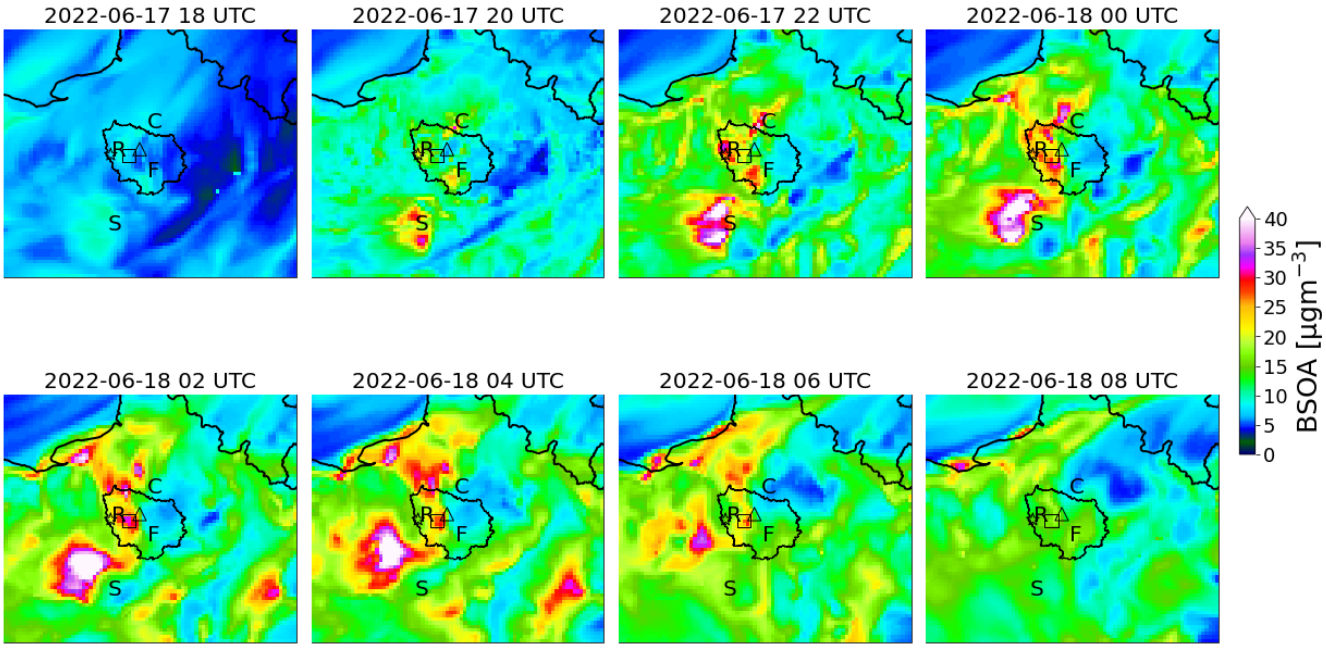

Figure 12: Simulated biogenic secondary organic aerosol (BSOA) mass concentration for the 17 and 18 June 2022. The letter "F" indicates the Fontainebleau forest, "R" indicates the Rambouillet forest, "S" indicates the Sologne forest and "C" indicates the Chantilly forest. The star, the square and the triangle markers indicate respectively the RambForest, SIRTA and PRG sites location.

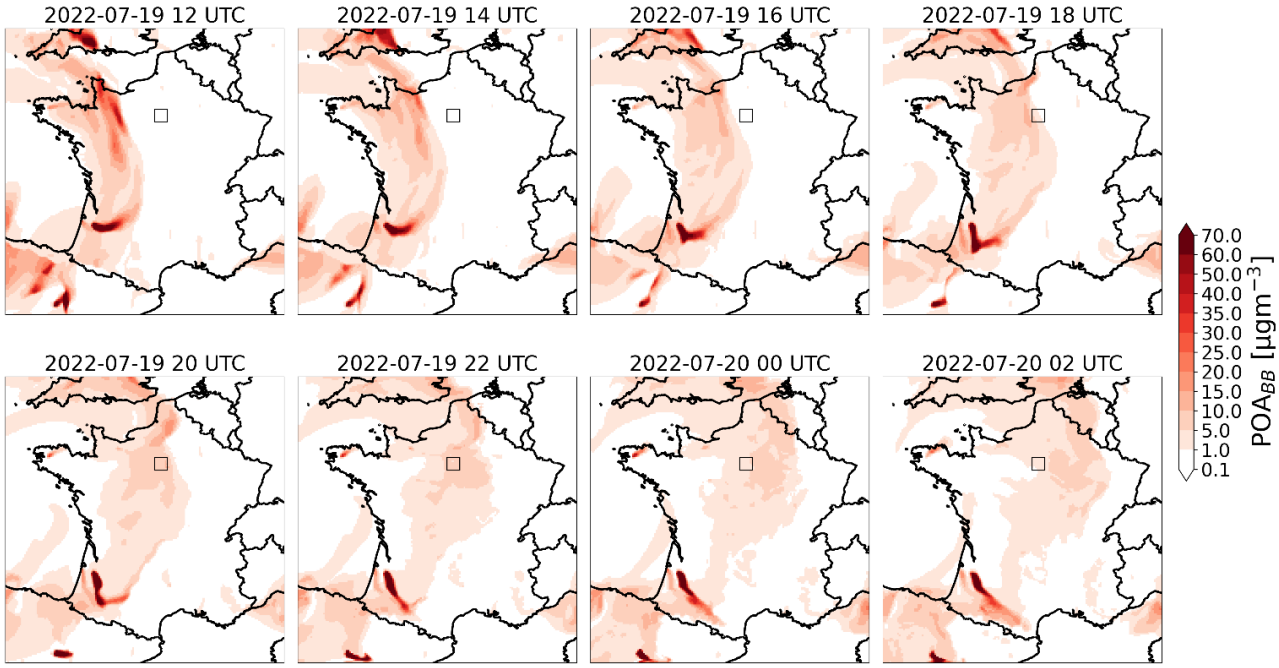

Figure 13: Simulated primary biomass burning organic aerosol mass concentration for the fire episode of the 19 and 20 July 2022. The square marker indicates the Paris-Rive Gauche location.

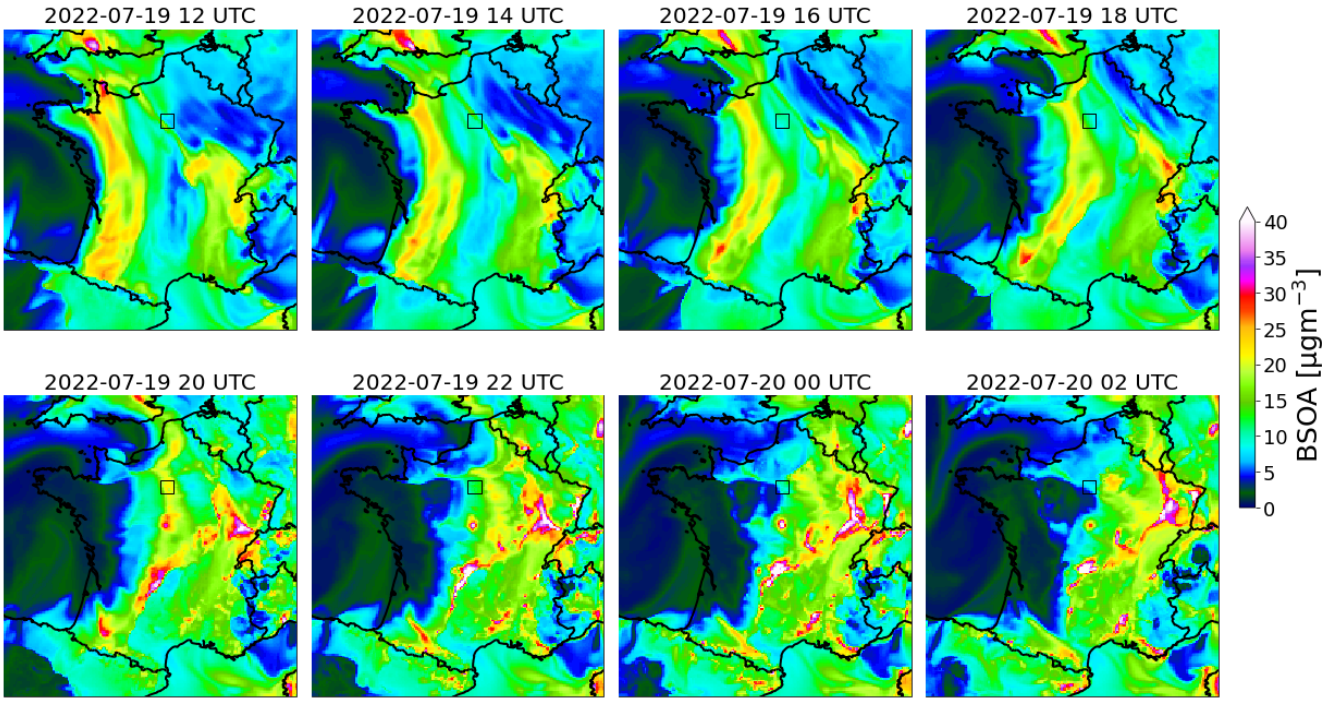

Figure 14: Simulated biogenic secondary organic aerosol (BSOA) mass concentration for the 19 and 20 July 2022. The square marker indicates the Paris-Rive Gauche location. Among the BSOA precursors, α-pinene both stems from fire and from forest emissions.

Tables

Inputs	Description	Spatial resolution
Meteorology	WRF v. 3.7.1 model forced with the NCEP initial and boundary condition	1°x1° (NCEP) WRF nested domains at 30, 6, 2 km
Initial and boundary conditions for chemistry	The CAMS reanalysis (EAC4)	0.75°x0.75°
Anthropogenic emissions	CAMS-GLOB-ANT v5.3	0.1°x0.1°
Biogenic emissions	Online with the MEGAN v. 2.04 model	WRF nested domains at 30, 6, 2 km
Fire Emissions	CAMS Global Fire Assimilation System (GFAS)	0.1°x0.1°
Land use	GLOBCOVER	~300 m

Table 1: Summary of the WRF-CHIMERE model inputs for the ACROSS field campaign 2022 simulation.

	Full period (15 June- 25 July)											
	PRG			SIRTA			RambForest (above the canopy)			RambForest (below the canopy)		
	N_{TOT}	R	NMB %	N_{TOT}	R	NMB %	N_{TOT}	R	NMB %	N_{TOT}	R	NMB %
Ammonium	943	0.52	8.2	904	0.50	0.7	506	0.07	251.8	772	0.27	89.3
Sulfate	942	0.25	-1.2	906	0.37	-12.0	506	0.01	95.9	772	0.17	36.7
Nitrate	943	0.47	15.2	906	0.39	21.0	506	0.21	325.4	772	0.29	148.1
Organic	943	0.61	-19.9	906	0.68	-3.1	506	0.62	21.3	772	0.77	9.7
Chloride	943	0.14	-1.7	888	0.11	7.9	506	0.139	59.4	772	0.06	32.8

Table 2: Summary of the comparison for the Paris-Rive Gauche (urban), SIRTA (peri-urban) and Rambouillet forest (rural) sites from the aerosol refractory chemical composition measurements. Statistical metrics are: Ntot, number of observations, R, correlation coefficient, NMB normalized mean bias.

	Full period (15 June- 25 July)					
	PRG			RambForest		
	NTOT	R	NMB %	NTOT	R	NMB %
eBC	70	0.48	27.0	41	0.36	65.7
EC	70	0.35	27.5	43	0.46	67.7
rBC	-	-	-	22	0.5	152.9
OM	72	0.74	-5.4	43	0.83	1.2

Table 3: Summary of the comparison of the black carbon concentration for the Paris-Rive Gauche and Rambouillet Forest (rural) sites averaged on the filters sampling datetimes. The eBC has been corrected for the ACTRIS harmonisation factor (H*=2.45). The OC has been converted to OM assuming the OM/OC ratio equal to 1.8. Statistical metrics are Ntot, number

5.2 Spectral optical properties validation of the ACROSS field campaign simulation

5.2.1 Evaluation of the PM1 surface complex refractive index and single scattering albedo

In this section, we address the WRF-CHIMERE model capacity to simulate (at 2kmx2km spatial resolution) the hourly PM_1 complex refractive index (CRI) and single scattering albedo (SSA) at 520 nm at the surface level compared to the hourly observations retrieved from the ACROSS field campaign and further described in Chapter 4 of this thesis manuscript. The complex refractive index from the WRF-CHIMERE model has been calculated as the volume-weighted average CRI (i.e. internal mixing) of each model species (see Chapter 2). Figures 5.2.1-5.2.3 show the simulated and observed time series of the real and imaginary CRI components at 520 nm respectively for the urban (PRG), peri-urban (SIRTA) and rural (RambForest) sites. The statistical analysis is summarised in Table 5.2.1 and the scatter plot at the three different sites is shown in Figure 5.2.4. The real CRI component is generally overestimated (MBE of 0.08 and NMB of 5.9%) at the urban site compared to the CRI optical retrieval, with maximum bias between the 20 June and 12 July 2022, which has been characterised by low aerosol loadings. Results from Chapter 4 have shown that this period was

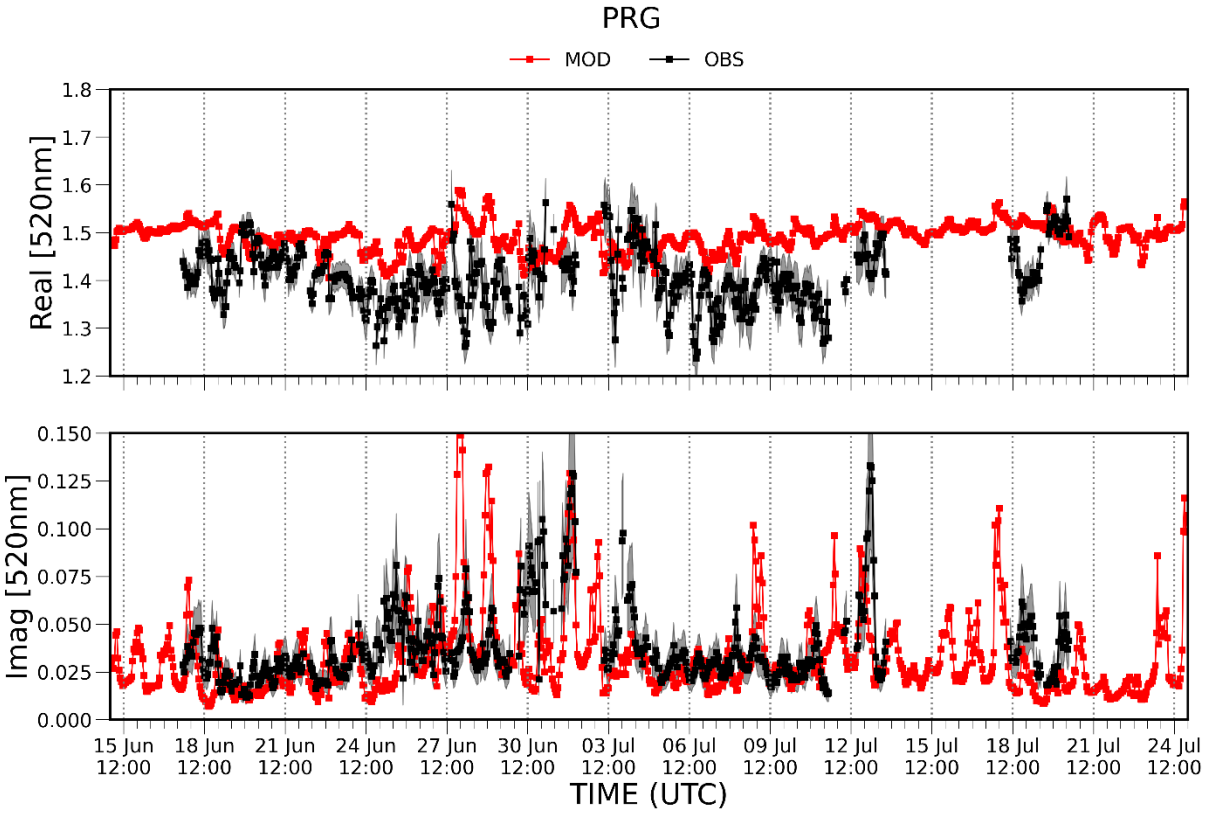

Figure 5.2.1 Time series of the volume-averaged PM1 simulated complex refractive index (real and imaginary) vs the complex refractive index retrieved from optical measurements at 520 nm for the Paris-Rive Gauche site. Shaded area represents the ±SD.

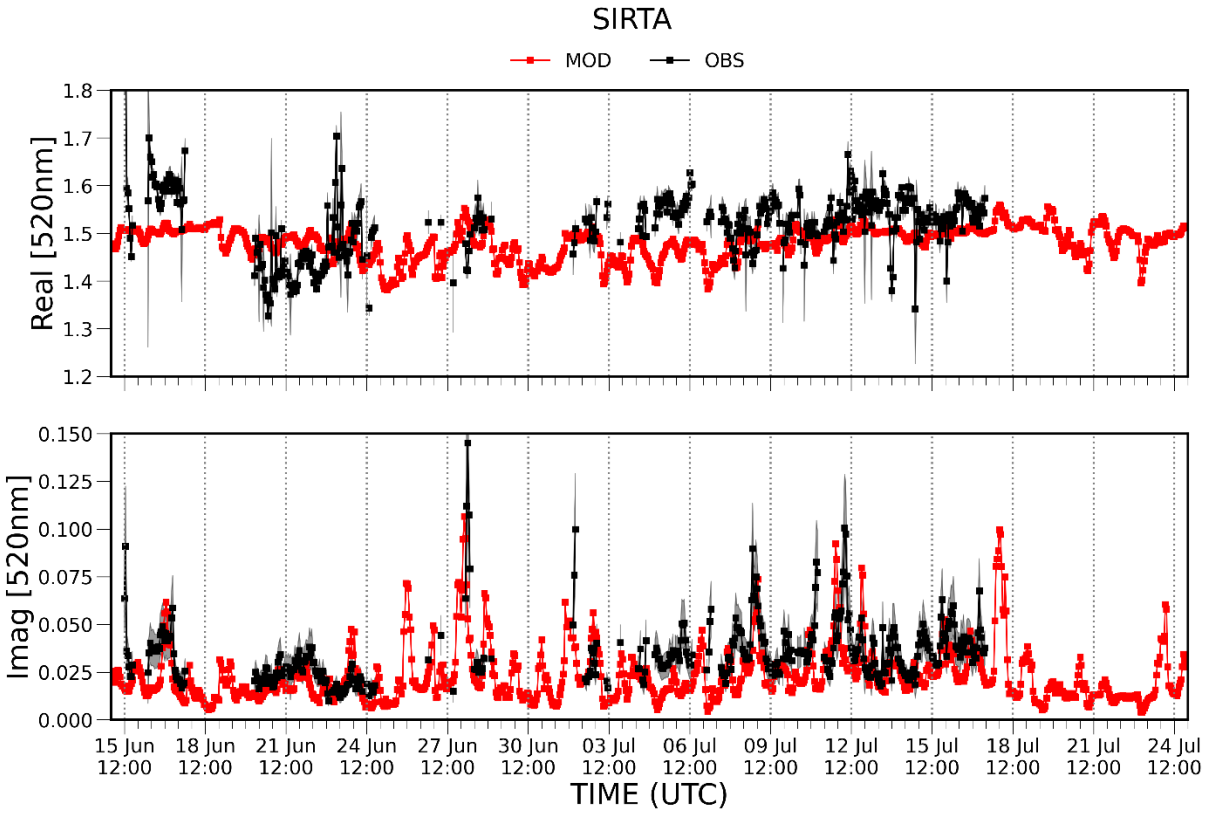

Figure 5.2.2 Time series of the volume-averaged PM_1 simulated complex refractive index vs the complex refractive index (real and imaginary) retrieved from optical measurements at 520 nm for the SIRTA site. Shaded area represents the ±SD.

characterised by higher primary emissions and higher humidity compared to the heat wave periods. This may have an impact on the real CRI, suggesting that the model is less sensitive to the local variability of the site due to aerosol emissions under low loading conditions. On the other hand, better, but still low (≤~0.5) correlation on the real CRI is observed at the peri-urban and rural sites. Concerning the imaginary CRI component, the model is better capable of reproducing its variability, even if correlation does not exceed an R value of about 0.4. Several strong peaks, with k values up to 0.15 are correctly simulated or shifted in time by several hours. As expected k values are larger for the urban site, than for the peri-urban, than for the rural sites (average k at 520 nm of 0.037, 0.035, 0.028 respectively at PRG, SIRTA and RambForest sites). Indeed, k values are primarily dominated by the black carbon absorption and spatial and temporal differences in k values reflect those of BC (see chapter 5.1). Results in Chapter 4 have shown that even a small contribution of BC may increase the CRI absorption. However, the value of k is underestimated in the model (from a NMB of -14.8 at the urban up to a NMB of -35% at the rural site) with a probable consequence on the particles absorption, resulting in an overestimation of the single scattering albedo. Figure 5.2.5 depicts the time series of the surface single scattering albedo calculated under the external and core-shell mixing assumption against field observations at PRG, SIRTA, and RambForest. The statistical analysis is

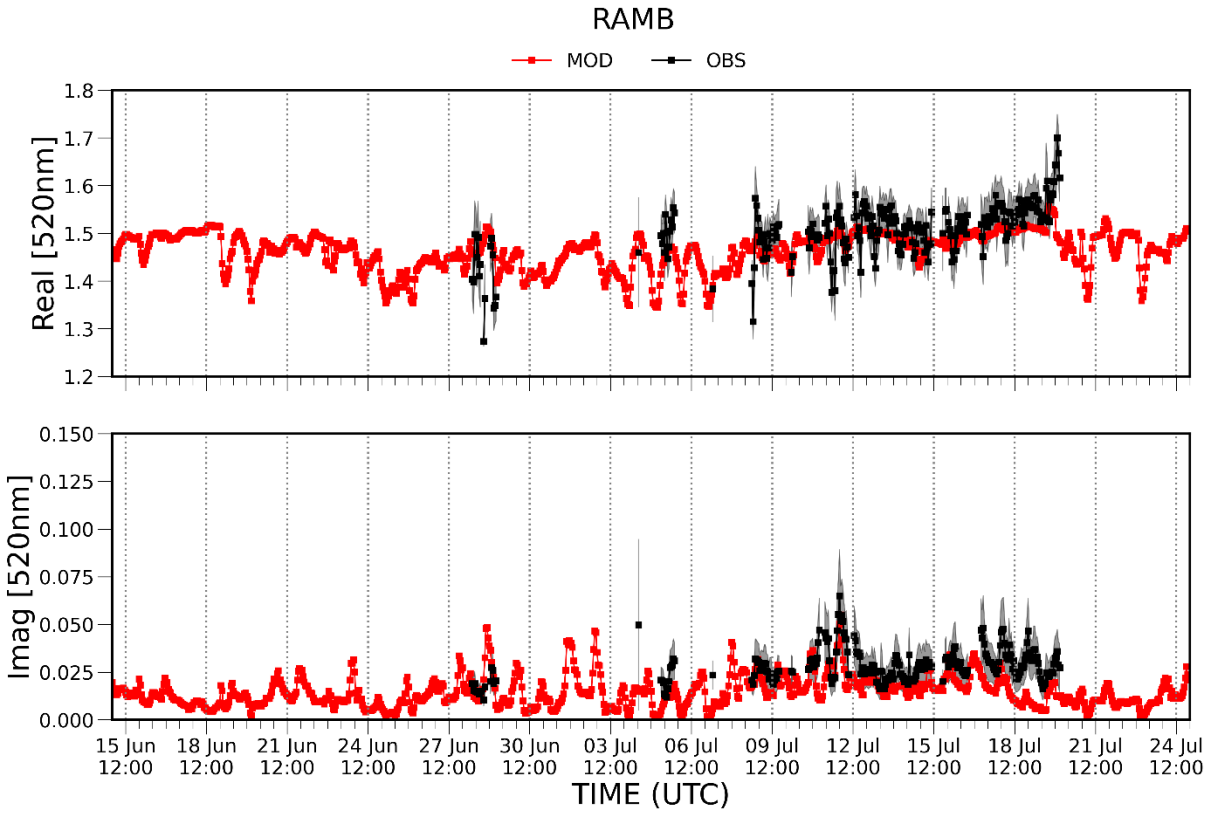

Figure 5.2.3: Time series of the volume-averaged PM_1 simulated complex refractive index vs the complex refractive index (real and imaginary) retrieved from optical measurements at 520 nm for the Rambouillet Forest site. Shaded area represents the ±SD.

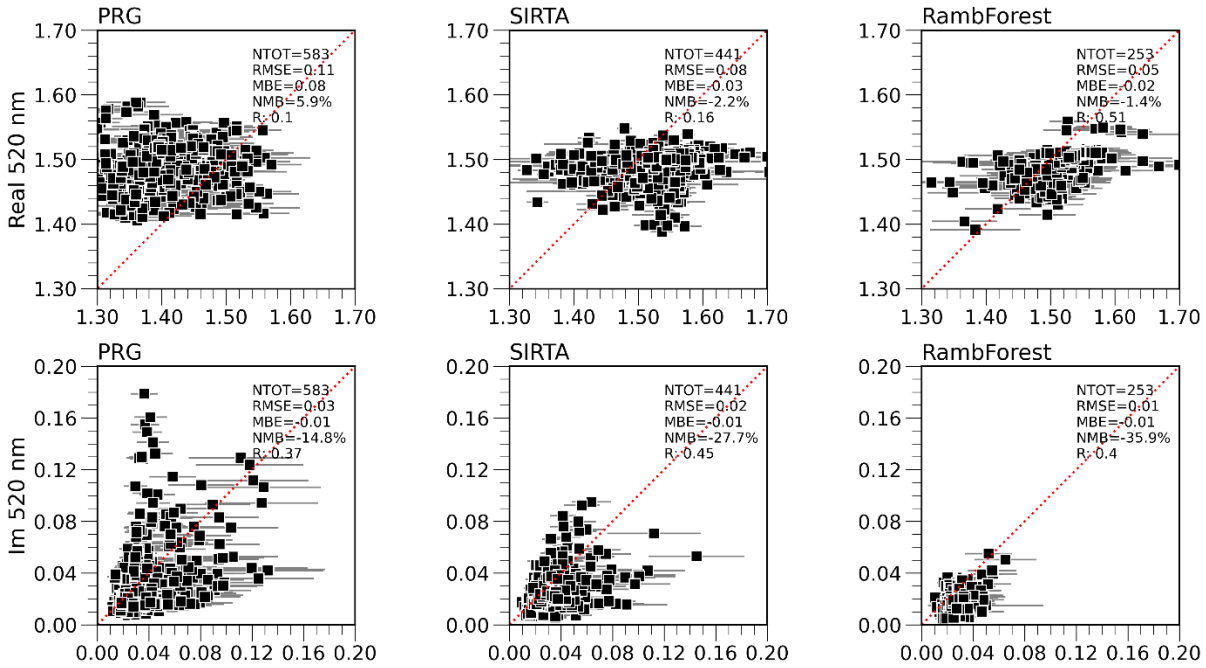

Figure 5.2.4 Scatter plot of the volume-averaged PM1 simulated complex refractive index (real and imaginary) vs the complex refractive index retrieved from optical measurements at 520 nm for the Paris-Rive Gauche, SIRTA and Rambouillet Forest site. Error bars represent the ±SD.

Site	Parameter [520 nm]	NTOT	R	RMSE	MBE	NMB [%]
PRG	n	583	0.10	0.11	0.08	5.9
	k	583	0.37	0.03	-0.01	-14.8
	SSA_{EXT}	809	0.45	0.21	0.19	25.4
	SSA_{CS}	809	0.14	0.23	0.21	28.5
SIRTA	n	441	0.16	0.08	-0.03	2.2
	k	441	0.45	0.02	-0.01	-27.7
	SSA_{EXT}	925	0.51	0.11	0.08	10.1
	SSA_{CS}	925	0.44	0.14	0.12	14.6
RambForest	n	253	0.51	0.05	-0.02	1.4
	k	253	0.40	0.01	-0.01	-35.9
	SSA_{EXT}	783	0.35	0.07	0.04	5.2
	SSA_{CS}	783	0.38	0.08	0.07	8.2

Table 5.2.1 Summary of the statistical analysis for the PM_1 complex refractive index and surface single scattering albedo at 520 nm

summarised in Table 5.2.1 and the scatter plot at the three different sites is shown in Figure 5.2.6. Overestimation of SSA is observed at all sites, with maxima at the urban site for both mixing assumptions between 0.19 and 0.21 for MBE and 25 % and 29% for NMB. Positive biases at PRG and SIRTA are most pronounced especially during the clean period where relative BC contributions to fine PM are largest. This SSA overestimation is striking and remains unexplained at this stage. In particular, black carbon simulations show a positive bias with respect to observations derived with different methods at PRG (between 27 and 28 %) and even more at Rambouillet (between 66 and 153 %), as shown in Figures 11 and 12 and Table 3 of Chapter 5.1. From this result, on the contrary, an underestimation in simulated SSA could have been expected. In addition, contrary to what expected, the absorption is generally lower under the core-shell assumption than positive SSA biases are even slightly larger for the core shell assumption. This result could be justified by the fact that the lensing effect may occur under significant aerosol loading in the shell and depend on the core-to-shell ratio in order to strongly enhance the absorption. In fact, the magnitude of the light absorption enhancement depends on the particle core diameter, the coating thickness of the shell and the complex refractive index (Zhao et al., 2020; Xie et al., 2019; Wu et al., 2018; Liu et al., 2017; Taylor et al., 2015). In fact, higher SSA values for the core shell occur especially for the clean period. On the contrary, during

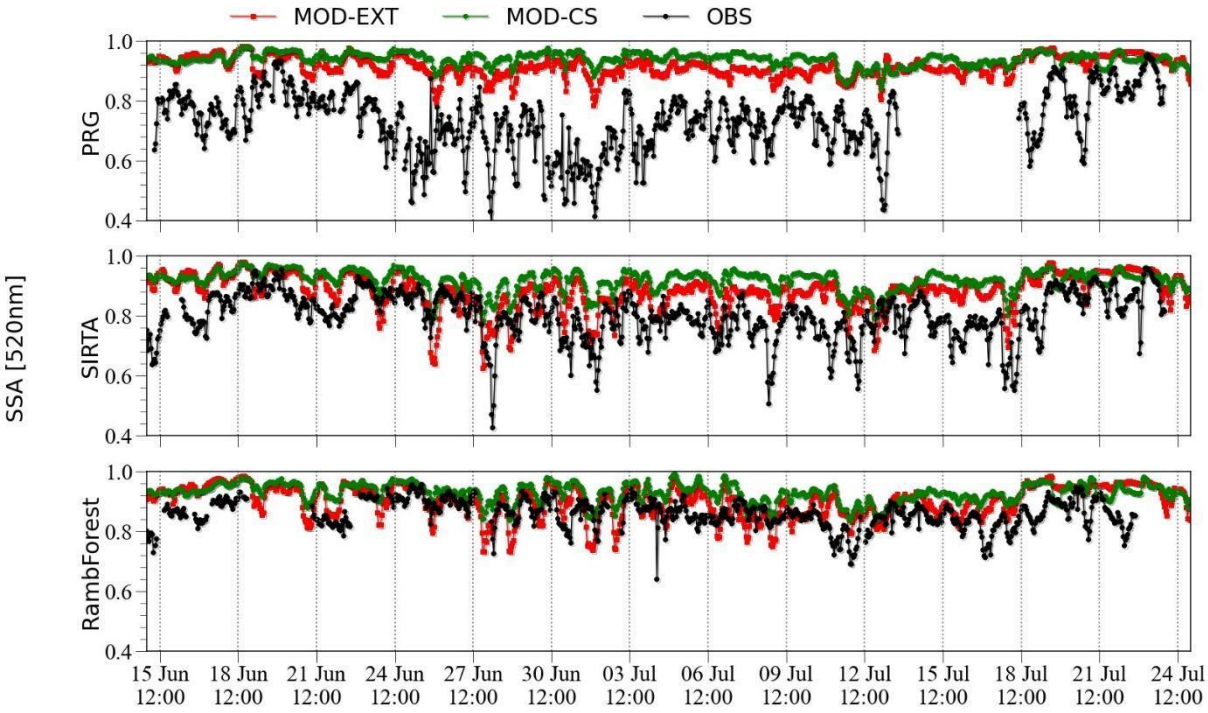

Figure 5.2.5: Comparison of the simulated vs retrieved PM1 surface single scattering albedo (SSA). EXT is the simulated external mixing with the FlexAOD model. CS is the core-shell plus dust in external mixing combining OPTSIM and FlexAOD.

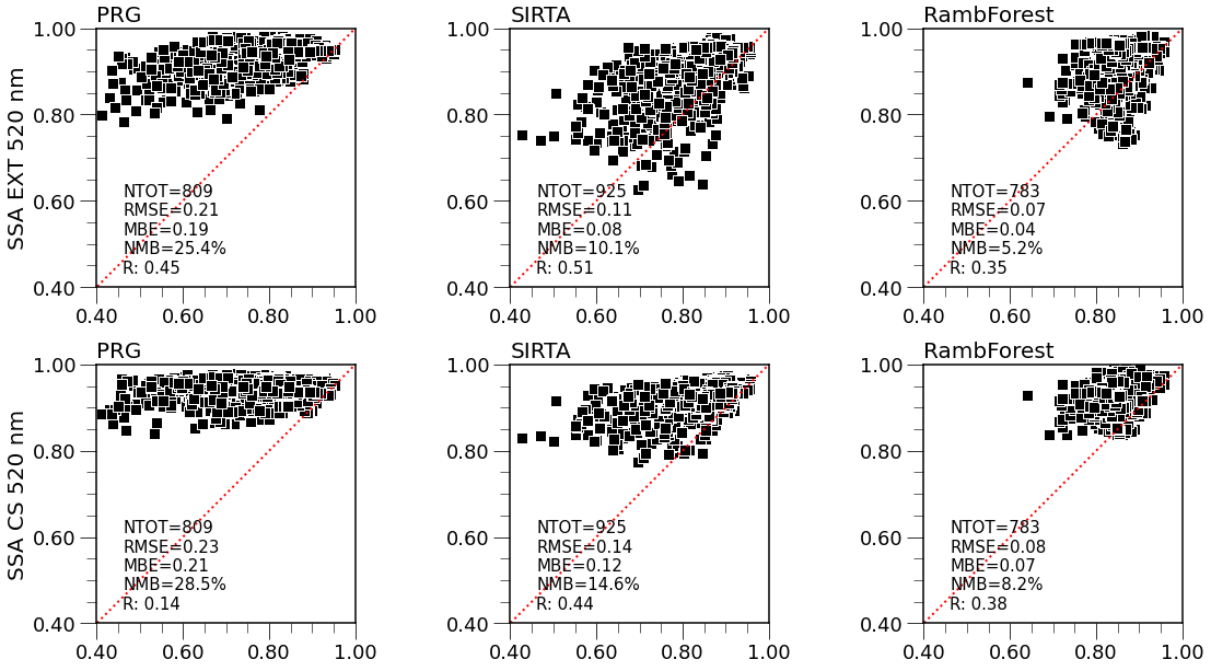

Figure 5.2.6: Scatter plot of the simulated surface single scattering albedo and the observed from optical measurements at 520 nm for the Paris-Rive Gauche, SIRTA and Rambouillet Forest site.

the heatwave periods (from 15 to 18 June 2022 or from 12 July to 25 July), the core-shell shows as expected lower SSA values than external mixing due to the presence of the poorly absorbing BSOAs in the shell enhancing the lensing effect. During the heatwave periods (from 15 to 18 June 2022 or from 12 July to 25 July), the core-shell shows equal or slightly lower SSA values (due to the presence of the poorly absorbing BSOAs) compared to the clean period (from 19 June up to 11 July 2022). The absolute value and temporal variation of the SSA is well reproduced at the peri-urban and rural sites than at the urban site, where a significant bias is obtained (MBE of 0.19 under external mixing), especially during the clean period where primary black carbon emissions dominate the absorption.

As a conclusion, our results suggest that surface aerosol absorption is underestimated by the model. However, since the SSA is calculated from the corrected scattering and absorption measurements, which need specific corrections (see Chapter 4), the uncertainty can be considerable (up to 20 % on SSA). For instance, the aerosol absorption coefficient has to be corrected for the multiple scattering effect (the multiple scattering effect due to aerosol within the filter fibres) with C_{ref} parameter. Indeed, the literature survey on the C_{ref} parameter, depicted in Chapter 4, has shown that the C_{ref} is site and wavelength dependent and may introduce up to 40% uncertainty in the absorption, thus leading to significant uncertainty in the SSA retrievals.

5.2.2 Evaluation of the columnar aerosol optical depth, single scattering albedo and absorption aerosol optical depth with AERONET

Since modelling the DRE also requires an accurate representation of the spectral optical properties within the aerosol column, in this section, we exploit the WRF-CHIMERE model capacity to represent the aerosol columnar spectral optical properties over France, at the 6kmx6km spatial resolution. We compare three main parameters at 440 nm and 675 nm with the columnar AERONET hourly averaged retrieval of: the i) aerosol optical depth (AOD) to validate the aerosol loading, ii) the absorption aerosol optical depth (AAOD) and iii) the single scattering albedo (SSA) to validate the scattering and absorption aerosol components.

The aerosol spectral optical properties have been calculated from the i) ONLINE simulation (i.e CHIMERE optical module under external mixing assumption); ii) OFFLINE with the FlexAOD (external mixing) and OPTSIM (core-shell) model. Results for the AOD, SSA and AAOD at 440 and 675 nm from the ONLINE simulation are presented in Figure 5.2.7 and further summarised in Table 5.2.2. For the simulation, the model reproduces reasonably well the columnar aerosol optical depth both at 440 and 675 nm showing a high correlation coefficient (0.81 at 440 nm and 0.84 at 675 nm)

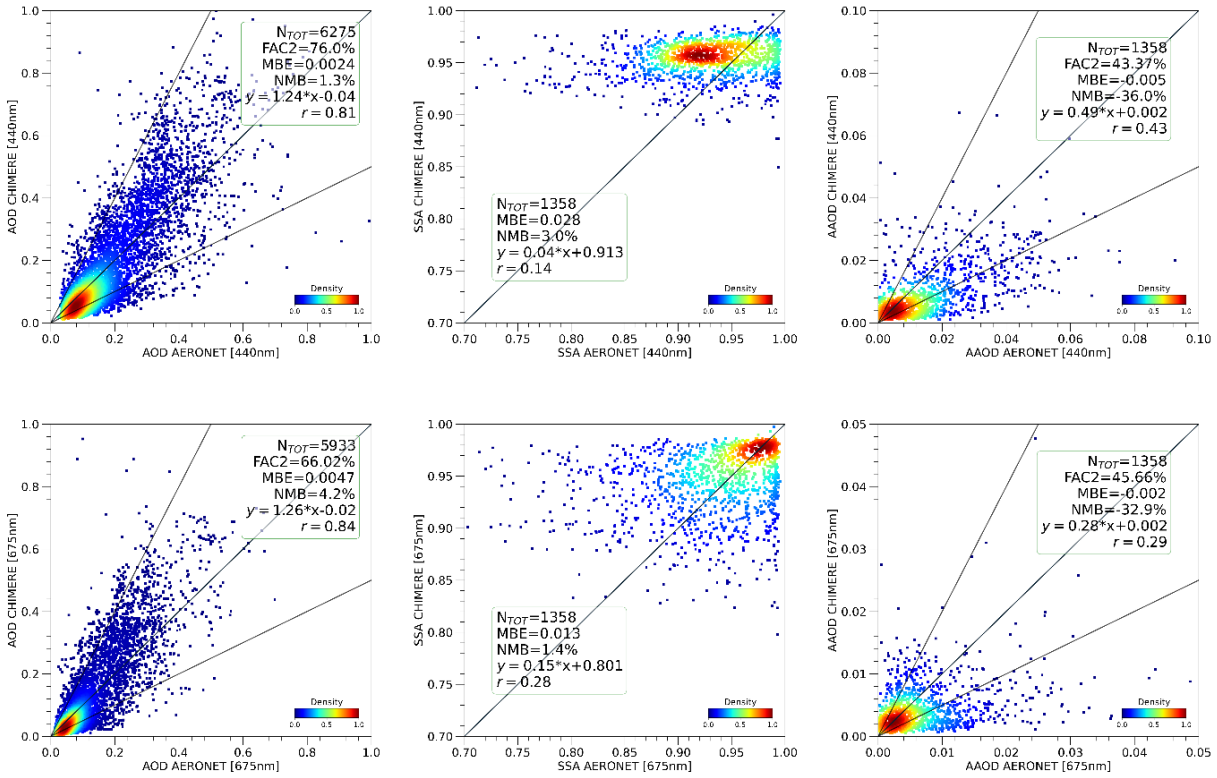

Figure 5.2.7: Comparison of the simulated (CHIMERE external mixing) vs observed (AERONET) aerosol optical depth (AOD), single scattering albedo (SSA) and absorbing aerosol optical depth (AAOD) at 440 nm and 675 nm for the 6km domain

and an only small mean bias error of 0.002 and 0.005 respectively (below 5 % in relative terms). Interestingly, Figure 5.2.7 shows a tendency of underestimation in simulated AOD for values below 0.15 where the maximum of points is located, and an overestimation for larger AOD values. Reasons for this behaviour could be manifold. This results could reflect that we found a stronger PM_1 and $PM_{2.5}$ overestimations during heatwave periods when strong AOD values are encountered than during the clean period. Furthermore, this overestimation could be also linked to the Saharan dust events occurred over the region. Regarding the absorption aerosol optical depth under external mixing assumption, the model is underestimating the columnar absorption both at 440 nm and 675 nm with NMB of -36% and -33% respectively. Dispersion of the comparison is relatively large as less than 50% of points lie within the FAC2 range. As a consequence of AAOD underestimation, the columnar single scattering albedo is overestimated, by +0.028 at 440 nm and + 0.013 at 675 nm. For both wavelengths and especially at 440 nm, correlation is low (0.28 at 675 nm and 0.13 at 440 nm), especially observations of low SSA below 0.85 are not reproduced by the model. Results from the OFFLINE calculations under external and core-shell mixing assumptions for AOD, SSA and AAOD are presented in Figures 5.2.8-2.10 and the statistical analysis summarised in Table 5.2.3.

Parameter	NTOT	R	MBE	NMB [%]	FAC2 [%]
AOD 440 nm	6275	0.81	0.0024	1.3	76.0
AOD 675 nm	5933	0.84	0.0047	4.2	66.0
SSA 440 nm	1358	0.14	0.028	3.0	100.0
SSA 675 nm	1358	0.28	0.013	1.4	100.0
AAOD 440 nm	1358	0.43	-0.005	-36.0	43.4
AAOD 675 nm	1358	0.29	-0.002	-32.9	45.7

Table 5.2.2: Summary of the statistical analysis for the aerosol optical depth, single scattering albedo and the absorption aerosol optical depth at 440 and 675 nm

		External mixing (EXT)				Core-shell plus dust in external mixing (CS+DUST_EXT)			
Parameter	NTOT	R	MBE	NMB [%]	FAC2 [%]	R	MBE	NMB [%]	FAC2 [%]
AOD 440 nm	6275	0.81	-0.0175	-9.5	65.42	0.81	-0.0197	-10.7	64.43
AOD 675 nm	5933	0.84	0.0004	0.4	59.38	0.84	-0.0013	-1.2	57.91
SSA 440 nm	1358	0.14	0.027	2.9	100.0	0.03	-0.003	-0.4	100.0
SSA 675 nm	1358	0.29	0.009	0.9	100.0	0.21	0.02	2.1	100.0
AAOD 440 nm	1358	0.43	-0.006	-43.0	38.88	0.36	-0.001	5.8	44.33
AAOD 675 nm	1358	0.30	-0.002	-34.9	48.09	0.28	-0.002	-23.6	40.06

Table 5.2.3: Summary of the statistical analysis for the aerosol optical depth, single scattering albedo and the absorption aerosol optical depth under external and core-shell mixing assumption at 440 and 675 nm

The agreement is again very good with relative biases below about 10%, and good correlation above 0.8. The aerosol optical depth validation under external (EXT) and core-shell (CS) is shown in Figure 5.2.8. The AOD at 440 nm is now slightly underestimated (up to a NMB of 11%) compared to the CHIMERE external mixing where it was slightly overestimated by 4%. This could be due to the difference in the optical calculation (i.e. the size distribution refinement before the optical calculation that is not performed by the OFFLINE module). On the contrary, the AOD at 675 nm shows good agreement with observations with a NMB of 0.4 and -1.2% respectively for the EXT and CS assumption. Furthermore, the AAOD validation (see Figure 5.10) shows that under the CS model the absorption variability is better reproduced and the difference from the EXT assumption is significantly lower. This enhancement has been further investigated and observed in literature (Curci et al., 2019). Indeed, the NMB at 440 nm decreases from -43% to 5.8% and from -34.9 to -23.6% at 675 nm, suggesting that the CS model is more suitable to reproduce the columnar aerosol absorption properties, although there remains a significant underestimation at 675 nm. Concerning the columnar

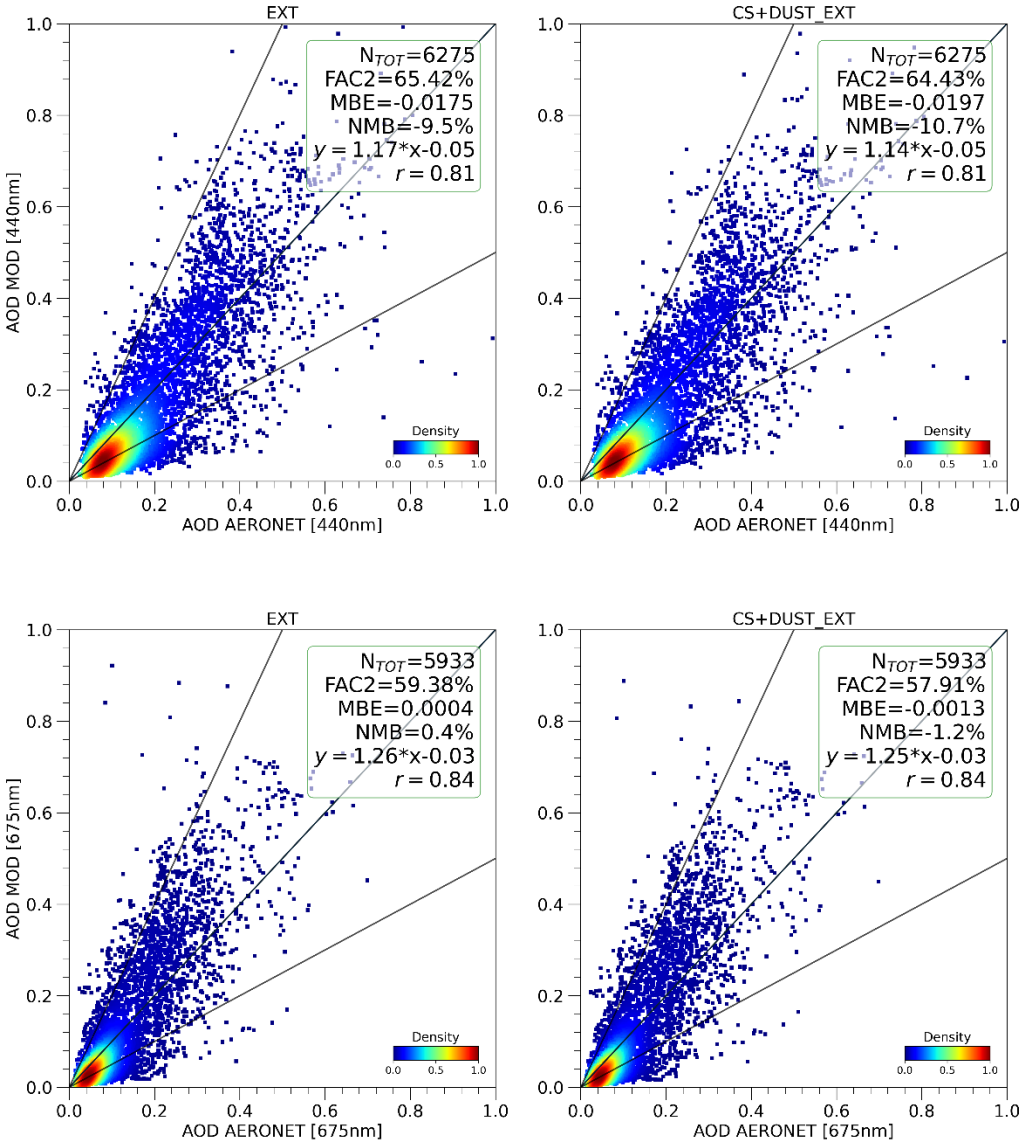

Figure 5.2.8: Comparison of the simulated vs observed (AERONET) aerosol optical depth (AOD) at 440 nm and 675 nm for the 6km domain. (left) Simulated external mixing with the FlexAOD model (right) Core-shell plus dust in external mixing combining OPTSIM and FlexAOD.

single scattering albedo, the SSA under external mixing is still overestimated and shows a similar behaviour compared to the ONLINE external mixing results with a mean bias of 0.0027 and 0.009 respectively for the 440 and 675 nm. On the contrary, the aerosol absorption is enhanced under the CS assumption, lowering the SSA (see Figure 5.2.9) and showing better agreement at 440 nm (CS NMB of -0.4 compared to the EXT NMB of 2.9). The opposite happens at 675 nm where the EXT model still performs better than the CS model. However, the density of points under the CS assumption is closer to the 1:1 line.

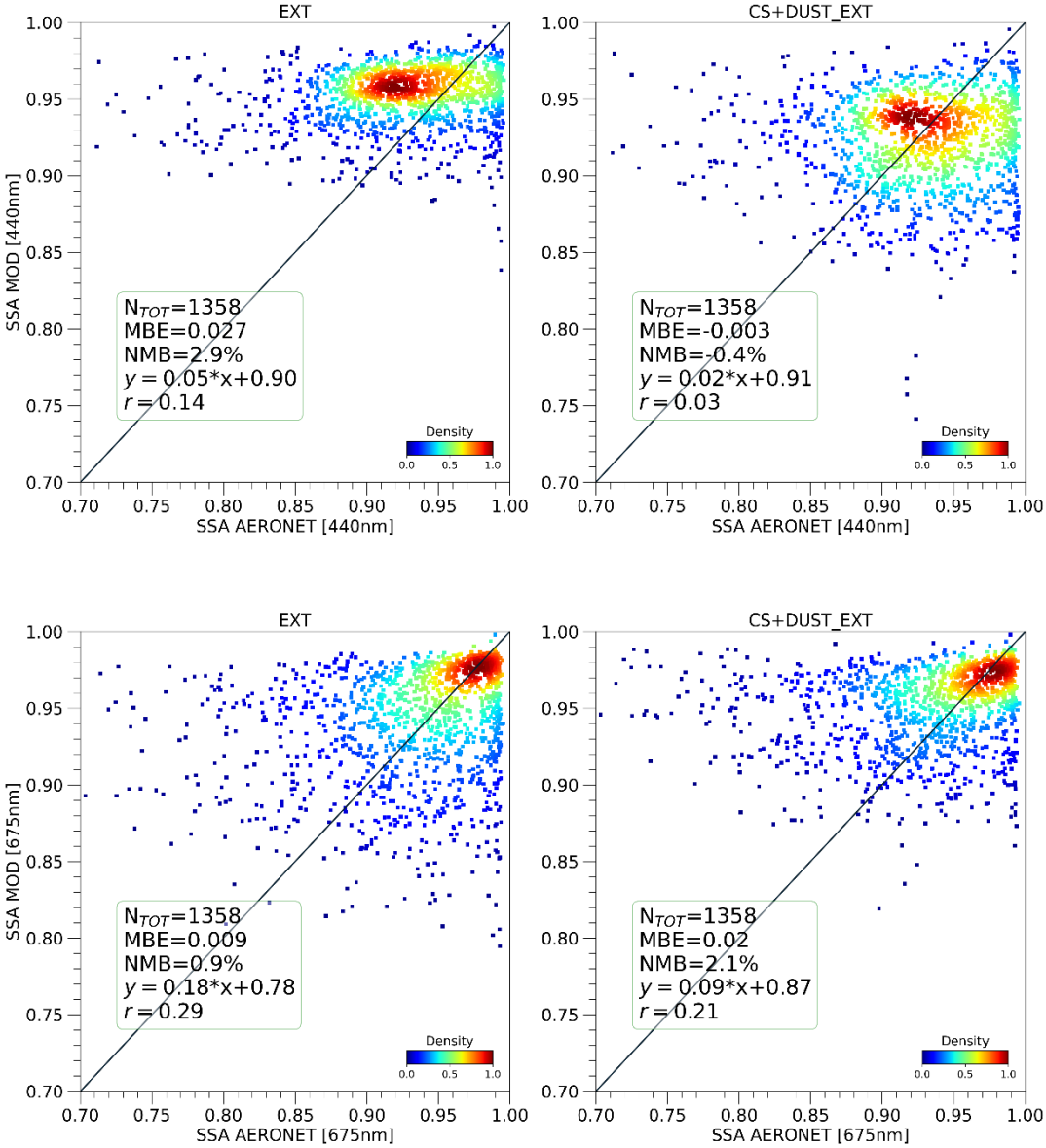

Figure 5.2.9 Comparison of the simulated vs observed (AERONET) single scattering albedo (SSA) at 440 nm and 675 nm for the 6km domain. (left) Simulated external mixing with the FlexAOD model (right) Core-shell plus dust in external mixing combining OPTSIM and FlexAOD.

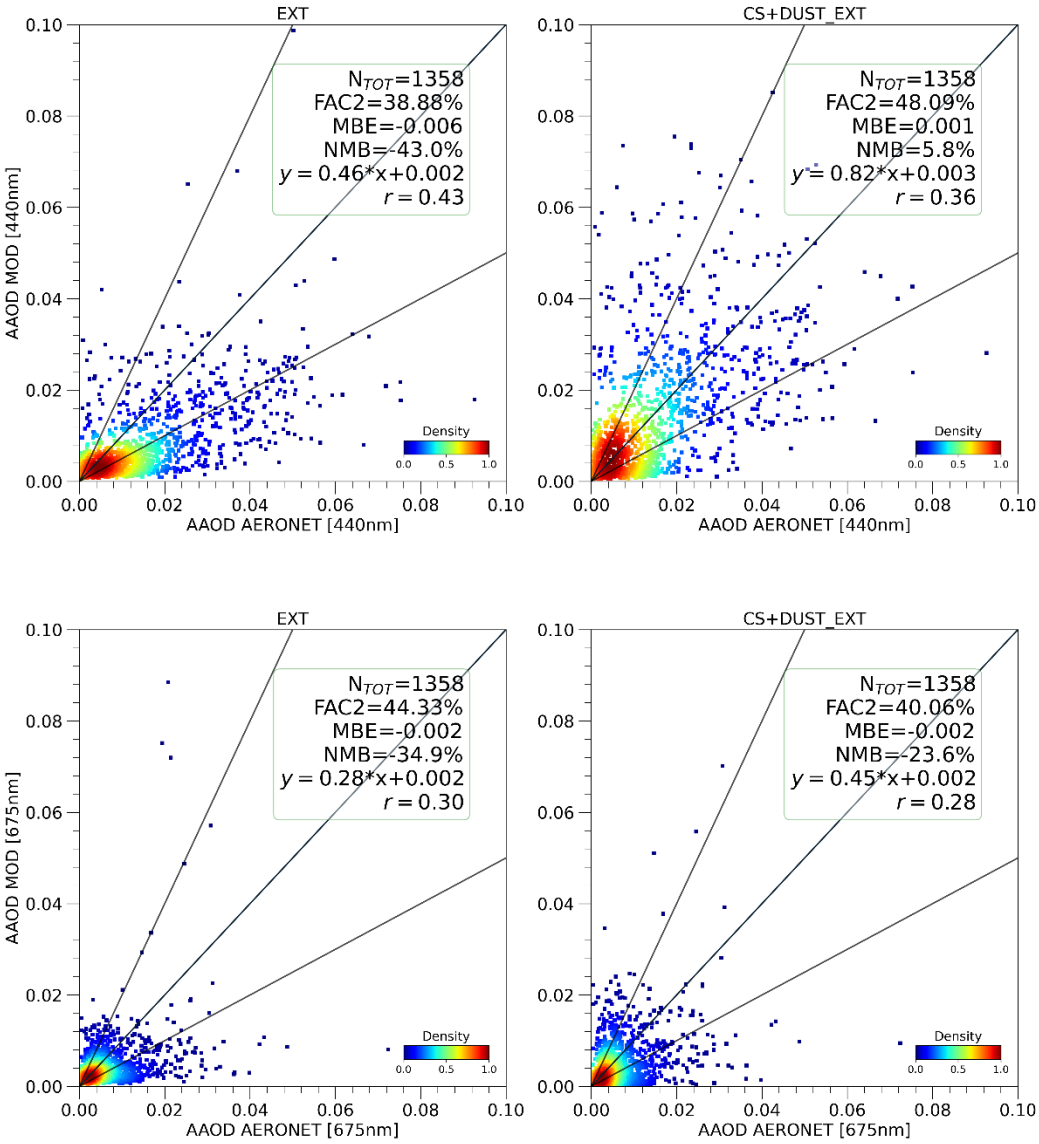

Figure 5.2.10: Comparison of the simulated vs observed (AERONET) absorbing aerosol optical depth (AAOD) at 440 nm and 675 nm for the 6km domain. (left) Simulated external mixing with the FlexAOD model (right) Core-shell plus dust in external mixing combining OPTSIM and FlexAOD.

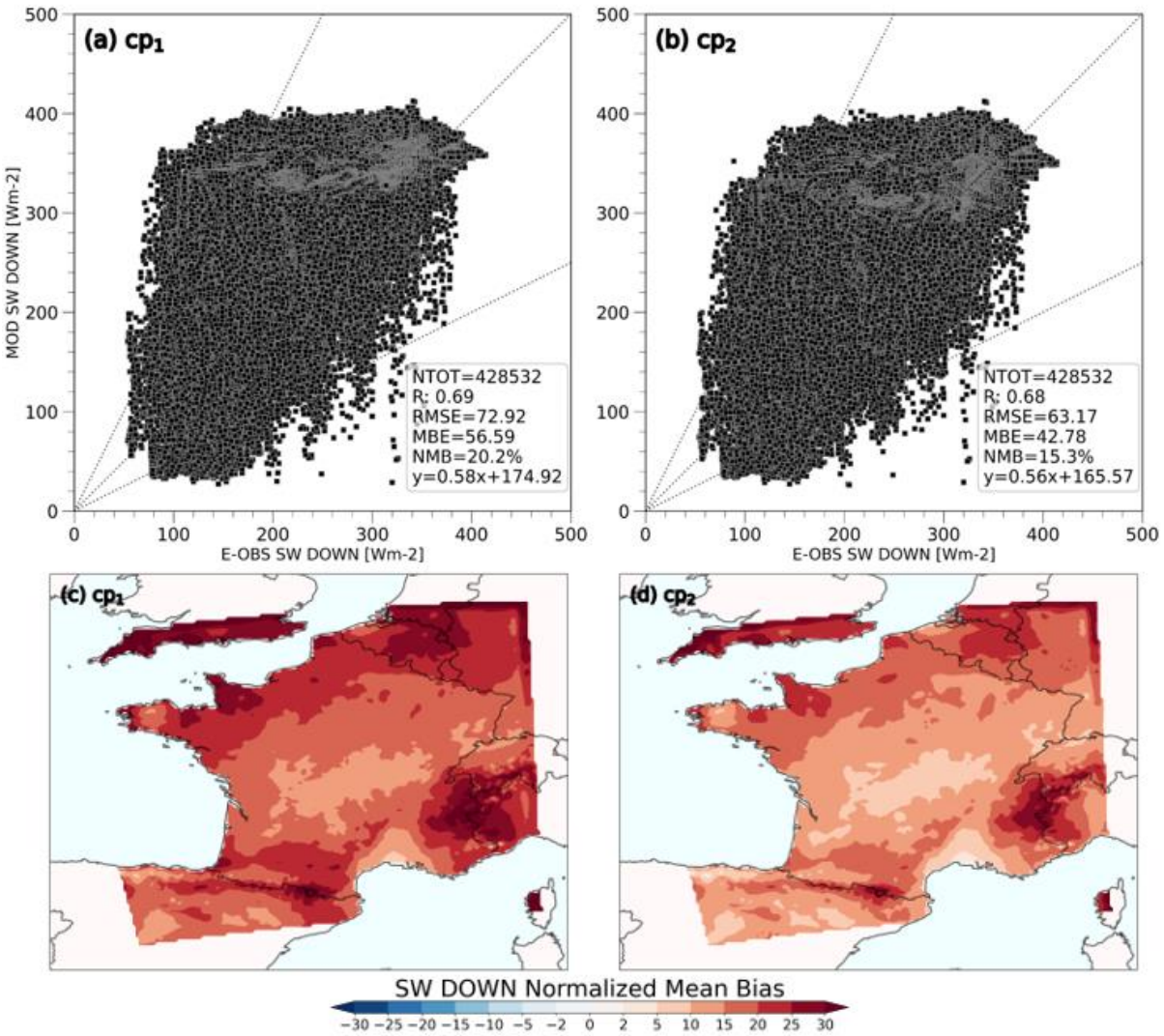

Figure 5.2.11: Shortwave downwelling radiation validation with E-OBS dataset for the 6km domain. Scatter plot of the modelled and observed for (a) not-coupled simulation (cp1) and the (b) coupled simulation (cp2). The normalised mean bias calculated during the entire simulation period respectively without (c) and with (d) the WRF-CHIMERE coupling

5.2.3 Evaluation of the surface downwelling radiation

In this paragraph we compare the simulated daily average downwelling shortwave irradiance at the surface from the WRF model, with the E-OBS daily gridded observations at 0.25x0.25° under the cp1 (no aerosol spectral optical properties exchange between WRF and CHIMERE, i.e. no aerosol direct effect activated) and the cp2 (aerosol direct effect activated) configurations. Figure 5.2.11 shows both the scatter plot and the spatially resolved normalised mean bias over the 6kmx6km domain. Results show that the WRF model overestimates the surface radiation with a positive NMB of 20% and a MBE of 57 Wm^{-2} if the aerosol direct effect is not included (cp1). Devaliya et al., (2023)

also found an overestimation of the radiation fields simulated by the WRF model and compared the CERES data up to 30% over India.

However, when allowing CHIMERE to send the spectral optical properties to the WRF model (cp2 case), the bias is reduced by the effect of aerosols on radiation and meteorology (NMB of 15.3 % and MBE of 43 Wm^{-2}). The spatial NMB shows that there is still an overestimation in the 5 to 20% range over the Ile-de-France region. This result suggests that an inaccurate simulation of parameters such as the cloud cover can lead to biases in the simulation of short wave surface radiation. The strongest model overestimation of mountainous regions (Alps or Pyrenees) could be also due a mismatch in surface characteristics (height of surface albedo) and difficulties in representing sub-grid convection.

5.2.4 Summary and conclusions

In section 5.2 we have shown the optical properties and radiation validation performed both with in-situ observations obtained during the ACROSS campaign and the existing observations from networks.

The comparison with the surface PM1 complex refractive index and the single scattering albedo have shown that the model is capable of reproducing their temporal variability, but that it tends to underestimate the absorption, increasing the SSA signal, particularly at the urban site. This result suggests that an accurate representation of the SSA variability near ground is difficult due to the challenges in the characterisation of the aerosol size distribution, especially at the urban sites, where primary emissions are predominant. On the contrary at the rural and peri-urban sites (i.e more background conditions), the model performs better as compared to the urban. On the contrary, the columnar single scattering albedo is better reproduced as compared to the surface observations due to the vertical integration, and finally this latter comparison is more relevant for assuring the correctness of the DRE estimations that will be performed in chapter 6. Concerning the columnar spectral optical properties, the ONLINE simulation describes reasonably well the aerosol optical depth variability compared to the AERONET database.

However, the OFFLINE models show a slight underestimation due to the missing size refinement in the optical calculation. Thus it might be advisable to incorporate this interpolation in future studies for a better comparison between the ONLINE and OFFLINE models. The columnar AAOD and SSA are better described under the core-shell assumption, suggesting that the CS model is more suitable to reproduce the columnar aerosol absorption properties.

Additionally, validation of surface radiation has shown that the model overestimates the shortwave downwelling flux, which may induce a bias both in the all-sky and clear-sky direct radiative effect estimation. Therefore, the validation of the simulated cloud fraction is also important for a better all-sky DRE assessment and would represent an added value to deepen the understanding of the surface downwelling radiation overestimation made evident. Additionally, in order to investigate the radiation fluxes, a further investigation using both surface pyrometers and satellite observations for the TOA upwelling fluxes (e.g. using SW and LW CERES observations) has to be performed.

Finally, another aspect which is not presented in this section and which will be useful to further investigate the spectral optical properties validation, consists in performing the validation of the number and volume size distribution, both with the AERONET observations and the ACROSS in-situ observations, since the size distribution represents a key parameter for the aerosol-radiation interaction.

Chapter 6

6. Modelling of the aerosol direct radiative effect during the ACROSS field campaign in summer 2022

In this chapter we present the results of the aerosol direct radiative effect (DRE) calculations for the ACROSS field campaign period. Figure 6.1 depicts the workflow strategy applied to estimate the DRE, as already detailed in Sec. 2.3. This strategy is based on two different approaches:

- **ONLINE.** This approach benefits from the interaction between the WRF model and the CHIMERE CTM model (which provides the aerosol optical depth, the single scattering albedo and the asymmetry parameter to WRF at each physical time step under the external mixing assumption) to provide shortwave and longwave (SW+LW) DRE, both under clear-sky and all-sky, accounting for meteorological rapid adjustments (i.e. temperature, wind, pressure…). This in turn has feedbacks also on the aerosols concentrations and emissions fields in the model. The DRE calculated from this approach additionally takes into account the possible aerosol semi-direct effect (SDRE, under all-sky conditions).
- **OFFLINE.** This approach requires the aerosol concentrations and size distribution simulated from the WRF-CHIMERE model to recalculate the vertically-resolved AOD, SSA and asymmetry factor field fields under two different mixing states (external and core-shell mixing), compared to the only external mixing assumption of the ONLINE (i.e. with the

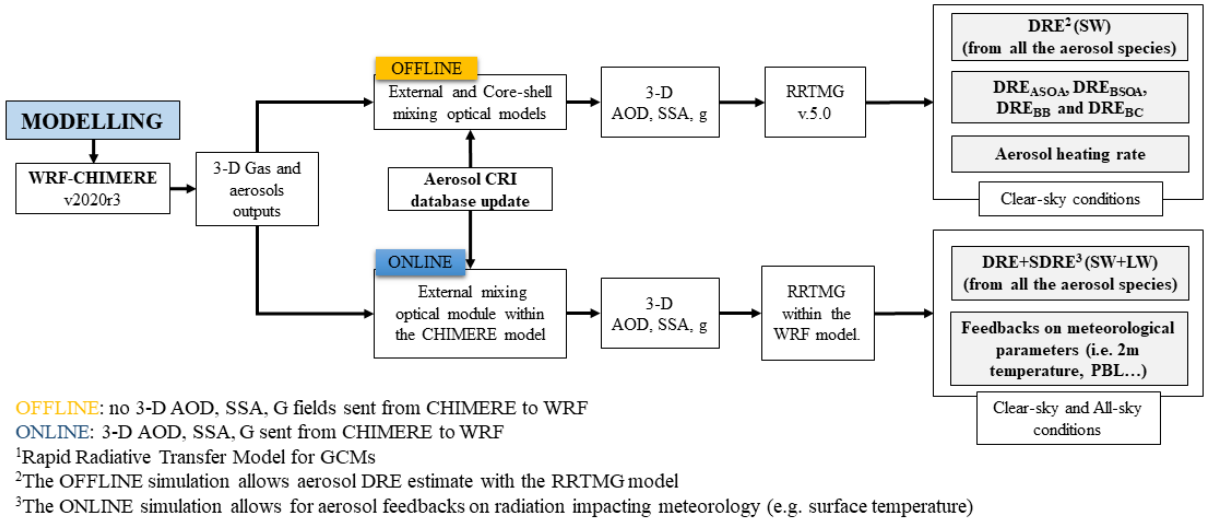

Figure 6.1: Schematic representation of the radiative effects modelling strategy. The ONLINE simulation benefits from the WRF-CHIMERE coupling to provide the DRE and SDRE (under all-sky conditions), together with the meteorological feedbacks. On the contrary, the OFFLINE simulation is used to process the WRF-CHIMERE outputs and recalculate the optical properties from the aerosol size distribution simulated from the model, allowing for sensitivity tests on the different aerosol species (e.g. black carbon, biogenic and anthropogenic SOA and biomass burning), as well as the aerosol heating rate.

WRF-CHIMERE model) approach. This method allows to perform several sensitivity tests. In particular, estimating the contribution to the DRE of different aerosol species (e.g. BC, BSOA) and evaluating the impact of the aerosol mixing state on the DRE. I developed this approach for the shortwave part of the spectrum and under clear-sky conditions only.

The spectral optical properties calculations from the OFFLINE and the ONLINE methods differ for a number of model assumptions detailed in Sec. 2.3. Most importantly, within the ONLINE approach, the WRF-CHIMERE model before the optical calculation applies a particle size distribution refinement. This size distribution refinement is not performed for the FlexAOD (external mixing model) and OPTSIM (core-shell mixing model) models, leading to possible differences in the AOD, DRE and DREE magnitude.

The results derived from the radiative simulations will be presented as follows: section 6.1 will discuss the DRE and Direct Radiative Effect Efficiency (DREE) outcomes from the ONLINE method, whereas section 6.2 presents the results from the OFFLINE method to estimate the DRE contribution of the BC, BSOA, ASOA and BB-POA at regional scale of France and Ile-de-France. Subsequently, section 6.3 analyses the impact of aerosols on the main meteorological parameters, such as temperature, wind, planetary boundary layer, and shortwave clear-sky aerosol heating rate.

6.1 Total aerosol direct radiative effect from the ONLINE WRF-CHIMERE coupling

6.1.1 Shortwave and longwave direct radiative effect and efficiency during the ACROSS field campaign at the France and Ile-de-France regional scale

In this paragraph, we present the results of the shortwave and longwave clear-sky and all-sky direct radiative effect (DRE) and efficiency (DREE) following the ONLINE approach at the France regional scale (See Figure 6.1).

Figures 6.2 to 6.4 show the shortwave (longwave and shortwave plus longwave results are available in Annex D) clear-sky and all-sky DRE and DREE simulated over the France domain (42°N, 51.15°N, 3.2°E, 8.5°W) at 6 km horizontal resolution and divided into different periods (heatwaves and clean period) defined during the ACROSS campaign. Clear-sky averages for the DRE and DREE values for the shortwave, longwave and shortwave plus longwave are also summarised in Tables 6.1 and D.1 for the France and specifically over the Ile-de-France region (48.1°N, 49.26 °N, 3.57°E, 1.47°W) at 6 km resolution.

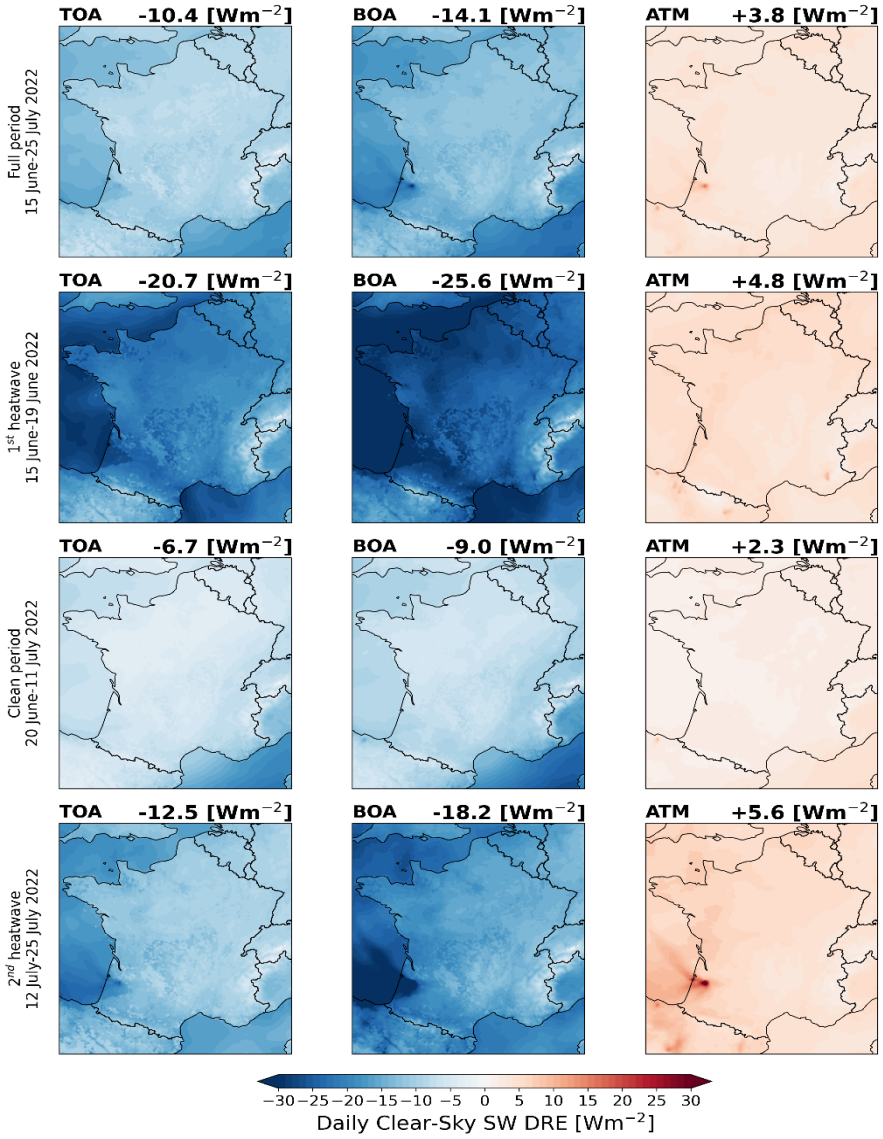

Figure 6.2: Daily Clear-Sky SW direct radiative effect at top of the atmosphere (TOA), bottom of the atmosphere (BOA) and atmosphere (ATM) for the France domain (42°N, 51.15°N, 3.2°E, 8.5°W) at 6km resolution, divided by the different periods during the ACROSS campaign. The aerosol optical depth at 550 nm averages over the France domain are 0.15, 0.32, 0.09, 0.20 respectively for the ACROSS full period, first heatwave, clean period and the second heatwave.

The DRE results are presented at the top of the atmosphere (TOA), bottom of the atmosphere (BOA) and within the atmosphere as average values of daily averages. Average values over the France domain shows that TOA Clear-sky SW DRE is maximum during the first heatwave (-20.7 Wm^{-2}), while lower during the clean period (-6.7 Wm^{-2}). Stronger negative values compared to the TOA are observed at surface (BOA), implying a warming within the atmosphere (ATM) up to +5.6 Wm^{-2} (obtained for the second heatwave). Indeed, as particles both scatter and absorb short-wave radiation, the atmosphere warms due to aerosol absorption (i.e. the direct radiative effect within the atmosphere is positive), DRE BOA is more strongly negative, because of the additive effect of scattering and absorption (corresponding to extinction), while DRE TOA corresponds to the subtractive effect of

		Clear-sky (France)								
		SW			LW			SW+LW		
		TOA	**BOA**	**ATM**	**TOA**	**BOA**	**ATM**	**TOA**	**BOA**	**ATM**
Full period (15 June-25 July)	DRE	-10.4	-14.1	+3.8	+1.2	+3.4	-2.2	-9.2	-10.8	+1.6
	DREE	-78.7	-117.3	+38.6	+7.1	+24.5	-17.5	-71.6	-92.8	+21.1
1st heatwave (15 June-19 June)	DRE	-20.7	-25.6	+4.8	+2.4	+6.5	-4.1	-18.4	-19.1	+0.7
	DREE	-69.3	-87.7	+18.4	+6.4	+20.3	-13.9	-63.0	-67.4	+4.5
Clean period (20 June-11 July)	DRE	-6.7	-9.9	+2.3	+0.6	+2.1	-1.5	-6.1	-6.9	+0.9
	DREE	-83.8	-126.8	+43.0	+6.2	+25.4	-19.2	-77.6	-101.4	+23.8
2nd heatwave (12 July-25 July)	DRE	-12.5	-18.2	+5.6	+1.6	+4.3	-2.7	-10.9	-13.9	+3.0
	DREE	-74.0	-112.9	+38.8	+8.6	+24.6	-15.9	-65.4	-88.3	+22.9

Table 6.1: Clear sky direct radiative effect and direct radiative efficiency averages for the ONLINE approach at top of the atmosphere (TOA), bottom of the atmosphere (BOA) and atmosphere (ATM) for the France domain (42°N, 51.15°N, 3.2°E, 8.5°W) divided by the different periods during the ACROSS campaign. The aerosol optical depth at 550 nm averages over the France domain are 0.15, 0.32, 0.09, 0.20 respectively for the ACROSS full period, first heatwave, clean period and the second heatwave.

scattering and absorption. The strongly negative DRE TOA and BOA signals obtained during the first and second heatwave and more strongly positive DRE ATM as compared to the clean period (average differences by a factor of two), demonstrate the different aerosol loading and chemical composition contribution to the DRE. During the heatwaves, the strong BSOA formation, biomass burning emissions and dust advection as presented in Chapter 5.1 leads to a general increase of the aerosol loading.

As the average simulated aerosol is globally only weakly absorbing (with SSA values of about 0.96 see chapter 5.2), this leads to enhanced negative DRE TOA. Nevertheless, enhanced BC concentrations due to wildfire and anthropogenic sources explain the enhanced DRE within the atmosphere (ATM). The contribution of the brown carbon (BrC) absorption due to biomass burning aerosols is included in the complex refractive index assigned to the primary biomass burning aerosol (BB-POA) and that will be analysed under different aerosol mixing state.

In particular, during the second heatwave the area over the Gironde region (Southern France) shows a more negative DRE at TOA and BOA, while more positive within the atmosphere (ATM) due to biomass burning aerosols associated to fires. This effect is amplified over the ocean (lower than -30 Wm^{-2} at the BOA) due to a lower surface albedo. However, although we have observed that the BC contribution is stronger at the surface (see Chapter 4) and dominates the PM_1 composition over the

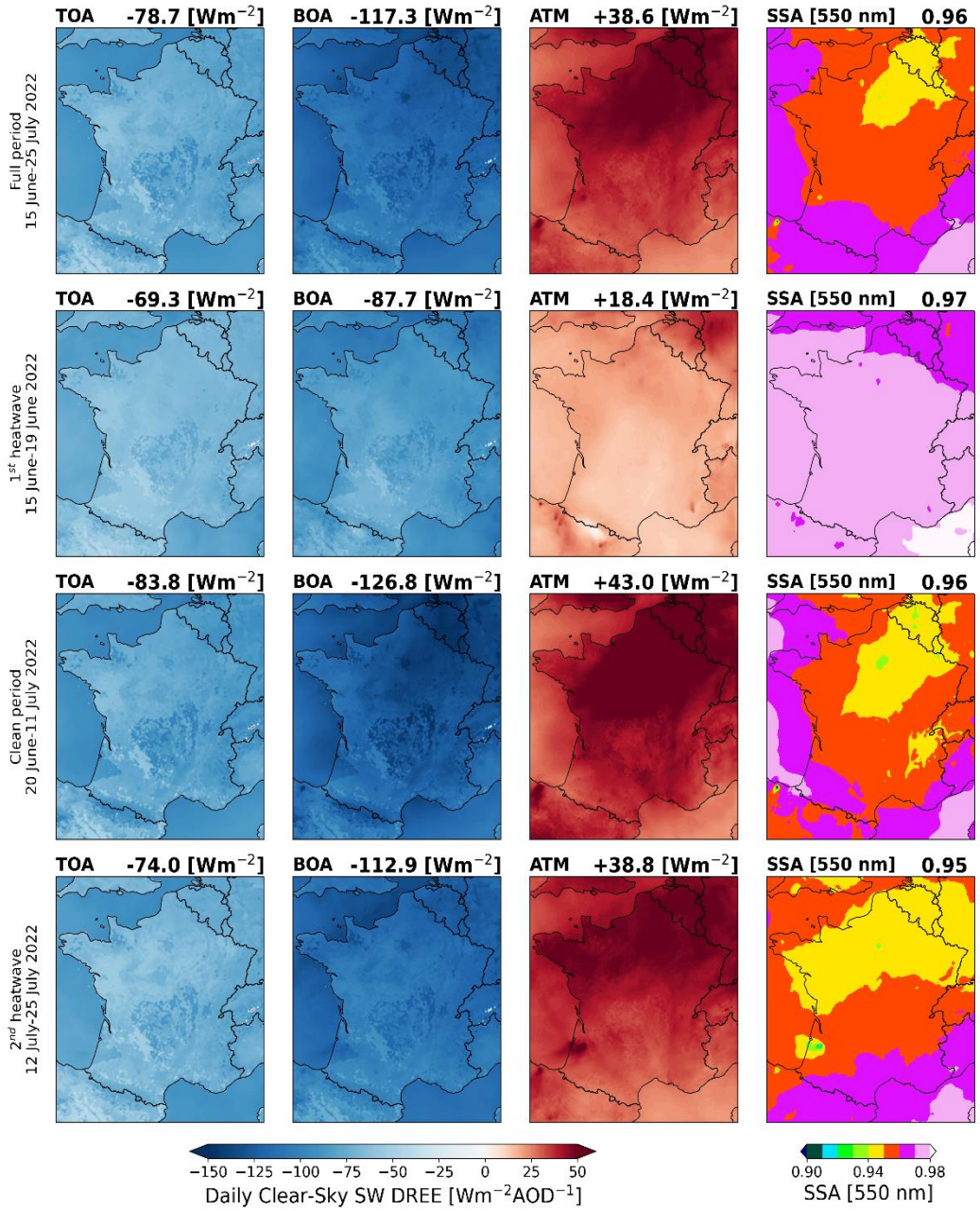

Figure 6.3: Daily Clear-Sky SW direct radiative efficiency at top of the atmosphere (TOA), bottom of the atmosphere (BOA) and atmosphere (ATM) and single scattering albedo at 550 nm for the France domain (42°N, 51.15°N, 3.2°E,8.5°W) at 6km resolution, divided by the different periods during the ACROSS campaign. The aerosol optical depth at 550 nm averages over the France domain are 0.15, 0.32, 0.09, 0.20 respectively for the ACROSS full period, first heatwave, clean period and the second heatwave.

urban sites, it does not strongly affect the columnar spectral optical properties, which in turn shows a weaker DRE signal over the clean period.

Regarding the Clear-sky SW DRE Efficiency (DREE, See Figure 6.3), a spatial heterogeneous signal at BOA and ATM due to the aerosol spatial distribution is observed, with maxima during the clean

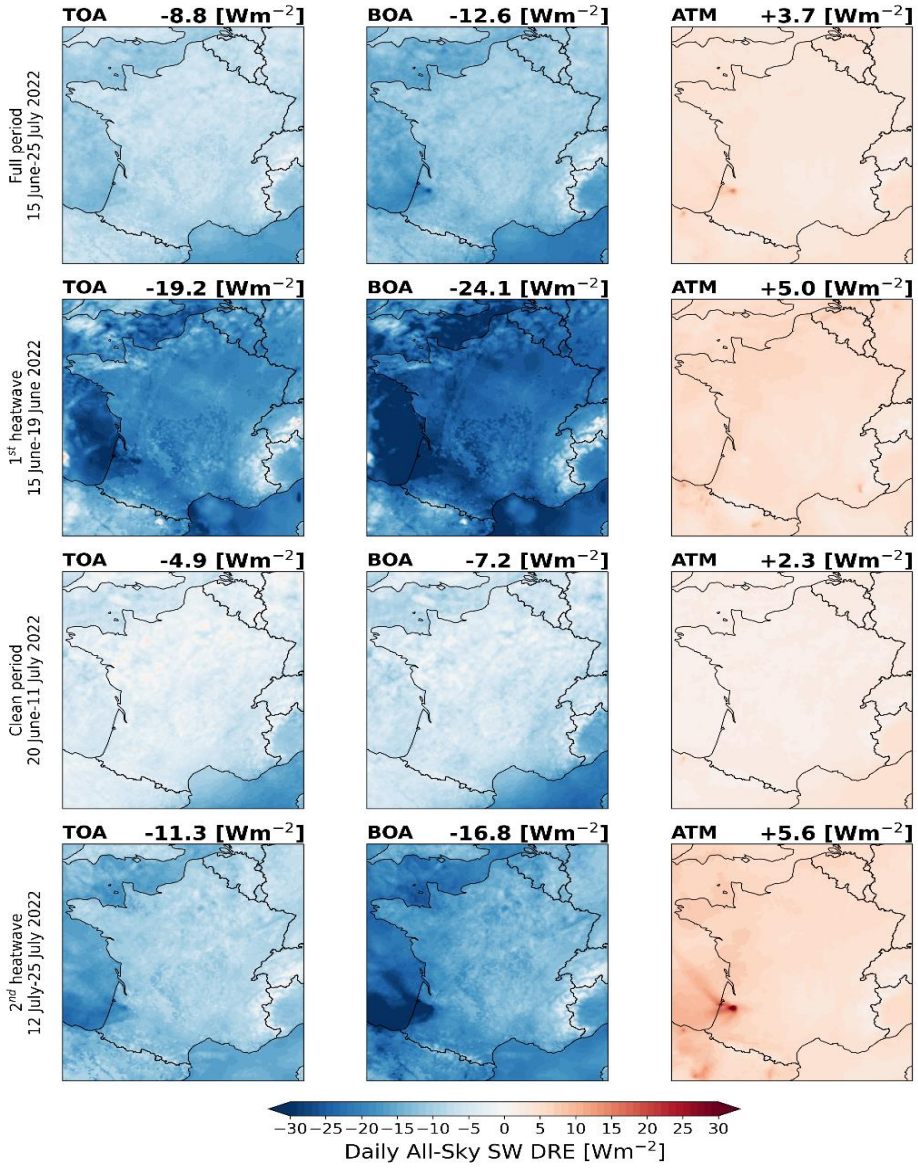

Figure 6.4 Daily All-Sky SW direct radiative effect at top of the atmosphere (TOA), bottom of the atmosphere (BOA) and atmosphere (ATM) for the France domain (42°N, 51.15°N, 3.2°E,8.5°W) at 6km resolution, divided by the different periods during the ACROSS campaign. Average aerosol optical depth at 550 nm over the France domain is 0.15, 0.32, 0.09, 0.20 respectively for the ACROSS full period, first heatwave, clean period and the second heatwave.

period (-126.8 Wm^{-2} at BOA and +43 Wm^{-2} within the atmosphere). The columnar simulated SSA at 550 nm also shown in Figure 6.3 is strongly correlated with the spatial distribution of the DREE within the ATM and explains the DREE ATM and BOA variability. A weaker single scattering albedo (SSA) induces a more positive DRE efficiency within the atmosphere, while a stronger SSA induces a more negative DREE at the BOA. On average, more absorbing aerosols are observed over northern France (reflected in a stronger DREE ATM) mainly during the clean period, when the black carbon fraction of PM_1 aerosol becomes larger due to lower regional background (See Chapter 4). The Paris

		All-sky (France)								
		SW			LW			SW+LW		
		TOA	BOA	ATM	TOA	BOA	ATM	TOA	BOA	ATM
Full period	DRE	-8.8	-12.6	+3.7	+1.0	+3.1	-2.1	-7.9	-9.5	+1.6
(15 June-25 July)	DREE	-67.9	-105.8	+38.0	+6.2	+22.9	-16.6	-61.6	-82.9	+21.3
1st heatwave	DRE	-19.2	-24.1	+5.0	+1.9	+6.2	-4.3	-17.3	-18.0	+0.7
(15 June-19 June)	DREE	-63.9	-82.6	+18.7	+4.2	+19.2	-15.0	-59.7	-63.4	+3.7
Clean period	DRE	-4.9	-7.2	+2.3	+0.5	+1.8	-1.3	-4.5	-5.5	+1.0
(20 June-11 July)	DREE	-68.5	-110.5	+42.0	+5.6	+23.1	-17.5	-62.9	-87.4	+24.5
2nd heatwave	DRE	-11.3	-16.8	+5.6	+1.5	+4.1	-2.6	-9.8	-12.7	+2.9
(12 July-25 July)	DREE	-68.2	-106.7	+38.5	+7.9	+23.8	-15.9	-60.3	-82.9	+22.6

Table 6.2: All-sky direct radiative effect and direct radiative efficiency averages for the ONLINE approach at top of the atmosphere (TOA), bottom of the atmosphere (BOA) and atmosphere (ATM) for the France domain (42°N, 51.15°N, 3.2°E,8.5°W) divided by the different periods during the ACROSS campaign. The aerosol optical depth at 550 nm averages over the France domain are 0.15, 0.32, 0.09, 0.20 respectively for the ACROSS full period, first heatwave, clean period and the second heatwave.

plume is also visible on the simulated columnar averaged SSA (showing values around 0.93 at 550 nm), suggesting that most of the aerosol loading over the column is located near the surface during this period. A similar effect is observed for the second heatwave were the Gironde biomass burning plume is visible on the SSA signal (values around 0.93) and due to transport of more absorbing aerosols (e.g. BC and biomass burning OA) are advected over the Northern France, leading to a weaker SSA signal. The clear sky DREE (at TOA, BOA and ATM) for the second heatwave differs from the first, which shows significantly weaker DREE (of a factor of two within the atmosphere) due to more scattering aerosols. This result can be justified by the fact that the presence of black carbon and organic aerosols over the column (due to BB-POA transport) induces an increase in the absorption compared to the first heatwave dominated mostly by BSOA aerosols (i.e. weak absorption) formed over central and northern France (See Chapter 5.1).

Contrary to the direct radiative efficiency within the atmosphere and BOA, the TOA DREE is more spatially homogeneous and appears to be less sensitive to the aerosol properties. A maximum is observed during the clean period (-83.8 Wm^{-2}) and a minimum during the heatwaves, with the highest values over the ocean.

One may note that, both at TOA and BOA the DREE signal over the Paris area is distinguishable from the regional surrounding, highlighting the impact of anthropogenic emissions on the regional domain. This result is complementary to what obtained in Chapter 3 where we observed a local-to-

regional enhancement on the columnar aerosol optical depth over the Paris area due to anthropogenic activities.

Concerning the longwave part of the spectrum, DRE averages show positive values at TOA and BOA, while negative within the atmosphere (Figure D.1), resulting in a weaker combined SW+LW net effect at TOA, BOA and ATM, than for SW alone (Figure D.3). The absolute ratio at the TOA of the SW/LW DRE is 8.7 (8.8) under clear-sky (all-sky) conditions across the France domain, indicating that the LW compensate for about 14% of the SW effect.

The introduction of clouds, thus under all-sky conditions, results in an attenuation of the TOA and BOA DRE and DREE values throughout the period for both SW, LW, and the net SW+LW. Results for the all-sky conditions are summarised in Tables 6.2 and D.2 for the France and Ile-de-France domains respectively. Figure 6.4 shows the SW all-sky DRE for the different periods of the ACROSS field campaign. Results highlights that clouds decrease the TOA and BOA DRE by around 20% on average for the full period, with weaker changes during heatwave periods when cloud cover was lower due to the stable anticyclonic weather conditions over France. The DRE within the atmosphere does not change significantly.

Average all-sky DRE results for the TOA, BOA and ATM are within the order of magnitude of the DRE results from (Péré et al., 2011) for western Europe (including France) for the heatwave episode occurred in August 2003. Péré et al. (2011) found a range of variability for the daily average SW TOA DRE of [-1,-12] Wm^{-2}, BOA DRE of [-10,-30] Wm^{-2} and ATM DRE of [+5,23] Wm^{-2}, which is comparable to the full period averages values that have been estimated in this work for the TOA (-8.8 Wm^{-2}), BOA (-12.6 Wm^{-2}) and ATM (+3.7 Wm^{-2}). First heatwave TOA DRE average is stronger (-19.2 Wm^{-2}) compared to what obtained from Péré et al. (2011) probably due to the strong BSOA contribution on a short time period (from 15 June to 19 June). On the contrary, the second heatwave DRE estimates are more consistent with what obtained in Péré et al. (2011).

A comparison with Mallet et al. (2022) literature survey for the Mediterranean region (where mixture of biogenic and anthropogenic aerosols occur as it is expected for the France and Ile-de-France regions) shows that the DRE is also comparable to what they report for the TOA and BOA for the SW DRE between [-9, -1.5] Wm^{-2} and [-66, -24] Wm^{-2} However, regional DRE signals are significantly heterogeneous and stronger than global averages where all-sky and clear-sky DRE TOA vary within the [-2.4, -1.46] and [-7.3, -2.6] Wm^{-2} (see literature survey in Table 1.1 from Chapter 1), demonstrating the importance of regional-scale aerosol direct radiative effect.

6.1.2 Shortwave clear-sky direct radiative effect and efficiency simulated at the urban, peri-urban and rural sites of the ACROSS campaign within the Ile-de-France region

In this paragraph, we present the results of the shortwave clear-sky direct radiative effect (DRE) and efficiency (DREE) following the ONLINE approach for the three sites characteristics of the Ile-de-France region (See Figure 6.1).

Figures 6.5 and 6.6 show the daily average SW DRE and DREE respectively for the urban Paris Rive Gauche (PRG), peri-urban (SIRTA) and rural Rambouillet Forest (RambForest) sites during the ACROSS campaign. Firstly, it can be noticed that DRE (TOA, BOA, ATM) values are very similar for the three sites, and they will thus not be distinguished in the following discussion. More strongly negative DRE values at TOA and BOA are observed during the two heatwave periods, as expected due to stronger aerosol loads (differences between the sites could be related to the different aerosol loading), while during the clean period, the DRE is close to zero. However, under heatwave conditions and with high aerosol loading, the signal becomes larger and reaches -38 Wm^{-2} for the DRE at TOA.

Concerning the TOA DREE, the day to day variability is rather low, albeit values at BOA are more negative during the clean period. Indeed, the daily BOA and ATM DREE variations are strongly anticorrelated. For positive peak values of ATM DREE, larger values occur at the urban PRG sites,

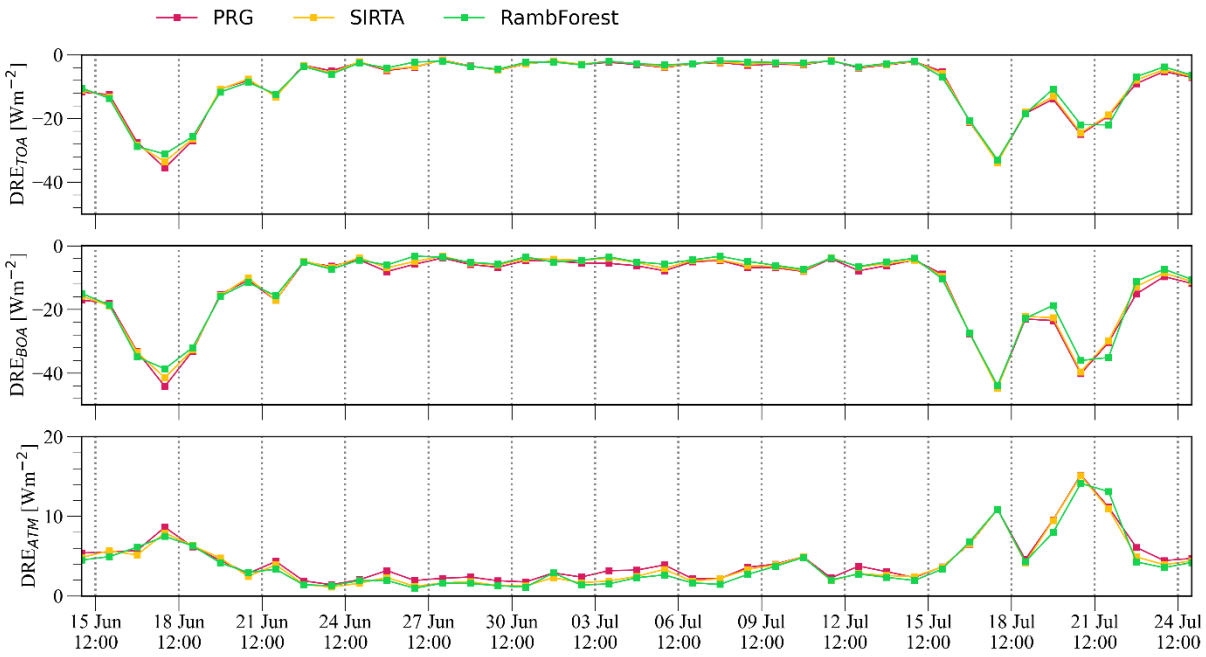

Figure 6.5 Time series of daily Clear-Sky SW direct radiative effect at top of the atmosphere (TOA), bottom of the atmosphere (BOA) and atmosphere (ATM) for the Paris Rive Gauche (PRG), SIRTA, Rambouillet Forest (RambForest) during the ACROSS campaign. The aerosol optical depth at 550 nm averages at the PRG, SIRTA and RambForest sites are 0.14, 0.35, 0.05, 0.19 respectively for the ACROSS full period (15 June-25 July), first heatwave (15 June-19 June), clean period (20 June-11 July) and the second heatwave (12 July-25 July).

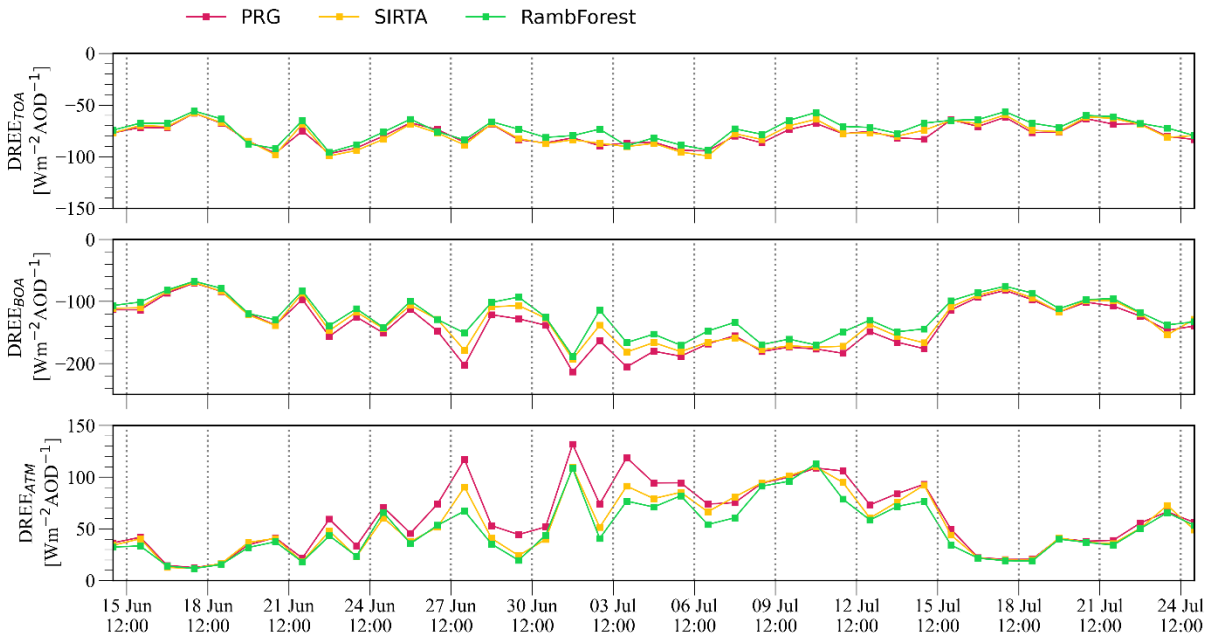

Figure 6.6 Time series of daily Clear-Sky SW direct radiative efficiency at top of the atmosphere (TOA), bottom of the atmosphere (BOA) and atmosphere (ATM) for the Paris Rive Gauche (PRG), SIRTA, Rambouillet Forest (RambForest) during the ACROSS campaign. The aerosol optical depth at 550 nm averages at the PRG, SIRTA and RambForest sites are 0.14, 0.35, 0.05, 0.19 respectively for the ACROSS full period (15 June-25 July), first heatwave (15 June-19 June), clean period (20 June-11 July) and the second heatwave (12 July-25 July).

and then at peri-urban SIRTA, and lower values at the forest site Rambouillet. These features are probably linked to larger BC to PM_1 ratios during specific days during the clean period where BC dominates the spectral optical properties. Results from the bulk chemical composition analysis (see Chapter 4), show how even a small BC concentration can decrease the surface single scattering albedo and increase the aerosol absorption, that is more pronounced at PRG urban site due to the stronger primary anthropogenic emissions.

6.2 The aerosol direct radiative effect and link to types and optical properties from WRF-CHIMERE OFFLINE coupling

6.2.1 Shortwave direct radiative effect from all the aerosol species from the OFFLINE method

In this paragraph, we present the results of the shortwave clear-sky direct radiative effect contribution estimated for several aerosol species (i.e. black carbon, BSOA, ASOA and biomass burning organic aerosols) following the OFFLINE approach (See Figure 6.1).

Firstly, we compare the OFFLINE DRE results with the ONLINE approach, which under clear-sky condition have to be similar (despite not exactly equal since the WRF-CHIMERE ONLINE coupling has an impact on the aerosol spectral optical properties and radiation fields, in turn impacting on the DRE, external or core-shell mixing assumption, numerical differences…). Successively, we present

the estimation of the DRE contribution of several simulated aerosol species such black carbon, biogenic and anthropogenic SOA and biomass burning organic aerosols.

The full period averages over the France domain and for the different ACROSS periods considering all the aerosol species are presented in Figure D.7 for the CHIMERE (external mixing), FlexAOD (external mixing) and OPTSIM (core-shell mixing) models (i.e. estimated applying the developed offline interface on the vertically resolved spectral optical properties) and compared to the results from the ONLINE simulation in Table D.3.

Small differences (of the order of 5%) are observed when comparing the direct radiative effect estimations from all the aerosol species calculated from the ONLINE and OFFLINE (external mixing) from the CHIMERE vertically-resolved spectral optical properties (i.e. applying the OFFLINE approach to the CHIMERE outputs directly). On the contrary, stronger differences (of the order of 15-20%) are observed between the ONLINE and the OFFLINE simulations when all species are simulated using the FlexAOD and OPTSIM models. These differences may be due to two combined effects: i) the ONLINE simulation rapidly adjusts to the meteorological changes due to aerosol effect on radiation and meteorology, impacting the radiative effect (and this could explain the 5% difference between the CHIMERE ONLINE and OFFLINE DRE simulations); ii) estimating the direct radiative effect from the offline optical properties may lead to numerical differences. For instance, some numerical differences may arise from i) the reproduction of the numerical calculations performed within the WRF-CHIMERE model from the OFFLINE approach, starting from the CHIMERE and WRF outputs (e.g. the estimation of the meteorological parameters such as the pressure and temperature model half and interface layers) and ii) the sensitivity to the size distribution interpolation that CHIMERE performs within the optical model (see Chapter 2) and that it is not included by the OPTSIM and FlexAOD models, leading to a 10% difference in the AOD at 440 nm (See Chapter 5.2), which in turn may propagate on the DRE estimation, leading to differences up to 20% (See Table D.3)

Due to these numerical effects, differences in the ONLINE and OFFLINE DRE estimations (for the same external mixing assumption) cannot be attributed to the semi-direct effect. Nevertheless, between the CHIMERE ONLINE and OFFLINE DRE estimations differs by less than 5% at TOA, BOA and ATM, and DRE spatial patterns are reproduced, suggesting that the OFFLINE model can be used to calculate the different contributions of aerosol species (DRE at TOA, BOA and ATM).

Indeed, the DRE has been estimated by excluding the specific aerosol species (i.e. difference between simulation with and without the specific aerosol species), both with the FlexAOD (external mixing) and OPTSIM (core-shell) models. Results both for the external mixing and core-shell average shortwave daily clear-sky ΔDRE (at TOA, BOA and within the atmosphere) due to black carbon

	SW Clear-sky ΔDRE for the France domain														
	All			**BC**			**BB-POA**			**BSOA**			**ASOA**		
	TOA	**BOA**	**ATM**	**TOA**	**BOA**	**ATM**	**TOA**	**BOA**	**ATM**	**TOA**	**BOA**	**ATM**	**TOA**	**BOA**	**ATM**
EXT_F[a]	-8.6	-12.7	+4.0	+0.50	-1.45	+1.94	-0.36	-0.72	+0.37	-1.92	-2.06	+0.14	-0.59	-0.60	+0.00
CS[a]	-8.0	-13.4	+5.3	/	/	/	-0.23	-0.77	+0.54	-1.52	-2.68	+1.16	-0.41	-0.84	+0.42
EXT_F[b]	-16.7	-22.1	+5.5	+0.49	-1.57	+2.06	-0.14	-0.30	+0.16	-3.73	-4.04	+0.30	-1.07	-1.11	+0.03
CS[b]	-15.8	-23.4	+7.7	/	/	/	-0.12	-0.28	+0.16	-3.12	-4.99	+1.87	-0.71	-1.61	+0.90
EXT_F[c]	-5.4	-8.0	+2.6	+0.40	-1.14	+1.54	-0.04	-0.08	+0.04	-0.94	-1.00	+0.06	-0.39	-0.39	+0.00
CS[c]	-5.5	-7.7	+2.3	/	/	/	-0.03	-0.07	+0.04	-0.83	-1.15	+0.32	-0.30	-0.50	+0.19
EXT[d]	-10.8	-16.7	+5.8	+0.66	-1.88	+2.54	-0.94	-1.89	+0.96	-2.80	-3.02	+0.22	-0.74	-0.74	-0.01
CS[d]	-9.3	-18.7	+9.3	/	/	/	-0.59	-2.05	+1.46	-2.03	-4.26	+2.24	-0.48	-1.09	+0.61

[a]Full period (15 June-25 July 2022)
[b]First heatwave (15 June-19 June 2022)
[c]Clean period (20 June-11 July 2022)
[d]2nd heatwave (12 July-25 July 2022)

Table 6.3: Summary of daily clear-sky SW direct radiative effect for all the species and specifically for the black carbon (BC), primary biomass burning (BB-POA), anthropogenic and biogenic SOA (BSOA and ASOA) calculated from the FlexAOD model (EXTF) and the Core-shell model (CS) for the France domain (42°N, 51.15°N, 3.2°E,8.5°W) at 6km resolution and during the ACROSS campaign. The slash sign indicates the missing data.

(BC), primary biomass burning organic aerosols (BB-POA), biogenic SOA (BSOA) and anthropogenic SOA (ASOA) are summarised in Table 6.3 for the different ACROSS periods and for the France domain. Additionally, spatial ΔDRE (at TOA, BOA and within the atmosphere patterns) for the France domain and for the aforementioned aerosol species are depicted in Figures 6.7-6.13 both under external and core-shell assumptions and divided by the different ACROSS periods. Notice that black carbon DRE has been estimated only under the external mixing assumption due to the core-shell model definition (i.e. BC in the core).

Black carbon. Black carbon absorbs the solar radiation within the atmospheric column, representing the major aerosol contributor in reducing (in absolute value) the TOA DRE. An average positive BC TOA ΔDRE of +0.50 Wm^{-2} over the France domain and of +0.65 Wm^{-2} for the Ile-de-France domain has been estimated for the full campaign period. This result is comparable to the literature survey in Saleh et al. (2015), which points out that the BC ΔDRE strongly depends on the BC mixing state (external or internal) and varies between +0.3 and +1.05 Wm^{-2} (if accounting for both model and observationally constrained studies), even if conditions in our study may be different than in Saleh et al., (2015).

Additionally, BC accounts for the most significant positive signal both at the TOA and within the atmosphere (up to 30% under external mixing assumption, showing that larger BC ΔDRE is observed

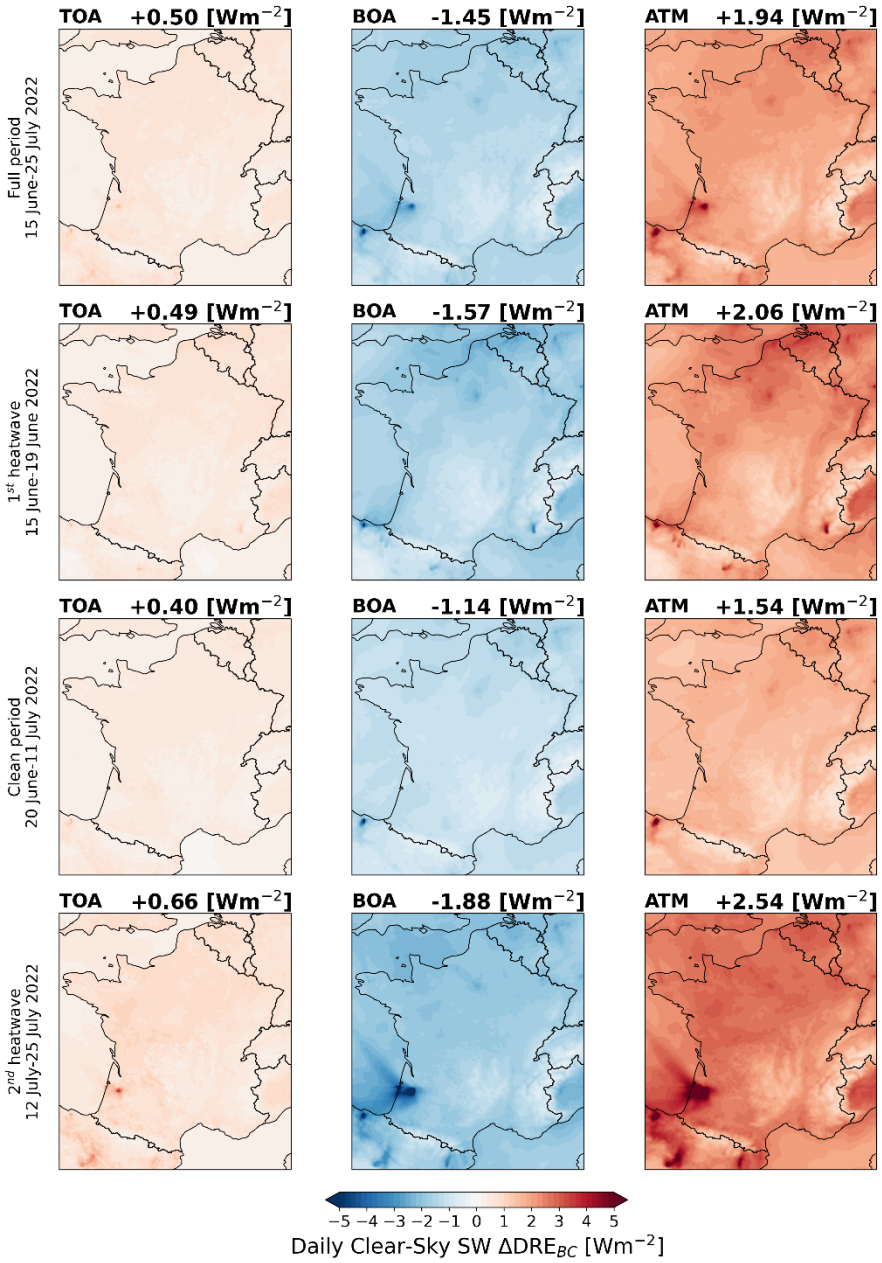

Figure 6.7 External mixing black carbon daily Clear-Sky SW direct radiative effect at top of the atmosphere (TOA), bottom of the atmosphere (BOA) and atmosphere (ATM) for the France domain (42°N, 51.15°N, 3.2°E,8.5°W) at 6km resolution, divided by the different periods during the ACROSS campaign.

over Northern France, further confirming our assumption in the discussion of Figure 6.3, which illustrates that the larger ATM contribution to the total absorption is obtained dividing the BC ATM ΔDRE with respect to the ATM DRE from all aerosol species). Figure 6.7 depicts the spatial and temporal distribution of the DRE values due to BC under external mixing assumption. Maximum BC ΔDRE is observed during the second heatwave (average BC ΔDRE of +0.66 Wm^{-2}, -1.88 Wm^{-2}, +2.54 Wm^{-2} respectively at the TOA, BOA and ATM over the France domain) due to the high black carbon concentration linked to the wildfires activity, in particular over the Aquitaine region in SW France during this period (Menut et al., 2023). Indeed, the wildfire hotspots are clearly visible within

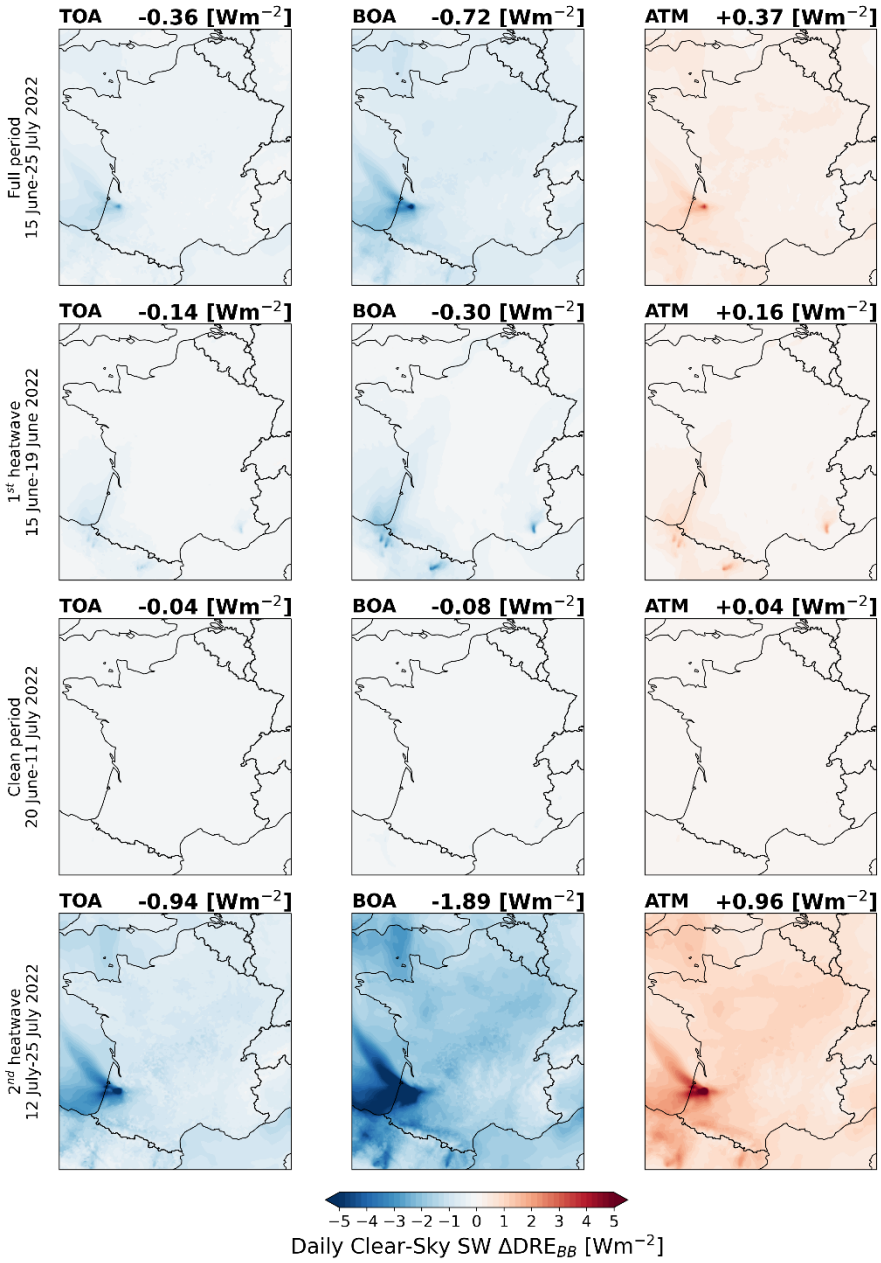

Figure 6.8 External mixing primary biomass burning (BB-POA) daily Clear-Sky SW direct radiative effect at top of the atmosphere (TOA), bottom of the atmosphere (BOA) and atmosphere (ATM) for the France domain (42°N, 51.15°N, 3.2°E,8.5°W) at 6km resolution, divided by the different periods during the ACROSS campaign.

Figure 6.7 at TOA, BOA and ATM. On the contrary, the minimum DRE BC contribution is observed during the clean period (average BC DRE of +0.40 Wm^{-2}, -1.14 Wm^{-2}, +1.54 Wm^{-2} respectively at the TOA, BOA and ATM over the France domain), with no clear spatial pattern. However, the Paris area is visible at BOA and ATM across all the field campaign periods, with less impact over the TOA DRE, where only the fire hotspot is visible.

Primary biomass burning. Figure 6.8 and 6.9 show the primary biomass burning organic aerosol DRE spatial distribution under the external mixing (EXT) and core-shell (CS) assumptions

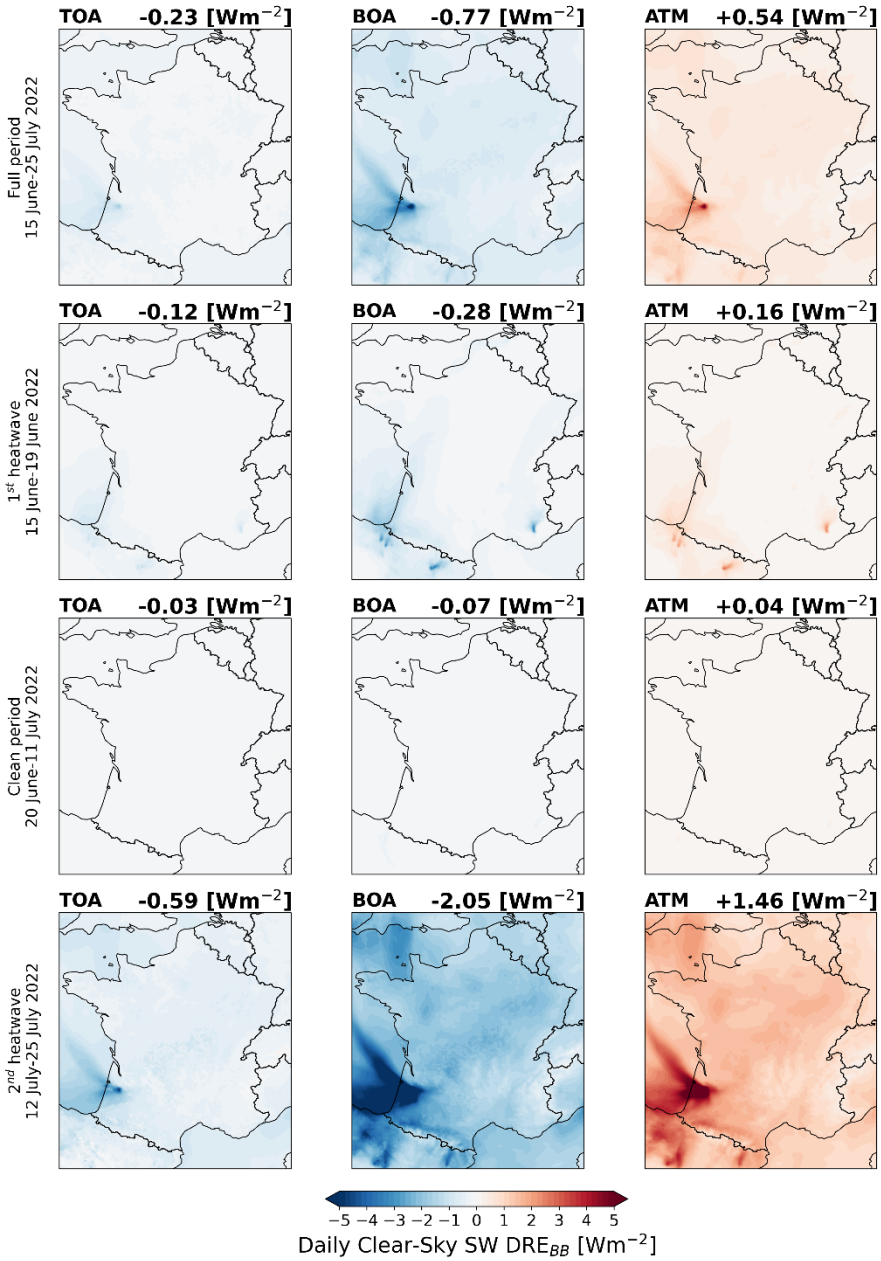

Figure 6.9 Core-shell mixing primary biomass burning (BB-POA) daily Clear-Sky SW direct radiative effect at top of the atmosphere (TOA), bottom of the atmosphere (BOA) and atmosphere (ATM) for the France domain (42°N, 51.15°N, 3.2°E,8.5°W) at 6km resolution, divided by the different periods during the ACROSS campaign.

respectively for the different periods of the ACROSS field campaign. This class of species has been isolated from primary organic emissions in order to specifically trace the wildfire impact within the simulated domain. Results show negative TOA and BOA ΔDRE (more negative at BOA) across all the periods with slightly different contributions under the two mixing state assumption (full period TOA ΔDRE averages of -0.36 and -0.23 Wm^{-2} respectively under EXT and CS assumptions). Although the complex refractive index attributed for this simulation for the BB-POA species from Saleh et al. (2015) includes the brown carbon absorption, the TOA signal is still negative, contrary

to what happens for BC (due to the stronger absorption of the latter). Biomass burning aerosols mostly negatively contribute to the total TOA DRE and may be enhanced over bright surfaces (Konovalov et al., 2023b). (Rap et al., 2013; Ward et al., 2012) estimated a global annual mean SW clear sky TOA DRE due to wildfire in the [-0.27, -0.06] Wm^{-2} range. However, the TOA BB-POA DRE magnitude can vary regionally and due to the intensity of the wildfire activity: Konovalov et al., (2023) estimated a SW TOA DRE between -5.96 and -2.77 Wm^{-2} for the Siberian fires, while Zhuravleva et al. (2019) shows that it can reach up to -17 Wm^{-2} over the region. Feng and Christopher (2014) reported a value range of -5.6 Wm^{-2} for biomass burning aerosols over the Southeast Asia, while monthly values between -7.6 and -9.1 Wm^{-2} over southern Africa (Abel et al., 2005).

During the second heatwave (such as for the black carbon DRE) due to the intense wildfire activity over Southern Western France the TOA DRE rises up to -0.94 and -0.59 Wm^{-2} for the EXT and CS cases respectively, when averaged over France. In particular, a strong positive atmospheric BB-POA ΔDRE of +0.96 and +1.46 Wm^{-2} respectively under the EXT and CS mixing assumptions is observed, reaching 40% compared to the ATM BC ΔDRE. The atmospheric ΔDRE is rather amplified in the CS compared to the EXT due to the "lensing effect" (Konovalov et al., 2023b; Liu et al., 2017; Saleh et al., 2015; Zhang et al., 2018) and reduces the TOA contribution (from -0.94 to -0.59 Wm^{-2}). Indeed, the black carbon absorbing core-surrounded by the scattering shell allows for absorption enhancement due to due multiple scattering redirection of the light towards the core.

The magnitude of the absorption enhancement depends on several factor such as the core-diameter, the coating thickness of the shell and also the complex refractive index (Zhao et al., 2020b). Denjean et al. (2020) show that the coating over the black carbon cores enhance the light absorption by a factor of about 2 for biomass burning fires over West Africa.

In our study, we find a factor of 1.5 absorption enhancement (with the simulated ΔDRE ATM) both over France and specifically over the Gironde fire hotspot (43.90°N, 44.80°N, 1.20°E, 0.05°E).

Biogenic SOA. Figure 6.10 and 6.11 depict the biogenic secondary organic aerosol (formed from forest and wildfire biogenic emissions) ΔDRE spatial distribution at the TOA, BOA and ATM under

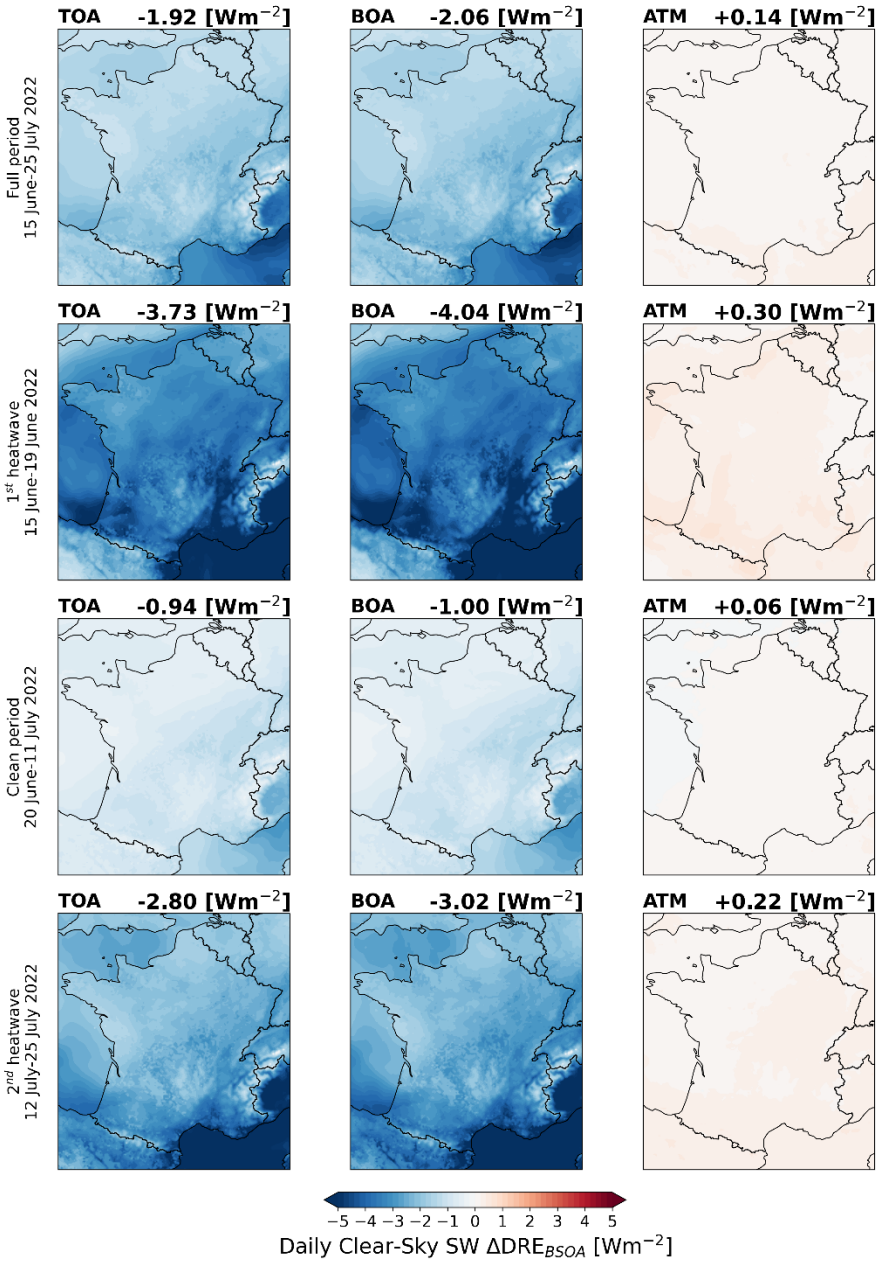

Figure 6.10: External mixing biogenic secondary organic aerosol daily Clear-Sky SW direct radiative effect at top of the atmosphere (TOA), bottom of the atmosphere (BOA) and atmosphere (ATM) for the France domain (42°N, 51.15°N, 3.2°E,8.5°W) at 6km resolution, divided by the different periods during the ACROSS campaign.

the EXT and CS respectively and for the different periods of the ACROSS field campaign. Strong TOA and BOA contribution of the BSOA is observed during the two heatwaves, with a maximum over the first heatwave period (TOA ΔDRE averages of -3.73 and -3.12 Wm^{-2} respectively under EXT and CS assumptions) due to the amplified BSOA formation with temperature (See Chapter 5.1). This value is significantly higher compared to the -0.29 Wm^{-2} global mean clear-sky DRE found from O'Donnell et al. (2011), the global all-sky DRE from Scott et al. (2014) between -0.08 and -0.78 Wm^{-2} (stronger at the tropics due to strong BVOC emissions) and the monthly averaged of China of -0.46 Wm^{-2} from Yin et al. (2015). The BSOA ΔDRE is stronger over Southern France, likely due to the

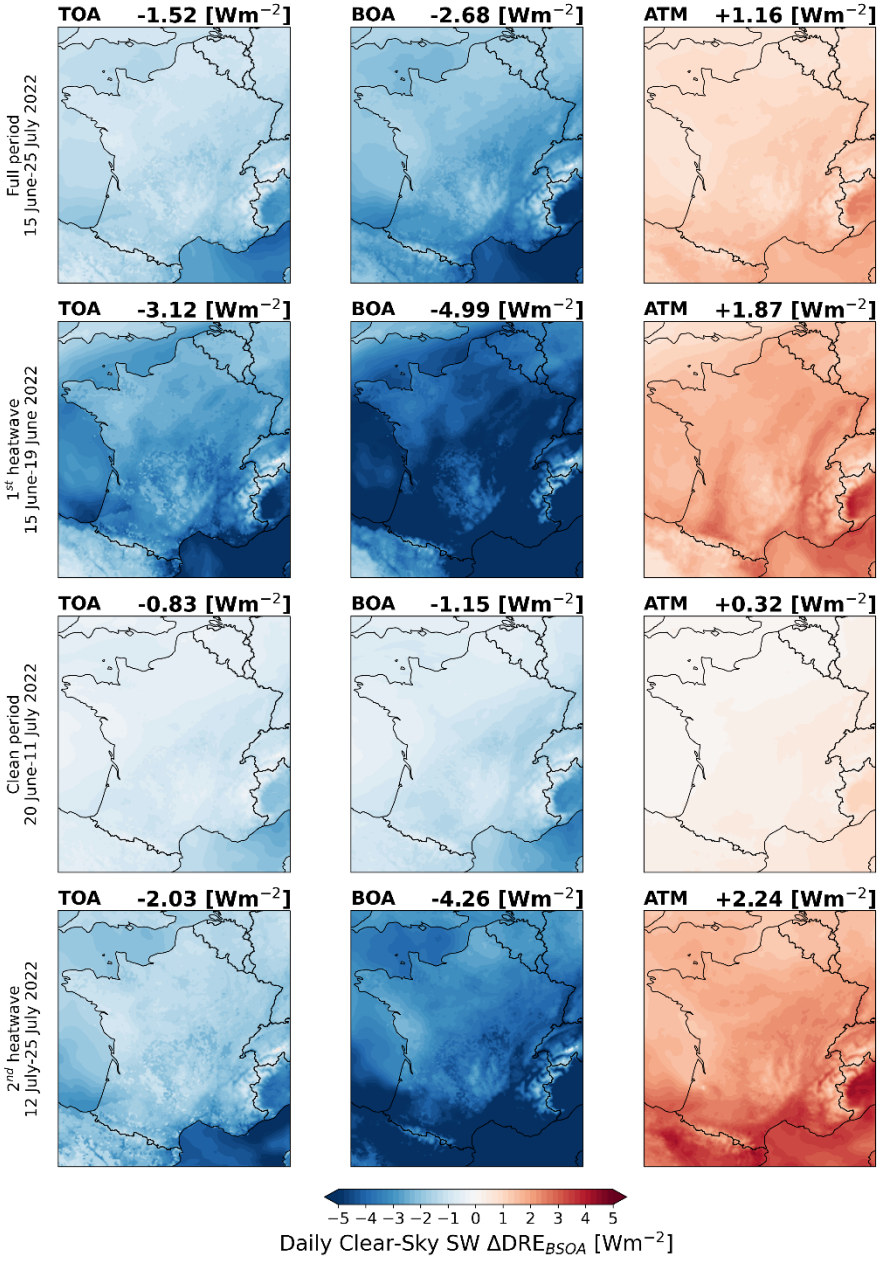

Figure 6.11: Core-shell mixing biogenic secondary organic aerosol Daily Clear-Sky SW direct radiative effect at top of the atmosphere (TOA), bottom of the atmosphere (BOA) and atmosphere (ATM) for the France domain (42°N, 51.15°N, 3.2°E,8.5°W) at 6km resolution, divided by the different periods during the ACROSS campaign.

concentration of forested areas and therefore biogenic emissions in that region. The strong signal over the ocean can be associated to the transport of the BSOA due to northerly winds during the period. On the contrary, the minimum contribution is estimated for the clean period with TOA DRE averages of -0.94 and -0.83 Wm^{-2} respectively under EXT and CS assumptions due to lack of intense BSOA formation.

Nevertheless, it is important to notice that the interaction between biogenic and anthropogenic aerosols leads to a strong absorption enhancement within the atmosphere. Under the EXT assumption the maximum average BSOA ATM ΔDRE attests at +0.30 Wm^{-2} during the first heatwave, which is

relatively weak due to the weak absorbing imaginary component (absorbing mainly at UV and much less in the visible attributed to the BSOA compounds, see Table 2.8 in Chapter 2 for the BSOA complex refractive index). However, under the CS assumption the BSOA ATM ΔDRE rises up to +1.87 Wm^{-2} which is a factor of six stronger than the EXT value. This is due to so-called the lensing effect (Saleh et al., 2015; Zhang et al., 2018): enhanced BSOA concentrations increase the thickness of the shell, which then focusses more radiation onto the BC core, and thus enhances the absorption of the particle. Taking into account this lensing effect is one of the strengths of the core-shell model.

The aforementioned absorption enhancement is therefore further amplified during the heatwave periods due to the increased biogenic secondary aerosol loadings (i.e. biogenic emissions may enhance due to the rise in temperature) and it reaches the maximum for the CS during the second heatwave (+2.24 Wm^{-2}), corresponding to the 24% of the total ATM ΔDRE (considering all the aerosol species), stronger compared to the 8% obtained with the EXT mixing assumption.

Anthropogenic SOA. Figure 6.12 and Figure 6.13 show the anthropogenic secondary organic aerosol (ASOA) ΔDRE spatial distribution at the TOA, BOA and ATM under the EXT and CS respectively and for the different periods of the ACROSS field campaign. The ASOAs negatively contribute to the TOA and BOA ΔDRE, showing full ACROSS campaign average TOA ΔDRE of -0.59 and -0.41 Wm^{-2} and BOA ΔDRE of -0.60 and -0.84 Wm^{-2} under the EXT and CS mixing respectively. Stronger DRE is also observed during the heatwaves, potentially due to the increase availability of oxidants (such as ozone), which may enhance the secondary aerosol formation. Spracklen et al. (2011) estimated a global mean all-sky TOA direct radiative effect of -0.26 Wm^{-2} for the ASOA, while Yin et al. (2015) estimated all-sky TOA DRE of -0.66 Wm^{-2} estimated over the China region, comparable to the clear-sky value obtained in this study.

However, it is important to notice that the ATM ASOA ΔDRE remains negligible under the external mixing assumption, while an absorption enhancement, such as for BB-POA and BSOA (resulting from the CS model) is observed, exhibiting an average value of +0.42 Wm^{-2}, 60% lower compared

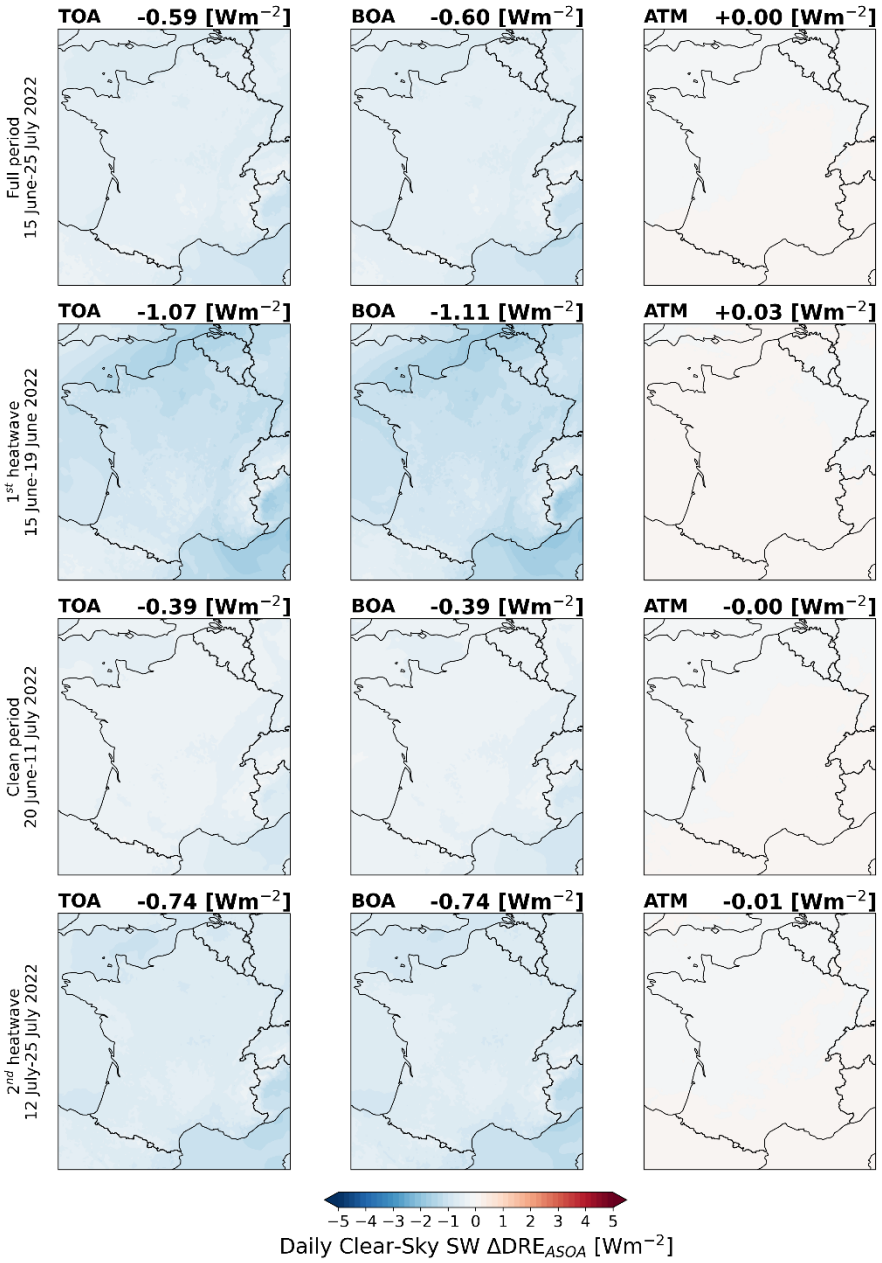

Figure 6.12 External mixing anthropogenic secondary organic aerosol Daily Clear-Sky SW direct radiative effect at top of the atmosphere (TOA), bottom of the atmosphere (BOA) and atmosphere (ATM) for the France domain (42°N, 51.15°N, 3.2°E,8.5°W) at 6km resolution, divided by the different periods during the ACROSS campaign.

to the BSOA contribution. This result could be linked to the different aerosol loadings between the ASOA and BSOA. In fact, surface ASOA concentrations are on average half of BSOA (even lower during the heatwave reaching the 37% of the BSOA loading) which in turn may contribute to a small ATM ASOA ΔDRE signal under the external mixing, although the ASOA absorption (i.e. imaginary complex refractive index) is higher (in the UV part of the spectrum) compared to the BSOA (See Chapter 2).

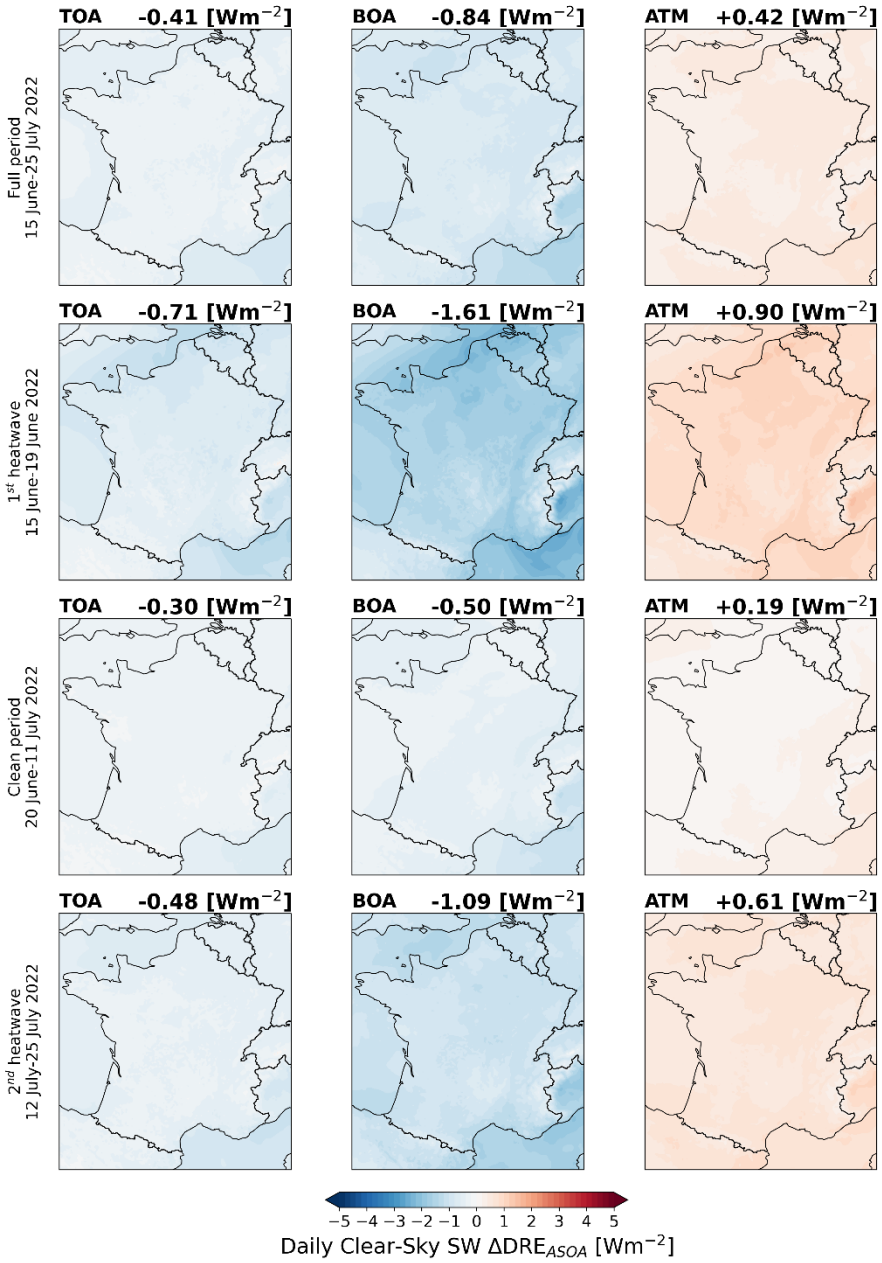

Figure 6.13 : Core-shell mixing anthropogenic secondary organic aerosol Daily Clear-Sky SW direct radiative effect at top of the atmosphere (TOA), bottom of the atmosphere (BOA) and atmosphere (ATM) for the France domain (42°N, 51.15°N, 3.2°E,8.5°W) at 6km resolution, divided by the different periods during the ACROSS campaign.

6.2.2 Shortwave direct radiative effect of BC, BSOA, ASOA and BB-POA in Ile-de-France region

In this paragraph, we present the black carbon, biogenic and anthropogenic secondary organic aerosols and primary biomass burning contribution to the DRE at the regional scale of the Ile-de-France. Figure 6.14 shows the average daily clear-sky ΔDRE averaged on the region on the for the

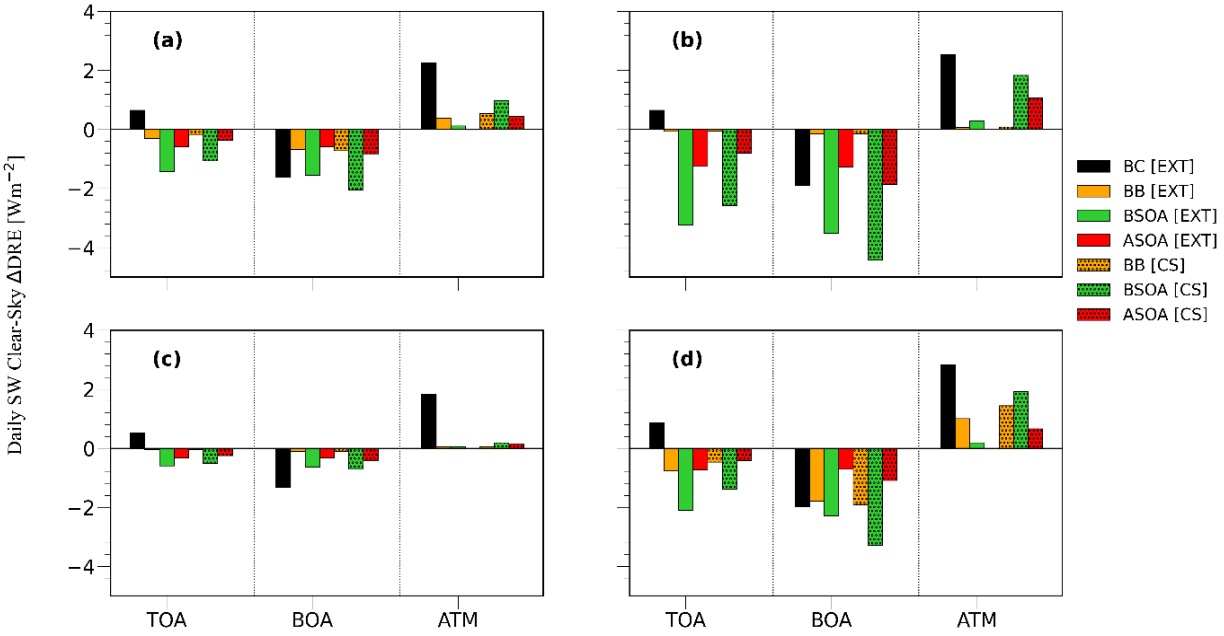

Figure 6.14 Summary of daily clear-sky SW ΔDRE for (a) the full ACROSS campaign from the 15 June to 25 July 2022, (b) the 15 June-19 June 2022 (first heatwave), (c) 20 June-11 July 2022 (clean period), (d) 12 July-25 July 2022 (second heatwave) of black carbon (BC), biomass burning (BB-POA), anthropogenic and biogenic SOA (BSOA and ASOA) direct radiative effect at the top of the atmosphere (TOA), bottom of the atmosphere (BOA) and atmosphere (ATM) from the FlexAOD model (EXT) and the Core-shell model (CS) for the Ile-de-France domain (48.1°N, 49.26 °N, 3.57°E, 1.47°W) at 6km resolution and during the ACROSS campaign. The term "BC [EXT]" stands for the direct radiative effect simulation performed with spectral AOD, SSA and g, calculated with and without including the black carbon under external mixing assumption. Analogous formulations can be obtained for the other legend labels.

TOA, BOA, and within the atmosphere and under the EXT and CS mixing assumption. Summary of the DRE is also available in Table 6.7.

Black carbon is the primary contributor at all levels (TOA, BOA, ATM). However, under heatwave conditions, BSOA aerosols exhibit a larger influence compared to black carbon (both under external and core-shell mixing state). In fact, the TOA and BOA BSOA DRE absolute values under external mixing assumption are higher compared to those of BC (by a factor of two at the TOA). This result does not occur during the clean period, characterised by low aerosol loading over the region (in particular low BSOA concentrations), indicating that the BOA DRE within the Ile-de-France is interestingly dominated by the black carbon extinction, which in turn reduces the overall negative DRE (considering all the aerosol species). Conversely, under heatwave conditions, BSOA plays a dominating role in contributing to negative DRE even at the Ile-de-France regional scale. Under the core-shell assumption, the absolute BSOA contribution within the atmosphere strongly increases (six times higher than external mixing), leading to a less negative BSOATOA ΔDRE contribution (less

	SW Clear-sky ΔDRE for the Ile-de-France domain														
	All			BC			BB-POA			BSOA			ASOA		
	TOA	BOA	ATM	TOA	BOA	ATM	TOA	BOA	ATM	TOA	BOA	ATM	TOA	BOA	ATM
EXT_F[a]	-6.8	-10.9	+4.1	+0.65	-1.61	+2.26	-0.30	-0.68	+0.38	-1.43	-1.55	+0.12	-0.58	-0.57	0.00
CS[a]	-6.3	-11.3	+5.0	/	/	/	-0.19	-0.72	+0.53	-1.07	-2.05	+0.98	-0.38	-0.82	+0.44
EXT_F[b]	-17.1	-23.5	+6.3	+0.65	-1.89	+2.54	-0.06	-0.15	+0.08	-3.23	-3.52	+0.29	-1.25	-1.27	+0.02
CS[b]	-16.2	-24.8	+8.6	/	/	/	-0.05	-0.14	+0.09	-2.58	-4.42	+1.84	-0.80	-1.87	+1.07
EXT_F[c]	-3.2	-5.6	+2.4	+0.52	-1.32	+1.84	-0.05	-0.10	+0.05	-0.59	-0.63	+0.04	-0.32	-0.32	0.00
CS[c]	-3.4	-5.1	+1.7	/	/	/	-0.04	-0.09	+0.05	-0.52	-0.71	+0.19	-0.25	-0.40	+0.16
EXT[d]	-8.8	-14.8	+6.0	+0.86	-1.97	+2.83	-0.77	-1.78	+1.01	-2.38	-3.30	+0.19	-0.73	-0.71	-0.02
CS[d]	-7.4	-16.4	+9.0	/	/	/	-0.47	-1.91	+1.44	-1.38	-3.30	+1.92	-0.43	-1.09	+0.66

[a]Full period (15 June-25 July 2022)
[b]First heatwave (15 June-19 June 2022)
[c]Clean period (20 June-11 July 2022)
[d]2nd heatwave (12 July-25 July 2022)

Table 6.4: Summary of daily clear-sky SW direct radiative effect for all the species and specifically for the black carbon (BC), primary biomass burning (BB-POA), anthropogenic and biogenic SOA (BSOA and ASOA) calculated from the FlexAOD model (EXTF) and the Core-shell model (CS) for the Ile-de-France domain (48.1°N, 49.26 °N, 3.57°E, 1.47°W) at 6km resolution and during the ACROSS campaign. The slash sign indicates the missing data.

radiation back to space compared to the external mixing case), and to a more negative one for BSOA BOA ΔDRE. Considering the anthropogenic secondary organic aerosols, significant DRE are observed only during the heatwave conditions probably due more favourable conditions for secondary pollutants build-up (increased local pollution accumulation, advection, higher availability of oxidants such as ozone. Indeed, a strong ATM DRE enhancement over the region is observed with maximum average value of +1.07 Wm^{-2} under the CS mixing (obtained for the second heatwave) and which is more than two times stronger than the average value obtained at the France domain scale.

Finally, it is important to investigate the primary biomass burning aerosol contribution over the Ile-de-France region mainly due to the intense fire activities over Europe (in particular South-Western France) during summer 2022 and that have been transported over the region on the 19 July 2022. Results show that during the second heatwave the BB-POA exhibits an ATM DRE of +1.01 Wm^{-2} and +1.44 Wm^{-2} respectively for the external and core-shell mixing, lower than the BSOA contribution, but higher than the ASOA, suggesting the important the BB-POA contribution over the region during this period.

6.3 Meteorological feedbacks

Aerosols impact meteorology and cloud microphysics through their interaction with solar radiation. In this paragraph, the WRF-CHIMERE model coupling capability is used to investigate the impact of aerosol radiative effect on various meteorological parameters, including surface temperature, wind speed and planetary boundary layer height. Figures 6.15-17 show the results for the temperature, wind speed and PBL differences (with and without aerosols) for the Ile-de-France domain, while Figures A8-A10 for the France domain, respectively for the different ACROSS periods. Figure 6.15 shows that introducing aerosols in the simulation (meteorological coupling activated), the daily surface temperature decreases (up to -0.28 K over the Ile-de-France and -0.48 K at the France domains respectively) especially where negative SW+LW BOA DRE occurs (Figure D.6), due to a reduction in the radiation reaching the surface.

Shortwave radiation contributes more during the day, whereas longwave radiation is present both day and night. In the Ile-de-France domain, the Paris metropolitan area is more pronounced compared to

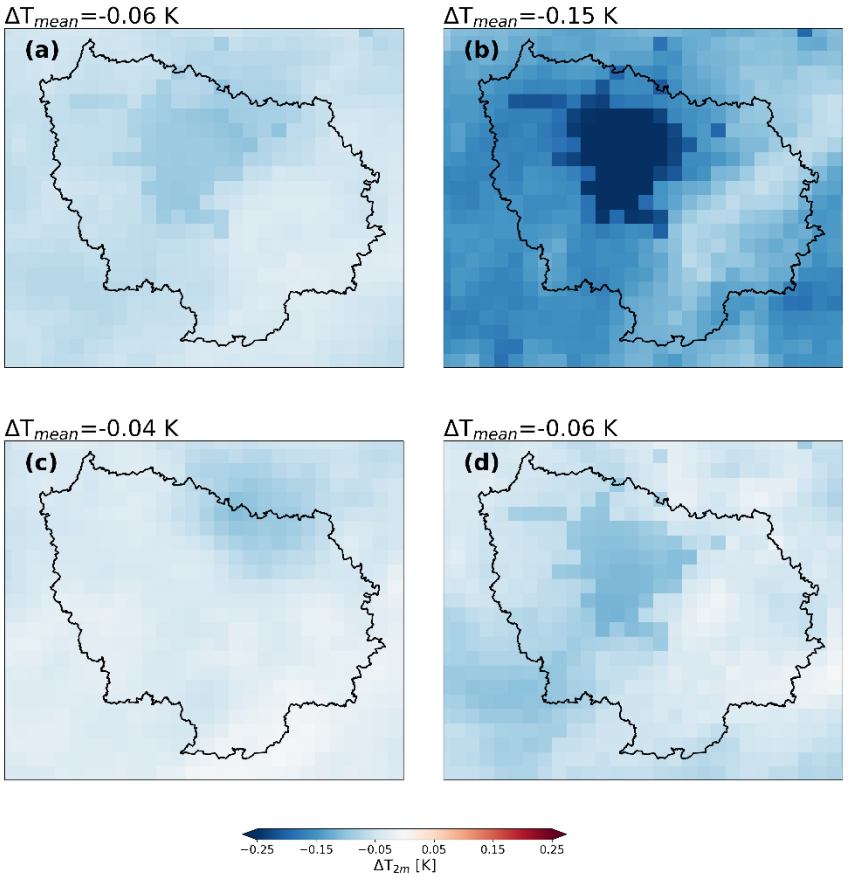

Figure 6.15: Daily mean 2m temperature differences between coupled and not-coupled simulations for (a) the full ACROSS campaign from the 15 June to 25 July 2022, (b) the 15 June-19 June 2022 (first heatwave), (c) 20 June-11 July 2022 (clean period), (d) 12 July-25 July 2022 (second heatwave) using the ONLINE approach for the Ile-de-France domain (48.1°N, 49.26 °N, 3.57°E, 1.47°W) divided by the different periods during the ACROSS campaign.

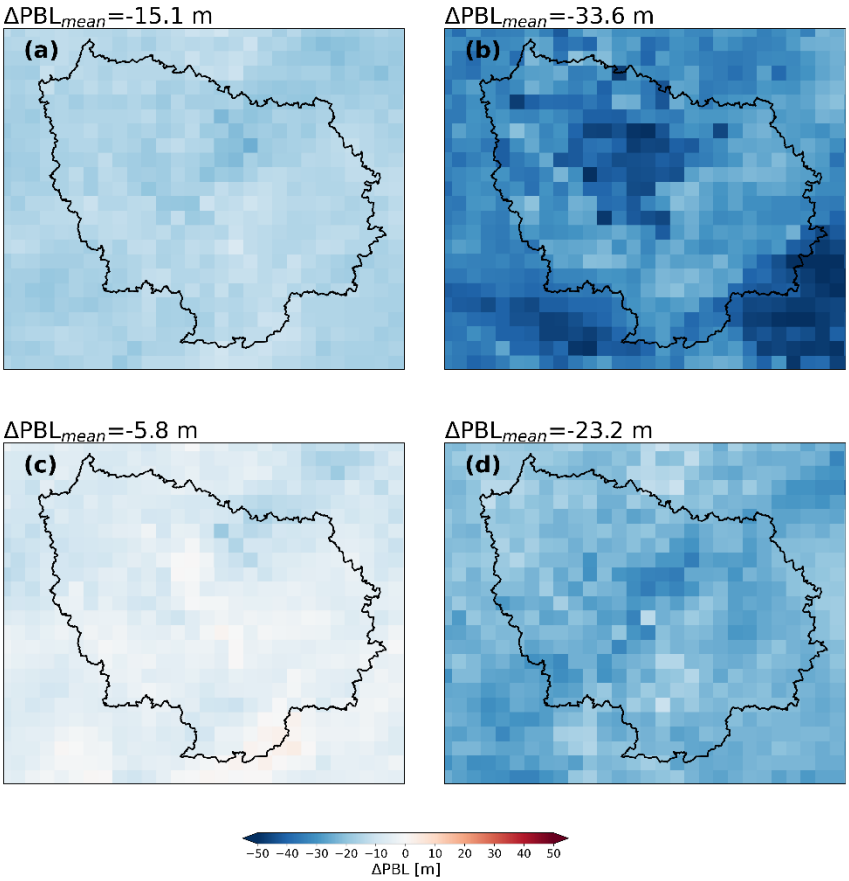

Figure 6.16: Daily mean planetary boundary layer differences between coupled and not-coupled simulations for (a) the full ACROSS campaign from the 15 June to 25 July 2022, (b) the 15 June-19 June 2022 (first heatwave), (c) 20 June-11 July 2022 (clean period), (d) 12 July-25 July 2022 (second heatwave) using the ONLINE approach for the for the Ile-de-France domain (48.1°N, 49.26 °N, 3.57°E, 1.47°W) divided by the different periods during the ACROSS campaign.

the surrounding area and with strongest surface temperature decrease under heatwave conditions (average value of -0.15 K and -0.06 K for the first and second heatwave respectively) compared to the clean period (-0.04 K), due to higher aerosol loadings during heatwave periods. Péré et al. (2011) observed a value of the order of -0.1 K for the Northern France (in particular over the Ile-de-France region), comparable to the heatwave conditions observed within the ACROSS field campaign (See Figure 6.16), while a stronger decrease between -0.1 and -0.3 K has been observed for Southern France, comparable to what it has been observed within this study (See Fig. A 8). Briant et al. (2017) also observed a decrease in the 2m temperature between 0 and -0.45 K over France for the June-July 2012 period.

A lower surface temperature may lead to a weaker development of the planetary boundary layer (PBL). Figure 6.16 show the PBL difference between coupled and not-coupled simulation, for the different periods of the ACROSS field campaign. Indeed, a PBL decrease of up to -34 and -133 m is simulated across the entire Ile-de-France and France domains respectively (obtained during the

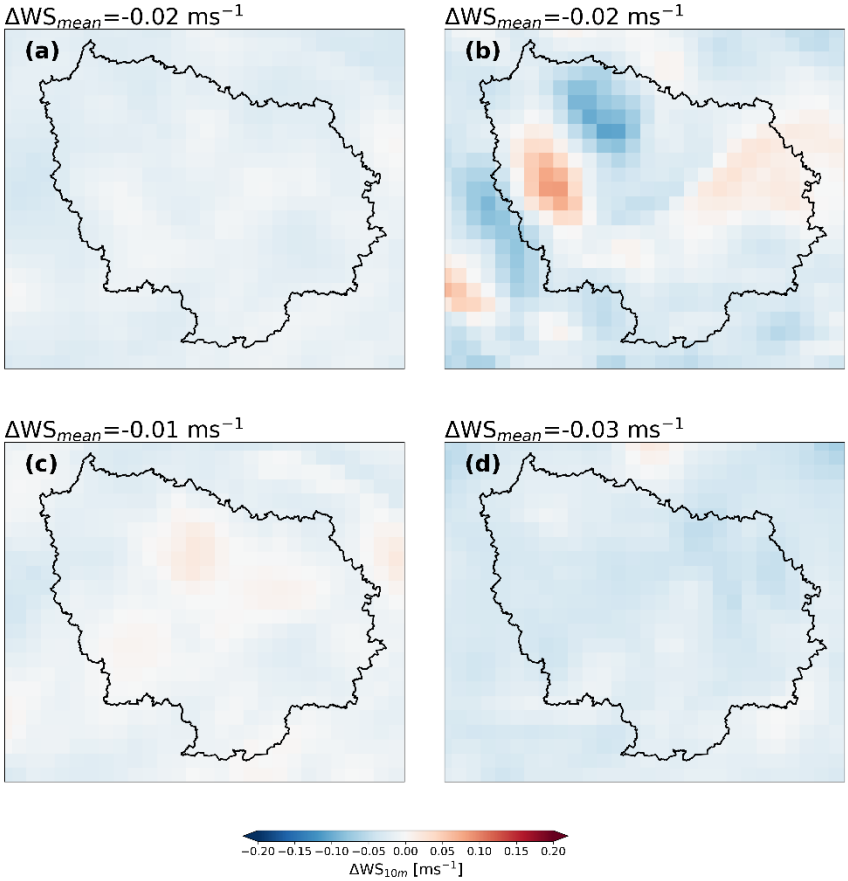

Figure 6.17: Daily mean 10 m wind speed differences between coupled and not-coupled simulations for (a) the full ACROSS campaign from the 15 June to 25 July 2022, (b) the 15 June-19 June 2022 (first heatwave), (c) 20 June-11 July 2022 (clean period), (d) 12 July-25 July 2022 (second heatwave) using the ONLINE approach for the for the Ile-de-France domain (48.1°N, 49.26 °N, 3.57°E, 1.47°W) divided by the different periods during the ACROSS campaign.

heatwave periods). Péré et al. (2011) observed a PBL decrease over Southern France ranging between 40 and 203 m, with the highest impact during the maximum extension of the PBL (between 12 and 14 h). However, the aerosol-PBL interaction can both favour or stabilize the PBL development, depending on the aerosol vertical distribution (Su et al., 2020).

Figure 6.17 shows that a more complex behaviour is observed for the wind speed changes, which can vary from negative (-0.54 ms^{-1}) to positive (+0.43 ms^{-1}) across the entire France domain. As boundary layer height, wind speed has an impact on aerosol dispersion and advection and to some extent also on emissions, particularly those of sea salt and mineral dust.

Under the WRF-CHIMERE radiative coupling, slightly weaker winds (10 m wind speed) are simulated for most of the campaign periods and places over the Ile-de-France region, but with nearly no effect on the average wind speed (-0.01 ms^{-1}). However, averages over the different ACROSS

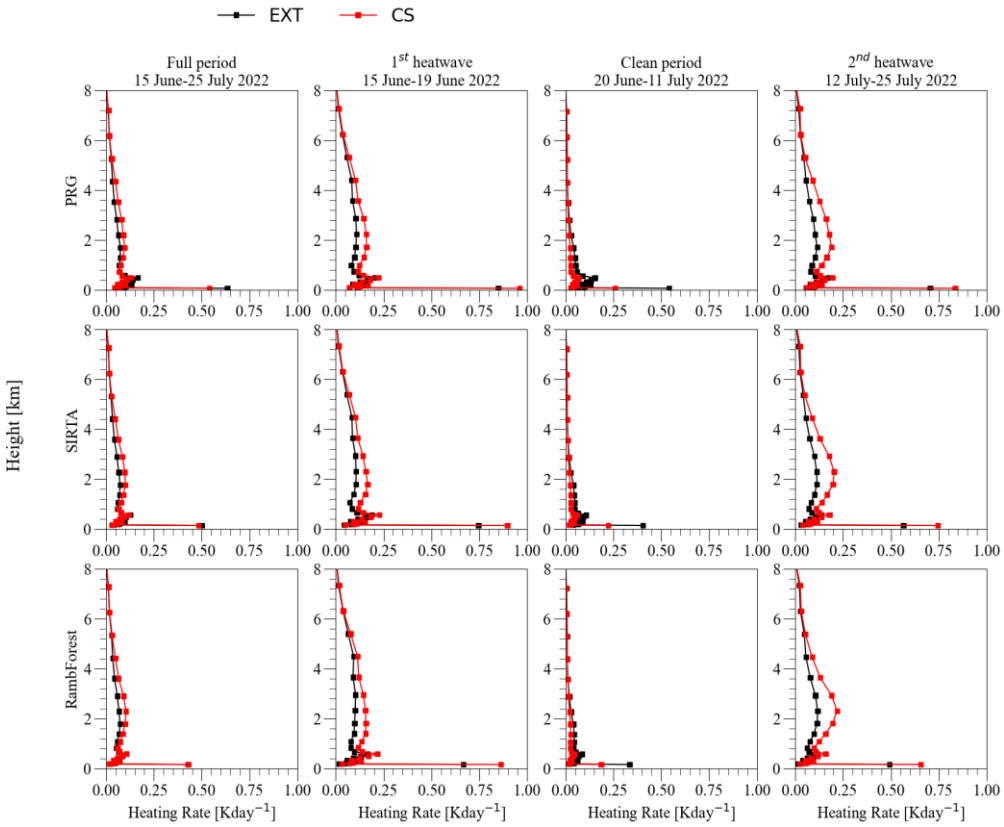

Figure 6.18 External mixing vs Core-shell mixing clear-sky aerosol heating rate at the Paris Rive Gauche (PRG), SIRTA, Rambouillet Forest (RambForest) sites during the ACROSS field campaign 2022.

periods show also areas of slightly enhanced wind speeds. These results are comparable to those found over France by Briant et al. (2017) for the June-July 2012 (ranging between ±0.5 ms^{-}1).

The effect of these modifications in meteorological parameters has not yet been explicitly investigated: the major probably antagonistic effects being a slight increase due to a lower boundary layer height, and a slight decrease due to lower temperature inducing lower BVOC emissions.

Another complementary result to the aerosol feedbacks on meteorology is the atmospheric heating rate (HR) due to aerosols. The vertically resolved shortwave atmospheric heating rate (HR, units of K day^{-1}) is obtained from the OFFLINE simulations and calculated as:

$$HR = \frac{\Delta T(z)}{\Delta t} = -\frac{g}{C_p}\frac{\Delta DRE(z)}{\Delta P(z)} \quad (6.1)$$

where g is the gravity acceleration, C_p the specific heat capacity and ΔP is the net pressure within the layer. The aerosol contribution (aerosol heating rate, AHR) is calculated subtracting the aerosol simulation with the pristine (no aerosol) simulation as:

$$AHR = \frac{\Delta T(z)}{\Delta t}_{aer} - \frac{\Delta T(z)}{\Delta t}_{clean} \quad (6.2)$$

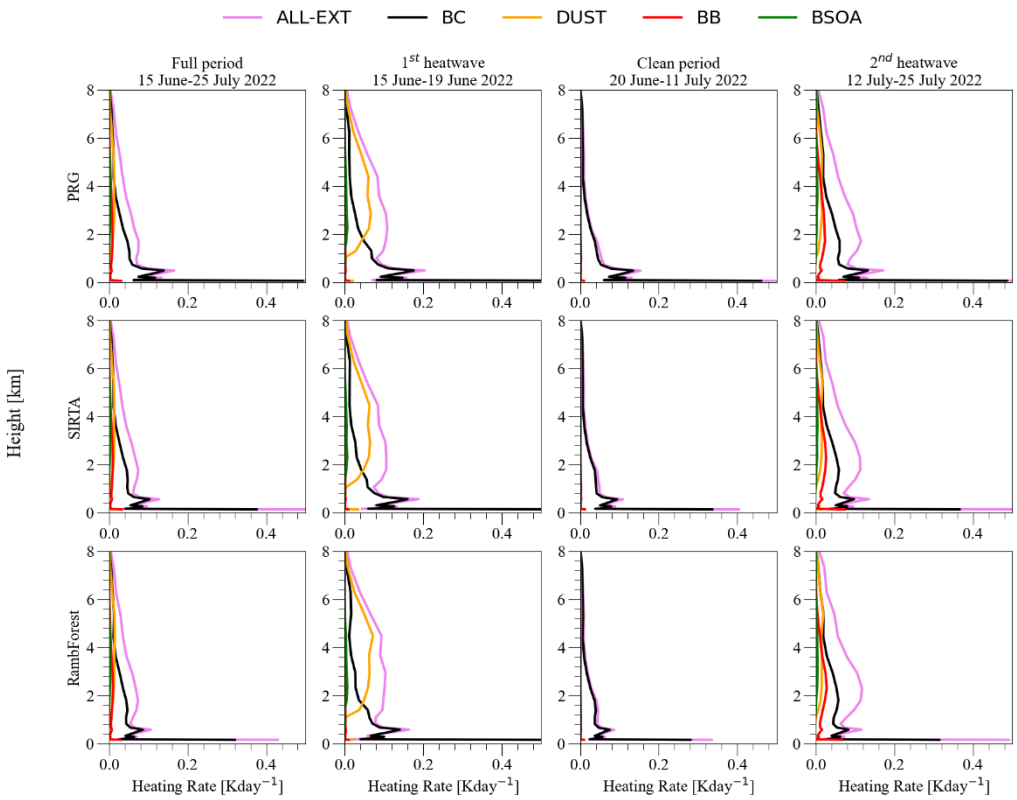

Figure 6.19: External mixing clear-sky aerosol heating rate considering all the species (ALL-EXT), only black carbon (BC), dust (DUST), primary biomass burning (BB-POA), biogenic secondary organic aerosols (BSOA) at the Paris Rive Gauche (PRG), SIRTA, Rambouillet Forest (RambForest) sites during the ACROSS field campaign 2022.

Figure 6.18 shows the atmospheric clear-sky heating rate at the PRG, SIRTA and RambForest sites under external and core-shell assumptions and for the different ACROSS campaign periods.

Maximum AHR values are observed near the surface (in the first model layer from surface to 20 m above ground), respectively of 0.96, 0.89, 0.86 $Kday^{-1}$ for the PRG, SIRTA and RambForest sites, during the first heatwave and under the core-shell assumption. The heating rate exhibits a complex altitude dependence: besides the close-to-surface peak, secondary peaks appear at about 500m height and a broader peak around 2 km altitude, enhanced under the core-shell mixing state compared to the external (up to 55% enhancement).

During heatwaves, this enhancement for the core-shell assumption is typically present, while during clean periods, the external mixing state induces a stronger heating rate. Monthly climatology from Wu et al. (2021) for the rural SGP (Southern Great) site in Oklahoma, shows that the clear-sky aerosol heating rate profiles during June-July show a maximum at the surface (~0.4 $Kday^{-1}$), while it is lower than 0.2 $Kday^{-1}$ above, comparable to what obtained for the RambForest site. Furthermore, as an extreme comparison, the SW AHR was also compared with results from Meloni et al. (2015) , where

they estimate the all-sky AHR during the Airborne Measurements of Aerosol Radiative Forcing (GAMARF) campaign in Lampedusa. Results show comparable values between 500 m and 1 km (less than 0.2 $Kday^{-1}$), while surface and above 1 km values differ due to the different nature of the sites. Above 1 km Meloni et al. (2015) found the largest heating of about 0.72 $Kday^{-1}$.

Figure 6.19 depicts the different contributors to the clear-sky aerosol heating rate under external mixing assumption, obtained following the same approach applied to the DRE (i.e. removing a specific aerosol from the simulation). Accordingly, it can be observed that below 1 km, black carbon dominates the absorption and is the primary contributor to the SW heating rate (AHR). In particular, this is relevant during the clean periods where the vertical heating rate profile due to black carbon (BC) is nearly overlapping with that of all the aerosol species (ALL-EXT). On the contrary, during the heatwaves dust and biomass burning OA represent a strong contribution above 1 km.

In fact, during the first heatwave dust plays a significant role, while during the second heatwave, biomass burning OA and BC (due to wildfires) are major contributors. Finally, due to the week absorption, BSOA do not significantly contribute to the heating rate even though the loadings are relevant (e.g. during the heatwaves).

6.4 Summary and conclusions

In this chapter we have investigated the aerosol direct radiative effect and feedbacks on meteorology during the ACROSS field campaign over France and Ile-de -France.

We estimate a maximum daily shortwave DRE TOA, BOA and ATM during the heatwaves under clear-sky (all-sky) of -20.7 (-19.2), -25.6 (-24.1) Wm^{-2} and +4.8 (+5.0) Wm^{-2}, more negative than the full period clear-sky (all-sky) averages values estimated in this work of -10.4 (-8.8) Wm^{-2}, -14.1 (-12.6) Wm^{-2} and +3.8 (+3.7) Wm^{-2} for the TOA, BOA and ATM respectively. Our results for the all-sky full period averages are comparable to the all-sky DRE obtained for Western Europe for the heatwave period of the 7–15 August 2003 from Péré et al. (2011), between (-1,-12) Wm^{-2}, for TOA, (-10,-30) Wm^{-2} for BOA and (+5,23) Wm^{-2} for ATM.

Additionally, DRE regional signals are significantly stronger compared to global averages, attesting the importance of fulfilling regional studies to better evaluate the DRE regional variability. In addition, even within our simulation domain the DRE is heterogeneous, with stronger signals over the Southern than over Northern France.

Thanks to the OFFLINE method developed within this thesis it has been possible to perform sensitivity tests useful to isolate the different aerosol species contribution to the DRE. Results shows that black carbon contributes to attenuate the SW TOA DRE negative signal on average by about 5%

and 10% of the total TOA DRE respectively for the France and Ile-de-France. On the contrary, the biomass burning POA, BSOA and ASOA enhance the DRE negative magnitude, contributing on average to the TOA respectively with 4%, 28% and 7%. The BB-POA contribution increased over the second heatwave period with an average value of 10%.

Of particular interest is the BSOA contribution to the DRE (both at the TOA, BOA, and ATM) due to the strong aerosol loading under heatwave conditions, which in absolute value becomes comparable to that of BC. The BSOA impact is stronger over Southern France, likely due to the concentration of forested areas and wildfire activities (mainly during the second heatwave) and therefore biogenic emissions in that region. The magnitude of the BSOA contribution strongly depends on the anthropogenic-biogenic interaction: the black carbon ATM DRE (anthropogenic) is enhanced by the biogenic SOA (whose formation is attributed to the biogenic emissions from forests and wildfires). Indeed, under the core-shell mixing (i.e. BC core surrounded by all the other species in the shell), due to the lensing effect the BSOA ΔDRE within the atmosphere increased by a factor between six and ten (under heatwave conditions) compared to the external mixing assumption and becomes comparable to that of BC under external mixing.
This strong absorption enhancement is observed also for the ASOA and biomass burning POA. In particular, the ASOA DRE within the atmosphere (ATM) at the Ile-de-France scale, changed from a negligible magnitude under external mixing (+0.02 Wm^{-2}) to a significant contribution (+1.07 Wm^{-2}) under the core-shell mixing, suggesting that even lower aerosol loading could lead to significant DRE contribution under core-shell mixing assumptions. However, the ASOA contribution to the direct radiative effect is much weaker compared to that of BSOA (more than a factor of two stronger at the TOA, BOA and within the atmosphere), and this even in regions with strong anthropogenic sources such as Ile-de-France.

A source of uncertainty in the calculation of the absorption enhancement of BSOA and ASOA may arise from the choice of the complex refractive index as the logarithmic average of the different curves from Liu et al. (2015), which will be the subject of further sensitivity analysis in latter studies.

Additionally, we found a factor of 1.5 absorption enhancement related to the primary biomass burning OA for the ATM DRE, which showed a significant contribution mainly during the second heatwave due to the strong fire episode of the 19 July 2022. This episode is also of considerable interest because brown carbon contribution was also observed in the Paris area due to the wildfire transport from the

Aquitaine region. This result, could be further refined by including the photochemical aging (such as bleaching or on the contrary, depending on browning) within the complex refractive index (since the fire has travelled for several hundreds of km before arriving to the Ile-de-France region), which is not taken into account by the constant (over time) complex refractive index applied within this study. Nevertheless, the important impacts obtained within this study suggest that under heatwave conditions, the increasing frequency of the wildfire activity due to the temperature increase, may strongly contribute to the DRE within regions even far from the sources (such as Ile-de-France in this case) due to the atmospheric transport.

Finally, exploiting the WRF-CHIMERE coupling and the OFFLINE approach has allowed us estimating the aerosol feedbacks on meteorology and the aerosol heating rate under clear-sky conditions. A moderate negative daily surface temperature decrease has been observed, maximum under the heatwave conditions (up to -0.15K over the region), reflected in a weaker PBL development everywhere in the Ile-de-France domain, in particular over the Paris metropolitan area. This suggests that under heatwave conditions aerosols may attenuate the heat island effect within megacities to a small extent. Indeed, the introduction of the aerosol decreased the simulated hourly 2m temperature of about 1° over the Paris metropolitan area under heatwave conditions.

The aerosol contribution to the atmospheric heating rate shows that under the external mixing the maximum absorption at the three sites within the Ile-de-France is observed at the surface where BC dominates mostly over the clean period of the ACROSS campaign. However, maximum heating rate values are observed between one and two km above the ground. A possible explanation may be related to i) the Saharan dust outbreaks and ii) the primary biomass burning and biogenic SOA transport from the Southern France during the ACROSS campaign and in particular during the heatwaves. In fact, during these periods, the aerosol heating rate shows a strong absorption enhancement under the core-shell compared to the external mixing, mostly observed above 1 km.
Future studies should evaluate the possible impact of this absorption enhancement on atmospheric stability under all-sky conditions, and therefore their effect on cloudiness.

Chapter 7

7. Conclusions and perspectives

7.1 Conclusions

A deeper understanding of the aerosol particles' role in the climate system requires an accurate characterisation of the spatial and temporal variability of the aerosol distribution, physico-chemical properties and radiative effects under diverse atmospheric conditions, particularly within densely populated areas where millions of people are every day exposed to considerable pollution levels. These areas may be situated in proximity to forested and rural environments, thereby favouring the interaction of anthropogenic and biogenic pollution sources, which may potentially result in alterations of the physical-chemical and spectral optical properties of aerosols.

The work presented in this thesis manuscript contributes to get deeper understanding of the distribution, spectral optical properties and direct radiative effect (DRE) of aerosols at the regional scale of the Ile-de-France region by a coupled measurement-modelling approach. The Ile-de-France region represents an ideal case study for investigating the effects of biogenic and anthropogenic interactions and regional implications. On the one hand, the Paris urban area is characterized by a high population density. On the other hand, the surrounding area is predominantly rural and forested, forming a natural buffer zone around the metropolitan ring.

The decision of conducting these kind of studies within the Ile-de-France region is further supported by the occurrence of the international ACROSS project and an intense field campaign over the Paris area, which took place during summer 2022 and that characterise the framework of this thesis project. Indeed, this thesis has benefited from a comprehensive set of measurements, which have enabled a detailed characterisation of the aerosol distribution, physico-chemical and spectral optical properties at different sites characteristics of the region. Complemented by remote sensing and larger network datasets, the in situ surface observations from ACROSS are used to evaluate three-dimensional chemistry-transport modelling studies of the aerosol DRE with the WRF-CHIMERE model.

This thesis work aimed at addressing three main scientific questions, which are:

1. *Can we better constrain the regional scale DRE magnitude and sign over a region affected by the mixing of anthropogenic and biogenic emissions?*
2. *How sensitive is the DRE to the aerosol composition and mixing state and the possible contribution of the biogenic-anthropogenic interaction?*
3. *Which aerosol species contribute the most to the DRE in such mixed regions? What is the specific contribution of the BC, ASOA, BSOA and BB-POA to the DRE?*

Conclusions are drawn in the following paragraphs to provide elements of answers to these questions, based on the integrated results from the performed analyses.

7.1.1 Climatological studies of the aerosol optical depth at the European, regional and local scale from the long-term satellite record

In a first phase, we conducted a climatological study on the aerosol optical depth (AOD), on which the direct radiative effect strongly depends. We performed a climatological analysis based on twenty-one years of high resolution satellite data (from February 2000 to August 2021) at different spatial scales (European, regional and local), to quantify the order of magnitude of the AOD that we might expect a mixed anthropogenic-biogenic region (such as the Paris area and the Ile-de-France region) and place it into a wider European framework.

We observed a generalized seasonal pattern of the AOD, with the highest values occurring during the summer (JJA) and the lowest during the winter (DJF). This pattern is accompanied by a strong positive north-south gradient in the AOD, both at the European scale (in terms of background values) and within the major cities under investigation. Average AOD values at 550 nm within the cities varies in the 0.06-0.18 range with lower values observed at Oslo and higher at Athens. The AOD for Paris is located in the middle of the average range of values an average value at 550 nm of 0.12.

In addition, in this study we conducted for the first time an evaluation of the impact of twenty-one cities aerosol burden on their regional background by defining a quantity called the AOD local-to-regional ratio (LTRR), where the "regional" and the "local" scales represent respectively an area about 100x100 km^2 and 3x3 km^2 around city centers. The analysis of the LTRR shows that most of the cities contribute to the enhancement of the AOD loading in comparison to their regional background. In contrast, for some cities a slightly negative LTRR is observed and could be explained by either specific removal processes or inhomogeneity of the regional background. In relative terms, the city's contribution to regional AOD is higher during the winter season, as the ratio of primary-to-secondary aerosol is expected to be the largest. Concerning Paris, which is characterized by a major isolated agglomeration with respect to the surrounding area, the long-term analysis conducted in this study indicates an average LTRR of 39 %, suggesting a non-negligible impact of the city emissions in addition to the regional aerosol burden.

Finally, we also performed an AOD trend analysis at the European, regional and local scale, observing a decreasing trend all over Europe. The AOD regional background is decreasing faster compared to the local scale AOD, in the range of $[-0.5, -1.7]\ \% \ yr^{-1}$ at the city level compared to the $[-0.9, -2.0]\ \% \ yr^{-1}$ of the regional surroundings. We attributed this difference to the possible effect of the more stringent control of aerosol precursor emissions (SO_2, NO_x, VOCs) with respect to primary aerosol emissions in cities.

7.1.2 The complex refractive index and single scattering albedo from the ACROSS field campaign observations

In a second phase, we benefited of the ACROSS field campaign observations, occurred from the 15 June to the 25 of July 2022, to retrieve the aerosol spectral optical properties at the surface level over the Ile-de-France region. These results are of strong interest for the ACROSS project and the scientific community: they provide the experimental estimate of the aerosol properties in an urban-to-rural gradient environment, and can be used to compare with the simulated WRF-CHIMERE spectral optical properties for a better evaluation of the DRE estimation.

We retrieved the surface PM_1 complex refractive index (CRI) and single scattering albedo (SSA) at seven different wavelengths in the spectral range of 370−950 nm, at three different sites characteristics of the region: i) the Paris-Rive Gauche located within the urban agglomeration of the Paris city and having urban-background features; ii) the SIRTA observatory, located in a semi-industrialised area and having peri-urban features and iii) the site within the Rambouillet forest having rural characteristics. We applied an iterative optical retrieval, based on the Mie Theory for homogenous spherical particles, in order to simulate the measured absorption and scattering coefficients at the three different sites.

Highly diversified weather conditions occurred during the campaign: 1) two strong heat waves leading to high aerosol loads; 2) an intermediate period of low aerosol concentrations; 3) a long-distance transported fire episode. These contrasted conditions lead to varying optical properties and spatial gradients.

Concerning the CRI, an average value at 520 nm of 1.45-0.043i (urban), 1.56-0.041i (peri-urban), 1.52-0.026i (rural) is retrieved under heatwave conditions, while an average CRI of 1.39-0.039i (urban), 1.52-0.038i (peri-urban), 1.47-0.023i (rural) under low aerosol concentrations. Concerning the SSA, an average value of 0.76 (urban), 0.81 (peri-urban), 0.87 (rural) is retrieved under heatwave conditions, while an average SSA of 0.69 (urban), 0.79 (peri-urban), 0.87 (rural) under low aerosol concentrations.

From this analysis, we show that the surface CRI and SSA have a gradient from the urban to the rural site, which depends on the meteorological conditions and air mass origin. In particular, we observed that under north-easterly winds, i.e. the rural and peri-urban sites under the influence of the Parisian urban plume, the SSA gradient is attenuated (~0.1 difference between the urban and rural) and the imaginary component at the urban site decreases (k at 520 nm of 0.028), while it increases at the peri-urban (0.039) and rural sites (0.026).

This result is supported by comparison of the retrieved CRI and SSA with the simulated BC-local-to-regional ratio from the WRF-CHIMERE model, a parameter used to trace the simulated Paris black carbon concentration from the metropolitan Grand Paris area, allowing for investigating the extent to which measurements at different points are influenced by the Parisian plume. Indeed, we observed that an increase of the BC-to-PM_1 concentration led to a decrease (increase) in the SSA (k) at the rural and peri-urban sites, which makes evident the impact of the Paris plume on aerosol properties at the peri-urban and rural sites. On the contrary, under south-westerly winds (i.e. cleaner air masses over the region) the SSA gradient between urban and rural is enhanced with a difference of about 0.2, showing the lower SSA average value of 0.67 at the urban site (due to the higher BC-to-PM_1 ratio and low aerosol concentrations) and the higher SSA of 0.90 at the rural site (due to the lower BC-to-PM_1 ratio and low aerosol concentrations).

Finally, we correlated the retrieved spectral optical properties to the bulk aerosol chemical composition from the aerosol mass spectrometers observations, showing that the imaginary component of the CRI is strongly correlated to the eBC fractions. This suggests the key role of primary emissions and even low eBC concentrations in affecting absorption, as particularly evident at the urban and peri-urban sites. Nevertheless, organics contribute to more than 50% of the aerosol mass concentration at the three sites, indicating the significant contribution of brown carbon (BrC) to total spectral absorption. The BrC is estimated to contribute on average up to 10% (urban), 17% (peri-urban) and 22% (rural) to the absorption coefficient at 370 nm during the full campaign. A particularly high BrC contribution to absorption at the ACROSS sites was observed during the long-range transport biomass burning episode which occurred on the 19 July 2022, representing 45%, 42% and 52% of the total absorption coefficient at 370 nm respectively at the urban, peri-urban and rural sites.

7.1.3 The WRF-CHIMERE modelling during the ACROSS field campaign 2022

A 3D simulation with the WRF-CHIMERE model was performed using three nested domains respectively at 30 km (covering Europe and part of the North Africa), 6 km (covering France), and at 2 km (centred over the Ile-de-France region) spatial resolution for the ACROSS field campaign period (from 15 June to 25 July 2022).

The WRF-CHIMERE model was used to achieve three main objectives:

- investigate the gas and aerosol temporal and spatial variability at the regional scale of France and Ile-de-France region;
- assist the interpretation of the observations from the ACROSS ground-based and aircraft scientific community with high resolution modelling;

- provide an estimation of the aerosol direct radiative effect at the regional scale of France and the Ile-de-France region in a mixed biogenic-anthropogenic framework, isolating the different aerosol contribution to the DRE and studying the impact of mixing state on the DRE.

To this aim, two different simulation approaches were used to model the spectral optical properties and the direct radiative effect were during the ACROSS campaign:

- the ONLINE simulation, where the WRF meteorological model is coupled with the CHIMERE chemistry-transport model.
- The OFFLINE simulation, where only the WRF model provides the meteorological fields to the CHIMERE model at each physical time step, while CHIMERE does not send the spectral optical properties to WRF. In this case two optical model have been employed to recalculate the spectral optical properties under two different mixing states: external and core-shell. In order to calculate the DRE under clear-sky conditions from the OFFLINE simulation, I have developed an interface between the Rapid Radiative Transfer model for GCMs (RRTMG) and the WRF-CHIMERE and optical models output (AOD, SSA and g) to provide sensitivity test on the aerosol mixing state and isolate the different aerosol contribution to the DRE.

7.1.3.1 The evaluation of the simulated meteorology, dynamics and chemical composition

The WRF-CHIMERE model simulation of gas and aerosol spatial and temporal variability at 6 km and 2 km spatial resolution has been extensively evaluated against observations from the ACROSS field observations and existing networks for the meteorology, dynamics and aerosol chemical composition.

The WRF model has shown to satisfactorily simulate the key meteorological variables and to follow the meteorological variability during the campaign, and in particular the two heat waves towards the beginning and the end of the campaign. Maximum daily temperature is in general simulated within ± 1°C, while the planetary boundary layer is generally underestimated by about 200 m for most of the days of the simulation period. The adequate simulation of temperature is important as this parameter is a general indicator for the model ability to catch the meteorological conditions, mainly under heatwave conditions, and as in particular it governs among others the intensity of biogenic VOC emissions in the MEGAN module.

Also high and low wind periods and evolution of wind direction are reasonably well simulated (within ±1 ms^{-1}), in particular for the Ile-de-France region. This allows the simulation of different transport regimes during the campaign period, including the simulation of the direction of the pollution plume originating in the Paris region.

We further performed an exhaustive evaluation of the simulated aerosol chemical composition against the in-situ measurements at the France regional scale, under the challenging heatwave conditions of summer 2022, taking advantage of both the ACROSS field campaign observations and the online measurements from the GEOD'AIR national network.

Since the organic aerosols (OA) represents a major fraction within the fine aerosol particulate matter, we employed the Volatility Basis Set (VBS) scheme to provide a more realistic treatment of the primary and secondary organic aerosols species. This scheme classifies the organic aerosols based on their volatility, allowing for the functionalisation and fragmentation processes, as well as the formation of non-volatile organic products. Results from model simulations were compared to observations at the France scale, showing that all the major aerosol species are overestimated: +21% is obtained for organic aerosol, +16% for sulfate, + 37% for ammonium, +53% for nitrate, but only +7% for black carbon. For the OA, the biases are larger during the two heatwave periods (+49% and +38%), while slightly negative (-8%) during the clean period. However, the high resolution (2 km x 2 km) validation at the three sites in Ile-de-France shows that model overestimations are less systematic. Biases are -20% to +21% for OA, -12% to +37% for sulfate, +1% to 89% for ammonium, +15% to +148% for nitrate and +27% to 66% for BC. Large positive biases are obtained for the Rambouillet rural site, where concentrations are very small (for example 0.38 µg m^{-3} for ammonium, 0.16 µg m^{-3} for nitrate and 0.14 µg m^{-3} for BC). We attribute the possible bias in the organic aerosols to the temperature increase, inducing a corresponding bias in the biogenic VOC emissions, or within the VBS scheme. Since the VOCs measurements from the ACROSS field campaign will be available in the coming months, an evaluation of the VOCs emissions will be expected in the near future and beneficial for a better comprehension of this overestimation.

Finally, we prove the usefulness of the WRF-CHIMERE simulation to investigate specific events during the ACROSS campaign period, as for example during the two major heatwave days of:

- **18 June 2022.** Together with a strong dust episode reaching the surface, a series of organic aerosol peaks were simulated and partially observed at the campaign sites during the night of 17 to 18 June. These peaks were associated with the build-up of biogenic secondary organic aerosol (BSOA) above forested areas within and south of Ile-de-France, as well as the further advection of these BSOA-rich air masses to the campaign sites.
- **19 July 2022.** On the 19 July, together with the dust and biomass burning episodes, it is evident that the Aquitaine region in south-western France is responsible for a considerable formation of biogenic SOA due to both forest and wildfire biogenic emissions that are being transported regionally, reaching the Ile-de-France region by the end of the same day. This

episode represents a unique case study due to the mixing of Saharan dust, biomass burning and anthropogenic aerosols over the region, with a strong visibility and air quality reduction, possible proxy of a future climate scenario under climate change conditions.

7.1.3.2 The evaluation of the simulated surface and columnar spectral optical properties and surface radiation

Before performing the WRF-CHIMERE model simulation, since the model attributes the same spectral invariant complex refractive index to the biogenic and anthropogenic SOA, we decided to update the complex refractive index database of these species following the study from (Liu et al, 2015), which suggest that there is an order of magnitude of difference between the BSOA and ASOA absorption. Furthermore, we included a primary biomass burning (BB-POA) tracer species within the simulation, to follow the evolution of the wildfire activity during the ACROSS campaign period (due to the strong wildfire activity of summer 2022), attributing a specific complex refractive index following the formulation from Saleh et al. (2015), which further included the brown carbon absorption. This allowed for the estimation of the DRE due to primary biomass burning aerosols.

The evaluation of the simulated surface PM_1 complex refractive index and single scattering albedo at 520 nm against the ACROSS retrievals shows that the model is capable of reproducing the temporal variability, but it tends to underestimate the surface absorption (NMB of -15¨%, -28%, -36 % for k), increasing the SSA signal, with higher overestimation at urban site (NMB of +25% and 29% respectively under the external mixing and core-shell assumption) and significantly lower at the rural site (NMB of +5% and +8%) respectively under the external mixing and core-shell assumption. This result suggests that an accurate representation of the SSA surface variability is difficult due to the challenges in the characterisation of the aerosol local scale fluctuations of the refractive index, together with the size distribution, especially at the urban sites, where primary emissions are predominant.

Nevertheless, the columnar parameters, such as the AOD, SSA and AAOD, are more accurately reproduced than the surface observations. In particular, the AOD is well simulated from the WRF-CHIMERE model showing a NMB of 1.3% and 4.2% at 440 and 675 nm.
Recalculating the aerosol optical depth from the WRF-CHIMERE size-resolved (ten sectional bins between 0.01 μm and 40 μm) aerosol concentrations outputs, using the offline optical models we obtain an underestimation of the AOD mainly at 440 nm (-10% and -11% for the external and core-shell mixing assumptions respectively). The offline optical models do not include the size distribution

refinement in the shortwave, which in turn is performed only for the optical calculations in the WRF-CHIMERE model (from ten to twelve sectional bins between 0.04 µm and 10 µm with finer resolution over the near-visible part of the spectrum).

Nevertheless, we observed that the columnar AAOD and SSA are more accurately described under the core-shell (CS) assumption (the NMB for the AAOD changes from -43% under external to +6% for the core-shell mixing assumptions at 440 nm), indicating that the CS model is more suitable for reproducing the columnar aerosol absorption properties due to the lensing effect which enhances the particle absorption (Zhang et al., 2018).

Finally, the surface radiation evaluation against the E-OBS daily gridded dataset shows that the WRF-CHIMERE model overestimates the downwelling surface radiation both for the ONLINE (NMB of +15%) and OFFLINE (NMB of +20%). The overestimation of the ONLINE is reduced compared to the OFFLINE due to the presence of aerosols which reduced the radiation reaching the surface (i.e. contrary to the OFFLINE case, for the ONLINE case, the spectral optical properties are transferred from CHIMERE to WRF, affecting the radiation fields).

7.1.3.3 Aerosol direct radiative effect (DRE) modelling and feedbacks on meteorology

The WRF-CHIMERE model was used to estimate the aerosol direct radiative effect at the 6 km spatial resolution domain and at the regional scale of France and Ile-de-France, during the challenging conditions of the ACROSS field campaign, both using the ONLINE and OFFLINE approaches.

Using the WRF-CHIMERE coupling (ONLINE) at the France regional scale and for the ACROSS campaign period (15 June-25 July 2022), we estimated an average shortwave daily clear-sky of -10.4 and -14.1 Wm^{-2} at the TOA and BOA, while +1.2 and +3.4 Wm^{-2} for the longwave. The introduction of clouds, thus under all-sky conditions lead to a lower DRE of -8.8 and -12.6 Wm^{-2} for the shortwave, and +1.0 and +3.1 Wm^{-2} for the longwave. The SW DRE at the TOA and BOA were maximum during the heatwaves (maximum averages of -20.7 and -24.1 Wm^{-2} at the TOA and BOA). Similar DRE patterns were observed averaging on the Ile-de-France domain.

Considering the clear-sky shortwave direct radiative efficiency, we estimated a daily clear-sky DREE at the TOA and BOA of -79 and -117 $Wm^{-2}AOD^{-1}$ for the shortwave and +7 and +25 $Wm^{-2}AOD^{-1}$ for the LW for the France domain. We found that the spatial distribution of the shortwave DREE within the atmosphere (DREE ATM) is strongly correlated with the spatial distribution of the single scattering albedo, showing higher values where the SSA is lower (i.e. indicating the presence of more absorbing aerosols). A weaker single scattering albedo (SSA) induces a more positive DRE efficiency within the atmosphere, while a stronger SSA induces a more negative DREE at the BOA. In fact, the

clear-sky SW DREE within the atmosphere at the Ile-de-France scale is stronger (+52 $Wm^{-2}AOD^{-1}$ daily clear-sky average for the ACROSS period) compared to the France scale (+38 $Wm^{-2}AOD^{-1}$) scale due to more absorbing aerosols over the Ile-de-France region. In fact, this difference is maximised during the clean period of the ACROSS campaign (averages of +61 $Wm^{-2}AOD^{-1}$ for the Ile-de-France compared to the +42$Wm^{-2}AOD^{-1}$ over France), which was characterised by low aerosol regional background loadings. This lead to an increased black carbon fraction, causing the SSA decrease and the DREE ATM increase.

Thanks to the OFFLINE approach developed during the thesis we were further able to investigate the DRE sensitivity to the aerosol mixing state: external (EXT) and core-shell (CS) internal mixing states. Under the CS assumption, the direct radiative effect is less intense at the top of the atmosphere, and more intense at the bottom of the atmosphere compared to the external mixing, highlighting that a stronger amount of the radiation is absorbed within the atmospheric column.

This is due to the lensing effect on BC cores. The full ACROSS period ATM DRE average at the France regional scale is +5.3 Wm^{-2} for the CS assumption compared to the +4.0 Wm^{-2} of the EXT approximation. Values reach up to +9.3 Wm^{-2} for the CS compared to the +5.8 Wm^{-2} for EXT during the heatwave periods, resulting in a stronger BOA (i.e. less solar radiation reaching the surface) and weaker TOA signal (i.e. less radiation reflected back to space) due to the enhanced absorption within the atmospheric column.

Thanks to the OFFLINE development, it has been possible to perform the sensitivity tests to isolate the DRE contribution (under the EXT and CS mixing states) of several aerosol species.

Results show that black carbon is the only simulated aerosol species that contributes to attenuate the SW TOA DRE total negative signal on average by a 5% and 10 % of the total SW TOA DRE for the France and Ile-the-France domains (full period averages of +0.50 Wm^{-2} over France and +0.65 Wm^{-2} at the Ile-de-France domain). On the contrary, the biomass burning POA (BB-POA), BSOA and ASOA enhance the DRE TOA negative magnitude. The contribution to the TOA DRE under the CS mixing state is weaker due to the stronger absorption within the atmospheric column. Indeed, the BB-POA, BSOA and ASOA contribute on average to the TOA respectively with 4%, 22%, 7% and 3%, 19%, 5% for the France domain under the external and core-shell mixing state. Similar contributions to the TOA DRE are obtained for the Ile-de-France domain. At this regional scale, the aerosol species which dominates the contribution to the TOA, BOA and ATM DRE (in terms of absolute magnitude) changes according to the different periods of the ACROSS campaign: black carbon represents the dominant contribution to the DRE only within the atmosphere (ATM DRE) for the entire ACROSS campaign due to absorption. This does not occur at the TOA and BOA. The magnitude of the BC

BOA and TOA DRE (in terms of absolute values) is consistently weaker than that of the BSOA. At the BOA, the BC shows a stronger contribution only during the clean period, due to the low BSOA loadings. The ASOA shows a significant contribution only during heatwaves, but it never plays a dominant role in the overall DRE contributions across the region. The BB-POA exhibits a non-negligible contribution, comparable to that of BC and BSOA, primarily at the bottom of the atmosphere and within the atmospheric column and only during the second heatwave over the region. In fact, during this period, the BB-POA and BSOA loadings and DRE signals increased due to the strong temperature increase and wildfire activity over the Southern France, inducing a stronger signal at the TOA, BOA and within the atmosphere over the entire domain of simulation. However, this signal was never stronger than the BC contribution.

In consideration of these findings, it is of particular interest to consider the BSOA contribution to the DRE, given the strong aerosol loading observed under heatwave conditions. Under heatwave conditions, the biogenic secondary aerosol formation is significantly enhanced by the increase in biogenic VOC emissions, as a consequence of the rise in temperature, the presence of oxidants (such as the ozone) stagnant atmospheric conditions. The BSOA impact is stronger over Southern France, likely due to the concentration of forested areas and wildfire activities (mainly during the second heatwave) and therefore biogenic emissions in that region. It is important to notice that the magnitude of the BSOA direct radiative effect within the atmospheric column (ATM DRE) is enhanced under the core-shell mixing state by a factor between six and ten compared to the external mixing. This happens for all the periods of the ACROSS campaign with the highest enhancement under heatwave conditions due to the stronger BSOA loadings compared to the clean period.

This strong absorption enhancement within the atmosphere is observed also for the ASOA and biomass burning POA. In particular, the ASOA DRE within the atmosphere increased significantly under CS mixing, from a negligible magnitude under the EXT mixing to a significant contribution (+1.07 Wm^{-2} at the Ile-de-France scale).

Concerning the fire episode of the 19 July 2022 over Southern France, we found a factor of 1.5 absorption enhancement (with the CS compared to the EXT) for the BB-POA DRE within the atmosphere (ATM DRE), due to the coating of BB-POA on BC. This episode is also of considerable interest since the brown carbon contribution was also observed at the Paris urban site due to the long-range transport over the Ile-de-France region. This BB-POA DRE estimation could be further refined by accounting for the evolution of BrC optical properties during ageing, such as (photo) bleaching (Saleh et al. 2015), as the fire has travelled for hundreds of km before arriving to the Ile-de-France, which is not taken into account within this simulation. Nevertheless, the key results obtained within

this study suggest that under heatwave conditions, the increasing frequency of the wildfire activity due to the temperature increase, may strongly contribute to the DRE.

As a matter of fact, results from this thesis show that in order to better constrain the aerosol DRE in a mixed biogenic-anthropogenic environment, an accurate representation of the evolution of the aerosol mixing state within atmospheric models is required. We found that the mixing state is of significant importance under all weather conditions, with less, but still significant contribution under low aerosol loadings (i.e. clean period). However, under a future climate scenario, an increase in frequency of the BSOA and biomass burning events over Europe may occur, inducing an increase in the aerosol loading within regions even far from the sources (such as Ile-de-France in this case) due to the atmospheric transport. Moreover, the discrepancy between the two extremes mixing states varies according to the aerosol type and complex refractive index assigned, which influence the strength of the contribution to the DRE, suggesting the necessity also of an accurate simulation of the aerosol chemical composition and spectral optical properties.

Finally, by exploiting the interaction capabilities between the WRF and the CHIMERE model (ONLINE approach), it was possible to estimate the aerosol feedback on meteorological parameters such as the temperature, wind speed and planetary boundary layer height. A moderate negative surface daily temperature decrease has been observed, reaching its greatest extent during the heatwave period (up to -0.15 K over the region) and which can weaken the heat island effect over the Paris area. Indeed, the introduction of the aerosol decreased the simulated hourly 2m temperature of about 1° over the Paris metropolitan area under heatwave conditions. This phenomenon has been accompanied by a generalized weakening of the PBL across the Ile-de-France domain, with the Paris metropolitan area exhibiting the most pronounced decline.

7.2 Perspectives

The work conducted during this thesis opens to a wide range of perspectives both from the modelling and measurements point of view. Further analyses and observations will be forthcoming from the ACROSS field campaign concerning the chemical and optical aerosol characterization and gas phase chemistry, which will be useful not only for evaluating the model simulation, but also for interpreting the results obtained and deeply investigating the anthropogenic-biogenic aerosol interaction.

A validation of the anthropogenic and biogenic VOCs concentrations, which was not performed in this thesis manuscript due to lack of measurements at this stage of the campaign exploitation, could be essential to improve understanding of the possible pathways of biogenic aerosol formation.

Although the integration of the various SOA formation patterns may prove computationally expensive, it would be beneficial to gain a deeper understanding of the most likely BSOA and ASOA formation pathways in the region, accompanied by a more detailed development of the chemical mechanism within the CHIMERE model. It is important to note that there is currently a simplified treatment of VOCs chemistry and emissions within CTMs, particularly within the CHIMERE model. Concerning the biogenic SOA, not all the species simulated by the MEGAN biogenic model are included, which does not allow for a detailed and effective comparison with in-situ observations. This issue will be the focus of future projects that will be an extension of the ACROSS project. In particular of the ADEME Acacia ECLAT project (Tirer les leçons de l'**É**té 2022 : quelle qualité de l'air dans un **CL**im**AT** futur?), where the implementation of the explicit chemical mechanisms with the Generator for Explicit Chemistry and Kinetics of Organics in the Atmosphere (GECKO-A) model within the WRF-CHIMERE model is foreseen.

Since the aerosol organic fraction constitutes over 60% of the total fraction in the fine part of the surface size distribution, it is important to simulate it correctly within CTMs in order to accurately represent the aerosol spectral optical properties. The VBS scheme applied under the challenging conditions of summer 2022 has proven to generally overestimate the organic fraction. Alternatively, an inaccurate simulation of biogenic emissions could also lead to an overestimation of BSOA (e.g. the biogenic model does not account for drought conditions, which could potentially constrain VOC emissions), and thus merits further investigation, particularly in the context of heat waves conditions, proxy of a future climate scenario.

The complex refractive index and single scattering albedo datasets produced in the framework of the ACROSS field campaign, together with the complementary measurements from the aircraft ACROSS campaign (not analysed in this work), provide a unique dataset that can be used to better constrain the spectral aerosol optical properties representation in climate models and satellite retrievals under challenging climate conditions. Beyond work performed in this thesis, a more detailed analysis is necessary to provide insight on the particle mixing state and composition taking advantage of the aircraft observations and more advanced chemical molecular scale analyses at the various sites of the ACROSS campaign. This could additionally help relating spectral absorption to the presence of different chromophores, such as nitro-aromatics, at the different sites and under different conditions. In addition, a more detailed characterization of the particle mixing state by particle-level in-situ measurements would be advantageous to better understand the particle chemical and optical evolution far from the emission sources, where more aged and internally mixed aerosols are expected.

Additionally, the simulation performed during the ACROSS campaign, will represent a useful tool for the ACROSS scientific community for the interpretation of the observations during the campaign. The CHIMERE simulation can support the activities carried out during the aircraft campaign, such as explaining the possible variations in the BSOA and ASOA when passing over a specific area of the region, the spatial and temporal evolution of the Parisian plume and the aerosol concentrations variations at the ground level of the ACROSS measurement sites.

The development of the OFFLINE scheme for radiative transfer estimations opens up to applications in other regions, under diverse aerosol load and properties, to extend the results of the present analysis to other climate-relevant conditions and to assess the contributions related to different aerosol sources.

Specifically to this work and the estimate of the DRE for the ACROSS period over France, however we stress on specific tasks that remains necessary and that we encourage for future studies. Among those we mention:

- the spatial validation of the aerosol optical depth, single scattering albedo and absorption aerosol optical depth using high-resolution satellite data and ACROSS aircraft observations for a better characterization of the spatial and temporal aerosol variability;
- the realisation of sensitivity tests on the choice of complex refractive index for a better characterisation of the direct radiative effect sensitivity to the CRI assumptions for pure species and for the absorption uncertainty analysis;
- the estimation of the black carbon internal mixing contribution to the DRE using a homogenous internal mixing model;
- the validation of cloud coverage and radiation fields from satellite measurements for a better reliability of the all-sky and clear-sky conditions DRE;
- the use of lidar measurements for model validation of the aerosol vertical distribution (such as the dust transport from lower latitudes) as it represents a key factor in the DRE estimation;
- the evaluation of the surface aerosol size distribution which we argue to explain the difficulties in reproducing the surface single scattering albedo at the urban site;

Finally, it is important to note that the aerosol direct radiative effect represents only a portion of the total aerosol contribution within the climate system. In order to accurately assess the overall impact of aerosols on the regional scale of Ile-de-France during the ACROSS campaign, it will be necessary to consider other radiative effects, such as the semi-direct and the indirect effects on the microphysics of cloud formation and precipitation patterns. This could be addressed by future studies.

As a final conclusion, the results obtained within this thesis demonstrate the benefits of an integrated measurement and modelling approach to perform an effective and a more detailed evaluation on the aerosol direct radiative effect, particularly at regional scale under the effect of varying and extreme conditions, as observed during the ACROSS campaign in summer 2022. The necessity of an accurate representation of the aerosol chemical composition, spectral optical properties and mixing state is mandatory for a better constrain on the DRE temporal and spatial variability in models. This requires a comprehensive comparison with observations and a more thorough understanding of the interaction between anthropogenic and biogenic compounds in regions where the mixing occurs. The work realized during this thesis provides advances on the investigation of the regional scale aerosol radiative effects in areas affected by mixing and under challenging conditions proxies of a future climate scenario. It represents a thorough base for guiding and support more extended analysis within the ACROSS project and the scientific community in the coming years.

Annex

Annex A. Supplementary to the Chapter 3

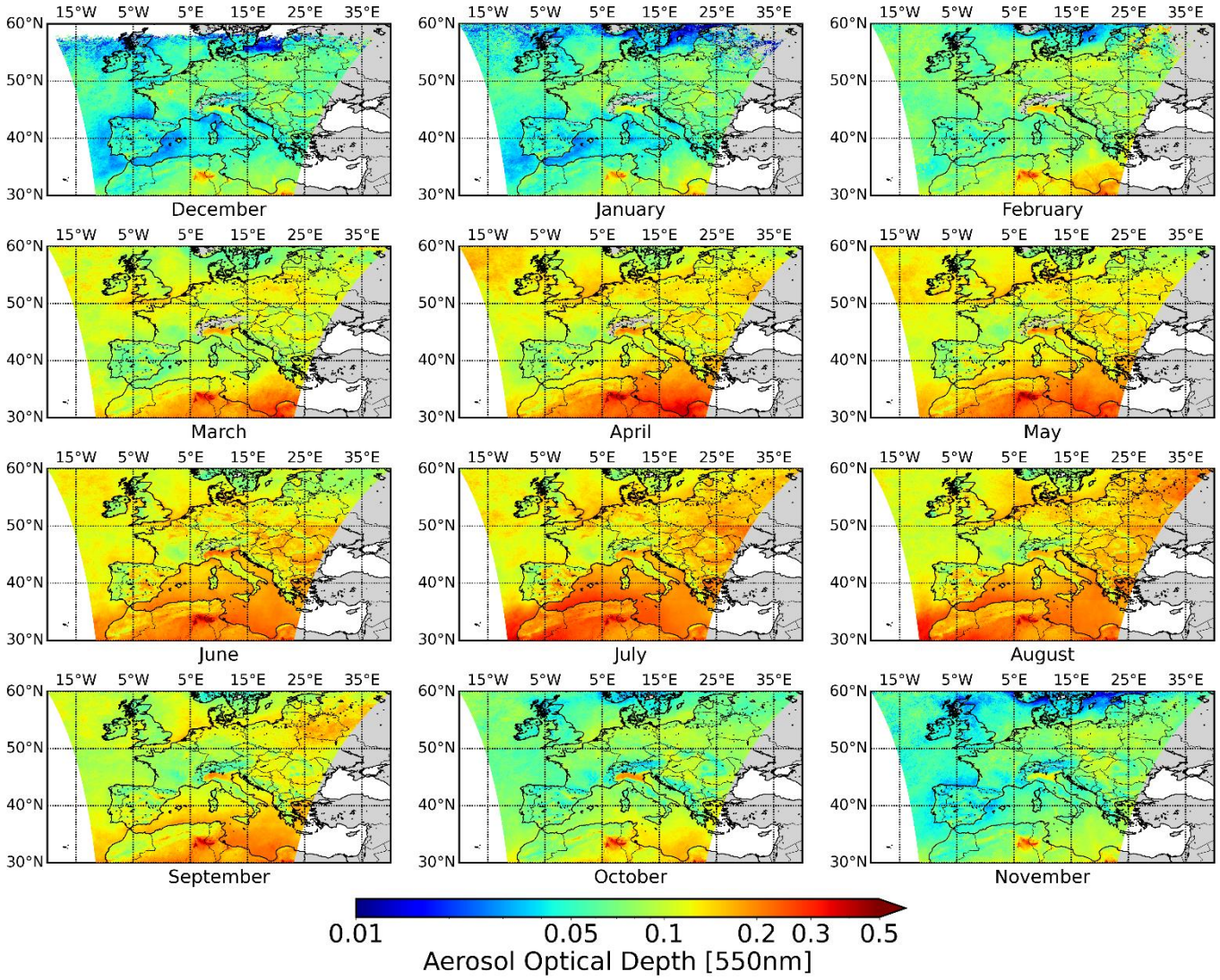

Figure S1: Climatological monthly mean of the Aerosol Optical Depth at 550 nm over the period 2000–2021.

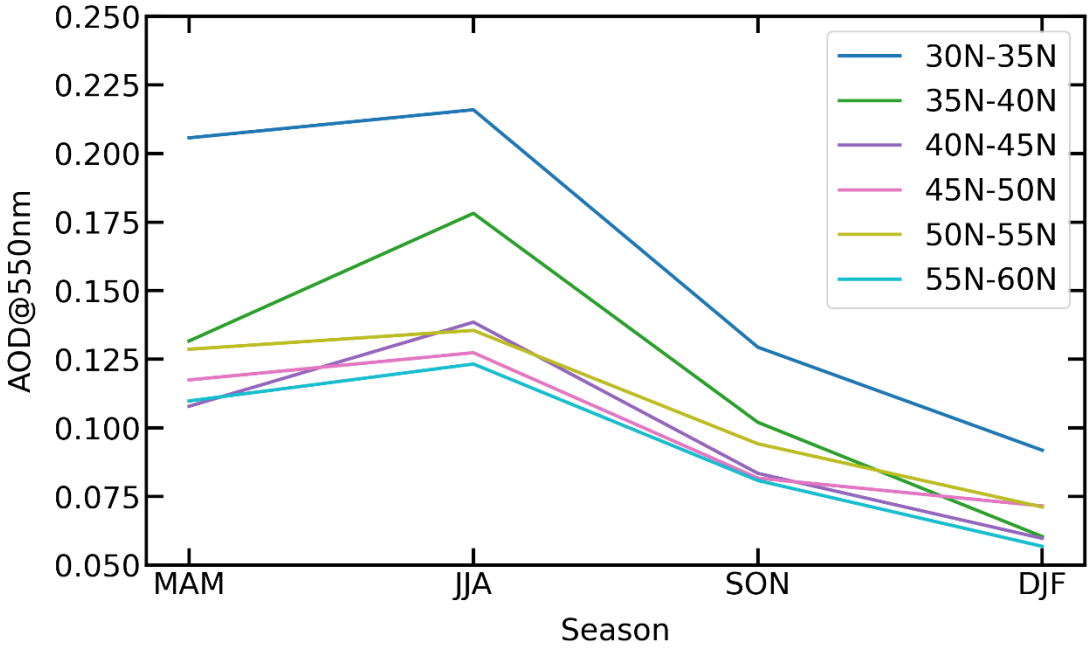

Figure S2: Seasonal and latitudinal climatological averages of Aerosol Optical Depth at 550 nm from the MAIAC product.

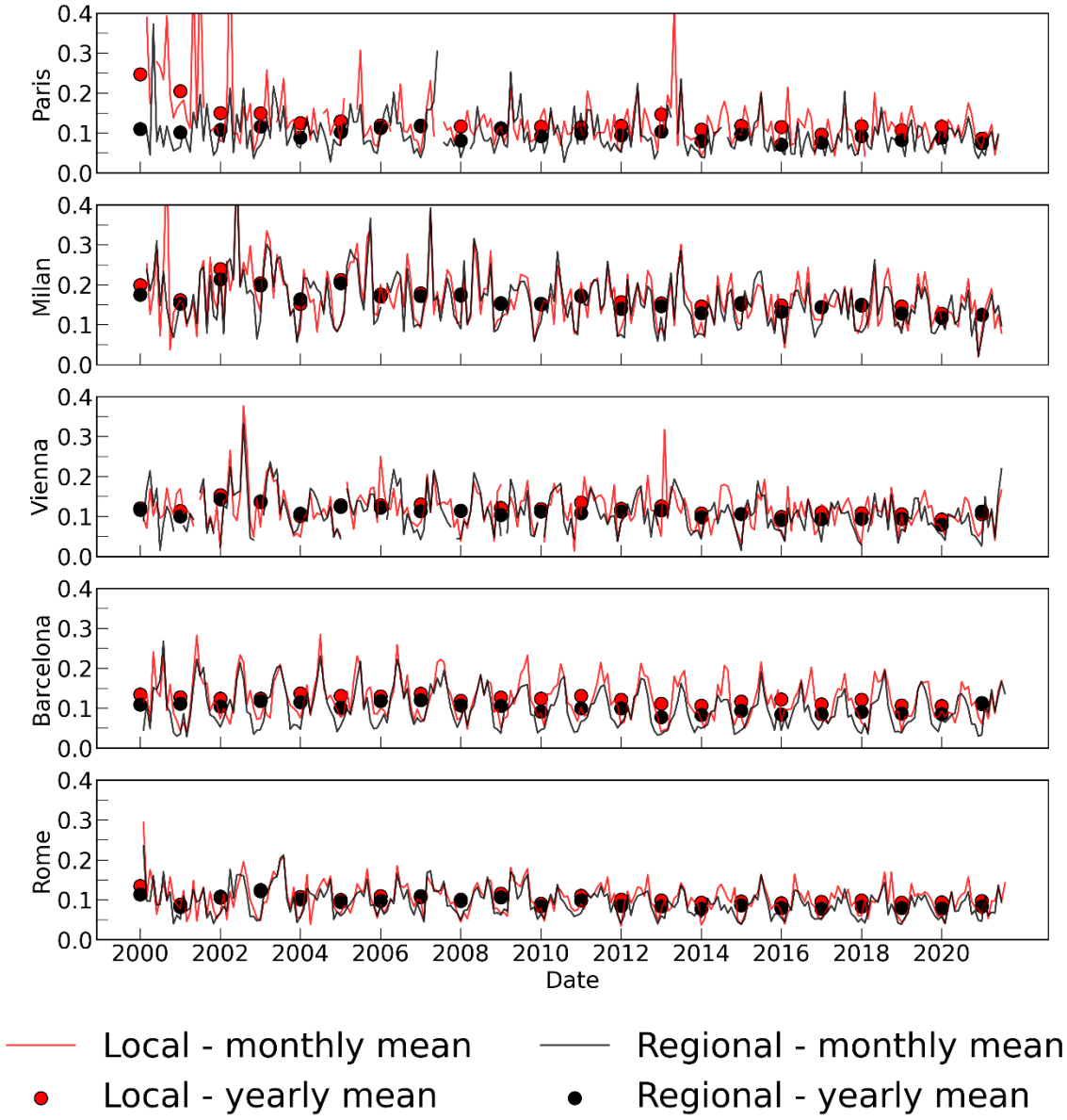

Figure S3: Time series of monthly and yearly local and regional Aerosol Optical Depth at 550 nm from the MAIAC product for five different cities: Paris, Milan, Vienna, Barcelona, Rome.

Annex B. Supplementary to the Chapter 4

Supplementary Text 1. Detailed procedure for CRI retrieval from optical-iterative method

Starting from the data LEVEL 2 data, the following treatment was applied:

- The $\beta_{sca}(\lambda, \theta_1 - \theta_2)$ (non truncation–corrected) was extrapolated at the seven β_{abs} wavelengths (370, 470, 520, 590, 660, 880, 950) using the SAE following Eq. (2) and Eq. (3);
- The SMPS aerosol number size distribution ($dN(Dm)/dlogDm$) was converted into $dN(Dg)/dlogDg$ assuming spherical particles (χ=1). For the SIRTA site the size distribution data within the 8.9-829 nm range has been extrapolated with a cubic spline on a constant dlog=1/64 (to be consistent with the dlog of the PRG and RambForest sites) and normalised to conserve the total number of particles (N_{tot});
- The β_{abs} was corrected for multiple–scattering (C_{ref}) using the C_{ref}=2.45 following the ACTRIS recommendation
- Iteration on n in the [1.2, 2.0] range and a dn=0.01 resolution and on k in [0, 0.02] range and a dk=0.001, in order to model the no truncation–corrected scattering and absorption coefficients ($\beta_{sca}(\lambda, \theta_1 - \theta_2), \beta_{abs}$) through a Mie code for homogeneous spherical particles. $C_{sca}(\lambda) = \beta_{sca}(\lambda, 0° - 180°)/\beta_{sca}(\lambda, \theta_1 - \theta_2)$

Minimisation of the root mean squared difference (RMSD) between observed and modelled β_{sca} and β_{abs} to find the optimal n_1 and k_1 pair; The RMSD between observation and modelling was calculated as:

$$\mathrm{RMSD} = \sqrt{\left(\frac{\beta_{sca-obs} - \beta_{sca-mod}}{\beta_{sca-mod}}\right)^2 + \left(\frac{\beta_{abs-obs} - \beta_{abs-mod}}{\beta_{abs-mod}}\right)^2}$$

- Estimation of the truncation correction coefficient $C_{sca}(\lambda) = \beta_{sca}(\lambda, 0° - 180°)/\beta_{sca}(\lambda, \theta_1 - \theta_2)$;
- Sensitivity to the input parameters, as well as the C_{ref} variability were performed to provide the n and k uncertainty. Those consisted in repeating the iterative method by using as input the first and third quartiles, the median and the mean to take into account the variability of the dataset within the averaged hour, and the systematic error of the measurement. The final value for n and k have been estimated as the average of the n and k from the sensitivity tests, and the total uncertainty has been estimated as the standard deviation of the n and k from all the tests performed.

$$\mathrm{RMSD} = \sqrt{\left(\frac{\beta_{sca-obs} - \beta_{sca-mod}}{\beta_{sca-mod}}\right)^2 + \left(\frac{\beta_{abs-obs} - \beta_{abs-mod}}{\beta_{abs-mod}}\right)^2} \quad \text{(S1)}$$

Supplementary Text 2. Detailed procedure for CRI retrieval from GRIMM OPC – SMPS comparison

The following treatment on the GRIMM OPC and SMPS data was applied:

- The GRIMM OPC not CRI corrected $dN(Dopt)/dlogDopt$ was interpolated over the SMPS geometrical diameters;
- The imaginary part of the refractive index was fixed to that of the optical retrieval.
- The optical−to−geometrical correction on the GRIMM OPC size distribution was performed varying the diameters corrections in the [1.33, 1.74] real refractive index range;
- Estimation of the root mean squared error (RMSE) and mean absolute error (MAE) between the GRIMM OPC and SMPS $dN(Dg)/dlogDg$ at each iteration after applying the aforementioned corrections;
- Average of the real refractive index on all the values within the 15th percentile distribution of RMSE and MAE;
- The retrieval uncertainty was calculated performing simulations taking into account i) the size distribution statistical error due to counting (detailed in Sec 2.2.3) and ii) the imaginary part uncertainty from the complex refractive index retrieval.

The RMSE stands for the root mean squared error and was calculated as:

$$\mathrm{RMSE} = \sqrt{\frac{\sum\left(\frac{dN}{dlog(D)_{SMPS}} - \frac{dN}{dlog(D)_{GRIMM\ OPC}}\right)^2}{N}} \quad \text{(S2)}$$

where N is the number of points in the overlapping region. The MAE is the mean absolute error and it has been estimated as:

$$\mathrm{MAE} = \frac{1}{N}\left|\frac{dN}{dlog(D)_{SMPS}} - \frac{dN}{dlog(D)_{GRIMM\ OPC}}\right| \quad \text{(S3)}$$

Supplementary Text 3. Mass concentration threshold for CRI retrieval: optical closure versus OPC–SMPS overlap methods

Figure 2 in the main manuscript shows the 1:1 comparison between the real refractive index retrieved at 780 and 655 nm at PRG and RambForest based on optical closure versus OPC–SMPS overlap method (the time series of the retrieved n at PRG and RambForest with the two methods is shown in Fig. S7). Considering all data points (panel (a) and (b)) a slope of 0.77 and 0.23 and a correlation coefficient of 0.82 and 0.15 are obtained respectively for the PRG and RambForest, indicating a limited correlation at rural site. A closer look at the data suggest that periods with very low aerosol load, significantly influence the comparison. This is not surprising since the lower the aerosol load, the lower the constraint given by the measured optical signal and number concentration to the retrieval procedure. The correlation significantly improves at the RambForest site (a slope of 0.93 and a correlation coefficient of 0.6, panel (d)), while showing a weak impact on the PRG site (a slope of 0.75 and a correlation coefficient of 0.84 at the RambForest site, panel (c)), by applying a threshold to the dataset at 3 µg m^{-3} (based on mass concentration from SMPS data and assuming an aerosol uniform density of 1.4 g cm^{-3}). This threshold corresponds to a β_{ext} of 12 Mm^{-1} (assuming a mass extinction efficiency, MEE, of 4 m^2g^{-1}), corresponding to the 25th, 35th and 52th percentile of the β_{ext} distribution at PRG, SIRTA and RambForest sites. This analysis, which compares the real refractive index data derived based on independent calculations and different inputs (SMPS, β_{abs} and β_{sca} on one side, while SMPS versus OPC on the other side), suggests that a minimum in the aerosol load is necessary to provide a well constrained retrievals. Applying the 3 µg m^{-3} threshold reduces the total number of valid CRI retrieval of 5%, 37% and 43% respectively for the urban, peri−urban and rural sites.

Supplementary Tables

INPUTS	SIMULATION LABELS	SITE	RESULT
$dN(D_g)/dlogD_g$ from SMPS β_{sca} β_{abs}	mean, q1, median, q3, errp, errm	Paris Rive Gauche (PRG) SIRTA Rambouillet	n–ik (mean±SD)

Table S1 : List of all simulations performed using the different inputs to retrieve the final CRI. The simulation labels represents the attributed name to the sensitivity tests performed: "mean" represents the test using the hourly mean inputs, "q1" represents the test using 1st quartile values of the inputs, "q3" represents the test using 3rd quartile values of the inputs, "median" represents the test using the median values of the inputs, "errp" represents the test performed on the median values plus the instrumental error due to noise and SD of the inputs, "errm" "represents the test performed on the median values minus the instrumental error due to noise and SD of the inputs. The final CRI is retrieved as the mean σ±SD.

Wind direction	SSA ± SD			n ± SD			k ± SD		
	PRG	**SIRTA**	**Ramb Forest**	**PRG**	**SIRTA**	**Ramb Forest**	**PRG**	**SIRTA**	**Ramb Forest**
N	0.73 ±0.08	0.79 ±0.06	0.86 ±0.03	1.40 ±0.07	1.56 ±0.05	1.48 ±0.05	0.035± 0.016	0.039± 0.010	0.021 ±0.004
NNE	0.77 ±0.06	0.80 ±0.07	0.85 ±0.03	1.39 ±0.05	1.52 ±0.08	1.50 ±0.03	0.027± 0.007	0.038 ±0.015	0.023 ±0.004
NE	0.75 ±0.09	0.78 ±0.08	0.83 ±0.03	1.40 ±0.05	1.50 ±0.07	1.48 ±0.06	0.031 ±0.015	0.040 ±0.014	0.024± 0.005
ENE	0.78 ±0.07	0.79 ±0.07	0.82 ±0.04	1.40 ±0.05	1.51 ±0.07	1.50 ±0.05	0.025 ±0.008	0.039 ±0.012	0.028 ±0.007
E	0.77 ±0.10	0.73 ±0.11	0.80 ±0.05	1.38 ±0.06	1.50 ±0.06	1.50 ±0.04	0.031 ±0.015	0.051 ±0.031	0.032 ±0.008
ESE	0.73 ±0.08	0.76 ±0.08	0.82 ±0.04	1.42 ±0.04	1.51 ±0.09	1.53 ±0.03	0.038 ±0.015	0.044 ±0.019	0.030± 0.008
SE	0.71 ±0.10	0.75 ±0.12	0.85 ±0.05	1.43 ±0.04	1.55 ±0.06	1.54 ±0.04	0.044 ±0.024	0.059 ±0.029	0.027± 0.004
SSE	0.69 ±0.11	0.81 ±0.10	0.88 ±0.05	1.42 ±0.04	1.53 ±0.06	1.55 ±0.02	0.049 ±0.030	0.065 ±0.026	0.021± 0.003
S	0.70 ±0.08	0.84 ±0.05	0.90 ±0.02	1.42 ±0.06	1.56 ±0.04	1.51 ±0.08	0.043 ±0.013	0.031 ±0.014	0.018 ±0.005
SSW	0.69 ±0.10	0.84 ±0.05	0.90 ±0.03	1.41 ±0.06	1.55 ±0.05	1.51 ±0.02	0.050 ±0.021	0.022 ±0.008	0.021 ±0.002
SW	0.66 ±0.10	0.85 ±0.05	0.89 ±0.03	1.39 ±0.06	1.55 ±0.06	1.51 ±0.05	0.051 ±0.026	0.024 ±0.008	0.020 ±0.004
WSW	0.67 ±0.10	0.83 ±0.06	0.90 ±0.03	1.39 ±0.04	1.51 ±0.06	1.49 ±0.06	0.044 ±0.022	0.024 ±0.006	0.018 ±0.005
W	0.73 ±0.12	0.83 ±0.06	0.87 ±0.04	1.44 ±0.06	1.50 ±0.07	1.54 ±0.10	0.040 ±0.024	0.024 ±0.006	0.021 ±0.006
WNW	0.72 ±0.12	0.81 ±0.08	0.87 ±0.04	1.42 ±0.07	1.56 ±0.05	1.48 ±0.11	0.038 ±0.018	0.027 ±0.006	0.020 ±0.004
NW	0.82 ±0.10	0.85 ±0.08	0.89 ±0.03	1.43 ±0.06	1.51 ±0.07	1.52 ±0.02	0.033 ±0.021	0.032 ±0.010	0.018 ±0.006
NNW	0.77 ±0.10	0.82 ±0.06	0.86 ±0.04	1.41 ±0.08	1.56 ±0.04	1.50 ±0.04	0.033 ±0.012	0.033 ±0.009	0.023 ±0.007

Table S2: Single scattering albedo and complex refractive index averages ±SD at 520 nm and for the urban (PRG), peri−urban (SIRTA) and rural (RambForest) sites and under different wind direction regimes.

Supplementary Figures

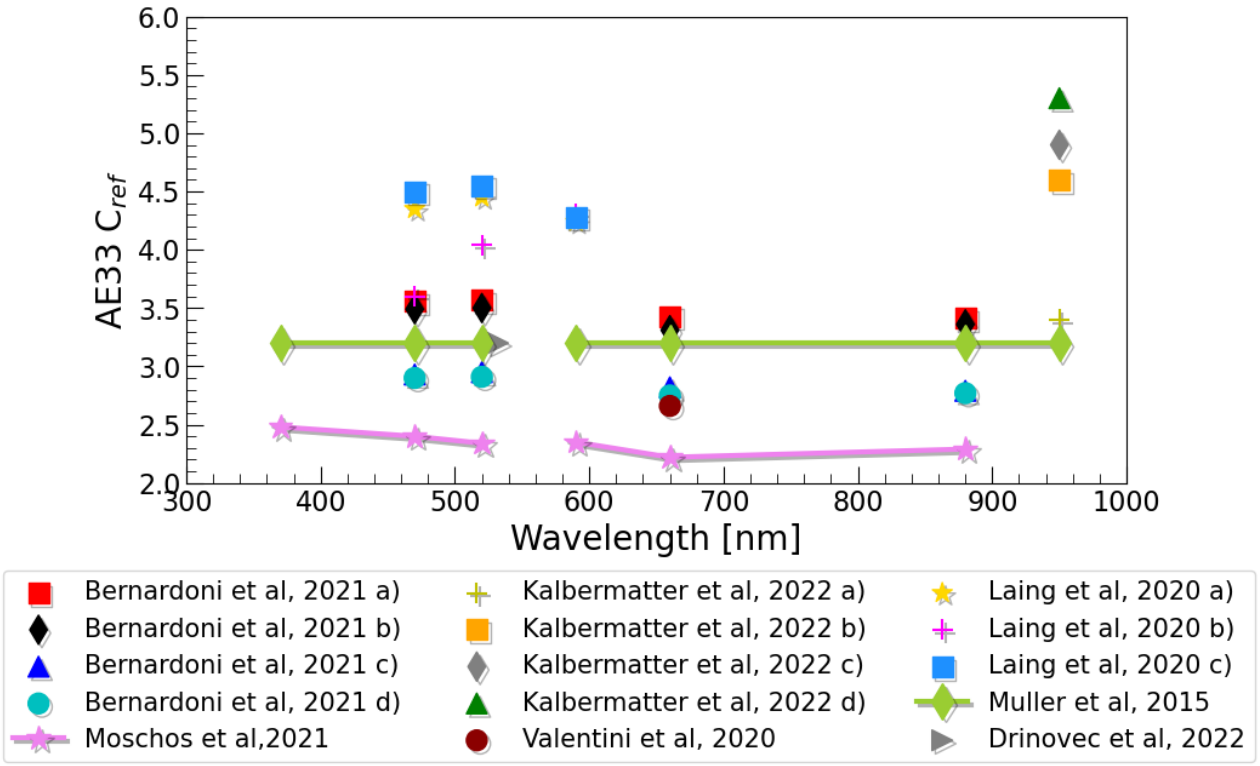

Figure S1: Multiple scattering coefficient C_{ref} values from the recent literature as a function of the wavelength. The (Bernardoni et al., 2021) different cases represent a) day PP, b) night PP, c) day PaM, d) night paM approaches. The (Kalbermatter et al., 2022) different cases report C_{ref} values at different SSA a) 0.03 b) 0.13 c) 0.5 and d) 0.68. (Laing et al., 2020) different cases in Oregon considering a) all the aerosol species b) only biomass burning events c) only non−biomass burning events.

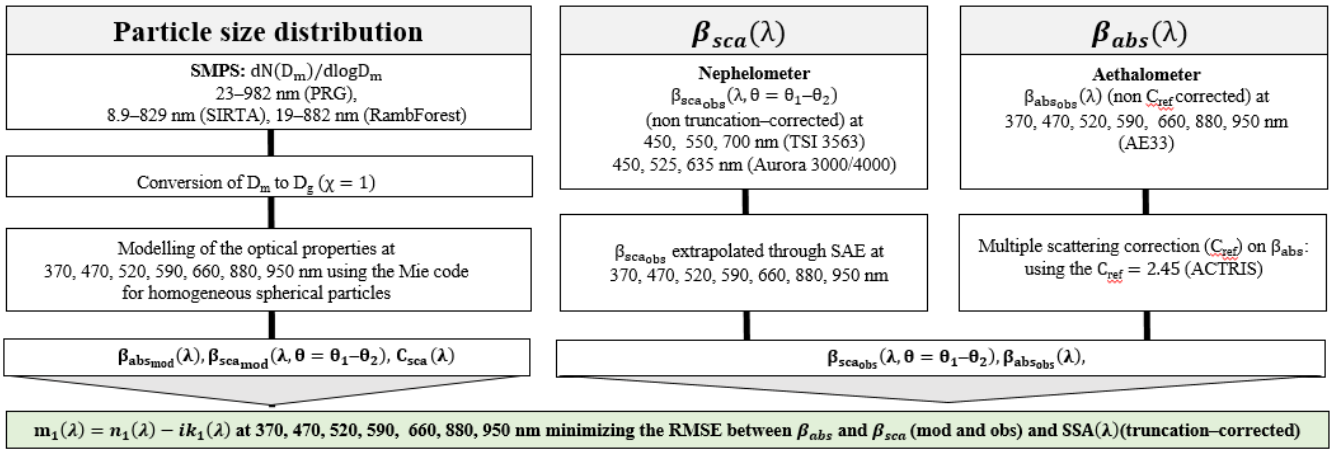

Figure S2: Flowchart of optical complex refractive index retrieval (CRI, m=n–ik) by means of the iterative method. See main text for details. dN(Dm)/dlogDm is the SMPS particle size distribution measured through the mobility diameter (Dm) range. βsca(λ,θ1–θ2) is the spectral aerosol scattering coefficient integrated within the measured angles θ1 and θ2. The subscript obs and mod represent respectively the modelled and observed parameter. βsca(λ,0°–180°) is the spectral aerosol scattering coefficient integrated over the 0°–180° range. βabs(λ) is the spectral aerosol absorption coefficient measured. Csca(λ) is the spectral truncation correction coefficient for the measured βsca(λ,θ1–θ2). m1(λ) is the spectral complex refractive index estimated using only the SMPS size distribution. The Cref is the multiple scattering paremater

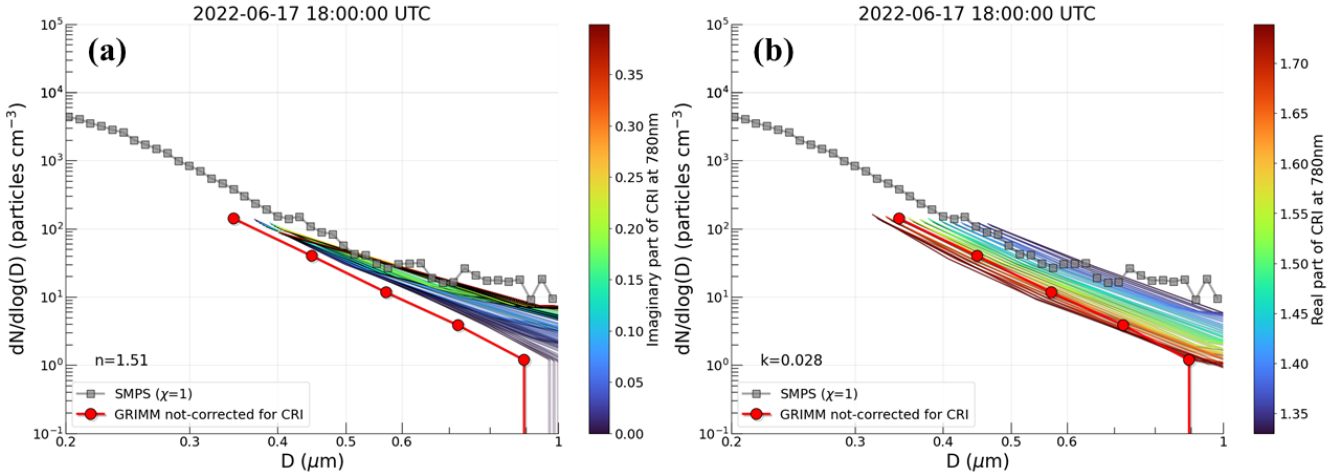

Figure S3: Sensitivity of the GRIMM OPC (model 1.108) particle size distribution (<1µm) $dN(D_o)/dlogD_o$ at the Paris Rive Gauche site to a) the imaginary part of the CRI used for the optical–to–geometrical diameters correction, fixing the real part at the optical retrieved value of 1.51 for the 17 June 2022 at 18 UTC b) the real part of the CRI used for the optical–to–geometrical diameters correction, fixing the imaginary part at the optical retrieved value of 0.028 for the 17 June 2022 at 18 UTC. Grey squares represent the SMPS particle size distribution. The red circles, the GRIMM OPC not–corrected size distribution, while the colorbar refers to the variability of the imaginary and real part respectively for a) and b).

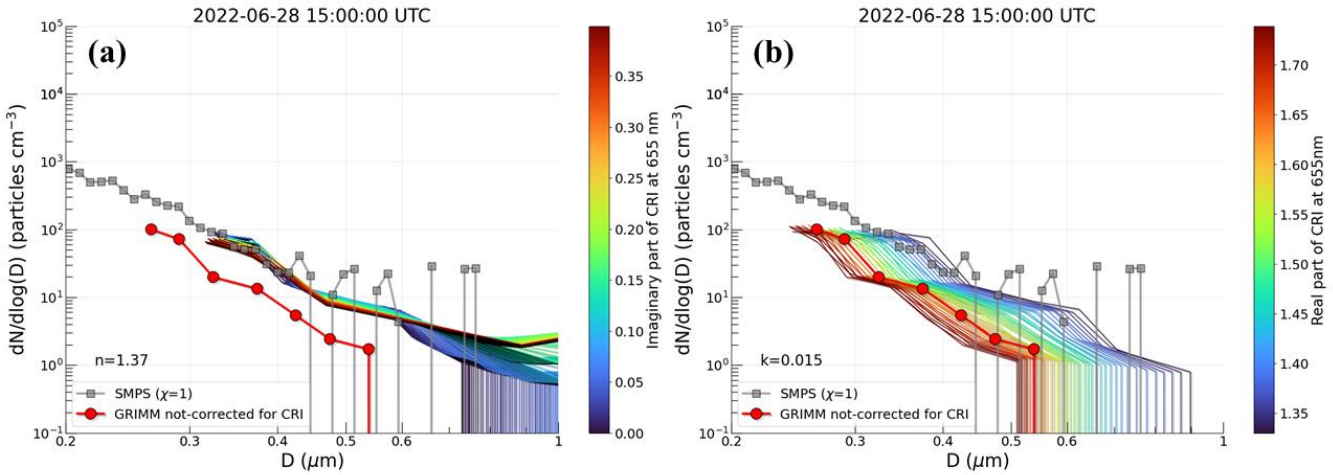

Figure S4: Sensitivity of the GRIMM OPC (model 1.109) particle size distribution (<1µm) $dN(D_o)/dlogD_o$ at the Rambouillet site to a) the imaginary part of the CRI used for the optical–to–geometrical diameters correction, fixing the real part at the optical retrieved value of 1.51 for the 17 June 2022 at 18 UTC b) the real part of the CRI used for the optical–to–geometrical diameters correction, fixing the imaginary part at the optical retrieved value of 0.028 for the 17 June 2022 at 18 UTC. Grey squares represent the SMPS particle size distribution. The red circles, the GRIMM OPC not–corrected size distribution, while the colorbar refers to the variability of the imaginary and real part respectively for a) and b).

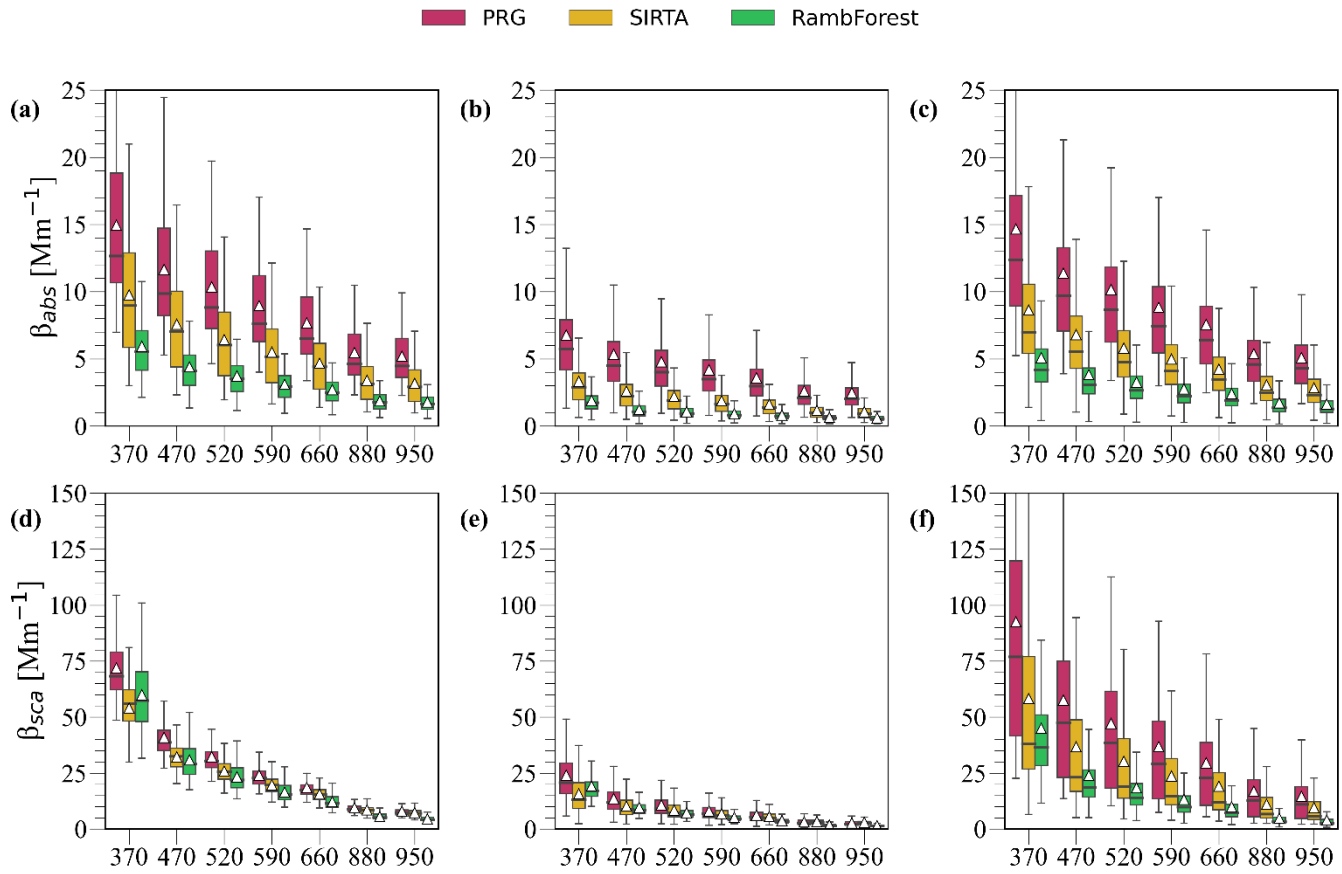

Figure S5: Wavelength dependence of β_{abs}, and β_{sca} and splitted by the different sites and under the first heatwave, the clean period and the second heatwave: a) and d), for the Paris Rive gauche (PRG) site; b) and e) for the SIRTA site; c), and f) for the Rambouillet (RambForest) site. The absorption and scattering coefficient are decreasing with the wavelength for all the three sites, showing an urban–to–rural gradient. The white triangles represent the mean values, while the median has been reported as the line crossing the boxplot. Outliers are not shown for the sake of readability.

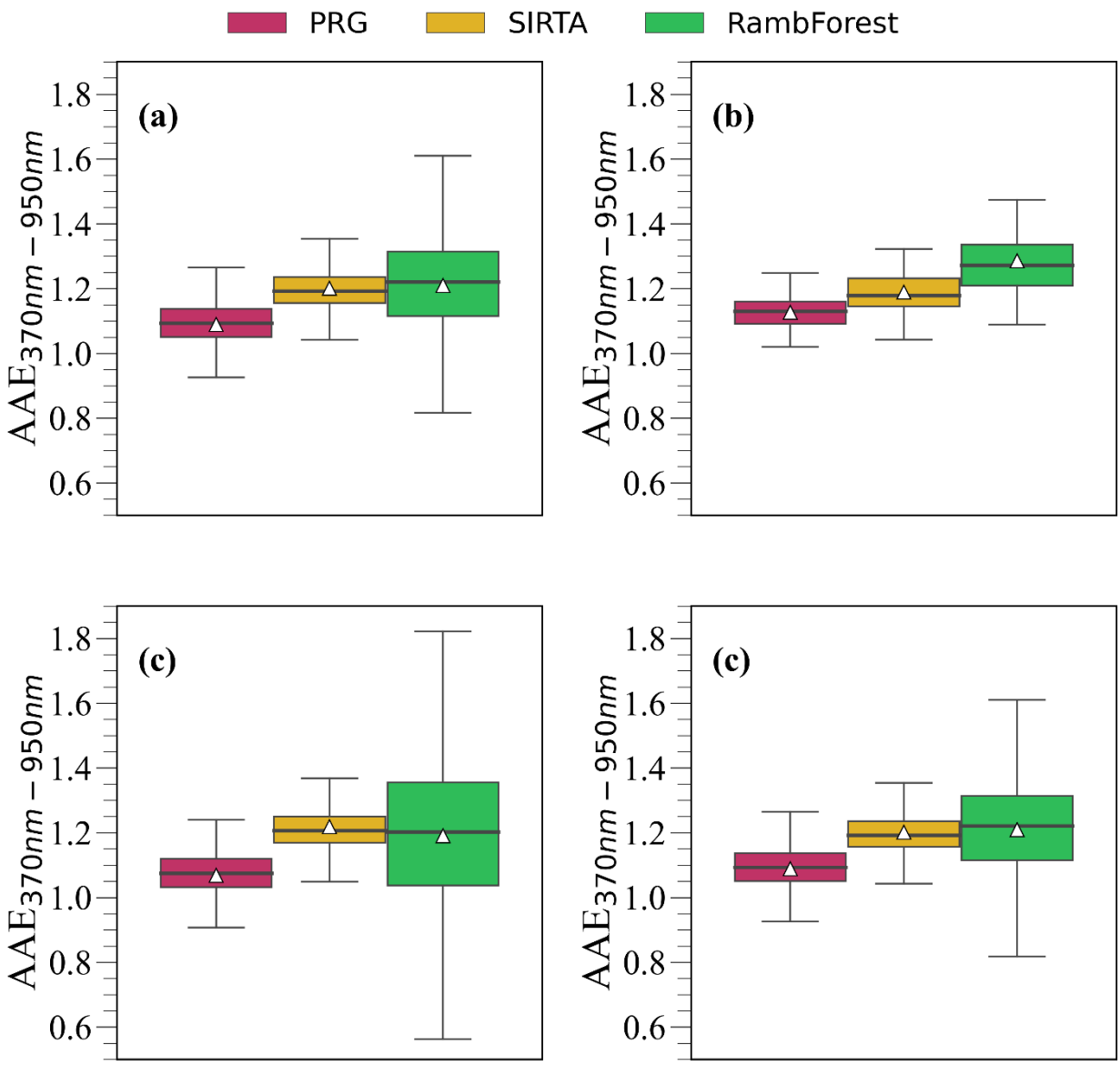

Figure S6: Absorption angstrom exponent between 370 and 950 nm variability for (a) full period (b) first heatwave (c) clean period and (d) second heatwave for the PRG, SIRTA and RambForest sites. Higher values are observed at the rural site compared to the urban site. Black lines represent the boxplot median, while white triangles represent the boxplot mean.

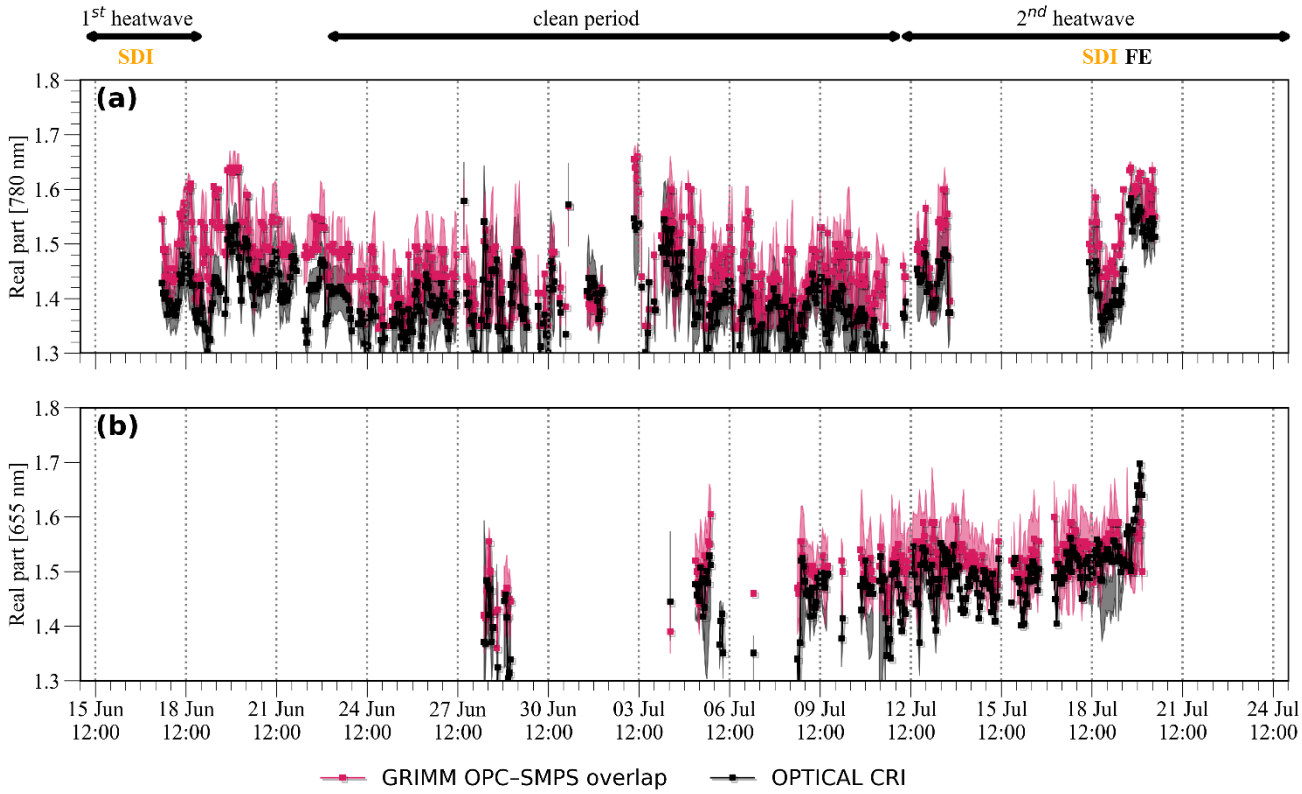

Figure S7: Time series of the real part of the refractive index at the a) PRG (urban) site and b) Rambouillet Rambouillet sites using the two retrievals detailed in Sec. 3. Shaded area represents the uncertainty of the retrievals. Panels c) and d) show the scatter plot of the CRI real retrieval at the urban and rural respectively, colored by the particle mass calculated from the SMPS data and assuming an aerosol particle density of 1.4 g/cm3. SDI (colored in orange) and FE (colored in black) stands for the Saharan dust intrusion from the upper levels down to the ground and the Gironde fire episode (started from the southern part of France) respectively. Red dotted line represents the fit line, while the blue line represents the 1:1 line.

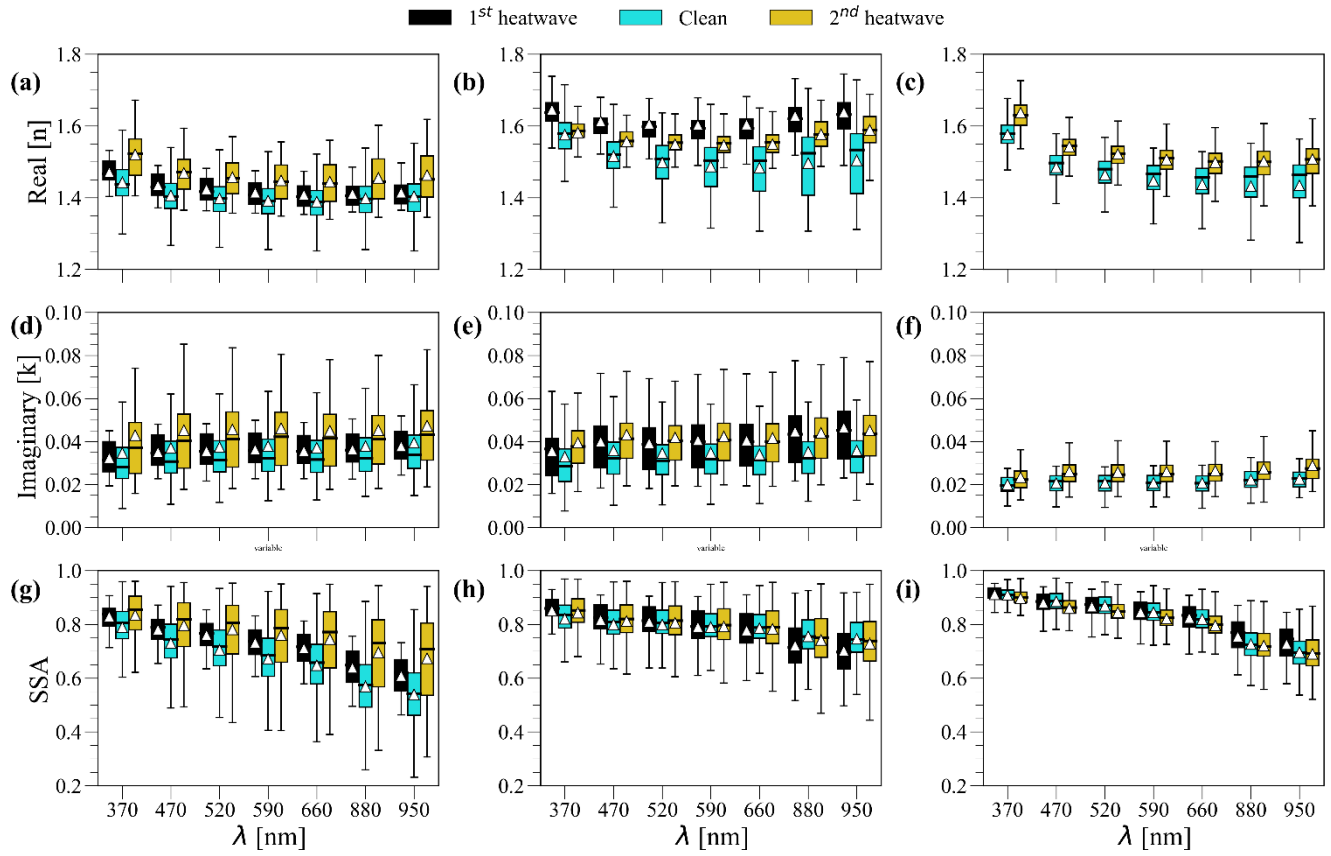

Figure S8: Wavelength dependence of the single scattering albedo (SSA) and complex refractive index (CRI) for all the available points in the period under investigation for the PRG (panels (a), (d), (g)), SIRTA (panels (b), (e), (h)), RambForest (panels (c), (f), (i)) ground−based sites. White triangles show the average value, while black lines show the median values. Outliers are not shown for the sake of readability.

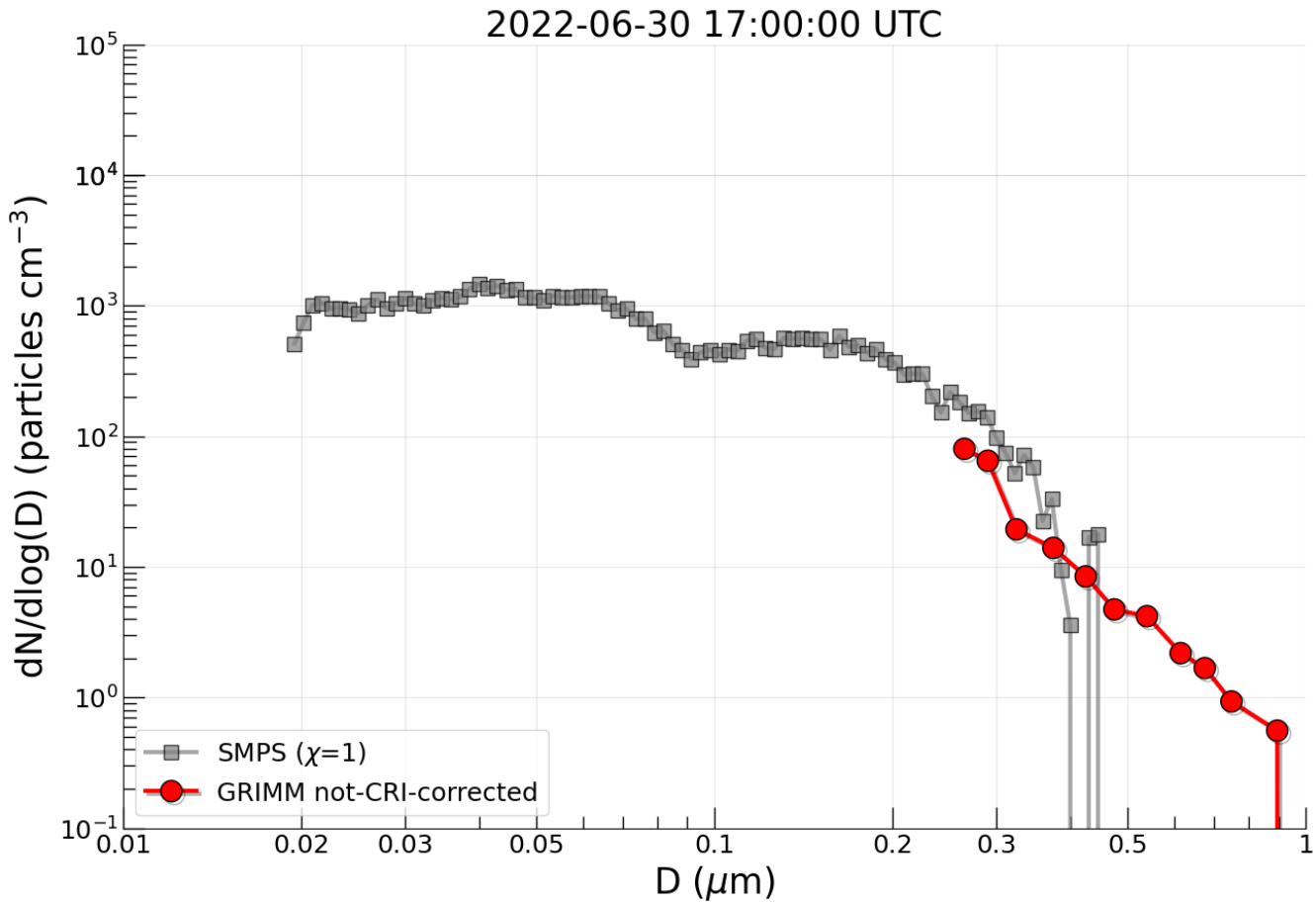

Figure S9: SMPS and GRIMM OPC not−CRI−corrected particle size distribution (<1µm) dN(D)/dlogD hourly median measured at RambForest site for the 30 June at 17 UTC. SMPS shows no particles above 0.5 µm, compared to the OPC.

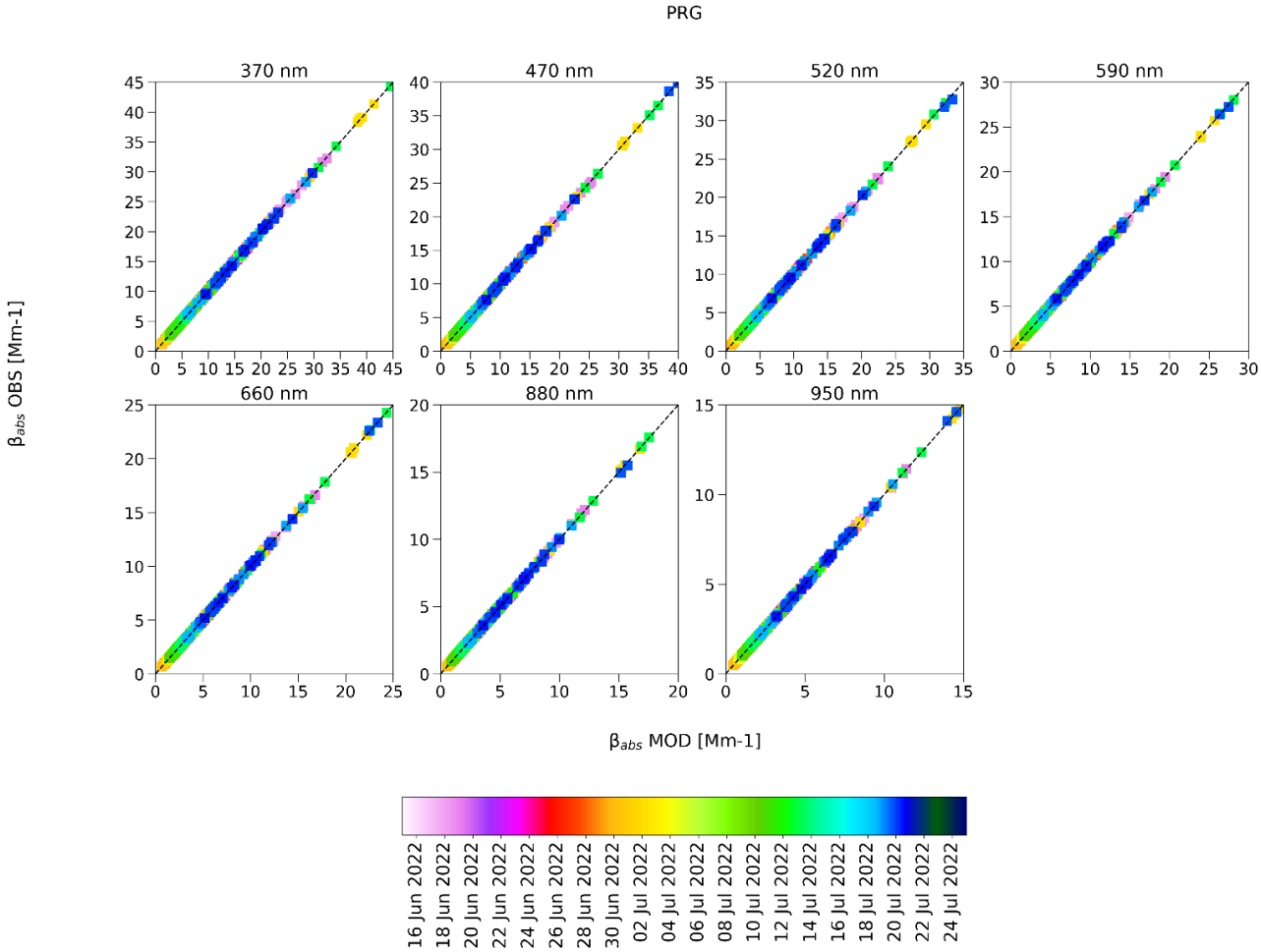

Figure S10: Scatter plot of the hourly median observed absorption coefficient vs modelled at seven different wavelengths and during the all ACROSS campaign at the Paris Rive Gauche (urban site). The colorbar represents the time. The absorption coefficient has been calculated using a Mie code for spherical particles varying the real part (n) and imaginary part (k) in the [1.3,2] and [0,0.2] respectively. The modelled value represents the value that minimizes the root mean squared difference (RMSD) of Eq. 4. Only SMPS data has been taken into account.

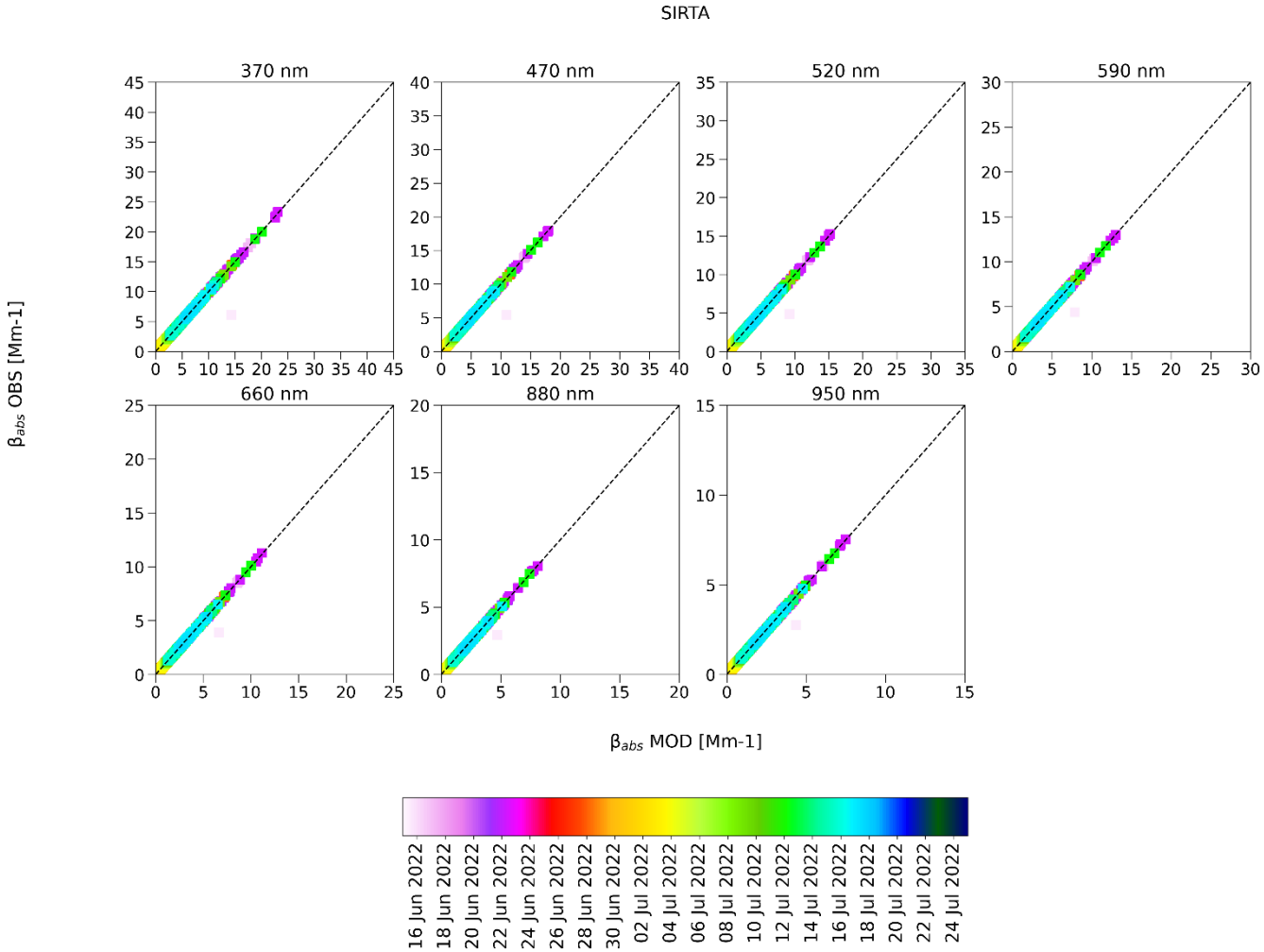

Figure S11: Scatter plot of the hourly median observed absorption coefficient vs modelled at seven different wavelengths and during the all ACROSS campaign at the SIRTA (peri–urban site). The colorbar represents the time. The absorption coefficient has been calculated using a Mie code for spherical particles varying the real part (n) and imaginary part (k) in the [1.3,2] and [0,0.2] respectively. The modelled value represents the value that minimizes the root mean squared difference (RMSD) of Eq. 4. Only SMPS data have been taken into account.

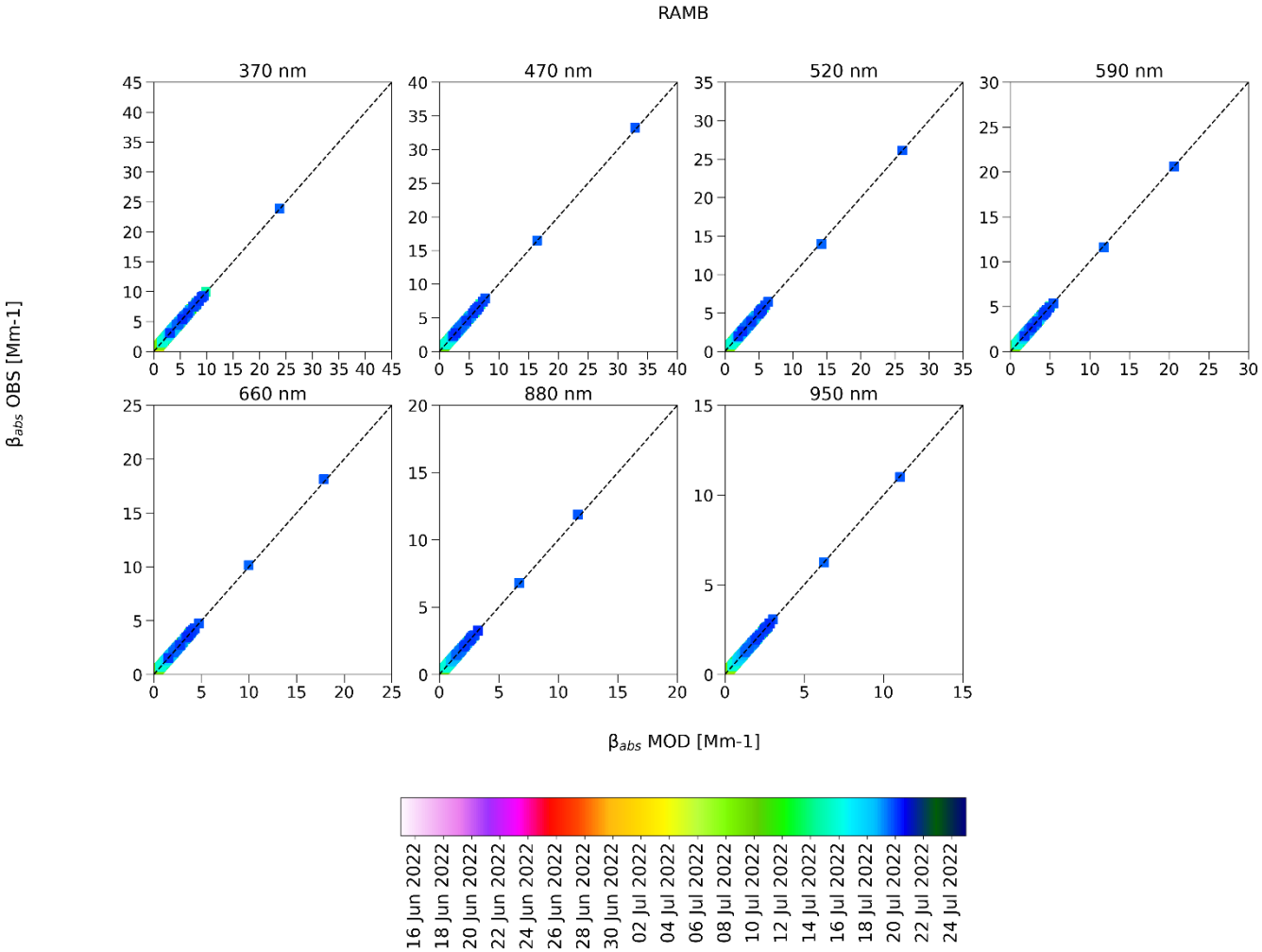

Figure S12: Scatter plot of the hourly median absorption coefficient observed vs modelled at seven different wavelengths and during the all ACROSS campaign at the Rambouillet (rural site). The colorbar represents the time. The absorption coefficient has been calculated using a Mie code for spherical particles varying the real part (n) and imaginary part (k) in the [1.3,2] and [0,0.2] respectively. The modelled value represents the value that minimises the root mean squared difference (RMSD) of Eq. 4. Only SMPS data have been taken into account.

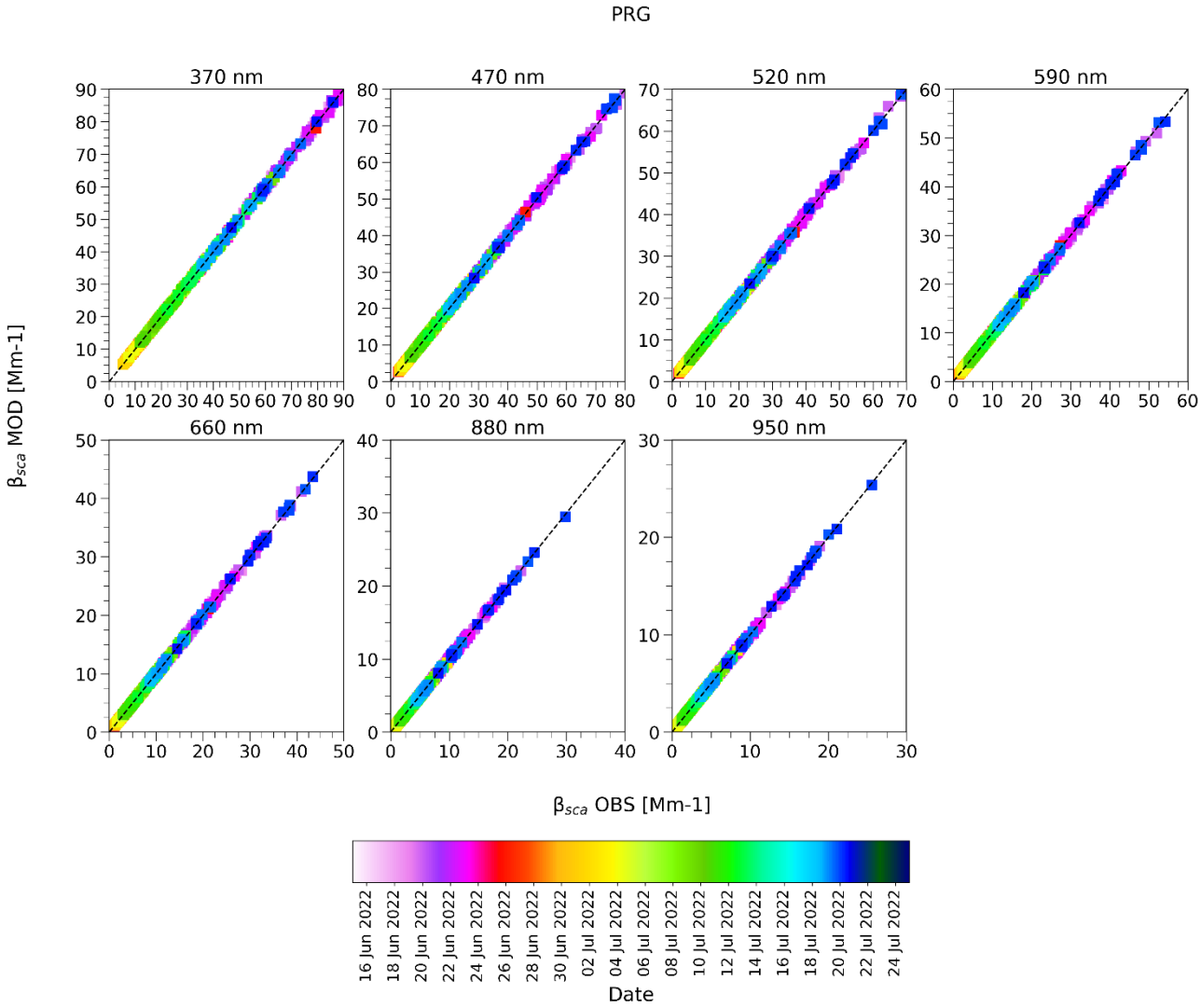

Figure S13: Scatter plot of the hourly median observed scattering coefficient vs modelled at seven different wavelengths and during the all ACROSS campaign at the Paris Rive Gauche (urban site). The colorbar represents the time. The scattering coefficient has been calculated using a Mie code for spherical particles varying the real part (n) and imaginary part (k) in the [1.3,2] and [0,0.2] respectively. The modelled value represents the value that minimises the root mean squared difference (RMSD) of Eq. 4. Only SMPS data has been taken into account.

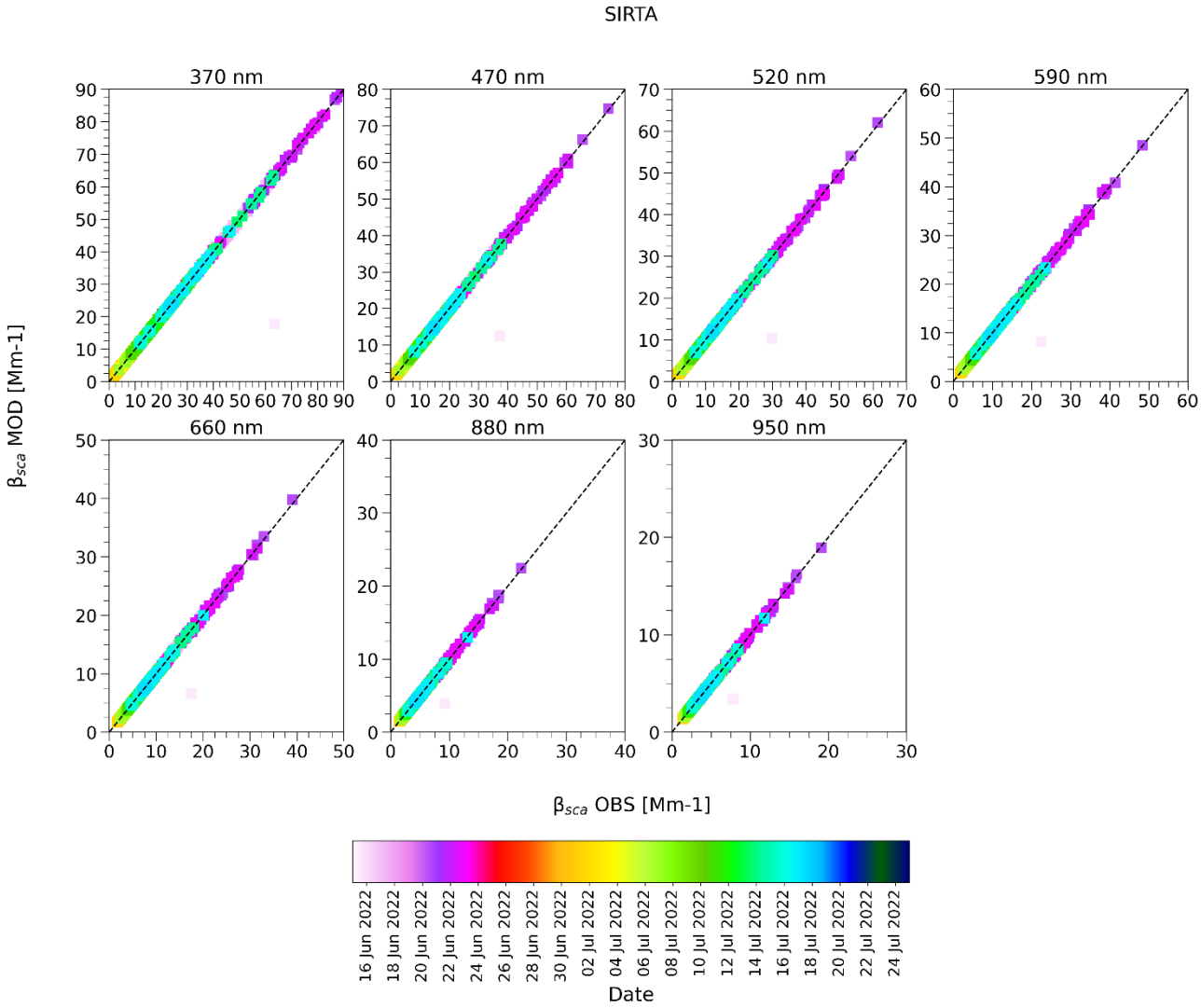

Figure S14: Scatter plot of the hourly median observed scattering coefficient vs modelled at seven different wavelengths and during the all ACROSS campaign at the SIRTA (peri–urban site). The colorbar represents the time. The scattering coefficient has been calculated using a Mie code for spherical particles varying the real part (n) and imaginary part (k) in the [1.3,2] and [0,0.2] respectively. The modelled value represents the value that minimises the root mean squared error of Eq. x. Only SMPS data has been taken into account.

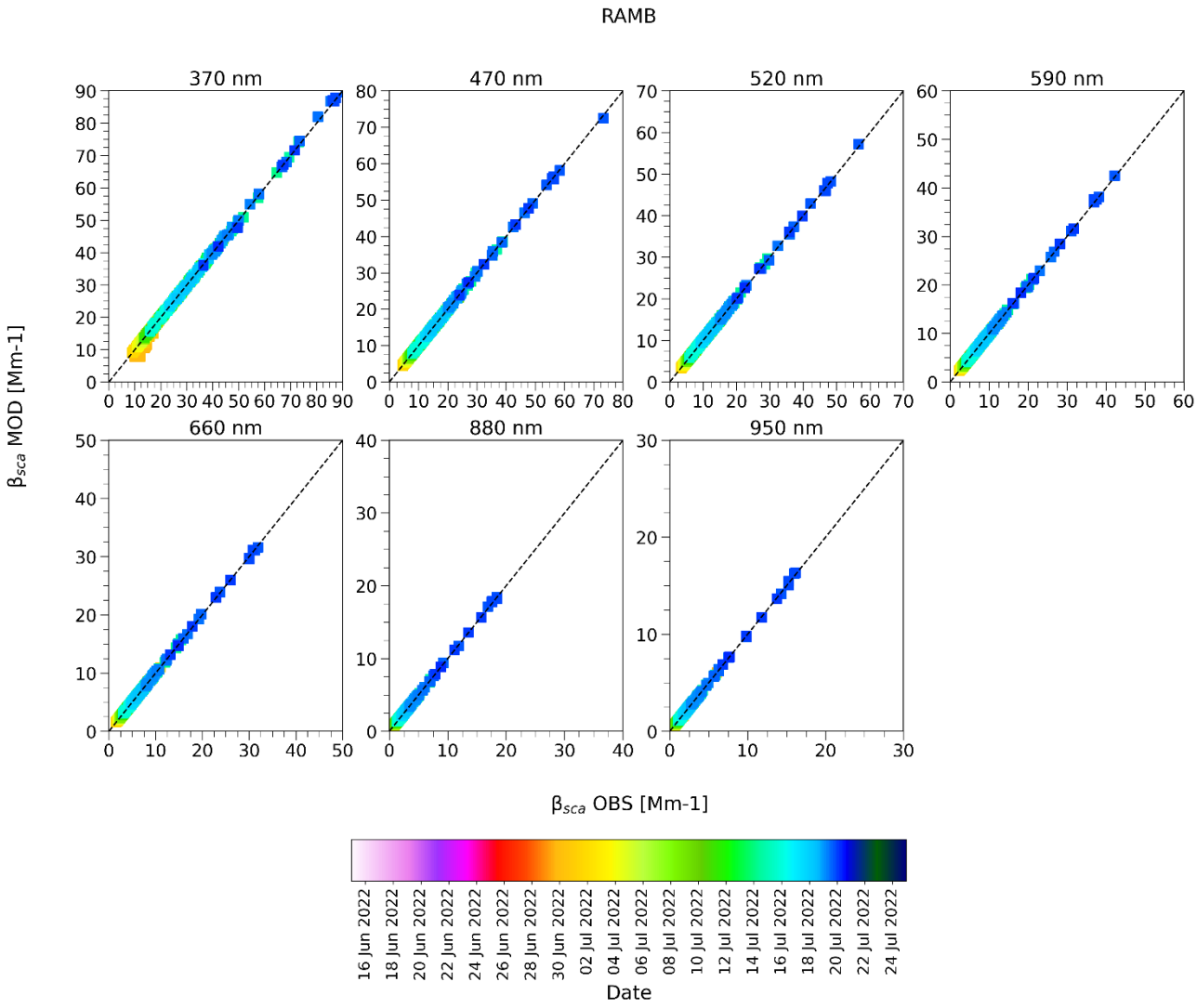

Figure S15: Scatter plot of the hourly median observed scattering coefficient vs modelled at seven different wavelengths and during the all ACROSS campaign at the Rambouillet (rural site). The colorbar represents the time. The scattering coefficient has been calculated using a Mie code for spherical particles varying the real part (n) and imaginary part (k) in the [1.3,2] and [0,0.2] respectively. The modelled value represents the value that minimises the root mean squared difference (RMSD) of Eq. 4. Only SMPS data has been taken into account.

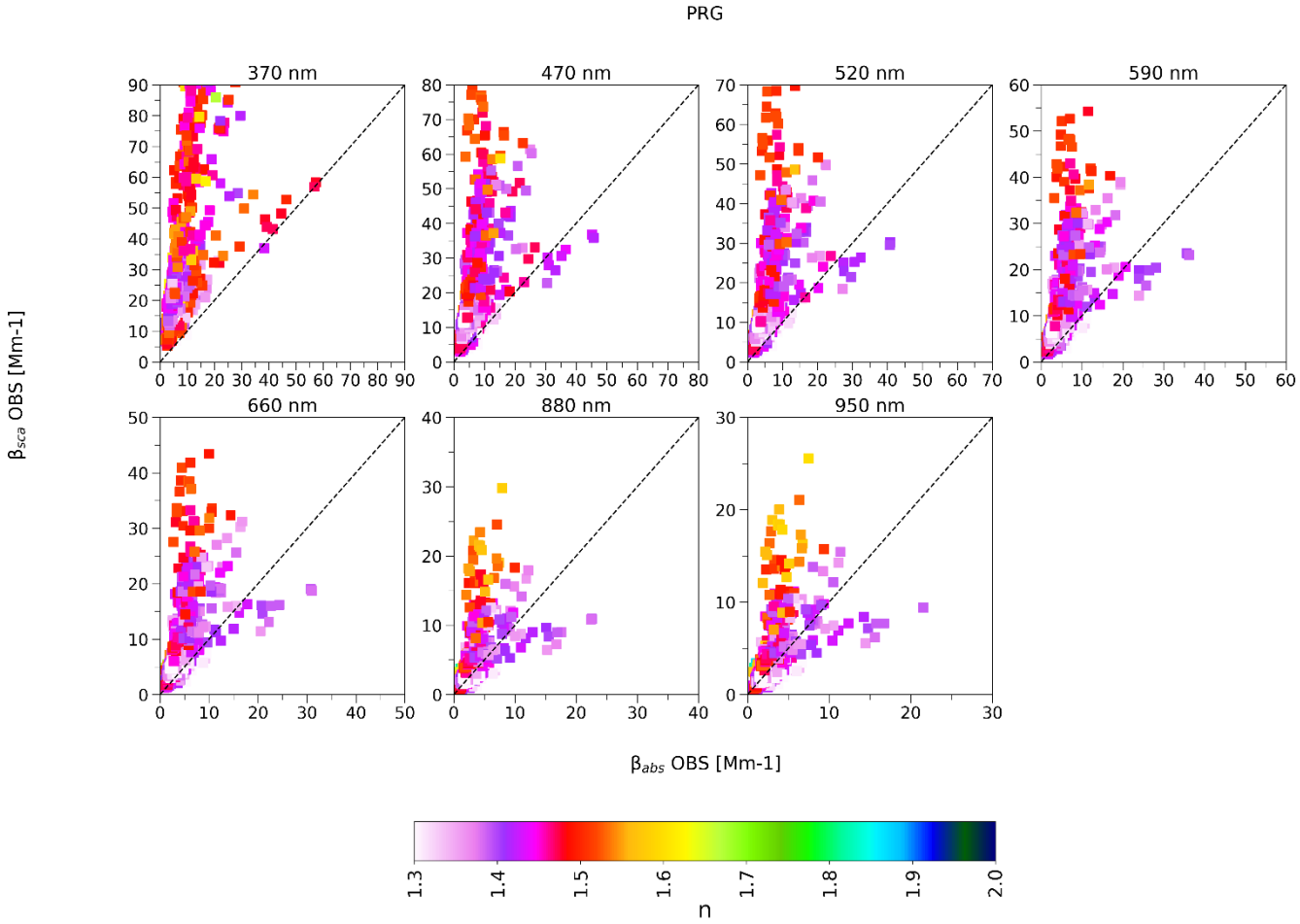

Figure S16: Scatter plot of hourly median observed scattering and absorption coefficient at seven different wavelengths and during the all ACROSS campaign at the Paris Rive Gauche (urban site). The colors represent the simulated real (n) part of CRI simulated using a Mie code for spherical particles varying n and k in the [1.3,2] and [0,0.2] respectively. The modelled value represents the value that minimizes root mean squared difference (RMSD) of Eq. 4. Only SMPS data has been taken into account for optical calculations.

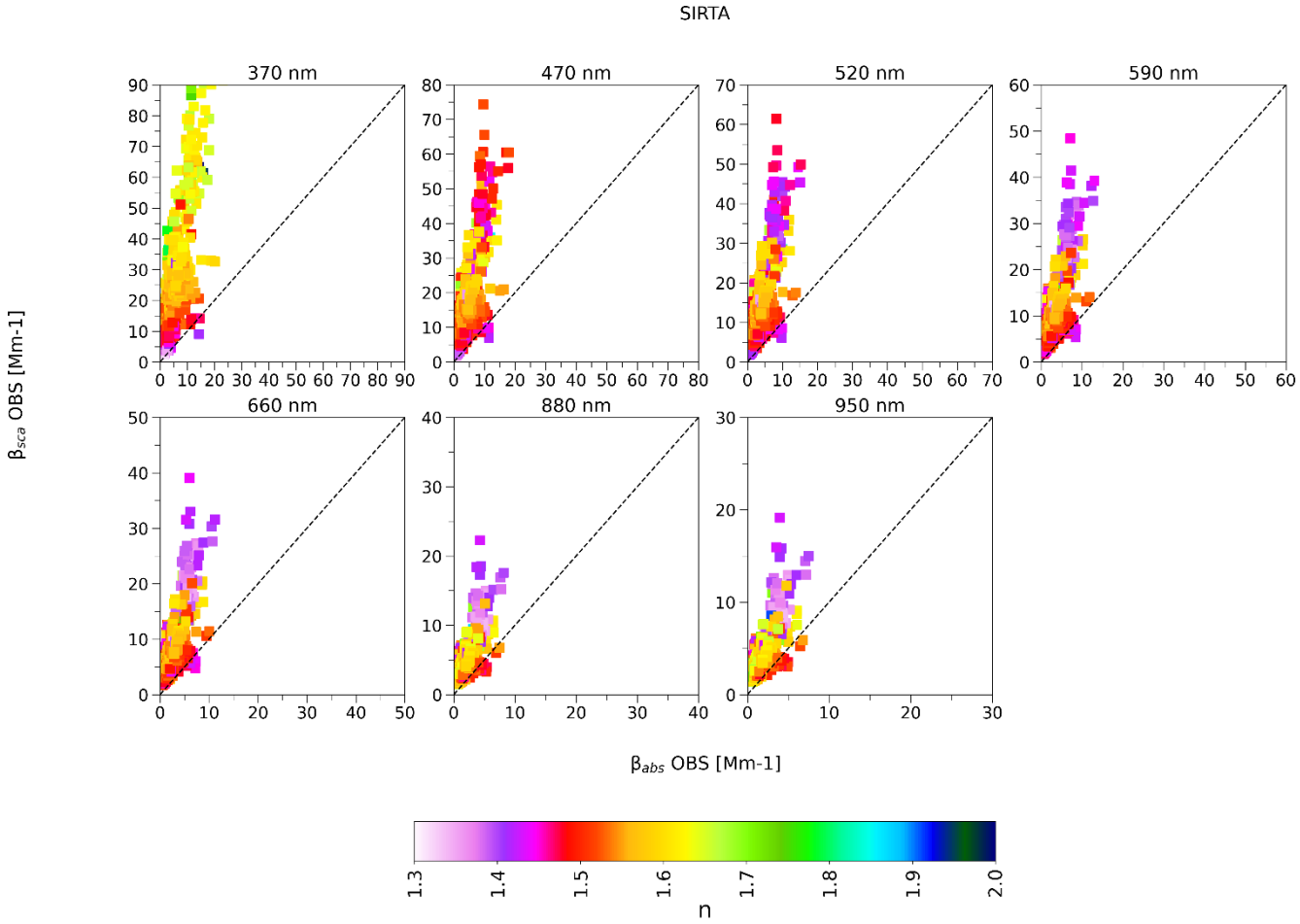

Figure S17: Scatter plot of hourly median observed scattering and absorption coefficient at seven different wavelengths and during the all ACROSS campaign at the SIRTA (peri–urban site). The colours represent the simulated n. The real (n) part of CRI has been simulated using a Mie code for spherical particles varying n and k in the [1.3,2] and [0,0.2] respectively. The modelled value represents the value that minimises the root mean squared difference (RMSD) of Eq. 4. Only SMPS data has been taken into account.

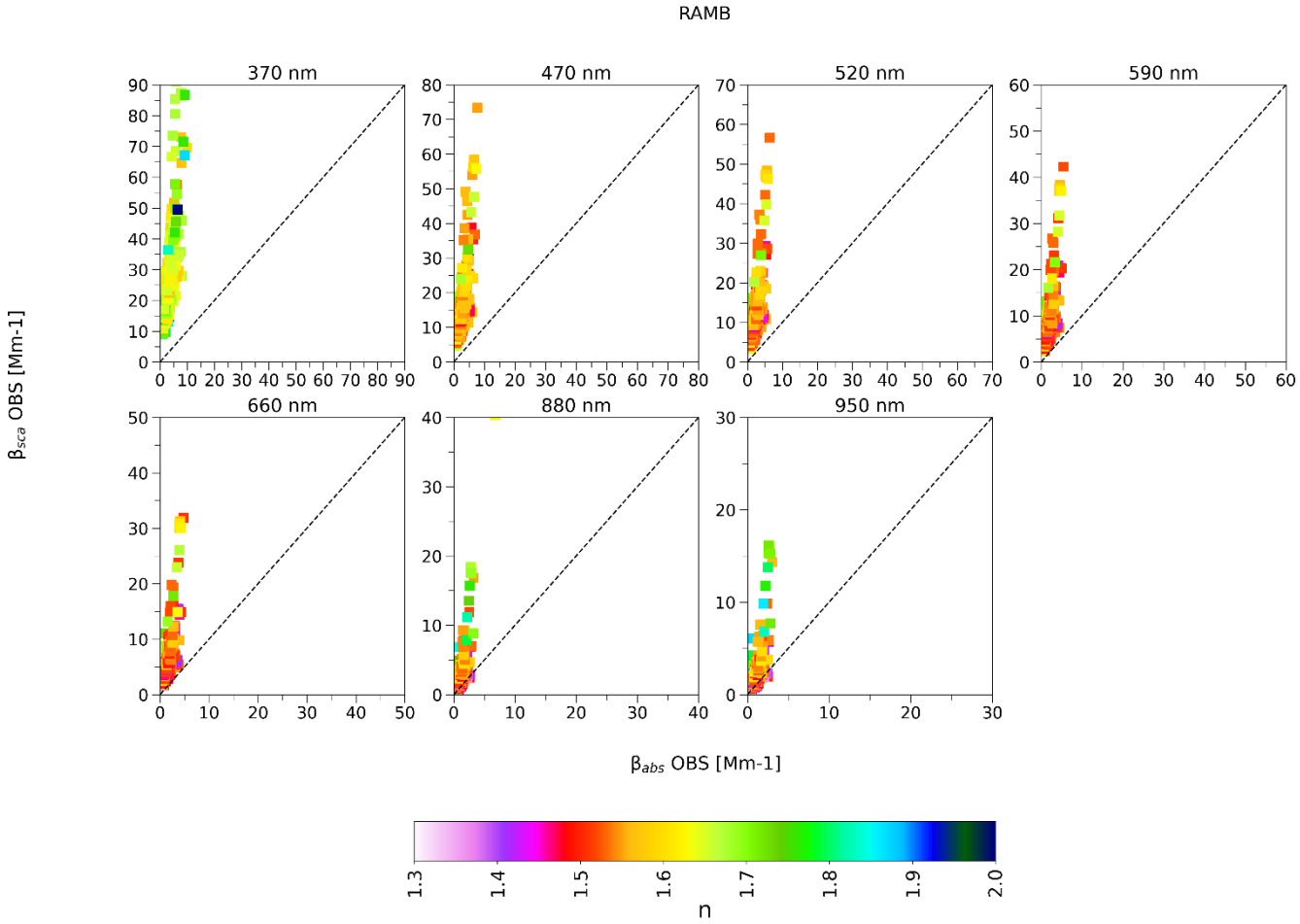

Figure S18: Scatter plot of hourly median observed scattering and absorption coefficient at seven different wavelengths and during the all ACROSS campaign at the Rambouillet (rural site). The colours represent the simulated n. The real (n) part of CRI has been simulated using a Mie code for spherical particles varying n and k in the [1.3,2] and [0,0.2] respectively. The modelled value represents the value that minimises the root mean squared difference (RMSD) of Eq. 4. Only SMPS data has been taken into account.

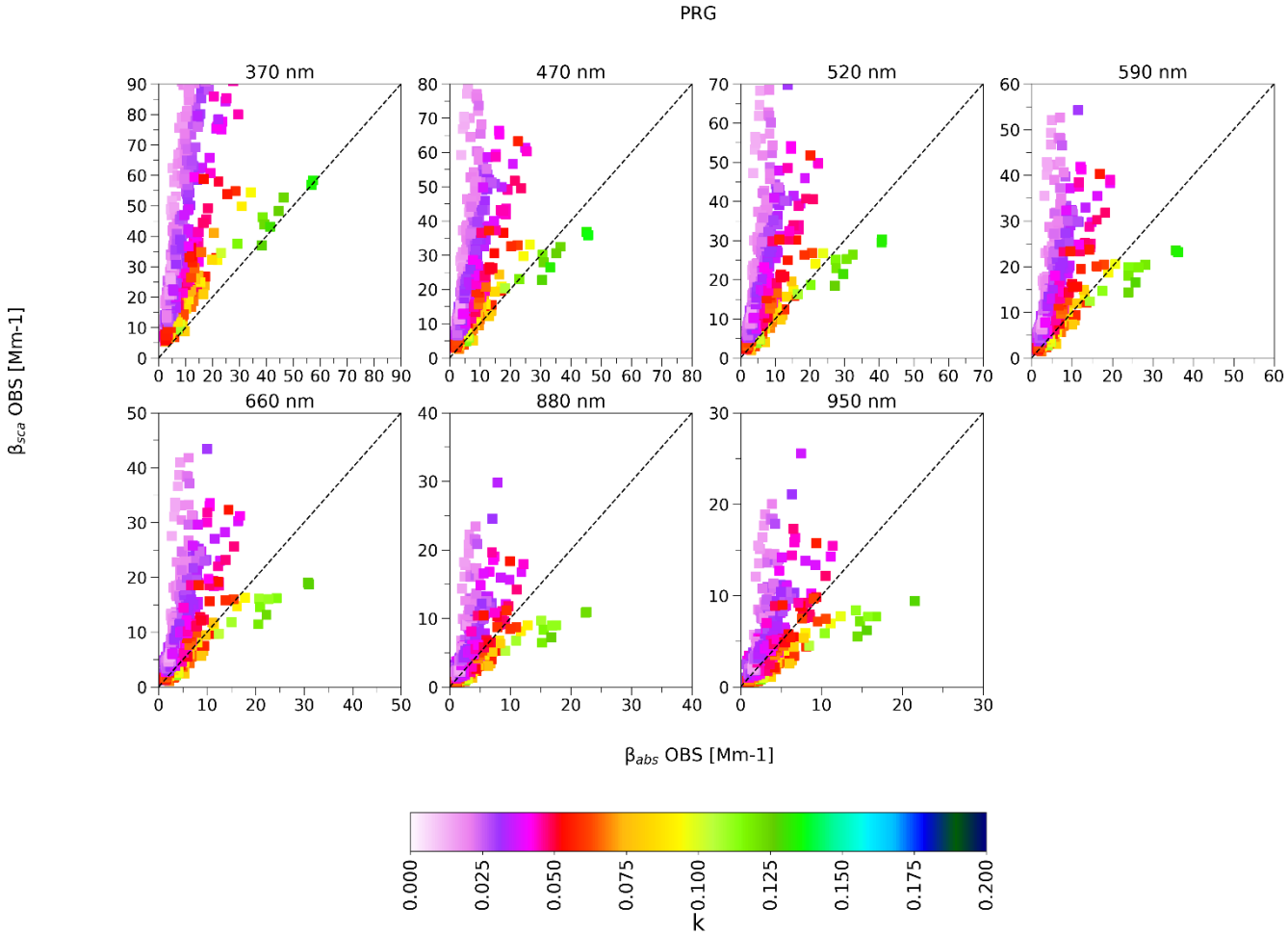

Figure S19: Scatter plot of hourly median observed scattering and absorption coefficient at seven different wavelengths and during the all ACROSS campaign at the Paris Rive Gauche (urban site). The colours represent the simulated k. The imaginary (k) part of CRI has been simulated using a Mie code for spherical particles varying n and k in the [1.3,2] and [0,0.2] respectively. The modelled value represents the value that minimises the root mean squared difference (RMSD) of Eq. 4. Only SMPS data has been taken into account.

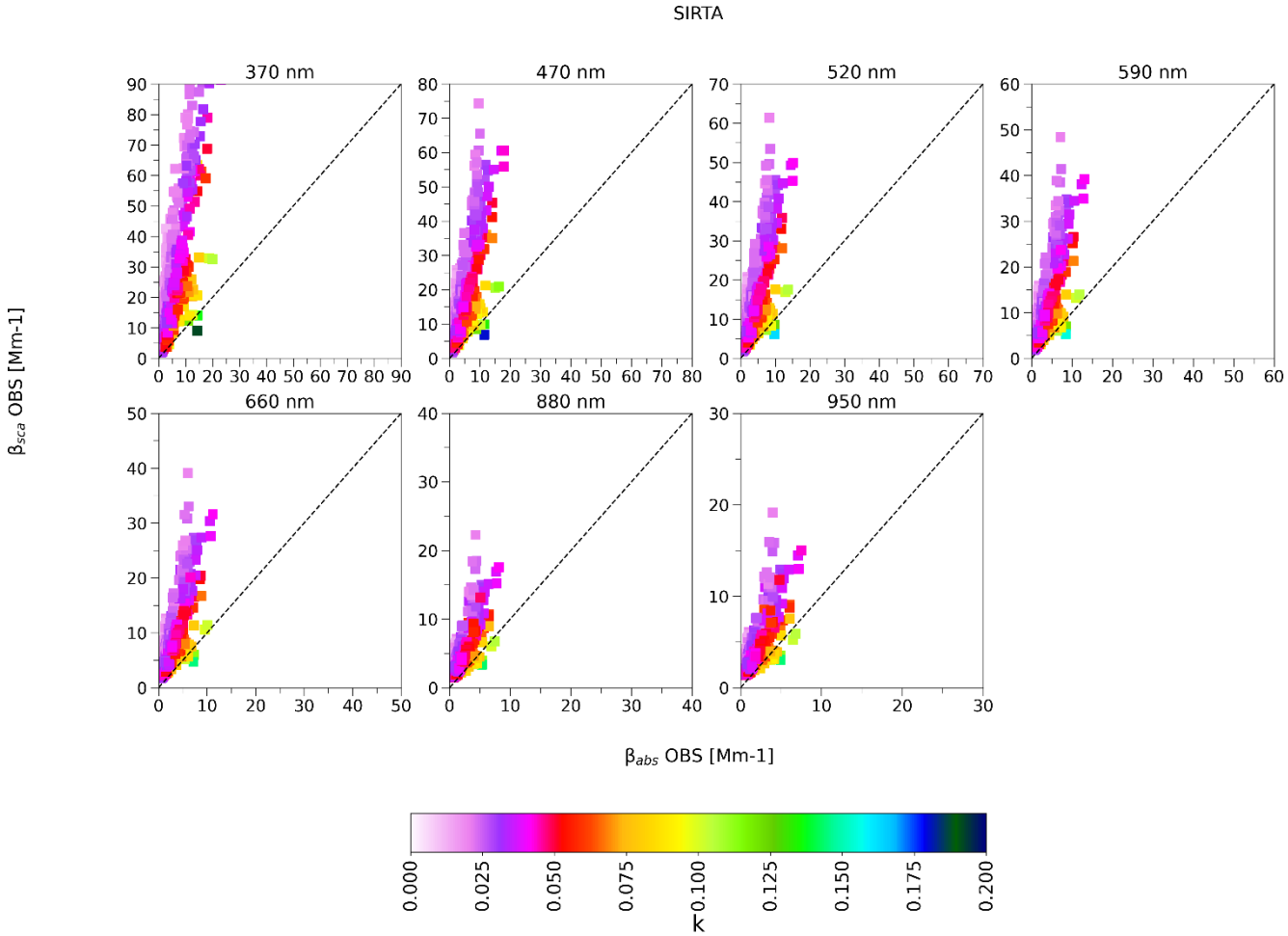

Figure S20: Scatter plot of hourly median observed scattering and absorption coefficient at seven different wavelengths and during the all ACROSS campaign at the SIRTA (peri–urban site). The colours represent the simulated k. The imaginary (k) part of CRI has been simulated using a Mie code for spherical particles varying n and k in the [1.3,2] and [0,0.2] respectively. The modelled value represents the value that minimises the root mean squared difference (RMSD) of Eq. 4. Only SMPS data has been taken into account.

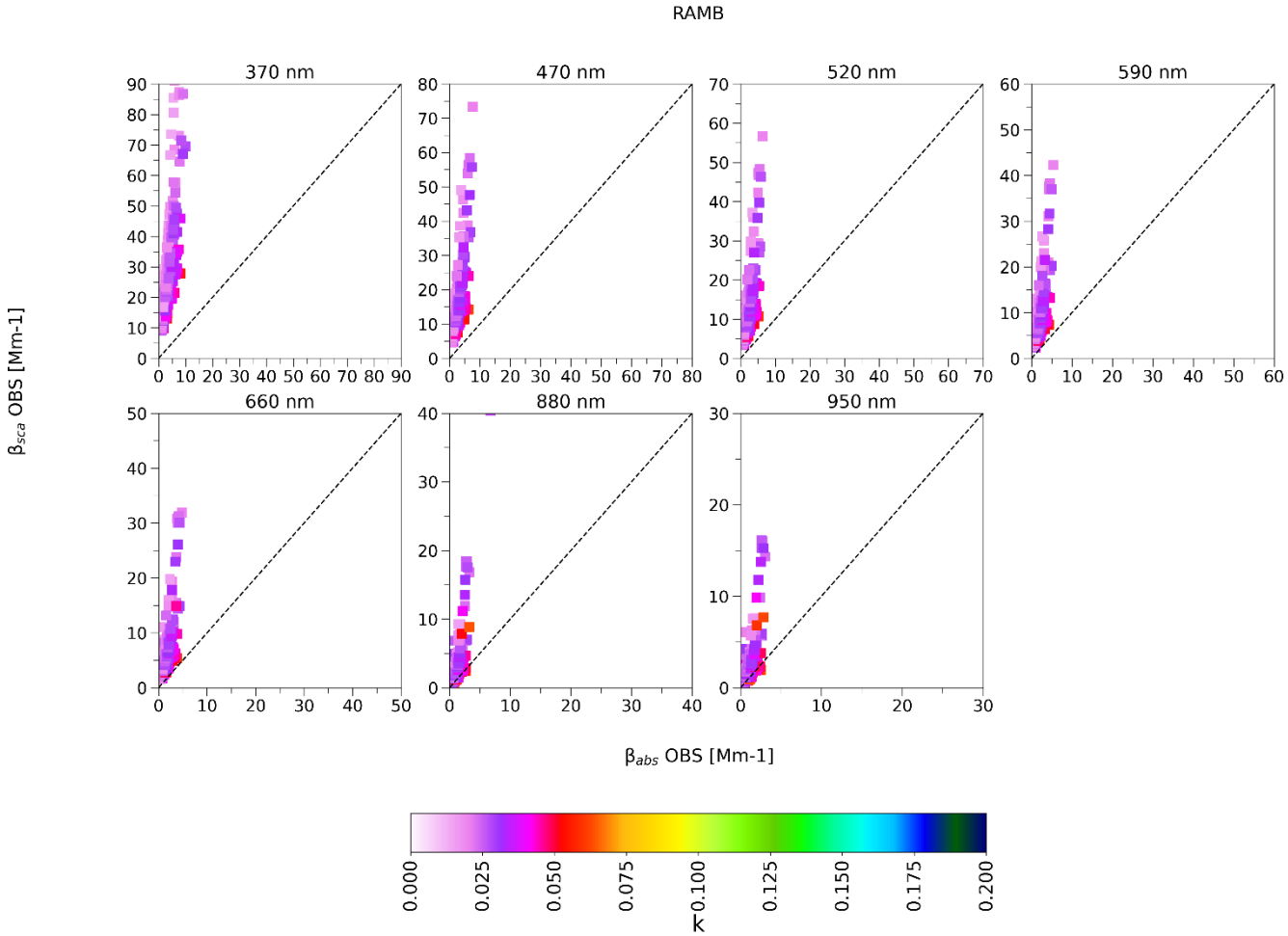

Figure S21: Scatter plot of hourly median observed scattering and absorption coefficient at seven different wavelengths and during the all ACROSS campaign at the Rambouillet (rural site). The colours represent the simulated k. The imaginary (k) part of CRI has been simulated using a Mie code for spherical particles varying n and k in the [1.3,2] and [0,0.2] respectively. The modelled value represents the value that minimises the root mean squared difference (RMSD) of Eq. 4. Only SMPS data has been taken into account.

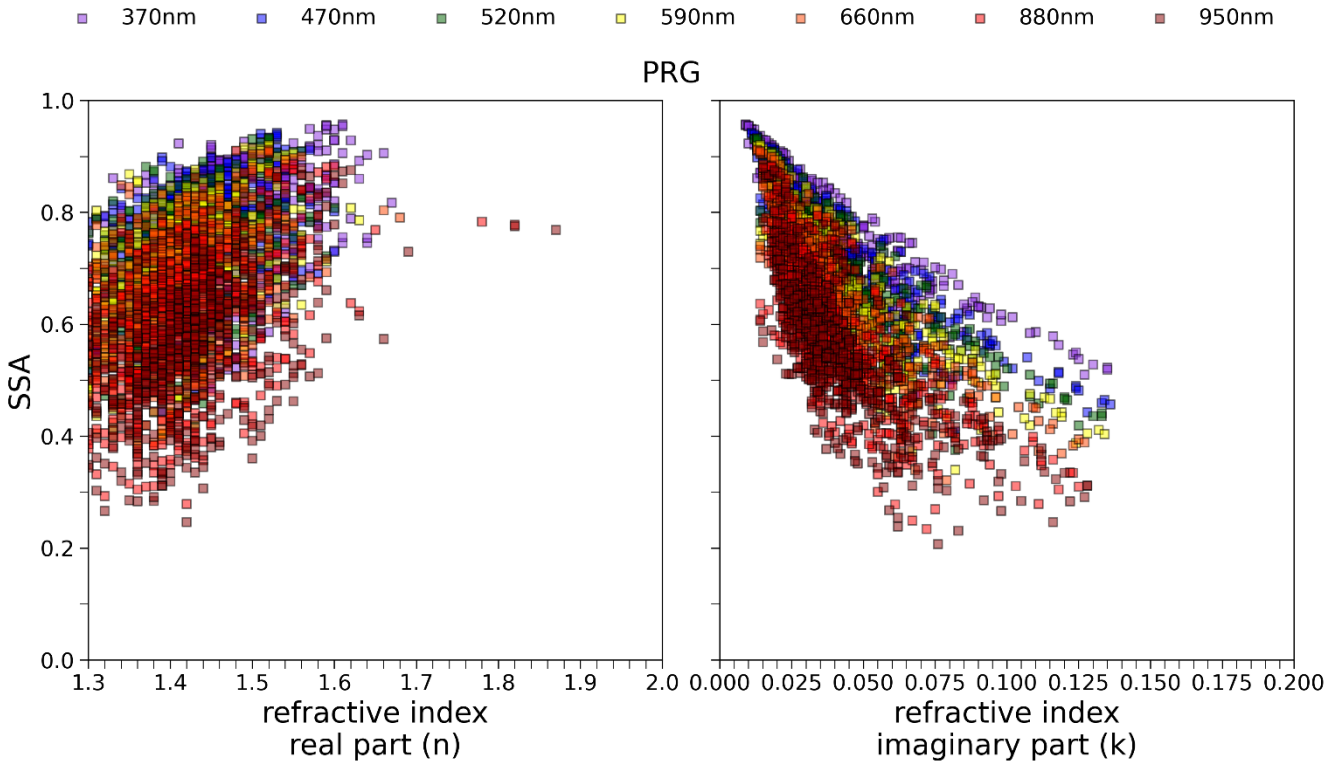

Figure S22: Scatter plot of (left) hourly median observed single scattering albedo vs modelled real part and (right) hourly median observed single scattering albedo vs modelled imaginary part and of the refractive index at seven different wavelengths and during the all ACROSS campaign at the Paris Rive Gauche (urban site). The colours represent the different wavelengths. The real (n) and imaginary (k) part of CRI have been simulated using a Mie code for spherical particles varying n and k in the [1.3,2] and [0,0.2] respectively. The modelled value represents the value that minimises the root mean squared difference (RMSD) of Eq. 4. Only SMPS data has been taken into account.

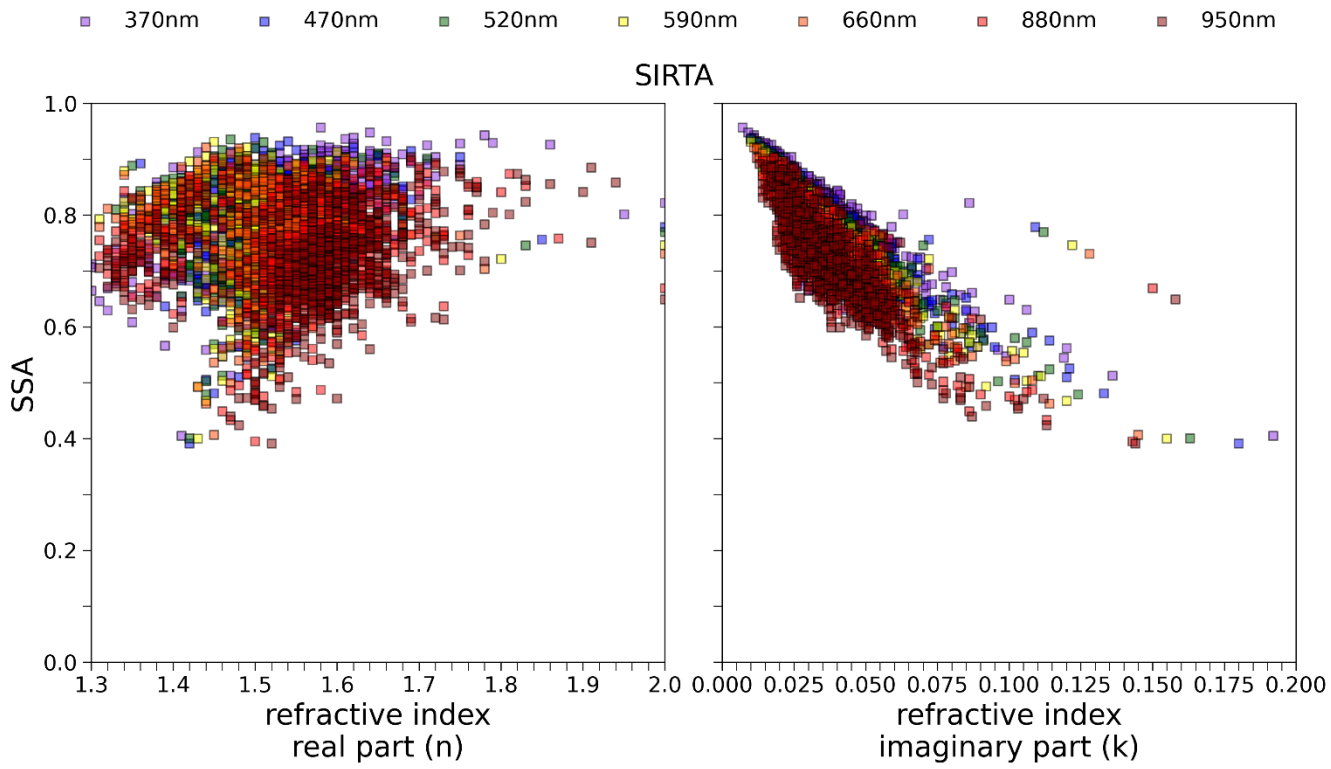

Figure S23: Scatter plot of (left) hourly median observed single scattering albedo vs modelled real part and (right) hourly median observed single scattering albedo vs modelled imaginary part and of the refractive index at seven different wavelengths and during the all ACROSS campaign at the SIRTA (peri–urban site). The colours represent the different wavelengths. The real (n) and imaginary (k) part of CRI have been simulated using a Mie code for spherical particles varying n and k in the [1.3,2] and [0,0.2] respectively. The modelled value represents the value that minimises the root mean squared difference (RMSD) of Eq. 4. Only SMPS data has been taken into account.

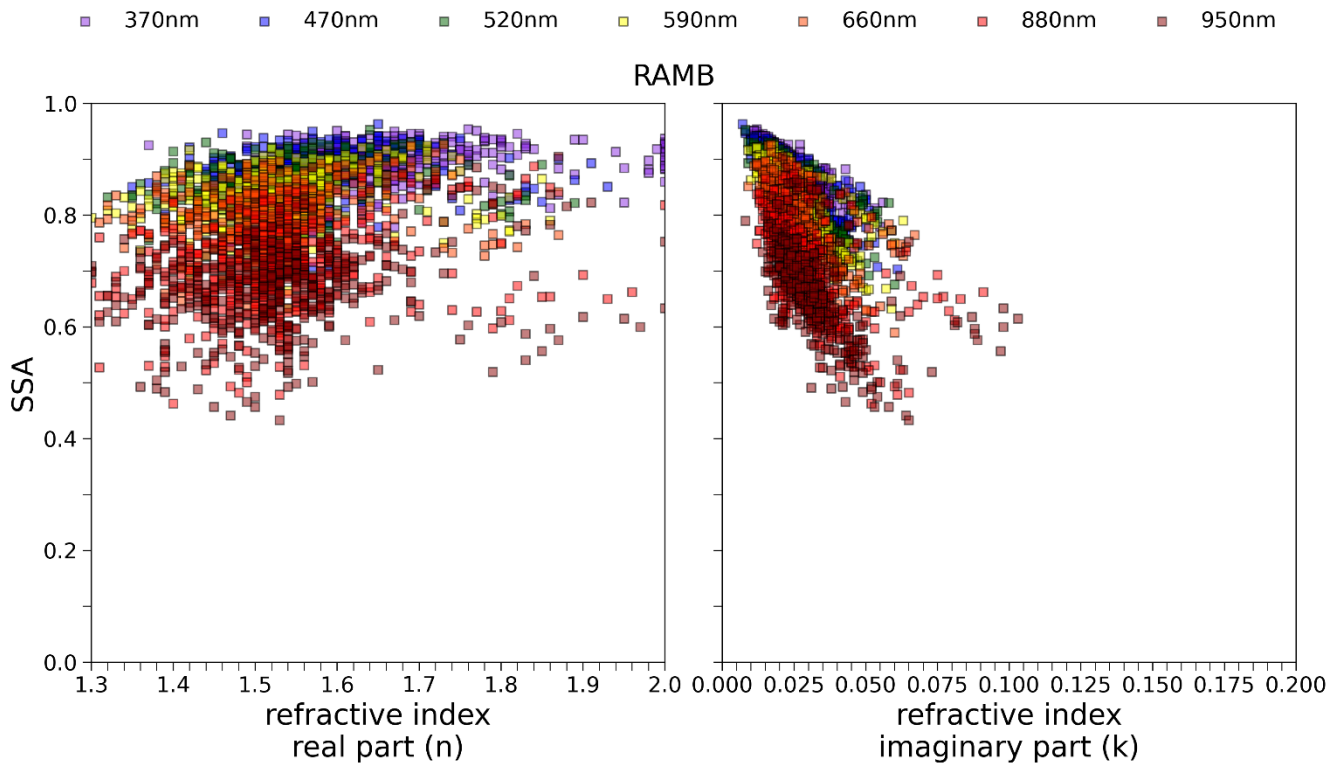

Figure S24: Scatter plot of (left) hourly median observed single scattering albedo vs modelled real part and (right) hourly median observed single scattering albedo vs modelled imaginary part and of the refractive index at seven different wavelengths and during the all ACROSS campaign at the Rambouillet (rural site). The colours represent the different wavelengths. The real (n) and imaginary (k) part of CRI have been simulated using a Mie code for spherical particles varying n and k in the [1.3,2] and [0,0.2] respectively. The modelled value represents the value that minimises the root mean squared difference (RMSD) of Eq. 4. Only SMPS data has been taken into account.

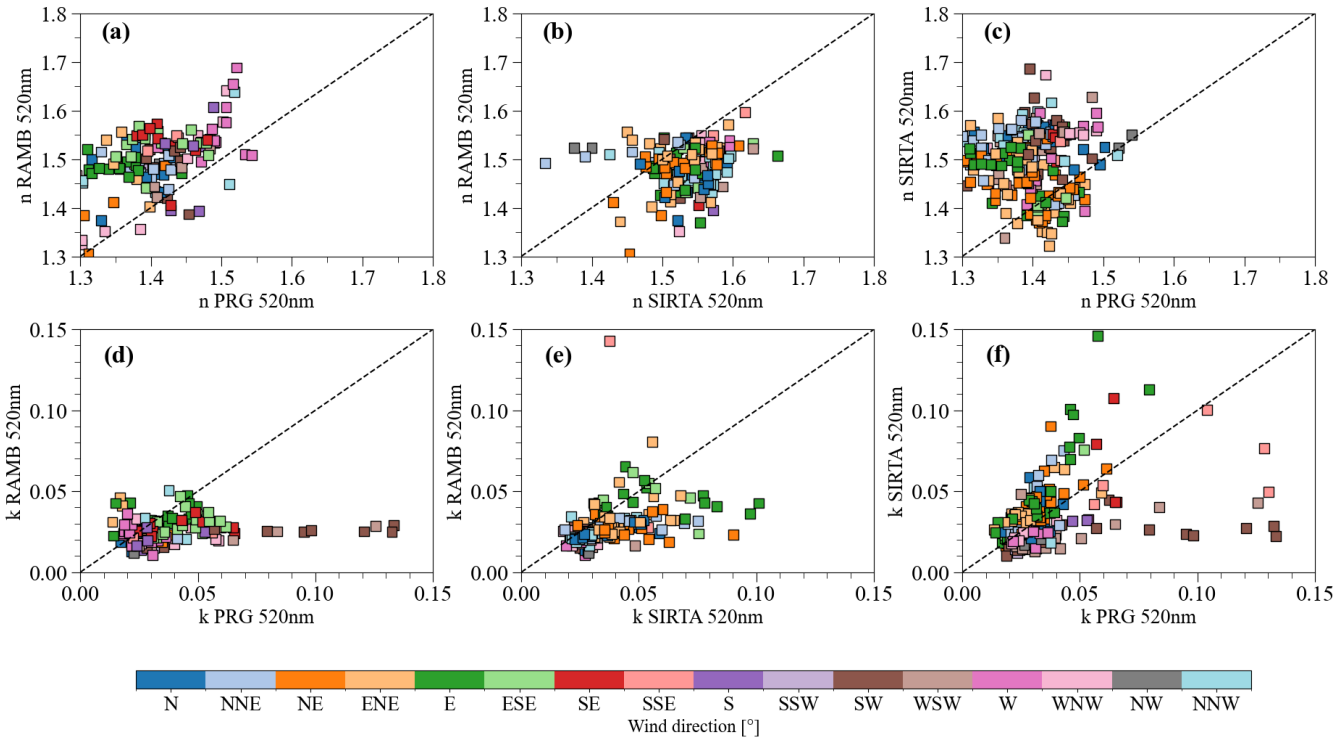

Figure S25: Scatter plot of real (n) and imaginary (k) part of the complex refractive index at 520 nm and at the three different sites: Paris Rive Gauche (PRG, urban), SIRTA (peri–urban) and Rambouillet (RambForest, rural). Dashed line represents the 1:1 line. The CRI has been calculated as the mean of all simulations listed in Tab. 1. Colors represent the different wind directions.

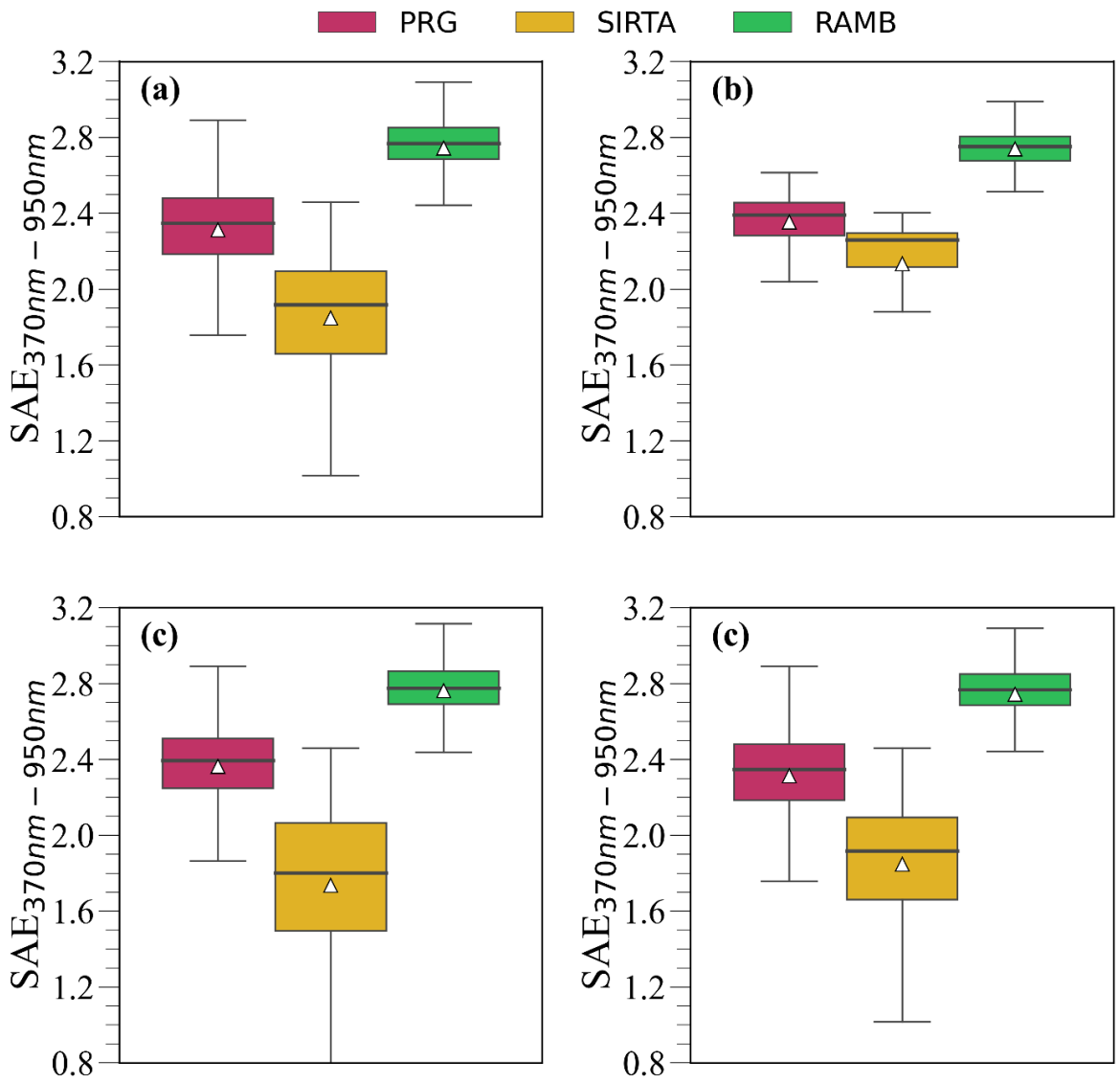

Figure S26: Scattering angstrom exponent between 370 and 950 nm variability for (a) full period (b) first heatwave (c) clean period and (d) second heatwave. Black lines represent the boxplot median, while white triangles represent the boxplot mean.

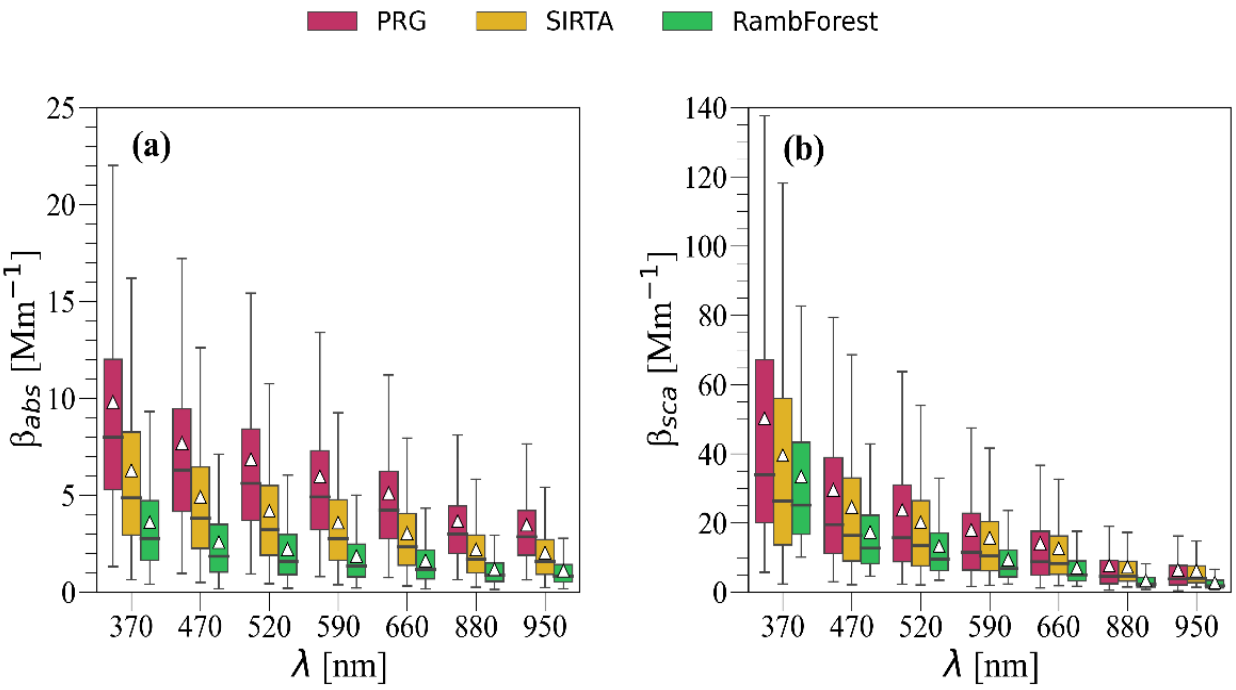

Figure S27: Wavelength dependence of a) β_{abs}, b) β_{sca} at Paris Rive Gauche (PRG,urban site), SIRTA (peri–urban site) and Rambouillet (RambForest, rural site) for the 15 June–24 July 2022 period. The white triangles represent the mean values, while the median has been reported as the line crossing the boxplot.

Annex C. Supplementary to the Chapter 5

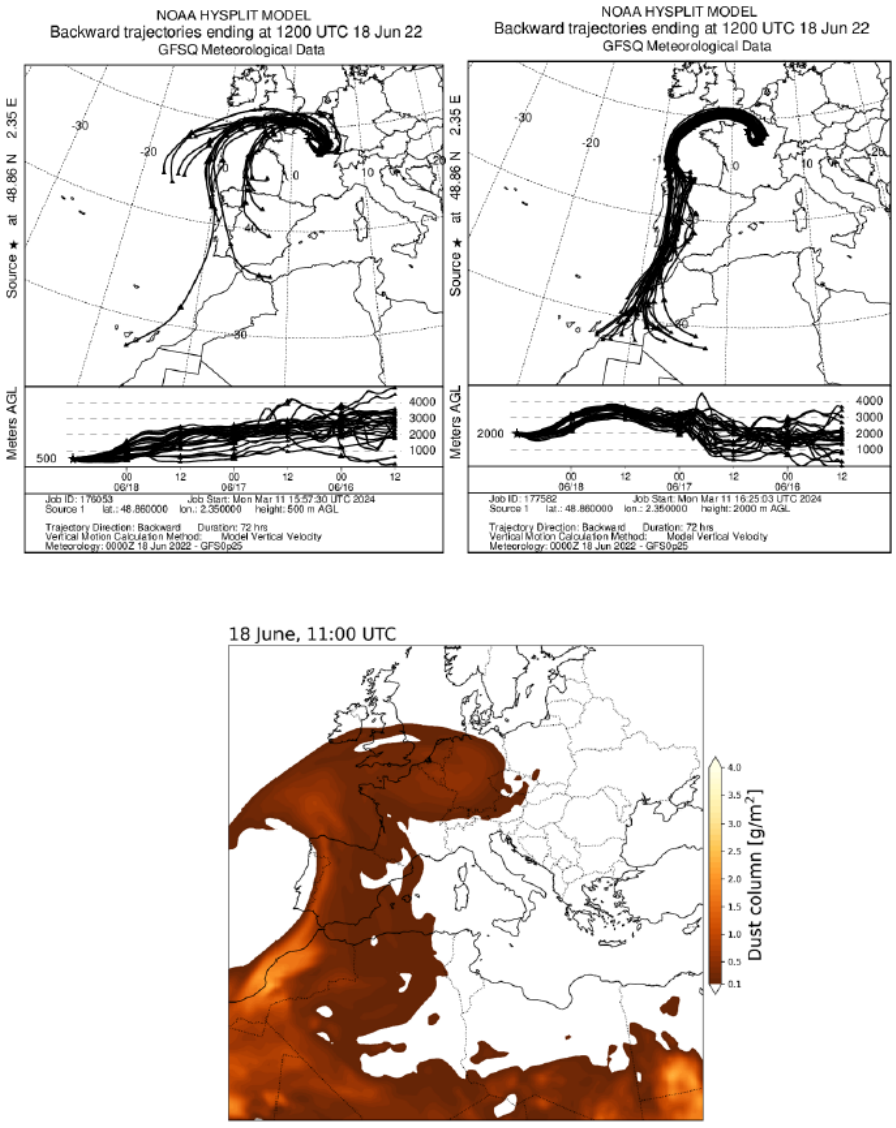

Figure S1: (top) 3 day HYSPLIT backward trajectory simulation for the 18 June 2022 starting in the center of Paris at an altitude of 500m (left) and 2000 m (right). (Bottom) Simulated dust columnar concentration on the 18 June 2022 at 11:00 UTC. The dust plume reached northern Europe and the Paris area during the day.

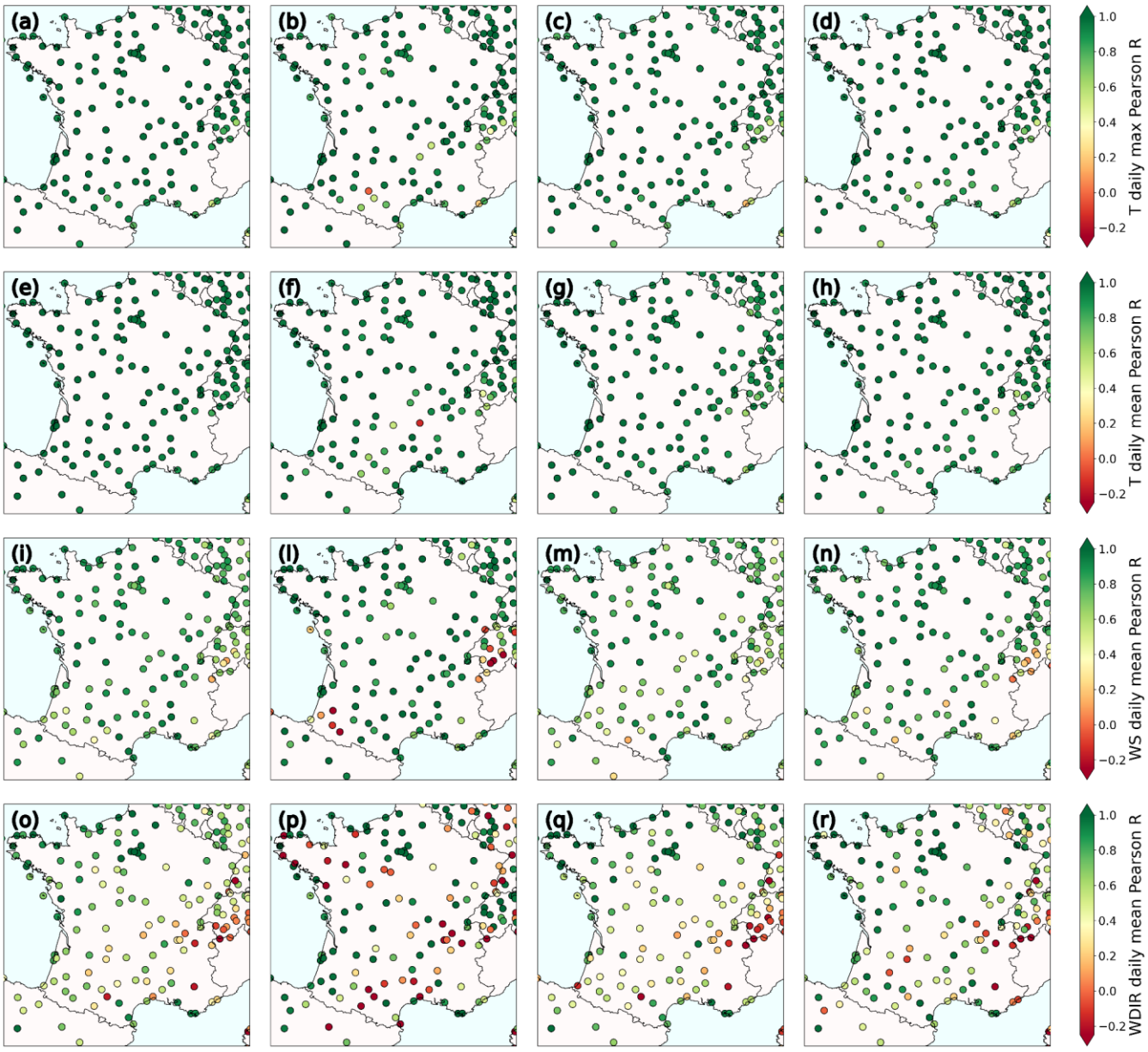

Figure S2: Daily Pearson correlation coefficient between WRF-CHIMERE model output and observations of the MIDAS database respectively for the full period (left column), the first heatwave (middle left column), the clean period (middle right column) and the second heatwave (right column); (a)-(d) for the temperature daily max, (e) - (h) temperature daily mean, (i)-(n) wind speed daily mean and (o)-(r) wind speed daily mean.

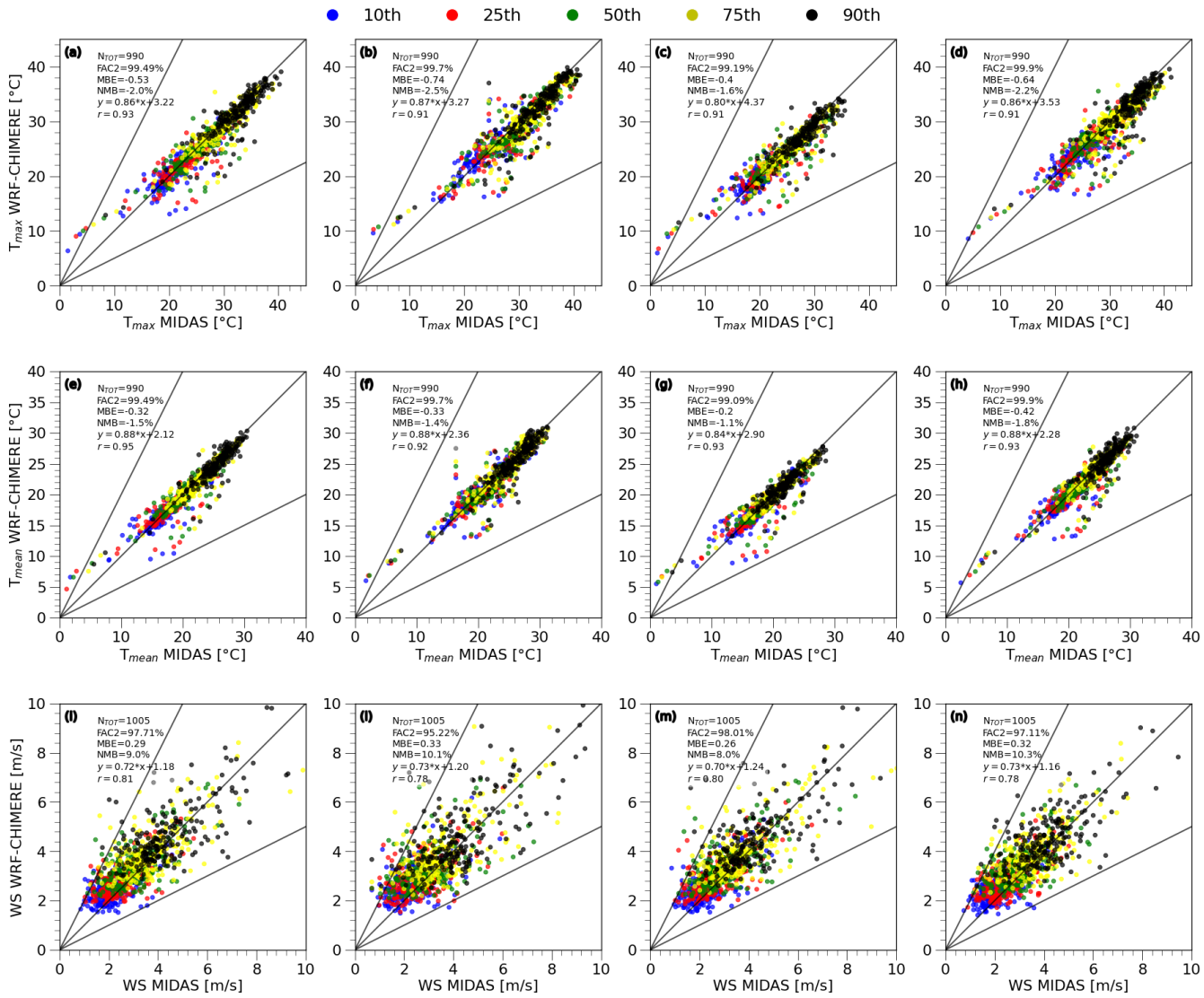

Figure S3: Percentiles analysis of WRF-CHIMERE simulated meteorological parameters compared to the MIDAS database observations, respectively for the full period (left column), the first heatwave (middle left column), the clean period (middle right column) and the second heatwave (right column)for the (a)-(d) temperature max, (e) - (h) temperature mean, (i)-(n) wind speed. Statistical metrics are calculated from data merged for all sites: Ntot, number of observations, FAC2 fraction of points within a factor 2 limit, MBE mean bias error, NMB normalized mean bias, linear fit equation, R correlation coefficient.

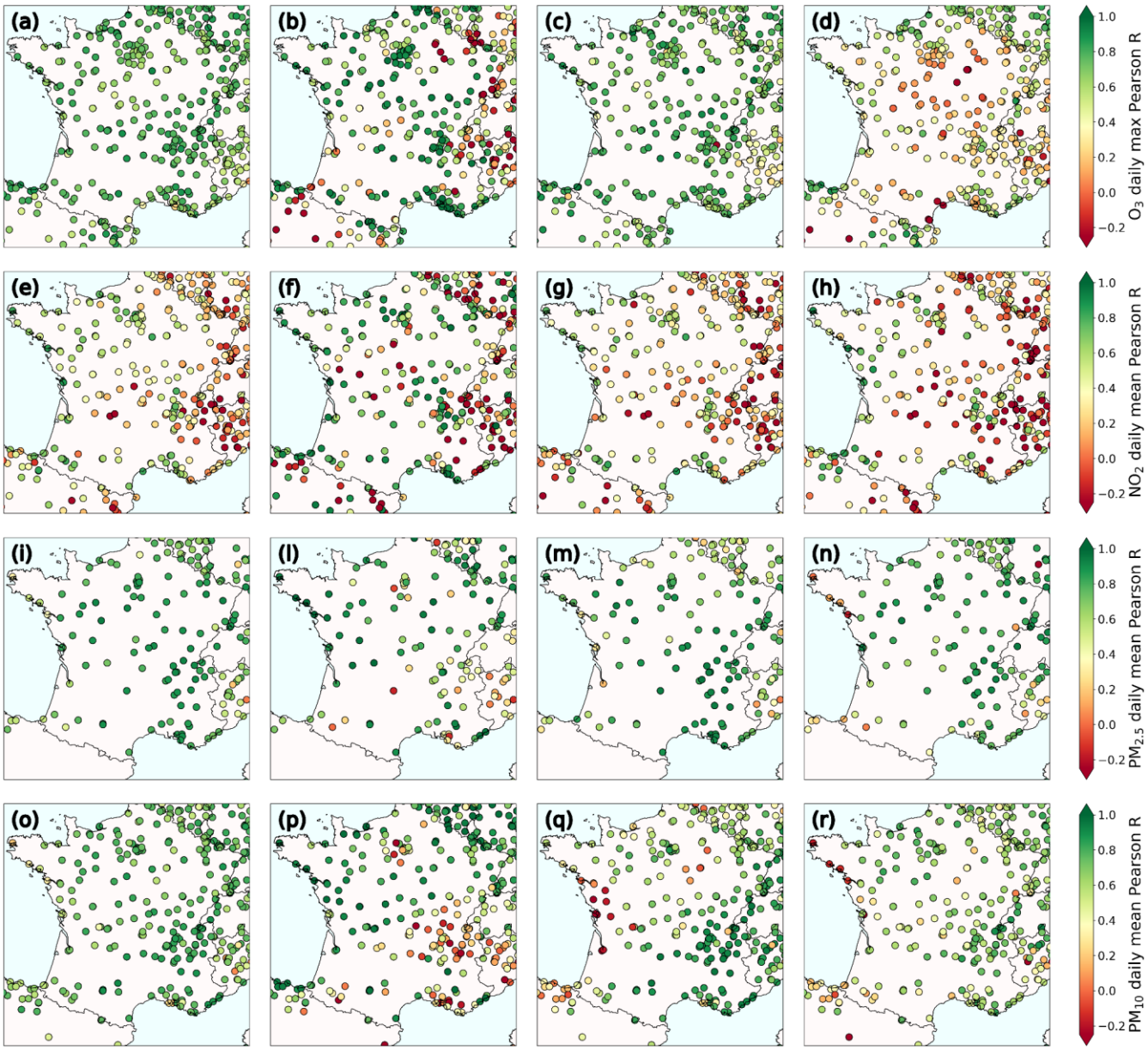

Figure S4: Daily Pearson correlation coefficient between WRF-CHIMERE output and EEA observations respectively for the full period (left column), the first heatwave (middle left column), the clean period (middle right column) and the second heatwave (right column) for the (a)-(d) O_3 daily max, (e) - (h) NO_2 daily mean, (i)-(n) $PM_{2.5}$ daily mean and (o)-(r) PM_{10} daily mean.

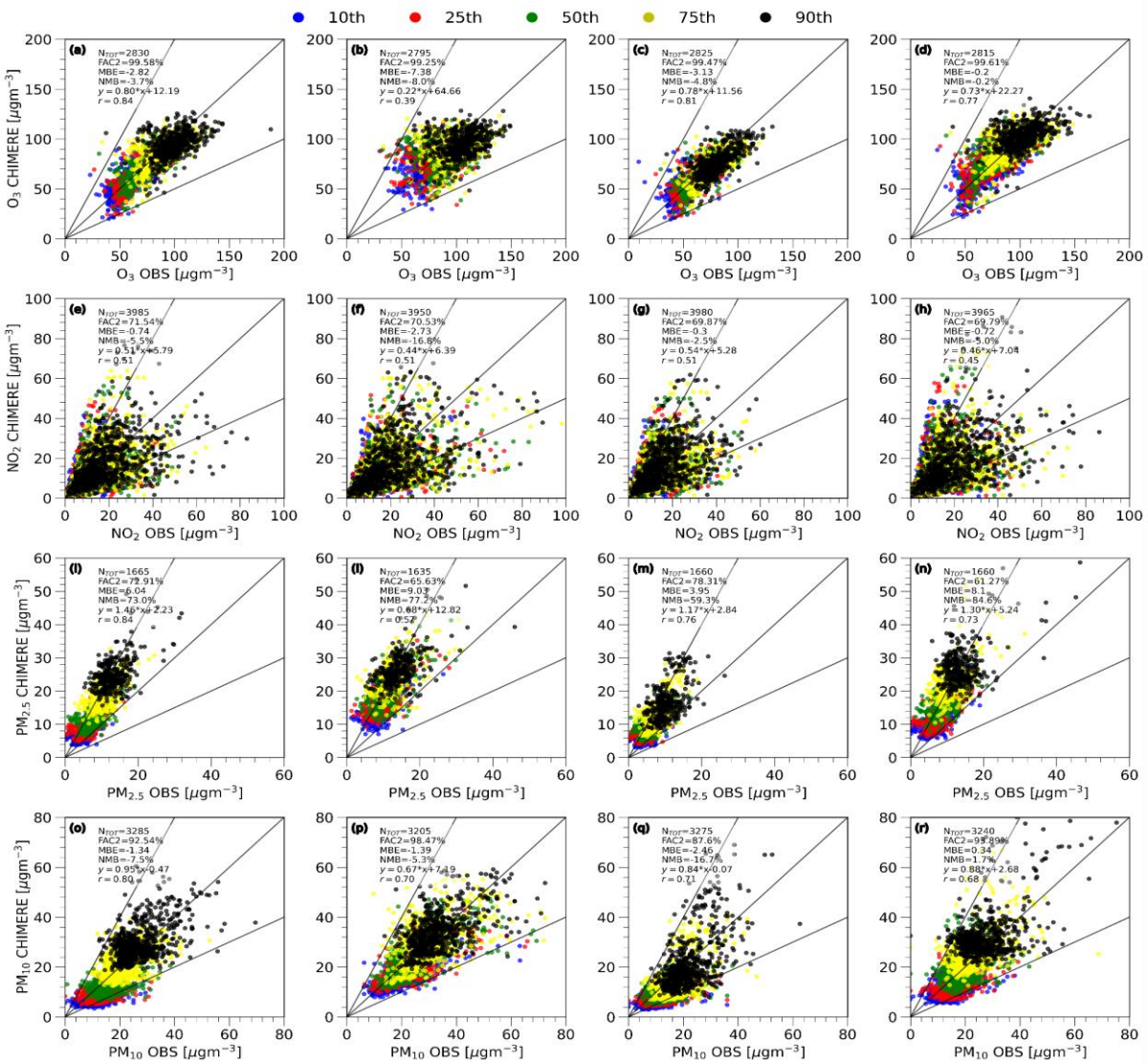

Figure S5: Percentiles analysis of WRF-CHIMERE simulated aerosol load and gaseous compounds compared to EEA observations, respectively for the full period (left column), the first heatwave (middle left column), the clean period (middle right column) and the second heatwave (right column) for the (a)-(d) O_3, (e) - (h) NO_2, (i)-(n) $PM_{2.5}$, (o)-(r) PM_{10}. Statistical metrics are calculated from data merged for all sites: Ntot, number of observations, FAC2 fraction of points within a factor 2 limit, MBE mean bias error, NMB normalized mean bias, linear fit equation, R correlation coefficient. Percentiles are calculated from the daily max values for O_3, while from the daily mean for PM_{10}, NO_2, $PM_{2.5}$.

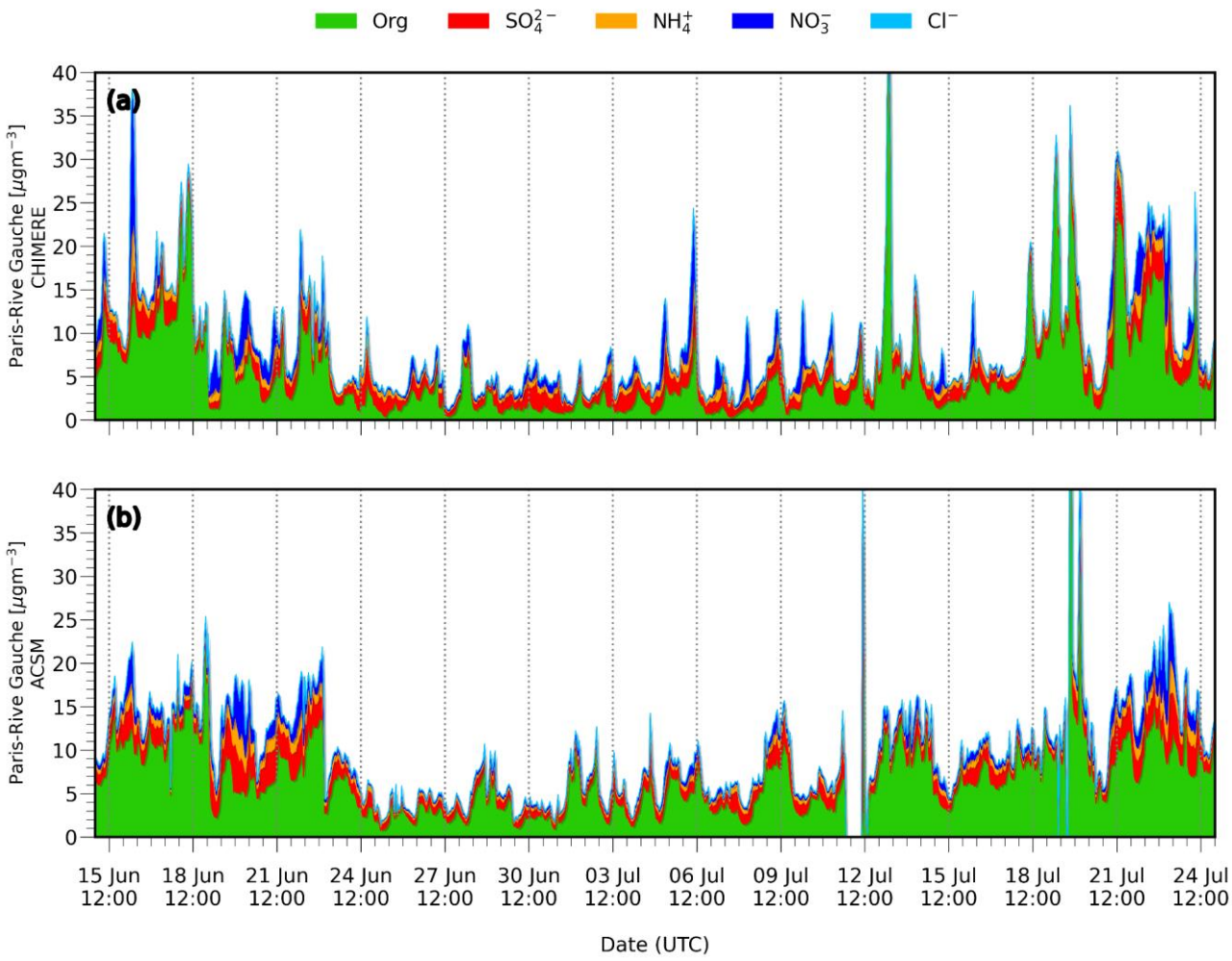

Figure S6: Timeseries of the chemical composition (organics, sulfate, nitrate, ammonium and chloride) simulated (a) and observed (b) at the Paris-Rive Gauche (PRG) urban background site.

, :

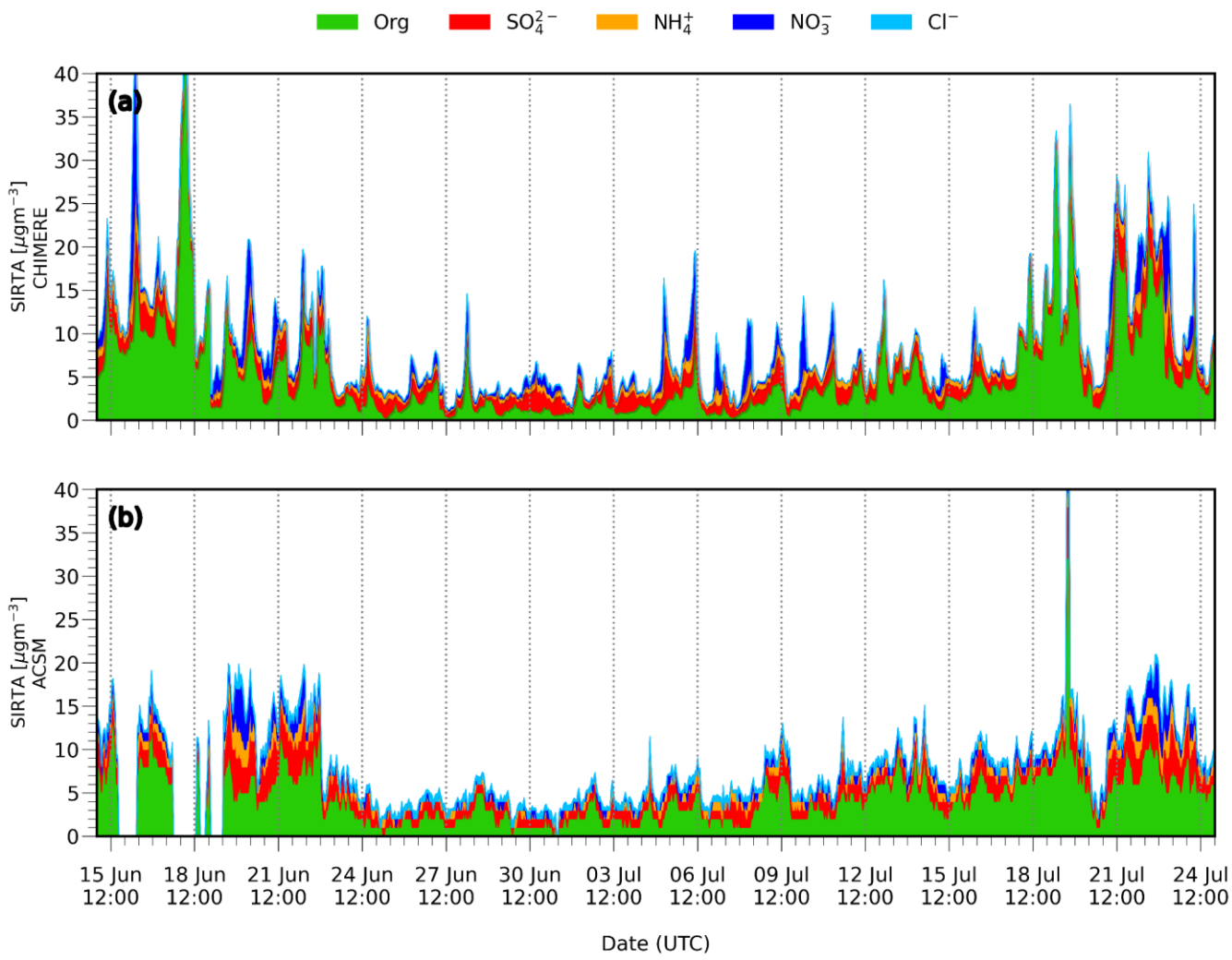

Figure S7: Timeseries of the chemical composition (organics, sulfate, nitrate, ammonium and chloride) simulated (a) and observed (b) at the SIRTA peri-urban site.

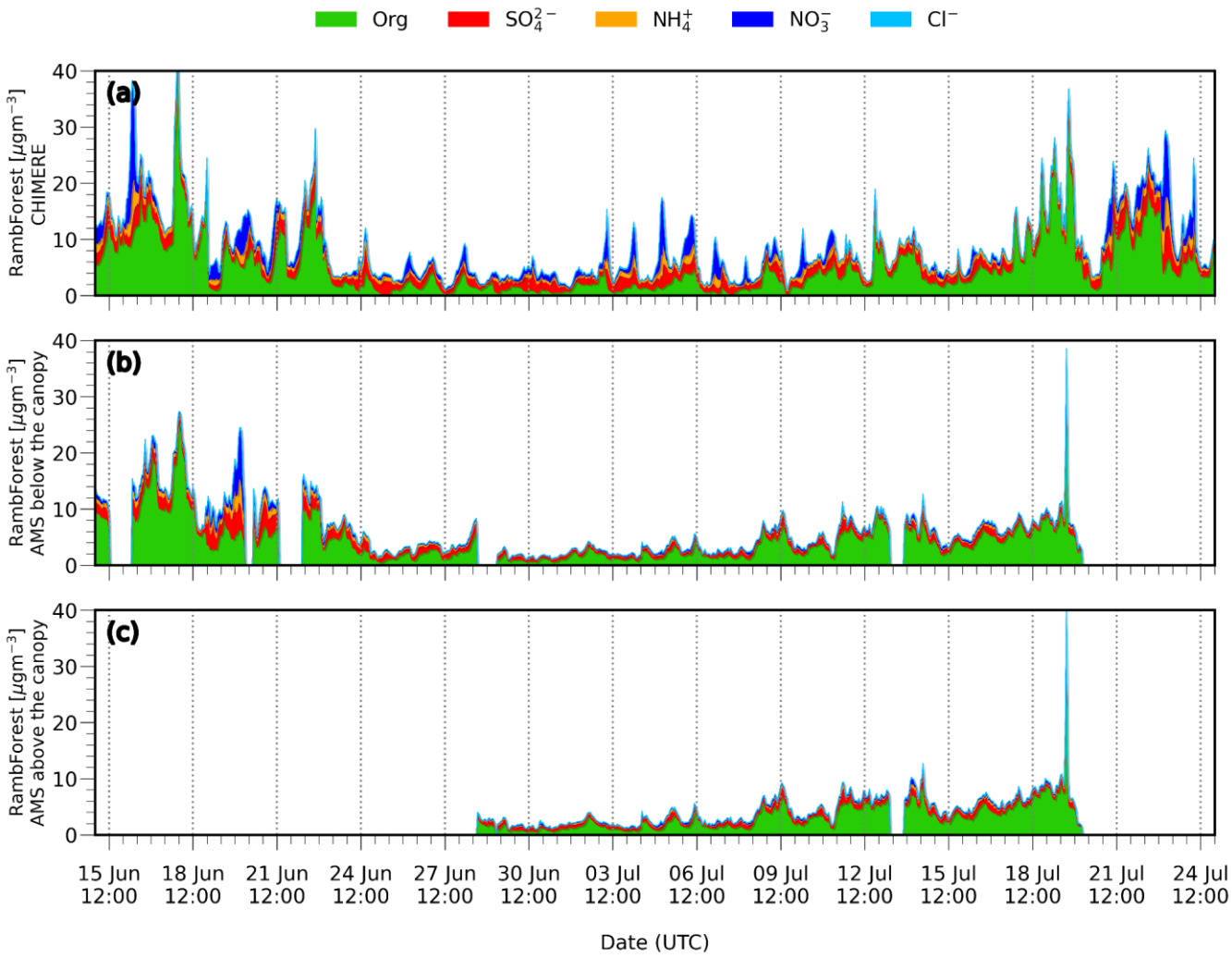

Figure S8: Timeseries of the chemical composition (organics, sulfate, nitrate, ammonium and chloride) simulated (a) and observed below the canopy (b) and above the canopy (c) at the Rambouillet forest (RambForest) site.

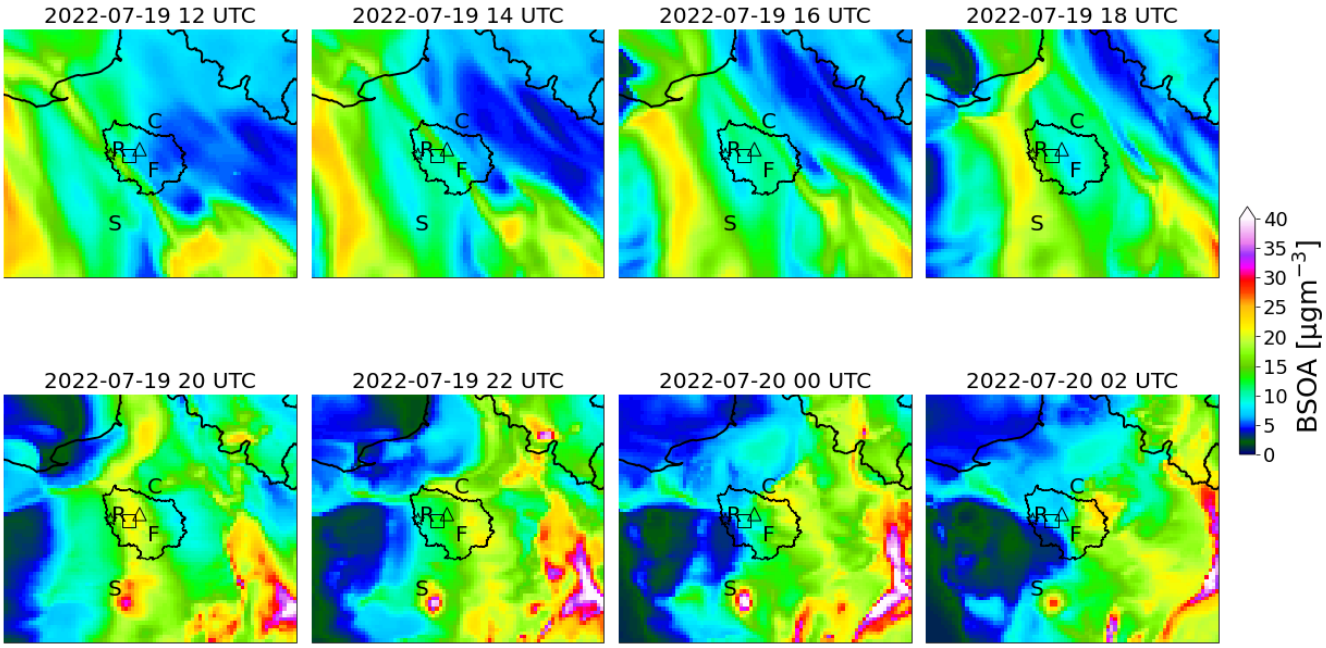

Figure S9: Simulated biogenic secondary organic aerosol (BSOA) mass concentration for the 19 and 20 July 2022. The "F" indicates the Fontainebleau forest, the "R" indicates the Rambouillet forest, the "S" indicates the Sologne forest and the "C" indicates the Chantilly forest. The star, the square and the triangle markers indicate respectively the RambForest, SIRTA and PRG sites location. Please note that BSOA stems both from BVOC compounds emitted by fires and forests.

Name	Longitude	Latitude	Features
Calais	1.84° E	50.94	Urban
Creil	2.47° E	49.25	Urban
Metz	6.22° E	49.11	Urban
Paris Les Halles	2.34° E	48.86	Urban
Strasbourg	7.76° E	48.57	Urban
Poitiers	0.34° E	46.58	Urban
Lyon	4.85° E	45.75	Urban
Toulouse	1.43° E	43.62	Urban
Marseille	5.39° E	43.30	Urban

Table S1: GEOD'AIR sites available to validate the aerosol chemical composition.

	Full period (15 June- 25 July)				**First heatwave (15 June-19 June)**				**Clean period (20 June-11 July)**				**Second heatwave (12 July-25 July)**			
	N_{TOT}	R	MBE µgm-3	NMB %	N_{TOT}	R	MBE µgm-3	NMB %	N_{TOT}	R	MBE µgm-3	NMB %	N_{TOT}	R	MBE µgm-3	NMB %
Ammonium	943	0.52	0.06	8.2	120	0.39	0.11	12.8	524	0.40	0.10	16.5	299	0.71	-0.03	-3.9
Sulfate	942	0.25	-0.02	-1.2	120	-0.18	-0.21	-10.6	524	0.10	0.08	5.3	298	0.36	-0.11	-5.7
Nitrate	943	0.47	0.11	15.2	120	0.65	0.27	28.7	524	0.46	0.30	55.6	299	0.53	-0.29	-29.8
Organic	943	0.61	-1.39	-19.9	120	0.54	0.02	0.10	524	0.53	-1.78	-37.7	299	0.44	-1.26	-13.3
Chloride	943	0.14	-0.001	-1.7	120	0.56	-0.02	-45.2	524	-0.10	0.01	44.0	299	0.39	-0.02	-35.4
	OBS		MOD		OBS		MOD		OBS		MOD		OBS		MOD	
Ammonium	0.72		0.78		0.87		0.98		0.60		0.70		0.86		0.83	
Sulfate	1.66		1.64		2.9		1.79		1.42		1.50		1.93		1.82	
Nitrate	0.72		0.83		0.94		1.22		0.54		0.84		0.96		0.68	
Organic	6.97		5.58		10.60		10.61		4.71		2.93		9.46		8.20	
Chloride	0.04		0.04		0.04		0.02		0.03		0.05		0.06		0.04	

Table S2: Summary of the comparison of model output to observations for the Paris-Rive Gauche (urban) site from the ACSM; Statistical metrics are: Ntot, number of observations, R, correlation coefficient, MBE, mean bias error, NMB, normalized mean bias.

	Full period (15 June- 25 July)				**First heatwave (15 June-19 June)**				**Clean period (20 June-11 July)**				**Second heatwave (12 July-25 July)**			
	N_{TOT}	R	MBE µgm-3	NMB %	N_{TOT}	R	MBE µgm-3	NMB %	N_{TOT}	R	MBE µgm-3	NMB %	N_{TOT}	R	MBE µgm-3	NMB %
Ammonium	904	0.50	0.01	0.7	68	0.002	-0.15	-13.7	524	0.35	0.10	17.9	412	0.73	-0.13	-14.4
Sulfate	906	0.37	-0.22	-12.0	68	-0.37	-0.63	-22.9	526	0.20	-0.11	-6.9	312	0.64	-0.32	-15.6
Nitrate	906	0.39	0.13	21.0	68	0.13	-0.24	-28	526	037	0.33	63.8	312	0.50	-0.12	-15.5
Organic	906	0.68	-0.16	-3.1	68	0.08	1.93	22.6	526	0.65	-0.90	-24.5	312	0.52	0.64	9.1
Chloride	888	0.11	0.003	7.9	68	-0.01	-0.01	-38.1	511	-0.49	0.01	30.5	309	0.71	-0.01	-17.3
	OBS		MOD		OBS		MOD		OBS		MOD		OBS		MOD	
Ammonium	0.75		0.75		1.07		092		0.60		0.71		0.93		0.80	
Sulfate	1.86		1.63		2.73		2.10		1.62		1.51		2.07		1.74	
Nitrate	0.62		0.75		0.87		0.63		0.51		0.84		0.76		0.64	
Organic	5.18		5.03		8.54		10.48		3.68		2.78		7.00		7.64	
Chloride	0.038		0.041		0.035		0.021		0.037		0.048		0.041		0.033	

Table S3: As Table S2, but for the SIRTA (peri-urban) site

	Full period (15 June- 25 July)				**First heatwave (15 June-19 June)**				**Clean period (20 June-11 July)**				**Second heatwave (12 July-25 July)**			
	N_{TOT}	R	MBE µgm-3	NMB %	N_{TOT}	R	MBE µgm-3	NMB %	N_{TOT}	R	MBE µgm-3	NMB %	N_{TOT}	R	MBE µgm-3	NMB %
Above the canopy																
Ammonium	506	0.07	0.46	251.8	-				319	0.16	0.57	396.0	187	0.36	0.26	106.5
Sulfate	506	0.01	0.67	95.9	-				319	0.01	0.81	130.7	187	0.31	0.43	51.3
Nitrate	506	0.21	0.52	325.4	-				319	0.52	0.84	632.7	187	0.17	-0.02	-6.9
Organic	506	0.62	0.7	21.3	-				319	0.57	-0.04	-1.7	187	0.41	1.99	36.7
Chloride	506	0.139	0.015	59.4	-				319	0.12	0.027	99.6	187	0.20	-0.005	-21.4
Below the canopy																
Ammonium	772	0.27	0.33	89.3	101	0.18	0.19	23.3	484	0.22	0.40	123.2	187	0.43	0.24	93.0
Sulfate	772	0.17	0.40	36.7	101	-0.12	-0.18	-8.8	484	0.11	0.51	51.4	187	0.38	0.44	53.3
Nitrate	772	0.29	0.48	148.1	101	0.25	0.64	105.5	484	0.32	0.64	214.4	187	0.45	-0.035	-15.3
Organic	772	0.77	0.45	9.7	101	0.76	1.22	11.9	484	0.76	-0.13	-4.5	187	0.43	1.52	26.0
Chloride	772	0.06	0.01	32.8	101	0.61	-0.021	67.6	484	-0.08	0.02	67.6	187	0.39	0.0	-1.4

	OBS	MOD	OBS	MOD	OBS	MOD	OBS	MOD
Ammonium	0.18/0.38	0.64/0.71	0.83	1.02	0.14/0.33	0.71/0.73	0.25/0.26	0.51/0.61
Sulfate	0.70/1.09	1.38/1.49	2.08	1.90	0.63/0.99	1.45/1.49	0.83/0.82	1.26/1.26
Nitrate	0.16/0.32	0.69/0.80	0.61	1.25	0.13/0.30	0.97/0.94	0.21/0.23	0.19/0.19
Organic	3.34/4.59	4.05/5.04	10.35	11.58	2.13/2.90	2.09/2.77	5.40/5.87	7.39/7.40
Chloride	0.025/0.031	0.040/0.041	0.052	0.028	0.027/0.031	0.05/0.053	0.023/0.018	0.018/0.017

Table S4: As Table S2, but for the Rambouillet (forest) and from AMS measurements below and above the canopy. Average concentrations are reported both for the above and below canopy respectively divided by a slash sign.

	Full period (15 June- 25 July)				**First heatwave (15 June-19 June)**				**Clean period (20 June-11 July)**				**Second heatwave (12 July-25 July)**			
	N_{TOT}	R	MBE µgm-3	NMB %	N_{TOT}	R	MBE µgm-3	NMB %	N_{TOT}	R	MBE µgm-3	NMB %	N_{TOT}	R	MBE µgm-3	NMB %
eBC	70	0.48	0.12	27.0	10	0.60	0.20	33.8	36	0.28	0.14	45.3	23	0.45	0.003	0.5
EC	70	0.35	0.12	27.5	10	0.6	0.18	29.2	36	-0.13	0.17	57.4	23	0.34	-0.02	-3.5
OM	72	0.74	-0.31	-5.4	10	0.53	2.2	26.9	37	0.45	-1.16	-29.0	24	0.65	-0.048	-0.7
	OBS		MOD		OBS		MOD		OBS		MOD		OBS		MOD	
eBC	0.45		0.57		0.60		0.78		0.31		0.46		0.59		0.59	
EC	0.45				0.62				0.29				0.61			
OM	5.7		5.4		8.2		10.4		3.99		2.83		7.31		7.27	

Table S5: Summary of the comparison of the black carbon concentration for the Paris-Rive Gauche (urban) site averaged on the filters sampling times (daytime 6 – 22 UTC, night time 22- 6 UTC). The eBC has been corrected for the ACTRIS harmonisation factor (H*=2.45). The OC has been converted to OM assuming the OM/OC ratio equal to 1.8. Statistical metrics are: Ntot, number of observations, R, correlation coefficient, MBE, mean bias error, NMB, normalized mean bias.

	Full period (15 June- 25 July)				**First heatwave (15 June-19 June)**				**Clean period (20 June-11 July)**				**Second heatwave (12 July-25 July)**			
	N_{TOT}	R	MBE µgm-3	NMB %	N_{TOT}	R	MBE µgm-3	NMB %	N_{TOT}	R	MBE µgm-3	NMB %	N_{TOT}	R	MBE µgm-3	NMB %
eBC	41	0.36	0.09	65.7	-				22	0.41	0.11	124.4	19	0.13	0.07	35.5
EC	43	0.46	0.1	67.7	-				22	0.39	0.12	149.9	21	0.31	0.07	34.1
rBC	22	0.5	0.16	152.9	-				2	-	0.15	274.5	20	0.47	0.16	147.0
OM	43	0.83	0.06	1.2	-				22	0.73	-1.09	-33.0	21	0.70	1.27	18.8
	OBS		MOD		OBS		MOD		OBS		MOD		OBS		MOD	
eBC	0.14		0.24		-				0.09		0.20		0.20		0.27	
EC	0.14				-				0.08				0.21			
rBC	0.11				-				0.05				0.11			
OM	4.99		5.04		-				3.31		2.22		6.74		8.01	

Table S6: As for Table S5, but for the Rambouillet (forest) site.

Annex D. Supplementary to the Chapter 6

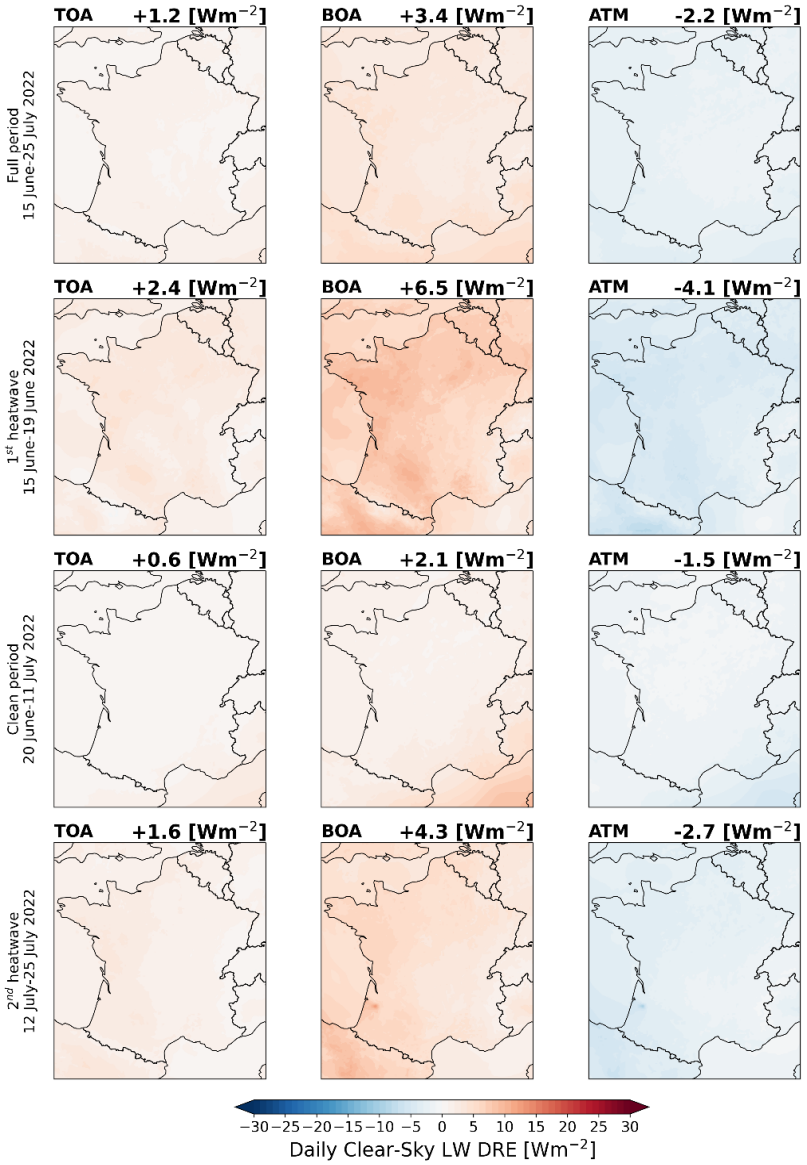

Figure D.1 Daily Clear-Sky LW direct radiative effect at top of the atmosphere (TOA), bottom of the atmosphere (BOA) and atmosphere (ATM) for the France domain (42°N, 51.15°N, 3.2°E,8.5°W) at 6km resolution, divided by the different periods during the ACROSS campaign.

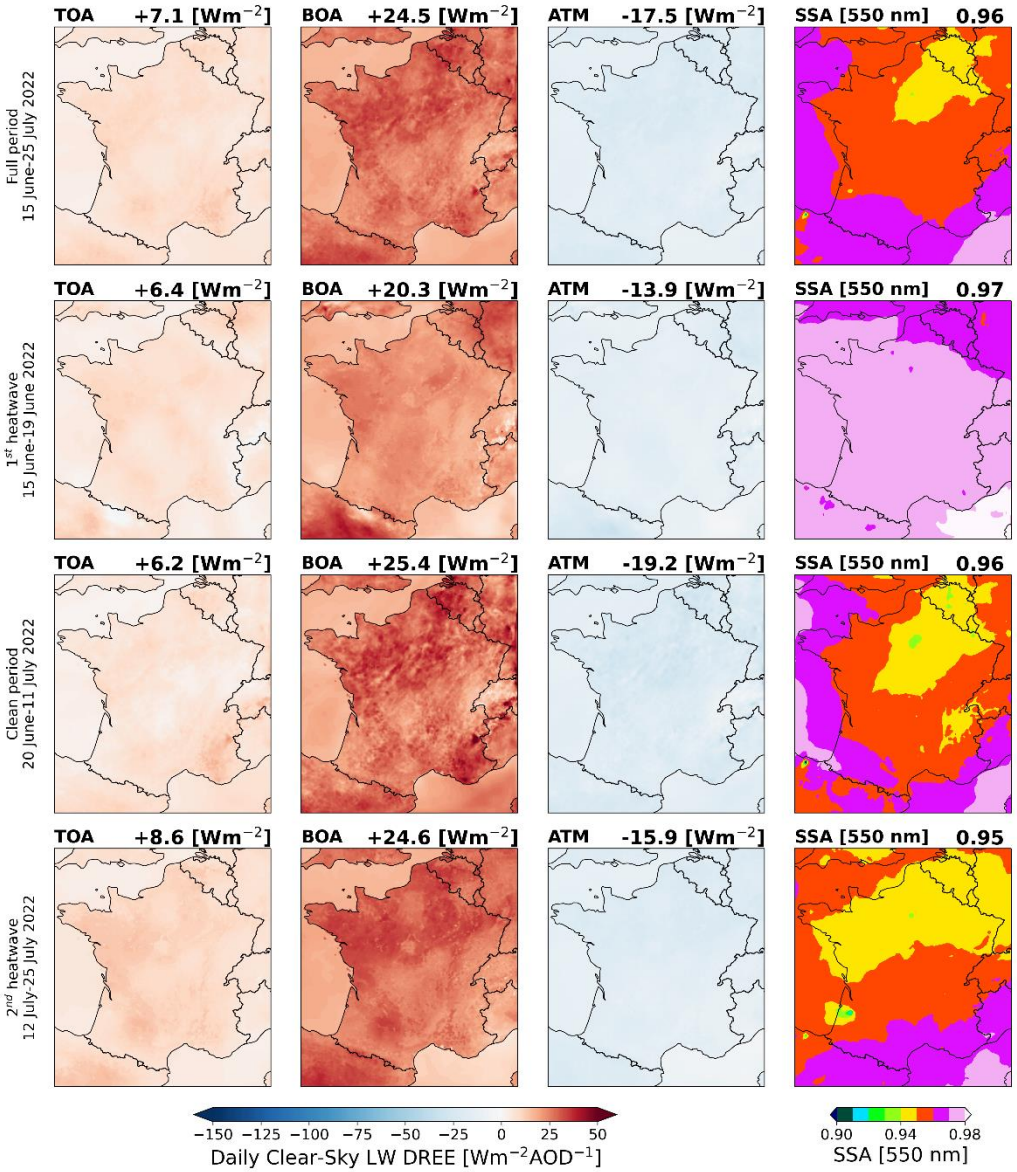

Figure D.2 Daily Clear-Sky LW direct radiative efficiency at top of the atmosphere (TOA), bottom of the atmosphere (BOA) and atmosphere (ATM) and single scattering albedo at 550 nm for the France domain (42°N, 51.15°N, 3.2°E,8.5°W) at 6km resolution, divided by the different periods during the ACROSS campaign.

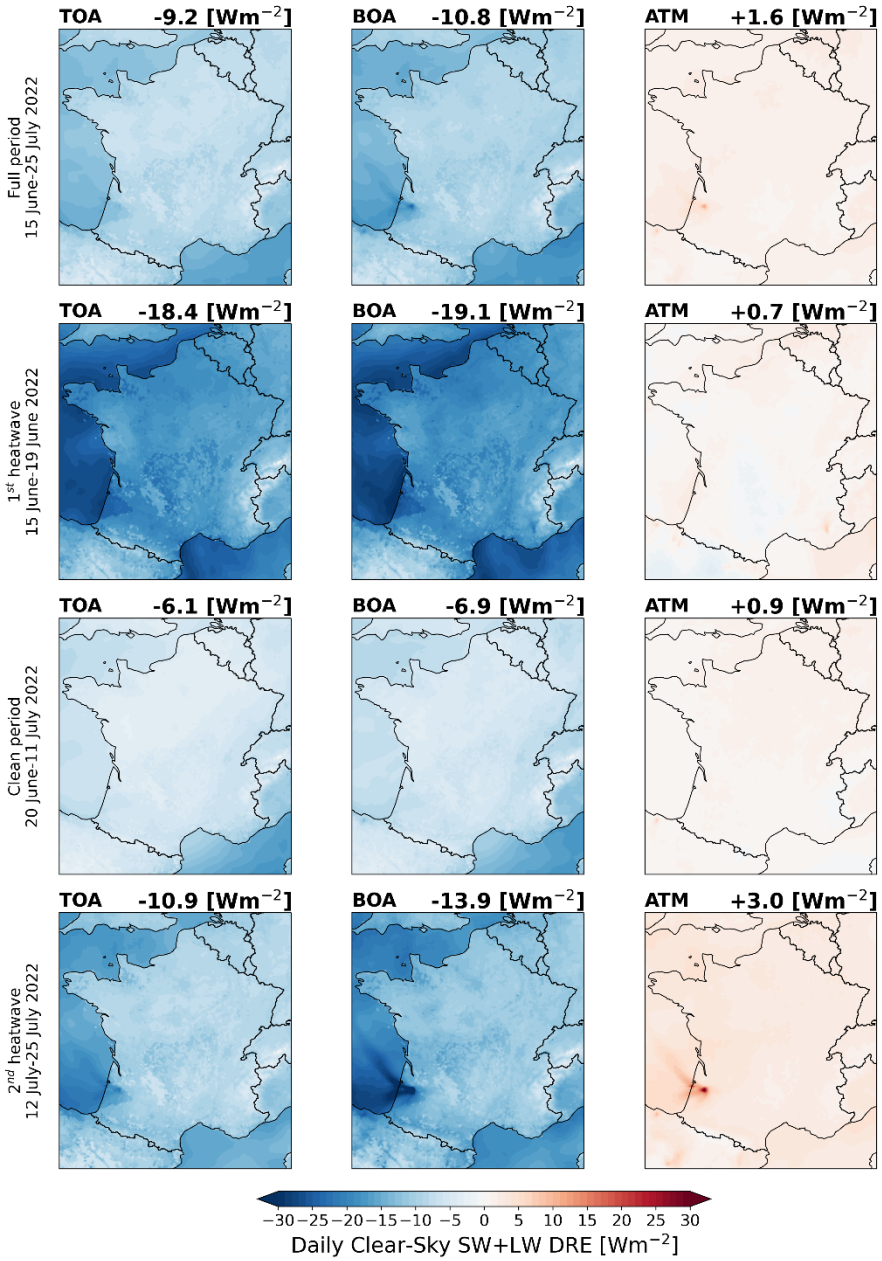

Figure D.3 Daily Clear-Sky SW+LW direct radiative effect at top of the atmosphere (TOA), bottom of the atmosphere (BOA) and atmosphere (ATM) for the France domain (42°N, 51.15°N, 3.2°E,8.5°W) at 6km resolution, divided by the different periods during the ACROSS campaign.

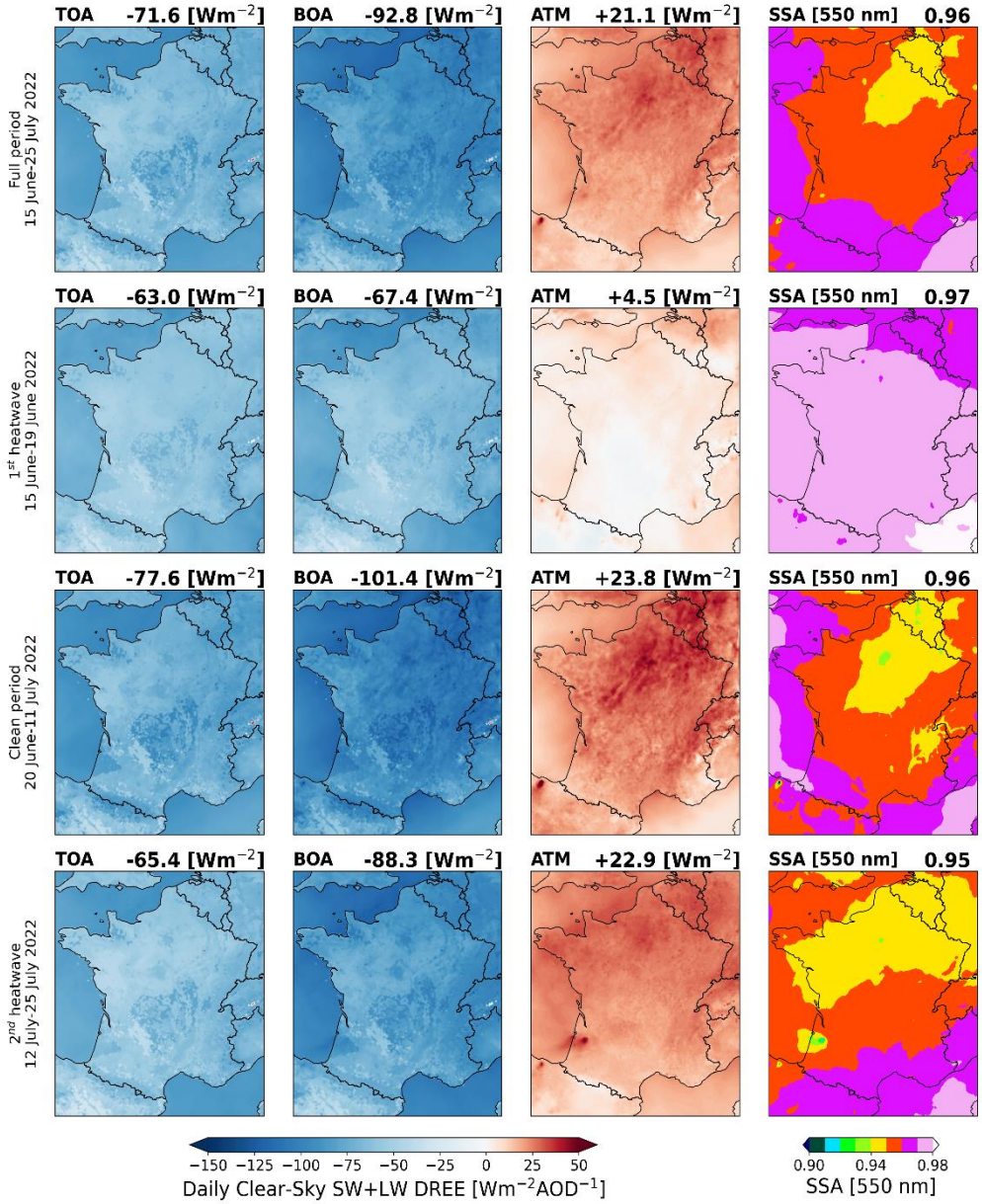

Figure D.4 Daily Clear-Sky SW+LW direct radiative efficiency at top of the atmosphere (TOA), bottom of the atmosphere (BOA) and atmosphere (ATM) and single scattering albedo at 550 nm for the France domain (42°N, 51.15°N, 3.2°E,8.5°W) at 6km resolution, divided by the different periods during the ACROSS campaign.

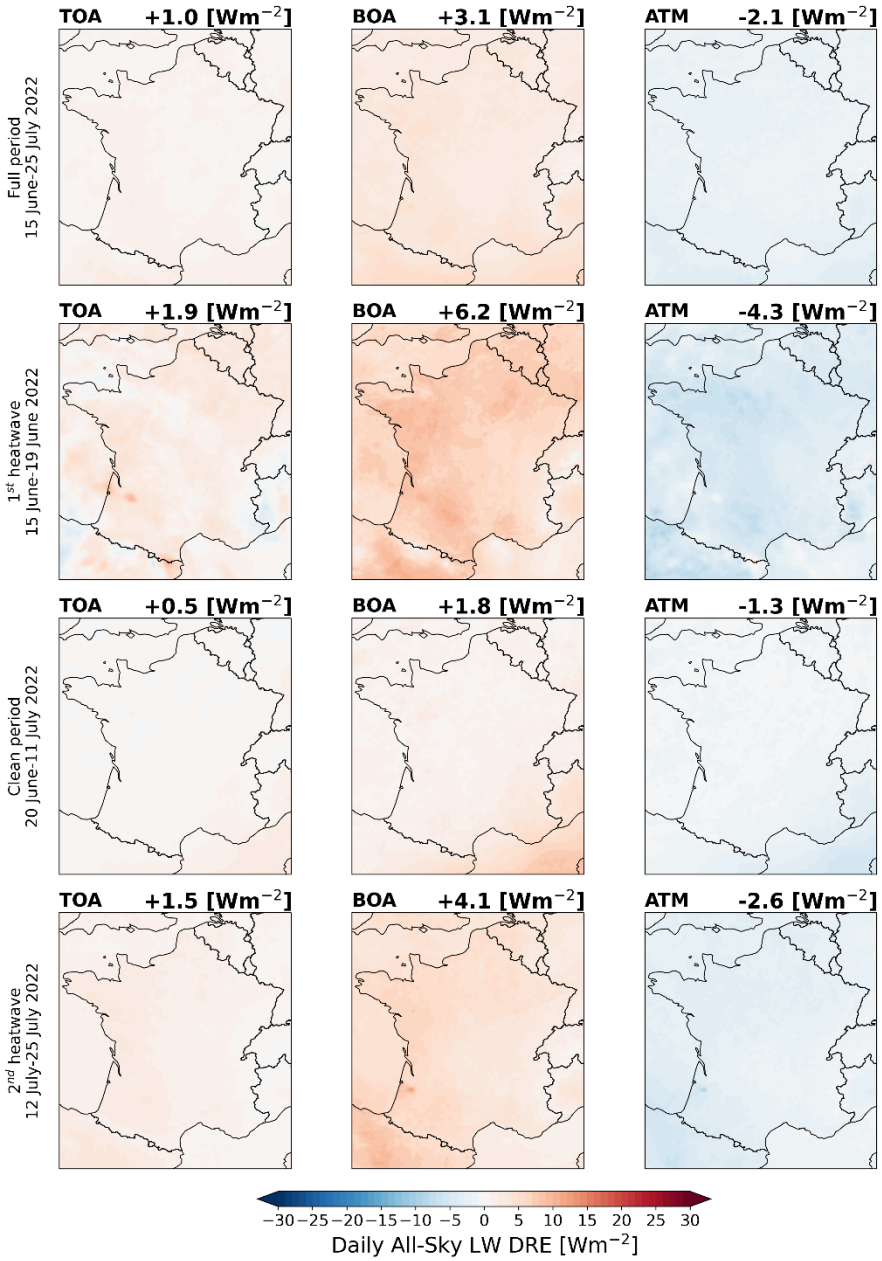

Figure D.5 Daily All-Sky LW direct radiative effect at top of the atmosphere (TOA), bottom of the atmosphere (BOA) and atmosphere (ATM) for the France domain (42°N, 51.15°N, 3.2°E,8.5°W) at 6km resolution, divided by the different periods during the ACROSS campaign.

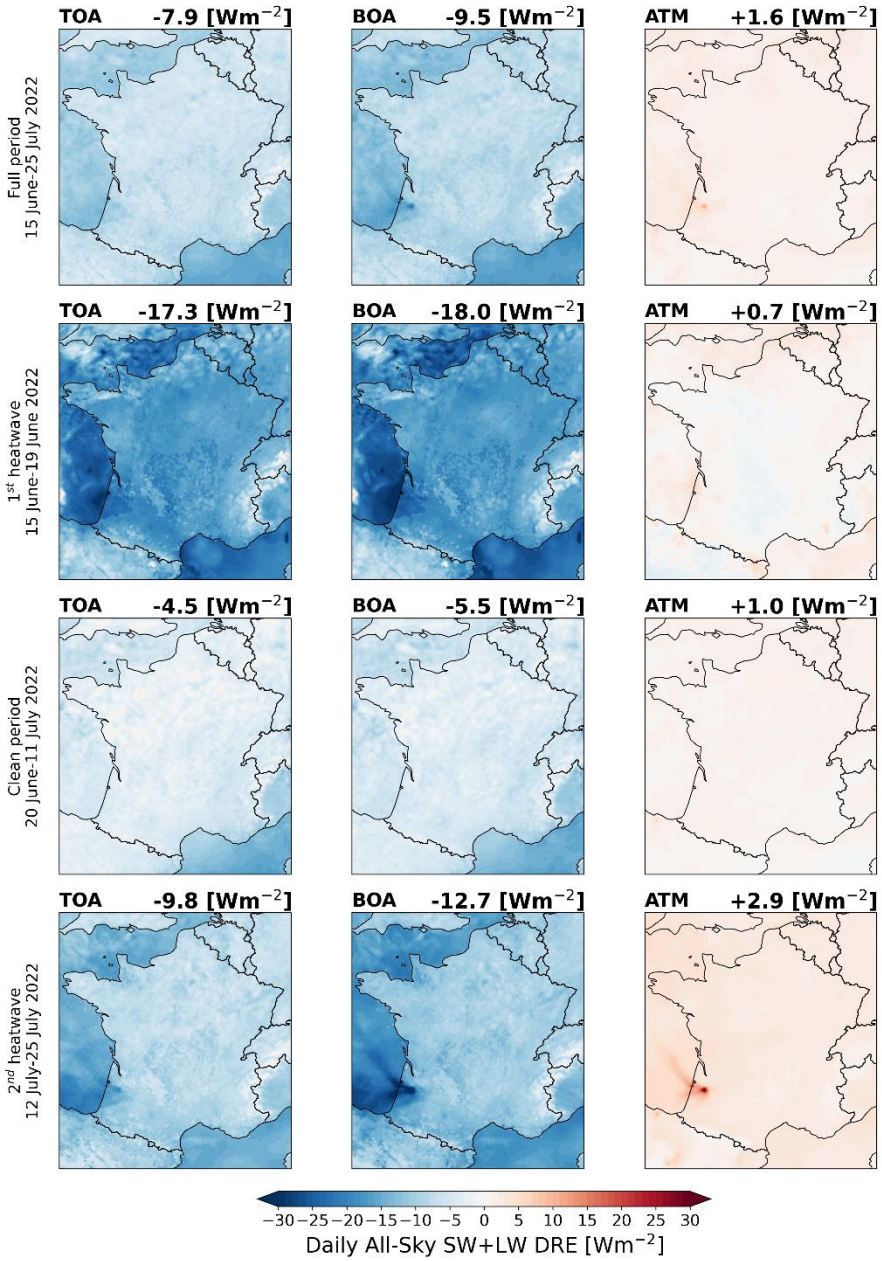

Figure D.6 Daily All-Sky SW+LW direct radiative effect at top of the atmosphere (TOA), bottom of the atmosphere (BOA) and atmosphere (ATM) for the France domain (42°N, 51.15°N, 3.2°E,8.5°W) at 6km resolution, divided by the different periods during the ACROSS campaign.

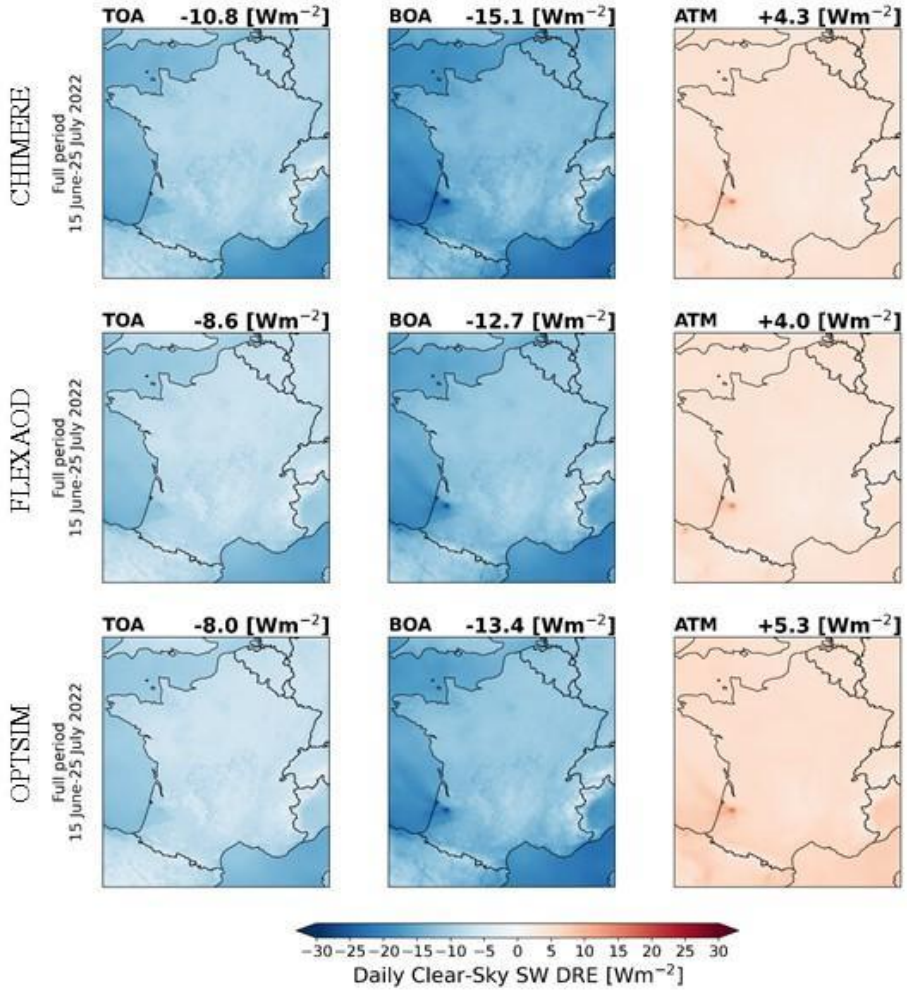

Figure D.7 Full ACROSS period averages OFFLINE Daily Clear-Sky SW direct radiative effect at top of the atmosphere (TOA), bottom of the atmosphere (BOA) and atmosphere (ATM) for the France domain (42°N, 51.15°N, 3.2°E,8.5°W) at 6km resolution with the CHIMERE, FlexAOD and OPTSIM models.

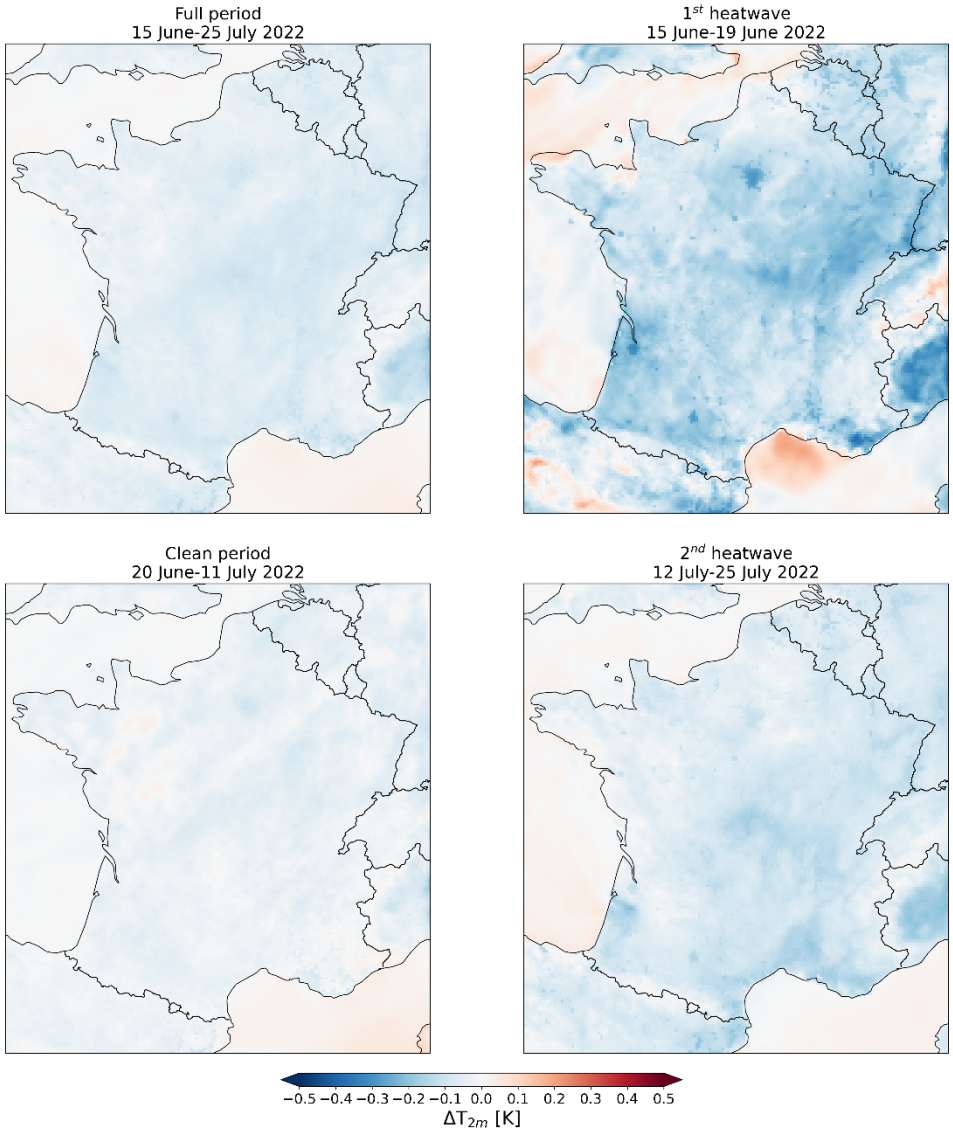

Figure D.8 Temperature differences feedbacks between coupled and not-coupled simulation during the ONLINE approach for the France domain (42°N, 51.15°N, 3.2°E,8.5°W) at 6km resolution, divided by the different periods during the ACROSS campaign.

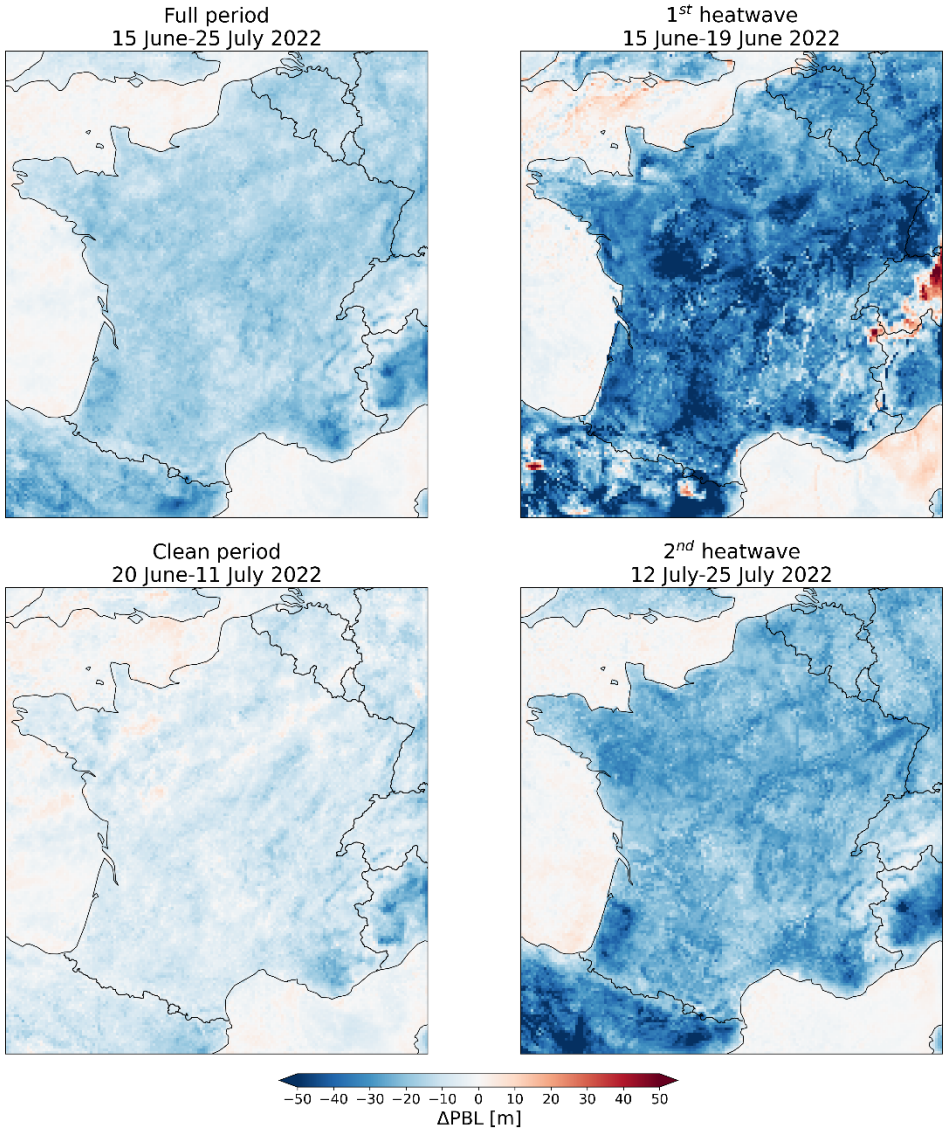

Figure D.9 Planetary boundary layer differences between coupled and not-coupled simulation during the ONLINE approach for the France domain (42°N, 51.15°N, 3.2°E,8.5°W) at 6km resolution, divided by the different periods during the ACROSS campaign.

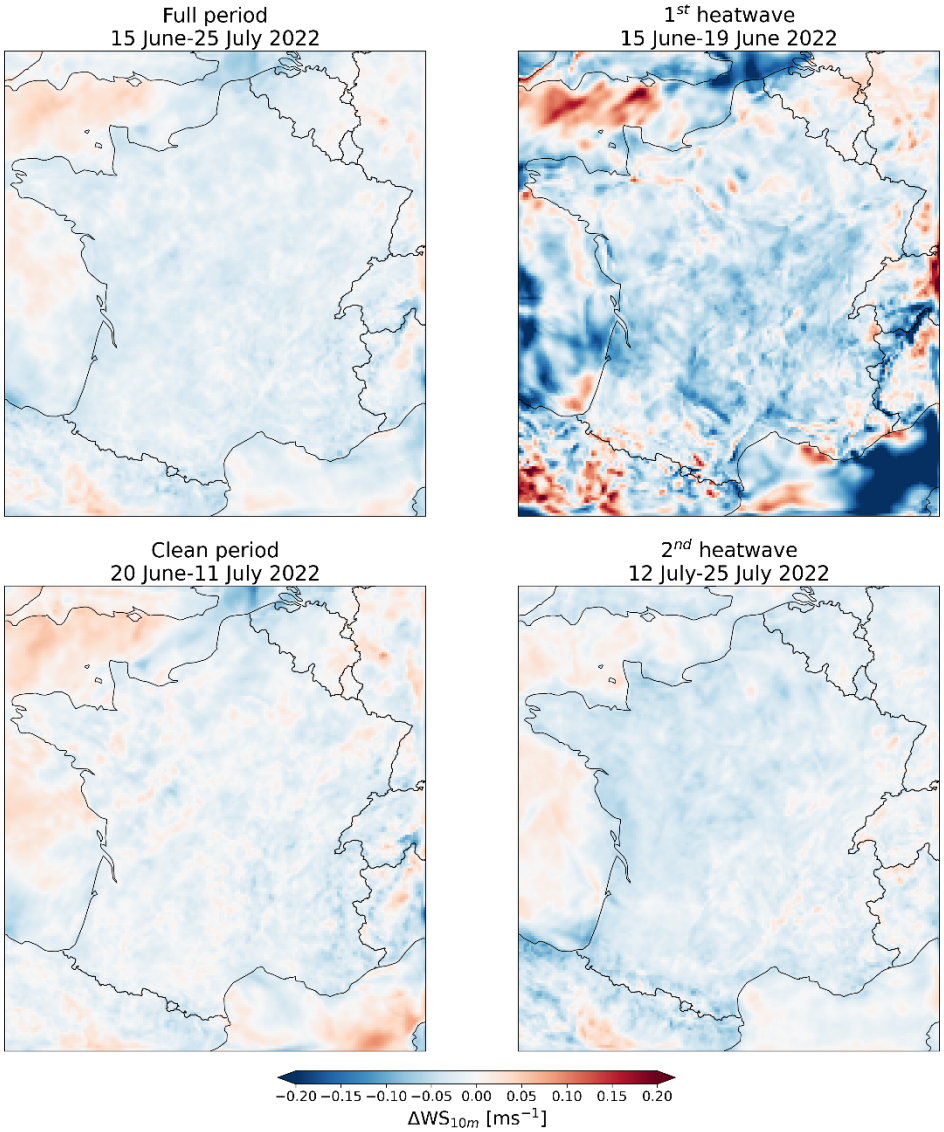

Figure D.10: 10 m wind speed differences between coupled and not-coupled simulation during the ONLINE approach for the France domain (42°N, 51.15°N, 3.2°E,8.5°W) at 6km resolution, divided by the different periods during the ACROSS campaign.

Tables

		All-sky (Ile-de-France)								
		SW			LW			SW+LW		
		TOA	BOA	ATM	TOA	BOA	ATM	TOA	BOA	ATM
Full period (15 June-25 July)	DRE	-6.7	-10.4	+3.7	+0.8	+2.9	-2.1	-5.9	-7.5	+1.6
	DREE	-61.7	-111.6	+49.8	+6.6	+28.9	-22.4	-55.2	-82.6	+27.5
1st heatwave (15 June-19 June)	DRE	-19.5	-25.3	+5.8	+1.8	+7.3	-5.5	-17.7	-18.0	+0.3
	DREE	-60.9	-83.4	+22.5	+3.4	+21.4	-18.0	-57.5	-62.0	+4.5
Clean period (20 June-11 July)	DRE	-2.1	-4.2	+2.0	+0.1	+0.8	-0.7	-2.1	-3.4	+1.3
	DREE	-61.2	-117.8	+56.7	+5.0	+30.1	-25.1	-56.2	-87.7	+31.6
2nd heatwave (12 July-25 July)	DRE	-9.4	-15.0	+5.6	+1.7	+4.7	-3.0	-7.7	-10.3	+2.6
	DREE	-62.9	-111.7	+48.8	+10.1	+29.8	-19.6	-52.7	-81.9	+29.2

Table D.1: All-sky direct radiative effect and direct radiative efficiency averages for the ONLINE approach at top of the atmosphere (TOA), bottom of the atmosphere (BOA) and atmosphere (ATM) for the Ile-de-France domain (48.1°N, 49.26 °N, 3.57°E, 1.47°W) divided by the different periods during the ACROSS campaign.

		Clear-sky (Ile-de-France)								
		SW			LW			SW+LW		
		TOA	BOA	ATM	TOA	BOA	ATM	TOA	BOA	ATM
Full period (15 June-25 July)	DRE	-8.2	-12.0	+3.8	+1.2	+3.2	-2.0	-7.0	-8.8	+1.8
	DREE	-72.3	-124.6	+52.3	+8.3	+29.9	-21.5	-64.0	-94.7	+30.7
1st heatwave (15 June-19 June)	DRE	-21.3	-26.7	+5.4	+3.1	+7.6	-4.5	-18.2	-19.1	+0.9
	DREE	-66.6	-87.9	+21.2	+8.0	+22.2	-14.2	-58.6	-65.7	+7.0
Clean period (20 June-11 July)	DRE	-3.9	-6.1	+2.3	+0.3	+1.2	-0.9	-3.6	-5.0	+1.4
	DREE	-78.0	-139.1	+61.1	+7.1	+31.6	-24.5	-70.8	-07.5	+36.7
2nd heatwave (12 July-25 July)	DRE	-10.3	-16.0	+5.7	+1.8	+4.7	-2.9	-8.5	-11.3	+2.8
	DREE	-65.4	-114.9	+49.5	+10.4	+30.0	-19.6	-55.0	-84.9	+29.9

Table D.2: Clear sky direct radiative effect and direct radiative efficiency averages for the ONLINE approach at top of the atmosphere (TOA), bottom of the atmosphere (BOA) and atmosphere (ATM) for the Ile-de-France domain (48.1°N, 49.26 °N, 3.57°E, 1.47°W) divided by the different periods during the ACROSS campaign.

		DRE SW (Clear-sky)			DREE SW (Clear-sky)			
		TOA	**BOA**	**ATM**	**TOA**	**BOA**	**ATM**	**AOD [550nm]**
Full period (15 June-25 July)	$EXT_{C\text{-}ONLINE}$	-10.4	-14.1	+3.8	-78.0	-115.8	+37.8	0.15
	$EXT_{C\text{-}OFFLINE}$	-10.8	-15.1	+4.3	-82.0	-125.1	+43.0	
	EXT_F	-8.6	-12.7	+4.0	-75.1	-120.4	+46.3	0.14
	CS	-8.0	-13.4	+5.3	-77.6	-121.8	+44.2	0.14
1st heatwave (15 June-19 June)	$EXT_{C\text{-}ONLINE}$	-20.7	-25.6	+4.8	-68.7	-86.0	+17.3	0.32
	$EXT_{C\text{-}OFFLINE}$	-21.7	-27.4	+5.7	-72.2	-93.6	+21.4	
	EXT_F	-16.7	-22.1	+5.5	-58.8	-79.9	+21.1	0.31
	CS	-15.8	-23.4	+7.7	-56.5	-84.9	+28.4	0.31
Clean period (20 June-11 July)	$EXT_{C\text{-}ONLINE}$	-6.7	-9.0	+2.3	-83.1	-125.5	+42.4	0.09
	$EXT_{C\text{-}OFFLINE}$	-6.9	-9.6	+2.8	-87.3	-136.1	+48.8	
	EXT_F	-5.4	-8.0	+2.6	-80.7	-134.4	+53.7	0.08
	CS	-5.5	-7.7	+2.3	-91.0	-127.8	+36.8	0.08
2nd heatwave (12 July-25 July)	$EXT_{C\text{-}ONLINE}$	-12.5	-18.2	+5.6	-73.3	-111.2	+37.9	0.20
	$EXT_{C\text{-}OFFLINE}$	-13.1	-19.2	+6.1	-77.3	-119.0	+41.7	
	EXT_F	-10.8	-16.7	+5.8	-69.3	-112.9	+43.6	0.17
	CS	-9.3	-18.7	+9.3	-64.2	-125.5	+61.3	0.17

Table D.3: Summary of daily clear-sky SW direct radiative effect, direct radiative efficiency and aerosol optical depth at 550 nm averages for the ONLINE approach ($EXT_{C\text{-}ONLINE}$) and OFFLINE calculate with the CHIMERE spectral optical properties output ($EXT_{C\text{-}OFFLINE}$), the FlexAOD model (EXT_F) and the Core-shell model (CS) for the France domain (42°N, 51.15°N, 3.2°E, 8.5°W) at 6km resolution and during the ACROSS campaign.

Annex E. Pilot study of the summer 2019 heatwave and first DRE evaluation with the WRF-CHIMERE model

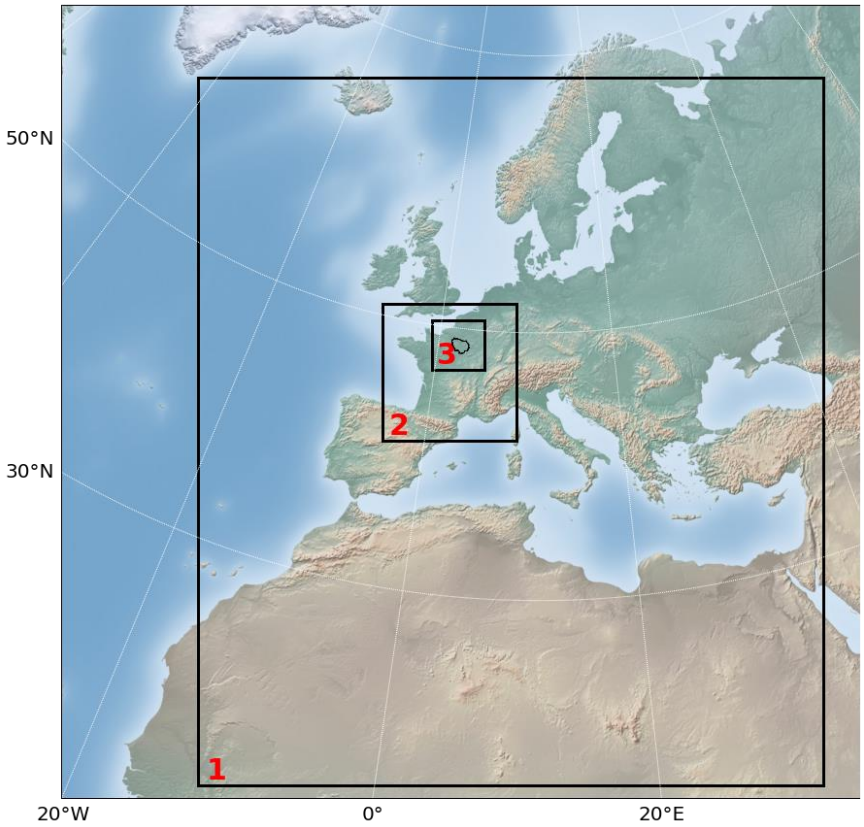

Figure E.1: Domain configuration for the ACROSS-like TEST case using: 30,6, and 2 km of spatial resolution respectively.

A first simulation with three nested domains having a resolution of 30, 6 and 2 km respectively, (centered in the Paris area) was configured (Fig. E.1) on a case study of June-July 2019 with the chemistry and transport WRF-CHIMERE model. The case study, defined as "pilot study" has been chosen by considering an intense heatwave that hit the Paris region during the summer 2019. In this regard, high values of ozone have been registered by the AIRPARIF network (https://data-airparif-asso.opendata.arcgis.com/, last access: 18 May 2024). This case is interesting for the ACROSS campaign, where the ideal condition would be the presence of a high pressure system centered on England, such that the wind originates from North-East and links the Paris urban and the Rambouillet forest site. The validation of the control simulation (CTRL) has been carried out by comparing some of the available data from existing databases: AIRPARIF (O_3, $PM_{2.5}$, PM_{10}), EBAS (O_3, $PM_{2.5}$, PM_{10}, EEA (O_3, $PM_{2.5}$, PM_{10}, SIRTA observatory (wind direction) and AERONET (optical properties, AOD), E-OBS (temperature). An example of the validation performed for the aerosol optical depth is shown in the Figure E2.

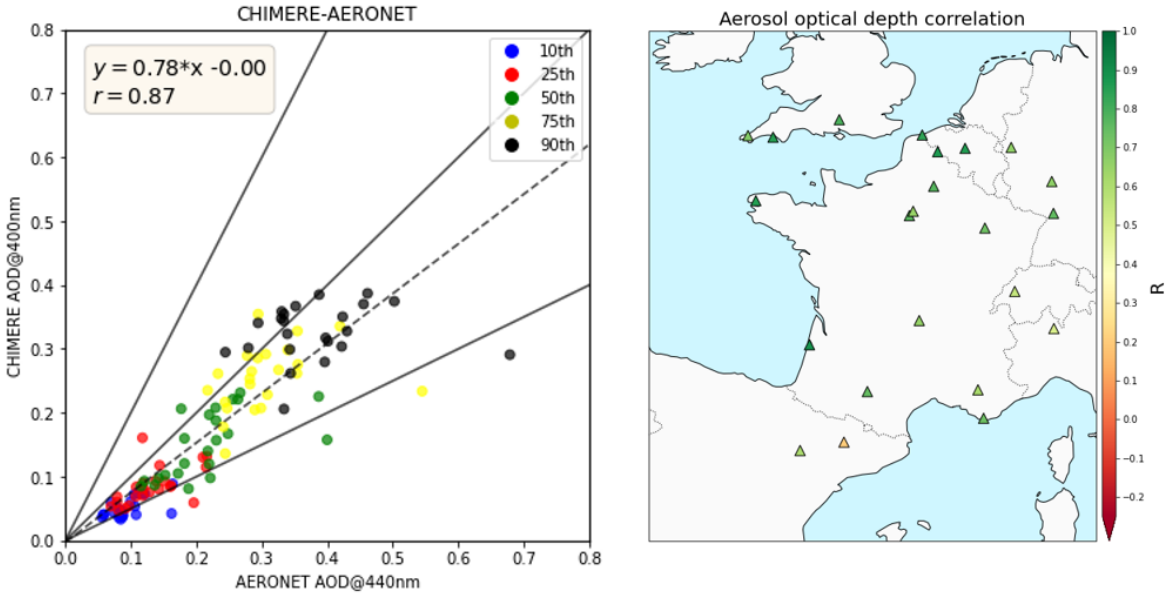

Figure E.2: (Left) CHIMERE vs AERONET AOD scatter plot and percentiles' analysis on the available AERONET station data in the domain during the case study June-July 2019, (Right) AOD Pearson coefficient on the case study June-July 2019.

The objective of this simulation was to test the model under the ideal conditions of the campaign which took place in July 2022. This phase was essential to study the capacities and weaknesses of the model and to propose possible improvements.

A climatology of the aerosol size distribution was built based on available measurements in the region and used to compare to the aerosol size distribution from the model simulation (Figure E.3). The climatological size distribution shows two main modes: the fine mode D=0.2-0.3µm and the coarse mode D=5-6 µm. The comparison with the WRF-CHIMERE chemically-speciated simulated columnar volume size distribution, showed that the model simulated finer particles with a diameter of approximately 0.15 µm, in contrast to in situ measurements on the region whose diameter was about 0.25µm, leading to a possible underestimation in the aerosol optical depth estimation (Figure E. 2). The size distribution comparison also revealed the presence of a strong coarse mode due to dust aerosols, during the summer 2019 heatwave period, which was identified also in the AERONET optical inversion measurements. In order to investigate the underestimation of the fine part of the particle size distribution, sensitivity tests were conducted: the size distribution was right-shifted by about 0.07 µm. This resulted in a more accurate representation of the aerosol optical depth. However, at the same time a bug was identified causing the AOD underestimation. This bug was fixed by the

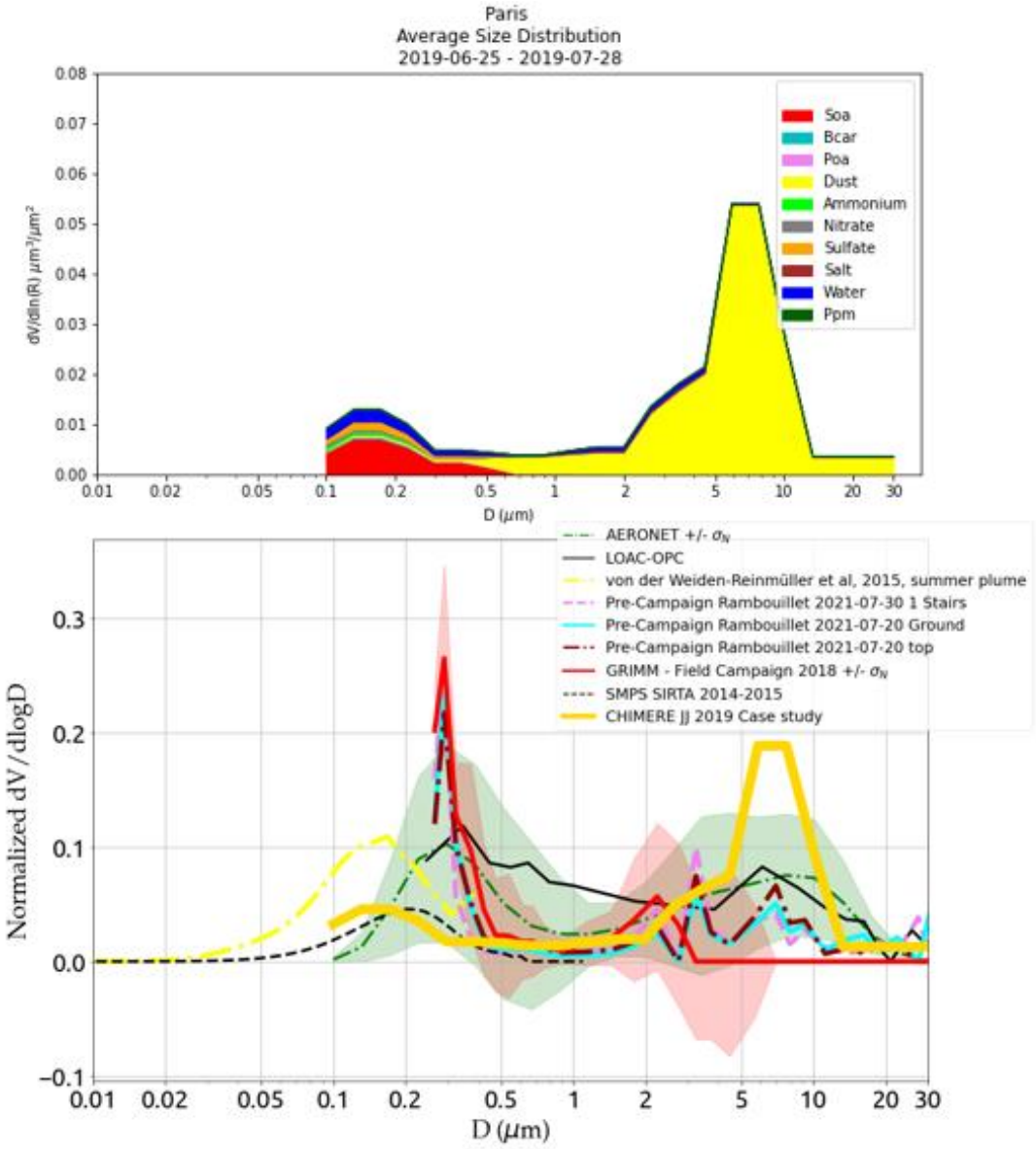

Figure E.3: (top) Chemically-speciated simulated columnar volume size distribution from the CHIMERE model for the summer 2019: secondary organic aerosol (SOA), primary organic aerosol (POA) , primary particulate matter (PPM); (bottom) size distribution comparison with literature and the pre-campaign of the ACROSS field campaign.

CHIMERE development team by implementing a dust emission correction in the fine part of the size distribution. This correction was then implemented in the simulation for the ACROSS campaign 2022.

Finally, a first direct radiative effect estimation using the WRF-CHIMERE coupling (Fig. E.4) has been performed.

Thanks to the ACROSS-like case-study we were able to estimate a daily average shortwave TOA DRE for all the aerosol species of -18.4 Wm^{-2} over l'Ile-de-France and -17.1 Wm^{-2} over Paris for the

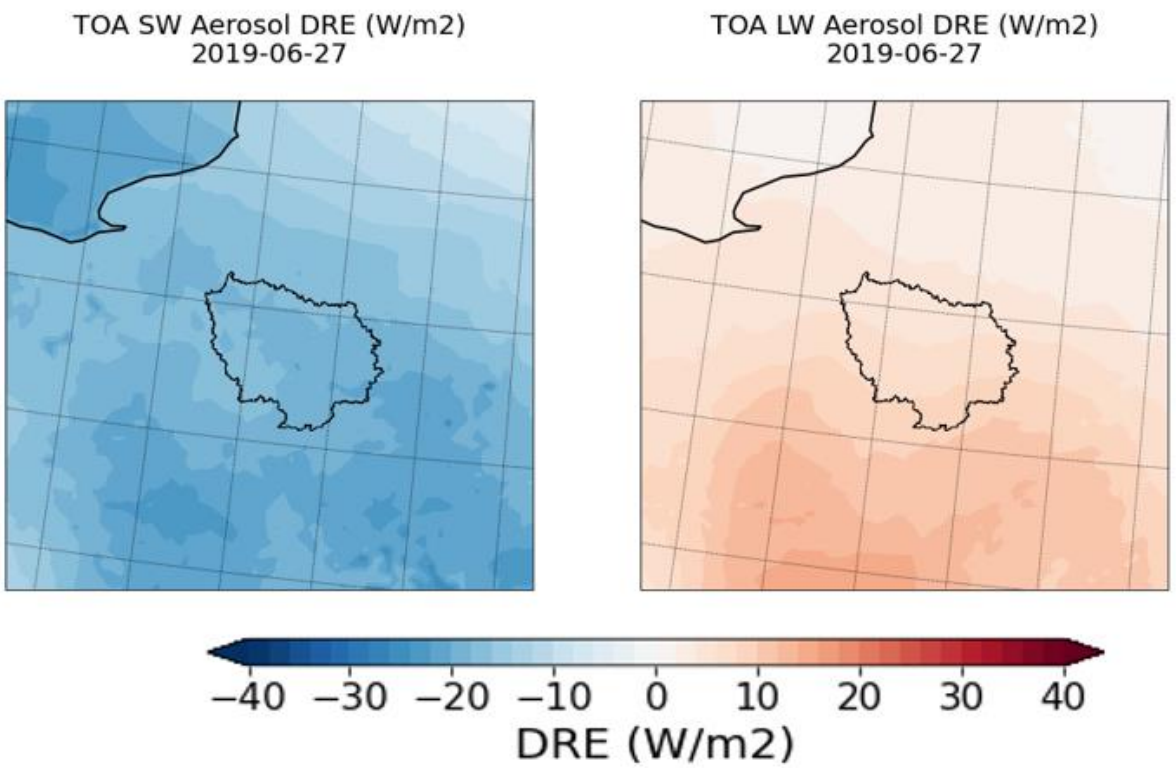

Figure E.4: shortwave and (right) longwave direct radiative effect at the top of the atmosphere for the 27 June 2019 over the Ile-de-France region

27 June 2019. The results of this test proved to be beneficial, as it indicated that under heatwave conditions and high aerosol loading, the DRE becomes significant even in regions where the AOD climatological averages are relatively low, such as the Ile-de-France region.

Annex F. Example forecast report for the ACROSS aircraft field campaign

ACROSS forecast report

21 June 2022

Members present: C. Cantrell, M. Beekmann, G. Siour, **L. Di Antonio**

Report Author: **L. Di Antonio**, M. Beekmann

General situation

The low pressure cut-off centered on the Northern part of Spain, will lead to unstable weather conditions over France, in particular over the Ile-de-France region, where rain and thunderstorms may not be excluded, mainly in the late afternoon. **NE winds will prevail, of gentle breeze intensity both at surface and at 950hPa, with the relative formation of a pollution plume, over the south west direction. Temperatures between 26/29 °C. The chance of flight over the SW direction may not be excluded.**

Figure F.1: Geopotential Height at 500 hPa for Tuesday 21/06 12Z

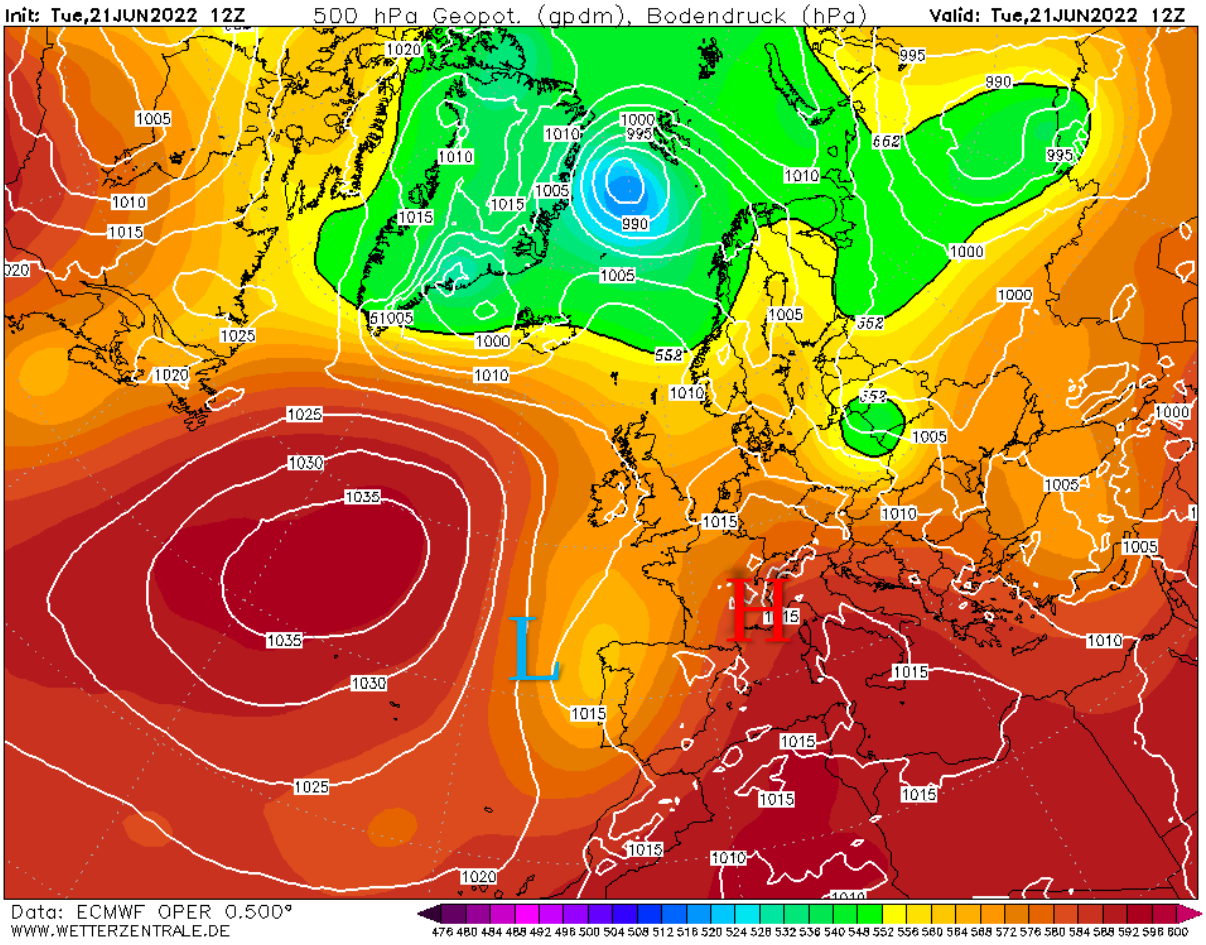

22 June 2022 (J+1)

The day will begin with scattered clouds and variable weather over all the IDF region, with no remarkable precipitation events expected in the morning. The cloud cover will increase during the day. The latter will lead to the possible formation of intense rainy events in the late afternoon, located over S-SW of the region, due to moderate instability (CAPE~2200 J/Kg). NE Winds prevailing, between 10/15 Km/h. Temperatures between 26/29 °C. The chance of a possible shorter flight during the 13-17h LT window may be discussed.

Figure F.2: (left) CAPE and LI for 13 UTC, (right) O3 and ASOA at 13 UTC from Prevair

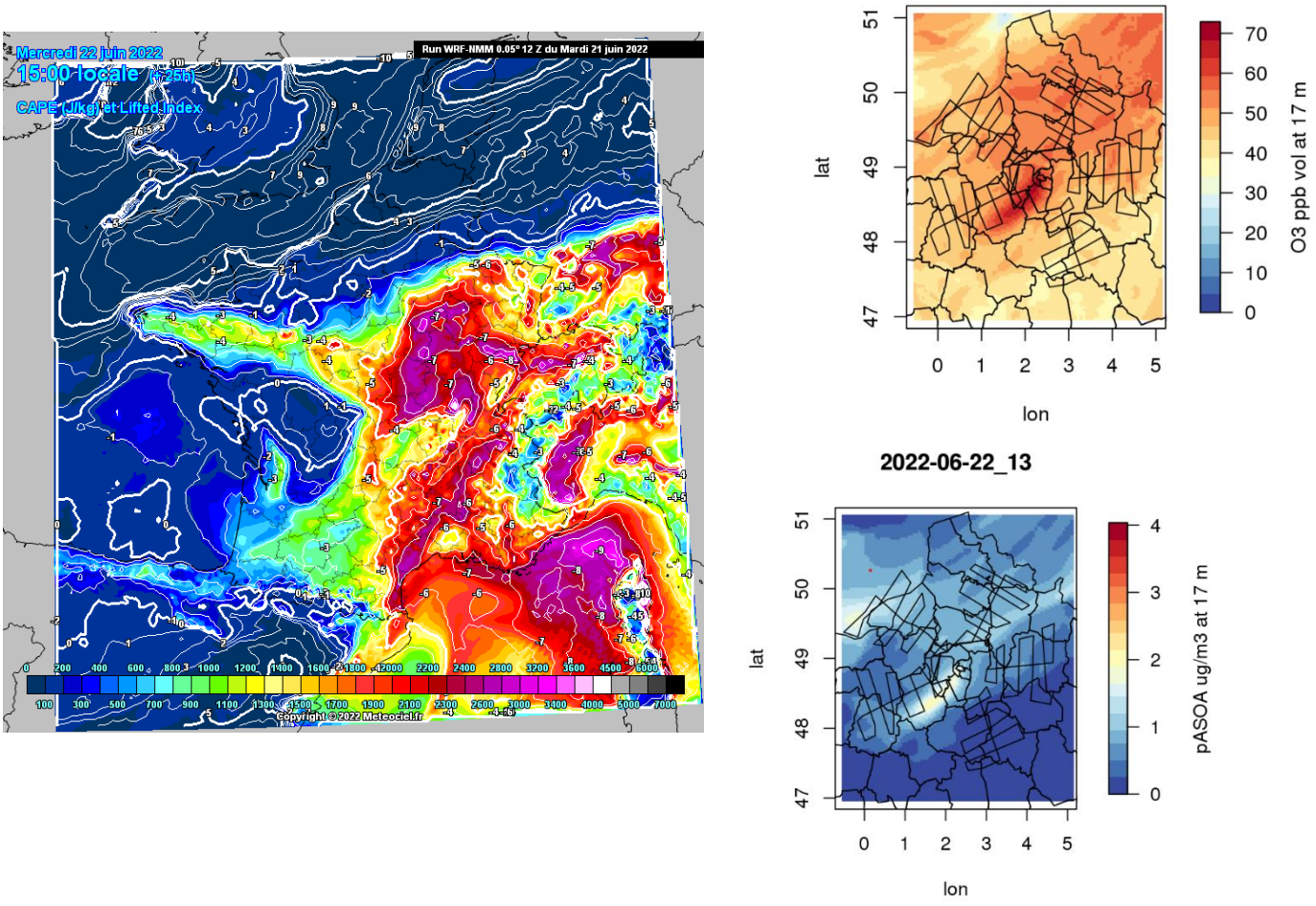

23 June 2022 (J+2)

The low pressure system will be still localized over the Atlantic Ocean. The day will start with scattered low clouds and residual rain from the antecedent night. Weather conditions will improve during the central part of the day over the IDF and the NE direction, with a new consequent deterioration in the late evening over the S-SW of the region. The wind will turn from the northern quadrants to the southern quadrants, in particular the SW. Temperatures 22/26 °C. **Pollution plume will form over the NE direction. A NE direction's flight may be envisaged.**

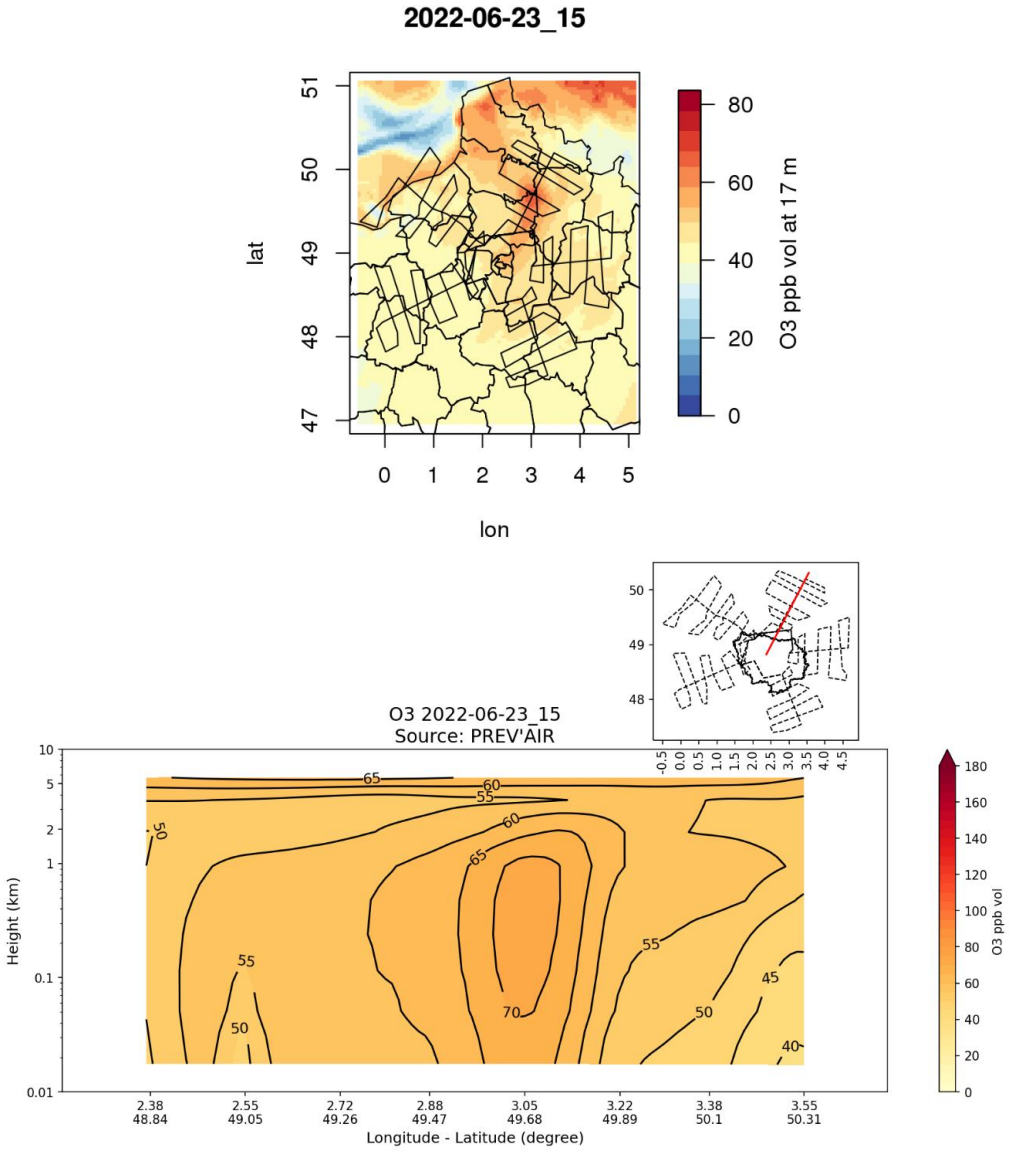

Figure F.3: O_3 and NE O_3 cross section from Prevair for Wednesday 23/06 15 UTC. O3 NE cross section

24 June 2022 (J+3)

The cut-off system will be absorbed by the persistent low pressure system over the North Atlantic Ocean. The latter will move down in latitude, bringing a decrease in temperature 18/22 °C and rainy events over the Ile-de-France region. **The region will still be under SW flow, and a SW flight direction may be discussed. Pollution plume over the SW direction, low level of particulate matter.**

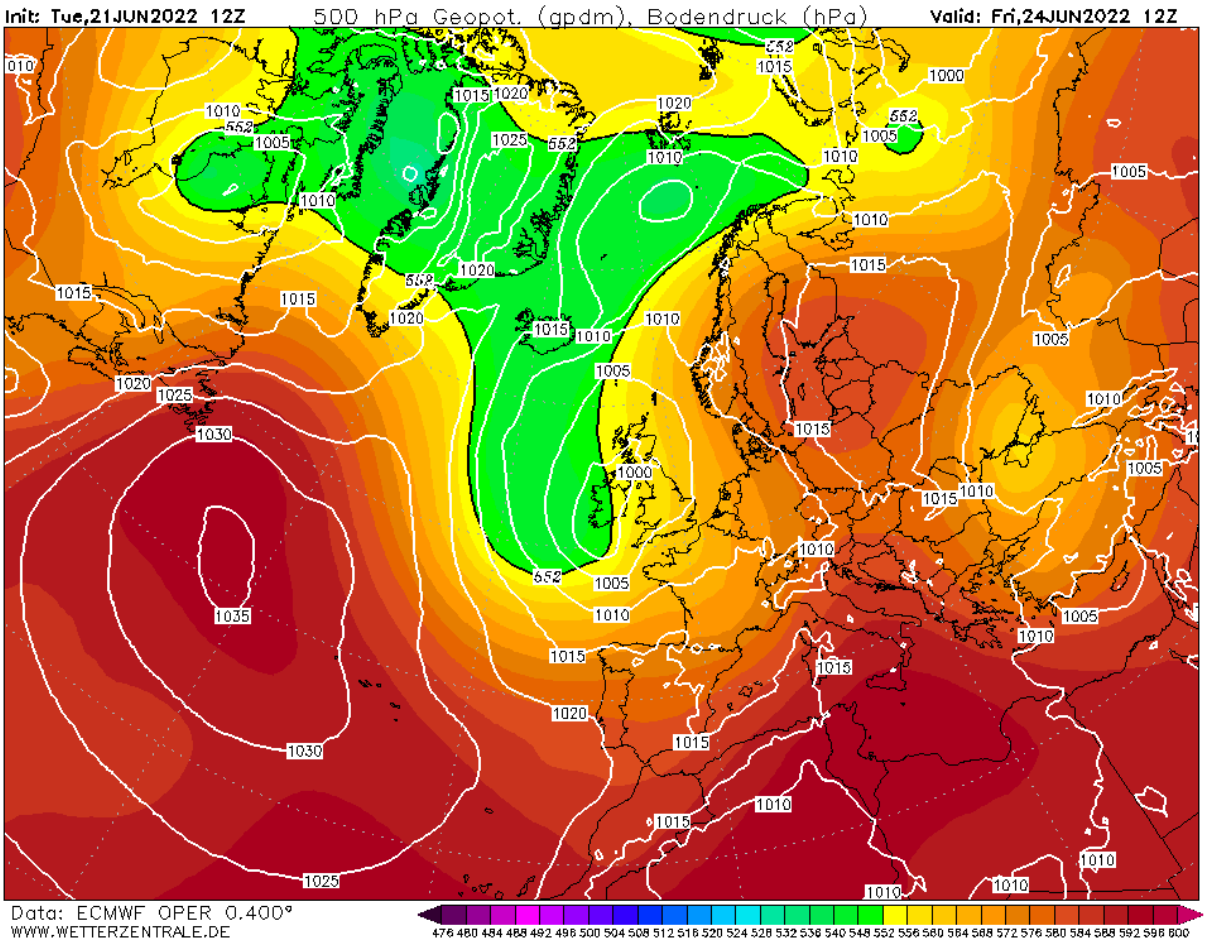

Figure F.4: Geopotential Height at 500 hPa for Tuesday Fri 24/06 12Z

25 June 2022 (J+4) and after

The low pressure system will continue to displace down, settling its center over Ireland. The latter will mainly induce a SW-W flow for the following days and rainy events at the interface of the cold front's passage. **Possible window of flight after the passage of the front.**

Recommendations:

- NE flights pattern could be discussed for the 22/06, final decision on the 22 June 9h LT meeting.
- SW flight pattern could be discussed for the 23/06

Next meeting 22 June 2022 9h LT

Annex G. Publications, peer review, conferences, abstracts, poster, oral presentations and formations

Scientific papers

- G. Curci, J.A. Guijarro, **L. Di Antonio**, M. Di Bacco, B. Di Lena, AR. Scorzini, "Building a local climate reference dataset: Application to the Abruzzo region (Central Italy), 1930–2019". Int J Climatol. 2021; 41: 4414– 4436. https://doi.org/10.1002/joc.7081
- **Di Antonio, L**., Di Biagio, C., Foret, G., Formenti, P., Siour, G., Doussin, J.-F., and Beekmann, M.: Aerosol optical depth climatology from the high-resolution MAIAC product over Europe: differences between major European cities and their surrounding environments, Atmos. Chem. Phys., 23, 12455–12475, https://doi.org/10.5194/acp-23-12455-2023 , 2023.

Datasets

- **Di Antonio, L**., Di Biagio, C. & Gratien, A. (2023). ACROSS_LISA_PRG_AETH-Abs_PM1_1-Min_L2. [Dataset]. Aeris. https://doi.org/10.25326/574
- **Di Antonio, L.,** Di Biagio, C. & Gratien, A. (2023). ACROSS_LISA_PRG_AETH-eBC_PM1_1-Min_L2. [Dataset]. Aeris. https://doi.org/10.25326/575
- **Di Antonio, L**., Di Biagio, C. & Gratien, A. (2023). ACROSS_LISA_PRG_FIDAS-PM_PM1_1-Min_L2. [Dataset]. Aeris. https://doi.org/10.25326/572
- **Di Antonio, L.,** Di Biagio, C., Gratien, A., Hawkins, L.N., Bergé, A. & Riley, S. (2023). ACROSS_LISA_PRG_METEO_1-Min_L2. [Dataset]. Aeris. https://doi.org/10.25326/573
- **Di Antonio, L.,** Di Biagio, C. & Gratien, A. (2023). ACROSS_LISA_PRG_OPC-Sizedistr_PM1_1-Min_L2. [Dataset]. Aeris. https://doi.org/10.25326/539
- **Di Antonio, L.,** Di Biagio, C. & Gratien, A. (2023). ACROSS_LISA_PRG_NEPH-Scatt-Backscatt_PM1_1-Min_L2. [Dataset]. Aeris. https://doi.org/10.25326/538
- **Di Antonio**, Siour, G. & Beekmann, M. (2023). ACROSS_LISA_CHIMERE_BCRatio_1H. [Dataset]. Aeris. https://doi.org/10.25326/529
- Siour, G. & **Di Antonio, L.** (2023). ACROSS_LISA_WRF-CHIMERE_HYSPLIT_Backtraj_1H. [Dataset]. Aeris. https://doi.org/10.25326/543

Publications submitted and under review:

- Lombardi, A., Tomassetti, B., Colaiuda, V., **Di Antonio, L**., Tuccella, P., Montopoli, M., Ravazzani, G., Marzano, F. S., Lidori, R., and Panegrossi, G.: On the combined use of rain gauges and GPM IMERG satellite rainfall products: testing cellular automata-based interpolation methodology on the Tanaro river basin in Italy, Hydrol. Earth Syst. Sci. Discuss. [preprint], https://doi.org/10.5194/hess-2023-214, in review, 2023.

Publications in preparation:

- **Di Antonio et al.**: Aerosol spectral optical properties in the Paris urban area and its peri−urban and forested surroundings from ACROSS surface observations during summer 2022

- **Di Antonio et al**: Modelling of atmospheric variability of gas and aerosols during the ACROSS campaign 2022 in the greater Paris area: evaluation of the meteorology, dynamics and chemistry
- **Di Antonio et al.**: Modelling of the aerosol direct radiative effect during the ACROSS field campaign

Peer review:

- Peer review for the Atmospheric Chemistry and Physics (ACP) journal on the 3 November 2023, https://portal.issn.org/resource/ISSN/1680-7316

Conferences, abstracts, poster and oral presentations:

- **L. Di Antonio** et al, Aerosol complex refractive index retrieval in the Paris urban area and its forested surroundings during the ACROSS field campaign: variability and constraint for direct radiative effect estimation in regional models – ACTRIS 13-16 May 2024 (Oral presentation)
- **L. Di Antonio** et al, Constraining the aerosol direct radiative effect in the framework of the ACROSS campaign held during the June-July 2022 intense summer heatwave period, Workshop CHIMERE, Paris, 22-23 June 2023 (Oral presentation)
- **L. Di Antonio** et al, Constraining the aerosol direct radiative effect in the framework of the ACROSS campaign held during the June-July 2022 intense summer heatwave period– AMA2023, Toulouse, 9-11 May 2023 (Oral presentation)
- **L. Di Antonio** et al, Aerosol optical depth climatology from the high-resolution MAIAC observations product over Europe: difference between major European cities and their surrounding environment– Workshop Lille 2023 & GRASP ACE Summer School, 22-26 May 2023 (Poster presentation)
- **L. Di Antonio** et al, Aerosol complex refractive index retrieval in the Paris urban area and its forested surroundings during the ACROSS field campaign: variability and constraint for direct radiative effect estimation in regional models– EGU2023, 23-28 April 2023 (Oral presentation)
- M. Beekman, G. Siour**, L. Di Antonio**, …, Meteorological variability and regional pollutant distributions during the summer 2022 ACROSS/PANAME campaign. – EGU2023 23-28 April 2023 (Oral presentation)
- D. Pereira, A. Gratien, …, **L. Di Antonio**, …, Addressing the chemical composition of secondary organic aerosol in the rural/ urban Paris area – EGU2023 23-28 April 2023 (Poster presentation)
- P. Formenti, …, **L. Di Antonio**, …, Hygroscopic and optical properties of complex aerosol mixtures at the Rambouillet forest super-site of the ACROSS project. – EGU2023 23-28 April 2023 (Poster presentation)
- C. Cantrell, V. Michoud, J-F Doussin, P. Formenti, M. Cirtog, P. Coll, **L. Di Antonio**, …, Overview of the ACROSS Campaign near Paris in Summer 2022 – EGU2023 23-28 April

2023 (Poster presentation)

- J.F. De Brito, …, **L. Di Antonio**, …, Contrasting aerosol composition in and out of Paris plume during the ACROSS campaign at the Rambouillet supersite. – EGU2023 (Oral presentation)
- **L. Di Antonio** et al, Aerosol complex refractive index retreival during the ACROSS campaign – Workshop ACROSS February 2023 (Oral presentation)
- **L. Di Antonio** et al, Modelling of aerosol and radiative effects during the ACROSS campaign 2022 – Workshop ACROSS February 2023 (Oral presentation)
- **L. Di Antonio** et al, Radiative effects of carbonaceous aerosols on the Euro-Mediterranean region – ASIAM conference 2021 (Oral presentation)

Seminars

- **L. Di Antonio** et al, Properties, size distribution and radiative effects of the aerosols in Ile-de-France: a synergistic measurements-modelling approach (oral) – Lille (October 2022)
- **L. Di Antonio** et al, Properties, size distribution and radiative effects of the aerosols in Ile-de-France: a synergistic measurements-modelling approach (oral) – 1st and 3rd PhD year seminar at LISA (May 2022)

List of followed formations

1. CHIMERE Training (4-5 July 2022)
2. TP, Vacation en Python dans le Master « Modelisation des systemes Environnementaux » - 21 heures
3. Modélisation Numérique de l'Écoulement Atmosphérique et Assimilation de Données – 16 heures
4. Anglais - Module Academic English - B2 - 12 heures
5. Anglais : Module Professional English - B2 – 12 heures
6. Cours : Nuages Aérosols Précipitations - 30 heures
7. Convective and Volcanic Clouds detection, monitoring and modeling - 26 heures
8. TRAVAUX EN HAUTEUR ET PORT DU HARNAIS - R 430 et R431 - 7 heures
9. Intégrité scientifique et éthique de la recherche - 6 heures
10. Prise en main du calculateur Joliot-Curie - 8 heures
11. CHIMERE training course - 12 heures
12. SSH-aerosol training - 5 heures
13. Francais : Cours Francais Langue Etrangère niveau intermédiaire – 20 heures
14. Formation : Rediger des documents scientifiques avec LATEX – 7h

Annex H. My contribution to the ACROSS field campaign 2022 and CHIMERE model simulations and developments

In this paragraph, I summarize my contributions, both in terms of measurements and modelling work, during the thesis.

My contribution to the ground-based ACROSS field campaign can be described as follows:

- Contribution to the setup, deployment, operation and maintain of the instrumentation (e.g. nephelometers, aethalometer…) at the two supersites of the ACROSS campaign: Paris Rive Gauche (PRG, urban) and Rambouillet Forest (rural). In particular, I have participated to the whole campaign, acting as a focal point of the daily activities at the PRG site, ensuring correct operations throughout most of the campaign period.
- Software development for data acquisition and processing of gas and aerosol instruments such as nephelometers, aethalometers and particle counters (OPC), at the Paris Rive Gauche urban site, and processing of aerosol observations at the Rambouillet site.
- Support in scientific and technical activities (e.g. quartz filters changes the early morning and the late afternoon at the PRG site).
- Data submission and publication on the AERIS website for the in situ measurements during the ACROSS campaign, including, but not limited to, aerosol and gas observations (see to the annex for further details on the published datasets).

My contribution to the ACROSS campaign through the modelling:

- Setup, run, validation and full analysis of the high resolution WRF-CHIMERE model simulations (three nested domains up to 2 km x 2km spatial resolution over the Ile-de-France region) to estimate the aerosol DRE, also used to support the ACROSS aircraft and ground-based teams in the interpretation of the field campaign results. The model simulations served also as input to the HYSPLIT back trajectories model.
- Development of a tracer analysis aiming at supporting the ground-based and aircraft teams in following the Paris plume evolution (BCRatio) detailed in Sec 2.3.5.

My contribution to the ACROSS aircraft campaign consisted in:

- a production of daily forecast reports (See Annex), as part of the forecasting cell, on meteorological and chemical conditions, aimed at assisting the scientific team in selecting the right time and flight pattern to follow the direction of the Paris plume to achieve the scientific goals of the campaign.

For each flight, the research team had to choose, with the support of the weather forecasting and the pilot teams, one the five possible flights patterns (See Fig. H.1), based on the wind direction and

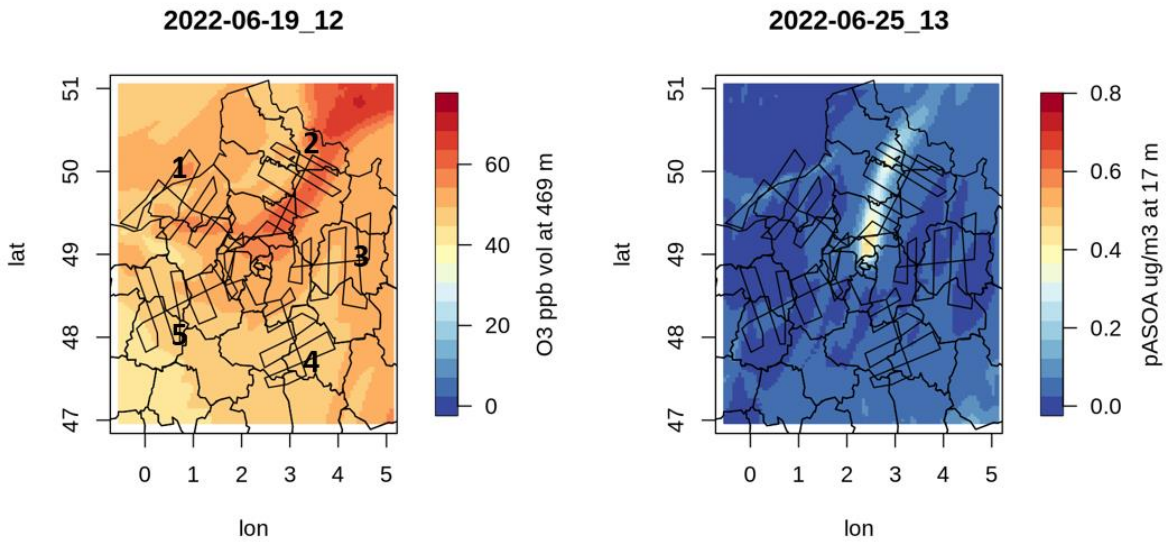

Figure H.1 The SAFIRE ATR-42 research aircraft deployed during the ACROSS campaign 2022. (b) and (c) represent the ozone (O3) and anthropogenic secondary organic aerosol (pASOA) output of the CHIMERE simulation from PREV'AIR operation facility. In black there are the five (1-5) possible flight patterns that the aircraft could follow. A forecasting cell was specifically created to help the scientific tem in choosing the right flight pattern to follow the Paris plume. Flight pattern 2 was rather the best choice for the 19 June 2022 and the 25 June 2022.

therefore the direction of the Parisian plume. Two examples of the CHIMERE simulation from the PREV'AIR (www.prevair.org) operational product used to choose the flight pattern is shown in Figure 2.22. For both the cases, the suggested flight pattern was the number 2 (i.e. NE). The flight pattern number 5 have been chosen 5 times, flying in proximity of the Rambouillet forest supersite.

Regarding the other activities outlined in this manuscript I performed:

- Analysis of long term data series from remote sensing observations (ground-based, satellite) to perform preliminary climatological analyses and to support model simulation validation (Chapter 3).
- The retrieval and the data analysis of the spectral optical properties and complex refractive index at three different sites in the Ile-de-France region (Chapter 4).
- Two high resolution WRF-CHIMERE modelling along with all its offline developments for two case studies i) the June-July 2019 heatwave period simulation (pilot study), not reported in this thesis manuscript but which served to test the WRF-CHIMERE configuration finally set-up for simulating summer 2022 ii) the June-July 2022 ACROSS field campaign period.
- I developed the WRF-CHIMERE RRTMG interface in the SW for the OFFLINE ca (detailed in Sec 2.3.4).
- I handled the processing of the datasets used for the WRF-CHIMERE validation and its validation (Chapter 5).

Some observations datasets are already available on the LISA server (i.e. EEA data). However, for some other datasets, I also took care of the downloading process (i.e. TROPOMI, E-OBS, AERONET).

References

Abel, S. J., Highwood, E. J., Haywood, J. M., and Stringer, M. A.: The direct radiative effect of biomass burning aerosols over southern Africa, Atmospheric Chem. Phys., 5, 1999–2018, https://doi.org/10.5194/acp-5-1999-2005, 2005.

ACTRIS: ACTRIS, https://www.actris-ecac.eu/particle-light-absorption.html, 2023.

Adebiyi, A., Kok, J. F., Murray, B. J., Ryder, C. L., Stuut, J.-B. W., Kahn, R. A., Knippertz, P., Formenti, P., Mahowald, N. M., Pérez García-Pando, C., Klose, M., Ansmann, A., Samset, B. H., Ito, A., Balkanski, Y., Di Biagio, C., Romanias, M. N., Huang, Y., and Meng, J.: A review of coarse mineral dust in the Earth system, Aeolian Res., 60, 100849, https://doi.org/10.1016/j.aeolia.2022.100849, 2023.

Ait-Helal, W., Borbon, A., Sauvage, S., de Gouw, J. A., Colomb, A., Gros, V., Freutel, F., Crippa, M., Afif, C., Baltensperger, U., Beekmann, M., Doussin, J.-F., Durand-Jolibois, R., Fronval, I., Grand, N., Leonardis, T., Lopez, M., Michoud, V., Miet, K., Perrier, S., Prévôt, A. S. H., Schneider, J., Siour, G., Zapf, P., and Locoge, N.: Volatile and intermediate volatility organic compounds in suburban Paris: variability, origin and importance for SOA formation, Atmospheric Chem. Phys., 14, 10439–10464, https://doi.org/10.5194/acp-14-10439-2014, 2014.

Aldhaif, A. M., Stahl, C., Braun, R. A., Moghaddam, M. A., Shingler, T., Crosbie, E., Sawamura, P., Dadashazar, H., Ziemba, L., Jimenez, J. L., Campuzano-Jost, P., and Sorooshian, A.: Characterization of the Real Part of Dry Aerosol Refractive Index Over North America From the Surface to 12 km, J. Geophys. Res. Atmospheres, 123, 8283–8300, https://doi.org/10.1029/2018JD028504, 2018.

Allen, R. J., Amiri-Farahani, A., Lamarque, J.-F., Smith, C., Shindell, D., Hassan, T., and Chung, C. E.: Observationally constrained aerosol–cloud semi-direct effects, Npj Clim. Atmospheric Sci., 2, 1–12, https://doi.org/10.1038/s41612-019-0073-9, 2019.

Anderson, T. L. and Ogren, J. A.: Determining Aerosol Radiative Properties Using the TSI 3563 Integrating Nephelometer, Aerosol Sci. Technol., 29, 57–69, https://doi.org/10.1080/02786829808965551, 1998.

Anderson, T. L., Covert, D. S., Marshall, S. F., Laucks, M. L., Charlson, R. J., Waggoner, A. P., Ogren, J. A., Caldow, R., Holm, R. L., Quant, F. R., Sem, G. J., Wiedensohler, A., Ahlquist, N. A., and Bates, T. S.: Performance Characteristics of a High-Sensitivity, Three-Wavelength, Total Scatter/Backscatter Nephelometer, J. Atmospheric Ocean. Technol., 13, 967–986, https://doi.org/10.1175/1520-0426(1996)013<0967:PCOAHS>2.0.CO;2, 1996.

Ångström, A.: On the Atmospheric Transmission of Sun Radiation and on Dust in the Air, Geogr. Ann., 11, 156–166, https://doi.org/10.1080/20014422.1929.11880498, 1929.

Aouizerats, B., Thouron, O., Tulet, P., Mallet, M., Gomes, L., and Henzing, J. S.: Development of an online radiative module for the computation of aerosol optical properties in 3-D atmospheric models: validation during the EUCAARI campaign, Geosci. Model Dev., 3, 553–564, https://doi.org/10.5194/gmd-3-553-2010, 2010.

Arino, O., Bicheron, P., Achard, F., Latham, J., WITT, R., and WEBER, J.-L.: GLOBCOVER: The Most Detailed Portrait of Earth, ESA Bull. 136, 24–31, 2008.

Ayash, T., Gong, S., and Jia, C. Q.: Direct and Indirect Shortwave Radiative Effects of Sea Salt Aerosols, J. Clim., 21, 3207–3220, https://doi.org/10.1175/2007JCLI2063.1, 2008.

Bahadur, R., Praveen, P. S., Xu, Y., and Ramanathan, V.: Solar absorption by elemental and brown carbon determined from spectral observations, Proc. Natl. Acad. Sci., 109, 17366–17371, https://doi.org/10.1073/pnas.1205910109, 2012.

Baklanov, A., Lawrence, M., Pandis, S., Mahura, A., Finardi, S., Moussiopoulos, N., Beekmann, M., Laj, P., Gomes, L., Jaffrezo, J.-L., Borbon, A., Coll, I., Gros, V., Sciare, J., Kukkonen, J., Galmarini, S., Giorgi, F., Grimmond, S., Esau, I., Stohl, A., Denby, B., Wagner, T., Butler, T., Baltensperger, U., Builtjes, P., van den Hout, D., van der Gon, H. D., Collins, B., Schluenzen, H., Kulmala, M., Zilitinkevich, S., Sokhi, R., Friedrich, R., Theloke, J., Kummer, U., Jalkinen, L., Halenka, T., Wiedensholer, A., Pyle, J., and Rossow, W. B.: MEGAPOLI: concept of multi-scale modelling of megacity

impact on air quality and climate, in: Advances in Science and Research, 9th EMS Annual Meeting and 9th European Conference on Applications of Meteorology 2009 -, 115–120, https://doi.org/10.5194/asr-4-115-2010, 2010.

Baldo, C., Formenti, P., Di Biagio, C., Lu, G., Song, C., Cazaunau, M., Pangui, E., Doussin, J.-F., Dagsson-Waldhauserova, P., Arnalds, O., Beddows, D., MacKenzie, A. R., and Shi, Z.: Complex refractive index and single scattering albedo of Icelandic dust in the shortwave part of the spectrum, Atmospheric Chem. Phys., 23, 7975–8000, https://doi.org/10.5194/acp-23-7975-2023, 2023.

Barker, H. W., Cole, J. N. S., Morcrette, J.-J., Pincus, R., Räisänen, P., von Salzen, K., and Vaillancourt, P. A.: The Monte Carlo Independent Column Approximation: an assessment using several global atmospheric models, Q. J. R. Meteorol. Soc., 134, 1463–1478, https://doi.org/10.1002/qj.303, 2008.

Baudic, A., Gros, V., Sauvage, S., Locoge, N., Sanchez, O., Sarda-Estève, R., Kalogridis, C., Petit, J.-E., Bonnaire, N., Baisnée, D., Favez, O., Albinet, A., Sciare, J., and Bonsang, B.: Seasonal variability and source apportionment of volatile organic compounds (VOCs) in the Paris megacity (France), Atmospheric Chem. Phys., 16, 11961–11989, https://doi.org/10.5194/acp-16-11961-2016, 2016.

Bedoya-Velásquez, A. E., Titos, G., Bravo-Aranda, J. A., Haeffelin, M., Favez, O., Petit, J.-E., Casquero-Vera, J. A., Olmo-Reyes, F. J., Montilla-Rosero, E., Hoyos, C. D., Alados-Arboledas, L., and Guerrero-Rascado, J. L.: Long-term aerosol optical hygroscopicity study at the ACTRIS SIRTA observatory: synergy between ceilometer and in situ measurements, Atmospheric Chem. Phys., 19, 7883–7896, https://doi.org/10.5194/acp-19-7883-2019, 2019.

Beekmann, M., Chiappini, L., Favez, O., Aymoz, G., Bessagnet, B., Rouil, L., and Rossignol, S.: The megapoli paris campaign for urban aerosol characterisation - a comprehensive data set for air quality model evaluation, in: 13. International Conference on Harmonisation within Atmospheric Dispersion Modelling for Regulatory Purposes (HARMO 13), Paris, France, 519–523, 2010.

Beekmann, M., Prévôt, A. S. H., Drewnick, F., Sciare, J., Pandis, S. N., Denier van der Gon, H. a. C., Crippa, M., Freutel, F., Poulain, L., Ghersi, V., Rodriguez, E., Beirle, S., Zotter, P., von der Weiden-Reinmüller, S.-L., Bressi, M., Fountoukis, C., Petetin, H., Szidat, S., Schneider, J., Rosso, A., El Haddad, I., Megaritis, A., Zhang, Q. J., Michoud, V., Slowik, J. G., Moukhtar, S., Kolmonen, P., Stohl, A., Eckhardt, S., Borbon, A., Gros, V., Marchand, N., Jaffrezo, J. L., Schwarzenboeck, A., Colomb, A., Wiedensohler, A., Borrmann, S., Lawrence, M., Baklanov, A., and Baltensperger, U.: In situ, satellite measurement and model evidence on the dominant regional contribution to fine particulate matter levels in the Paris megacity, Atmospheric Chem. Phys., 15, 9577–9591, https://doi.org/10.5194/acp-15-9577-2015, 2015.

Beelen, R., Raaschou-Nielsen, O., Stafoggia, M., Andersen, Z. J., Weinmayr, G., Hoffmann, B., Wolf, K., Samoli, E., Fischer, P., Nieuwenhuijsen, M., Vineis, P., Xun, W. W., Katsouyanni, K., Dimakopoulou, K., Oudin, A., Forsberg, B., Modig, L., Havulinna, A. S., Lanki, T., Turunen, A., Oftedal, B., Nystad, W., Nafstad, P., De Faire, U., Pedersen, N. L., Östenson, C.-G., Fratiglioni, L., Penell, J., Korek, M., Pershagen, G., Eriksen, K. T., Overvad, K., Ellermann, T., Eeftens, M., Peeters, P. H., Meliefste, K., Wang, M., Bueno-de-Mesquita, B., Sugiri, D., Krämer, U., Heinrich, J., de Hoogh, K., Key, T., Peters, A., Hampel, R., Concin, H., Nagel, G., Ineichen, A., Schaffner, E., Probst-Hensch, N., Künzli, N., Schindler, C., Schikowski, T., Adam, M., Phuleria, H., Vilier, A., Clavel-Chapelon, F., Declercq, C., Grioni, S., Krogh, V., Tsai, M.-Y., Ricceri, F., Sacerdote, C., Galassi, C., Migliore, E., Ranzi, A., Cesaroni, G., Badaloni, C., Forastiere, F., Tamayo, I., Amiano, P., Dorronsoro, M., Katsoulis, M., Trichopoulou, A., Brunekreef, B., and Hoek, G.: Effects of long-term exposure to air pollution on natural-cause mortality: an analysis of 22 European cohorts within the multicentre ESCAPE project, The Lancet, 383, 785–795, https://doi.org/10.1016/S0140-6736(13)62158-3, 2014.

Bellouin, N., Quaas, J., Morcrette, J.-J., and Boucher, O.: Estimates of aerosol radiative forcing from the MACC re-analysis, Atmospheric Chem. Phys., 13, 2045–2062, https://doi.org/10.5194/acp-13-2045-2013, 2013.

Bellouin, N., Quaas, J., Gryspeerdt, E., Kinne, S., Stier, P., Watson-Parris, D., Boucher, O., Carslaw, K. S., Christensen, M., Daniau, A.-L., Dufresne, J.-L., Feingold, G., Fiedler, S., Forster, P., Gettelman, A., Haywood, J. M., Lohmann, U., Malavelle, F., Mauritsen, T., McCoy, D. T., Myhre, G., Mülmenstädt, J., Neubauer, D., Possner, A., Rugenstein, M., Sato, Y., Schulz, M., Schwartz, S. E., Sourdeval, O., Storelvmo, T., Toll, V., Winker, D., and Stevens, B.: Bounding Global Aerosol Radiative Forcing of Climate Change, Rev. Geophys., 58, e2019RG000660, https://doi.org/10.1029/2019RG000660, 2020.

Bender, F. A.-M.: Aerosol Forcing: Still Uncertain, Still Relevant, AGU Adv., 1, e2019AV000128, https://doi.org/10.1029/2019AV000128, 2020.

Bernardoni, V., Ferrero, L., Bolzacchini, E., Forello, A. C., Gregorič, A., Massabò, D., Močnik, G., Prati, P., Rigler, M., Santagostini, L., Soldan, F., Valentini, S., Valli, G., and Vecchi, R.: Determination of Aethalometer multiple-scattering enhancement parameters and impact on source apportionment during the winter 2017/18 EMEP/ACTRIS/COLOSSAL campaign in Milan, Atmospheric Meas. Tech., 14, 2919–2940, https://doi.org/10.5194/amt-14-2919-2021, 2021.

Betz, K. L., Calvert, C. T., Al-Mashala, H. H., and Schnitzler, E. G.: Hygroscopicity of Secondary Brown Carbon Aerosol from Aqueous Photo-Oxidation of Phenolic Precursors, ACS Earth Space Chem., 6, 2609–2618, https://doi.org/10.1021/acsearthspacechem.2c00132, 2022.

Boedicker, E. K., Andrews, E., Sheridan, P. J., and Quinn, P. K.: Climatology of aerosol properties at an atmospheric monitoring site on the northern California coast, Atmospheric Chem. Phys., 23, 9525–9547, https://doi.org/10.5194/acp-23-9525-2023, 2023.

Bohren et Huffman: Absorption and scattering of light by small particles, 1st edition., Wiley-VCH, 1983.

Bond, T. C. and Bergstrom, R. W.: Light Absorption by Carbonaceous Particles: An Investigative Review, Aerosol Sci. Technol., 40, 27–67, https://doi.org/10.1080/02786820500421521, 2006.

Bond, T. C., Habib, G., and Bergstrom, R. W.: Limitations in the enhancement of visible light absorption due to mixing state, J. Geophys. Res. Atmospheres, 111, https://doi.org/10.1029/2006JD007315, 2006.

Bond, T. C., Doherty, S. J., Fahey, D. W., Forster, P. M., Berntsen, T., DeAngelo, B. J., Flanner, M. G., Ghan, S., Kärcher, B., Koch, D., Kinne, S., Kondo, Y., Quinn, P. K., Sarofim, M. C., Schultz, M. G., Schulz, M., Venkataraman, C., Zhang, H., Zhang, S., Bellouin, N., Guttikunda, S. K., Hopke, P. K., Jacobson, M. Z., Kaiser, J. W., Klimont, Z., Lohmann, U., Schwarz, J. P., Shindell, D., Storelvmo, T., Warren, S. G., and Zender, C. S.: Bounding the role of black carbon in the climate system: A scientific assessment, J. Geophys. Res. Atmospheres, 118, 5380–5552, https://doi.org/10.1002/jgrd.50171, 2013.

Boucher, O., Randall, D., Artaxo, P., Bretherton, C., Feingold, G., Forster, P., Kerminen, V.-M., Kondo, Y., Liao, H., Lohmann, U., Rasch, P., Satheesh, S. K., Sherwood, S., Stevens, B., and Zhang, X. Y.: Clouds and aerosols, in: Climate Change 2013: The Physical Science Basis. Contribution of Working Group I to the Fifth Assessment Report of the Intergovernmental Panel on Climate Change, edited by: Stocker, T. F., Qin, D., Plattner, G.-K., Tignor, M., Allen, S. K., Doschung, J., Nauels, A., Xia, Y., Bex, V., and Midgley, P. M., Cambridge University Press, Cambridge, UK, 571–657, https://doi.org/10.1017/CBO9781107415324.016, 2013.

Bouma, F., Janssen, N. A., Wesseling, J., van Ratingen, S., Strak, M., Kerckhoffs, J., Gehring, U., Hendricx, W., de Hoogh, K., Vermeulen, R., and Hoek, G.: Long-term exposure to ultrafine particles and natural and cause-specific mortality, Environ. Int., 175, 107960, https://doi.org/10.1016/j.envint.2023.107960, 2023.

Bressi, M., Sciare, J., Ghersi, V., Mihalopoulos, N., Petit, J.-E., Nicolas, J. B., Moukhtar, S., Rosso, A., Féron, A., Bonnaire, N., Poulakis, E., and Theodosi, C.: Sources and geographical origins of fine aerosols in Paris (France), Atmospheric Chem. Phys., 14, 8813–8839, https://doi.org/10.5194/acp-14-8813-2014, 2014.

Briant, R., Tuccella, P., Deroubaix, A., Khvorostyanov, D., Menut, L., Mailler, S., and Turquety, S.: Aerosol–radiation interaction modelling using online coupling between the WRF 3.7.1 meteorological model and the CHIMERE 2016 chemistry-transport model, through the OASIS3-MCT coupler, Geosci. Model Dev., 10, 927–944, https://doi.org/10.5194/gmd-10-927-2017, 2017.

Budisulistiorini, S. H., Canagaratna, M. R., Croteau, P. L., Baumann, K., Edgerton, E. S., Kollman, M. S., Ng, N. L., Verma, V., Shaw, S. L., Knipping, E. M., Worsnop, D. R., Jayne, J. T., Weber, R. J., and Surratt, J. D.: Intercomparison of an Aerosol Chemical Speciation Monitor (ACSM) with ambient fine aerosol measurements in downtown Atlanta, Georgia, Atmospheric Meas. Tech., 7, 1929–1941, https://doi.org/10.5194/amt-7-1929-2014, 2014.

C3S: European State of the Climate 2022, Full report, Copernic. Clim. Change Serv., https://doi.org/10.24381/gvaf-h066, 2023.

Calderón-Garcidueñas, L., Kulesza, R. J., Doty, R. L., D'Angiulli, A., and Torres-Jardón, R.: Megacities air pollution problems: Mexico City Metropolitan Area critical issues on the central nervous system pediatric impact, Environ. Res., 137, 157–169, https://doi.org/10.1016/j.envres.2014.12.012, 2015.

Cantrell, C. and Michoud, V.: ACROSS: A Field Experiment to Study Atmospheric Oxidation Chemistry and Physics of Mixed Anthropogenic-Biogenic Air Masses in the Greater Paris Area, Bull. Am. Meteorol. Soc., 1, https://doi.org/10.1175/BAMS-D-21-0115.1, 2022.

Cappa, C. D., Zhang, X., Russell, L. M., Collier, S., Lee, A. K. Y., Chen, C.-L., Betha, R., Chen, S., Liu, J., Price, D. J., Sanchez, K. J., McMeeking, G. R., Williams, L. R., Onasch, T. B., Worsnop, D. R., Abbatt, J., and Zhang, Q.: Light Absorption by Ambient Black and Brown Carbon and its Dependence on Black Carbon Coating State for Two California, USA, Cities in Winter and Summer, J. Geophys. Res. Atmospheres, 124, 1550–1577, https://doi.org/10.1029/2018JD029501, 2019.

Carlton, A. G., Pye, H. O. T., Baker, K. R., and Hennigan, C. J.: Additional Benefits of Federal Air-Quality Rules: Model Estimates of Controllable Biogenic Secondary Organic Aerosol, Environ. Sci. Technol., 52, 9254–9265, https://doi.org/10.1021/acs.est.8b01869, 2018.

Carter, W. P. L.: Development of the SAPRC-07 chemical mechanism, Atmos. Environ., 44, 5324–5335, https://doi.org/10.1016/j.atmosenv.2010.01.026, 2010.

Cavalli, F., Viana, M., Yttri, K. E., Genberg, J., and Putaud, J.-P.: Toward a standardised thermal-optical protocol for measuring atmospheric organic and elemental carbon: the EUSAAR protocol, Atmospheric Meas. Tech., 3, 79–89, https://doi.org/10.5194/amt-3-79-2010, 2010.

Chahine, A., Dupont, E., Musson-Genon, L., Legorgeu, C., and Carissimo, B.: Long term modelling of the dynamical atmospheric flows over SIRTA site, J. Wind Eng. Ind. Aerodyn., 172, 351–366, https://doi.org/10.1016/j.jweia.2017.09.004, 2018.

Chakrabarty, R. K., Shetty, N. J., Thind, A. S., Beeler, P., Sumlin, B. J., Zhang, C., Liu, P., Idrobo, J. C., Adachi, K., Wagner, N. L., Schwarz, J. P., Ahern, A., Sedlacek, A. J., Lambe, A., Daube, C., Lyu, M., Liu, C., Herndon, S., Onasch, T. B., and Mishra, R.: Shortwave absorption by wildfire smoke dominated by dark brown carbon, Nat. Geosci., 16, 683–688, https://doi.org/10.1038/s41561-023-01237-9, 2023.

Chand, D., Wood, R., Anderson, T. L., Satheesh, S. K., and Charlson, R. J.: Satellite-derived direct radiative effect of aerosols dependent on cloud cover, Nat. Geosci., 2, 181–184, https://doi.org/10.1038/ngeo437, 2009.

Chang, Y., Du, T., Song, X., Wang, W., Tian, P., Guan, X., Zhang, N., Wang, M., Guo, Y., Shi, J., and Zhang, L.: Changes in physical and chemical properties of urban atmospheric aerosols and ozone during the COVID-19 lockdown in a semi-arid region, Atmos. Environ., 287, 119270, https://doi.org/10.1016/j.atmosenv.2022.119270, 2022.

Chauvigné, A., Waquet, F., Auriol, F., Blarel, L., Delegove, C., Dubovik, O., Flamant, C., Gaetani, M., Goloub, P., Loisil, R., Mallet, M., Nicolas, J.-M., Parol, F., Peers, F., Torres, B., and Formenti, P.: Aerosol above-cloud direct radiative effect and properties in the Namibian region during the AErosol, RadiatiOn, and CLOuds in southern Africa (AEROCLO-sA) field campaign – Multi-Viewing, Multi-Channel, Multi-Polarization (3MI) airborne simulator and sun photometer measurements, Atmospheric Chem. Phys., 21, 8233–8253, https://doi.org/10.5194/acp-21-8233-2021, 2021.

Chazette, P., Randriamiarisoa, H., Sanak, J., Couvert, P., and Flamant, C.: Optical properties of urban aerosol from airborne and ground-based in situ measurements performed during the Etude et Simulation de la Qualité de l'air en Ile de France (ESQUIF) program, J. Geophys. Res. Atmospheres, 110, https://doi.org/10.1029/2004JD004810, 2005.

Chazette, P., Totems, J., and Shang, X.: Transport of aerosols over the French Riviera – link between ground-based lidar and spaceborne observations, Atmospheric Chem. Phys., 19, 3885–3904, https://doi.org/10.5194/acp-19-3885-2019, 2019.

Che, H., Yang, Z., Zhang, X., Zhu, C., Ma, Q., Zhou, H., and Wang, P.: Study on the aerosol optical properties and their relationship with aerosol chemical compositions over three regional background stations in China, Atmos. Environ., 43, 1093–1099, https://doi.org/10.1016/j.atmosenv.2008.11.010, 2009.

Che, H., Qi, B., Zhao, H., Xia, X., Eck, T. F., Goloub, P., Dubovik, O., Estelles, V., Cuevas-Agulló, E., Blarel, L., Wu, Y., Zhu, J., Du, R., Wang, Y., Wang, H., Gui, K., Yu, J., Zheng, Y., Sun, T., Chen, Q., Shi, G., and Zhang, X.: Aerosol optical properties and direct radiative forcing based on measurements from the China Aerosol Remote Sensing Network (CARSNET) in eastern China, Atmospheric Chem. Phys., 18, 405–425, https://doi.org/10.5194/acp-18-405-2018, 2018.

Chen, C., Dubovik, O., Fuertes, D., Litvinov, P., Lapyonok, T., Lopatin, A., Ducos, F., Derimian, Y., Herman, M., Tanré, D., Remer, L. A., Lyapustin, A., Sayer, A. M., Levy, R. C., Hsu, N. C., Descloitres, J., Li, L., Torres, B., Karol, Y., Herrera, M., Herreras, M., Aspetsberger, M., Wanzenboeck, M., Bindreiter, L., Marth, D., Hangler, A., and Federspiel, C.: Validation of GRASP algorithm product from POLDER/PARASOL data and assessment of multi-angular polarimetry potential for aerosol monitoring, Earth Syst. Sci. Data, 12, 3573–3620, https://doi.org/10.5194/essd-12-3573-2020, 2020.

Chen, C., Dubovik, O., Schuster, G. L., Chin, M., Henze, D. K., Lapyonok, T., Li, Z., Derimian, Y., and Zhang, Y.: Multi-angular polarimetric remote sensing to pinpoint global aerosol absorption and direct radiative forcing, Nat. Commun., 13, 7459, https://doi.org/10.1038/s41467-022-35147-y, 2022a.

Chen, G., Canonaco, F., Tobler, A., Aas, W., Alastuey, A., Allan, J., Atabakhsh, S., Aurela, M., Baltensperger, U., Bougiatioti, A., De Brito, J. F., Ceburnis, D., Chazeau, B., Chebaicheb, H., Daellenbach, K. R., Ehn, M., El Haddad, I., Eleftheriadis, K., Favez, O., Flentje, H., Font, A., Fossum, K., Freney, E., Gini, M., Green, D. C., Heikkinen, L., Herrmann, H., Kalogridis, A.-C., Keernik, H., Lhotka, R., Lin, C., Lunder, C., Maasikmets, M., Manousakas, M. I., Marchand, N., Marin, C., Marmureanu, L., Mihalopoulos, N., Močnik, G., Nęcki, J., O'Dowd, C., Ovadnevaite, J., Peter, T., Petit, J.-E., Pikridas, M., Matthew Platt, S., Pokorná, P., Poulain, L., Priestman, M., Riffault, V., Rinaldi, M., Różański, K., Schwarz, J., Sciare, J., Simon, L., Skiba, A., Slowik, J. G., Sosedova, Y., Stavroulas, I., Styszko, K., Teinemaa, E., Timonen, H., Tremper, A., Vasilescu, J., Via, M., Vodička, P., Wiedensohler, A., Zografou, O., Cruz Minguillón, M., and Prévôt, A. S. H.: European aerosol phenomenology − 8: Harmonised source apportionment of organic aerosol using 22 Year-long ACSM/AMS datasets, Environ. Int., 166, 107325, https://doi.org/10.1016/j.envint.2022.107325, 2022b.

Chen, L., Wang, R., Wei, G., Han, J., and Zha, Y.: A surface reflectance correction model to improve the retrieval of MISR aerosol optical depth supported by MODIS data, Adv. Space Res., 67, 858–867, https://doi.org/10.1016/j.asr.2020.10.033, 2021.

Cheng, Y. F., Eichler, H., Wiedensohler, A., Heintzenberg, J., Zhang, Y. H., Hu, M., Herrmann, H., Zeng, L. M., Liu, S., Gnauk, T., Brüggemann, E., and He, L. Y.: Mixing state of elemental carbon and non-light-absorbing aerosol components derived from in situ particle optical properties at Xinken in Pearl River Delta of China, J. Geophys. Res. Atmospheres, 111, https://doi.org/10.1029/2005JD006929, 2006.

Cholakian, A., Beekmann, M., Colette, A., Coll, I., Siour, G., Sciare, J., Marchand, N., Couvidat, F., Pey, J., Gros, V., Sauvage, S., Michoud, V., Sellegri, K., Colomb, A., Sartelet, K., Langley DeWitt, H., Elser, M., Prévot, A. S. H., Szidat, S., and Dulac, F.: Simulation of fine organic aerosols in the western Mediterranean area during the ChArMEx 2013 summer campaign, Atmospheric Chem. Phys., 18, 7287–7312, https://doi.org/10.5194/acp-18-7287-2018, 2018.

Cholakian, A., Beekmann, M., Coll, I., Ciarelli, G., and Colette, A.: Biogenic secondary organic aerosol sensitivity to organic aerosol simulation schemes in climate projections, Atmospheric Chem. Phys., 19, 13209–13226, https://doi.org/10.5194/acp-19-13209-2019, 2019.

Claeys, M., Roberts, G., Mallet, M., Arndt, J., Sellegri, K., Sciare, J., Wenger, J., and Sauvage, B.: Optical, physical and chemical properties of aerosols transported to a coastal site in the western Mediterranean: a focus on primary marine aerosols, Atmospheric Chem. Phys., 17, 7891–7915, https://doi.org/10.5194/acp-17-7891-2017, 2017.

Clough, S. A., Shephard, M. W., Mlawer, E. J., Delamere, J. S., Iacono, M. J., Cady-Pereira, K., Boukabara, S., and Brown, P. D.: Atmospheric radiative transfer modeling: a summary of the AER codes, J. Quant. Spectrosc. Radiat. Transf., 91, 233–244, https://doi.org/10.1016/j.jqsrt.2004.05.058, 2005.

Collaud Coen, M., Weingartner, E., Apituley, A., Ceburnis, D., Fierz-Schmidhauser, R., Flentje, H., Henzing, J. S., Jennings, S. G., Moerman, M., Petzold, A., Schmid, O., and Baltensperger, U.: Minimizing light absorption measurement artifacts of the Aethalometer: evaluation of five correction algorithms, Atmospheric Meas. Tech., 3, 457–474, https://doi.org/10.5194/amt-3-457-2010, 2010.

Corbin, J. C., Pieber, S. M., Czech, H., Zanatta, M., Jakobi, G., Massabò, D., Orasche, J., El Haddad, I., Mensah, A. A., Stengel, B., Drinovec, L., Mocnik, G., Zimmermann, R., Prévôt, A. S. H., and Gysel, M.: Brown and Black Carbon Emitted by a Marine Engine Operated on Heavy Fuel Oil and Distillate Fuels: Optical Properties, Size Distributions, and Emission Factors, J. Geophys. Res. Atmospheres, 123, 6175–6195, https://doi.org/10.1029/2017JD027818, 2018.

Córdoba-Jabonero, C., Sicard, M., López-Cayuela, M.-Á., Ansmann, A., Comerón, A., Zorzano, M.-P., Rodríguez-Gómez, A., and Muñoz-Porcar, C.: Aerosol radiative impact during the summer 2019 heatwave produced partly by an

inter-continental Saharan dust outbreak – Part 1: Short-wave dust direct radiative effect, Atmospheric Chem. Phys., 21, 6455–6479, https://doi.org/10.5194/acp-21-6455-2021, 2021.

da Costa e Oliveira, J. R., Base, L. H., de Abreu, L. C., Filho, C. F., Ferreira, C., and Morawska, L.: Ultrafine particles and children's health: Literature review, Paediatr. Respir. Rev., 32, 73–81, https://doi.org/10.1016/j.prrv.2019.06.003, 2019.

Craig, A., Valcke, S., and Coquart, L.: Development and performance of a new version of the OASIS coupler, OASIS3-MCT_3.0, Geosci. Model Dev., 10, 3297–3308, https://doi.org/10.5194/gmd-10-3297-2017, 2017.

Crawford, J. H., Ahn, J.-Y., Al-Saadi, J., Chang, L., Emmons, L. K., Kim, J., Lee, G., Park, J.-H., Park, R. J., Woo, J. H., Song, C.-K., Hong, J.-H., Hong, Y.-D., Lefer, B. L., Lee, M., Lee, T., Kim, S., Min, K.-E., Yum, S. S., Shin, H. J., Kim, Y.-W., Choi, J.-S., Park, J.-S., Szykman, J. J., Long, R. W., Jordan, C. E., Simpson, I. J., Fried, A., Dibb, J. E., Cho, S., and Kim, Y. P.: The Korea–United States Air Quality (KORUS-AQ) field study, Elem. Sci. Anthr., 9, 00163, https://doi.org/10.1525/elementa.2020.00163, 2021.

Crenn, V., Sciare, J., Croteau, P. L., Verlhac, S., Fröhlich, R., Belis, C. A., Aas, W., Äijälä, M., Alastuey, A., Artiñano, B., Baisnée, D., Bonnaire, N., Bressi, M., Canagaratna, M., Canonaco, F., Carbone, C., Cavalli, F., Coz, E., Cubison, M. J., Esser-Gietl, J. K., Green, D. C., Gros, V., Heikkinen, L., Herrmann, H., Lunder, C., Minguillón, M. C., Močnik, G., O'Dowd, C. D., Ovadnevaite, J., Petit, J.-E., Petralia, E., Poulain, L., Priestman, M., Riffault, V., Ripoll, A., Sarda-Estève, R., Slowik, J. G., Setyan, A., Wiedensohler, A., Baltensperger, U., Prévôt, A. S. H., Jayne, J. T., and Favez, O.: ACTRIS ACSM intercomparison – Part 1: Reproducibility of concentration and fragment results from 13 individual Quadrupole Aerosol Chemical Speciation Monitors (Q-ACSM) and consistency with co-located instruments, Atmospheric Meas. Tech., 8, 5063–5087, https://doi.org/10.5194/amt-8-5063-2015, 2015.

Crippa, M., Canonaco, F., Lanz, V. A., Äijälä, M., Allan, J. D., Carbone, S., Capes, G., Ceburnis, D., Dall'Osto, M., Day, D. A., DeCarlo, P. F., Ehn, M., Eriksson, A., Freney, E., Hildebrandt Ruiz, L., Hillamo, R., Jimenez, J. L., Junninen, H., Kiendler-Scharr, A., Kortelainen, A.-M., Kulmala, M., Laaksonen, A., Mensah, A. A., Mohr, C., Nemitz, E., O'Dowd, C., Ovadnevaite, J., Pandis, S. N., Petäjä, T., Poulain, L., Saarikoski, S., Sellegri, K., Swietlicki, E., Tiitta, P., Worsnop, D. R., Baltensperger, U., and Prévôt, A. S. H.: Organic aerosol components derived from 25 AMS data sets across Europe using a consistent ME-2 based source apportionment approach, Atmospheric Chem. Phys., 14, 6159–6176, https://doi.org/10.5194/acp-14-6159-2014, 2014.

Cuesta-Mosquera, A., Močnik, G., Drinovec, L., Müller, T., Pfeifer, S., Minguillón, M. C., Briel, B., Buckley, P., Dudoitis, V., Fernández-García, J., Fernández-Amado, M., Ferreira De Brito, J., Riffault, V., Flentje, H., Heffernan, E., Kalivitis, N., Kalogridis, A.-C., Keernik, H., Marmureanu, L., Luoma, K., Marinoni, A., Pikridas, M., Schauer, G., Serfozo, N., Servomaa, H., Titos, G., Yus-Díez, J., Zioła, N., and Wiedensohler, A.: Intercomparison and characterization of 23 Aethalometers under laboratory and ambient air conditions: procedures and unit-to-unit variabilities, Atmospheric Meas. Tech., 14, 3195–3216, https://doi.org/10.5194/amt-14-3195-2021, 2021.

Cuevas-Agulló, E., Barriopedro, D., García, R. D., Alonso-Pérez, S., González-Alemán, J. J., Werner, E., Suárez, D., Bustos, J. J., García-Castrillo, G., García, O., Barreto, Á., and Basart, S.: Sharp increase in Saharan dust intrusions over the western Euro-Mediterranean in February–March 2020–2022 and associated atmospheric circulation, Atmospheric Chem. Phys., 24, 4083–4104, https://doi.org/10.5194/acp-24-4083-2024, 2024.

Curci, G.: FLEXAOD: A CHEMISTRY-TRANSPORT MODEL POST-PROCESSING TOOL FOR A FLEXIBLE CALCULATION OF AEROSOL OPTICAL PROPERTIES, 2012.

Curci, G., Hogrefe, C., Bianconi, R., Im, U., Balzarini, A., Baró, R., Brunner, D., Forkel, R., Giordano, L., Hirtl, M., Honzak, L., Jiménez-Guerrero, P., Knote, C., Langer, M., Makar, P. A., Pirovano, G., Pérez, J. L., San José, R., Syrakov, D., Tuccella, P., Werhahn, J., Wolke, R., Žabkar, R., Zhang, J., and Galmarini, S.: Uncertainties of simulated aerosol optical properties induced by assumptions on aerosol physical and chemical properties: An AQMEII-2 perspective, Atmos. Environ., 115, 541–552, https://doi.org/10.1016/j.atmosenv.2014.09.009, 2015.

Curci, G., Alyuz, U., Barò, R., Bianconi, R., Bieser, J., Christensen, J. H., Colette, A., Farrow, A., Francis, X., Jiménez-Guerrero, P., Im, U., Liu, P., Manders, A., Palacios-Peña, L., Prank, M., Pozzoli, L., Sokhi, R., Solazzo, E., Tuccella, P., Unal, A., Vivanco, M. G., Hogrefe, C., and Galmarini, S.: Modelling black carbon absorption of solar radiation: combining external and internal mixing assumptions, Atmospheric Chem. Phys., 19, 181–204, https://doi.org/10.5194/acp-19-181-2019, 2019.

Dayan, C., Fredj, E., Misztal, P. K., Gabay, M., Guenther, A. B., and Tas, E.: Emission of biogenic volatile organic compounds from warm and oligotrophic seawater in the Eastern Mediterranean, Atmospheric Chem. Phys., 20, 12741–12759, https://doi.org/10.5194/acp-20-12741-2020, 2020.

Debry, E., Fahey, K., Sartelet, K., Sportisse, B., and Tombette, M.: Technical Note: A new SIze REsolved Aerosol Model (SIREAM), Atmospheric Chem. Phys., 7, 1537–1547, https://doi.org/10.5194/acp-7-1537-2007, 2007.

DeCarlo, P. F., Slowik, J. G., Worsnop, D. R., Davidovits, P., and Jimenez, J. L.: Particle Morphology and Density Characterization by Combined Mobility and Aerodynamic Diameter Measurements. Part 1: Theory, Aerosol Sci. Technol., 38, 1185–1205, https://doi.org/10.1080/027868290903907, 2004.

Denjean, C., Brito, J., Libois, Q., Mallet, M., Bourrianne, T., Burnet, F., Dupuy, R., Flamant, C., and Knippertz, P.: Unexpected Biomass Burning Aerosol Absorption Enhancement Explained by Black Carbon Mixing State, Geophys. Res. Lett., 47, e2020GL089055, https://doi.org/10.1029/2020GL089055, 2020.

Devaliya, S., Bhate, J. N., Sunder Raman, R., Muduchuru, K., Sharma, A., Singh, V., Kesarkar, A. P., and Venkataraman, C.: Assessment of the impact of atmospheric aerosols and meteorological data assimilation on simulation of the weather over India during summer 2015, Atmos. Environ., 297, 119586, https://doi.org/10.1016/j.atmosenv.2023.119586, 2023.

Devi, A. and Satheesh, S. K.: Global maps of aerosol single scattering albedo using combined CERES-MODIS retrieval, Atmospheric Chem. Phys., 22, 5365–5376, https://doi.org/10.5194/acp-22-5365-2022, 2022.

Devi, J. J., Bergin, M. H., Mckenzie, M., Schauer, J. J., and Weber, R. J.: Contribution of particulate brown carbon to light absorption in the rural and urban Southeast US, Atmos. Environ., 136, 95–104, https://doi.org/10.1016/j.atmosenv.2016.04.011, 2016.

Di Antonio, L. and Siour, G.: ACROSS_LISA_WRF-CHIMERE_HYSPLIT_Backtraj_1H, https://doi.org/10.25326/543, 2023.

Di Antonio, L., Siour, G., and Beekmann, M.: ACROSS_LISA_CHIMERE_BCRatio_1H, https://doi.org/10.25326/529, 2023a.

Di Antonio, L., Di Biagio, C., and Gratien, A.: ACROSS_LISA_PRG_AETH-Abs_PM1_1-Min_L2, https://doi.org/10.25326/574, 2023b.

Di Antonio, L., Di Biagio, C., and Gratien, A.: ACROSS_LISA_PRG_AETH-eBC_PM1_1-Min_L2, https://doi.org/10.25326/575, 2023c.

Di Antonio, L., Di Biagio, C., and Gratien, A.: ACROSS_LISA_PRG_FIDAS_PM_1-Min_L2, https://doi.org/10.25326/572, 2023d.

Di Antonio, L., Di Biagio, C., Gratien, A., Hawkins, L. N., Bergé, A., and Riley, S.: ACROSS_LISA_PRG_METEO_1-Min_L2, https://doi.org/10.25326/573, 2023e.

Di Antonio, L., Di Biagio, C., and Gratien, A.: ACROSS_LISA_PRG_NEPH_Scatt-Backscatt_PM1_1-Min_L2, https://doi.org/10.25326/538, 2023f.

Di Antonio, L., Di Biagio, C., and Gratien, A.: ACROSS_LISA_PRG_OPC_Sizedistr_PM1_1-Min_L2, https://doi.org/10.25326/539, 2023g.

Di Antonio, L., Di Biagio, C., Foret, G., Formenti, P., Siour, G., Doussin, J.-F., and Beekmann, M.: Aerosol optical depth climatology from the high-resolution MAIAC product over Europe: differences between major European cities and their surrounding environments, Atmospheric Chem. Phys., 23, 12455–12475, https://doi.org/10.5194/acp-23-12455-2023, 2023h.

Di Biagio, C., Formenti, P., Cazaunau, M., Pangui, E., Marchand, N., and Doussin, J.-F.: Aethalometer multiple scattering correction C_{ref} for mineral dust aerosols, Atmospheric Meas. Tech., 10, 2923–2939, https://doi.org/10.5194/amt-10-2923-2017, 2017a.

Di Biagio, C., Formenti, P., Balkanski, Y., Caponi, L., Cazaunau, M., Pangui, E., Journet, E., Nowak, S., Caquineau, S., Andreae, M. O., Kandler, K., Saeed, T., Piketh, S., Seibert, D., Williams, E., and Doussin, J.-F.: Global scale variability of the mineral dust long-wave refractive index: a new dataset of in situ measurements for climate modeling and remote sensing, Atmospheric Chem. Phys., 17, 1901–1929, https://doi.org/10.5194/acp-17-1901-2017, 2017b.

Di Biagio, C., Formenti, P., Balkanski, Y., Caponi, L., Cazaunau, M., Pangui, E., Journet, E., Nowak, S., Andreae, M. O., Kandler, K., Saeed, T., Piketh, S., Seibert, D., Williams, E., and Doussin, J.-F.: Complex refractive indices and single-scattering albedo of global dust aerosols in the shortwave spectrum and relationship to size and iron content, Atmospheric Chem. Phys., 19, 15503–15531, https://doi.org/10.5194/acp-19-15503-2019, 2019.

Di Biagio, C., Balkanski, Y., Albani, S., Boucher, O., and Formenti, P.: Direct Radiative Effect by Mineral Dust Aerosols Constrained by New Microphysical and Spectral Optical Data, Geophys. Res. Lett., 47, e2019GL086186, https://doi.org/10.1029/2019GL086186, 2020.

Di Biagio, C., Doussin, J.-F., Cazaunau, M., Pangui, E., Cuesta, J., Sellitto, P., Ródenas, M., and Formenti, P.: Infrared optical signature reveals the source–dependency and along–transport evolution of dust mineralogy as shown by laboratory study, Sci. Rep., 13, 13252, https://doi.org/10.1038/s41598-023-39336-7, 2023.

Di Biagio, C., Gratien, A., and et al: Aerosol and gas in situ observations at the urban site of Paris Rive Gauche–PRG during the June–July 2022 ACROSS (Atmospheric Chemistry Of the Suburban Forest) field campaign, ESSD, Atmospheric Chem. Phys., in preparation.

Di Biagio et al., C.: ACROSS_LISA_PRG_ACSM_L2, 2024.

Dingle, J. H., Zimmerman, S., Frie, A. L., Min, J., Jung, H., and Bahreini, R.: Complex refractive index, single scattering albedo, and mass absorption coefficient of secondary organic aerosols generated from oxidation of biogenic and anthropogenic precursors, Aerosol Sci. Technol., 53, 449–463, https://doi.org/10.1080/02786826.2019.1571680, 2019.

Dockery, D. W.: Health Effects of Particulate Air Pollution, Ann. Epidemiol., 19, 257–263, https://doi.org/10.1016/j.annepidem.2009.01.018, 2009.

Donahue, N. M., Robinson, A. L., Stanier, C. O., and Pandis, S. N.: Coupled Partitioning, Dilution, and Chemical Aging of Semivolatile Organics, Environ. Sci. Technol., 40, 2635–2643, https://doi.org/10.1021/es052297c, 2006.

Douville, H., Raghavan, K., Renwick, J., Allan, R. P., Arias, P. A., Barlow, M., Cerezo-Mota, R., Cherchi, A., Gan, T. Y., Gergis, J., Jiang, D., Khan, A., Pokam Mba, W., Rosenfeld, D., Tierney, J., and Zolina, O.: Water Cycle Changes, edited by: Masson-Delmotte, V., Zhai, P., Pirani, A., Connors, S. L., Péan, C., Berger, S., Caud, N., Chen, Y., Goldfarb, L., Gomis, M. I., Huang, M., Leitzell, K., Lonnoy, E., Matthews, J. B. R., Maycock, T. K., Waterfield, T., Yelekçi, O., Yu, R., and Zhou, B., Clim. Change 2021 Phys. Sci. Basis Contrib. Work. Group Sixth Assess. Rep. Intergov. Panel Clim. Change, 1055–1210, https://doi.org/10.1017/9781009157896.010, 2021.

Drewnick, F., Hings, S. S., DeCarlo, P., Jayne, J. T., Gonin, M., Fuhrer, K., Weimer, S., Jimenez, J. L., Demerjian, K. L., Borrmann, S., and Worsnop, D. R.: A New Time-of-Flight Aerosol Mass Spectrometer (TOF-AMS)—Instrument Description and First Field Deployment, Aerosol Sci. Technol., 39, 637–658, https://doi.org/10.1080/02786820500182040, 2005.

Drinovec, L., Močnik, G., Zotter, P., Prévôt, A. S. H., Ruckstuhl, C., Coz, E., Rupakheti, M., Sciare, J., Müller, T., Wiedensohler, A., and Hansen, A. D. A.: The "dual-spot" Aethalometer: an improved measurement of aerosol black carbon with real-time loading compensation, Atmospheric Meas. Tech., 8, 1965–1979, https://doi.org/10.5194/amt-8-1965-2015, 2015.

Drinovec, L., Jagodič, U., Pirker, L., Škarabot, M., Kurtjak, M., Vidović, K., Ferrero, L., Visser, B., Röhrbein, J., Weingartner, E., Kalbermatter, D. M., Vasilatou, K., Bühlmann, T., Pascale, C., Müller, T., Wiedensohler, A., and Močnik, G.: A dual-wavelength photothermal aerosol absorption monitor: design, calibration and performance, Atmospheric Meas. Tech., 15, 3805–3825, https://doi.org/10.5194/amt-15-3805-2022, 2022.

Drugé, T., Nabat, P., Mallet, M., Michou, M., Rémy, S., and Dubovik, O.: Modeling radiative and climatic effects of brown carbon aerosols with the ARPEGE-Climat global climate model, Atmospheric Chem. Phys., 22, 12167–12205, https://doi.org/10.5194/acp-22-12167-2022, 2022.

Dubovik, O., Smirnov, A., Holben, B. N., King, M. D., Kaufman, Y. J., Eck, T. F., and Slutsker, I.: Accuracy assessments of aerosol optical properties retrieved from Aerosol Robotic Network (AERONET) Sun and sky radiance measurements, J. Geophys. Res. Atmospheres, 105, 9791–9806, https://doi.org/10.1029/2000JD900040, 2000.

Dubovik, O., Holben, B., Eck, T. F., Smirnov, A., Kaufman, Y. J., King, M. D., Tanré, D., and Slutsker, I.: Variability of Absorption and Optical Properties of Key Aerosol Types Observed in Worldwide Locations, J. Atmospheric Sci., 59, 590–608, https://doi.org/10.1175/1520-0469(2002)059<0590:VOAAOP>2.0.CO;2, 2002.

Dubovik, O., Sinyuk, A., Lapyonok, T., Holben, B. N., Mishchenko, M., Yang, P., Eck, T. F., Volten, H., Muñoz, O., Veihelmann, B., van der Zande, W. J., Leon, J.-F., Sorokin, M., and Slutsker, I.: Application of spheroid models to account for aerosol particle nonsphericity in remote sensing of desert dust, J. Geophys. Res. Atmospheres, 111, https://doi.org/10.1029/2005JD006619, 2006.

Dufour, G., Wittrock, F., Camredon, M., Beekmann, M., Richter, A., Aumont, B., and Burrows, J. P.: SCIAMACHY formaldehyde observations: constraint for isoprene emission estimates over Europe?, Atmospheric Chem. Phys., 9, 1647–1664, https://doi.org/10.5194/acp-9-1647-2009, 2009.

Ebert, M., Weinbruch, S., Rausch, A., Gorzawski, G., Helas, G., Hoffmann, P., and Wex, H.: Complex refractive index of aerosols during LACE 98#x2010; as derived from the analysis of individual particles, J. Geophys. Res. Atmospheres, 107, LAC 3-1-LAC 3-15, https://doi.org/10.1029/2000JD000195, 2002.

Ebert, M., Weinbruch, S., Hoffmann, P., and Ortner, H. M.: The chemical composition and complex refractive index of rural and urban influenced aerosols determined by individual particle analysis, Atmos. Environ., 38, 6531–6545, https://doi.org/10.1016/j.atmosenv.2004.08.048, 2004.

Elsey, J., Bellouin, N., and Ryder, C.: Sensitivity of global direct aerosol radiative forcing to uncertainties in aerosol optical properties, Aerosols/Atmospheric Modelling and Data Analysis/Troposphere/Physics (physical properties and processes), https://doi.org/10.5194/egusphere-2023-1096, 2023.

Espinosa, W. R., Martins, J. V., Remer, L. A., Dubovik, O., Lapyonok, T., Fuertes, D., Puthukkudy, A., Orozco, D., Ziemba, L., Thornhill, K. L., and Levy, R.: Retrievals of Aerosol Size Distribution, Spherical Fraction, and Complex Refractive Index From Airborne In Situ Angular Light Scattering and Absorption Measurements, J. Geophys. Res. Atmospheres, 124, 7997–8024, https://doi.org/10.1029/2018JD030009, 2019.

Falah, S., Mhawish, A., Sorek-Hamer, M., Lyapustin, A. I., Kloog, I., Banerjee, T., Kizel, F., and Broday, D. M.: Impact of environmental attributes on the uncertainty in MAIAC/MODIS AOD retrievals: A comparative analysis, Atmos. Environ., 262, 118659, https://doi.org/10.1016/j.atmosenv.2021.118659, 2021.

Feichter, J. and Stier, P.: Assessment of black carbon radiative effects in climate models, WIREs Clim. Change, 3, 359–370, https://doi.org/10.1002/wcc.180, 2012.

Feng, N. and Christopher, S. A.: Clear sky direct radiative effects of aerosols over Southeast Asia based on satellite observations and radiative transfer calculations, Remote Sens. Environ., 152, 333–344, https://doi.org/10.1016/j.rse.2014.07.006, 2014.

Ferrare, R., Turner, D., Clayton, M., Schmid, B., Redemann, J., Covert, D., Elleman, R., Ogren, J., Andrews, E., Goldsmith, J. E. M., and Jonsson, H.: Evaluation of daytime measurements of aerosols and water vapor made by an operational Raman lidar over the Southern Great Plains, J. Geophys. Res. Atmospheres, 111, https://doi.org/10.1029/2005JD005836, 2006.

Ferrare, R. A., Melfi, S. H., Whiteman, D. N., Evans, K. D., and Leifer, R.: Raman lidar measurements of aerosol extinction and backscattering: 1. Methods and comparisons, J. Geophys. Res. Atmospheres, 103, 19663–19672, https://doi.org/10.1029/98JD01646, 1998.

Ferreira de Brito, J., Riffault, V., Dusanter, S., and Jamar, M.: ACROSS_IMTNE_RambForest_AMS_AboveCanopy_L2, https://doi.org/10.25326/491, 2023a.

Ferreira de Brito, J., Riffault, V., Dusanter, S., and Jamar, M.: ACROSS_IMTNE_RambForest_AMS_BelowCanopy_L2, https://doi.org/10.25326/492, 2023b.

Ferreyra, M. F. G., Curci, G., and Lanfri, M.: First Implementation of the WRF-CHIMERE-EDGAR Modeling System Over Argentina, IEEE J. Sel. Top. Appl. Earth Obs. Remote Sens., 9, 5304–5314, https://doi.org/10.1109/JSTARS.2016.2588502, 2016.

Fiore, A. M., Naik, V., Spracklen, D. V., Steiner, A., Unger, N., Prather, M., Bergmann, D., Cameron-Smith, P. J., Cionni, I., Collins, W. J., Dalsøren, S., Eyring, V., Folberth, G. A., Ginoux, P., Horowitz, L. W., Josse, B., Lamarque, J.-F., MacKenzie, I. A., Nagashima, T., O'Connor, F. M., Righi, M., Rumbold, S. T., Shindell, D. T., Skeie, R. B., Sudo, K., Szopa, S., Takemura, T., and Zeng, G.: Global air quality and climate, Chem. Soc. Rev., 41, 6663–6683, https://doi.org/10.1039/C2CS35095E, 2012.

Flores, J. M., Trainic, M., Borrmann, S., and Rudich, Y.: Effective broadband refractive index retrieval by a white light optical particle counter, Phys. Chem. Chem. Phys. PCCP, 11, 7943–7950, https://doi.org/10.1039/b905292e, 2009.

Flores, J. M., Washenfelder, R. A., Adler, G., Lee, H. J., Segev, L., Laskin, J., Laskin, A., Nizkorodov, S. A., Brown, S. S., and Rudich, Y.: Complex refractive indices in the near-ultraviolet spectral region of biogenic secondary organic aerosol aged with ammonia, Phys. Chem. Chem. Phys., 16, 10629–10642, https://doi.org/10.1039/C4CP01009D, 2014a.

Flores, J. M., Zhao, D. F., Segev, L., Schlag, P., Kiendler-Scharr, A., Fuchs, H., Watne, Å. K., Bluvshtein, N., Mentel, T. F., Hallquist, M., and Rudich, Y.: Evolution of the complex refractive index in the UV spectral region in ageing secondary organic aerosol, Atmospheric Chem. Phys., 14, 5793–5806, https://doi.org/10.5194/acp-14-5793-2014, 2014b.

Formenti, P., Di Biagio, C., Huang, Y., Kok, J., Mallet, M. D., Boulanger, D., and Cazaunau, M.: Look−up tables resolved by complex refractive index to correct particle sizes measured by common research−grade optical particle counters, Atmospheric Meas. Tech. Discuss., 1–30, https://doi.org/10.5194/amt-2021-403, 2021.

Formenti, P., Di Biagio, C., and et al: Aerosol and gas in situ observations at the Rambouillet rural site (RambForest) during the June–July 2022 ACROSS (Atmospheric Chemistry Of the Suburban Forest) field campaign, ESSD, Atmospheric Chem. Phys., in preparation.

Forster, P., Storelvmo, T., Armour, K., Collins, W., Dufresne, J.-L., Frame, D., Lunt, D. J., Mauritsen, T., Palmer, M. D., Watanabe, M., Wild, M., and Zhang, H.: The Earth's Energy Budget, Climate Feedbacks, and Climate Sensitivity, edited by: Masson-Delmotte, V., Zhai, P., Pirani, A., Connors, S. L., Péan, C., Berger, S., Caud, N., Chen, Y., Goldfarb, L., Gomis, M. I., Huang, M., Leitzell, K., Lonnoy, E., Matthews, J. B. R., Maycock, T. K., Waterfield, T., Yelekçi, O., Yu, R., and Zhou, B., Clim. Change 2021 Phys. Sci. Basis Contrib. Work. Group Sixth Assess. Rep. Intergov. Panel Clim. Change, 923–1054, https://doi.org/10.1017/9781009157896.009, 2021.

Freedman, M. A., Hasenkopf, C. A., Beaver, M. R., and Tolbert, M. A.: Optical Properties of Internally Mixed Aerosol Particles Composed of Dicarboxylic Acids and Ammonium Sulfate, J. Phys. Chem. A, 113, 13584–13592, https://doi.org/10.1021/jp906240y, 2009.

Freney, E. J., Sellegri, K., Canonaco, F., Colomb, A., Borbon, A., Michoud, V., Doussin, J.-F., Crumeyrolle, S., Amarouche, N., Pichon, J.-M., Bourianne, T., Gomes, L., Prevot, A. S. H., Beekmann, M., and Schwarzenböeck, A.: Characterizing the impact of urban emissions on regional aerosol particles: airborne measurements during the MEGAPOLI experiment, Atmospheric Chem. Phys., 14, 1397–1412, https://doi.org/10.5194/acp-14-1397-2014, 2014.

Fröhlich, R., Cubison, M. J., Slowik, J. G., Bukowiecki, N., Prévôt, A. S. H., Baltensperger, U., Schneider, J., Kimmel, J. R., Gonin, M., Rohner, U., Worsnop, D. R., and Jayne, J. T.: The ToF-ACSM: a portable aerosol chemical speciation monitor with TOFMS detection, Atmospheric Meas. Tech., 6, 3225–3241, https://doi.org/10.5194/amt-6-3225-2013, 2013.

Fu, Q.: An Accurate Parameterization of the Solar Radiative Properties of Cirrus Clouds for Climate Models, J. Clim., 9, 2058–2082, https://doi.org/10.1175/1520-0442(1996)009<2058:AAPOTS>2.0.CO;2, 1996.

Giles, D. M., Sinyuk, A., Sorokin, M. G., Schafer, J. S., Smirnov, A., Slutsker, I., Eck, T. F., Holben, B. N., Lewis, J. R., Campbell, J. R., Welton, E. J., Korkin, S. V., and Lyapustin, A. I.: Advancements in the Aerosol Robotic Network (AERONET) Version 3 database – automated near-real-time quality control algorithm with improved cloud screening for Sun photometer aerosol optical depth (AOD) measurements, Atmospheric Meas. Tech., 12, 169–209, https://doi.org/10.5194/amt-12-169-2019, 2019.

Gkikas, A., Obiso, V., Pérez García-Pando, C., Jorba, O., Hatzianastassiou, N., Vendrell, L., Basart, S., Solomos, S., Gassó, S., and Baldasano, J. M.: Direct radiative effects during intense Mediterranean desert dust outbreaks, Atmospheric Chem. Phys., 18, 8757–8787, https://doi.org/10.5194/acp-18-8757-2018, 2018.

Goldstein, A. H., Koven, C. D., Heald, C. L., and Fung, I. Y.: Biogenic carbon and anthropogenic pollutants combine to form a cooling haze over the southeastern United States, Proc. Natl. Acad. Sci., 106, 8835–8840, https://doi.org/10.1073/pnas.0904128106, 2009.

Gomez, J., Allen, R. J., Turnock, S. T., Horowitz, L. W., Tsigaridis, K., Bauer, S. E., Olivié, D., Thomson, E. S., and Ginoux, P.: The projected future degradation in air quality is caused by more abundant natural aerosols in a warmer world, Commun. Earth Environ., 4, 1–11, https://doi.org/10.1038/s43247-023-00688-7, 2023.

Granados-Muñoz, M. J., Sicard, M., Román, R., Benavent-Oltra, J. A., Barragán, R., Brogniez, G., Denjean, C., Mallet, M., Formenti, P., Torres, B., and Alados-Arboledas, L.: Impact of mineral dust on shortwave and longwave radiation: evaluation of different vertically resolved parameterizations in 1-D radiative transfer computations, Atmospheric Chem. Phys., 19, 523–542, https://doi.org/10.5194/acp-19-523-2019, 2019.

Grand-Orly Seine Bièvre: APUR : Territoires de la Métropode du Grand Paris, https://geo.data.gouv.fr/fr/datasets/51999ae0c038079425a71fe28ec144c349e963b0, 2018.

Guenther, A., Hewitt, C. N., Erickson, D., Fall, R., Geron, C., Graedel, T., Harley, P., Klinger, L., Lerdau, M., Mckay, W. A., Pierce, T., Scholes, B., Steinbrecher, R., Tallamraju, R., Taylor, J., and Zimmerman, P.: A global model of natural volatile organic compound emissions, J. Geophys. Res., 100, 8873–8892, https://doi.org/10.1029/94jd02950, 1995.

Guenther, A., Karl, T., Harley, P., Wiedinmyer, C., Palmer, P. I., and Geron, C.: Estimates of global terrestrial isoprene emissions using MEGAN (Model of Emissions of Gases and Aerosols from Nature), Atmospheric Chem. Phys., 6, 3181–3210, https://doi.org/10.5194/acp-6-3181-2006, 2006.

Gupta, P., Levy, R. C., Mattoo, S., Remer, L. A., and Munchak, L. A.: A surface reflectance scheme for retrieving aerosol optical depth over urban surfaces in MODIS Dark Target retrieval algorithm, Atmospheric Meas. Tech., 9, 3293–3308, https://doi.org/10.5194/amt-9-3293-2016, 2016.

Ha, S., Liu, Z., Sun, W., Lee, Y., and Chang, L.: Improving air quality forecasting with the assimilation of GOCI aerosol optical depth (AOD) retrievals during the KORUS-AQ period, Atmospheric Chem. Phys., 20, 6015–6036, https://doi.org/10.5194/acp-20-6015-2020, 2020.

Haeffelin, M., Barthès, L., Bock, O., Boitel, C., Bony, S., Bouniol, D., Chepfer, H., Chiriaco, M., Cuesta, J., Delanoë, J., Drobinski, P., Dufresne, J.-L., Flamant, C., Grall, M., Hodzic, A., Hourdin, F., Lapouge, F., Lemaître, Y., Mathieu, A., Morille, Y., Naud, C., Noël, V., O'Hirok, W., Pelon, J., Pietras, C., Protat, A., Romand, B., Scialom, G., and Vautard, R.: SIRTA, a ground-based atmospheric observatory for cloud and aerosol research, Ann. Geophys., 23, 253–275, https://doi.org/10.5194/angeo-23-253-2005, 2005.

Hallquist, M., Wenger, J. C., Baltensperger, U., Rudich, Y., Simpson, D., Claeys, M., Dommen, J., Donahue, N. M., George, C., Goldstein, A. H., Hamilton, J. F., Herrmann, H., Hoffmann, T., Iinuma, Y., Jang, M., Jenkin, M. E., Jimenez, J. L., Kiendler-Scharr, A., Maenhaut, W., McFiggans, G., Mentel, T. F., Monod, A., Prévôt, A. S. H., Seinfeld, J. H., Surratt, J. D., Szmigielski, R., and Wildt, J.: The formation, properties and impact of secondary organic aerosol: current and emerging issues, Atmospheric Chem. Phys., 9, 5155–5236, https://doi.org/10.5194/acp-9-5155-2009, 2009.

Hamilton, D. S., Perron, M. M. G., Bond, T. C., Bowie, A. R., Buchholz, R. R., Guieu, C., Ito, A., Maenhaut, W., Myriokefalitakis, S., Olgun, N., Rathod, S. D., Schepanski, K., Tagliabue, A., Wagner, R., and Mahowald, N. M.: Earth, Wind, Fire, and Pollution: Aerosol Nutrient Sources and Impacts on Ocean Biogeochemistry, Annu. Rev. Mar. Sci., 14, 303–330, https://doi.org/10.1146/annurev-marine-031921-013612, 2022.

Hand, J. L. and Kreidenweis, S. M.: A New Method for Retrieving Particle Refractive Index and Effective Density from Aerosol Size Distribution Data, Aerosol Sci. Technol., 36, 1012–1026, https://doi.org/10.1080/02786820290092276, 2002.

Hansen, J., Sato, M., Kharecha, P., Russell, G., Lea, D. W., and Siddall, M.: Climate change and trace gases, Philos. Trans. R. Soc. Math. Phys. Eng. Sci., 365, 1925–1954, https://doi.org/10.1098/rsta.2007.2052, 2007.

Harrison, R. M., Dall'Osto, M., Beddows, D. C. S., Thorpe, A. J., Bloss, W. J., Allan, J. D., Coe, H., Dorsey, J. R., Gallagher, M., Martin, C., Whitehead, J., Williams, P. I., Jones, R. L., Langridge, J. M., Benton, A. K., Ball, S. M., Langford, B., Hewitt, C. N., Davison, B., Martin, D., Petersson, K. F., Henshaw, S. J., White, I. R., Shallcross, D. E., Barlow, J. F., Dunbar, T., Davies, F., Nemitz, E., Phillips, G. J., Helfter, C., Di Marco, C. F., and Smith, S.: Atmospheric chemistry and physics in the atmosphere of a developed megacity (London): an overview of the REPARTEE experiment and its conclusions, Atmospheric Chem. Phys., 12, 3065–3114, https://doi.org/10.5194/acp-12-3065-2012, 2012.

Haywood, J. M. and Shine, K. P.: The effect of anthropogenic sulfate and soot aerosol on the clear sky planetary radiation budget, Geophys. Res. Lett., 22, 603–606, https://doi.org/10.1029/95GL00075, 1995.

Haywood, J. M. and Shine, K. P.: Multi-spectral calculations of the direct radiative forcing of tropospheric sulphate and soot aerosols using a column model, Q. J. R. Meteorol. Soc., 123, 1907–1930, https://doi.org/10.1002/qj.49712354307, 1997.

He, Q., Tomaz, S., Li, C., Zhu, M., Meidan, D., Riva, M., Laskin, A., Brown, S. S., George, C., Wang, X., and Rudich, Y.: Optical Properties of Secondary Organic Aerosol Produced by Nitrate Radical Oxidation of Biogenic Volatile Organic Compounds, Environ. Sci. Technol., 55, 2878–2889, https://doi.org/10.1021/acs.est.0c06838, 2021.

He, Q., Li, C., Siemens, K., Morales, A. C., Hettiyadura, A. P. S., Laskin, A., and Rudich, Y.: Optical Properties of Secondary Organic Aerosol Produced by Photooxidation of Naphthalene under NOx Condition, Environ. Sci. Technol., 56, 4816–4827, https://doi.org/10.1021/acs.est.1c07328, 2022.

Heald, C. L., Ridley, D. A., Kroll, J. H., Barrett, S. R. H., Cady-Pereira, K. E., Alvarado, M. J., and Holmes, C. D.: Contrasting the direct radiative effect and direct radiative forcing of aerosols, Atmospheric Chem. Phys., 14, 5513–5527, https://doi.org/10.5194/acp-14-5513-2014, 2014.

Healy, R. M., Sciare, J., Poulain, L., Crippa, M., Wiedensohler, A., Prévôt, A. S. H., Baltensperger, U., Sarda-Estève, R., McGuire, M. L., Jeong, C.-H., McGillicuddy, E., O'Connor, I. P., Sodeau, J. R., Evans, G. J., and Wenger, J. C.: Quantitative determination of carbonaceous particle mixing state in Paris using single-particle mass spectrometer and aerosol mass spectrometer measurements, Atmospheric Chem. Phys., 13, 9479–9496, https://doi.org/10.5194/acp-13-9479-2013, 2013.

Hecobian, A., Zhang, X., Zheng, M., Frank, N., Edgerton, E. S., and Weber, R. J.: Water-Soluble Organic Aerosol material and the light-absorption characteristics of aqueous extracts measured over the Southeastern United States, Atmospheric Chem. Phys., 10, 5965–5977, https://doi.org/10.5194/acp-10-5965-2010, 2010.

Heim, M., Mullins, B. J., Umhauer, H., and Kasper, G.: Performance evaluation of three optical particle counters with an efficient "multimodal" calibration method, J. Aerosol Sci., 39, 1019–1031, https://doi.org/10.1016/j.jaerosci.2008.07.006, 2008.

Hersbach, H., Bell, B., Berrisford, P., Bilavati, G., Horányi, A., Muñoz Sabater, J., Nicolas, J., Peubey, C., Radu, R., Rozum, I., Schepers, D., Simmons, A., Soci, C., Dee, D., and Thépaut, J.-N.: ERA5 hourly data on pressure levels from 1940 to present. Copernicus Climate Change Service (C3S) Climate Data Store (CDS), https://doi.org/10.24381/cds.bd0915c, 2023a.

Hersbach, H., Bell, B., Berrisford, P., Bilavati, G., Horányi, A., Muñoz Sabater, J., Nicolas, J., Peubey, C., Radu, R., Rozum, I., Schepers, D., Simmons, A., Soci, C., Dee, D., and Thépaut, J.-N.: ERA5 hourly data on single levels from 1940 to present. Copernicus Climate Change Service (C3S) Climate Data Store (CDS), https://doi.org/10.24381/cds.adbb2d47, 2023b.

Hong, S.-Y.: A new stable boundary-layer mixing scheme and its impact on the simulated East Asian summer monsoon, Q. J. R. Meteorol. Soc., 136, 1481–1496, https://doi.org/10.1002/qj.665, 2010.

Houghton, J. E. T., Ding, Y., Griggs, D., Noguer, M., van der Linden, P., Dai, X., Maskell, M., and Johnson, C.: Climate Change 2001: The Scientific Basis, in: Contribution of Working Group I to the Third Assessment Report of the Intergovernmental Panel on Climate Change (IPCC), vol. 881., 881, 2001.

Hsu, N. C., Tsay, S.-C., King, M. D., and Herman, J. R.: Aerosol properties over bright-reflecting source regions, IEEE Trans. Geosci. Remote Sens., 42, 557–569, https://doi.org/10.1109/TGRS.2004.824067, 2004.

Hu, K., Liu, D., Tian, P., Wu, Y., Li, S., Zhao, D., Li, R., Sheng, J., Huang, M., Ding, D., Liu, Q., Jiang, X., Li, Q., and Tao, J.: Identifying the Fraction of Core–Shell Black Carbon Particles in a Complex Mixture to Constrain the Absorption Enhancement by Coatings, Environ. Sci. Technol. Lett., https://doi.org/10.1021/acs.estlett.2c00060, 2022.

Hu, W., Hu, M., Hu, W., Jimenez, J. L., Yuan, B., Chen, W., Wang, M., Wu, Y., Chen, C., Wang, Z., Peng, J., Zeng, L., and Shao, M.: Chemical composition, sources, and aging process of submicron aerosols in Beijing: Contrast between summer and winter, J. Geophys. Res. Atmospheres, 121, 1955–1977, https://doi.org/10.1002/2015JD024020, 2016.

Hu, Y. X. and Stamnes, K.: An Accurate Parameterization of the Radiative Properties of Water Clouds Suitable for Use in Climate Models, J. Clim., 6, 728–742, https://doi.org/10.1175/1520-0442(1993)006<0728:AAPOTR>2.0.CO;2, 1993.

Iacono, M. J., Delamere, J. S., Mlawer, E. J., Shephard, M. W., Clough, S. A., and Collins, W. D.: Radiative forcing by long-lived greenhouse gases: Calculations with the AER radiative transfer models, J. Geophys. Res. Atmospheres, 113, https://doi.org/10.1029/2008JD009944, 2008.

Intergovernmental Panel On Climate Change: Climate Change 2021 – The Physical Science Basis: Working Group I Contribution to the Sixth Assessment Report of the Intergovernmental Panel on Climate Change, 1st ed., Cambridge University Press, https://doi.org/10.1017/9781009157896, 2023.

IPCC: Climate Change 1995, Cambridge University Press, Cambridge New York, 572 pp., 1995.

IPCC: Climate Change 2013: The Physical Science Basis. Contribution of Working Group I to the Fifth Assessment Report of the Intergovernmental Panel on Climate Change, Cambridge University Press, Cambridge, 2013.

IPCC (Ed.): Anthropogenic and Natural Radiative Forcing, in: Climate Change 2013 – The Physical Science Basis, Cambridge University Press, 659–740, https://doi.org/10.1017/CBO9781107415324.018, 2014.

IPCC: Climate Change 2021: The Physical Science Basis. Contribution of Working Group I to the Sixth Assessment Report of the Intergovernmental Panel on Climate Change, , In Press, https://doi.org/10.1017/9781009157896, 2021.

IPCC: Climate Change 2022: Impacts, Adaptation and Vulnerability, 2022.

IPCC: Climate Change 2021 – The Physical Science Basis: Working Group I Contribution to the Sixth Assessment Report of the Intergovernmental Panel on Climate Change, Cambridge University Press, Cambridge, https://doi.org/10.1017/9781009157896, 2023.

Irvine, W. M.: The asymmetry of the scattering diagram of a spherical particle, Bull. Astron. Inst. Neth., 17, 176, 1963.

Jacobson, M. Z.: Strong radiative heating due to the mixing state of black carbon in atmospheric aerosols, Nature, 409, 695–697, https://doi.org/10.1038/35055518, 2001.

Jiang, B.: Simulation investigation on the indirect effects due to sea-salt aerosols on the cloud ice during a tropical cyclone, J. Atmospheric Sol.-Terr. Phys., 233–234, 105893, https://doi.org/10.1016/j.jastp.2022.105893, 2022.

Jo, D. S., Park, R. J., Lee, S., Kim, S.-W., and Zhang, X.: A global simulation of brown carbon: implications for photochemistry and direct radiative effect, Atmospheric Chem. Phys., 16, 3413–3432, https://doi.org/10.5194/acp-16-3413-2016, 2016.

Jurányi, Z., Tritscher, T., Gysel, M., Laborde, M., Gomes, L., Roberts, G., Baltensperger, U., and Weingartner, E.: Hygroscopic mixing state of urban aerosol derived from size-resolved cloud condensation nuclei measurements during the MEGAPOLI campaign in Paris, Atmospheric Chem. Phys., 13, 6431–6446, https://doi.org/10.5194/acp-13-6431-2013, 2013.

Just, A. C., Wright, R. O., Schwartz, J., Coull, B. A., Baccarelli, A. A., Tellez-Rojo, M. M., Moody, E., Wang, Y., Lyapustin, A., and Kloog, I.: Using high-resolution satellite aerosol optical depth to estimate daily PM2.5 geographical distribution in Mexico City, Environ. Sci. Technol., 49, 8576–8584, https://doi.org/10.1021/acs.est.5b00859, 2015.

Kahnert, M. and Kanngießer, F.: Modelling optical properties of atmospheric black carbon aerosols, J. Quant. Spectrosc. Radiat. Transf., 244, 106849, https://doi.org/10.1016/j.jqsrt.2020.106849, 2020.

Kaiser, J. W., Heil, A., Andreae, M. O., Benedetti, A., Chubarova, N., Jones, L., Morcrette, J.-J., Razinger, M., Schultz, M. G., Suttie, M., and van der Werf, G. R.: Biomass burning emissions estimated with a global fire assimilation system based on observed fire radiative power, Biogeosciences, 9, 527–554, https://doi.org/10.5194/bg-9-527-2012, 2012.

Kalbermatter, D. M., Močnik, G., Drinovec, L., Visser, B., Röhrbein, J., Oscity, M., Weingartner, E., Hyvärinen, A.-P., and Vasilatou, K.: Comparing black-carbon- and aerosol-absorption-measuring instruments – a new system using lab-generated soot coated with controlled amounts of secondary organic matter, Atmospheric Meas. Tech., 15, 561–572, https://doi.org/10.5194/amt-15-561-2022, 2022.

Kammer, J., Flaud, P.-M., Chazeaubeny, A., Ciuraru, R., Le Menach, K., Geneste, E., Budzinski, H., Bonnefond, J. M., Lamaud, E., Perraudin, E., and Villenave, E.: Biogenic volatile organic compounds (BVOCs) reactivity related to new particle formation (NPF) over the Landes forest, Atmospheric Res., 237, 104869, https://doi.org/10.1016/j.atmosres.2020.104869, 2020.

KAMMER, J., SHAHIN, M., D'Anna, B., and Temime-Roussel, B.: ACROSS_LCE_PRG_SMPS_Sizedistr_5-Min_L2, https://doi.org/10.25326/658, 2024.

Kanakidou, M., Seinfeld, J. H., Pandis, S. N., Barnes, I., Dentener, F. J., Facchini, M. C., Van Dingenen, R., Ervens, B., Nenes, A., Nielsen, C. J., Swietlicki, E., Putaud, J. P., Balkanski, Y., Fuzzi, S., Horth, J., Moortgat, G. K., Winterhalter, R., Myhre, C. E. L., Tsigaridis, K., Vignati, E., Stephanou, E. G., and Wilson, J.: Organic aerosol and global climate modelling: a review, Atmospheric Chem. Phys., 5, 1053–1123, https://doi.org/10.5194/acp-5-1053-2005, 2005.

Karydis, V. A., Tsimpidi, A. P., Pozzer, A., Astitha, M., and Lelieveld, J.: Effects of mineral dust on global atmospheric nitrate concentrations, Atmospheric Chem. Phys., 16, 1491–1509, https://doi.org/10.5194/acp-16-1491-2016, 2016.

Kasoar, M., Shawki, D., and Voulgarakis, A.: Similar spatial patterns of global climate response to aerosols from different regions, Npj Clim. Atmospheric Sci., 1, 1–8, https://doi.org/10.1038/s41612-018-0022-z, 2018.

Kelesidis, G. A., Neubauer, D., Fan, L.-S., Lohmann, U., and Pratsinis, S. E.: Enhanced Light Absorption and Radiative Forcing by Black Carbon Agglomerates, Environ. Sci. Technol., 56, 8610–8618, https://doi.org/10.1021/acs.est.2c00428, 2022.

Kim, H. and Paulson, S. E.: Real refractive indices and volatility of secondary organic aerosol generated from photooxidation and ozonolysis of limonene, α-pinene and toluene, Atmospheric Chem. Phys., 13, 7711–7723, https://doi.org/10.5194/acp-13-7711-2013, 2013.

Kinne, S.: Aerosol radiative effects with MACv2, Atmospheric Chem. Phys., 19, 10919–10959, https://doi.org/10.5194/acp-19-10919-2019, 2019.

Kirago, L., Gatari, M. J., Gustafsson, Ö., and Andersson, A.: Black carbon emissions from traffic contribute substantially to air pollution in Nairobi, Kenya, Commun. Earth Environ., 3, 1–8, https://doi.org/10.1038/s43247-022-00400-1, 2022.

Kirchstetter, T. W., Novakov, T., and Hobbs, P. V.: Evidence that the spectral dependence of light absorption by aerosols is affected by organic carbon, J. Geophys. Res. Atmospheres, 109, https://doi.org/10.1029/2004JD004999, 2004.

Kok, J. F., Ridley, D. A., Zhou, Q., Miller, R. L., Zhao, C., Heald, C. L., Ward, D. S., Albani, S., and Haustein, K.: Smaller desert dust cooling effect estimated from analysis of dust size and abundance, Nat. Geosci., 10, 274–278, https://doi.org/10.1038/ngeo2912, 2017.

Kok, J. F., Storelvmo, T., Karydis, V. A., Adebiyi, A. A., Mahowald, N. M., Evan, A. T., He, C., and Leung, D. M.: Mineral dust aerosol impacts on global climate and climate change, Nat. Rev. Earth Environ., 4, 71–86, https://doi.org/10.1038/s43017-022-00379-5, 2023.

Kondragunta, S., Lee, P., McQueen, J., Kittaka, C., Prados, A. I., Ciren, P., Laszlo, I., Pierce, R. B., Hoff, R., and Szykman, J. J.: Air Quality Forecast Verification Using Satellite Data, J. Appl. Meteorol. Climatol., 47, 425–442, 2008.

Konovalov, I. B., Golovushkin, N. A., Beekmann, M., and Andreae, M. O.: Insights into the aging of biomass burning aerosol from satellite observations and 3D atmospheric modeling: evolution of the aerosol optical properties in Siberian wildfire plumes, Atmospheric Chem. Phys., 21, 357–392, https://doi.org/10.5194/acp-21-357-2021, 2021.

Konovalov, I. B., Golovushkin, N. A., Zhuravleva, T. B., Nasrtdinov, I. M., Uzhegov, V. N., and Beekmann, M.: Application of the CHIMERE-WRF Model Complex to Study the Radiative Effects of Siberian Smoke Aerosol in the Eastern Arctic, Atmospheric Ocean. Opt., 36, 337–347, https://doi.org/10.1134/S1024856023040085, 2023a.

Konovalov, I. B., Golovushkin, N. A., Beekmann, M., Siour, G., Zhuravleva, T. B., Nasrtdinov, I. M., and Kuznetsova, I. N.: On the importance of the model representation of organic aerosol in simulations of the direct radiative effect of Siberian biomass burning aerosol in the eastern Arctic, Atmos. Environ., 119910, https://doi.org/10.1016/j.atmosenv.2023.119910, 2023b.

Korras-Carraca, M. B., Pappas, V., Hatzianastassiou, N., Vardavas, I., and Matsoukas, C.: Global vertically resolved aerosol direct radiation effect from three years of CALIOP data using the FORTH radiation transfer model, Atmospheric Res., 224, 138–156, https://doi.org/10.1016/j.atmosres.2019.03.024, 2019.

Korras-Carraca, M.-B., Gkikas, A., Matsoukas, C., and Hatzianastassiou, N.: Global Clear-Sky Aerosol Speciated Direct Radiative Effects over 40 Years (1980–2019), Atmosphere, 12, 1254, https://doi.org/10.3390/atmos12101254, 2021.

Kotthaus, S., Haeffelin, M., Bouffies-Cloche, S., Dupont, J.-C., Drouin, M.-A., and Kotthaus, S.: PANAME Mixed Layer Height from high-SNR Automatic Aerosol Lidars (1.0), https://doi.org/10.25326/501, 2023.

Kuang, Y., Zhao, C. S., Tao, J. C., Bian, Y. X., and Ma, N.: Impact of aerosol hygroscopic growth on the direct aerosol radiative effect in summer on North China Plain, Atmos. Environ., 147, 224–233, https://doi.org/10.1016/j.atmosenv.2016.10.013, 2016.

Kulmala, M., Laaksonen, A., and Pirjola, L.: Parameterizations for sulfuric acid/water nucleation rates, J. Geophys. Res. Atmospheres, 103, 8301–8307, https://doi.org/10.1029/97JD03718, 1998.

Lacagnina, C., Hasekamp, O. P., and Torres, O.: Direct radiative effect of aerosols based on PARASOL and OMI satellite observations, J. Geophys. Res. Atmospheres, 122, 2366–2388, https://doi.org/10.1002/2016JD025706, 2017.

Lachatre, M., Mailler, S., Menut, L., Turquety, S., Sellitto, P., Guermazi, H., Salerno, G., Caltabiano, T., and Carboni, E.: New strategies for vertical transport in chemistry transport models: application to the case of the Mount Etna eruption on 18 March 2012 with CHIMERE v2017r4, Geosci. Model Dev., 13, 5707–5723, https://doi.org/10.5194/gmd-13-5707-2020, 2020.

Laing, J. R., Jaffe, D. A., and Arthur J. Sedlacek, I. I. I.: Comparison of Filter-based Absorption Measurements of Biomass Burning Aerosol and Background Aerosol at the Mt. Bachelor Observatory, Aerosol Air Qual. Res., 20, 663–678, https://doi.org/10.4209/aaqr.2019.06.0298, 2020.

Laskin, A., Laskin, J., and Nizkorodov, S. A.: Chemistry of Atmospheric Brown Carbon, Chem. Rev., 115, 4335–4382, https://doi.org/10.1021/cr5006167, 2015.

LeBlanc, S. E., Segal-Rozenhaimer, M., Redemann, J., Flynn, C., Johnson, R. R., Dunagan, S. E., Dahlgren, R., Kim, J., Choi, M., da Silva, A., Castellanos, P., Tan, Q., Ziemba, L., Lee Thornhill, K., and Kacenelenbogen, M.: Airborne observations during KORUS-AQ show that aerosol optical depths are more spatially self-consistent than aerosol intensive properties, Atmospheric Chem. Phys., 22, 11275–11304, https://doi.org/10.5194/acp-22-11275-2022, 2022.

Lee, S., Park, S., Lee, M.-I., Kim, G., Im, J., and Song, C.-K.: Air Quality Forecasts Improved by Combining Data Assimilation and Machine Learning With Satellite AOD, Geophys. Res. Lett., 49, e2021GL096066, https://doi.org/10.1029/2021GL096066, 2022.

Lenschow, P., Abraham, H.-J., Kutzner, K., Lutz, M., Preuß, J.-D., and Reichenbächer, W.: Some ideas about the sources of PM10, Atmos. Environ., 35, S23–S33, https://doi.org/10.1016/S1352-2310(01)00122-4, 2001.

Li, J., Carlson, B. E., Yung, Y. L., Lv, D., Hansen, J., Penner, J. E., Liao, H., Ramaswamy, V., Kahn, R. A., Zhang, P., Dubovik, O., Ding, A., Lacis, A. A., Zhang, L., and Dong, Y.: Scattering and absorbing aerosols in the climate system, Nat. Rev. Earth Environ., 3, 363–379, https://doi.org/10.1038/s43017-022-00296-7, 2022a.

Li, J., Carlson, B. E., Yung, Y. L., Lv, D., Hansen, J., Penner, J. E., Liao, H., Ramaswamy, V., Kahn, R. A., Zhang, P., Dubovik, O., Ding, A., Lacis, A. A., Zhang, L., and Dong, Y.: Scattering and absorbing aerosols in the climate system, Nat. Rev. Earth Environ., 3, 363–379, https://doi.org/10.1038/s43017-022-00296-7, 2022b.

Li, S., Zhang, H., Wang, Z., and Chen, Y.: Advances in the Research on Brown Carbon Aerosols: Its Concentrations, Radiative Forcing, and Effects on Climate, Aerosol Air Qual. Res., 23, 220336, https://doi.org/10.4209/aaqr.220336, 2023.

Lindqvist, H., Jokinen, O., Kandler, K., Scheuvens, D., and Nousiainen, T.: Single scattering by realistic, inhomogeneous mineral dust particles with stereogrammetric shapes, Atmospheric Chem. Phys., 14, 143–157, https://doi.org/10.5194/acp-14-143-2014, 2014.

Liu, C. and Smith, M. H.: Urban and rural aerosol particle optical properties, Atmos. Environ., 29, 3293–3301, https://doi.org/10.1016/1352-2310(95)00236-R, 1995.

Liu, C., Chung, C. E., Yin, Y., and Schnaiter, M.: The absorption Ångström exponent of black carbon: from numerical aspects, Atmospheric Chem. Phys., 18, 6259–6273, https://doi.org/10.5194/acp-18-6259-2018, 2018.

Liu, D., Whitehead, J., Alfarra, M. R., Reyes-Villegas, E., Spracklen, D. V., Reddington, C. L., Kong, S., Williams, P. I., Ting, Y.-C., Haslett, S., Taylor, J. W., Flynn, M. J., Morgan, W. T., McFiggans, G., Coe, H., and Allan, J. D.: Black-carbon absorption enhancement in the atmosphere determined by particle mixing state, Nat. Geosci., 10, 184–188, https://doi.org/10.1038/ngeo2901, 2017.

Liu, J., Lin, P., Laskin, A., Laskin, J., Kathmann, S. M., Wise, M., Caylor, R., Imholt, F., Selimovic, V., and Shilling, J. E.: Optical properties and aging of light-absorbing secondary organic aerosol, Atmospheric Chem. Phys., 16, 12815–12827, https://doi.org/10.5194/acp-16-12815-2016, 2016.

Liu, L., Mishchenko, M. I., and Patrick Arnott, W.: A study of radiative properties of fractal soot aggregates using the superposition *T*-matrix method, J. Quant. Spectrosc. Radiat. Transf., 109, 2656–2663, https://doi.org/10.1016/j.jqsrt.2008.05.001, 2008.

Liu, P., Zhang, Y., and Martin, S. T.: Complex Refractive Indices of Thin Films of Secondary Organic Materials by Spectroscopic Ellipsometry from 220 to 1200 nm, Environ. Sci. Technol., 47, 13594–13601, https://doi.org/10.1021/es403411e, 2013.

Liu, P. F., Abdelmalki, N., Hung, H.-M., Wang, Y., Brune, W. H., and Martin, S. T.: Ultraviolet and visible complex refractive indices of secondary organic material produced by photooxidation of the aromatic compounds toluene and *m*-xylene, Atmospheric Chem. Phys., 15, 1435–1446, https://doi.org/10.5194/acp-15-1435-2015, 2015a.

Liu, S., Aiken, A. C., Gorkowski, K., Dubey, M. K., Cappa, C. D., Williams, L. R., Herndon, S. C., Massoli, P., Fortner, E. C., Chhabra, P. S., Brooks, W. A., Onasch, T. B., Jayne, J. T., Worsnop, D. R., China, S., Sharma, N., Mazzoleni, C., Xu, L., Ng, N. L., Liu, D., Allan, J. D., Lee, J. D., Fleming, Z. L., Mohr, C., Zotter, P., Szidat, S., and Prévôt, A. S. H.: Enhanced light absorption by mixed source black and brown carbon particles in UK winter, Nat. Commun., 6, 8435, https://doi.org/10.1038/ncomms9435, 2015b.

Liu, Y., Liu, Y., Wang, M., Dong, X., Zheng, Y., Shrivastava, M., Qian, Y., Bai, H., Li, X., and Yang, X.-Q.: Anthropogenic–biogenic interaction amplifies warming from emission reduction over the southeastern US, Environ. Res. Lett., 16, 124046, https://doi.org/10.1088/1748-9326/ac3285, 2021.

Luo, J., Li, Z., Fan, C., Xu, H., Zhang, Y., Hou, W., Qie, L., Gu, H., Zhu, M., Li, Y., and Li, K.: The polarimetric characteristics of dust with irregular shapes: evaluation of the spheroid model for single particles, Atmospheric Meas. Tech., 15, 2767–2789, https://doi.org/10.5194/amt-15-2767-2022, 2022.

Lyapustin, A., Wang, Y., Laszlo, I., and Korkin, S.: Improved cloud and snow screening in MAIAC aerosol retrievals using spectral and spatial analysis, Atmospheric Meas. Tech., 5, 843–850, https://doi.org/10.5194/amt-5-843-2012, 2012.

Lyapustin, A., Wang, Y., Korkin, S., and Huang, D.: MODIS Collection 6 MAIAC algorithm, Atmospheric Meas. Tech., 11, 5741–5765, https://doi.org/10.5194/amt-11-5741-2018, 2018.

Ma, Y., Xin, J., Zhang, W., Gong, C., Wen, T., Wu, X., Wang, Y., Wang, L., Wu, F., and Ding, X.: Uncertainties of Simulated Aerosol Direct Radiative Effect Induced by Aerosol Chemical Components: A Measurement-Based Perspective From Urban-Forest Transition Region in East China, J. Geophys. Res. Atmospheres, 126, e2020JD033688, https://doi.org/10.1029/2020JD033688, 2021.

Mack, L. A., Levin, E. J. T., Kreidenweis, S. M., Obrist, D., Moosmüller, H., Lewis, K. A., Arnott, W. P., McMeeking, G. R., Sullivan, A. P., Wold, C. E., Hao, W.-M., Collett, J. L. J., and Malm, W. C.: Optical closure experiments for biomass smoke aerosols, Atmospheric Chem. Phys., 10, 9017–9026, https://doi.org/10.5194/acp-10-9017-2010, 2010.

Mahowald, N.: Aerosol Indirect Effect on Biogeochemical Cycles and Climate, Science, 334, 794–796, https://doi.org/10.1126/science.1207374, 2011.

Mailler, S., Menut, L., Khvorostyanov, D., Valari, M., Couvidat, F., Siour, G., Turquety, S., Briant, R., Tuccella, P., Bessagnet, B., Colette, A., Létinois, L., Markakis, K., and Meleux, F.: CHIMERE-2017: from urban to hemispheric chemistry-transport modeling, Geosci. Model Dev., 10, 2397–2423, https://doi.org/10.5194/gmd-10-2397-2017, 2017.

Mallet, M., Pont, V., Liousse, C., Roger, J. C., and Dubuisson, P.: Simulation of aerosol radiative properties with the ORISAM-RAD model during a pollution event (ESCOMPTE 2001), Atmos. Environ., 40, 7696–7705, https://doi.org/10.1016/j.atmosenv.2006.08.031, 2006.

Mallet, M., Solmon, F., Nabat, P., Elguindi, N., Waquet, F., Bouniol, D., Sayer, A. M., Meyer, K., Roehrig, R., Michou, M., Zuidema, P., Flamant, C., Redemann, J., and Formenti, P.: Direct and semi-direct radiative forcing of biomass-burning aerosols over the southeast Atlantic (SEA) and its sensitivity to absorbing properties: a regional climate modeling study, Atmospheric Chem. Phys., 20, 13191–13216, https://doi.org/10.5194/acp-20-13191-2020, 2020.

Mallet, M., Nabat, P., di Sarra, A. G., Solmon, F., Gutiérrez, C., Mailler, S., Menut, L., Kaskaoutis, D., Rowlinson, M., Rap, A., and Dulac, F.: Aerosol and Tropospheric Ozone Direct Radiative Impacts, in: Atmospheric Chemistry in the Mediterranean Region: Volume 2 - From Air Pollutant Sources to Impacts, edited by: Dulac, F., Sauvage, S., and Hamonou, E., Springer International Publishing, Cham, 373–402, https://doi.org/10.1007/978-3-030-82385-6_19, 2022.

Mao, J., Zheng, Y., Horowitz, L. W., Menzel, R., Paynter, D., Naik, V., and Li, J.: Anthropogenic amplification of biogenic secondary organic aerosol formation, 2022, A42D-08, 2022a.

Mao, Q., Wang, L., Cao, W., and Chen, M.: Relationship between relative humidity and the hygroscopic growth characteristics of mixed clusters comprising black carbon and ammonium sulfate, Atmospheric Pollut. Res., 13, 101414, https://doi.org/10.1016/j.apr.2022.101414, 2022b.

Marinou, E., Amiridis, V., Binietoglou, I., Tsikerdekis, A., Solomos, S., Proestakis, E., Konsta, D., Papagiannopoulos, N., Tsekeri, A., Vlastou, G., Zanis, P., Balis, D., Wandinger, U., and Ansmann, A.: Three-dimensional evolution of Saharan dust transport towards Europe based on a 9-year EARLINET-optimized CALIPSO dataset, Atmospheric Chem. Phys., 17, 5893–5919, https://doi.org/10.5194/acp-17-5893-2017, 2017.

Martins, V. S., Lyapustin, A., de Carvalho, L. a. S., Barbosa, C. C. F., and Novo, E. M. L. M.: Validation of high-resolution MAIAC aerosol product over South America, J. Geophys. Res. Atmospheres, 122, 7537–7559, https://doi.org/10.1002/2016JD026301, 2017.

Martins, V. S., Lyapustin, A., Wang, Y., Giles, D. M., Smirnov, A., Slutsker, I., and Korkin, S.: Global validation of columnar water vapor derived from EOS MODIS-MAIAC algorithm against the ground-based AERONET observations, Atmospheric Res., 225, 181–192, https://doi.org/10.1016/j.atmosres.2019.04.005, 2019.

Masson, O., Piga, D., Gurriaran, R., and D'Amico, D.: Impact of an exceptional Saharan dust outbreak in France: PM10 and artificial radionuclides concentrations in air and in dust deposit, Atmos. Environ., 44, 2478–2486, https://doi.org/10.1016/j.atmosenv.2010.03.004, 2010.

Matsui, H., Hamilton, D. S., and Mahowald, N. M.: Black carbon radiative effects highly sensitive to emitted particle size when resolving mixing-state diversity, Nat. Commun., 9, 3446, https://doi.org/10.1038/s41467-018-05635-1, 2018.

Matus, A. V., L'Ecuyer, T. S., and Henderson, D. S.: New Estimates of Aerosol Direct Radiative Effects and Forcing From A-Train Satellite Observations, Geophys. Res. Lett., 46, 8338–8346, https://doi.org/10.1029/2019GL083656, 2019.

Meloni, D., di Sarra, A., Di Iorio, T., and Fiocco, G.: Direct radiative forcing of Saharan dust in the Mediterranean from measurements at Lampedusa Island and MISR space-borne observations, J. Geophys. Res. Atmospheres, 109, https://doi.org/10.1029/2003JD003960, 2004.

Meloni, D., Junkermann, W., di Sarra, A., Cacciani, M., De Silvestri, L., Di Iorio, T., Estellés, V., Gómez-Amo, J. L., Pace, G., and Sferlazzo, D. M.: Altitude-resolved shortwave and longwave radiative effects of desert dust in the Mediterranean during the GAMARF campaign: Indications of a net daily cooling in the dust layer, J. Geophys. Res. Atmospheres, 120, 3386–3407, https://doi.org/10.1002/2014JD022312, 2015.

Menut, L., Bessagnet, B., Briant, R., Cholakian, A., Couvidat, F., Mailler, S., Pennel, R., Siour, G., Tuccella, P., Turquety, S., and Valari, M.: The CHIMERE v2020r1 online chemistry-transport model, Geosci. Model Dev., 14, 6781–6811, https://doi.org/10.5194/gmd-14-6781-2021, 2021.

Menut, L., Cholakian, A., Siour, G., Lapere, R., Pennel, R., Mailler, S., and Bessagnet, B.: Impact of Landes forest fires on air quality in France during the 2022 summer, Atmospheric Chem. Phys., 23, 7281–7296, https://doi.org/10.5194/acp-23-7281-2023, 2023.

Merdji, A. B., Lu, C., Xu, X., and Mhawish, A.: Long-term three-dimensional distribution and transport of Saharan dust: Observation from CALIPSO, MODIS, and reanalysis data, Atmospheric Res., 286, 106658, https://doi.org/10.1016/j.atmosres.2023.106658, 2023.

Met Office: Met Office Integrated Data Archive System (MIDAS) Land and Marine Surface Stations Data (1853-current). NCAS British Atmospheric Data Centre, 2024., 2012.

Meteo France: Bilan climatique de l'été 2022, , https://meteofrance.fr/actualite/publications/2022-les-bilans-climatiques, 2022.

Mhawish, A., Banerjee, T., Sorek-Hamer, M., Lyapustin, A., Broday, D. M., and Chatfield, R.: Comparison and evaluation of MODIS Multi-angle Implementation of Atmospheric Correction (MAIAC) aerosol product over South Asia, Remote Sens. Environ., 224, 12–28, https://doi.org/10.1016/j.rse.2019.01.033, 2019.

Michoud, V., Sciare, J., Sauvage, S., Dusanter, S., Léonardis, T., Gros, V., Kalogridis, C., Zannoni, N., Féron, A., Petit, J.-E., Crenn, V., Baisnée, D., Sarda-Estève, R., Bonnaire, N., Marchand, N., DeWitt, H. L., Pey, J., Colomb, A., Gheusi, F., Szidat, S., Stavroulas, I., Borbon, A., and Locoge, N.: Organic carbon at a remote site of the western Mediterranean Basin: sources and chemistry during the ChArMEx SOP2 field experiment, Atmospheric Chem. Phys., 17, 8837–8865, https://doi.org/10.5194/acp-17-8837-2017, 2017.

Millet, D. B., Jacob, D. J., Boersma, K. F., Fu, T., Kurosu, T. P., Chance, K., Heald, C. L., and Guenther, A.: Spatial distribution of isoprene emissions from North America derived from formaldehyde column measurements by the OMI satellite sensor, J. Geophys. Res. Atmospheres, 113, 2007JD008950, https://doi.org/10.1029/2007JD008950, 2008.

Mishchenko, M. I., Dlugach, J. M., Yanovitskij, E. G., and Zakharova, N. T.: Bidirectional reflectance of flat, optically thick particulate layers: an efficient radiative transfer solution and applications to snow and soil surfaces, J. Quant. Spectrosc. Radiat. Transf., 63, 409–432, https://doi.org/10.1016/S0022-4073(99)00028-X, 1999.

Mohr, C., Lopez-Hilfiker, F. D., Yli-Juuti, T., Heitto, A., Lutz, A., Hallquist, M., D'Ambro, E. L., Rissanen, M. P., Hao, L., Schobesberger, S., Kulmala, M., Mauldin III, R. L., Makkonen, U., Sipilä, M., Petäjä, T., and Thornton, J. A.: Ambient observations of dimers from terpene oxidation in the gas phase: Implications for new particle formation and growth, Geophys. Res. Lett., 44, 2958–2966, https://doi.org/10.1002/2017GL072718, 2017.

Moise, T., Flores, J. M., and Rudich, Y.: Optical Properties of Secondary Organic Aerosols and Their Changes by Chemical Processes, Chem. Rev., 115, 4400–4439, https://doi.org/10.1021/cr5005259, 2015.

Molina, M. J. and Molina, L. T.: Megacities and Atmospheric Pollution, J. Air Waste Manag. Assoc., 54, 644–680, https://doi.org/10.1080/10473289.2004.10470936, 2004.

Moore, R. H., Wiggins, E. B., Ahern, A. T., Zimmerman, S., Montgomery, L., Campuzano Jost, P., Robinson, C. E., Ziemba, L. D., Winstead, E. L., Anderson, B. E., Brock, C. A., Brown, M. D., Chen, G., Crosbie, E. C., Guo, H., Jimenez, J. L., Jordan, C. E., Lyu, M., Nault, B. A., Rothfuss, N. E., Sanchez, K. J., Schueneman, M., Shingler, T. J., Shook, M. A., Thornhill, K. L., Wagner, N. L., and Wang, J.: Sizing response of the Ultra-High Sensitivity Aerosol Spectrometer (UHSAS) and Laser Aerosol Spectrometer (LAS) to changes in submicron aerosol composition and refractive index, Atmospheric Meas. Tech., 14, 4517–4542, https://doi.org/10.5194/amt-14-4517-2021, 2021.

Moschos, V., Gysel-Beer, M., Modini, R. L., Corbin, J. C., Massabò, D., Costa, C., Danelli, S. G., Vlachou, A., Daellenbach, K. R., Szidat, S., Prati, P., Prévôt, A. S. H., Baltensperger, U., and El Haddad, I.: Source-specific light absorption by carbonaceous components in the complex aerosol matrix from yearly filter-based measurements, Atmospheric Chem. Phys., 21, 12809–12833, https://doi.org/10.5194/acp-21-12809-2021, 2021.

Moteki, N., Ohata, S., Yoshida, A., and Adachi, K.: Constraining the complex refractive index of black carbon particles using the complex forward-scattering amplitude, Aerosol Sci. Technol., 57, 678–699, https://doi.org/10.1080/02786826.2023.2202243, 2023.

Müller, A., Miyazaki, Y., Aggarwal, S. G., Kitamori, Y., Boreddy, S. K. R., and Kawamura, K.: Effects of chemical composition and mixing state on size-resolved hygroscopicity and cloud condensation nuclei activity of submicron aerosols at a suburban site in northern Japan in summer, J. Geophys. Res. Atmospheres, 122, 9301–9318, https://doi.org/10.1002/2017JD027286, 2017.

Müller, D., Ansmann, A., Wagner, F., Franke, K., and Althausen, D.: European pollution outbreaks during ACE 2: Microphysical particle properties and single-scattering albedo inferred from multiwavelength lidar observations, J. Geophys. Res. Atmospheres, 107, AAC 3-1-AAC 3-11, https://doi.org/10.1029/2001JD001110, 2002.

Müller, T., Laborde, M., Kassell, G., and Wiedensohler, A.: Design and performance of a three-wavelength LED-based total scatter and backscatter integrating nephelometer, Atmospheric Meas. Tech., 4, 1291–1303, https://doi.org/10.5194/amt-4-1291-2011, 2011.

Myhre, G., Samset, B. H., Schulz, M., Balkanski, Y., Bauer, S., Berntsen, T. K., Bian, H., Bellouin, N., Chin, M., Diehl, T., Easter, R. C., Feichter, J., Ghan, S. J., Hauglustaine, D., Iversen, T., Kinne, S., Kirkevåg, A., Lamarque, J.-F., Lin, G., Liu, X., Lund, M. T., Luo, G., Ma, X., van Noije, T., Penner, J. E., Rasch, P. J., Ruiz, A., Seland, Ø., Skeie, R. B., Stier, P., Takemura, T., Tsigaridis, K., Wang, P., Wang, Z., Xu, L., Yu, H., Yu, F., Yoon, J.-H., Zhang, K., Zhang, H., and Zhou, C.: Radiative forcing of the direct aerosol effect from AeroCom Phase II simulations, Atmospheric Chem. Phys., 13, 1853–1877, https://doi.org/10.5194/acp-13-1853-2013, 2013.

Myhre, G., Samset, B. H., Mohr, C. W., Alterskjær, K., Balkanski, Y., Bellouin, N., Chin, M., Haywood, J., Hodnebrog, Ø., Kinne, S., Lin, G., Lund, M. T., Penner, J. E., Schulz, M., Schutgens, N., Skeie, R. B., Stier, P., Takemura, T., and Zhang, K.: Cloudy-sky contributions to the direct aerosol effect, Atmospheric Chem. Phys., 20, 8855–8865, https://doi.org/10.5194/acp-20-8855-2020, 2020.

Nair, V. S., Babu, S. S., Manoj, M. R., Moorthy, K. K., and Chin, M.: Direct radiative effects of aerosols over South Asia from observations and modeling, Clim. Dyn., 49, 1411–1428, https://doi.org/10.1007/s00382-016-3384-0, 2017.

Nakayama, T., Sato, K., Matsumi, Y., Imamura, T., Yamazaki, A., and Uchiyama, A.: Wavelength Dependence of Refractive Index of Secondary Organic Aerosols Generated during the Ozonolysis and Photooxidation of α-Pinene, Sola, 8, 119–123, https://doi.org/10.2151/sola.2012-030, 2012.

Nakayama, T., Sato, K., Tsuge, M., Imamura, T., and Matsumi, Y.: Complex refractive index of secondary organic aerosol generated from isoprene/NOx photooxidation in the presence and absence of SO2, J. Geophys. Res. Atmospheres, 120, 7777–7787, https://doi.org/10.1002/2015JD023522, 2015.

Nascimento, J. P., Bela, M. M., Meller, B. B., Banducci, A. L., Rizzo, L. V., Vara-Vela, A. L., Barbosa, H. M. J., Gomes, H., Rafee, S. A. A., Franco, M. A., Carbone, S., Cirino, G. G., Souza, R. A. F., McKeen, S. A., and Artaxo, P.: Aerosols from anthropogenic and biogenic sources and their interactions – modeling aerosol formation, optical properties, and impacts over the central Amazon basin, Atmospheric Chem. Phys., 21, 6755–6779, https://doi.org/10.5194/acp-21-6755-2021, 2021.

Nault, B. A., Jo, D. S., McDonald, B. C., Campuzano-Jost, P., Day, D. A., Hu, W., Schroder, J. C., Allan, J., Blake, D. R., Canagaratna, M. R., Coe, H., Coggon, M. M., DeCarlo, P. F., Diskin, G. S., Dunmore, R., Flocke, F., Fried, A., Gilman, J. B., Gkatzelis, G., Hamilton, J. F., Hanisco, T. F., Hayes, P. L., Henze, D. K., Hodzic, A., Hopkins, J., Hu, M., Huey, L. G., Jobson, B. T., Kuster, W. C., Lewis, A., Li, M., Liao, J., Nawaz, M. O., Pollack, I. B., Peischl, J., Rappenglück, B., Reeves, C. E., Richter, D., Roberts, J. M., Ryerson, T. B., Shao, M., Sommers, J. M., Walega, J., Warneke, C., Weibring, P., Wolfe, G. M., Young, D. E., Yuan, B., Zhang, Q., de Gouw, J. A., and Jimenez, J. L.: Secondary organic aerosols from anthropogenic volatile organic compounds contribute substantially to air pollution mortality, Atmospheric Chem. Phys., 21, 11201–11224, https://doi.org/10.5194/acp-21-11201-2021, 2021.

Navarro-Barboza, H., Pandolfi, M., Guevara, M., Enciso, S., Tena, C., Via, M., Yus-Díez, J., Reche, C., Pérez, N., Alastuey, A., Querol, X., and Jorba, O.: Uncertainties in source allocation of carbonaceous aerosols in a Mediterranean region, Environ. Int., 183, 108252, https://doi.org/10.1016/j.envint.2023.108252, 2024.

Nenes, A., Pandis, S. N., and Pilinis, C.: ISORROPIA: A New Thermodynamic Equilibrium Model for Multiphase Multicomponent Inorganic Aerosols, Aquat. Geochem., 4, 123–152, https://doi.org/10.1023/A:1009604003981, 1998.

O'Donnell, D., Tsigaridis, K., and Feichter, J.: Estimating the direct and indirect effects of secondary organic aerosols using ECHAM5-HAM, Atmospheric Chem. Phys., 11, 8635–8659, https://doi.org/10.5194/acp-11-8635-2011, 2011.

Oomen, G.-M., Müller, J.-F., Stavrakou, T., De Smedt, I., Blumenstock, T., Kivi, R., Makarova, M., Palm, M., Röhling, A., Té, Y., Vigouroux, C., Friedrich, M. M., Frieß, U., Hendrick, F., Merlaud, A., Piters, A., Richter, A., Van Roozendael, M., and Wagner, T.: Weekly derived top-down volatile-organic-compound fluxes over Europe from TROPOMI HCHO data from 2018 to 2021, Atmospheric Chem. Phys., 24, 449–474, https://doi.org/10.5194/acp-24-449-2024, 2024.

Pace, G., di Sarra, A., Meloni, D., Piacentino, S., and Chamard, P.: Aerosol optical properties at Lampedusa (Central Mediterranean). 1. Influence of transport and identification of different aerosol types, Atmospheric Chem. Phys., 6, 697–713, https://doi.org/10.5194/acp-6-697-2006, 2006.

Pandis, S. N., Wexler, A. S., and Seinfeld, J. H.: Secondary organic aerosol formation and transport — II. Predicting the ambient secondary organic aerosol size distribution, Atmospheric Environ. Part Gen. Top., 27, 2403–2416, https://doi.org/10.1016/0960-1686(93)90408-Q, 1993.

Pang, Y., Chen, M., Wang, Y., Chen, X., Teng, X., Kong, S., Zheng, Z., and Li, W.: Morphology and Fractal Dimension of Size-Resolved Soot Particles Emitted From Combustion Sources, J. Geophys. Res. Atmospheres, 128, e2022JD037711, https://doi.org/10.1029/2022JD037711, 2023.

Pankow, J. F.: An absorption model of the gas/aerosol partitioning involved in the formation of secondary organic aerosol, Atmos. Environ., 28, 189–193, https://doi.org/10.1016/1352-2310(94)90094-9, 1994.

Passant, N.: Speciation of UK emissions of non-methane volatile organic compounds, 2002.

Péré, J. C., Mallet, M., Pont, V., and Bessagnet, B.: Impact of aerosol direct radiative forcing on the radiative budget, surface heat fluxes, and atmospheric dynamics during the heat wave of summer 2003 over western Europe: A modeling study, J. Geophys. Res. Atmospheres, 116, https://doi.org/10.1029/2011JD016240, 2011.

Prahl, S.: miepython: Pure python implementation of Mie scattering, , https://doi.org/10.5281/zenodo.8023972, 2023.

Qin, W., Fang, H., Wang, L., Wei, J., Zhang, M., Su, X., Bilal, M., and Liang, X.: MODIS high-resolution MAIAC aerosol product: Global validation and analysis, Atmos. Environ., 264, 118684, https://doi.org/10.1016/j.atmosenv.2021.118684, 2021.

Räisänen, P., Merikanto, J., Makkonen, R., Savolahti, M., Kirkevåg, A., Sand, M., Seland, Ø., and Partanen, A.-I.: Mapping the dependence of black carbon radiative forcing on emission region and season, Atmospheric Chem. Phys., 22, 11579–11602, https://doi.org/10.5194/acp-22-11579-2022, 2022.

Ranaivombola, M., Bègue, N., Bencherif, H., Millet, T., Sivakumar, V., Duflot, V., Baron, A., Mbatha, N., Piketh, S., Formenti, P., and Goloub, P.: Aerosol Optical Properties and Types over Southern Africa and Reunion Island Determined from Ground-Based and Satellite Observations over a 13-Year Period (2008–2021), Remote Sens., 15, 1581, https://doi.org/10.3390/rs15061581, 2023.

Rao, S. and Dey, S.: Consistent signal of aerosol indirect and semi-direct effect on water clouds in the oceanic regions adjacent to the Indian subcontinent, Atmospheric Res., 232, 104677, https://doi.org/10.1016/j.atmosres.2019.104677, 2020.

Rap, A., Scott, C. E., Spracklen, D. V., Bellouin, N., Forster, P. M., Carslaw, K. S., Schmidt, A., and Mann, G.: Natural aerosol direct and indirect radiative effects, Geophys. Res. Lett., 40, 3297–3301, https://doi.org/10.1002/grl.50441, 2013.

Raut, J.-C. and Chazette, P.: Retrieval of aerosol complex refractive index from a synergy between lidar, sunphotometer and in situ measurements during LISAIR experiment, Atmospheric Chem. Phys., 7, 2797–2815, https://doi.org/10.5194/acp-7-2797-2007, 2007.

Raut, J.-C. and Chazette, P.: Vertical profiles of urban aerosol complex refractive index in the frame of ESQUIF airborne measurements, Atmospheric Chem. Phys., 8, 901–919, https://doi.org/10.5194/acp-8-901-2008, 2008.

Redemann, J., Turco, R. P., Liou, K. N., Russell, P. B., Bergstrom, R. W., Schmid, B., Livingston, J. M., Hobbs, P. V., Hartley, W. S., Ismail, S., Ferrare, R. A., and Browell, E. V.: Retrieving the vertical structure of the effective aerosol complex index of refraction from a combination of aerosol in situ and remote sensing measurements during TARFOX, J. Geophys. Res. Atmospheres, 105, 9949–9970, https://doi.org/10.1029/1999JD901044, 2000.

Remer, L. A., Kaufman, Y. J., Tanré, D., Mattoo, S., Chu, D. A., Martins, J. V., Li, R.-R., Ichoku, C., Levy, R. C., Kleidman, R. G., Eck, T. F., Vermote, E., and Holben, B. N.: The MODIS Aerosol Algorithm, Products, and Validation, J. Atmospheric Sci., 62, 947–973, https://doi.org/10.1175/JAS3385.1, 2005.

Remer, L. A., Levy, R. C., Mattoo, S., Tanré, D., Gupta, P., Shi, Y., Sawyer, V., Munchak, L. A., Zhou, Y., Kim, M., Ichoku, C., Patadia, F., Li, R.-R., Gassó, S., Kleidman, R. G., and Holben, B. N.: The Dark Target Algorithm for Observing the Global Aerosol System: Past, Present, and Future, Remote Sens., 12, 2900, https://doi.org/10.3390/rs12182900, 2020.

Ribes, A., Boé, J., Qasmi, S., Dubuisson, B., Douville, H., and Terray, L.: An updated assessment of past and future warming over France based on a regional observational constraint, Earth Syst. Dyn., 13, 1397–1415, https://doi.org/10.5194/esd-13-1397-2022, 2022.

Riemer, N., Ault, A. P., West, M., Craig, R. L., and Curtis, J. H.: Aerosol Mixing State: Measurements, Modeling, and Impacts, Rev. Geophys., 57, 187–249, https://doi.org/10.1029/2018RG000615, 2019.

Rizzo, L. V., Correia, A. L., Artaxo, P., Procópio, A. S., and Andreae, M. O.: Spectral dependence of aerosol light absorption over the Amazon Basin, Atmospheric Chem. Phys., 11, 8899–8912, https://doi.org/10.5194/acp-11-8899-2011, 2011.

Rizzo, L. V., Artaxo, P., Müller, T., Wiedensohler, A., Paixão, M., Cirino, G. G., Arana, A., Swietlicki, E., Roldin, P., Fors, E. O., Wiedemann, K. T., Leal, L. S. M., and Kulmala, M.: Long term measurements of aerosol optical properties at a primary forest site in Amazonia, Atmospheric Chem. Phys., 13, 2391–2413, https://doi.org/10.5194/acp-13-2391-2013, 2013.

Robinson, A. L., Donahue, N. M., Shrivastava, M. K., Weitkamp, E. A., Sage, A. M., Grieshop, A. P., Lane, T. E., Pierce, J. R., and Pandis, S. N.: Rethinking Organic Aerosols: Semivolatile Emissions and Photochemical Aging, Science, 315, 1259–1262, https://doi.org/10.1126/science.1133061, 2007.

Robotto, A., Barbero, S., Bracco, P., Cremonini, R., Ravina, M., and Brizio, E.: Improving Air Quality Standards in Europe: Comparative Analysis of Regional Differences, with a Focus on Northern Italy, Atmosphere, 13, 642, https://doi.org/10.3390/atmos13050642, 2022.

Ryder, C. L., Marenco, F., Brooke, J. K., Estelles, V., Cotton, R., Formenti, P., McQuaid, J. B., Price, H. C., Liu, D., Ausset, P., Rosenberg, P. D., Taylor, J. W., Choularton, T., Bower, K., Coe, H., Gallagher, M., Crosier, J., Lloyd, G., Highwood, E. J., and Murray, B. J.: Coarse-mode mineral dust size distributions, composition and optical properties from AER-D aircraft measurements over the tropical eastern Atlantic, Atmospheric Chem. Phys., 18, 17225–17257, https://doi.org/10.5194/acp-18-17225-2018, 2018.

Saleh, R., Robinson, E. S., Tkacik, D. S., Ahern, A. T., Liu, S., Aiken, A. C., Sullivan, R. C., Presto, A. A., Dubey, M. K., Yokelson, R. J., Donahue, N. M., and Robinson, A. L.: Brownness of organics in aerosols from biomass burning linked to their black carbon content, Nat. Geosci., 7, 647–650, https://doi.org/10.1038/ngeo2220, 2014.

Saleh, R., Marks, M., Heo, J., Adams, P. J., Donahue, N. M., and Robinson, A. L.: Contribution of brown carbon and lensing to the direct radiative effect of carbonaceous aerosols from biomass and biofuel burning emissions, J. Geophys. Res. Atmospheres, 120, 10,285-10,296, https://doi.org/10.1002/2015JD023697, 2015.

Samset, B. H., Stjern, C. W., Andrews, E., Kahn, R. A., Myhre, G., Schulz, M., and Schuster, G. L.: Aerosol Absorption: Progress Towards Global and Regional Constraints, Curr. Clim. Change Rep., 4, 65–83, https://doi.org/10.1007/s40641-018-0091-4, 2018.

Sand, M., Samset, B. H., Myhre, G., Gliß, J., Bauer, S. E., Bian, H., Chin, M., Checa-Garcia, R., Ginoux, P., Kipling, Z., Kirkevåg, A., Kokkola, H., Le Sager, P., Lund, M. T., Matsui, H., van Noije, T., Olivié, D. J. L., Remy, S., Schulz, M., Stier, P., Stjern, C. W., Takemura, T., Tsigaridis, K., Tsyro, S. G., and Watson-Parris, D.: Aerosol absorption in global models from AeroCom phase III, Atmospheric Chem. Phys., 21, 15929–15947, https://doi.org/10.5194/acp-21-15929-2021, 2021.

Sandrini, S., van Pinxteren, D., Giulianelli, L., Herrmann, H., Poulain, L., Facchini, M. C., Gilardoni, S., Rinaldi, M., Paglione, M., Turpin, B. J., Pollini, F., Bucci, S., Zanca, N., and Decesari, S.: Size-resolved aerosol composition at an urban and a rural site in the Po Valley in summertime: implications for secondary aerosol formation, Atmospheric Chem. Phys., 16, 10879–10897, https://doi.org/10.5194/acp-16-10879-2016, 2016.

Santese, M., Perrone, M. R., Zakey, A. S., De Tomasi, F., and Giorgi, F.: Modeling of Saharan dust outbreaks over the Mediterranean by RegCM3: case studies, Atmospheric Chem. Phys., 10, 133–156, https://doi.org/10.5194/acp-10-133-2010, 2010.

di Sarra, A., Di Biagio, C., Meloni, D., Monteleone, F., Pace, G., Pugnaghi, S., and Sferlazzo, D.: Shortwave and longwave radiative effects of the intense Saharan dust event of 25–26 March 2010 at Lampedusa (Mediterranean Sea), J. Geophys. Res. Atmospheres, 116, https://doi.org/10.1029/2011JD016238, 2011.

Sartelet, K. N., Couvidat, F., Seigneur, C., and Roustan, Y.: Impact of biogenic emissions on air quality over Europe and North America, Atmos. Environ., 53, 131–141, https://doi.org/10.1016/j.atmosenv.2011.10.046, 2012.

Satheesh, S. K. and Ramanathan, V.: Large differences in tropical aerosol forcing at the top of the atmosphere and Earth's surface, Nature, 405, 60–63, https://doi.org/10.1038/35011039, 2000.

Schuster, G. L., Dubovik, O., and Holben, B. N.: Angstrom exponent and bimodal aerosol size distributions, J. Geophys. Res. Atmospheres, 111, https://doi.org/10.1029/2005JD006328, 2006.

Schutgens, N. A. J.: Site representativity of AERONET and GAW remotely sensed aerosol optical thickness and absorbing aerosol optical thickness observations, Atmospheric Chem. Phys., 20, 7473–7488, https://doi.org/10.5194/acp-20-7473-2020, 2020.

Sciare, J., d'Argouges, O., Sarda-Estève, R., Gaimoz, C., Dolgorouky, C., Bonnaire, N., Favez, O., Bonsang, B., and Gros, V.: Large contribution of water-insoluble secondary organic aerosols in the region of Paris (France) during wintertime, J. Geophys. Res. Atmospheres, 116, https://doi.org/10.1029/2011JD015756, 2011.

Scott, C. E., Rap, A., Spracklen, D. V., Forster, P. M., Carslaw, K. S., Mann, G. W., Pringle, K. J., Kivekäs, N., Kulmala, M., Lihavainen, H., and Tunved, P.: The direct and indirect radiative effects of biogenic secondary organic aerosol, Atmospheric Chem. Phys., 14, 447–470, https://doi.org/10.5194/acp-14-447-2014, 2014.

Seinfeld and Pandis: Atmospheric Chemistry and Physics: From Air Pollution to Climate Change, 3rd Edition., Wiley, 1152 pp., 2016.

Seinfeld, J. H., Bretherton, C., Carslaw, K. S., Coe, H., DeMott, P. J., Dunlea, E. J., Feingold, G., Ghan, S., Guenther, A. B., Kahn, R., Kraucunas, I., Kreidenweis, S. M., Molina, M. J., Nenes, A., Penner, J. E., Prather, K. A., Ramanathan, V., Ramaswamy, V., Rasch, P. J., Ravishankara, A. R., Rosenfeld, D., Stephens, G., and Wood, R.: Improving our fundamental understanding of the role of aerosol−cloud interactions in the climate system, Proc. Natl. Acad. Sci., 113, 5781–5790, https://doi.org/10.1073/pnas.1514043113, 2016.

Sellegri, K. and Mallet, M.: Sea Spray Emissions, in: Atmospheric Chemistry in the Mediterranean Region: Volume 2 - From Air Pollutant Sources to Impacts, edited by: Dulac, F., Sauvage, S., and Hamonou, E., Springer International Publishing, Cham, 13–23, https://doi.org/10.1007/978-3-030-82385-6_2, 2022.

Shamjad, P. M., Tripathi, S. N., Thamban, N. M., and Vreeland, H.: Refractive Index and Absorption Attribution of Highly Absorbing Brown Carbon Aerosols from an Urban Indian City-Kanpur, Sci. Rep., 6, 37735, https://doi.org/10.1038/srep37735, 2016.

Shamjad, P. M., Satish, R. V., Thamban, N. M., Rastogi, N., and Tripathi, S. N.: Absorbing Refractive Index and Direct Radiative Forcing of Atmospheric Brown Carbon over Gangetic Plain, ACS Earth Space Chem., 2, 31–37, https://doi.org/10.1021/acsearthspacechem.7b00074, 2018.

Shi, T., Cui, J., Chen, Y., Zhou, Y., Pu, W., Xu, X., Chen, Q., Zhang, X., and Wang, X.: Enhanced light absorption and reduced snow albedo due to internally mixed mineral dust in grains of snow, Atmospheric Chem. Phys., 21, 6035–6051, https://doi.org/10.5194/acp-21-6035-2021, 2021.

Shingler, T., Crosbie, E., Ortega, A., Shiraiwa, M., Zuend, A., Beyersdorf, A., Ziemba, L., Anderson, B., Thornhill, L., Perring, A. E., Schwarz, J. P., Campazano-Jost, P., Day, D. A., Jimenez, J. L., Hair, J. W., Mikoviny, T., Wisthaler, A., and Sorooshian, A.: Airborne characterization of subsaturated aerosol hygroscopicity and dry refractive index from the surface to 6.5 km during the SEAC4RS campaign, J. Geophys. Res. Atmospheres, 121, 4188–4210, https://doi.org/10.1002/2015JD024498, 2016.

Shrivastava, M., Zelenyuk, A., Imre, D., Easter, R., Beranek, J., Zaveri, R. A., and Fast, J.: Implications of low volatility SOA and gas-phase fragmentation reactions on SOA loadings and their spatial and temporal evolution in the atmosphere, J. Geophys. Res. Atmospheres, 118, 3328–3342, https://doi.org/10.1002/jgrd.50160, 2013.

Shrivastava, M., Easter, R. C., Liu, X., Zelenyuk, A., Singh, B., Zhang, K., Ma, P.-L., Chand, D., Ghan, S., Jimenez, J. L., Zhang, Q., Fast, J., Rasch, P. J., and Tiitta, P.: Global transformation and fate of SOA: Implications of low-volatility SOA and gas-phase fragmentation reactions, J. Geophys. Res. Atmospheres, 120, 4169–4195, https://doi.org/10.1002/2014JD022563, 2015.

Shrivastava, M., Andreae, M. O., Artaxo, P., Barbosa, H. M. J., Berg, L. K., Brito, J., Ching, J., Easter, R. C., Fan, J., Fast, J. D., Feng, Z., Fuentes, J. D., Glasius, M., Goldstein, A. H., Alves, E. G., Gomes, H., Gu, D., Guenther, A., Jathar, S. H., Kim, S., Liu, Y., Lou, S., Martin, S. T., McNeill, V. F., Medeiros, A., de Sá, S. S., Shilling, J. E., Springston, S. R., Souza, R. a. F., Thornton, J. A., Isaacman-VanWertz, G., Yee, L. D., Ynoue, R., Zaveri, R. A., Zelenyuk, A., and Zhao, C.: Urban pollution greatly enhances formation of natural aerosols over the Amazon rainforest, Nat. Commun., 10, 1046, https://doi.org/10.1038/s41467-019-08909-4, 2019.

Sindelarova, K., Granier, C., Bouarar, I., Guenther, A., Tilmes, S., Stavrakou, T., Müller, J.-F., Kuhn, U., Stefani, P., and Knorr, W.: Global data set of biogenic VOC emissions calculated by the MEGAN model over the last 30 years, Atmospheric Chem. Phys., 14, 9317–9341, https://doi.org/10.5194/acp-14-9317-2014, 2014.

Sinyuk, A., Holben, B. N., Eck, T. F., Giles, D. M., Slutsker, I., Korkin, S., Schafer, J. S., Smirnov, A., Sorokin, M., and Lyapustin, A.: The AERONET Version 3 aerosol retrieval algorithm, associated uncertainties and comparisons to Version 2, Atmospheric Meas. Tech., 13, 3375–3411, https://doi.org/10.5194/amt-13-3375-2020, 2020.

Skamarock, W., Klemp, J., Dudhia, J., Gill, D., Barker, D., Wang, W., Huang, X.-Y., and Duda, M.: A Description of the Advanced Research WRF Version 3, UCAR/NCAR, https://doi.org/10.5065/D68S4MVH, 2008.

Smirnov, A., Holben, B. N., Eck, T. F., Slutsker, I., Chatenet, B., and Pinker, R. T.: Diurnal variability of aerosol optical depth observed at AERONET (Aerosol Robotic Network) sites, Geophys. Res. Lett., 29, 30-1-30–4, https://doi.org/10.1029/2002GL016305, 2002.

Sokolik, I. N. and Toon, O. B.: Incorporation of mineralogical composition into models of the radiative properties of mineral aerosol from UV to IR wavelengths, J. Geophys. Res. Atmospheres, 104, 9423–9444, https://doi.org/10.1029/1998JD200048, 1999.

Song, J., Xia, X., Che, H., Wang, J., Zhang, X., and Li, X.: Daytime variation of aerosol optical depth in North China and its impact on aerosol direct radiative effects, Atmos. Environ., 182, 31–40, https://doi.org/10.1016/j.atmosenv.2018.03.024, 2018.

Song, Q., Zhang, Z., Yu, H., Kok, J. F., Di Biagio, C., Albani, S., Zheng, J., and Ding, J.: Size-resolved dust direct radiative effect efficiency derived from satellite observations, Atmospheric Chem. Phys., 22, 13115–13135, https://doi.org/10.5194/acp-22-13115-2022, 2022.

Song, S.-K., Choi, Y.-N., Choi, Y., Flynn, J., and Sadeghi, B.: Characteristics of aerosol chemical components and their impacts on direct radiative forcing at urban and suburban locations in Southeast Texas, Atmos. Environ., 246, 118151, https://doi.org/10.1016/j.atmosenv.2020.118151, 2021.

Sorensen, C. M., Yon, J., Liu, F., Maughan, J., Heinson, W. R., and Berg, M. J.: Light scattering and absorption by fractal aggregates including soot, J. Quant. Spectrosc. Radiat. Transf., 217, 459–473, https://doi.org/10.1016/j.jqsrt.2018.05.016, 2018.

Soulie, A., Granier, C., Darras, S., Zilbermann, N., Doumbia, T., Guevara, M., Jalkanen, J.-P., Keita, S., Liousse, C., Crippa, M., Guizzardi, D., Hoesly, R., and Smith, S.: Global Anthropogenic Emissions (CAMS-GLOB-ANT) for the Copernicus Atmosphere Monitoring Service Simulations of Air Quality Forecasts and Reanalyses, Earth Syst. Sci. Data Discuss., 1–45, https://doi.org/10.5194/essd-2023-306, 2023.

Spracklen, D. V., Jimenez, J. L., Carslaw, K. S., Worsnop, D. R., Evans, M. J., Mann, G. W., Zhang, Q., Canagaratna, M. R., Allan, J., Coe, H., McFiggans, G., Rap, A., and Forster, P.: Aerosol mass spectrometer constraint on the global secondary organic aerosol budget, Atmospheric Chem. Phys., 11, 12109–12136, https://doi.org/10.5194/acp-11-12109-2011, 2011.

Srivastava, D., Vu, T. V., Tong, S., Shi, Z., and Harrison, R. M.: Formation of secondary organic aerosols from anthropogenic precursors in laboratory studies, Npj Clim. Atmospheric Sci., 5, 1–30, https://doi.org/10.1038/s41612-022-00238-6, 2022.

Stein, A. F., Draxler, R. R., Rolph, G. D., Stunder, B. J. B., Cohen, M. D., and Ngan, F.: NOAA's HYSPLIT Atmospheric Transport and Dispersion Modeling System, Bull. Am. Meteorol. Soc., 96, 2059–2077, https://doi.org/10.1175/BAMS-D-14-00110.1, 2015.

Stier, P., Schutgens, N. a. J., Bellouin, N., Bian, H., Boucher, O., Chin, M., Ghan, S., Huneeus, N., Kinne, S., Lin, G., Ma, X., Myhre, G., Penner, J. E., Randles, C. A., Samset, B., Schulz, M., Takemura, T., Yu, F., Yu, H., and Zhou, C.: Host model uncertainties in aerosol radiative forcing estimates: results from the AeroCom Prescribed intercomparison study, Atmospheric Chem. Phys., 13, 3245–3270, https://doi.org/10.5194/acp-13-3245-2013, 2013.

Stone, R. S., Augustine, J. A., Dutton, E. G., O'Neill, N. T., and Saha, A.: Empirical determinations of the longwave and shortwave radiative forcing efficiencies of wildfire smoke, J. Geophys. Res. Atmospheres, 116, https://doi.org/10.1029/2010JD015471, 2011.

Stromatas, S., Turquety, S., Menut, L., Chepfer, H., Péré, J. C., Cesana, G., and Bessagnet, B.: Lidar signal simulation for the evaluation of aerosols in chemistry transport models, Geosci. Model Dev., 5, 1543–1564, https://doi.org/10.5194/gmd-5-1543-2012, 2012.

Su, T., Li, Z., Li, C., Li, J., Han, W., Shen, C., Tan, W., Wei, J., and Guo, J.: The significant impact of aerosol vertical structure on lower atmosphere stability and its critical role in aerosol–planetary boundary layer (PBL) interactions, Atmospheric Chem. Phys., 20, 3713–3724, https://doi.org/10.5194/acp-20-3713-2020, 2020.

Su, X., Cao, M., Wang, L., Gui, X., Zhang, M., Huang, Y., and Zhao, Y.: Validation, inter-comparison, and usage recommendation of six latest VIIRS and MODIS aerosol products over the ocean and land on the global and regional scales, Sci. Total Environ., 884, 163794, https://doi.org/10.1016/j.scitotenv.2023.163794, 2023.

Subba, T., Gogoi, M. M., Pathak, B., Bhuyan, P. K., and Babu, S. S.: Recent trend in the global distribution of aerosol direct radiative forcing from satellite measurements, Atmospheric Sci. Lett., 21, e975, https://doi.org/10.1002/asl.975, 2020.

Sun, J., Xie, C., Xu, W., Chen, C., Ma, N., Xu, W., Lei, L., Li, Z., He, Y., Qiu, Y., Wang, Q., Pan, X., Su, H., Cheng, Y., Wu, C., Fu, P., Wang, Z., and Sun, Y.: Light absorption of black carbon and brown carbon in winter in North China Plain: comparisons between urban and rural sites, Sci. Total Environ., 770, 144821, https://doi.org/10.1016/j.scitotenv.2020.144821, 2021.

Sun, Y.-L., Zhang, Q., Schwab, J. J., Demerjian, K. L., Chen, W.-N., Bae, M.-S., Hung, H.-M., Hogrefe, O., Frank, B., Rattigan, O. V., and Lin, Y.-C.: Characterization of the sources and processes of organic and inorganic aerosols in New York city with a high-resolution time-of-flight aerosol mass apectrometer, Atmospheric Chem. Phys., 11, 1581–1602, https://doi.org/10.5194/acp-11-1581-2011, 2011.

Szopa, S., Naik, V., Adhikary, B., Artaxo, P., Berntsen, T., Collins, W. D., Fuzzi, S., Gallardo, L., Kiendler-Scharr, A., Klimont, Z., Liao, H., Unger, N., and Zanis, P.: Short-Lived Climate Forcers, edited by: Masson-Delmotte, V., Zhai, P., Pirani, A., Connors, S. L., Péan, C., Berger, S., Caud, N., Chen, Y., Goldfarb, L., Gomis, M. I., Huang, M., Leitzell, K.,

Lonnoy, E., Matthews, J. B. R., Maycock, T. K., Waterfield, T., Yelekçi, O., Yu, R., and Zhou, B., Clim. Change 2021 Phys. Sci. Basis Contrib. Work. Group Sixth Assess. Rep. Intergov. Panel Clim. Change, 817–922, https://doi.org/10.1017/9781009157896.008, 2021a.

Szopa, S., Naik, V., Adhikary, B., Artaxo, P., Berntsen, T., Collins, W. D., Fuzzi, S., Gallardo, L., Kiendler-Scharr, A., Klimont, Z., Liao, H., Unger, N., and Zanis, P.: Short-Lived Climate Forcers Supplementary Material, edited by: Masson-Delmotte, V., Zhai, P., Pirani, A., Connors, S. L., Péan, C., Berger, S., Caud, N., Chen, Y., Goldfarb, L., Gomis, M. I., Huang, M., Leitzell, K., Lonnoy, E., Matthews, J. B. R., Maycock, T. K., Waterfield, T., Yelekçi, O., Yu, R., and Zhou, B., Clim. Change 2021 Phys. Sci. Basis Contrib. Work. Group Sixth Assess. Rep. Intergov. Panel Clim. Change, 2021b.

Tafuro, A. M., Kinne, S., De Tomasi, F., and Perrone, M. R.: Annual cycle of aerosol direct radiative effect over southeast Italy and sensitivity studies, J. Geophys. Res. Atmospheres, 112, https://doi.org/10.1029/2006JD008265, 2007.

Tao, M., Wang, J., Li, R., Wang, L., Wang, L., Wang, Z., Tao, J., Che, H., and Chen, L.: Performance of MODIS high-resolution MAIAC aerosol algorithm in China: Characterization and limitation, Atmos. Environ., 213, 159–169, https://doi.org/10.1016/j.atmosenv.2019.06.004, 2019.

Tazaki, R., Tanaka, H., Okuzumi, S., Kataoka, A., and Nomura, H.: LIGHT SCATTERING BY FRACTAL DUST AGGREGATES. I. ANGULAR DEPENDENCE OF SCATTERING, Astrophys. J., 823, 70, https://doi.org/10.3847/0004-637X/823/2/70, 2016.

Teri, M., Müller, T., Gasteiger, J., Valentini, S., Horvath, H., Vecchi, R., Bauer, P., Walser, A., and Weinzierl, B.: Impact of particle size, refractive index, and shape on the determination of the particle scattering coefficient – an optical closure study evaluating different nephelometer angular truncation and illumination corrections, Atmospheric Meas. Tech., 15, 3161–3187, https://doi.org/10.5194/amt-15-3161-2022, 2022.

Thomas, G. E., Chalmers, N., Harris, B., Grainger, R. G., and Highwood, E. J.: Regional and monthly and clear-sky aerosol direct radiative effect (and forcing) derived from the GlobAEROSOL-AATSR satellite aerosol product, Atmospheric Chem. Phys., 13, 393–410, https://doi.org/10.5194/acp-13-393-2013, 2013.

Thompson, G., Field, P. R., Rasmussen, R. M., and Hall, W. D.: Explicit Forecasts of Winter Precipitation Using an Improved Bulk Microphysics Scheme. Part II: Implementation of a New Snow Parameterization, Mon. Weather Rev., 136, 5095–5115, https://doi.org/10.1175/2008MWR2387.1, 2008.

Thorsen, T. J., Ferrare, R. A., Kato, S., and Winker, D. M.: Aerosol Direct Radiative Effect Sensitivity Analysis, J. Clim., 33, 6119–6139, https://doi.org/10.1175/JCLI-D-19-0669.1, 2020.

Thorsen, T. J., Winker, D. M., and Ferrare, R. A.: Uncertainty in Observational Estimates of the Aerosol Direct Radiative Effect and Forcing, J. Clim., 34, 195–214, https://doi.org/10.1175/JCLI-D-19-1009.1, 2021.

Tian, P., Yu, Z., Cui, C., Huang, J., Kang, C., Shi, J., Cao, X., and Zhang, L.: Atmospheric aerosol size distribution impacts radiative effects over the Himalayas via modulating aerosol single-scattering albedo, Npj Clim. Atmospheric Sci., 6, 1–9, https://doi.org/10.1038/s41612-023-00368-5, 2023.

Toon, O. B. and Ackerman, T. P.: Algorithms for the calculation of scattering by stratified spheres, Appl. Opt., 20, 3657–3660, https://doi.org/10.1364/AO.20.003657, 1981.

Tozer, B., Sandwell, D. T., Smith, W. H. F., Olson, C., Beale, J. R., and Wessel, P.: Global Bathymetry and Topography at 15 Arc Sec: SRTM15+, Earth Space Sci., 6, 1847–1864, https://doi.org/10.1029/2019EA000658, 2019a.

Tozer, B., Sandwell, D. T., Smith, W. H. F., Olson, C., Beale, J. R., and Wessel, P.: Global bathymetry and topography at 15 arc sec: SRTM15+. Distributed by OpenTopography, , https://doi.org/10.5069/G92R3PT9., 2019b.

Tsyro, S., Mortier, A., Schulz, M., Valdebenito, A., and Benedictow, A.: Wildfires PM episode of 14-23 July 2022, CAMS, 2023.

Tuccella, P., Menut, L., Briant, R., Deroubaix, A., Khvorostyanov, D., Mailler, S., Siour, G., and Turquety, S.: Implementation of Aerosol-Cloud Interaction within WRF-CHIMERE Online Coupled Model: Evaluation and Investigation of the Indirect Radiative Effect from Anthropogenic Emission Reduction on the Benelux Union, Atmosphere, 10, 20, https://doi.org/10.3390/atmos10010020, 2019.

Tuccella, P., Curci, G., Pitari, G., Lee, S., and Jo, D. S.: Direct Radiative Effect of Absorbing Aerosols: Sensitivity to Mixing State, Brown Carbon, and Soil Dust Refractive Index and Shape, J. Geophys. Res. Atmospheres, 125, e2019JD030967, https://doi.org/10.1029/2019JD030967, 2020.

Tuccella, P., Pitari, G., Colaiuda, V., Raparelli, E., and Curci, G.: Present-day radiative effect from radiation-absorbing aerosols in snow, Atmospheric Chem. Phys., 21, 6875–6893, https://doi.org/10.5194/acp-21-6875-2021, 2021.

Turpin, B. J. and Huntzicker, J. J.: Identification of secondary organic aerosol episodes and quantitation of primary and secondary organic aerosol concentrations during SCAQS, Atmos. Environ., 29, 3527–3544, https://doi.org/10.1016/1352-2310(94)00276-Q, 1995.

Updyke, K. M., Nguyen, T. B., and Nizkorodov, S. A.: Formation of brown carbon via reactions of ammonia with secondary organic aerosols from biogenic and anthropogenic precursors, Atmos. Environ., 63, 22–31, https://doi.org/10.1016/j.atmosenv.2012.09.012, 2012.

Usha, K. H., Nair, V. S., and Babu, S. S.: Effects of Aerosol–Induced Snow Albedo Feedback on the Seasonal Snowmelt Over the Himalayan Region, Water Resour. Res., 58, e2021WR030140, https://doi.org/10.1029/2021WR030140, 2022.

Valentini, S., Barnaba, F., Bernardoni, V., Calzolai, G., Costabile, F., Di Liberto, L., Forello, A. C., Gobbi, G. P., Gualtieri, M., Lucarelli, F., Nava, S., Petralia, E., Valli, G., Wiedensohler, A., and Vecchi, R.: Classifying aerosol particles through the combination of optical and physical-chemical properties: Results from a wintertime campaign in Rome (Italy), Atmospheric Res., 235, 104799, https://doi.org/10.1016/j.atmosres.2019.104799, 2020.

Valenzuela, A., Olmo, F. J., Lyamani, H., Antón, M., Titos, G., Cazorla, A., and Alados-Arboledas, L.: Aerosol scattering and absorption Angström exponents as indicators of dust and dust-free days over Granada (Spain), Atmospheric Res., 154, 1–13, https://doi.org/10.1016/j.atmosres.2014.10.015, 2015.

Vautard, R., Beekmann, M., Roux, J., and Gombert, D.: Validation of a hybrid forecasting system for the ozone concentrations over the Paris area, Atmos. Environ., 35, 2449–2461, https://doi.org/10.1016/S1352-2310(00)00466-0, 2001.

Veefkind, J. P., Aben, I., McMullan, K., Förster, H., de Vries, J., Otter, G., Claas, J., Eskes, H. J., de Haan, J. F., Kleipool, Q., van Weele, M., Hasekamp, O., Hoogeveen, R., Landgraf, J., Snel, R., Tol, P., Ingmann, P., Voors, R., Kruizinga, B., Vink, R., Visser, H., and Levelt, P. F.: TROPOMI on the ESA Sentinel-5 Precursor: A GMES mission for global observations of the atmospheric composition for climate, air quality and ozone layer applications, Remote Sens. Environ., 120, 70–83, https://doi.org/10.1016/j.rse.2011.09.027, 2012.

Viana, M., Pey, J., Querol, X., Alastuey, A., de Leeuw, F., and Lükewille, A.: Natural sources of atmospheric aerosols influencing air quality across Europe, Sci. Total Environ., 472, 825–833, https://doi.org/10.1016/j.scitotenv.2013.11.140, 2014.

Volkamer, R., Jimenez, J. L., San Martini, F., Dzepina, K., Zhang, Q., Salcedo, D., Molina, L. T., Worsnop, D. R., and Molina, M. J.: Secondary organic aerosol formation from anthropogenic air pollution: Rapid and higher than expected, Geophys. Res. Lett., 33, https://doi.org/10.1029/2006GL026899, 2006.

Vratolis, S., Fetfatzis, P., Argyrouli, A., Papayannis, A., Müller, D., Veselovskii, I., Bougiatioti, A., Nenes, A., Remoundaki, E., Diapouli, E., Manousakas, M., Mylonaki, M., and Eleftheriadis, K.: A new method to retrieve the real part of the equivalent refractive index of atmospheric aerosols, J. Aerosol Sci., 117, 54–62, https://doi.org/10.1016/j.jaerosci.2017.12.013, 2018.

Wang, R., Balkanski, Y., Boucher, O., Ciais, P., Schuster, G. L., Chevallier, F., Samset, B. H., Liu, J., Piao, S., Valari, M., and Tao, S.: Estimation of global black carbon direct radiative forcing and its uncertainty constrained by observations, J. Geophys. Res. Atmospheres, 121, 5948–5971, https://doi.org/10.1002/2015JD024326, 2016.

Wang, X., Heald, C. L., Ridley, D. A., Schwarz, J. P., Spackman, J. R., Perring, A. E., Coe, H., Liu, D., and Clarke, A. D.: Exploiting simultaneous observational constraints on mass and absorption to estimate the global direct radiative forcing of black carbon and brown carbon, Atmospheric Chem. Phys., 14, 10989–11010, https://doi.org/10.5194/acp-14-10989-2014, 2014.

Wang, X., Heald, C. L., Liu, J., Weber, R. J., Campuzano-Jost, P., Jimenez, J. L., Schwarz, J. P., and Perring, A. E.: Exploring the observational constraints on the simulation of brown carbon, Atmospheric Chem. Phys., 18, 635–653, https://doi.org/10.5194/acp-18-635-2018, 2018.

Wang, Y., Lyapustin, A. I., Privette, J. L., Cook, R. B., SanthanaVannan, S. K., Vermote, E. F., and Schaaf, C. L.: Assessment of biases in MODIS surface reflectance due to Lambertian approximation, Remote Sens. Environ., 114, 2791–2801, https://doi.org/10.1016/j.rse.2010.06.013, 2010.

Ward, D. S., Kloster, S., Mahowald, N. M., Rogers, B. M., Randerson, J. T., and Hess, P. G.: The changing radiative forcing of fires: global model estimates for past, present and future, Atmospheric Chem. Phys., 12, 10857–10886, https://doi.org/10.5194/acp-12-10857-2012, 2012.

Weihs, P., Laimighofer, J., Formayer, H., and Olefs, M.: Influence of snow making on albedo and local radiative forcing in an alpine area, Atmospheric Res., 255, 105448, https://doi.org/10.1016/j.atmosres.2020.105448, 2021.

Weingartner, E., Saathoff, H., Schnaiter, M., Streit, N., Bitnar, B., and Baltensperger, U.: Absorption of light by soot particles: determination of the absorption coefficient by means of aethalometers, J. Aerosol Sci., 34, 1445–1463, https://doi.org/10.1016/S0021-8502(03)00359-8, 2003.

WHO, W. H. O.: WHO Air quality guidelines for particulate matter, ozone, nitrogen dioxide and sulfur dioxide : global update 2005 : summary of risk assessment, , WHO/SDE/PHE/OEH/06.02, 2006.

Willis, P. T. and Tattelman, P.: Drop-Size Distributions Associated with Intense Rainfall, J. Appl. Meteorol. Climatol., 28, 3–15, https://doi.org/10.1175/1520-0450(1989)028<0003:DSDAWI>2.0.CO;2, 1989.

Wu, X., Balmes, K. A., and Fu, Q.: Aerosol Direct Radiative Effects at the ARM SGP and TWP Sites: Clear Skies, J. Geophys. Res. Atmospheres, 126, e2020JD033663, https://doi.org/10.1029/2020JD033663, 2021.

Wu, Y., Cheng, T., Zheng, L., and Chen, H.: Black carbon radiative forcing at TOA decreased during aging, Sci. Rep., 6, 38592, https://doi.org/10.1038/srep38592, 2016.

Xia, C., Sun, J., Hu, X., Shen, X., Zhang, Y., Zhang, S., Wang, J., Liu, Q., Lu, J., Liu, S., and Zhang, X.: Effects of hygroscopicity on aerosol optical properties and direct radiative forcing in Beijing: Based on two-year observations, Sci. Total Environ., 857, 159233, https://doi.org/10.1016/j.scitotenv.2022.159233, 2023.

Xie, C., Xu, W., Wang, J., Liu, D., Ge, X., Zhang, Q., Wang, Q., Du, W., Zhao, J., Zhou, W., Li, J., Fu, P., Wang, Z., Worsnop, D., and Sun, Y.: Light absorption enhancement of black carbon in urban Beijing in summer, Atmos. Environ., 213, 499–504, https://doi.org/10.1016/j.atmosenv.2019.06.041, 2019.

Xiong, R., Li, J., Zhang, Y., Zhang, L., Jiang, K., Zheng, H., Kong, S., Shen, H., Cheng, H., Shen, G., and Tao, S.: Global brown carbon emissions from combustion sources, Environ. Sci. Ecotechnology, 12, 100201, https://doi.org/10.1016/j.ese.2022.100201, 2022.

Xu, L., Fukushima, S., Sobanska, S., Murata, K., Naganuma, A., Liu, L., Wang, Y., Niu, H., Shi, Z., Kojima, T., Zhang, D., and Li, W.: Tracing the evolution of morphology and mixing state of soot particles along with the movement of an Asian dust storm, Atmospheric Chem. Phys., 20, 14321–14332, https://doi.org/10.5194/acp-20-14321-2020, 2020.

Yamasoe, M. A., Kaufman, Y. J., Dubovik, O., Remer, L. A., Holben, B. N., and Artaxo, P.: Retrieval of the real part of the refractive index of smoke particles from Sun/sky measurements during SCAR-B, J. Geophys. Res. Atmospheres, 103, 31893–31902, https://doi.org/10.1029/98JD01211, 1998.

Yang, Z., Tsona, N. T., George, C., and Du, L.: Nitrogen-Containing Compounds Enhance Light Absorption of Aromatic-Derived Brown Carbon, Environ. Sci. Technol., 56, 4005–4016, https://doi.org/10.1021/acs.est.1c08794, 2022.

Yao, Y., Curtis, J. H., Ching, J., Zheng, Z., and Riemer, N.: Quantifying the effects of mixing state on aerosol optical properties, Atmospheric Chem. Phys., 22, 9265–9282, https://doi.org/10.5194/acp-22-9265-2022, 2022.

Yin, C., Wang, T., Solmon, F., Mallet, M., Jiang, F., Li, S., and Zhuang, B.: Assessment of direct radiative forcing due to secondary organic aerosol over China with a regional climate model, Tellus B Chem. Phys. Meteorol., 67, 24634, https://doi.org/10.3402/tellusb.v67.24634, 2015.

Yli-Juuti, T., Mielonen, T., Heikkinen, L., Arola, A., Ehn, M., Isokääntä, S., Keskinen, H.-M., Kulmala, M., Laakso, A., Lipponen, A., Luoma, K., Mikkonen, S., Nieminen, T., Paasonen, P., Petäjä, T., Romakkaniemi, S., Tonttila, J., Kokkola, H., and Virtanen, A.: Significance of the organic aerosol driven climate feedback in the boreal area, Nat. Commun., 12, 5637, https://doi.org/10.1038/s41467-021-25850-7, 2021.

Yu, C. and Formenti, P.: ACROSS_LISA_RambForest_SP2_rBC_0220614_20220722, https://doi.org/10.25326/527, 2023.

Yu, H., Kaufman, Y. J., Chin, M., Feingold, G., Remer, L. A., Anderson, T. L., Balkanski, Y., Bellouin, N., Boucher, O., Christopher, S., DeCola, P., Kahn, R., Koch, D., Loeb, N., Reddy, M. S., Schulz, M., Takemura, T., and Zhou, M.: A review of measurement-based assessments of the aerosol direct radiative effect and forcing, Atmospheric Chem. Phys., 6, 613–666, https://doi.org/10.5194/acp-6-613-2006, 2006.

Yu, Q. and Huang, Y.: Distributions and Trends of the Aerosol Direct Radiative Effect in the 21st Century: Aerosol and Environmental Contributions, J. Geophys. Res. Atmospheres, 128, e2022JD037716, https://doi.org/10.1029/2022JD037716, 2023.

Yuan, H., Dai, Y., Xiao, Z., Ji, D., and Shangguan, W.: Reprocessing the MODIS Leaf Area Index products for land surface and climate modelling, Remote Sens. Environ., 115, 1171–1187, https://doi.org/10.1016/j.rse.2011.01.001, 2011.

Yus-Díez, J., Bernardoni, V., Močnik, G., Alastuey, A., Ciniglia, D., Ivančič, M., Querol, X., Perez, N., Reche, C., Rigler, M., Vecchi, R., Valentini, S., and Pandolfi, M.: Determination of the multiple-scattering correction factor and its cross-sensitivity to scattering and wavelength dependence for different AE33 Aethalometer filter tapes: a multi-instrumental approach, Atmospheric Meas. Tech., 14, 6335–6355, https://doi.org/10.5194/amt-14-6335-2021, 2021.

Zeng, L., Zhang, A., Wang, Y., Wagner, N. L., Katich, J. M., Schwarz, J. P., Schill, G. P., Brock, C., Froyd, K. D., Murphy, D. M., Williamson, C. J., Kupc, A., Scheuer, E., Dibb, J., and Weber, R. J.: Global Measurements of Brown Carbon and Estimated Direct Radiative Effects, Geophys. Res. Lett., 47, e2020GL088747, https://doi.org/10.1029/2020GL088747, 2020.

Zhang, A., Wang, Y., Zhang, Y., Weber, R. J., Song, Y., Ke, Z., and Zou, Y.: Modeling the global radiative effect of brown carbon: a potentially larger heating source in the tropical free troposphere than black carbon, Atmospheric Chem. Phys., 20, 1901–1920, https://doi.org/10.5194/acp-20-1901-2020, 2020.

Zhang, G., Bi, X., Qiu, N., Han, B., Lin, Q., Peng, L., Chen, D., Wang, X., Peng, P., Sheng, G., and Zhou, Z.: The real part of the refractive indices and effective densities for chemically segregated ambient aerosols in Guangzhou measured by a single-particle aerosol mass spectrometer, Atmospheric Chem. Phys., 16, 2631–2640, https://doi.org/10.5194/acp-16-2631-2016, 2016.

Zhang, H., Li, L., Song, J., Akhter, Z. H., and Zhang, J.: Understanding aerosol–climate–ecosystem interactions and the implications for terrestrial carbon sink using the Community Earth System Model, Agric. For. Meteorol., 340, 109625, https://doi.org/10.1016/j.agrformet.2023.109625, 2023.

Zhang, L., Gong, S., Padro, J., and Barrie, L.: A size-segregated particle dry deposition scheme for an atmospheric aerosol module, Atmos. Environ., 35, 549–560, https://doi.org/10.1016/S1352-2310(00)00326-5, 2001.

Zhang, L., Li, J., Jiang, Z., Dong, Y., Ying, T., and Zhang, Z.: Clear-Sky Direct Aerosol Radiative Forcing Uncertainty Associated with Aerosol Optical Properties Based on CMIP6 Models, J. Clim., 35, 3007–3019, https://doi.org/10.1175/JCLI-D-21-0479.1, 2022.

Zhang, M., Wang, L., Gong, W., Ma, Y., and Liu, B.: Aerosol Optical Properties and Direct Radiative Effects over Central China, Remote Sens., 9, 997, https://doi.org/10.3390/rs9100997, 2017.

Zhang, Q., Jimenez, J. L., Canagaratna, M. R., Allan, J. D., Coe, H., Ulbrich, I., Alfarra, M. R., Takami, A., Middlebrook, A. M., Sun, Y. L., Dzepina, K., Dunlea, E., Docherty, K., DeCarlo, P. F., Salcedo, D., Onasch, T., Jayne, J. T., Miyoshi, T., Shimono, A., Hatakeyama, S., Takegawa, N., Kondo, Y., Schneider, J., Drewnick, F., Borrmann, S., Weimer, S., Demerjian, K., Williams, P., Bower, K., Bahreini, R., Cottrell, L., Griffin, R. J., Rautiainen, J., Sun, J. Y., Zhang, Y. M., and Worsnop, D. R.: Ubiquity and dominance of oxygenated species in organic aerosols in anthropogenically-influenced Northern Hemisphere midlatitudes, Geophys. Res. Lett., 34, https://doi.org/10.1029/2007GL029979, 2007.

Zhang, T., Shen, Z. X., Su, H., Liu, S. X., Zhou, J. M., Zhao, Z. Z., Wang, Q. Y., Prévôt, A. S. H., and Cao, J. J.: Effects of Aerosol Water Content on the formation of secondary inorganic aerosol during a Winter Heavy PM2.5 Pollution Episode in Xi'an, China, Atmos. Environ., 252, 118304, https://doi.org/10.1016/j.atmosenv.2021.118304, 2021a.

Zhang, X., Huang, Y., Rao, R., and Wang, Z.: Retrieval of effective complex refractive index from intensive measurements of characteristics of ambient aerosols in the boundary layer, Opt. Express, 21, 17849–17862, https://doi.org/10.1364/OE.21.017849, 2013.

Zhang, X., Jiang, H., and Mao, M.: Absorption Angstrom Exponent of Dust Aerosols Over the Tarim Basin, Pure Appl. Geophys., 178, 4549–4560, https://doi.org/10.1007/s00024-021-02874-0, 2021b.

Zhang, Y., Favez, O., Canonaco, F., Liu, D., Močnik, G., Amodeo, T., Sciare, J., Prévôt, A. S. H., Gros, V., and Albinet, A.: Evidence of major secondary organic aerosol contribution to lensing effect black carbon absorption enhancement, Npj Clim. Atmospheric Sci., 1, 1–8, https://doi.org/10.1038/s41612-018-0056-2, 2018.

Zhang, Y., Favez, O., Petit, J.-E., Canonaco, F., Truong, F., Bonnaire, N., Crenn, V., Amodeo, T., Prévôt, A. S. H., Sciare, J., Gros, V., and Albinet, A.: Six-year source apportionment of submicron organic aerosols from near-continuous highly time-resolved measurements at SIRTA (Paris area, France), Atmospheric Chem. Phys., 19, 14755–14776, https://doi.org/10.5194/acp-19-14755-2019, 2019.

Zhao, G., Li, F., and Zhao, C.: Determination of the refractive index of ambient aerosols, Atmos. Environ., 240, 117800, https://doi.org/10.1016/j.atmosenv.2020.117800, 2020a.

Zhao, G., Shen, C., and Zhao, C.: Technical note: Mismeasurement of the core-shell structure of black carbon-containing ambient aerosols by SP2 measurements, Atmos. Environ., 243, 117885, https://doi.org/10.1016/j.atmosenv.2020.117885, 2020b.

Zheng, Y., Horowitz, L. W., Menzel, R., Paynter, D. J., Naik, V., Li, J., and Mao, J.: Anthropogenic amplification of biogenic secondary organic aerosol production, Atmospheric Chem. Phys., 23, 8993–9007, https://doi.org/10.5194/acp-23-8993-2023, 2023.

Zhou, C., Zhang, H., Zhao, S., and Li, J.: On Effective Radiative Forcing of Partial Internally and Externally Mixed Aerosols and Their Effects on Global Climate, J. Geophys. Res. Atmospheres, 123, 401–423, https://doi.org/10.1002/2017JD027603, 2018.

Zhuravleva, T. B., Nasrtdinov, I. M., and Vinogradova, A. A.: Direct Radiative Effects of Smoke Aerosol in the Region of Tiksi Station (Russian Arctic): Preliminary Results, Atmospheric Ocean. Opt., 32, 296–305, https://doi.org/10.1134/S1024856019030187, 2019.

Ziemann, P. J. and Atkinson, R.: Kinetics, products, and mechanisms of secondary organic aerosol formation, Chem. Soc. Rev., 41, 6582–6605, https://doi.org/10.1039/C2CS35122F, 2012.

List of Figures

List of Tables

Résumé

Les aérosols atmosphériques sont l'une des composantes clés du système climatique et sont également des acteurs majeurs de la pollution atmosphérique. L'interaction entre les aérosols et le rayonnement solaire et infrarouge (l'Effet Radiatif Direct, ERD) reste l'une des principales incertitudes dans la compréhension du système climatique à l'échelle régionale et globale. Le dernier rapport du Groupe d'experts intergouvernemental sur l'évolution du climat (GIEC) atteste que l'Interaction Aérosols-Rayonnement (IAR) représente un forçage effectif global négatif moyen de -0.22±0.25 Wm-2 qui s'oppose et contrebalance une fraction du forçage radiatif direct positif des gaz à effet de serre. À ce jour, l'estimation de l'intensité et du signe de l'ERD des aérosols reste très incertain, en particulier à l'échelle régionale et lorsque des aérosols d'origine et de type différents se mélangent. Ceci est particulièrement le cas pour les environnements mixtes anthropogéniques et biogéniques, tels que les flux sortants des grandes agglomérations urbaines. La façon dont les composants anthropogéniques et biogéniques interagissent et affectent les propriétés des aérosols et l'ERD est une question majeure et ouverte, pour laquelle les connaissances scientifiques sont encore faibles.

L'objectif de cette thèse est de mettre en œuvre une approche synergique de mesure et de modélisation afin d'atteindre deux objectifs principaux: i) mieux comprendre les propriétés optiques spectrales des aérosols (épaisseur optique des aérosols, albédo de diffusion simple et indice de réfraction complexe) à l'échelle régionale où se produit le mélange entre les aérosols anthropogéniques et biogéniques, et évaluer leur variabilité temporelle et spatiale dans des conditions variables ; ii) produire une estimation robuste de l'effet radiatif direct des aérosols et étudier la dépendance de l'ERD à l'état de mélange des aérosols et à la contribution des différentes espèces d'aérosols. Le cadre d'application de cette étude est l'Ile-de-France, une zone très peuplée d'Europe théâtre de l'interaction entre les émissions anthropiques de l'agglomération métropolitaine Parisienne et biogéniques des zones forestières limitrophes.

La stratégie de ce travail se base sur la combinaison des observations de la campagne internationale ACROSS (Atmospheric ChemistRy Of the Suburban ForeSt) et des observations des bases de données existantes au sol et par satellite, avec les simulations du modèle de chimie-transport 3-D WRF-CHIMERE, permettant une évaluation la plus complète possible de la masse d'aérosol simulée, de la composition chimique et des propriétés optiques spectrales, qui sont des paramètres clés pour l'estimation de l'ERD.

Mot-clé : aérosols, interaction aérosol-rayonnement, iar, effet radiatif direct, mesure, modélisation, synergie, propriétés optiques spectrales, indice de réfraction complexe, albédo de diffusion simple, ACROSS, campagne de terrain, modèle de chimie-transport, WRF, CHIMERE

Abstract

Atmospheric aerosols are one of the key components of the climate system and also major contributors to air pollution. One of the most significant uncertainties in the understanding of the climate system at both regional and global scales is the interaction between aerosols and solar and infrared radiation (the Direct Radiative Effect, DRE). The latest Intergovernmental Panel on Climate Change (IPCC) report attests that the aerosol Aerosol-Radiation Interaction (ARI) represents an average negative global effective forcing of -0.22±0.25 Wm-2, which opposes and counteracts a fraction of the positive direct radiative forcing by greenhouse gases. At present, there is still large uncertainty in estimating the magnitude and sign of the aerosol DRE, in particular at the regional scale, where aerosol of different origin and types mix. This is particularly the case for the mixed anthropogenic-biogenic environments, such as in the outflow of big urban agglomerations. How the anthropogenic and biogenic components interact and affect aerosol properties and DRE is an open and relevant question, for which scientific knowledge is still low.

The objective of this thesis work is to apply a synergistic measurement-modelling approach in order to achieve two main objectives: i) get more deeper understanding of the aerosol spectral optical properties (aerosol optical depth, single scattering albedo and complex refractive index) at the regional scale where the mixing between anthropogenic and biogenic aerosols occurs and evaluate their temporal and spatial variability under varying conditions; ii) produce a robust direct radiative effect estimate in the region and investigate the DRE dependency on the aerosol mixing state and the contribution of the different aerosol species.

This thesis focuses on the Ile-de-France region, a densely populated area in central Europe affected by the interaction between anthropogenic emissions from the Paris metropolitan area and biogenic emissions from surrounding forested areas. The strategy of this work is based on the combination of field campaign observations from the international ACROSS (Atmospheric ChemistRy Of the Suburban ForeSt) campaign and observations from ground-based and remote sensing existing databases with the WRF-CHIMERE 3-D chemistry transport model (CTM), allowing for a comprehensive evaluation of the simulated aerosol loading, chemical composition and spectral optical properties, which are key parameters to drive the DRE estimation.

Keywords: aerosols, aerosol-radiation interaction, ari, direct radiative effect, measurement, modelling, synergy, spectral optical properties, complex refractive index, single scattering albedo, ACROSS, field campaign, CTM, WRF, CHIMERE